Proceedings Book of 16th International Foundrymen Conference: Global Foundry Industries – Perspectives for the Future

University of Zagreb
Faculty of Metallurgy
Sisak, Croatia

University of Ljubljana
Faculty of Natural Sciences and Engineering
Ljubljana, Slovenia

University North
Koprivnica, Croatia

ELKEM AS
Norway

PROCEEDINGS BOOK

16th INTERNATIONAL FOUNDRYMEN CONFERENCE

Global Foundry Industry – Perspectives for the Future

Opatija, May 15th – 17th 2017

PREFACE

Foundry industry as a base branch represents an important factor contributing to the economic potential of each country. Current market development as well as technical and economic objective, the production of high-quality, low-cost and environmentally friendly casting, requires application of recent and advanced materials, as well as production technologies, followed and supported by understanding of production process.

The forecast for 2020 for global foundry industry indicated in *Foundry Industry 2020: Trends and Challenges* (IKB Deutsche Industriebank AG, GIFA, 2015, Düsseldorf, DE) is a rising global production of grey, ductile and steel casting to nearly 96 million tons and aluminium to 17 million tons till 2020. The profitability of foundries tend to decrease due to increasing pricing pressure of the leading customer industry - vehicle manufacturing. Overcapacities still exist in individual sub-segments, e.g. construction – related casting applications or castings for wind turbine components, especially for offshore plants. In addition, energy costs significantly burden foundries. There is an ongoing consolidation process in the global foundry industry due to pressure for globalization, and increasing of investment requirements. Report also indicates strategic challenges as follows:

Globalization	• Major part of the demand growth will occur in emerging markets • Especially the automotive industry is increasingly demanding local presence outside of Europe • Increases the need for a global footprint
Technological leadership	• Maintaining the technological leadership is of great importance for European foundries • Pressure on unit weights will continue • This changes the material mix and increases the requirements for the alloy competence
Retain qualified personnel	• Many qualified foundry workers will retire during the next years • Competition for staff intensifies due to changing age structure • Requires new worker loyalty programs (pension schemes, profit-sharing, flexibility regarding family & job)
Investment requirements	• Growing trend towards completely finished cast parts will necessitate respective investments • Complexity of foundry materials will grow and consequently drive investment requirements • Globalizing market requires increased investments in logistics processes
Margin pressure	• Growing international competition in the vehicle manufacturing industry • This limits the possibility of passing on cost increases to end consumers • On the part of OEMs this pressure could be passed through to suppliers
Industry consolidation	• Thus the industry consolidation is expected to continue • Main reasons, besides the pressure for globalization, are increasing investment requirements • Also, many family businesses face succession-related problems from our point of view

Source: IKB Deutsche Industriebank AG, https://www.heat-processing.com/fileadmin/HPO/Dateien_Redaktion/Selected_Reports/150616_GIFA_Presentation_EN.pdf

The World Economic Forum indicates five directions for measuring the Global Competitiveness Index (GCI) of particular country in *The Global Competitiveness Report 2016-2017* as follows:

1. Productivity remains a key driver of prosperity. Prosperity can increase if inputs of production are used in smarter and more efficient ways to fulfill constantly evolving human demands.
2. Future orientation is central. The primary feature of successful economies will be their capacity to be agile, adapt to changes, and respond to shocks relatively smoothly and speedily. These aspects are meant to be captured by the education and skills, labour market, and goods market pillars that measure the extent to which a country's regulations and human capital support structural change and industrial revamp.
3. Innovation – The capacity of a country to be innovative is an ecosystem which produces scientific knowledge but also enables all industries, service sector and society at large to be

more flexible, interconnected, and open to new ideas and business models. To be truly innovative, a country should not only file patents and support research and development in science and technology, but should also provide a networking and connecting environment that promotes creativity and entrepreneurship, fosters collaboration, and rewards individuals who are open-minded and embrace new ways to perform tasks. In such an ecosystem the modernization of the educational framework also plays a pivotal role: it must offer life-long learning opportunities and teach students to think critically, collaborate with individuals of different backgrounds, and expose them to different points of view and ideas.

4. ICT infrastructure is an imperative. As ICT-based business models become more prevalent, countries that fail to transition to a digital economy will be at a substantial competitive disadvantage, not only commercially but also in terms of innovation. Hence the technology adoption, business agility, and innovation capacity pillars have been reformed, considering them to be all part of the innovation ecosystem. ICT infrastructure measures have also been added to the infrastructure pillar as they now play a prerequisite role for development as much as transport infrastructure.

5. The Fourth Industrial Revolution recognizes that all competitiveness factors matter for countries at all income levels and the exercise of policy prioritization is more complex.

The updated GCI is based on 12 pillars weight. An example for Croatia has been indicated as follows:
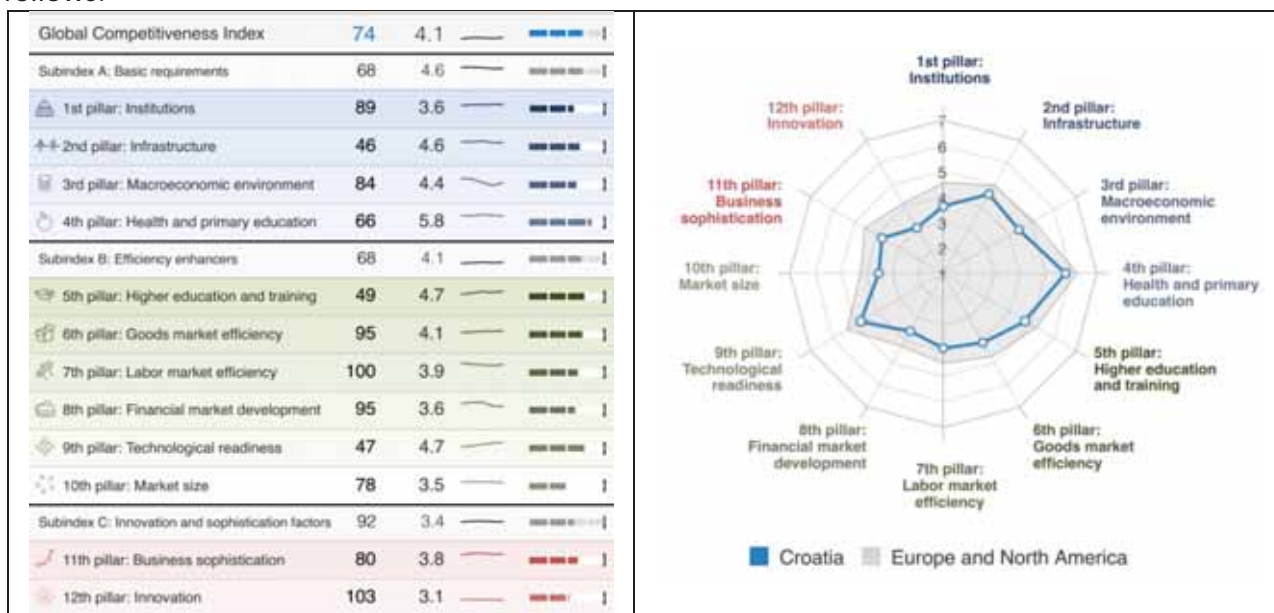
Most problematic factors for doing business
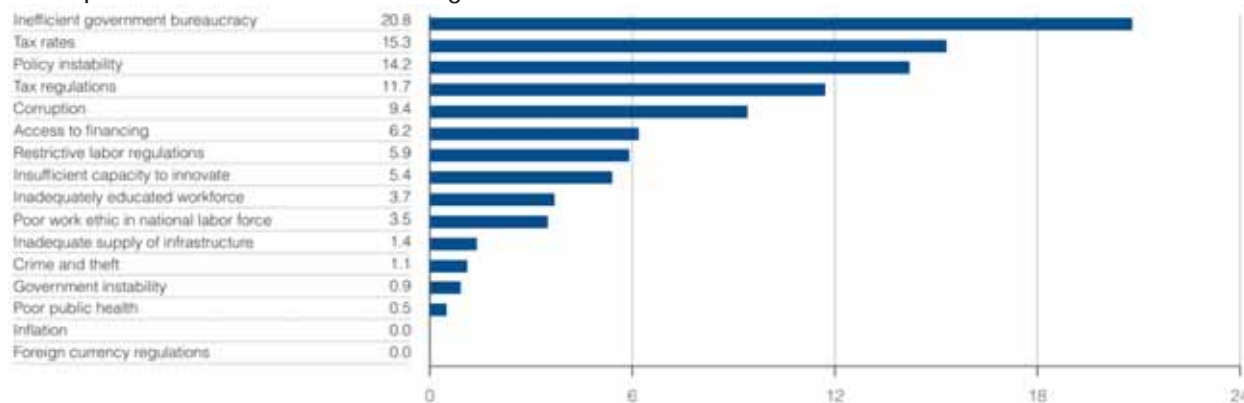
Source: World Economic Forum, http://www3.weforum.org/docs/GCR2016-2017/05FullReport/TheGlobalCompetitivenessReport2016-2017_FINAL.pdf

Within the industrial production of castings special significance is dedicated to the development of products based on innovative research activities. The Conference topics were designed as presentations of the current "state of the art" research in collaboration with industry, and production innovation with the aim to improve the competitiveness.

The scope of *16th International Foundrymen Conference (IFC)* covers scientific, technological and practical aspects concerning research, development and application of casting technology with the common perspective – increase of competitiveness. Special attention will be focused towards the competitiveness ability of foundries, improvement of materials features and casting technologies, environmental protection as well as subjects connected to the application of castings.

During this Conference 31 paper will be presented. Book of Abstracts of the 16th International Foundrymen Conference includes summaries of the papers. The Proceedings book consists of papers *in extenso* published in electronic format (CD). Full length papers have undergone the international review procedure, done by eminent experts from corresponding fields, but have not undergone linguistic proof reading. Sequence of papers in Proceedings book has been done by category of papers in following order: plenary lectures, invited lectures, oral and poster presentation, and inside the category alphabetically by the first author's surname.

This occasion represents the opportunity to discuss and increase the mutual collaboration between HEIs' and industry with the aim of information exchange related to advanced experience in foundry processes and technologies, gaining the new experience in presentation and / or teaching process within lifelong learning process.

The organizers of the Conference would like to thank all participants, reviewers, sponsors, auspices, media coverage and all those who have contributed to this Conference in any way.

President of Organizing Board

Assoc.Prof. Zdenka Zovko Brodarac, PhD

THE HEAD OF ORIENTAL GOD (ATIS?)
bronza
2nd century AD
SISCIA (modern Sisak, Croatia)

ILLYRIAN HELMET
iron
6th century BC

UNDER THE PATRONAGE

Ministry of Science, Education of Republic of Croatia
University of Zagreb
Croatian Foundry Association
AD KLASTER
Mittel Europäische Giesserei Initiative (MEGI)
Chamber of Commerce of Republic of Croatia
Sisak – Moslavina County
City of Sisak

SPONSORED BY

GOLDEN SPONSOR

COMET d.o.o., Novi Marof (HR) & SWATYCOMET d.o.o., Maribor (SI)
NETZSCH GmbH, Graz (AT) & ASOLUTIC d.o.o., Zagreb (HR)
MIKROLUX d.o.o., Zaprešić (HR)

SILVER SPONSOR

ANALYSIS d.o.o., Beograd (RS)
HAGI GmbH, Pyhra (AT)
LABTIM ADRIA d.o.o., Sesvete (HR)

BRONZE SPONSOR

BENTOPRODUCT d.o.o., Šipovo (BiH)
BITUS d.o.o., Zagreb (HR)
EDC d.o.o., Zagreb (HR)
EKW – KREMEN d.o.o., Šentjerej (SI)
IDEF d.o.o., Zagreb (HR)
INDUCTOTHERM EUROPE Ltd, Worcestershire (GB)
ISTRABENZ PLINI d.o.o., Bakar (HR)
KONTROLTEST INTERNATIONAL d.o.o., Zagreb (HR)
MECAS ESI s.r.o., Plzen (CZ) & TC LIVARSTVO d.o.o., Ljubljana (SI)
TOPOMATIKA d.o.o., Zagreb (HR)
WERNER METAL – Export Import d.o.o., Zlatar Bistrica (HR)

MEDIA COVER

IRT 3000
Foundry Planet
Foundry Lexicon

SUPPORTING ASSOCIATION AND COMPANIES

Croatian Foundry Association
Slovenian Foundry Association
FerroČrtalič d.o.o., Dolenjske Toplice (SI)

ORGANIZING COMMITTEE

Zdenka Zovko Brodarac
Ladislav Lazić
Primož Mrvar
Jožef Medved
Marin Milković
Mario Tomiša
Anita Begić Hadžipašić
Natalija Dolić
Stjepan Kožuh
Gordana Gojsević Marić

PROGRAM COMMITTEE

Željko Alar (HR)	Zoran Kožuh (HR)
Hasan Avdušinović (BiH)	Milisav Lalović (ME)
Branko Bauer (HR)	Ladislav Lazić (HR)
Anita Begić Hadžipašić (HR)	Martina Lovrenić – Jugović (HR)
Ana Beroš (BiH)	Srećko Manasijević (RS)
Ivan Budić (HR) †	Srđan Marković (RS)
Ivica Buljeta (BiH)	Jožef Medved (SI)
Jaka Burja (SI)	Daniel Novoselović (HR)
Franjo Cajner (HR)	Mitja Petrič (SI)
Peter Cvahte (SI)	Bojan Podgornik (SI)
Lidija Ćurković (HR)	Žarko Radović (ME)
Mile Djurdjević (AT)	Karlo T. Raić (RS)
Natalija Dolić (HR)	Vera Rede (HR)
Regina Fuchs – Godec (SI)	Milenko Rimac (BiH)
Matjaž Godec (SI)	Zdravko Schauperl (HR)
Mirko Gojić (HR)	Ljerka Slokar (HR)
Dario Iljkić (HR)	Božo Smoljan (HR)
Željko Kamberović (RS)	Tahir Sofilić (HR)
Sebastjan Kastelic (SI)	Davor Stanić (HR)
Varužan Kevorkijan (SI)	Iveta Vaskova (SK)
Ivica Kladarić (HR)	Maja Vončina (SI)
Borut Kosec (SI)	Franc Zupanič (SI)
Dražan Kozak (HR)	Zdenka Zovko Brodarac (HR)
Stjepan Kožuh (HR)	Dragana Živković (RS) †

REVIEW COMMITTEE

Vesna Alar (HR)

Sandra Babić (HR)

Branko Bauer (HR)

Anita Begić Hadžipašić (HR)

Ana Beroš (BiH)

Ivan Brnardić (HR)

Natalija Dolić (HR)

Regina Fuchs-Godec (SI)

Tomislav Galeta (HR)

Mirko Gojić (HR)

Tamara Holjevac Grgurić (HR)

Dario Iljkić (HR)

Ivan Jandrlić (HR)

Sebastjan Kastelic (SI)

Varužan Kevorkijan (SI)

Ivica Kladarić (HR)

Borut Kosec (SI)

Stjepan Kožuh (HR)

Ladislav Lazić (HR)

Martina Lovrenić-Jugović (HR)

Ivana Marković (RS)

Srećko Manasijević (RS)

Daniel Novoselović (HR)

Mitja Petrič (SI)

Milena Premović (RS)

Žarko Radović (ME)

Stoja Rešković (HR)

Zdravko Schauperl (HR)

Tahir Sofilić (HR)

Davor Stanić (HR)

Juraj Šipušić (HR)

Iveta Vaskova (SK)

Darja Volšak (SI)

Maja Vončina (SI)

Zdenka Zovko Brodarac (HR)

CONTENTS

THE GLOBAL CASTINGS INDUSTRY

Mark Fenyes[1], Andrew Turner[2]

[1]Chairman - Omega Foundry Machinery and Vice President of the
World Foundry Organization, United Kingdom
[2]General Secretary of the World Foundry Organization, United Kingdom

<u>**Plenary lecture**</u>
<u>*Subject review*</u>

Abstract

The Paper discusses the state of the global castings industry and contrasts the production in the leading countries of the world, in addition it highlights some of the current socio-economic trends that are affecting the industry and how the World Foundry Organization is working with the international associations and global industry to identify and assist with issues affecting everyone.

Keywords: *training, statistics, support*

*Corresponding author (e-mail address): markf@ofml.net

THE GLOBAL CASTINGS INDUSTRY

Mark Fenyes FICME

Chairman – Omega Foundry Machinery

Vice President – The WFO

TO BE ADDRESSED IN PRESENTATION:

▲ Overview of the World Foundry Organization

▲ Global Uncertainties

▲ General Thoughts on the Global castings Industry

▲ Specific Statistics on the leading nations

▲ Thoughts for the future

THE WORLD FOUNDRY ORGANIZATION

▲ Global Technical Association

▲ Supporting 30 Member Countries

▲ Annual Technical Event

▲ Working Groups

MEMBERS

Austria
Australia
Belarus
Bosnia and Herzegovina
Germany
Spain
France
Great Britain
India
Italy
Mexico
Poland
Sweden
South Africa
United States of America

Switzerland
China
Croatia
Czech Republic
Denmark
Egypt
Finland
Hungary
Japan
Korea
Norway
Romania
Slovenia
Turkey

WFO

TECHNICAL FORUM

▲ Held every 2 years 2017, 2019, 2021

▲ 2017 Held In South Africa – over 300 delegates

▲ 2019 In Conjunction Slovenian Foundry Event

▲ 2021 In India

SOUTH AFRICAN
METAL CASTING
CONFERENCE 2017

World Cast in Africa - Innovate for Sustainability

14 - 17 March 2017 | Emperors Palace, Gauteng, South Africa

WORLD FOUNDRY CONGRESS

The 72nd
World Foundry Congress
May 21 – 25 , 2016

- ▲ 2016 in Nagoya Japan over 1000 delegates
- ▲ 2018 will be in Krakow, Poland 23rd Sept
- ▲ 2020 will be in Korea
- ▲ 2022 will be Italy

WORKING GROUPS

- ▲ Training and Professional Development

- ▲ Energy Saving and the Environment

- ▲ Cast Composites

- ▲ Non Ferrous Metals

- ▲ Ferrous Metals

- ▲ Moulding Materials

*The Die Casting & Non Ferrous Alloys Working Group developed and held a two-day conference July 10-11, 2016. The latest technology and market information relating to the global die casting and non ferrous alloys was shared.

GLOBAL UNCERTAINTIES

▲ Markets affected by > 50 global conflicts, ie:

    * Russia   * Iraq

    * Ukraine   * Pakistan

    * Syria   * Turkey

    * Iran

▲ Unease in Global Financial Markets still exist

▲ Industry still shows uncertainty and pessimism

▲ Capital Investment still generally on hold

▲ Exchange rate fluctuations

GLOBAL INDUSTRY

We should remember that our industry:

▲ Is the oldest production process

▲ Fascinates those people who involved in it

▲ Exhibits a level of passion from those who are working in it

▲ Is unique in its ability to recycle

GLOBAL INDUSTRY

We should remember that:

- ▲ Virtually every nation in the world has a casting industry

- ▲ Worldwide output of castings now exceeds 105M tons

- ▲ Metalcasting is key to the improvement in the standard of living

- ▲ Metalcasting is vital to the drive in both aerospace and automotive for fuel efficiency

- ▲ Metalcasting is the oldest production process

GLOBAL INDUSTRY

Global Industry

- China 50%
- USA 11%
- India 11%
- Japan 6%
- Germany 6%
- Russia 4%
- Brazil 3%
- Korea 3%
- Mexico 2%
- Italy 2%
- Turkey 2%

WFO

GLOBAL INDUSTRY (Million Tonnes)

1 China 46.2
12th for Efficiency

2 USA 10.5
2nd for Efficiency

3 India 10.0
8th for Efficiency

4 Japan 5.5
7th for Efficiency

5 Germany 5.2
1st for Efficiency

6 Russia 4.2
4th for Efficiency

7 Brazil 2.7
9th for Efficiency

8 Korea 2.6
5th for Efficiency

9 Mexico 2.3
6th for Efficiency

10 Italia 2.0
11th for Efficiency

11 Turkey 1.7
10th for Efficiency

W F O

Figures from Modern castings Dec 2015.
Efficiency is tonnage / No of plants

GLOBAL INDUSTRY

Effects on regional production

- Affected by Build near demand
- Mercedes Cars in China
- Bombardier Aircraft in China
- Hyundai Cars in India

GLOBAL INDUSTRY

Influences on Export Markets

▲ Currency effects – Strong Euro

▲ Energy costs in Europe double that of USA

▲ Devaluation in BRICS Countries

▲ Growth of MINT Countries

▲ Brexit Effects – Devaluation of the £

▲ European Uncertainties

GLOBAL INDUSTRY

Europe

▲ Low GDP Growth

▲ High Unemployment (Italy 13% & 43% of Youth)

▲ High Energy Costs

▲ EU Commission Influences

▲ Recognizes need for:

Industrial Renaissance

Solid Manufacturing base to provide growth

and employment

The centrality of manufacturing & competitive

integration

GLOBAL INDUSTRY

Automotive Industry Impact

▶ More than half of castings produced autos

▶ Increasing customer demand for comfort, technology and performance

▶ Cars need bigger engines, bigger fuel tanks and stiffer chassis all adding weight

▶ Casting Industry meets weight reduction challenge with:

* material substitution

* thinner walls

* converting fabrications to castings

COUNTRY SPECIFICS

China

▲ 22% growth in 2002 -2003

▲ 8% growth since 2010

▲ 4% growth last year to 46.2M T

▲ Only 27% goes to Automotive

▲ Production by metal:
  * 46% Grey Iron
  * 26% Ductile Iron
  * 12% Steel
  * 12% Aluminum

WFO

COUNTRY SPECIFICS

China

▲ New Government initiatives for development and growth in the sector

▲ Industry will have access to support for the achievement of improvements in 9 key areas

▲ Foundries closed or merged due to program to push for high productivity & productivity as well as greater focus on quality.

WFO

COUNTRY SPECIFICS

Europe

▲ 15.2 M T production similar to 2013

▲ 5000 Foundries value of €41.3 B

▲ Ferrous output fallen (China +274%)

▲ Auto Sector driver for non ferrous increasing

▲ Number of foundries falling as is employment. (Aluminum sector trend in upward trajectory - unit numbers stable and manpower growing.)

COUNTRY SPECIFICS

Europe

▲ 85% of castings made in Europe used in Europe

▲ 15% direct export

▲ High growth for castings 2014 – 2018 from Automotive, General Engineering and Construction

▲ Optimism is high in Europe for 2016

▲ Future growth driven by:
* development of substitution
* smart engineering
* additive manufacturing

COUNTRY SPECIFICS

USA

▲ 10.5 M T produced by 1978 foundries €27 B

▲ Additional 2.3 M T Mexico and .71 M T Canada

▲ 2008 – 2010 falling output due to off shoring and high energy costs

▲ Currently optimistic with high growth forecasts due to:

    * low energy costs
    * high productivity
    * reduced shipping costs
    * trend toward re-shoring

▲ Imports: 1998 7%
           2008 24%
             currently 21%

WFO

COUNTRY SPECIFICS

India

- 9.5 M T from 4600 foundries

- 32% automotive, 8% each in agriculture, paper and sanitary castings

- Output: 68% grey iron, 9% Al

- 2012 – 13 economic stagnation in India but 10 – 12% growth in foundry sector

- Industry has many new foundries and some major expansions taking place currently

- New government strongly supporting industry

COUNTRY SPECIFICS

India

India

other
44%

sanitary
8%

paper
8%

agriculture
8%

0%

automotive
32%
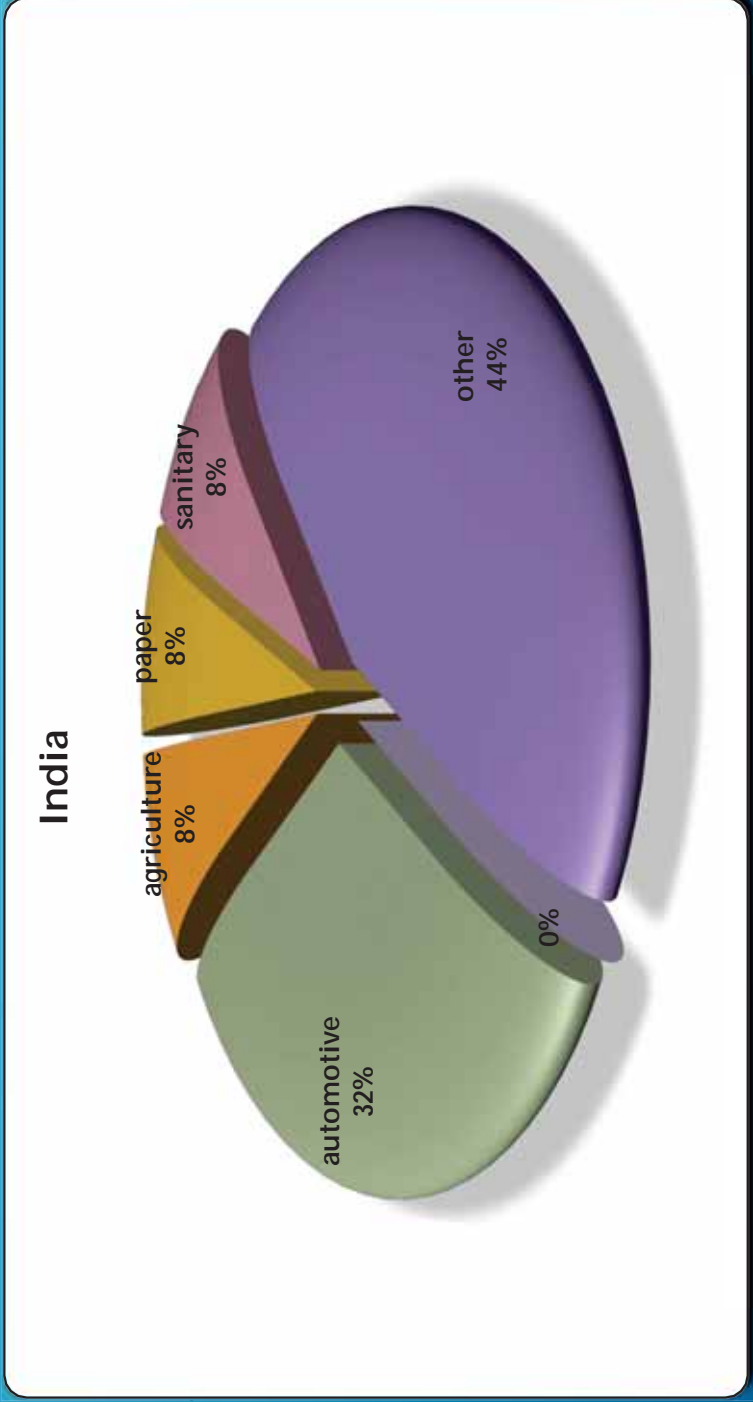
COUNTRY SPECIFICS

Japan

▲ 5.5 M T by 2085 foundries

▲ Significant problems in Japan:
  * Economy moving from deflation to inflation
  * Yen moving from strong position to weak
  * Country as a whole is in New Territory
  * Energy costs have risen by 73% (Tokyo area by 92%) since great earthquake in 2011

▲ Still 70% of castings for Automotive industry

▲ Current new industry vision with 6 points including Management, People, Environmental and Energy

WFO

COUNTRY SPECIFICS

Brazil

- 2.7 M T 1300 foundries
- Major difficulties in Brazil (lowest output for 10 years):
  - * Presidential Elections causing uncertainty
  - * Little or no Economic or structural policy in place
  - * Output in 2014 reduced from 2013 which was no better than 2008
  - * 73% of all castings in variable Automotive sector
  - * Energy costs concerns even though 75% comes from Hydro and renewables
  - * High taxation and interest rates affected by exchange rates
- Expectation of doubling vehicle output by 2020 needing an additional 0.5 M T of castings annually

WFO

THOUGHT FOR THE FUTURE

▲ German car industry in 2001 50% of cars made in Germany 50% in rest of the world

▲ In 2013 that was 35% Germany 65% ROW

▲ In Europe Casting production flat between 2004 and 2012 in China 100% growth

▲ Casting is still the most important process for manufacturing net shape products

▲ We still don't really understand the physics / chemistry of the casting process

▲ Huge potential for improvement in all aspects of foundry production

▲ Still areas for research available into Die and Tool life, simulation of mechanical properties

THOUGHT FOR THE FUTURE

- ▲ Track, watch, and respond to industry trends
- ▲ China has governmental control over foundry development
- ▲ India developing regional clusters for services, which is highly efficient Training, Testing, Simulation, re-cycling
- ▲ Global output predicted to be 110 M T in 2016
- ▲ Foundry Industry in general more efficient than national economy

FORWARD THINKING SPONSORS

THE GLOBAL CASTINGS INDUSTRY

Thanks for your attention

Any Questions

Eur Ing Andrew Turner FICME
General Secretary – The WFO

INVESTING IN EDUCATION AND RESEARCH IN STEM FIELD AS THE KEY TO ECONOMIC DEVELOPMENT OF CROATIA

Dražan Kozak, Željko Ivandić

Josip Juraj Strossmayer University of Osijek Mechanical Engineering Faculty
in Slavonski Brod, Slavonski Brod, Croatia

<u>Plenary lecture</u>
Subject review

Abstract

The article gives a subject review of recent investment to research and development (R&D) in Republic of Croatia related to other world countries, paying special attention to STEM field. It analyzes current number of the students and graduates at higher education institutions in Croatia with refer to EU and world. There is a lack of all technical professions, including ICT. Employability of the graduates in STEM field is in increasing in economically developed countries what could be the sign to decision makers in Croatia what kind of study programs should be promoted. There is one of the key-questions how to stop the brain drain of the experts in STEM field out from Croatia due to the fact that average salary in EU developed countries is even three times more. Is in that case unconditional free higher education investment to the development of other countries, indeed? Croatia stands very bad regarding the number of researchers per million inhabitants and also by investment to R&D. These data are looking still worse in its structure, where 80% of money allocated from public sector for education and R&D is spending for salaries of employees. Investments to R&D from business sector are also relatively small, in particular if they are compared to those in developed countries. This paper is trying to find out is there any correlation between defended doctoral thesis and economic development in Croatian counties, and also between study programs profile and export. It analyzes the influence of investment to R&D on the economic recovering and draw a parallel between current study programs in Croatia and its innovativeness level. There are given particularly some comments regarding the students quota to the study programs in STEM field related to others, that are approximately in the ratio 40:60. At the end of work some examples of good practice are given and steps taken so far to fix the today's situation in direction of economic recovering of Republic of Croatia.

Key words: *STEM field, research and development, Croatia, economic recovering*

*Corresponding author (e-mail address): dkozak@sfsb.hr

Prof. dr. sc. Dražan Kozak:

Ulaganje u obrazovanje i istraživanje u STEM području kao ključ gospodarskog razvoja Hrvatske

- plenarno predavanje u sklopu 16th International Foundrymen Conference 2017 -

Opatija, 16. svibnja 2017.

efinicija se razlikuje u pojedinim zemljama članicama EU.

emeljno: matematika, kemija, računalne znanosti, biologija, fizika, strojarstvo, ektronika i elektrotehnika, komunikacije, kemijsko inženjerstvo.

odatno: medicina, arhitektura, građevina, poljoprivreda, prehrambeno ženjerstvo, kineziologija.

TEM je pojam iz 20. stoljeća, STEAM iz 21. stoljeća.

odatak: *"Arts & design"* jer pridonose razvoju *"4C"* osobina: *creativity, ollaboration, critical thinking, and communication.*

STEM diplomanti u EU

Bilježi se porast broja diplomanata u STEM području u odnosu na ukupan broj u periodu od 2007. do 2012. kako slijedi:

❖ EU porast od **22%** na **23%**

❖ SAD i Japan porast od **16%** na **22%**

❖ U 2012. EU prosjek je **22,8%**, prednjače: Austrija, Švedska, Njemačka i Finska (27,6%), Slovenija (24,7%), Rumunjska, Portugal, **Hrvatska 23.8%**

❖ Uočljiva razlika u zastupljenosti spolova kod STEM diplomanata - najmanja razlika od **25%** više muškaraca u odnosu na žene.

Srednjoškolski učenici i STEM područje

- Prema PISA (**P**rogram for International **S**tudent **A**ssessment) testovima gotovo svaki peti učenik (18%) u EU ima nedovoljna znanja iz ovog područja, dok je ta vrijednost za učenike iz Koreje 7% odnosno Japana 8%.

- Tako su primjerice 2015. godine u matematičkoj pismenosti u dobi od 15 godina bili najbolji učenici iz Singapura (564 boda), dok se Hrvatska s 464 boda plasirala na 41. mjesto što je bio nešto ispodprosječan rezultat.

- Ipak, Hrvatska je sa 17,2% neuspješnih učenika _bolja_ od prosjeka EU28.

- Razlike među spolovima gotovo da nema među neuspješnim učenicima.

STEM zapošljavanje 2003.-2013.

- Porast broja zaposlenih u STEM području (visokoobrazovani i srednjoškolci) u periodu od 2003. do 2013. godine na razini EU je bio 12% (1,8 milijuna), dok je ukupni broj zaposlenih rastao samo 4%. 2013. godine broj zaposlenih u STEM područjima je bio svega 7% u odnosu na ukupan broj zaposlenih.

- U periodu od 2008. do 2013. godine unatoč recesiji samo su tri EU države zabilježile pad ukupnog broja zaposlenih: Belgija, Grčka i Španjolska.

- Izuzetno niska stopa nezaposlenosti među STEM stručnjacima – uglavnom daleko ispod 5%.

- Prisutan je nedostatak svih tehničkih zanimanja, uključujući ICT. Nema nedostatka stručnjaka iz biologije, ali postoji osjetni nedostatak kadrova iz matematike i fizike, inženjera i posebno nastavnika.

- Premalen postotak djevojaka među upisanima na STEM studije.

Očekivani porast poslova u STEM područjima u razdoblju 2012.-2022. prema projekciji američkog Ministarstva za rad

STEM projekcija zapošljavanja 2015.-2025.

Izvor: Cedefop (2015)	2015	2025	Promjena
STEM viša i visoka školska sprema	4 420 000	5 086 000	13%
STEM srednja školska sprema	10 666 000	11 434 000	7%
Sva zanimanja	227 072 000	234 340 000	3%

Jedno od ključnih pitanja je kako zaustaviti odljev STEM stručnjaka iz RH kada je prosječna plaća koju mogu dobiti u razvijenim članicama EU i tri puta veća?

Postaje li bezuvjetno besplatno visoko obrazovanje zapravo ulaganje u razvoj drugih država?

Bruto društveni proizvod u mlrd USD
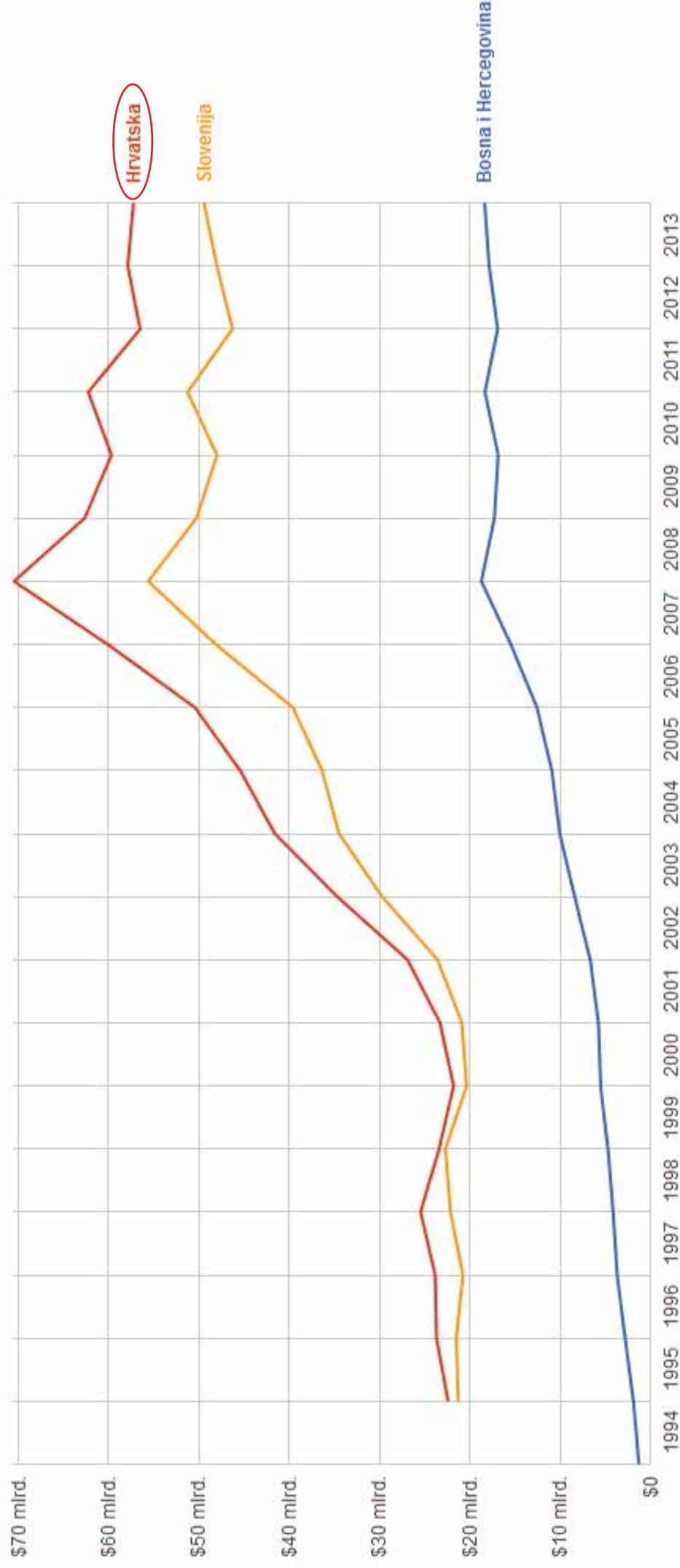
Bruto društveni proizvod po stanovniku u USD

Slovenija

Hrvatska

Bosna i Hercegovina

20.000

15.000

10.000

5.000

0

1994 1995 1996 1997 1998 1999 2000 2001 2002 2003 2004 2005 2006 2007 2008 2009 2010 2011 2012 2013
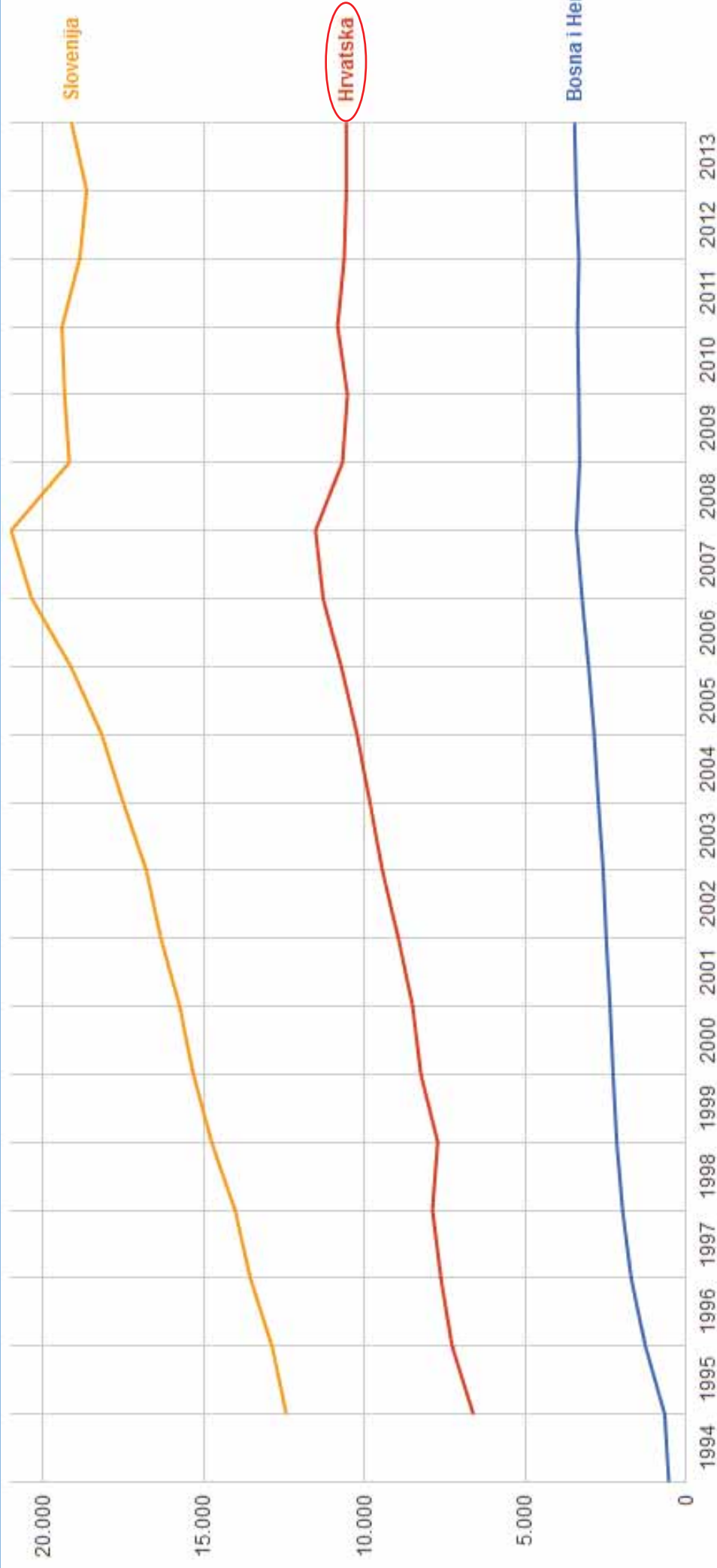
Razlike u bruto društvenom proizvodu u mlrd USD

Usporedbe vrijednosti BDP po državama

- Austrijski BDP u 2013. veći **8x** nego BDP Hrvatske! Uz pretpostavku da Austrija nastavi dugoročno rasti 1,5 % godišnje, Hrvatskoj bi uz dvostruko veću stopu od 3 % rasta godišnje trebalo **57** godina da dostigne austrijsku razinu BDP-a po glavi stanovnika.

- Njemački BDP u 2014. čak 3.250 mlrd USD ili **9x** veći od Austrije, odnosno **72x** veći od HR!

- Američki BDP je u 2014. iznosio 17.419 mlrd USD ili 5,35x veći od Njem. ili **355x** veći od HR.

- Hrvatski BDP je **0,3%** američkog BDP-a i smješten je oko **80.** mjesta svih država svijeta

- Po glavi stanovnika smo na **57.** mjestu (MMF)!

GDP PPP
IMF for 2014

EU · DE · FR · UK · Japan · India · United States · China · ID · ASEAN · BR · UNASUR · RU · EaEU
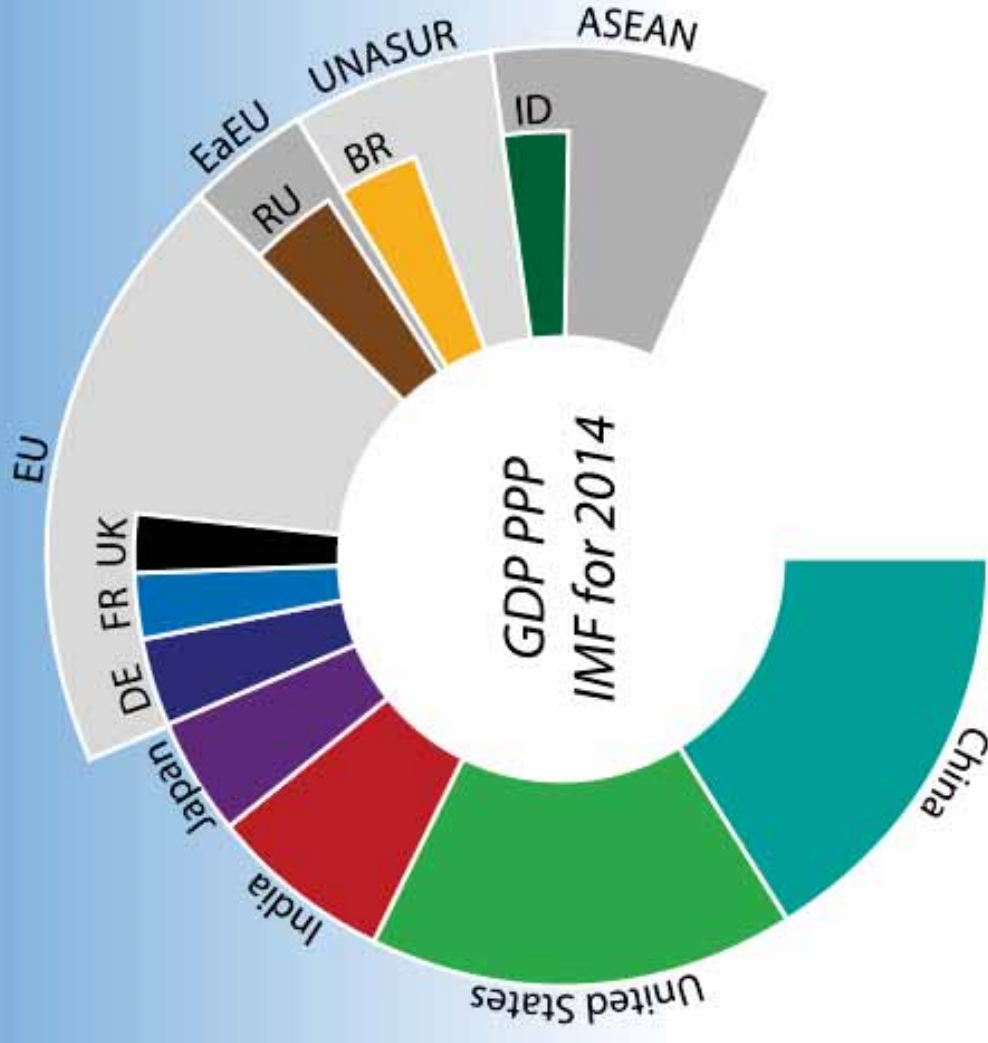
Nominalna vrijednost BDP po državama (MMF) za 2016.

Rank	Country/Economy	GDP Nominal (billions of $)						
		2016	share	2017	2018	2019	2020	2021
1	United States	18,558.130	25.081	19,285	20,145	21,016	21,874	22,766
2	China	11,383.030	15.384	12,263	13,338	14,605	16,144	17,762
3	Japan	4,412.600	5.963	4,514	4,562	4,676	4,800	4,895
4	Germany	3,467.780	4.687	3,592	3,697	3,822	3,959	4,066
5	United Kingdom	2,760.960	3.731	2,885	2,999	3,123	3,256	3,374
6	France	2,464.790	3.331	2,538	2,609	2,700	2,804	2,895
7	India	2,288.720	3.093	2,488	2,725	3,007	3,315	3,660
8	Italy	1,848.690	2.498	1,902	1,943	1,994	2,051	2,092
9	Brazil	1,534.780	2.074	1,556	1,609	1,677	1,749	1,829
10	Canada	1,462.330	1.976	1,531	1,596	1,667	1,740	1,804
80	Croatia	49.928	0.067	52	54	56	59	62
81	Bulgaria	49.364	0.067	51	54	56	59	62
82	Tanzania	45.899	0.062	50	54	58	63	69
83	Belarus	45.887	0.062	49	52	56	59	61
84	Tunisia	43.989	0.059	44	44	46	49	52
85	Slovenia	43.791	0.059	46	47	49	51	53

Najveći gubitnici i dobitnici proračuna: Za znanost i obrazovanje 158 milijuna kn manje

Orešković: Uštedjeli smo 2,5 milijardi kuna, a to nije malo. Mislim da donijeli balansirani i optimizirani plan

Trendovi?

BDP (RH) = 49,928 mlrd USD ili oko **340 mlrd kuna** (80. mjesto u svijetu)

Prihodi proračuna RH za 2016. godinu su planirani u **114,9** milijardi kuna (33,8% BDP), dok su planirani rashodi **122,4** milijardi kuna. Deficit iznosi **7,5** milijardi kuna ili 2,2 posto BDP-a.

Ministarstvo znanosti, obrazovanja i sporta je u proračunu za 2016. godinu planirano s iznosom od **13,8 milijardi kuna** (12% prihoda) od čega se 80% troši na plaće).
To je **158,1 milijun** ili **1,1 posto manje** od plana za prošlu godinu.

Gdje je Hrvatska po broju istraživača na 1.000.000 stanovnika i ulaganjima u istraživanje i razvoj?
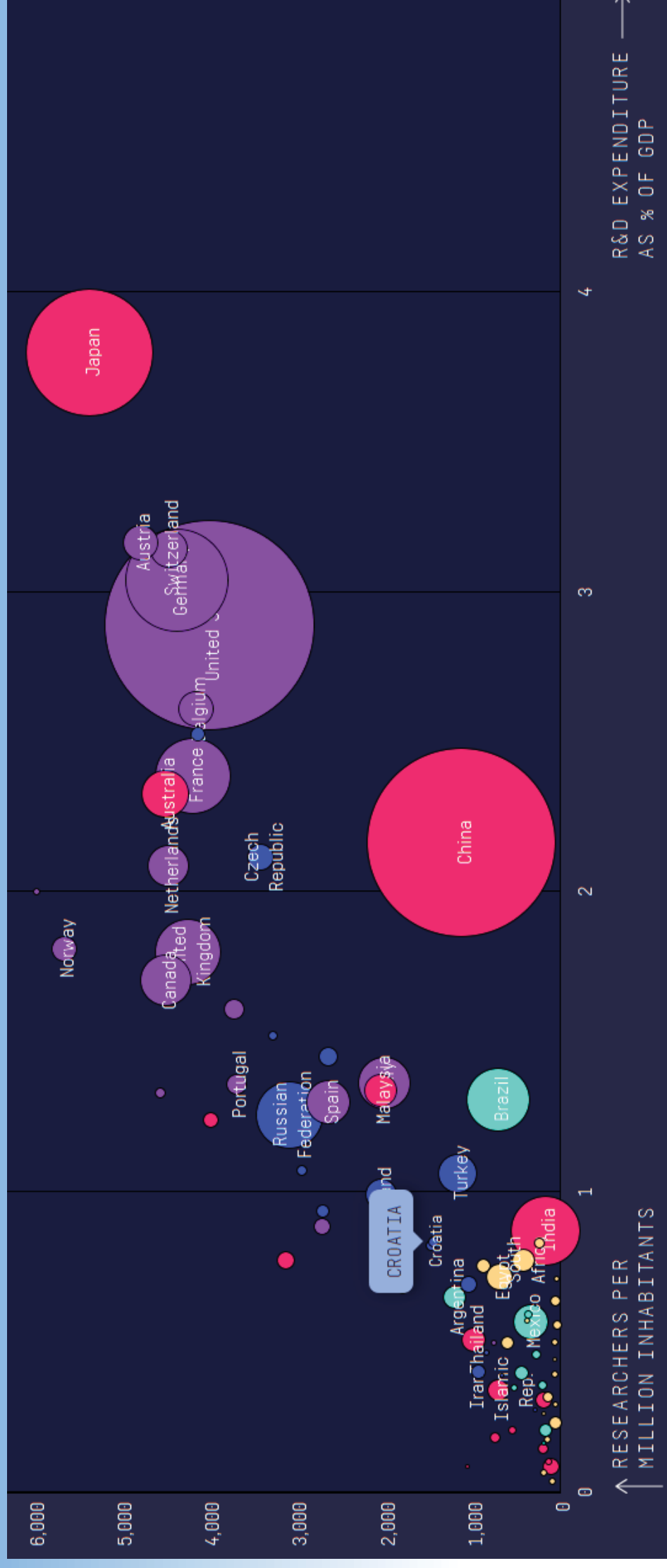
15 prvih država svijeta po % **BDP** u ulaganja u R&D

Ulaga[n]
pos[...]
sekt[...]

Korea, Rep.	Israel	Japan	Finland	Sweden
Denmark	Austria	Switzerland	Germany	United States
Belgium	Slovenia	France	Australia	Singapore
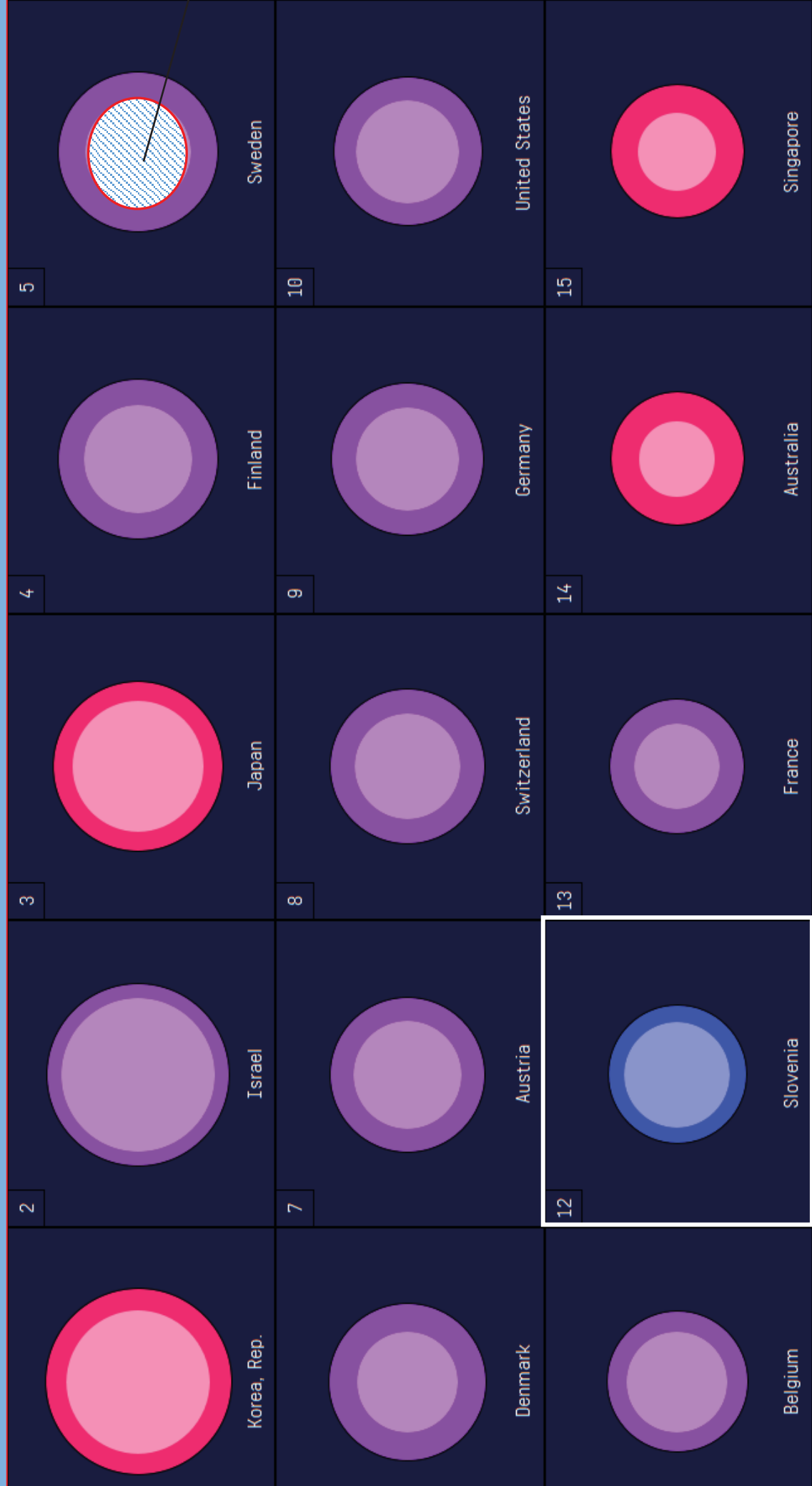
Kako stoji Hrvatska?

- Hrvatska ima 4.284.889 stanovnika i 10.027 istraživača (FTE) za 2014. godinu (oko 2.340 istraživača na 1 milijun stanovnika)

- svega **0.8% BDP** se ulaže u istraživanje i razvoj (55% od toga iz javnog sektora)

- 93% svih poduzeća su tzv. mikropoduzeća (oko 50.000) koja zapošljavaju oko 45% svih zaposlenih u HR s prosjekom od 1.9 zaposlenih, i s udjelom od čak 34% u ukupnom BDP

- u zadnjih 5-6 godina je iznos sredstava koji se ulaže u znanstvene aktivnosti konstantan i iznosi oko svega 75 milijuna eur/godišnje

Top 10 hrvatskih izvoznika

	2013.	2014.	2015.	Promjena
Izvoz (u mil. kn)				
INA	8 324 Kn	7 686 Kn	6 291 Kn	-18,15 %
Pliva Hrvatska	2 194 Kn	2 861 Kn	3 054 Kn	6,75 %
Boxmark Leather	1 923 Kn	2 541 Kn	2 655 Kn	4,49 %
Petrokemija	1 626 Kn	1 554 Kn	1 800 Kn	15,83 %
Valamar Riviera	716 Kn	977 Kn	1 087 Kn	11,26 %
Croatia Airlines	1 015 Kn	1 002 Kn	1 041 Kn	3,89 %
Prvo Plinarsko Društvo		0 Kn	1 018 Kn	/
Podravka	811 Kn	819 Kn	874 Kn	6,72 %
Ericsson NT	968 Kn	901 Kn	854 Kn	-5,22 %
AD Plastik		589 Kn	746 Kn	26,66 %
Ukupno	-	18 930 Kn	19 420 Kn	

Hrvatski izvoznici (www.hrvatski-izvoznici.hr) - HIZ

...Z dodijelio je 2015. deveti put zaredom nagrade po najvažnijim izvoznim tržištima te 'novim' tržištima za ...atske tvrtke, pa je tako **"Zlatni ključ"** za rastuća tržišta, odnosno najboljeg izvoznika u:

...usku federaciju dobila splitska tvrtka **Adria Winch**,

...jevernu, srednju i južnu Ameriku, odnosno Kanadu tvrtka **Omco Croatia** iz Huma na Sutli

...iričke zemlje, odnosno u Egipat je **MIV - Metalska industrija Varaždin**,

...ziju i Pacifik, odnosno Tursku Županjska tvrtka **Same Deutz-Fahr Žetelice**.

Nizozemsku je lani najbolji izvoznik bio **ACG Lukaps iz Ludbrega**,

...SAD karlovački **HS Produkt**,

Francusku **AD Plastik**, - u Mađarsku **Feroimpex automobilska tehnika** iz Bregane,

Srbiju dobila je **Saponia**, - u Austriju **Ivančica**, a - u BiH **Podravka**, dok je kao najbolji izvoznik - u Njemač...

...ka **Vivera. LTH Metalni lijev** iz Benkovca nagrađen je za izvoz - u Sloveniju, a **Rockwoll Adriatic** za izvo...

...najvažnije vanjskotrgovinsko tržište za hrvatske proizvode, - Italiju.

...iinovativniji izvoznik u 2015. po izboru HIZ-a je **AD Plastik**, a **bolji** mali **Nanobit**, srednji **Industrius**, i veliki **Pliva Hrvatska**

Br. istraživača na 1000 radno aktivnih stanovnika 2000. i 2009.
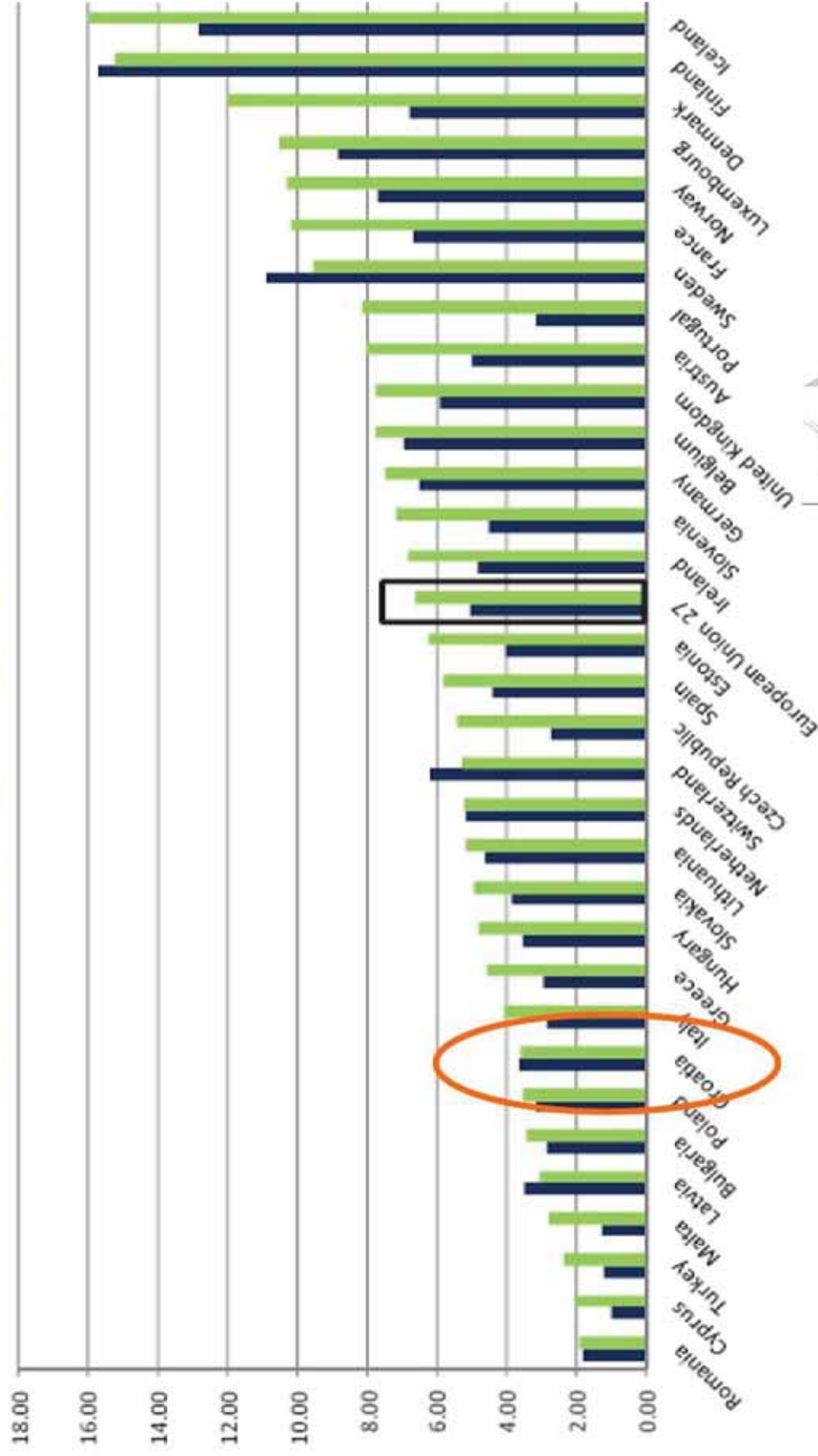
Researchers' Report 2012
DG Research and Innovation

Postoji li korelacija između obranjenih doktorata znanosti i gospodarskog razvoja?
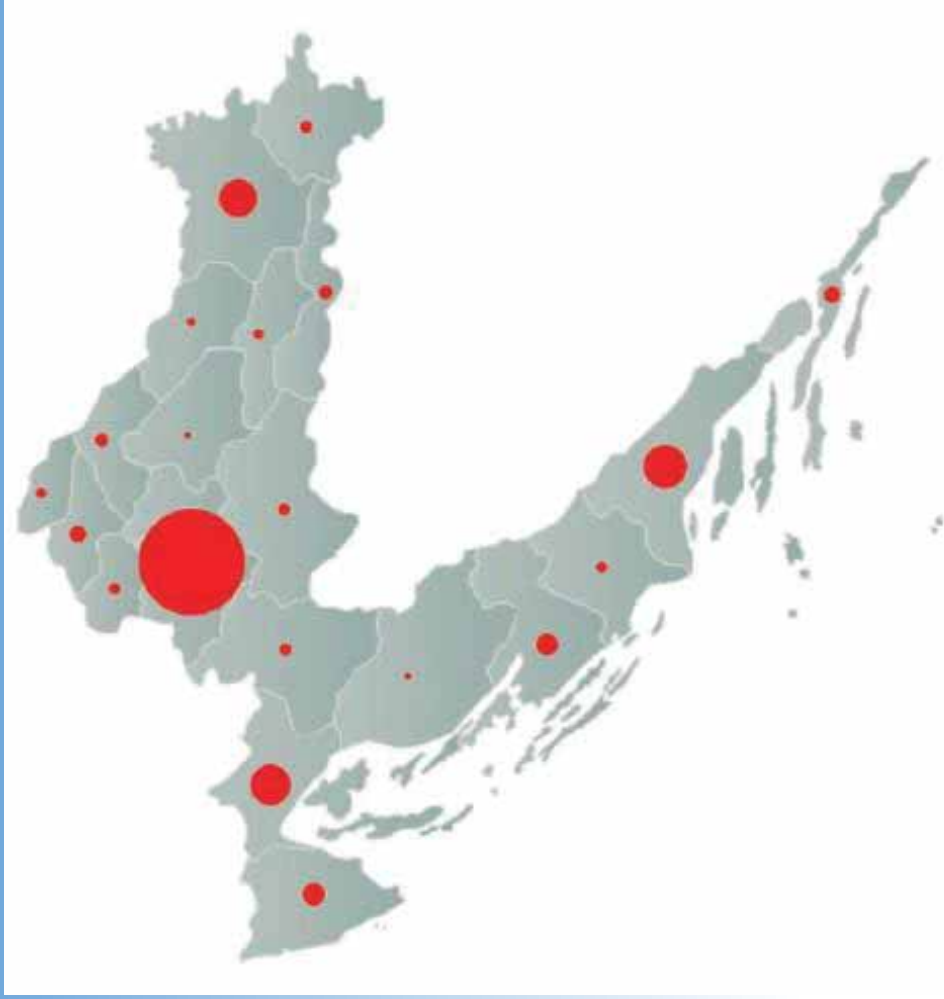
Figure 4. *Doctors of science (PhDs) by county of usual residence that graduated in 2000-2012 at Croatian universities (source Croatian Bureau of Statistics). Surface area of the circles is proportional to the number of PhD graduates.*

C-1. BRUTO DOMAĆI PROIZVOD PO STANOVNIKU U 2011.
GROSS DOMESTIC PRODUCT PER CAPITA, 2011
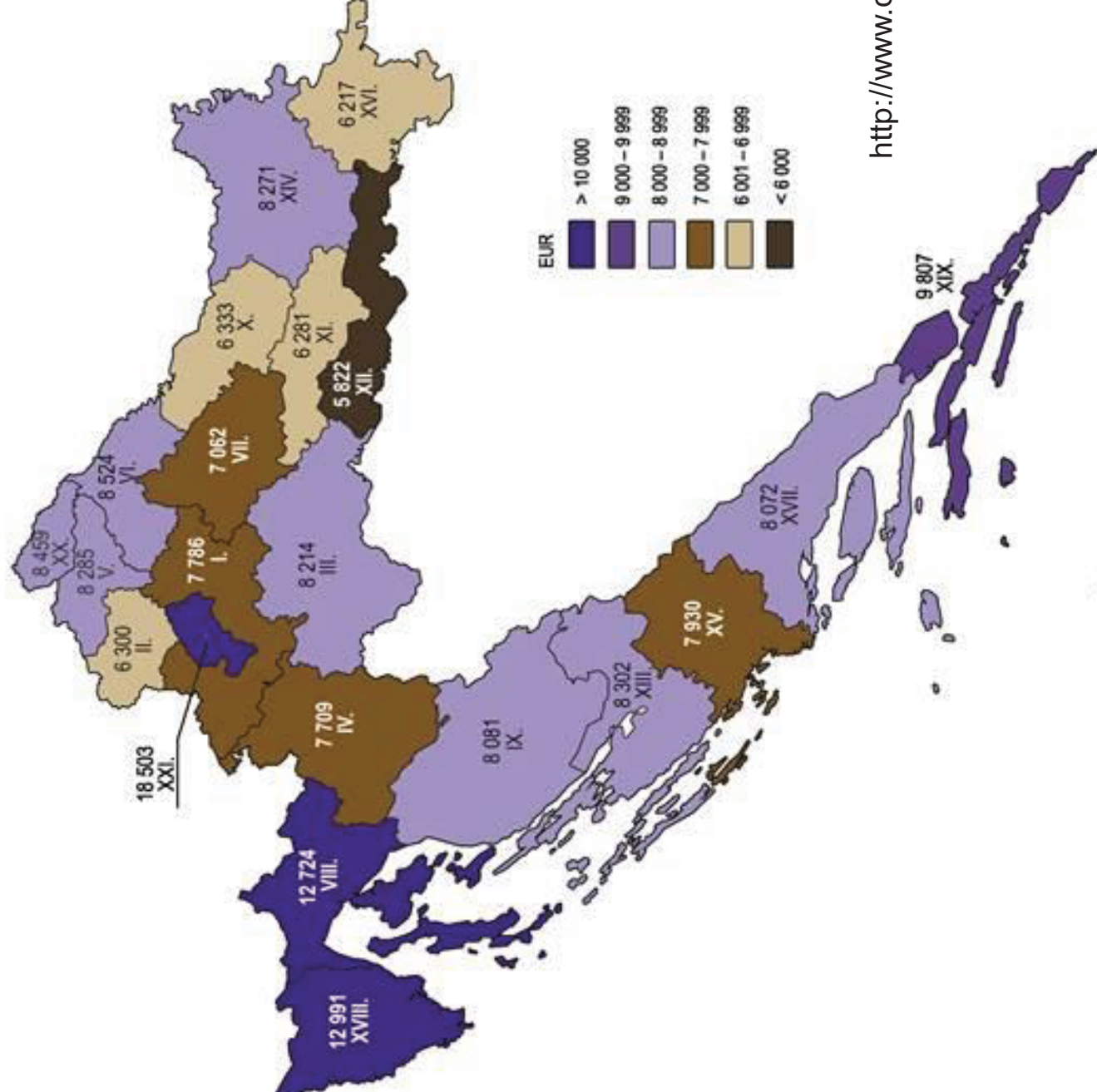
Bruto domaći proizvod po stanovniku u 2011. po Županijama

Izvor: Državni zavod za statistiku RH

http://www.dzs.hr/Hrv_Eng/publication/2014/12-01-02_01_2014.htm

EUR
- > 10 000
- 9 000 – 9 999
- 8 000 – 8 999
- 7 000 – 7 999
- 6 001 – 6 999
- < 6 000

Map labels:

- 6 217 XVI.
- 8 271 XIV.
- 6 333 X.
- 6 281 XI.
- 5 822 XII.
- 8 524 VI.
- 7 062 VII.
- 8 459 XX.
- 8 285 V.
- 7 786 I.
- 8 214 III.
- 6 300 II.
- 18 503 XXI.
- 7 709 IV.
- 8 081 IX.
- 8 302 XIII.
- 7 930 XV.
- 8 072 XVII.
- 9 807 XIX.
- 12 724 VIII.
- 12 991 XVIII.

ċaj ulaganja u istraživanje i razvoja (R&D) na gospodarski oporavak u 2010.
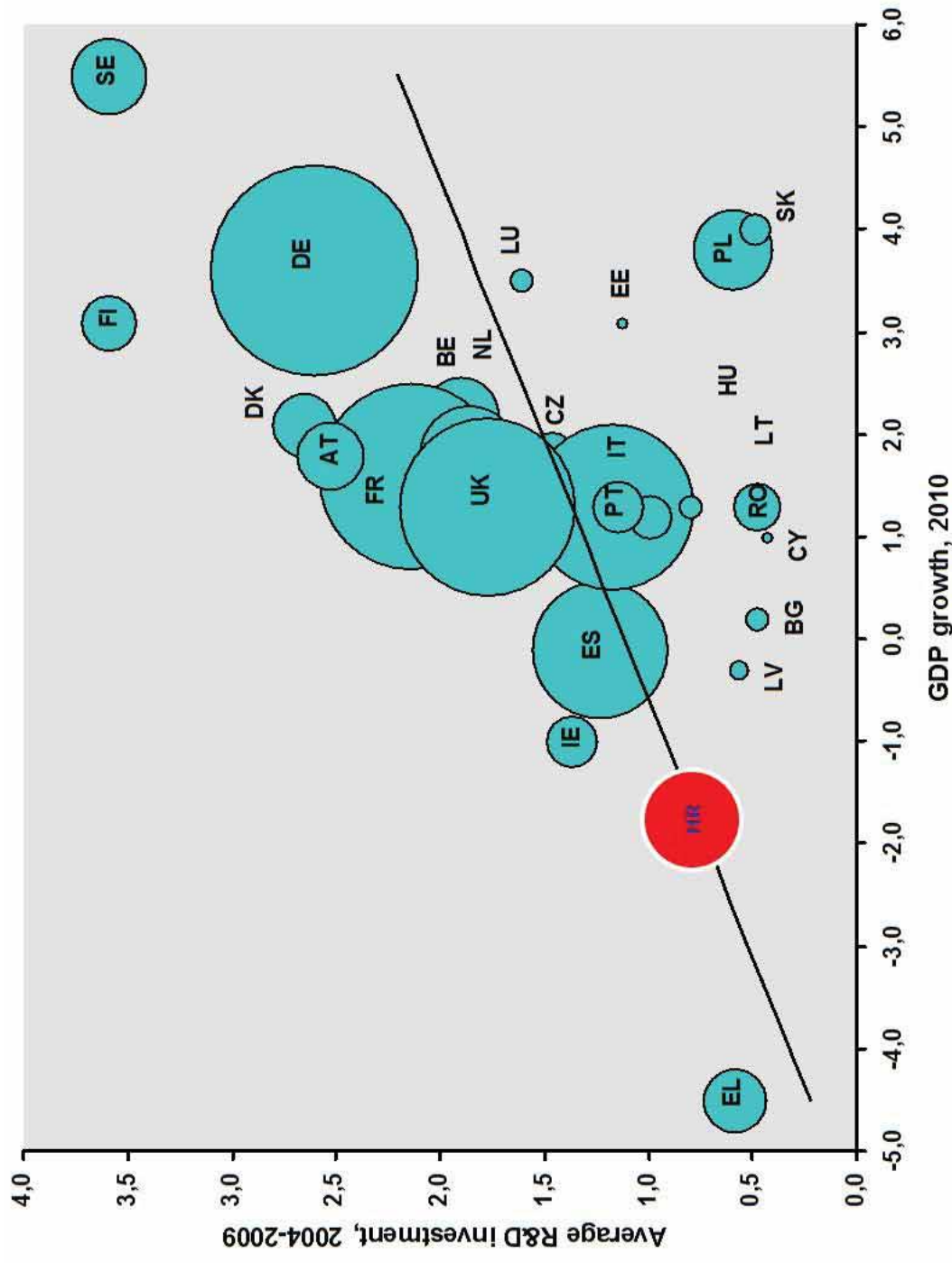
Figure 10: European countries' innovation performance
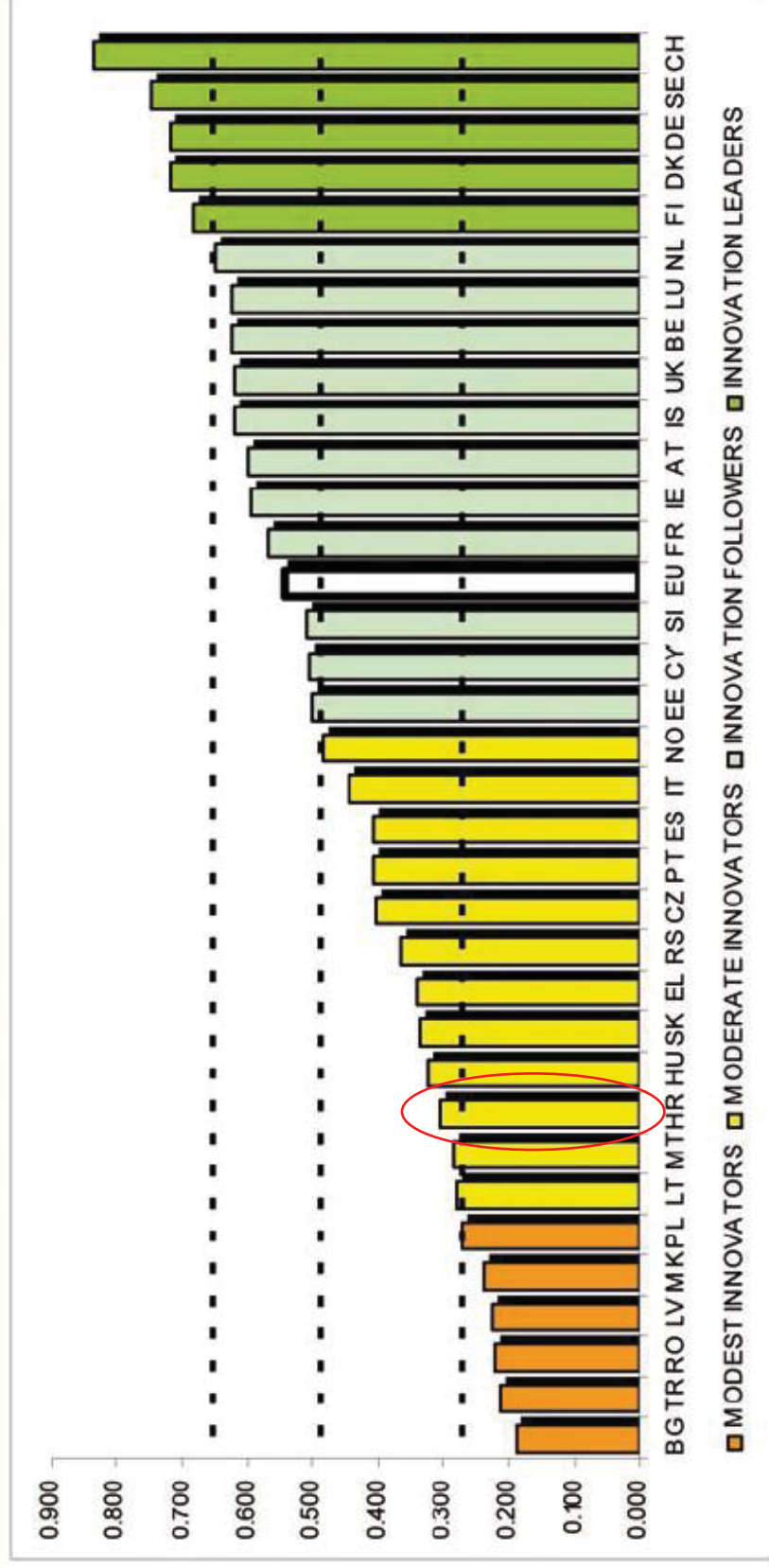
Note: Average performance is measured using a composite indicator building on data for 24 indicators ranging from a lowest possible performance of 0 to a maximum possible performance of 1. Average performance reflects performance in 2010/2011 due to a lag in data availability. The performance of Innovation leaders is 20% or more above that of the EU27; of Innovation followers it is less than 20% above but more than 10% below that of the EU27; of Moderate innovators it is less than 10% below but more than 50% below that of the EU27; and for Modest innovators it is below 50% that of the EU27.

Posto uključenih u cjeloživotno obrazovanje u dobi od 25-64 godine
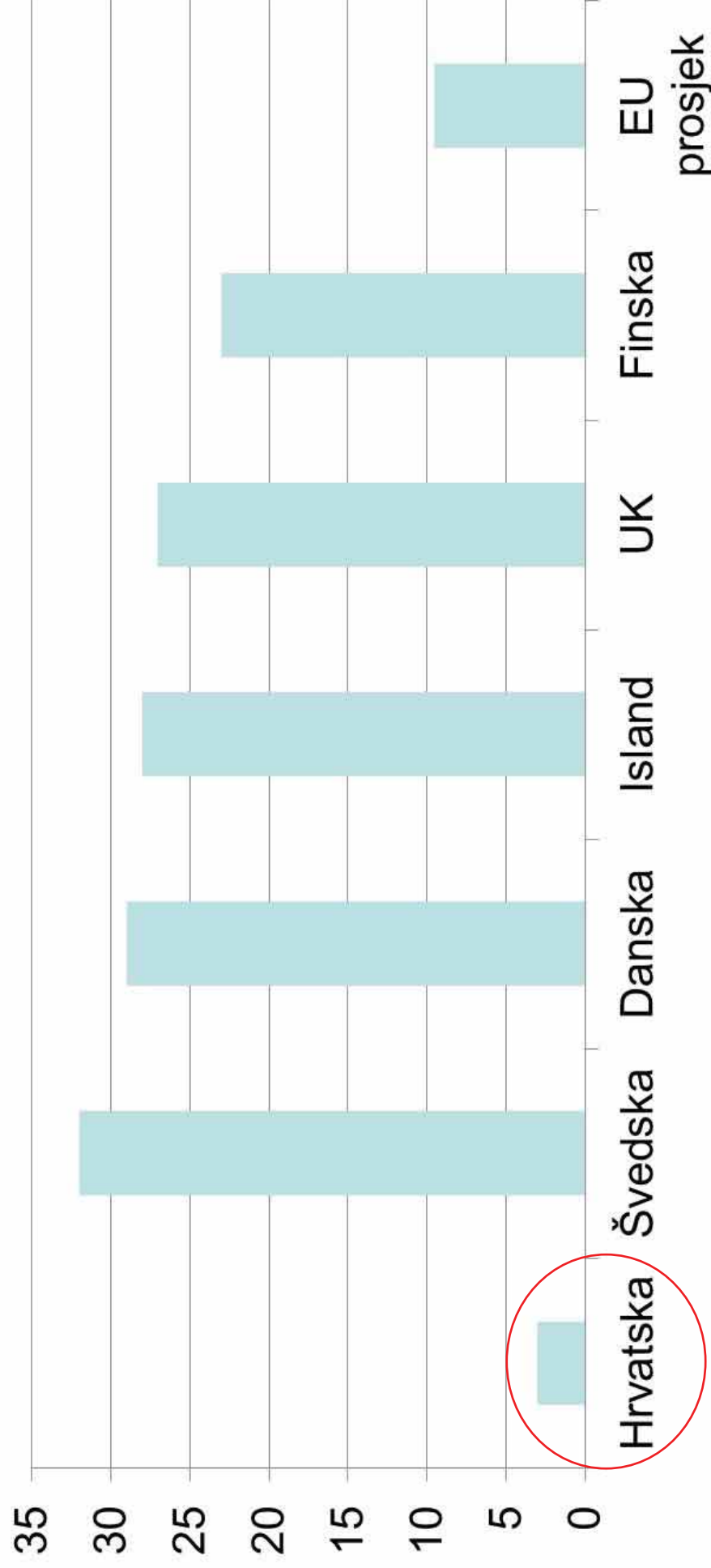
ašto je Hrvatska ispod 50% inovativnosti prosjeka EU28?

Danas u Hrvatskoj djeluje ukupno **119** visokih učilišta sa statusom ustanove:

- **8** (9) javnih i **2** privatna sveučilišta na kojima studira oko 79% studenata
- **68** fakulteta i umjetničkih akademija te 1 sveučilišni centar na javnim sveučilištima
- **11** javnih i 4 privatna veleučilišta
- **22** privatne visoke škole i **3** javne visoke škole te
- **25** javnih instituta, kao i drugi legalni R&D instituti

Akreditirano je više od **1200** studijskih programa u visokom obrazovanju.

Za osiguravanje kvalitete u visokom obrazovanju brine Agencija za znanost i visoko obrazovanje (www.azvo.hr).

ostoji li korelacija inovativnosti i broja studenata po znanstvenom području studija?

Udio studenata prema znanstvenom području studija
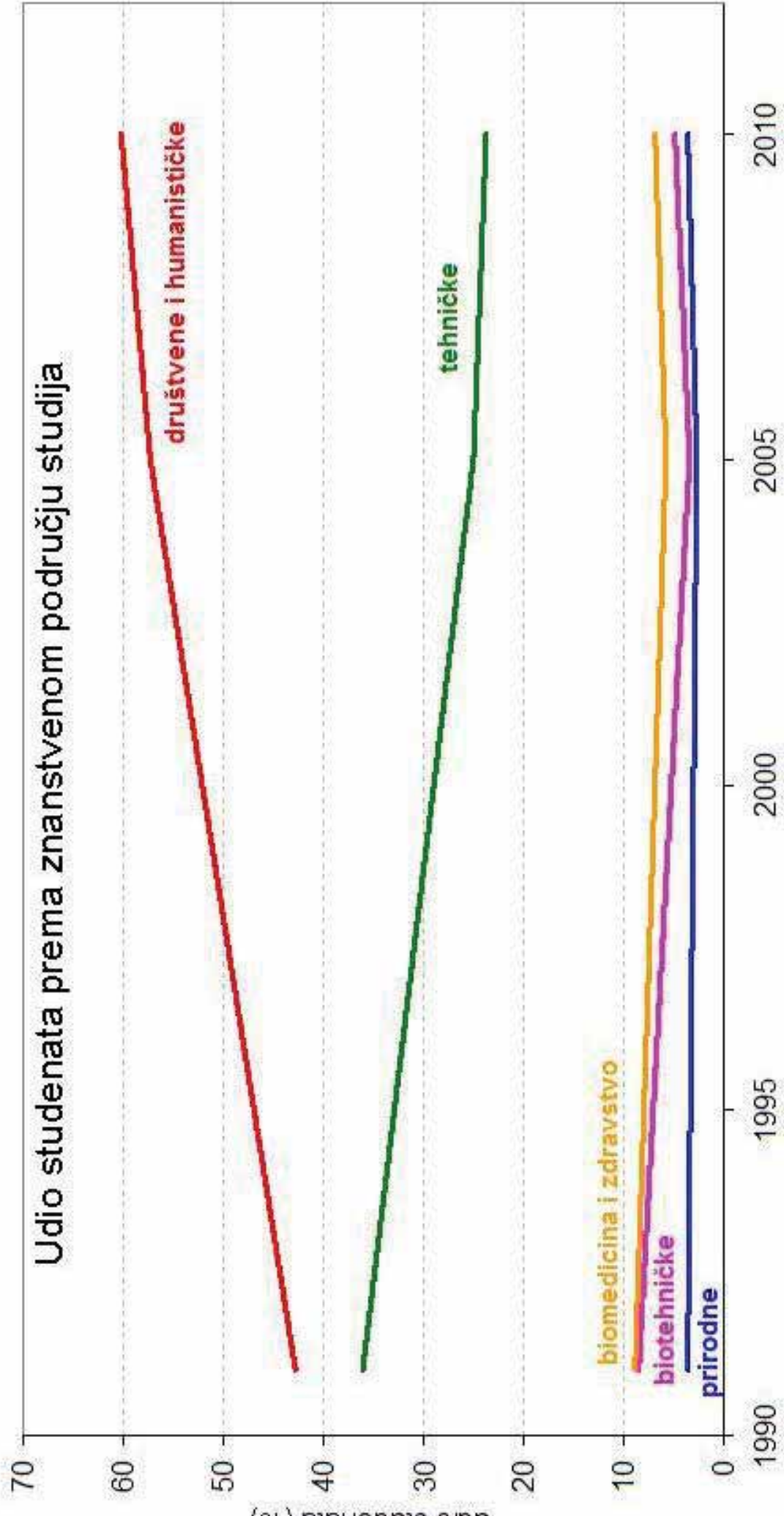
Omjer STEM:drugi = 40:60

Ukupno upisani studenti po područjima

- Tehničke znanosti
- Biomedicina i zdravstvo
- Umjetničko područje
- Biotehničke znanosti
- Humanističke znanosti
- Prirodne znanosti
- Društvene znanosti

51,68%

23,52%

6,73%

1,77%

4,89%

7,83%

3,58%
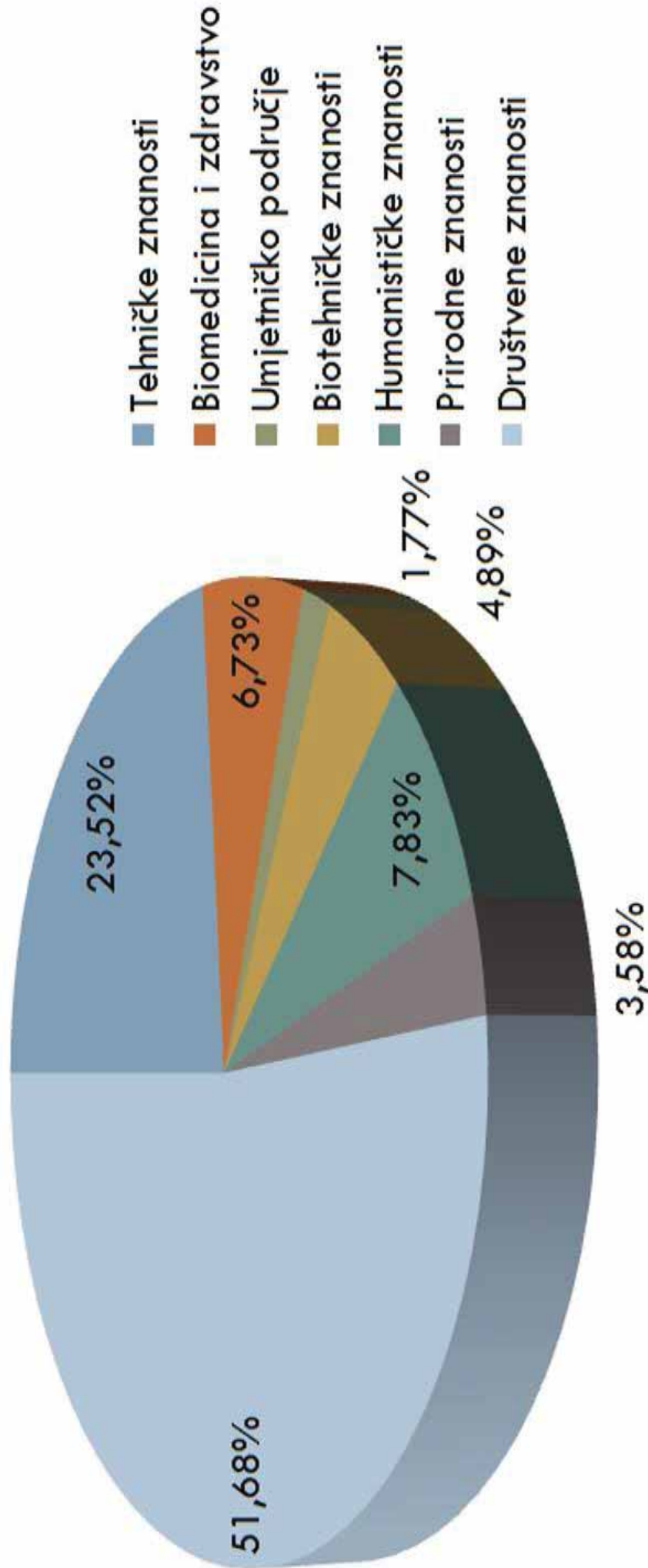
Deset najvećih fakulteta u Hrvatskoj po broju studenata (podatci za ak.g. 2013./2014.):

1. Ekonomski fakultet u Zagrebu – 11.181

2. Pravni fakultet u Zagrebu – 9.403

3. Filozofski fakultet u Zagrebu – 5.738

4. Prirodoslovno-matematički fakultet u Zagrebu – 4.309

5. Pravni fakultet u Splitu – 3.894

6. Ekonomski fakultetu u Splitu – 3.568

7. Ekonomski fakultet u Osijeku – 3.362

8. Fakultet elektrotehnike i računarstva u Zagrebu – 3.358

9. Fakultet organizacije i informatike u Varaždinu – 3.148

10. Fakultet prometnih znanosti u Zagrebu – 3.059

STEM

STEM

Što se čini kako bi se stvari popravile?

Usvojena je Nacionalna strategija obrazovanja, znanosti i tehnologije (siječanj 2014.)

Povećanje upisnih kvota u STEM području i broja osoba sa završenim studijem u tehničkim, biomedicinskim, biotehničkim i prirodnim (STEM) područjima te u informatičko-komunikacijskom području i u interdisciplinarnim studijima vezanim uz ova područja putem programskih ugovora s visokim učilištima

Potpora putem državnih stipendija (primjer dobre prakse su stipendije za studente u STEM/IT području koje daje Sveučilište u Rijeci!)

Gospodarski subjekti doniraju i stipendiraju razvoj STEM stručnjaka (dobar primjer HT, koji je osnovao STEM HUB kao inkubator za poticanje razvoja vještina u STEM-u, kojim se želi stvoriti aktivnu akademsko-gospodarsku zajednicu mladih stručnjaka iz prirodoslovnog i znanstvenog područja)

Što se čini kako bi se stvari popravile?

- Osnivanje Znanstvenih centara izvrsnosti (10/13 u STEM području)
- Osnovana Hrvatska zaklada za znanost (HRZZ) koja od 2004. financira samo najbolje projekte (www.hrzz.hr), nakon stroge međunarodne evaluacije

- Već 20 godina djeluje Hrvatska agencija za malo gospodarstvo, inovacije i investicije HAMAG-BICRO) (www.hamagbicro.hr), koja pruža podršku poduzetnicima kroz sve razvojne faze njihovog poslovanja – od istraživanja i razvoja ideje pa sve do komercijalizacije i plasmana na tržište

- Dodijeljeni ugovori u okviru natječaja ESF dodjele bespovratnih sredstava "*Promocija kvalitete i unapređenje sustava odgoja i obrazovanja na srednjoškolskoj razini*", koji bi kroz nove kurikulume, praktikume i edukaciju trebali učiniti studije u STEM području privlačnijim maturantima

TRADICIJA, KONTINUITET I KVALITETA

HVALA NA PAŽNJI

STROJARSKI FAKULTET

SIMULTANEOUS COOLING / CONTRACTION CURVE ANALYSIS IN DUCTILE IRON QUALITY CONTROL

Stelian Stan, Mihai Chisamera, Iulian Riposan

Politehnica University of Bucharest, Bucharest, Romania

Abstract

Commercial cast iron [more than 70% of the total world metal casting production] is a typical multi-phase, natural metal matrix composite. Analysis of recent literature shows that for both lamellar and nodular graphite morphologies, complex compounds act as nucleation sites in commercial cast irons, in a general three-stage graphite formation, but in a different sequence: oxide/sulphide – sulphide/oxide – graphite, respectively. Consequently, there are different sources of active elements to sustain graphite formation in commercial cast irons: base iron [C, Si, Mn, S, Al, O, N, etc], preconditioner [Al, Zr, Si, Ba, SiC, etc], nodulizer [Mg, RE, Al, Si, Ca, etc], inoculant [Ca, Ba, Sr, Ce, La, Zr, Si, Al, Mn, etc], inoculant enhancer [S, O, Al, Ca, Si, Mg, etc].

The cooling curve and its first derivative display patterns that can be used to predict the characteristics of a cast iron. The effects of active elements in the base iron [S, Al], preconditioning with oxide forming elements, inoculation and inoculation enhancing by adding S, O and oxy-sulphides forming elements with commercial Ca-FeSi inoculants were explored by thermal analysis as their capacity to restore solidification with low eutectic undercooling in ductile iron solidification.

An experimental device was developed with a technique to simultaneously evaluate cooling curves and expansion or contraction of cast metals during solidification. Undercooling at the end of solidification relative to the metastable (carbidic) equilibrium temperature and the expansion within the solidification sequence appear to have a strong influence on the susceptibility to macro - and micro - shrinkage in ductile iron castings. Green sand moulds, as less rigid moulds, encourage the formation of contraction defects, not only because of high initial expansion values, but also because of a higher cooling rate during solidification and, consequently, increased undercooling below the metastable equilibrium temperature up to the end of solidification.

Keywords: *graphite formation, grey and ductile cast iron, solidification, thermal analysis, cooling curves, contraction curves, undercooling, contraction defects, casting mould, carbides*

POLITEHNICA University of Bucharest, ROMANIA

Simultaneous Cooling / Contraction Curve Analysis in Ductile Iron Quality Control

[From Thermal Analysis to Simultaneous Cooling / Contraction / Expansion Curves Analysis]

S. Stan, M. Chisamera, I. Riposan

POLITEHNICA University of Bucharest, ROMANIA

POLITEHNICA University of Bucharest, ROMANIA
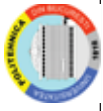
OUTLINE

● **INTRODUCTION**

*Cast iron in world metalcasting industry

*Graphite formation in commercial ductile iron – active elements contributions

● **THERMAL ANALYSIS CONTROL IN Mg - TREATED IRONS**

- peculiar influencing factors

*Base Iron: Sulphur, Superheating

*Aluminium Benefits: Preconditioning, Inoculation

*Inoculation Enhancing – Oxy-sulphides forming elements

● **SIMULTANEOUS THERMAL / CONTRACTION ANALYSIS**

*Mould rigidity influence on contraction defects sensitiveness

● **CONCLUSIONS**

POLITEHNICA University of Bucharest, ROMANIA

2015 WORLD METALCASTING PRODUCTION
[104.13 Million Metric Tons]

GI
44.89%

DI
24.56%

Steel
10.50%

Al
15.42%

Mg O.N
Zn
Cu

MI

70.30%
CAST IRON

Steel
10.50%

NON-FERROUS
19.20%

3
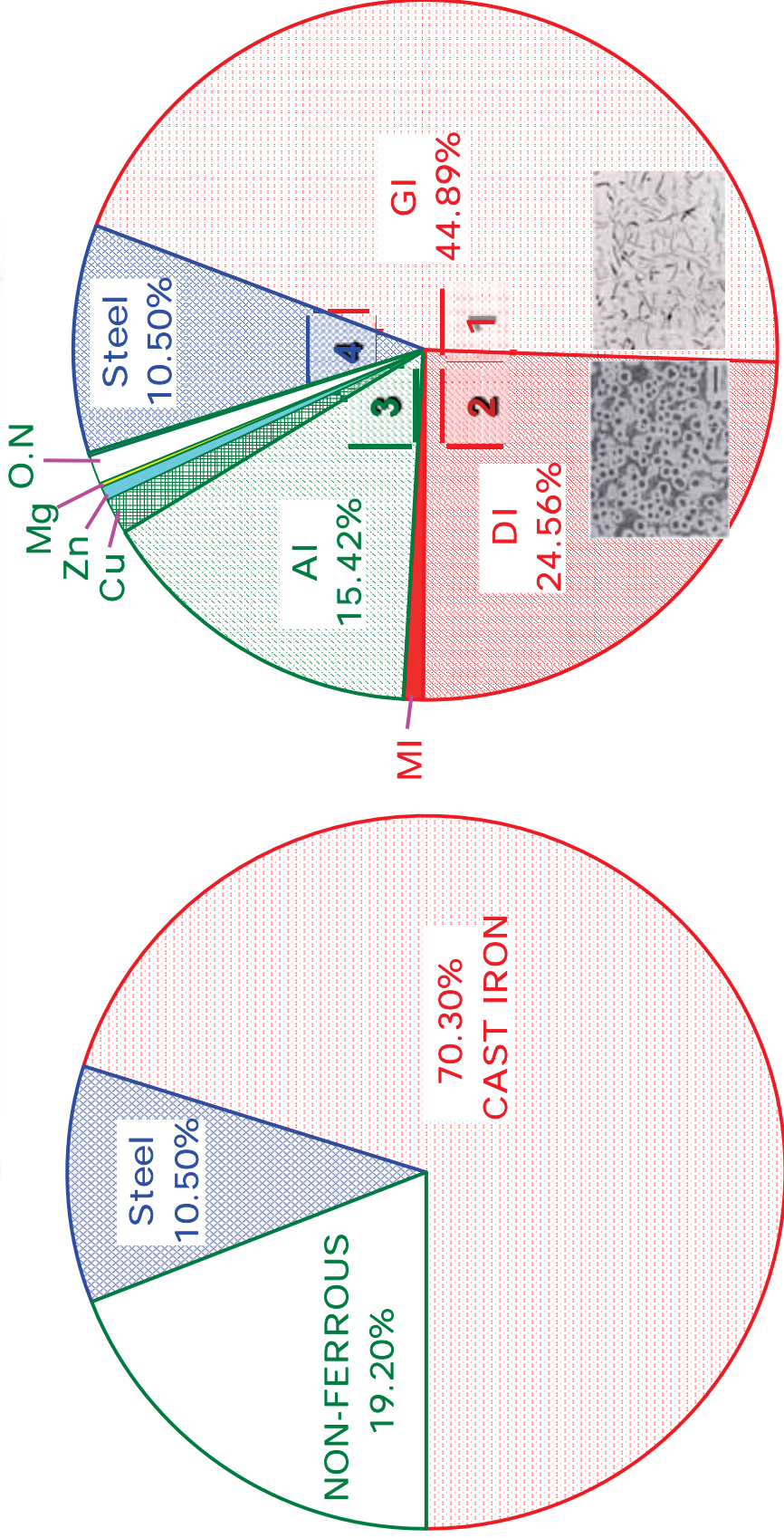
Ductile Iron Production Flow Chart *and* Typical Structures

BASE IRON

S < 0.02%; P < 0.05%
C = 3.2 - 3.8%
Si=1.5-3%; Mn=0.1-0.6%

NODULIZING TREATMENT
[0.1 – 3.0wt.% alloy]

[0.03-0.06%Mg_{res}]

Mg_{met}; Mg_{met} + REE
Mg – FeSi; Mg, REE - FeSi
Mg – Ni (Si); Mg - Cu

INOCULATION TREATMENT
[0.1 – 1.0wt.% alloy]

X – FeSi
X=Al, Ca, Ba, Sr, Zr, REE
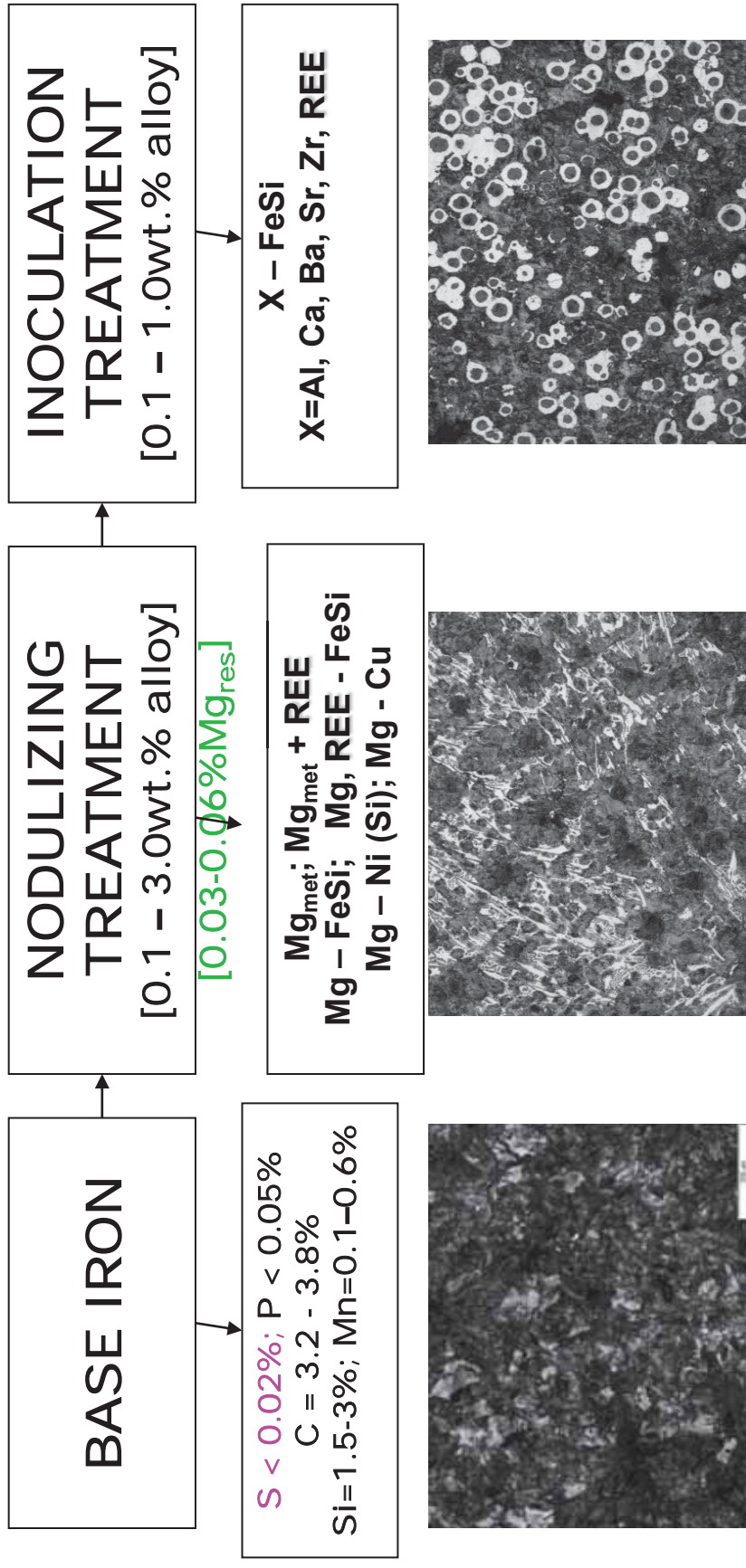
DUCTILE IRON STUCTURE FORMATION

NODULARIZATION

[Mg; MgFeSi(Al); MgFeSiCa(Al) MgFeSiCaRE(Al)]

IV. Graphite — Skaland, 1992

III. [XO·SiO₂; $XO·Al_2O_3·2SiO_2$]
Ca,Ba-FeSi(Al)]
[X = Ca,Sr,Ba]

NODULARIZATION + INOCULATION

[Ca-FeSi(Al); Ba-FeSi(Al); Sr-FeSi
Ca,Ba-FeSi(Al)]

III. Graphite

II. Shell
[MgO·SiO₂
2MgO·SiO₂]

I. Core
[MgS; CaS]

II. Shell
[MgO·SiO₂
2MgO·SiO₂]

I. Core
[MgS; CaS]
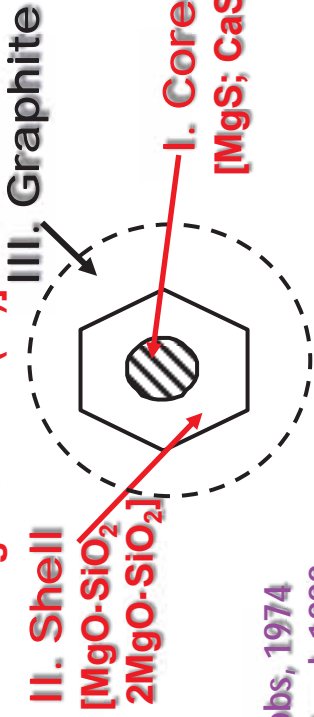
Jacobs, 1974
Skaland, 1992

MISMATCH, δ, % [(001)$_G$ – Substance]

Nodularization + Inoculation

$MgO·SiO_2 + X = XO·SiO_2 + Mg$
$2(MgO·SiO_2) + X + 2Al = XO·Al_2O_3·2SiO_2 + 4Mg$

[X = Ca, Sr, Ba]

Skaland, 1992

Mg – treatment
MgO·SiO₂
2MgO·SiO₂

MgO·SiO₂ 2MgO·SiO₂

CaO·SiO₂ SrO·SiO₂ BaO·SiO₂ CaO·Al₂O₃ SrO·Al₂O₃ BaO·Al₂O₃
                                          2SiO₂   2SiO₂   2SiO₂

Mismatch, δ, %

[S, O, Al, Si, Mg, Ca, Ba, Sr, Ce, La, ...]

5
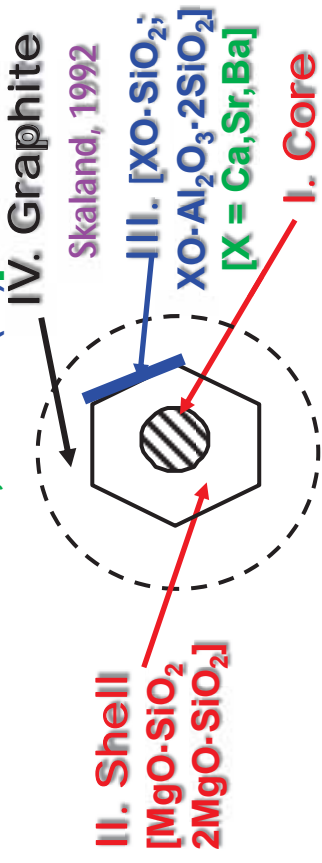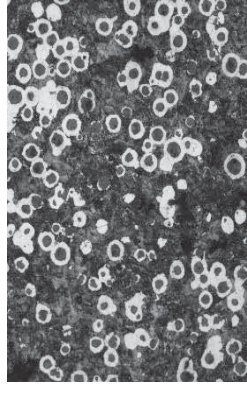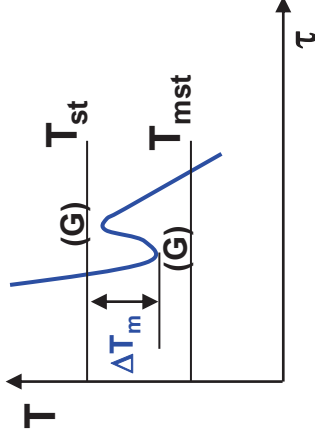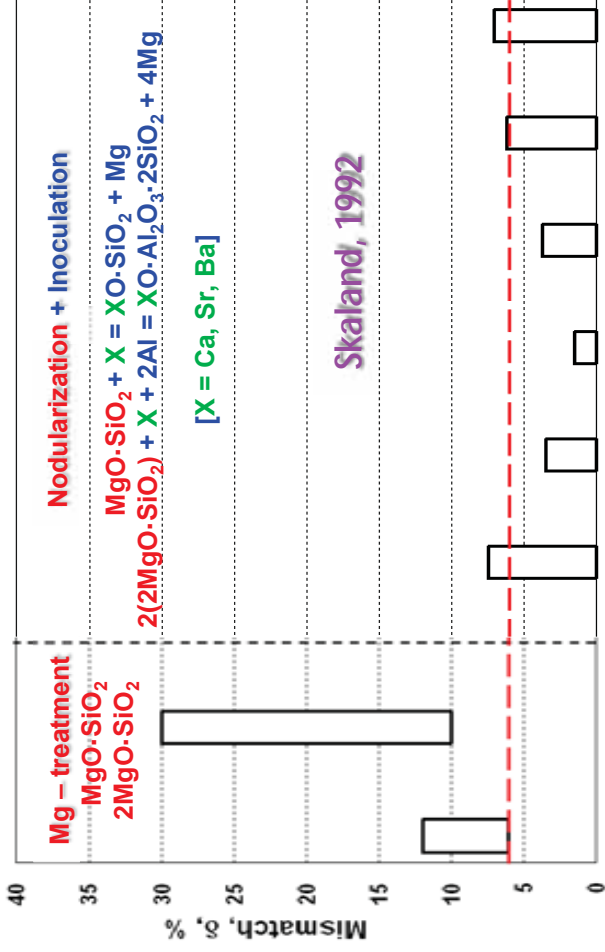
POLITEHNICA University of Bucharest, ROMANIA

SOURCES OF ACTIVE ELEMENTS IN GRAPHITE FORMATION IN CAST IRONS

- **BASE IRON: C, Si, Mn, S, Al, O, N ……**

- **PRECONDITIONER: Al, Zr, Si, Ba, SiC …….**

- **NODULIZER: Mg, Ce, La, Pr, Nd, Y, Ca, Al, Si…**

- **INOCULANT: Ca, Ba, Sr, Ce, La, Zr, Si, Al, Mn.….**

- **INOCULANT ENHANCER: S, O, Al, Ca, Si………**
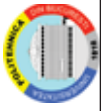
THERMAL ANALYSIS CONTROL IN

Mg - TREATED IRONS

- peculiar influencing factors

*Base Iron: Sulphur, Superheating

*Aluminium Benefits: Preconditioning, Inoculation

*Inoculation Enhancing – Oxy-sulphides forming elements

Base Iron: Sulphur / Superheating

Ductile Iron [DI] *vs* Grey Iron [GI]: DI = 0.005 - 0.01%S *vs* GI = 0.07 - 0.09%S

$[\Delta T_1 = TEU - Tmst; \Delta T_2 = TER - Tmst]$

SUPERHEATING

WI - White Iron
MI - Mottled Iron

ΔT_1 ΔT_2

S = 0.005 - 0.010 %
S = 0.07 - 0.09 %

Inoculated

Un-Inoculated
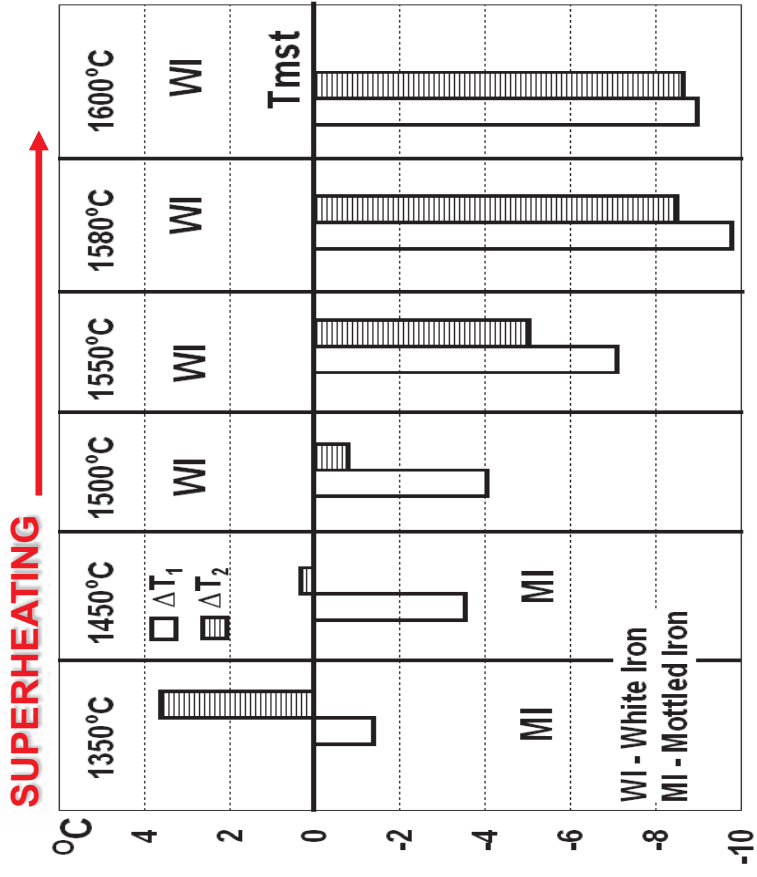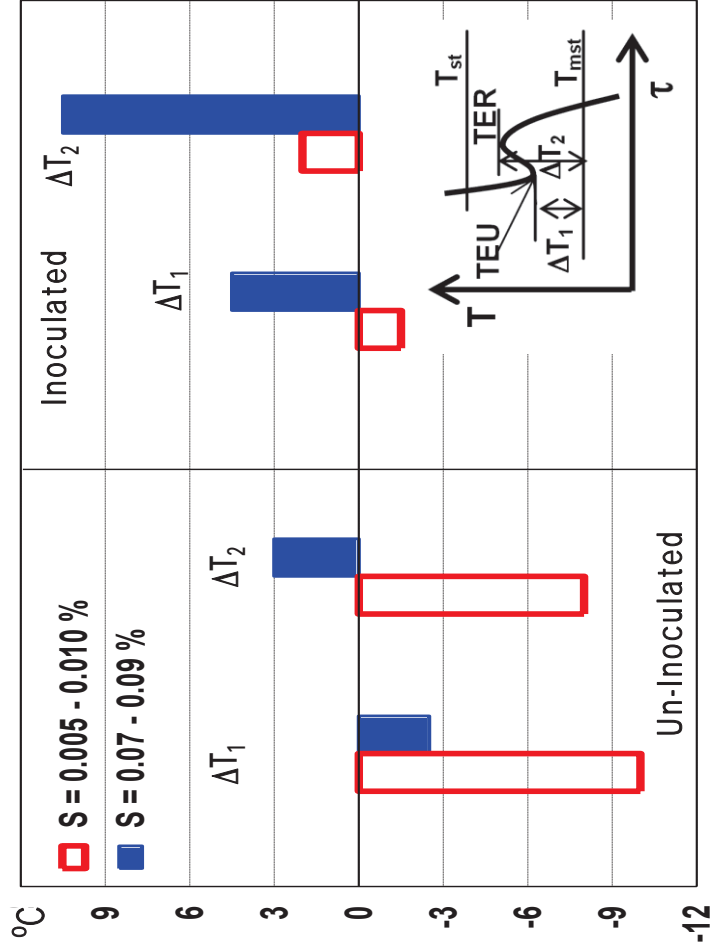
Al-FeSi preconditioning

[0.4wt.% Al-FeSi Preconditioning; 2.5wt. FeSiCaMg Nodulization; 0.5wt.% Ca-FeSi Inoculation; CE = 3.95 – 4.25%]

POLITEHNICA University of Bucharest, ROMANIA
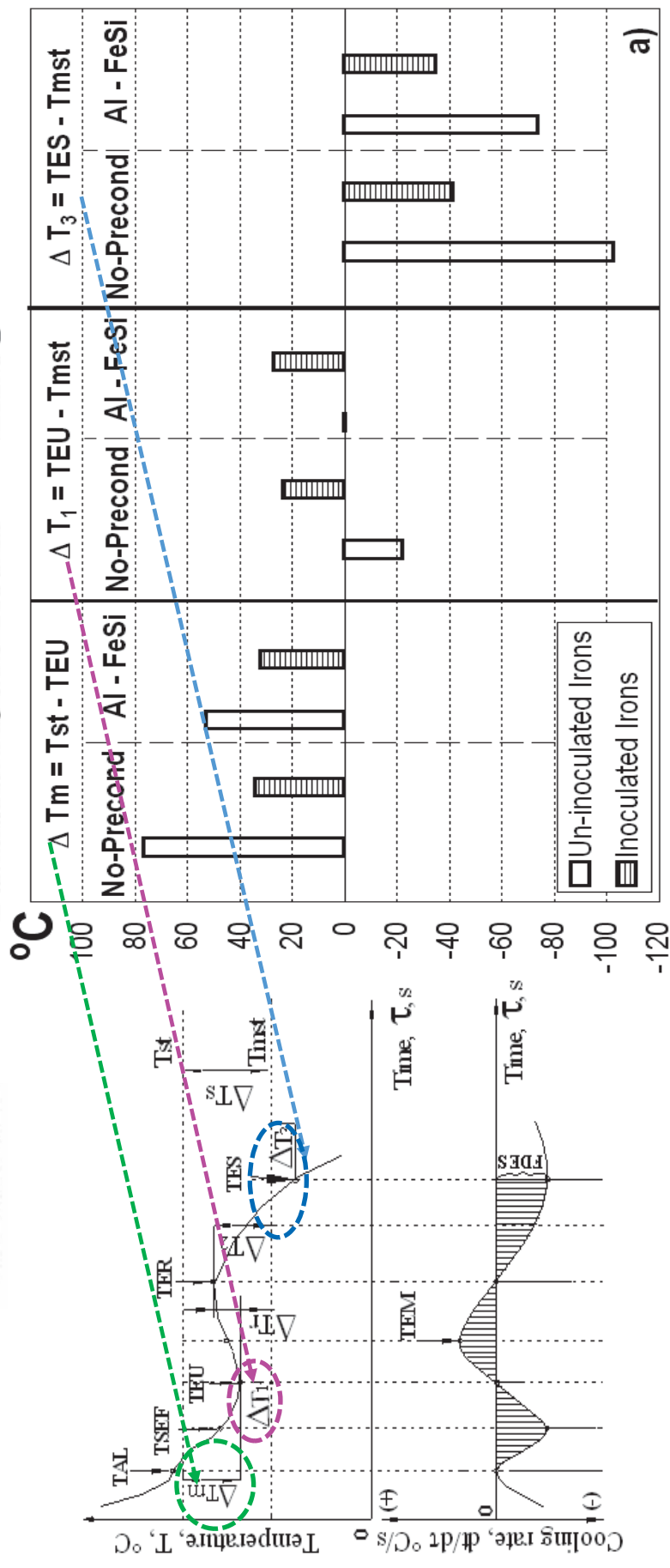
Al,Ca,Zr – FeSi Preconditioning

[0.1wt.% Al,Ca,Zr-FeSi preconditioning; 1.5wt.% FeSiCaAlMgRE Ladle Nodulization;
0.10wt.% Ca-FeSi In – Mould / In-Cup Inoculation; W_3 – ASTM A 367 Wedge Test – Resin Sand Mould]
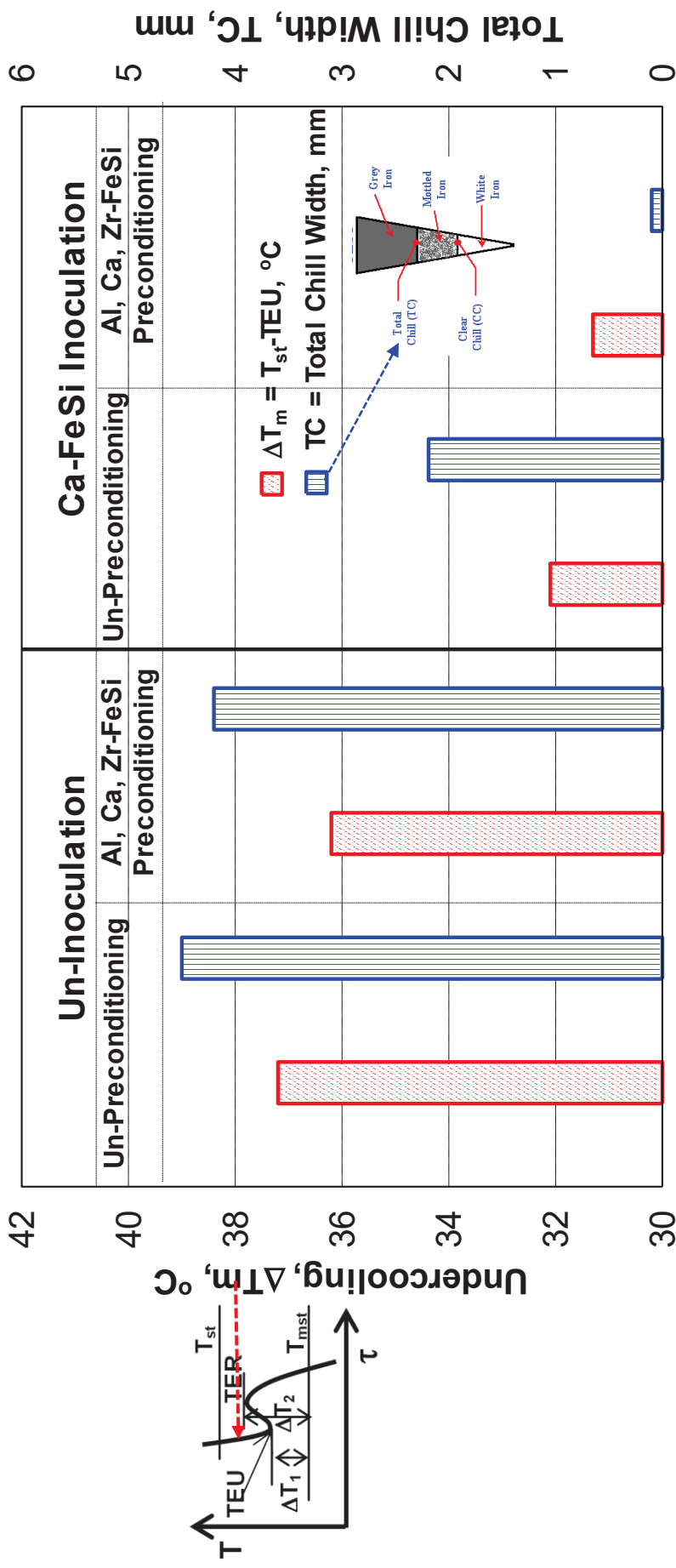
[S. Ojo, I. Riposan, Materi. Science and Technology, 2012, 28 (5), 576 – 581]

Ductile irons inoculated with low and high Al - content CaFeSi [CE = 3.95 – 4.25%]
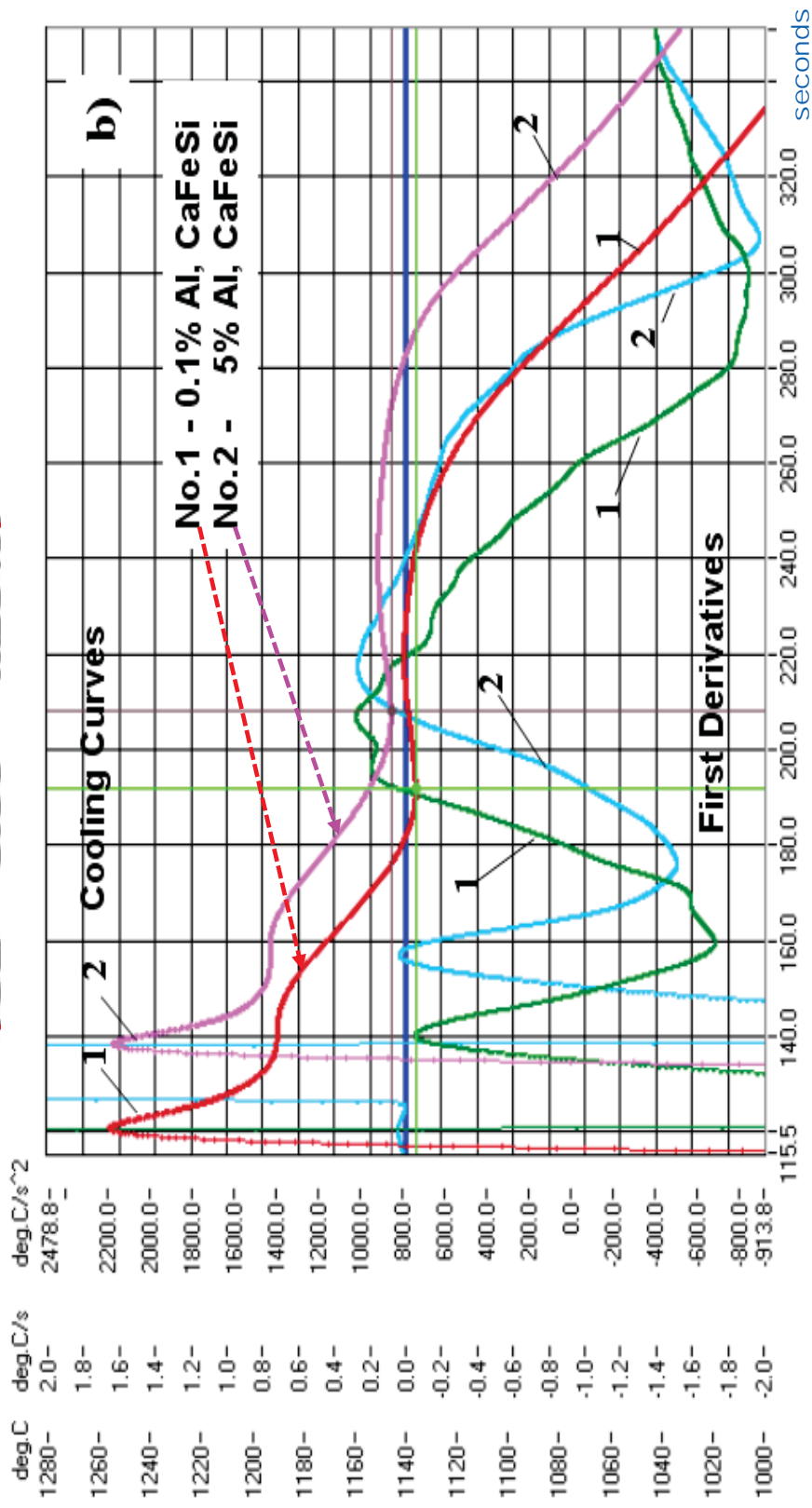
Al-residual [0.005–0.02 wt%]: medium potency graphitizing factor
- in both un-inoculated & inoculated irons; the most representative parameters of thermal analysis were improved;
- carbides amount decreased / nodule count increased

[I. Riposan, M. Chisamera, S. Stan, P. Toboc, G. Grasmo, D. White, C. Ecob, C. Hartung, AFS Trans., 2007, 115, 423]

INOCULATION / INOCULATION ENHANCING

[4.3 – 4.4%CE, 0.019 – 0.023%Mg$_{res}$, 30 – 50% Nodularity; Inoc. Enhancer: S,O,Al,Mg–CaSi]

COOLING CURVES ANALYSIS: TE$_{low}$ [TEU]
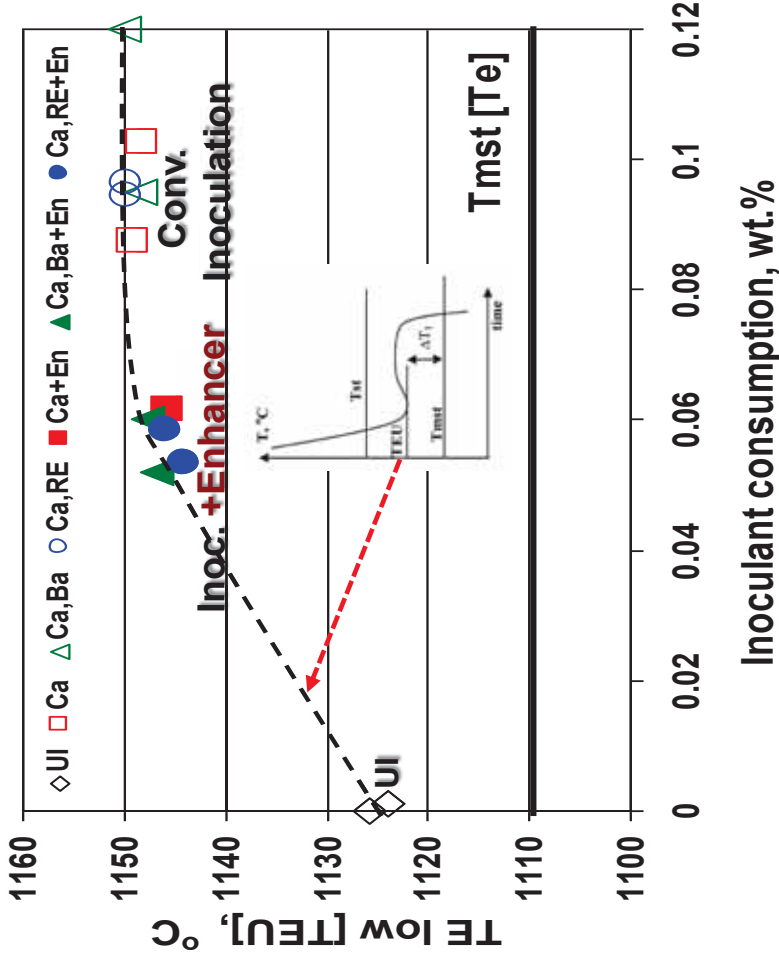
INOCULATION SPECIFIC FACTOR, ISF

$$ISF = \Delta TEU / [\text{wt.\% Inoculant}] = [TEU_{[I]} - TEU_{[UI]}] / [\text{wt.\%q Inoc.}]$$

Chart 1 (bar chart): Inoculation Specific Factor, ISF [TE low/TEU] vs Inoculation Variant

Inoc. + Enhancer / Conv. Inoculation

Variants: Ca, Ca,Ba, Ca,RE, Ca+En, Ca,Ba+En, Ca,RE+En

Y-axis: 0, 50, 100, 150, 200, 250, 300, 350, 400, 450

Chart 2 (scatter plot): TE low [TEU], °C vs Inoculant consumption, wt.%

Legend: ◇ UI, □ Ca, △ Ca,Ba, ○ Ca,RE, ■ Ca+En, ▲ Ca,Ba+En, ● Ca,RE+En

Inoc. +Enhancer / Conv. Inoculation

Tmst [Te]

Y-axis: 1100, 1110, 1120, 1130, 1140, 1150, 1160
X-axis: 0, 0.02, 0.04, 0.06, 0.08, 0.1, 0.12

POLITEHNICA University of Bucharest, ROMANIA

SIMULTANEOUS THERMAL / CONTRACTION ANALYSIS – SHRINKAGE SENSITIVENESS

*Twin mould cooling and contraction / expansion curve analysis

*Mould rigidity influence on contraction defects sensitiveness

*Adaptable instrument to foundry application

Typical shrinkage porosity in ductile iron casting

**(a) micro - shrinkage
[inter eutectic cells regions]**
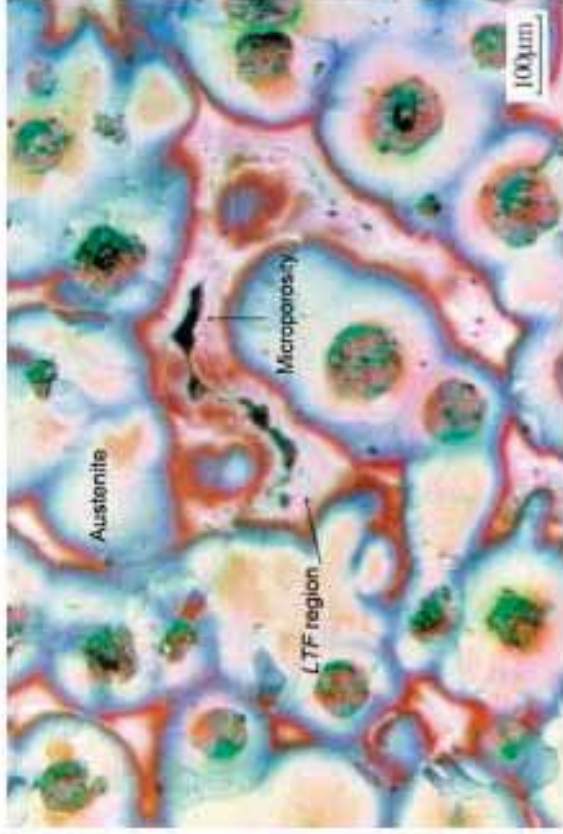
(b) macro - shrinkage

(a) Micro porosity
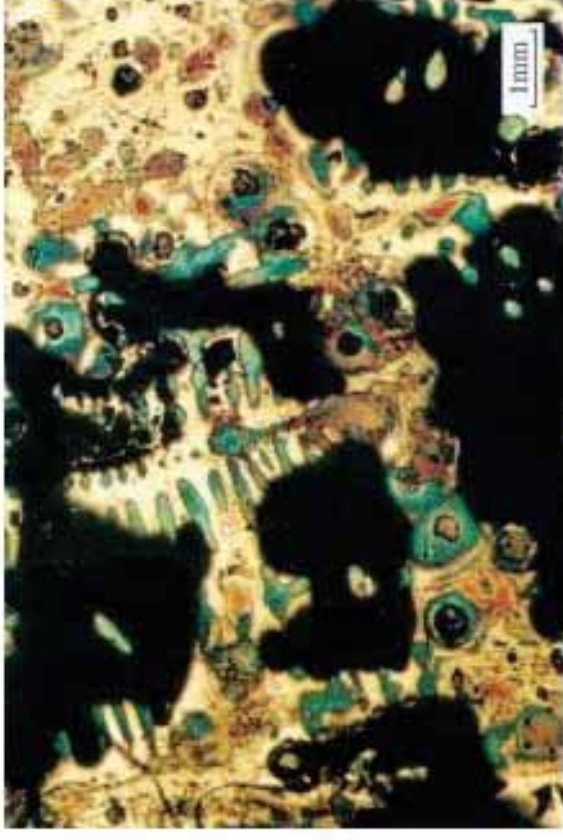
(b) Macro porosity

[Jiyang Z, 2010, Colour metallography of cast iron, China Foundry, 7(2), 183-198]

Factors Associated with Shrinkage in Ductile Iron Castings

➢ Chemistry

* Compositional Factor: CE = C+ 1/7 Si

  (CE < 3.9% - greater sensitivity)

* Mg_{res} [>]; Minor elements

➢ Mould

* Rigidity [<]; Hardness stability
  Cooling rate [<]

➢ Casting geometry

* Cooling modulus [>]; Feeding path

➢ Charge & melting

* Steel scrap / Pig iron ratio [>]; practice
* Superheat level [>]

➢ Pouring practice

* Pouring temperature [>]

➢ Inoculation

* Nodule count [>] & size distribution [<]

Typical Mould Media in Iron Castings Production

[MDH – Mould Dietert Hardness; MTD – Mould Thermal Diffusivity]
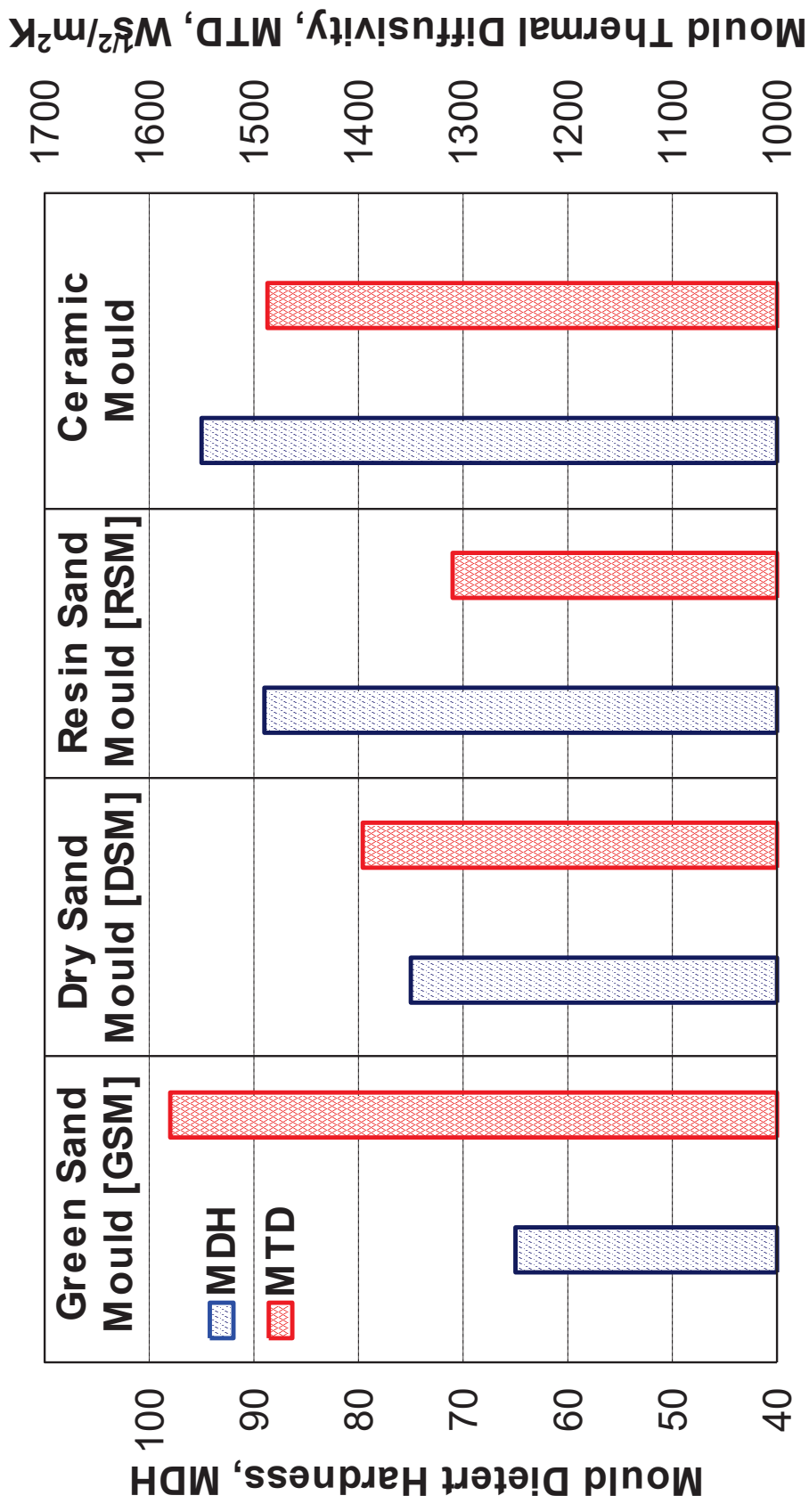
TWIN MOULD COOLING AND CONTRACTION / EXPANSION CURVE ANALYZER [CCCA]
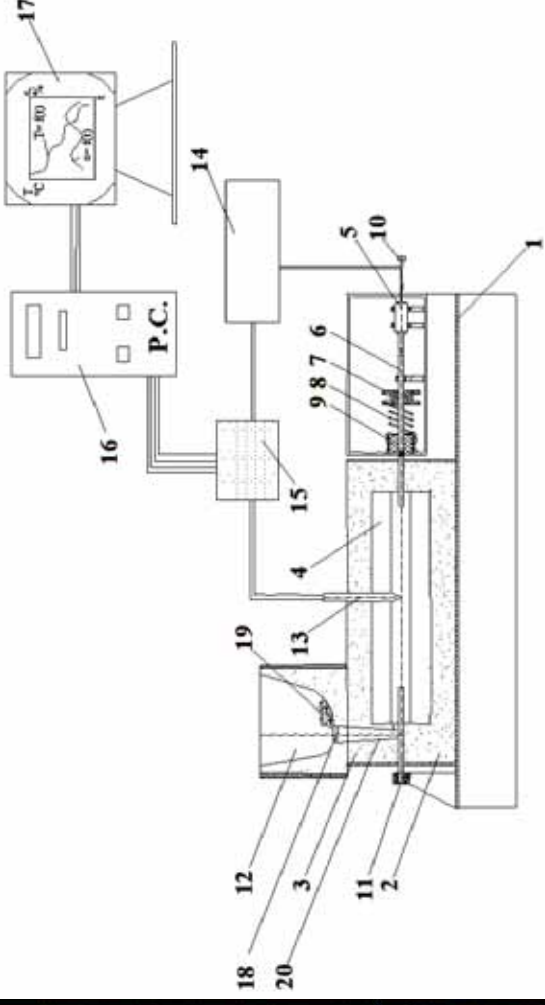
1. Stand; 2. Lower mold; 3. Upper mold; 4. Sample (bar); 5. Displacement transducer;
6. Mobile rod; 7. Thermal radiant; 8. Pretensioning spring; 9. Spring tensioning screw;
10. Fine regulation screw; 11. Rigid rod; 12. Pouring basin; 13. K- type thermocouple;
14. L.V.D.T. amplifier; 15. Connector box; 16. Computer (AT- MIO 10 interface);
17. Display monitor; 18. Fusible steel plate; 19. Inoculant; 20. Sprue.

POLITEHNICA University of Bucharest, ROMANIA

Schematic of Cooling / Contraction Curves and their First Derivatives for Ductile Iron
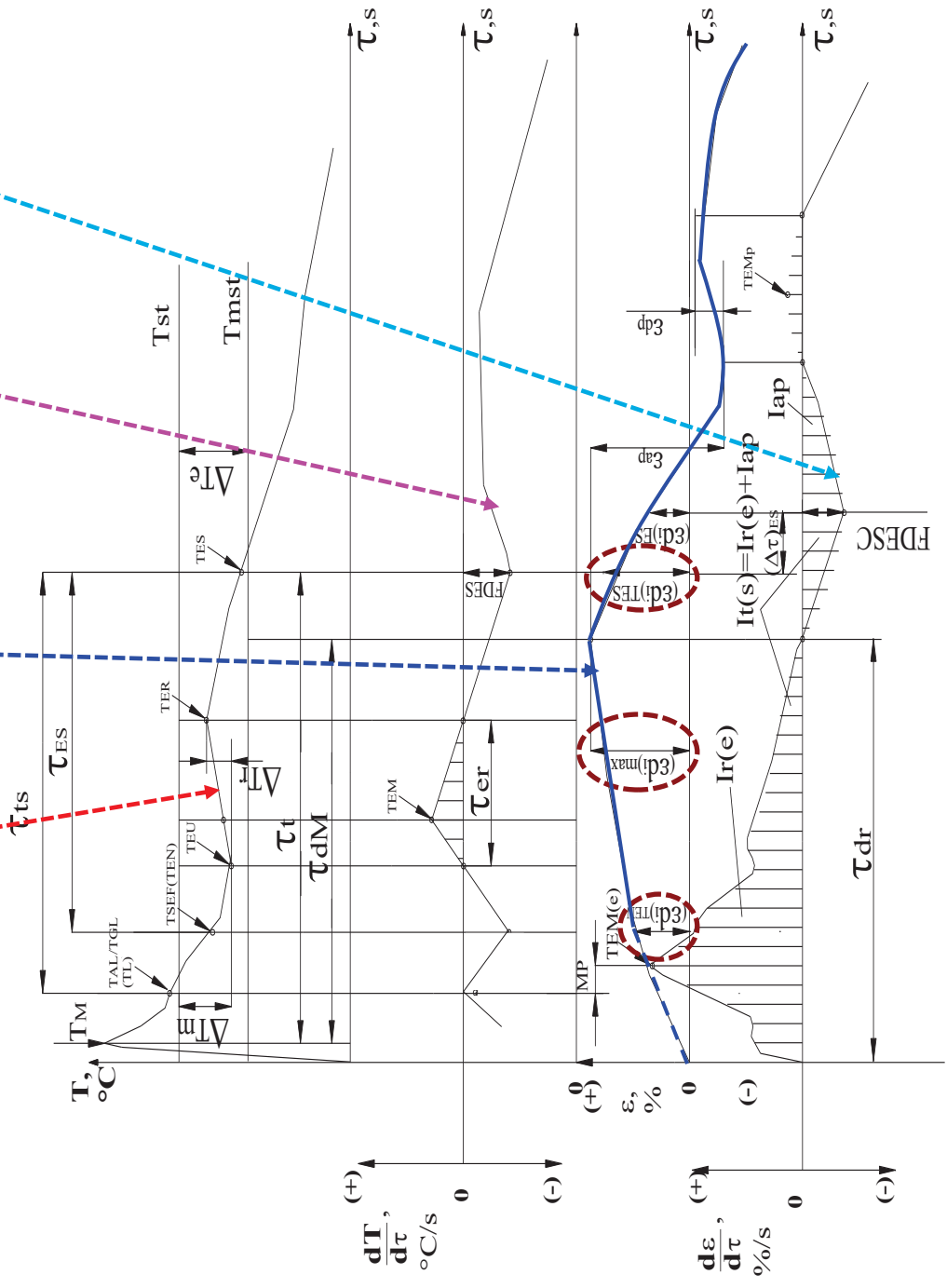
Typical Cooling and Contraction / Expansion Curves and their first derivatives
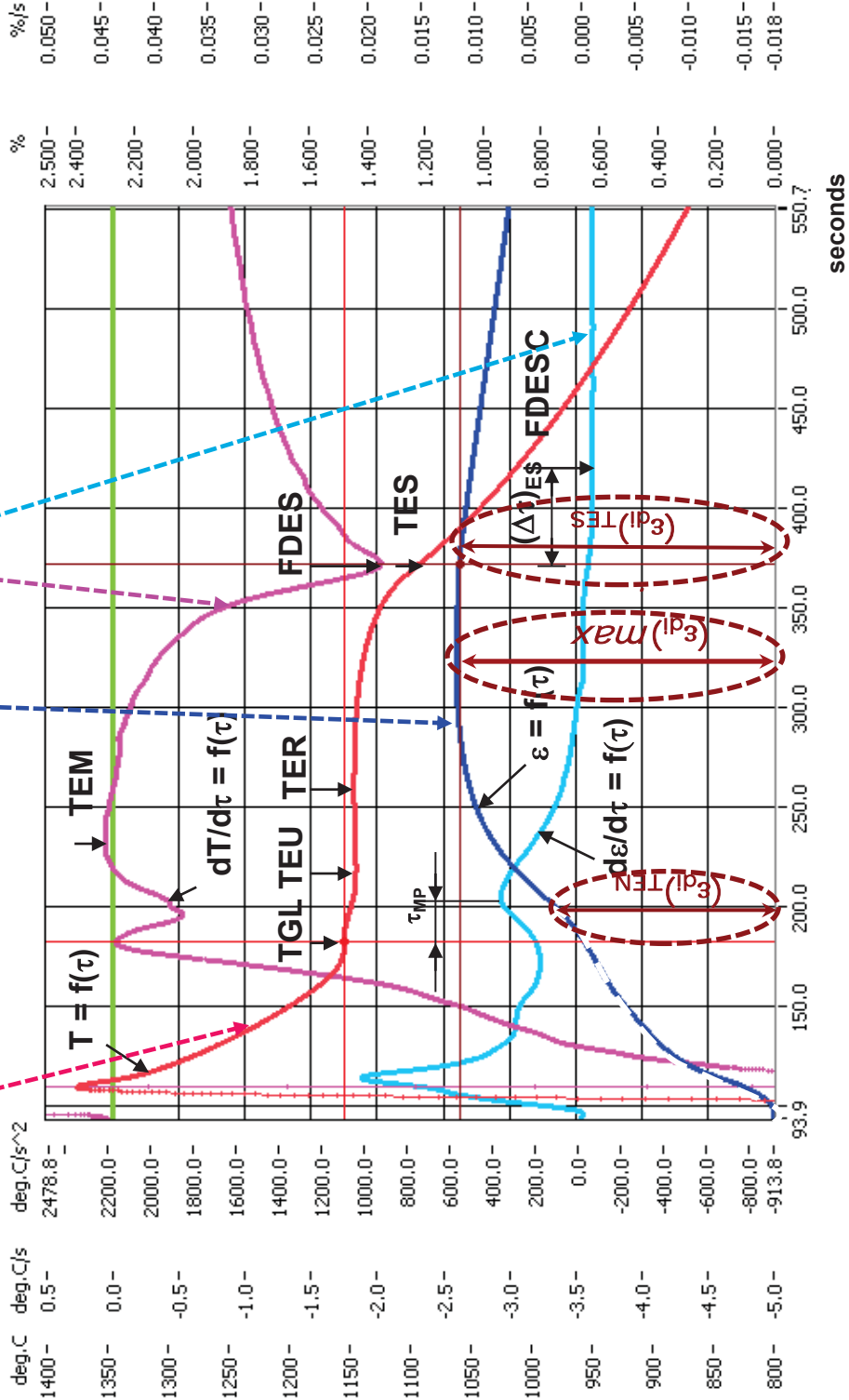
❖CCCA – REPRESENTATIVE PARAMETERS

*Temperature: Max. Eut. Underc. (TEU), Recalescence (TER), End Solidif. (TES)

*Eutectic Undercooling:

$\Delta Tm = Tst - TEU$; $\Delta T_1 = TEU - Tmst$; $\Delta T_2 = TER - Tmst$; $\Delta T_3 = TES - Tmst$

*Eutectic Recalescence: $\Delta Tr = TER - TEU$

*First Derivative: Cooling (FDES) / Contraction (FDESC) Curves, at (TES)

*Maximum Rate of Recalescence (TEM) / Eutectic Expansion [TEM (e)]

*Maximum Initial Expansion, $(\varepsilon di)_{max}$

*Expansion in the moment of the Start $(\varepsilon di)_{TEN}$ / End $(\varepsilon di)_{TES}$ of Eutectic freezing

*The First Derivative of the Contraction Curve *during* Eutectic Expansion, Ir(e)

*Total integral of the First Contraction Curve Derivative, It(s) = Ir(e) + Iap

(up to the end of ante-pearlitic contraction)

❖ CCCA - EXPERIMENTAL PARAMETERS

❖ Two work positions:

*Simultaneous testing of two inoculants / two mould media / two addition rates

❖ Two different mould media tested:

*GSM - Green Sand Mould (60-70 Dietert Hardness, 125 N/cm^2 Compressive Strength)
*FRM - Furan Resin Mould (89 Dietert Hardness 1400 N/cm^2 Tensile Strength)

❖ Oblong Iron Samples:

*30 mm square cross section bar x 200 mm length / 0.72 cm Cooling Modulus [CM = V / A]
*Structure and Shrinkage / Micro-shrinkage evaluation

❖ LABVIEW Program – Specialized Software :

*Transducer for Temp. Recording: 5000 readings / sec
*Linear Displacement Transducer: 0.001mm precision

√ Induction Melting / Tundish Cover treatment

- 8kg iron, 1500-1520°C, 2.5wt.% FeSiMg6RE 0.6

√ Pouring Basin [CCCA] Inoculation

- 1350 - 1380°C, 0.2wt% Inoculant, 0.2 - 0.7 mm grain size, FeSi-based alloys

√ Final Ductile Irons: CE = 4.5 - 4.6%, Mg$_{res}$ = 0.06 – 0.07%

POLITEHNICA University of Bucharest, ROMANIA

Typical Shrinkage view in the frontal longitudinal plane of the CCCA bars:

I – dispersed macro-shrinkage; II – concentrated shrinkage

RSM – Resin Sand Mould

GSM – Green Sand Mould

POLITEHNICA University of Bucharest, ROMANIA
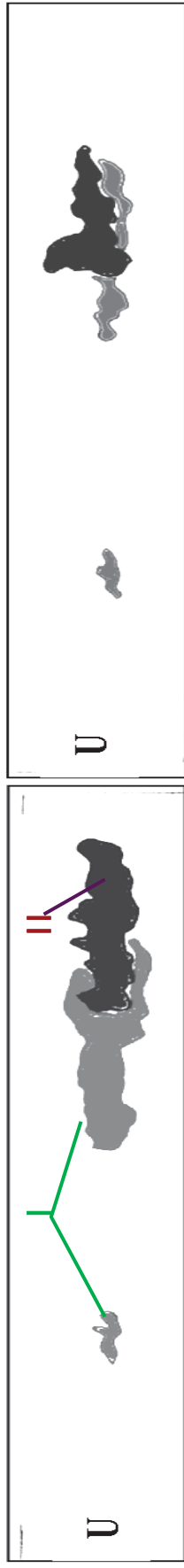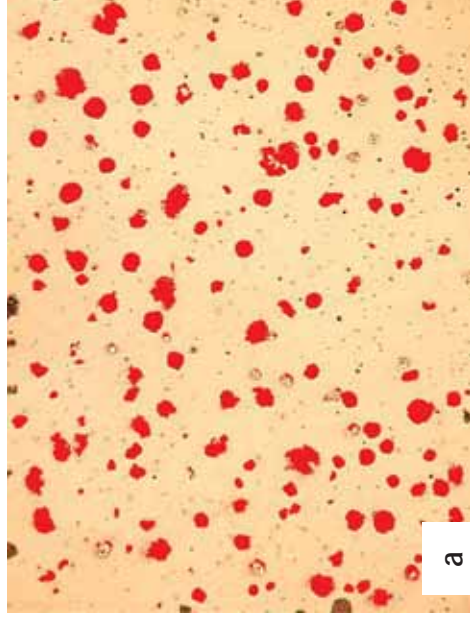
Maxim. Initial Expansion – Mould Hardness Relationship
[GSM = Green Sand Mould vs RSM = Resin Sand Mould]

$y = -0.0174x + 1.7606$
$R^2 = 0.8371$

RSM

GSM

$(\varepsilon_{di})_{max}$, %

Mould Dietert Hardness

POLITEHNICA University of Bucharest, ROMANIA
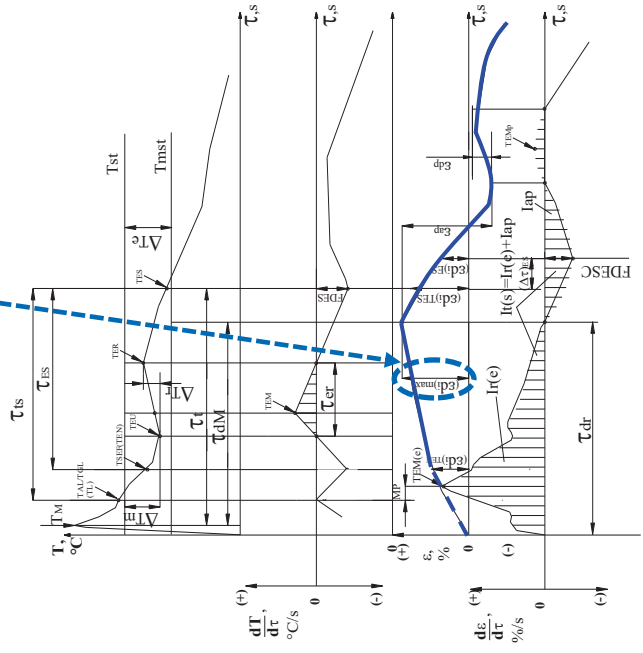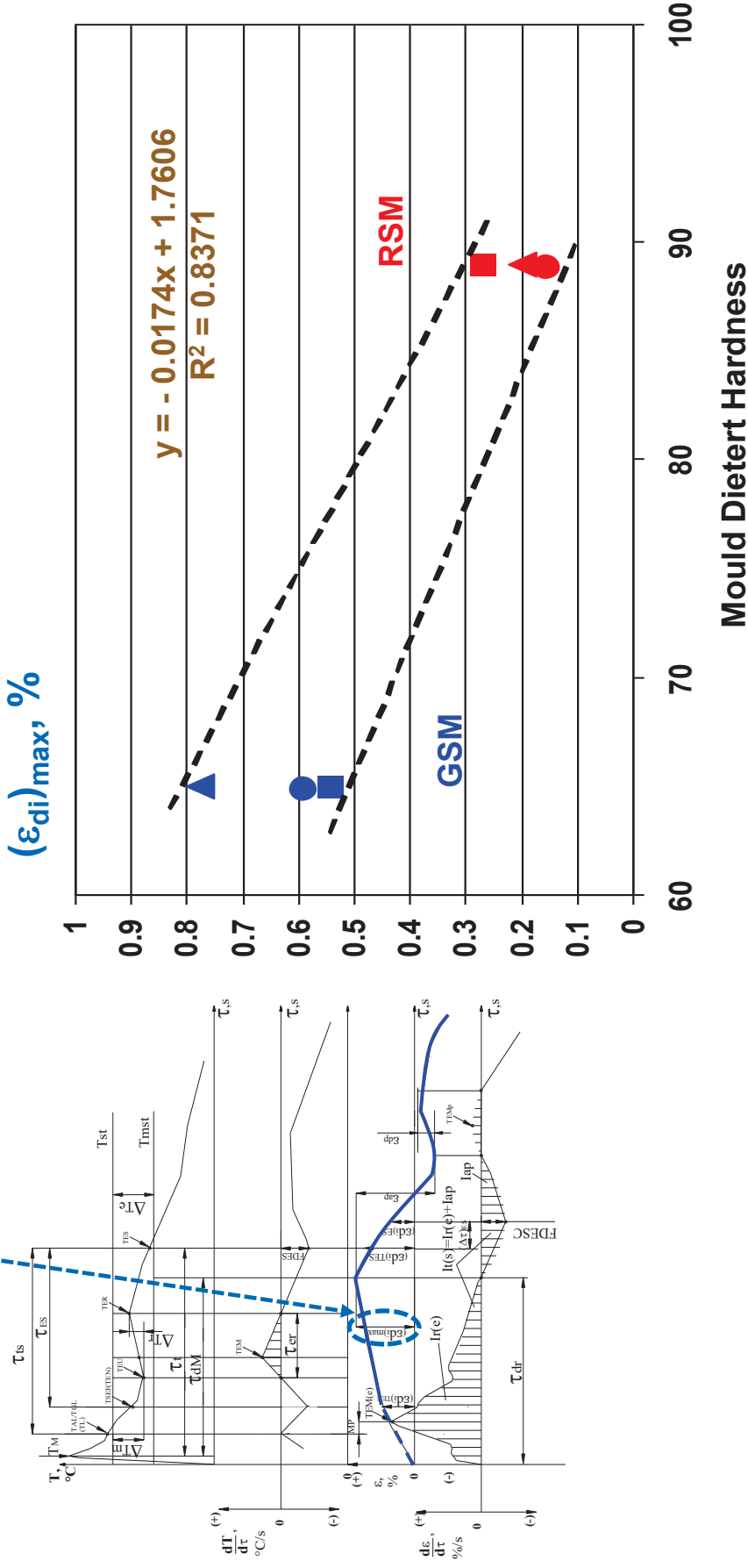
EFFECTS OF MAXIMUM INITIAL EXPANSION [$(\varepsilon di)_{max}$, %]
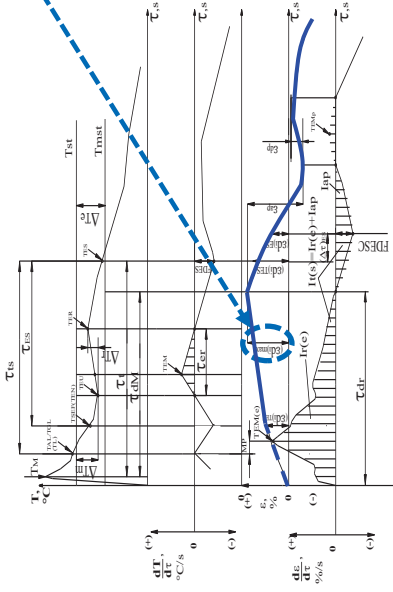
[GSM = Green Sand Mould vs RSM = Resin Sand Mould]

[Cshv, vol.%] Conc. Shrinkage Vol.; [ρ, g/cm^3] Apparent Density

[ρ_1 – all Shrinkage Types / ρ_2 – only Microshrinkage]

$y = -0.4371x + 7.2276$
$R^2 = 0.7947$

ρ_2

GSM

ρ_1

$y = -0.2872x + 6.8881$ $R^2 = 0.4436$

RSM

ρ, g/cm^3

$(\varepsilon di)_{max}$, %

$y = 3.2621x + 0.6821$
$R^2 = 0.7537$

GSM

RSM

Cshv, %

$(\varepsilon di)_{max}$, %
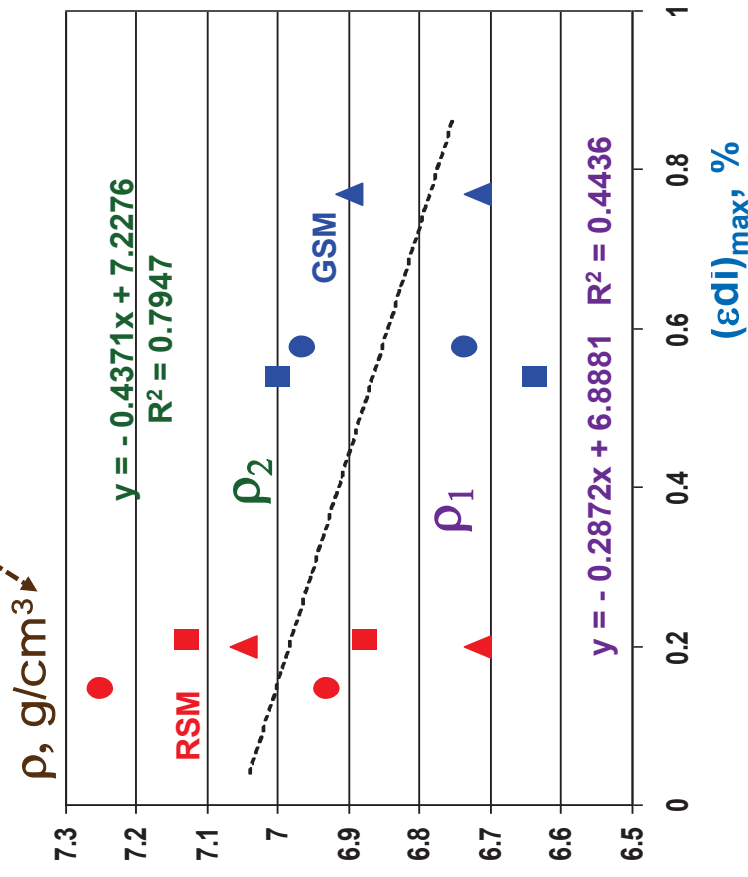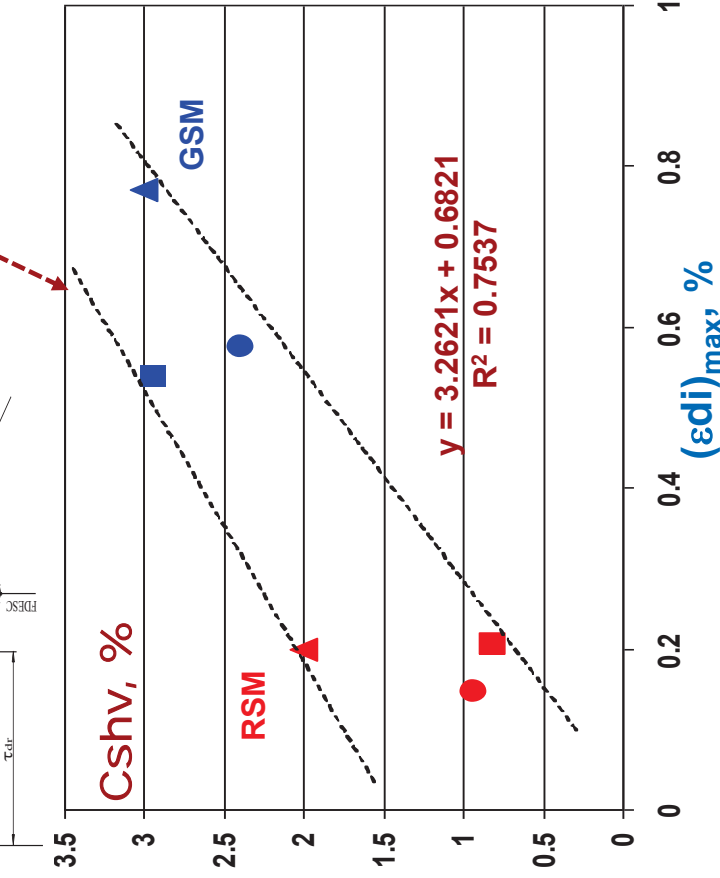
Ir(e)-The First Derivative of the Contraction Curve, Eutectic Expansion
– Mould Hardness Relationship
[GSM = Green Sand Mould vs RSM = Resin Sand Mould]
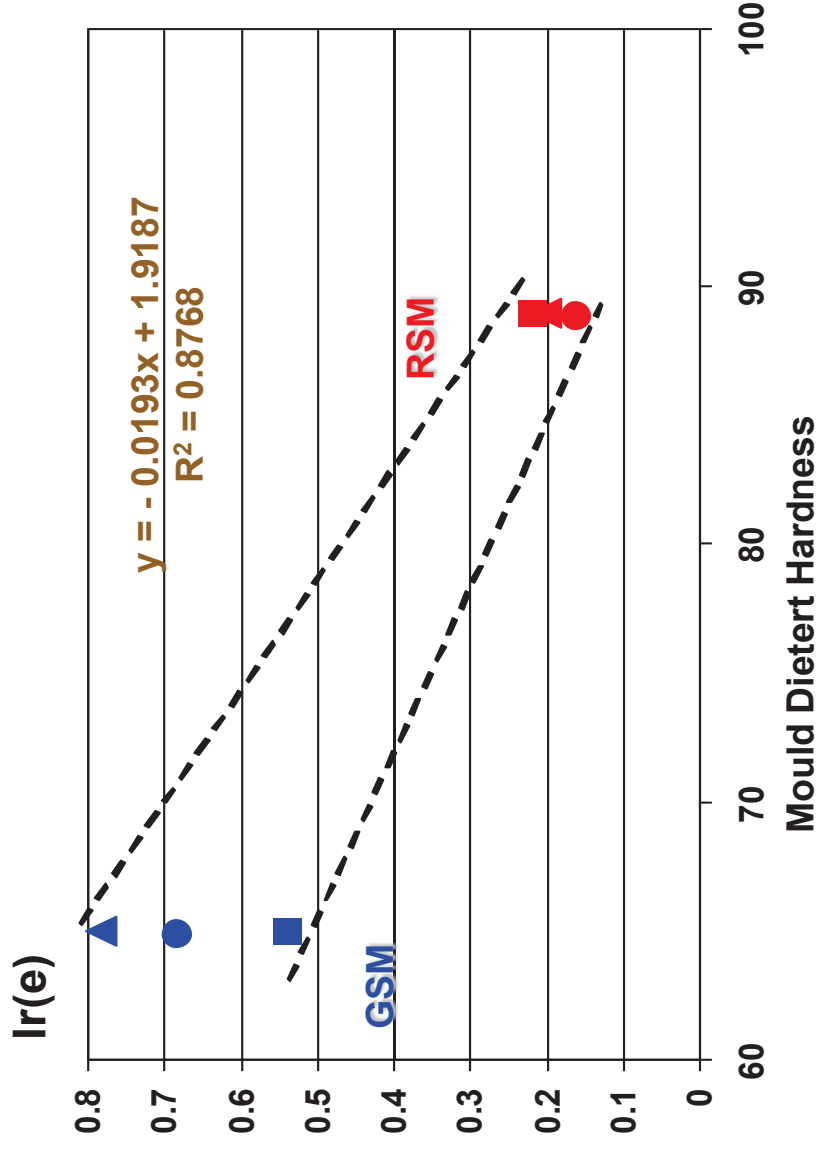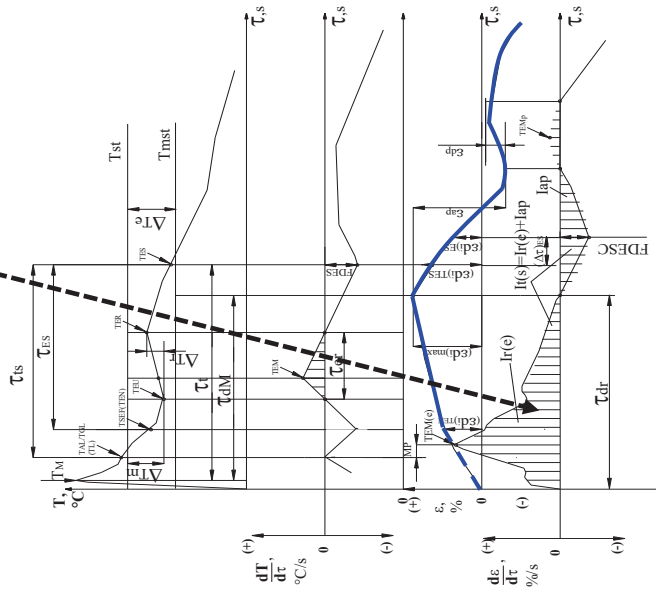
$$y = -0.0193x + 1.9187$$
$$R^2 = 0.8768$$

RSM

GSM

Ir(e)

Mould Dietert Hardness

Ir(e) - Effects of The First Derivative of the Contraction Curve during Eutectic Expansion

[GSM = Green Sand Mould *vs* RSM = Resin Sand Mould]

[Cshv, vol.%] Conc. Shrinkage Vol.; [ρ, g/cm³] Apparent Density

[ρ₁ – all Shrinkage Types / ρ₂ – only Microshrinkage]

$y = -0.4334x + 7.229$
$R^2 = 0.7854$

$y = -0.2802x + 6.8871$ $R^2 = 0.4245$

$y = 3.2397x + 0.6751$
$R^2 = 0.7393$

ρ, g/cm³

ρ₂

ρ₁

GSM

RSM

Cshv, %

Ir(e)

POLITEHNICA University of Bucharest, ROMANIA

Total integral of the First Contraction Curve Derivative,

It(s) = Ir(e) + Iap (up to the end of ante-pearlitic contraction).

[GSM = Green Sand Mould vs RSM = Resin Sand Mould]

$y = -0.0194x + 1.5077$

$R^2 = 0.8468$

POLITEHNICA University of Bucharest, ROMANIA
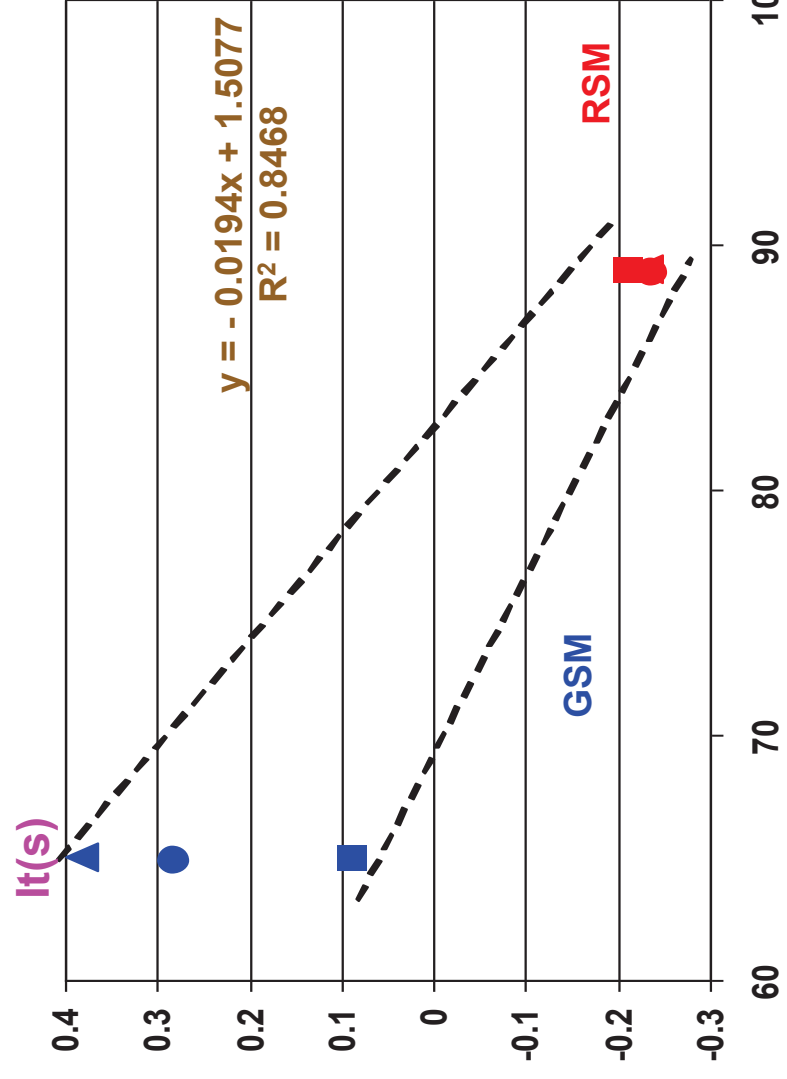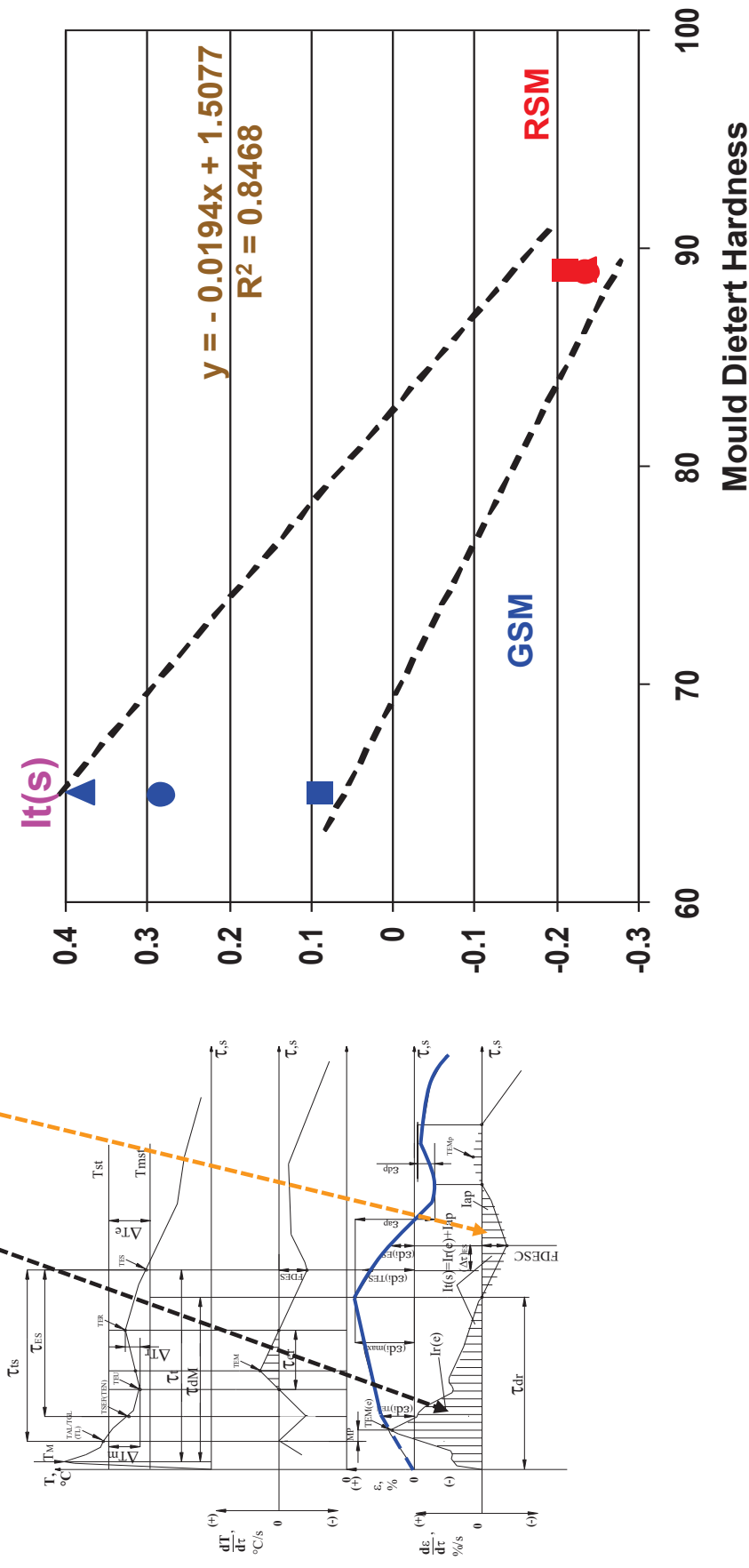
EFFECTS OF TOTAL INTEGRAL OF THE FIRST CONTRACTION CURVE DERIVATIVE [It(s) = Ir(e) + Iap]
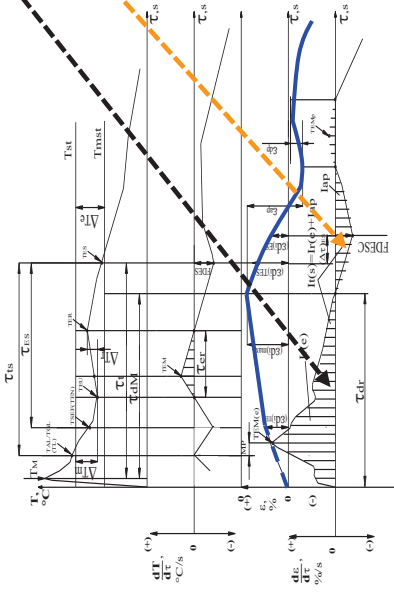
[GSM = Green Sand Mould *vs* RSM = Resin Sand Mould]

[Cshv, vol.%]Conc. Shrinkage;[ρ, g/cm³] Apparent Density

[ρ₁ – all Shrinkage Types / ρ₂ – only Microshrinkage]

ρ, g/cm³

$y = - 0.4104x + 7.0444$
$R^2 = 0.7137$

GSM

ρ₂

ρ₁

RSM

$y = - 0.2534x + 6.7679$ $R^2 = 0.3516$

It(s)

Cshv, %

GSM

$y = 3.1125x + 2.0453$
$R^2 = 0.6901$

RSM

It(s)
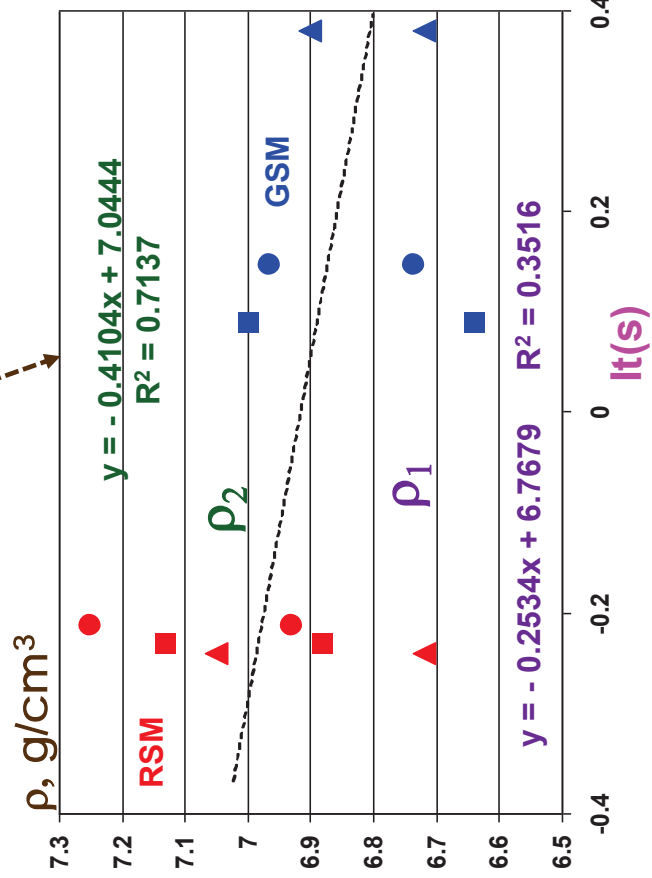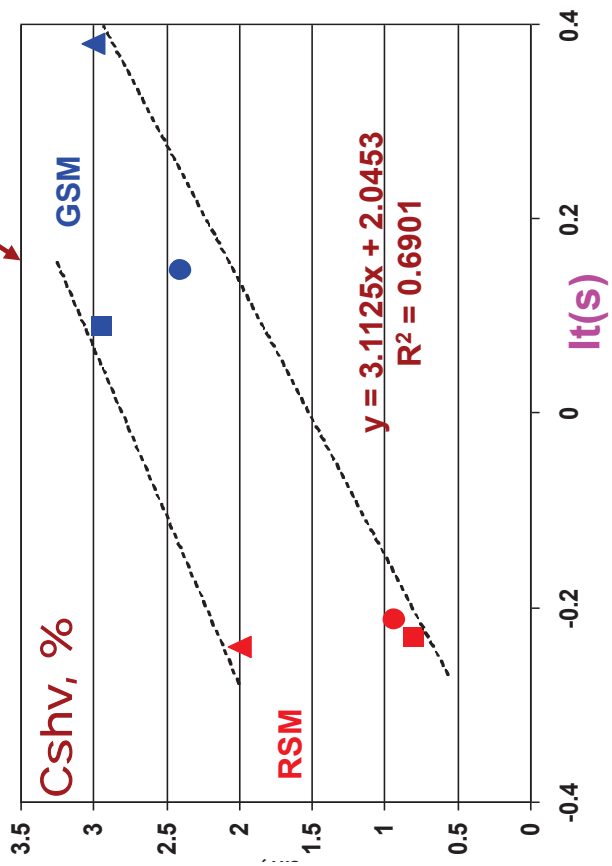
EFFECTS OF UNDERCOOLING AT THE END OF SOLIDIFICATION
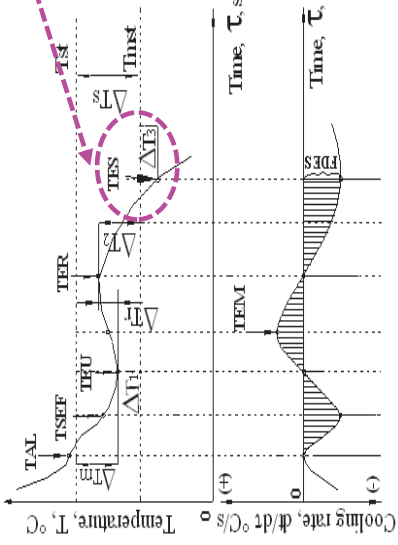
$\Delta T_3 = TES - Tmst, \, ^\circ C$

[GSM = Green Sand Mould vs RSM = Resin Sand Mould]

[Cshv, vol.%] Conc. Shrinkage Vol.; [ρ, g/cm^3] Apparent Density
[ρ_1 – all Shrinkage Types / ρ_2 – only Microshrinkage]

ρ, g/cm^3

$y = 0.0121x + 7.1399$
$R^2 = 0.3406$

ρ_2

ρ_1

$y = 0.0127x + 6.8666 \quad R^2 = 0.4904$

$\Delta T_3, \, ^\circ C$

Cshv, %

$y = -0.0487x + 2.3283$
$R^2 = 0.9762$

GSM

$y = -0.1097x + 0.6197$
$R^2 = 0.9979$

RSM

$\Delta T_3, \, ^\circ C$

Temperature, T, °C

Cooling rate, dt/dt °C/s

Time, τ, s

TAL
TSEF
TEU
TER
TES
Tst
Tmst
ΔT_m
ΔT_1
ΔT_2
ΔT_3
ΔT_5

TEM
FDES
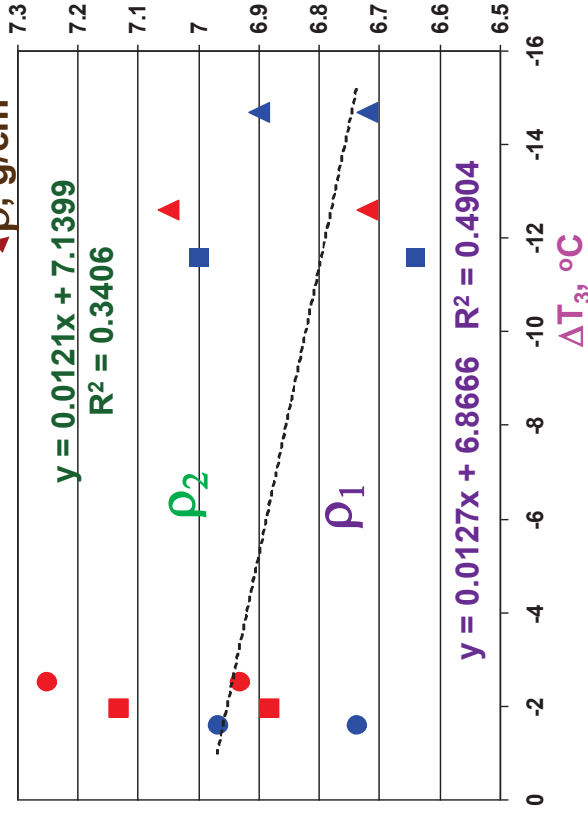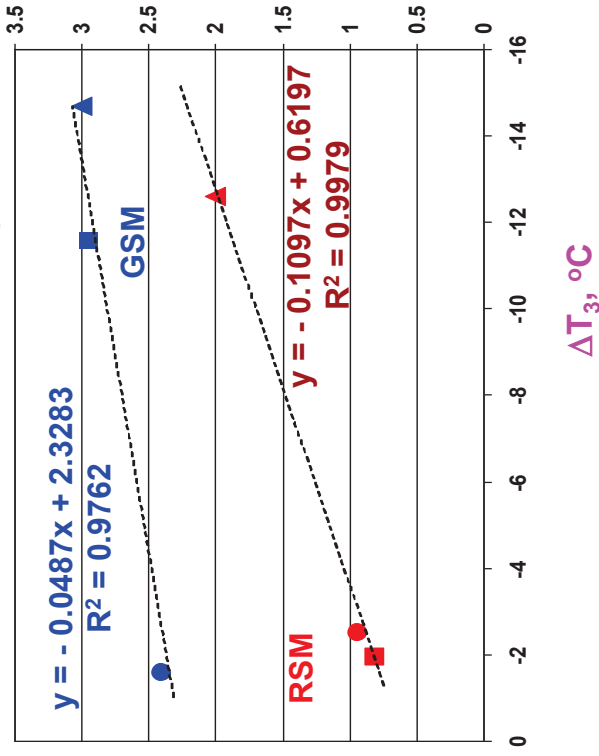
SUMMARY

❖ The technique incorporating Cooling & Contraction / Expansion Analysis, *is useful to test*

- different mould media,

- different iron chemistries

- different inoculants,

- different inoculant additions,

side by side, under otherwise constant conditions,
      in laboratory or plant environments

Its application is illustrated by shrinkage tendency results in ductile iron *as affected by*

- mould rigidity (Green Sand *vs* Resin Sand Moulds)

SUMMARY

➤ [ΔT_3 = TES – Tmst] - **Undercooling at the end of solidification**
  - relative to the metastable (carbidic) equilibrium temperature *and*

*The expansion within the solidification sequence [$(\varepsilon_{dil})max$]
  - appear to have a strong influence on the susceptibility to
    macro – *and* micro – shrinkage in ductile iron castings

➤ **With higher Maximum Initial Expansion [$(\varepsilon_{dil})max$] *and / or***
  - shortly before the end of eutectic solidification *and / or*
More negative Undercooling *at the* End of Solidification [ΔT_3],
  - there is an increase in concentrated & dispersed shrinkage volumes,
  - which lowers the apparent density of ductile iron castings.
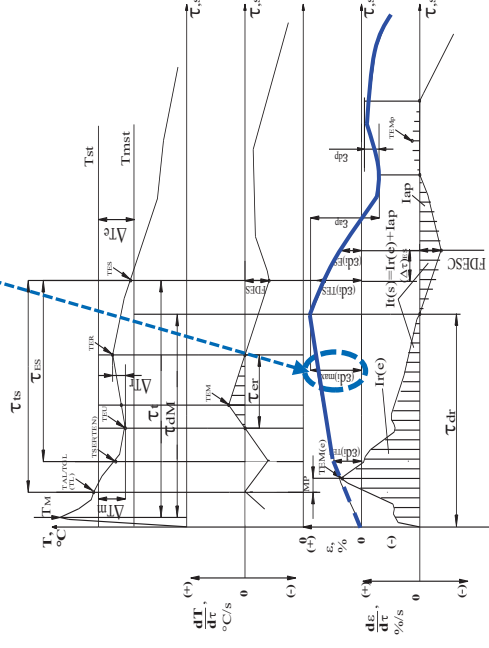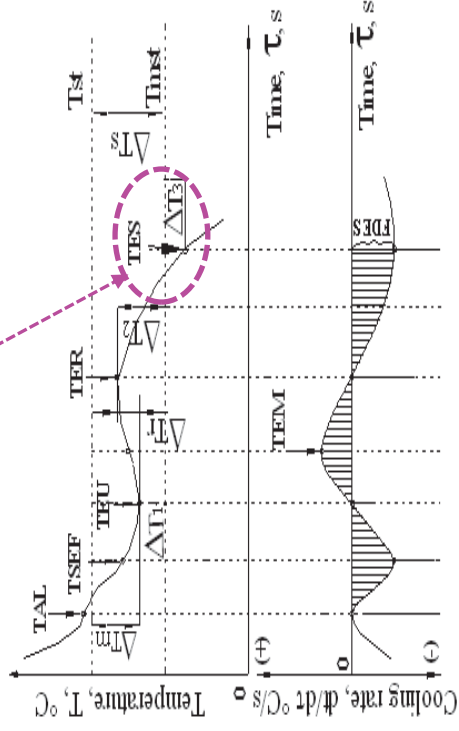
Future Actions to Improve the Performances of Iron Melt

Solidification Thermal Analysis / Contraction System

∆ **Higher number of un-treated and treated iron experiments, for statistical approach**

∆ **Cooling Curve *and* Contraction Curve parameters relationship**

∆ **The most representatives CCCA parameters selection**

∆ **Special hardware / software, simultaneous CCCA recording and reading data**

∆ **Casting microstructure and casting defects foreseen**

∆ **Effects of representative technological influencing factors evaluation**
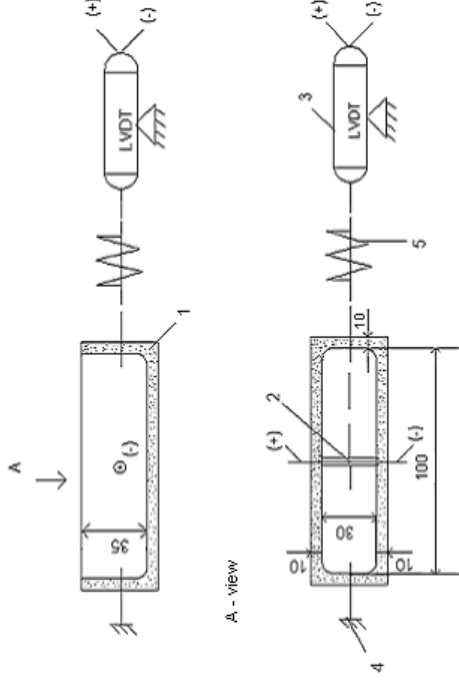
ACKNOWLEDGEMENT

POLITEHNICA University of Bucharest, ROMANIA
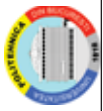
THANK YOU

16th **INTERNATIONAL FOUNDRYMEN CONFERENCE**
Global Foundry Industry – Perspectives for the Future
Opatija, May 15th-17th, 2017

BIG-DATA ANALYTICS FOR THE PREDICTIVE MODELLING
OF ALUMINIUM ALLOYS

Varužan Kevorkijan[1], **Sara Hmelak**[2], **Branko Hmelak**[2], **Peter Cvahte**[1],
Borislav Hostej[1], **Irena Lesjak**[1]

[1]Impol Aluminium Industry, Slovenska Bistrica, Slovenia
[2]Alcad d.o.o., IT Company, Slovenska Bistrica, Slovenia

Abstract

An industrial tool developed within the Impol Aluminium Group for a cognitive modelling of wrought aluminium alloys is OPTIAl – the cognitive computing algorithm for correlating the properties of wrought aluminium alloys, the chemical composition and the processing parameters. The inductive learning of the algorithm was performed by applying the experimentally confirmed equivalency of different technological paths, able to provide the same combination of properties. In the first step, through a process of data mining, a data matrix was created, consisting of the results of standard, room-temperature tensile tests and the corresponding technological paths for different production lots of the AA 6110 alloy. Next, based on cognitive processing of the accumulated data, the most probable technological path-property correlations were identified. Finally, various standard (and some non-standard) alloy compositions, derived from the alloy AA 6110, and the processing parameters were cognitively inducted to provide the desired combination of properties.

The so far existing validation of the above-described methodology was performed through regular production of more than 30 cognitively computed alloys of the standard chemical composition and their detailed characterization. It was found that by applying the cognitive-computing methodology on proper experimentally determined values, either the chemical composition or the mechanical properties can be predicted with high accuracy, sufficient for most industrial applications.

Keywords: big data, predictive modelling, cognitive computing, aluminium alloys

*Corresponding author (e-mail address): <u>*varuzan.kevorkijan@impol.si*</u>

INTRODUCTION

To remain competitive with other advanced materials, e.g., high-strength steels, in solutions with "the proper materials in the proper place", wrought aluminium alloys must provide

superior functional and cost-effective solutions. To achieve this, it will be necessary to design and develop new, wrought aluminium alloys, focusing on the desired performance – and not on the exact chemical composition [1]. A fundamental change in the design of advanced, wrought aluminium alloys would be the introduction of new chemical compositions with broader intervals of concentration for the critical alloying elements, i.e., iron and silicon, as well as other alloying elements and trace elements [2]. However, for the successful formulation of these new alloys, experimentally established relations between the changes in the chemical composition and the processing (heat treatment and forming), on the one hand, and the properties, on the other, are necessary [3].

In this paper an algorithm for finding the correlation between the properties of wrought aluminium alloys, the chemical composition and the processing parameters will be presented and validated.

THE MAIN PRINCIPLES OF MODELLING RECYCLING-FRIENDLY ALLOYS

MODELLING THE CHEMICAL COMPOSITION

From the point of view of modelling, it is important to note that in the functional correlation between a selected alloy property, e.g., the tensile strength (TS), and the compositional and processing variables, all the variables appear as intervals with a normal (Gaussian) distribution.

Therefore, we can write:

$$TS\,(\mu, \sigma) = \, f[C_1(\mu_1, \sigma_1), .., C_n(\mu_n, \sigma_n), P_1(\pi_1, \Theta_1), .., P_m(\pi_m, \Theta_m)] \tag{1}$$

where $C_i(\mu_i, \sigma_i)\, i = 1,2, \dots, n$ represents the concentration intervals with a Gaussian distribution of concentrations for the individual alloying elements, while $P_j(\pi_j, \Theta_j)\, j = 1,2, \dots, m$ represents the individual processing parameters that are also given as intervals with a Gaussian distribution. Here, μ_i and π_j are the mean or expectation of the distribution of the individual variable (the concentration or processing parameter), while σ_i and Θ_j represent the standard deviations of the concentrations and the processing parameters, respectively.

The complexity in the formulation of non-standard compositions of wrought aluminium alloys necessary to achieve the desired combination of properties is mainly in the large number of variables involved in the methical development of the properties and the proper combination of properties. The only useful strategy in an industrial environment is data mining, performed on the existing results of chemical analyses and measurements of the mechanical properties from the regular quality control of wrought aluminium alloys and the corresponding semi-products, in combination with the parameters of the heat treatment and forming. These data are available, but only collected for alloys having the *standard* composition. Thus, the question is: how can we use these values to extrapolate to the alternative, i.e., non-standard, compositions?

If the correlation between the properties and the corresponding technological path (chemical composition and technological parameters) is known within the standard

5

□

intervals, then the values obtained by the extrapolation from the existing data can apply for tailoring the composition and/or properties of non-standard aluminium alloys.

For the practical application of such an extrapolation cognitive computing technique it is important to ensure that the extrapolated values are sufficiently reliable, i.e., that they are comparable with the experimental findings. To achieve this, it is reasonable to validate the cognitive modelling by creating the interpolated values of the mechanical properties and after that, if these fit well with the experimental findings for the standard compositions, to apply the same methodology for extrapolating the properties of an alloy of the non-standard composition. The basic idea of the process is illustrated in Figure 1.
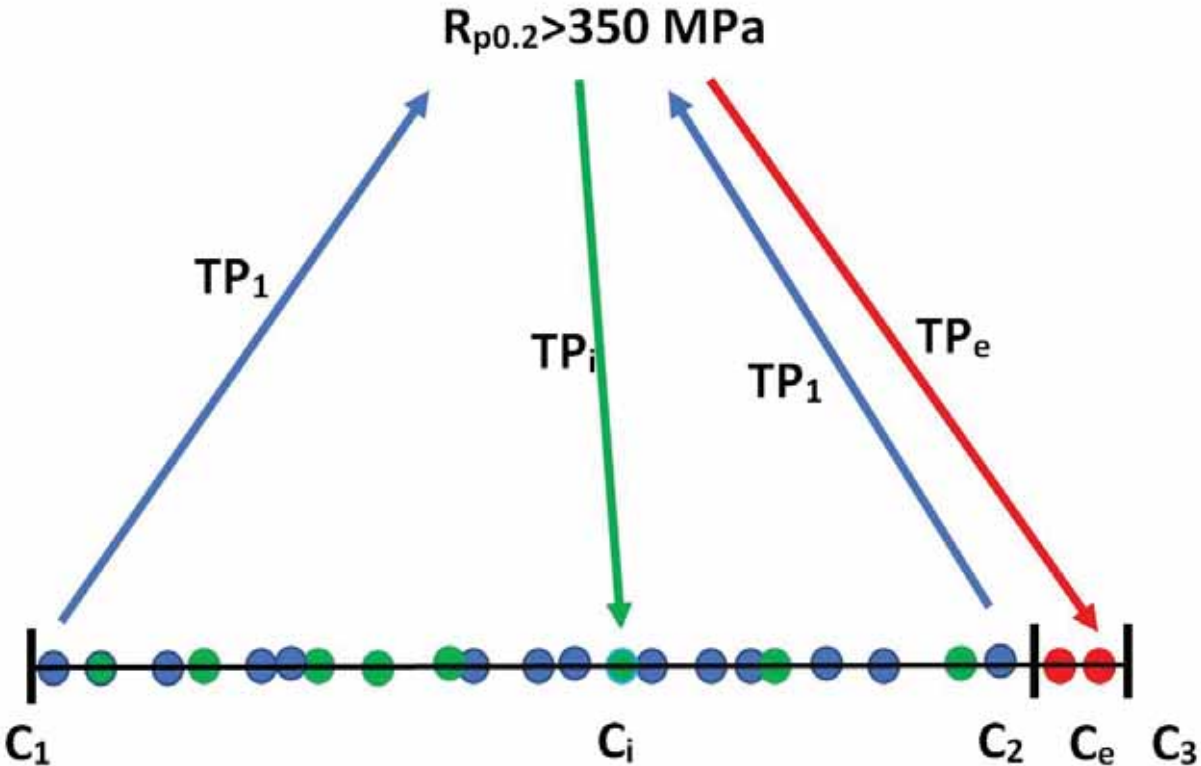
Figure 1. Schematic presentation of the alloy-properties modelling process based on the required values of the selected mechanical properties. Here, the TP_s represent the corresponding technological paths, while the C_s are the concentrations of the selected alloying element

The first step in the modelling is the calculation of the interpolated values of the TS for various standard compositions. The final step is the calculation of an extrapolated value of TS for an alloy of the non-standard composition.
Note that increasing the upper concentration limits of the alloying elements, outside of the standard compositions, should be limited to just below some critical value: in practice, typically less than 20%. Under these boundary conditions, the extrapolated values of the alloy's properties, caused by the non-standard alloy composition, provide a reliable prediction of the alloy's properties, and are suitable for industrial use.

To ensure sufficient accuracy in the prediction of the alloy's properties, the cognitive extrapolation should be performed on the appropriately classified big data. The methodology used in this work is illustrated in Figures 2 and 3.

Two kinds of classification for the big data were performed: (i) clustering of the data with almost the same values, and (ii) selection of the data intervals with the same or similar widths as the extrapolated ones.

The classification based on clustering of the data is illustrated in Figure 2. The difference in the concentration of the alloying element for the data in the cluster is negligible ($\Delta C \to 0$).
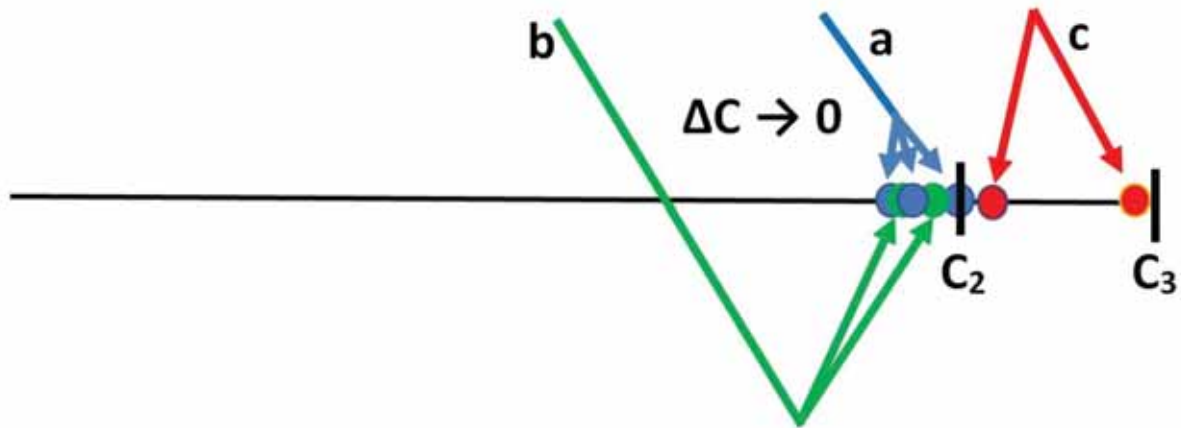
Figure 2. Cognitive predictions of the chemical composition based on the data cluster at the edge of the standard concentration interval. Note that the b values are the interpolated predictions, while the c values are extrapolated

The classification of data through the selection of data intervals is represented in Figure 3.
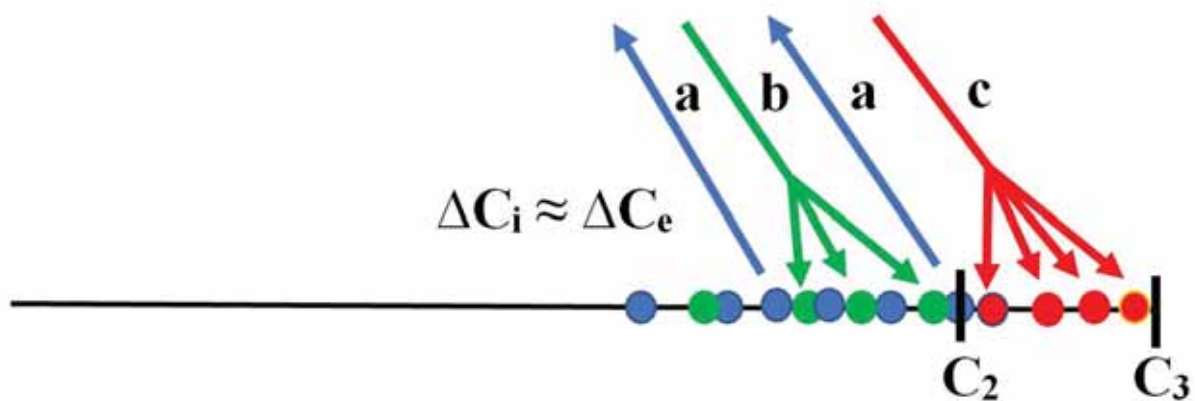
Figure 3. Cognitive predictions of the chemical composition based on the interpolated and the extrapolated data intervals of similar widths ($\Delta C_i \approx \Delta C_e$)

MODELLING THE CONCENTRATION INTERVALS

Let us consider that the concentration of the alloying element in a wrought aluminium alloy of the standard composition is C (μ, σ), while in the wrought aluminium alloy with the alternative composition, the concentration of that element will be C′ ($\mu′$, $\sigma′$). The precondition for the same level of uniformity and reproducibility, i.e., the same level of quality, is the same (or similar) standard deviation. Therefore, we can write:

$$\sigma′ \approx \sigma \tag{2}$$

In addition, the standard deviation for the alloy with the alternative composition should be lower than critical:

$$\sigma < \sigma_{critical} \tag{3}$$

At the same time, let us denote the average concentration of the alloying element in the alloy of the standard composition with μ, and the average concentration of the same alloying element in the alloy having the alternative composition with $\mu′$.
To enable a greater replacement of the primary aluminium and alloying elements with scrap, it should be:

$$\mu′ > \mu \tag{4}$$

Figures 4 and 5 present some of the ways of formulating alternative concentrations for the selected alloying element. The first option (the example b in Figure 4) is based on increasing the average concentration of the alloying element without changing its *minimum* concentration. Of course, the result of such a formulation for the alternative concentration interval is an increase in the average concentration and the maximum allowed concentration, while the minimum allowed concentration remains the same, as is clear from Figure 4. In that case, the increase in the standard deviation is the same as the increase in the average concentration of the alloying element.
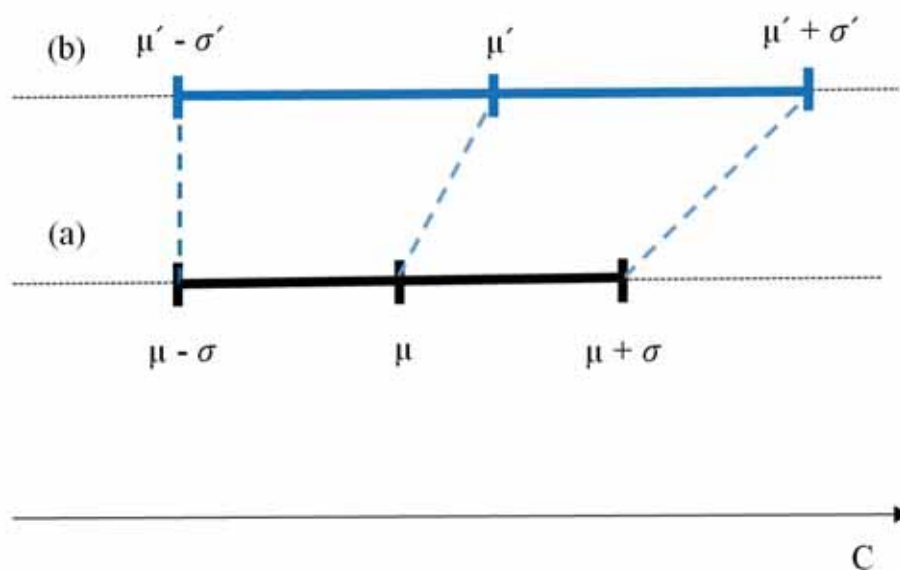
Figure 4. Example of a non-standard concentration interval with the same left-edge concentration (b) as in the standard one (a)

8

The second option, as presented in Figure 5 (example b), is an increase in the average concentration of the alloying element, keeping its standard deviation constant. The consequences of that are changes to the minimum, maximum and average concentrations of the alloying element, as shown in Figure 5, with the composition b. An advantage of this way of tailoring the alternative concentration interval is in preserving the same (i.e., comparable) degree of quality, i.e., the alloy's uniformity and the reproducibility of its properties.
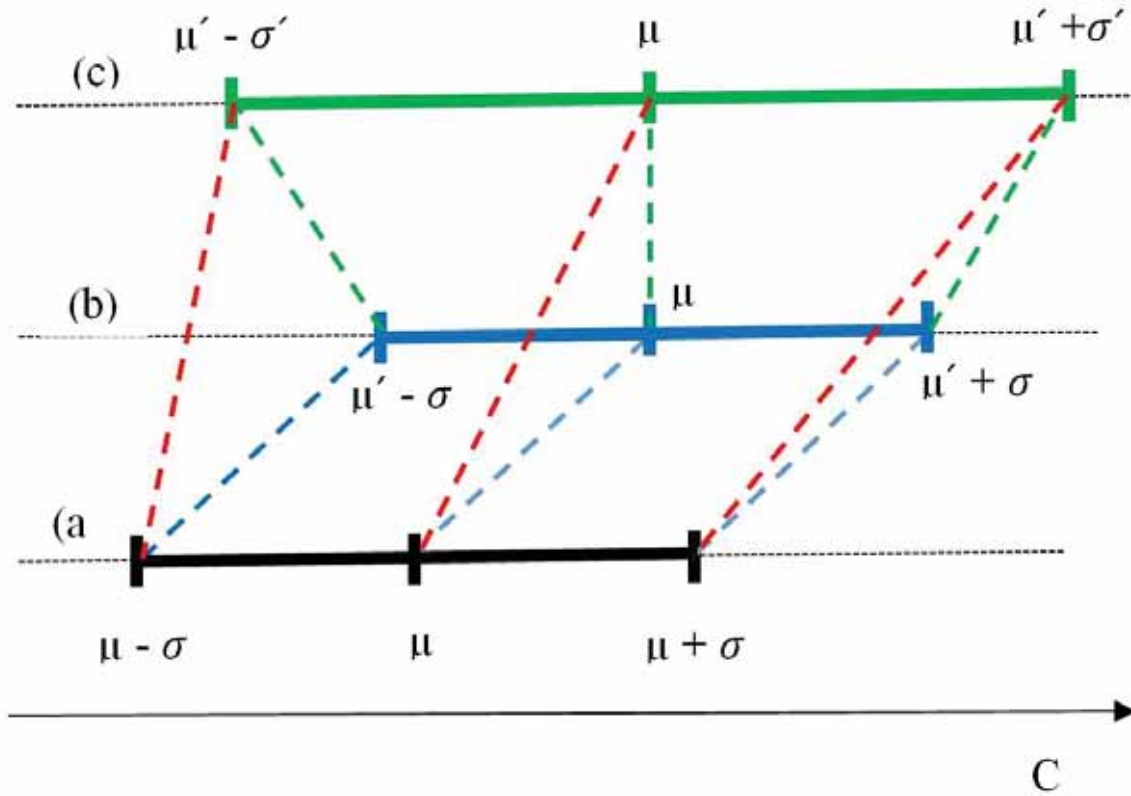
Figure 5. Possibilities for designing non-standard concentration intervals starting from the standard one

(a) Standard concentration interval with an average concentration of the alloying element, μ, and the standard deviation, σ;

(b) Non-standard interval with an increased average concentration of the alloying element, μ', and the same standard deviation, σ;

(c) Non-standard interval with an already increased average concentration, μ', and an additionally increased standard deviation, σ'.

Finally, we can simultaneously increase both the average concentration of the alloying element and its standard deviation, which corresponds to the composition c in Figure 5. Such a solution enables fully-independent changes to all the variables and freedom when it comes to tailoring an alternative composition.

It is important to note that the same principles are also applicable in formulating the intervals (minimum and maximum values) for all the other variables, i.e., the different processing variables or parameters involved in the modelling of the selected properties of the recycling-friendly alloys. Mathematically, this is expressed using Eq.1, in which all the variables and the tensile strength (TS) on the right-hand side of the equation appear as

9

Gaussian intervals. It is important to note that the parameters of the Gaussian distribution of UTS, on the left-hand side of Eq. 1, are prescribed by the customer, while all the other variables, appearing on the right-hand side of Eq. 1, are formulated by the producer of the alloy.

To enable the highest possible replacement of the primary aluminium and the alloying elements with scrap, while maintaining the value of UTS inside the required interval UTS (μ, σ), it will be necessary to formulate some more scrap-friendly compositions. This is usually achieved by increasing the average concentrations and the standard deviations of some of the alloying elements and, especially, the impurities. However, in this case it is important to ensure a production process with "narrower" processing parameters (i.e., a lower standard deviation), which is, in practice, not an easy task. The opposite solution – narrowing the intervals of the concentrations of the alloying and trace elements (i.e., impurities) – significantly reduces the possibilities for introducing scrap, which is the current situation in many wrought-aluminium-alloy casting houses.

ALGORITHM

In principle, the modelling of wrought aluminium alloys with the desired combination of properties is based on finding the surjective and inverse correlation T (C, PP) ↔ P between the properties, P, of the final product and the different technological paths T (C, PP) capable of providing it (and vice-versa), as illustrated in Figure 6.
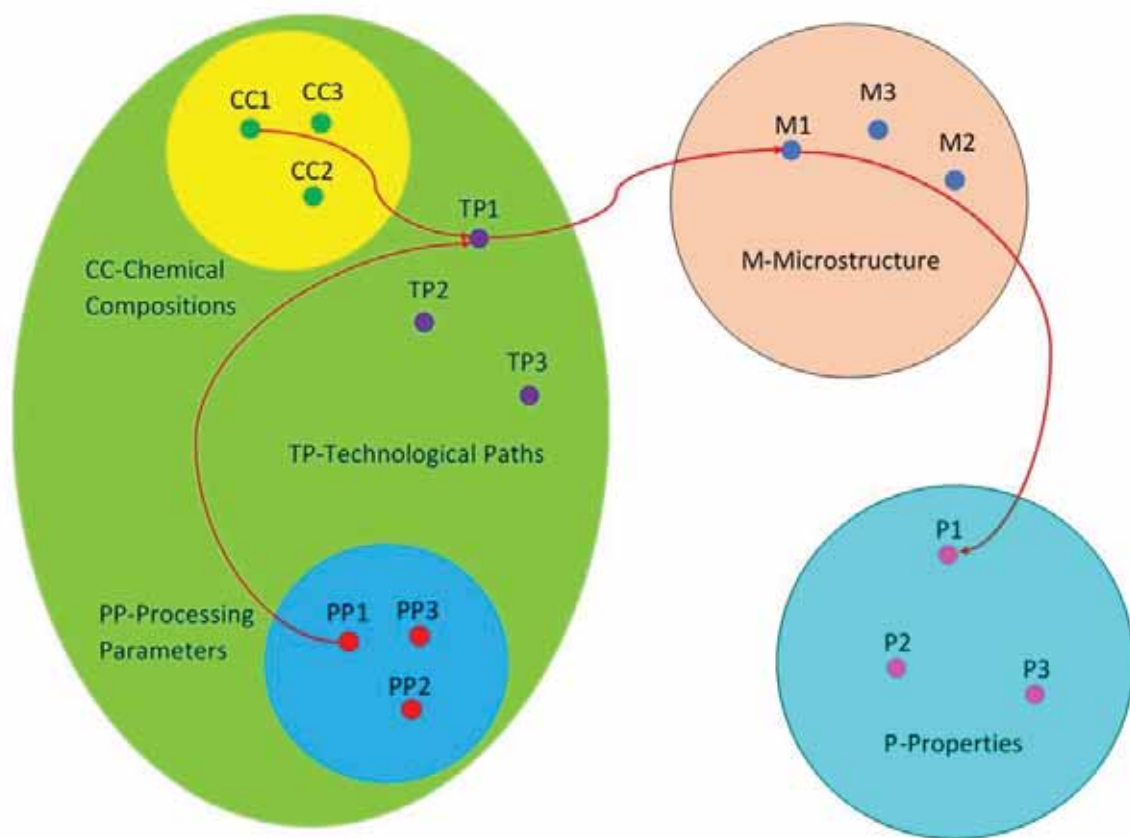
Figure 6. Schematic presentation of the relations existing between the technological path (TP), the microstructure and the end-product properties

10

Here, C represents the chemical composition of the alloy and PP is the processing parameters. The algorithm presented here is based on the functional equivalency of two different technological paths, T1 and T2, able to provide the same combination of properties, written as P (T1) = P(T2), where P(T1) and P(T2) represent the properties obtained using the various paths T1 and T2 in vector space. The selection of the best among the functionally equivalent technological paths, T, was performed by applying the minimum-cost criterion.

The cognitive system applied in this work includes the tools for (i) extracting structured data (process parameters, concentrations of alloying elements, and mechanical properties), (ii) finding the correlations between the individual processing paths and the end-product properties, and finally, (iii) learning the algorithm to perform the predictions on the composition of new alloys and the processing parameters for matching the required mechanical properties. The additional details of the modelling methodology can be found in Refs. [2,3].

PREDICTIONS OF THE TECHNOLOGICAL PATHS BASED ON BAYESIAN DATA MINING

Let the event of interest A happen under any of the hypotheses H_i with a known (conditional) probability $P(A\backslash H_i)$.

Let us further define that the event A happens when the cognitive predicted alloy has a yield strength higher than 350 MPa (Event A: $R_{p0.2} > 350$ MPa), while the hypothesis H_i represents an event that is among n available, and the technological path i will be selected to produce an alloy with the required $R_{p0.2}$.

We also assume that the probabilities of the hypotheses H_1, ..., H_n are known (*prior* probabilities) and H_1, ..., H_n form a set of mutually exclusive events in the sample space, i.e., $\sum_{i=1}^{n} P(H_i) = 1$.

Then the conditional (*posterior*) probability of the hypothesis H_i, i= 1, 2, ..., n, given that event A happened, is:

$$P(H_i \backslash A) = \frac{P(H_i)\, P(A\backslash H_i)}{P(A)} \qquad (5)$$

$$P(A) = \sum_{i=1}^{n} P(H_i)\, P(A\backslash H_i) \qquad (6)$$

Usually, the Bayesian data mining is performed in the form of a Bayesian Additive Regression Tree (BART) and Bayesian Networking (BN). The result is the selection of the processing paths, i.e., the interpolated (TP_i) and the extrapolated (TP_e), with the highest probability of achieving the required mechanical properties ($R_{p0.2} > 350$ MPa).

RESULTS AND DISCUSSION

The main purpose of the case study performed on the cognitive derivative compositions of the base alloy AA6110 was to validate the algorithm developed in this investigation.

As a first step, data mining was applied to obtain the results for standard, room-temperature, tensile tests and the corresponding concentrations of the alloying elements for

the 130 different technological paths of the AA 6110A alloy. The standard chemical composition of AA6110 is reported in Table 1.

The measurements of the mechanical properties were performed in the T1, T5 and T6 conditions by using standard, room-temperature, tensile tests. The chemical compositions of the samples were analysed using optical emission spectroscopy (OES), with an average accuracy of ±10 ppm.

Next, based on the accumulated data obtained for all three tempers, as illustrated in Fig. 7, the property-composition correlation was established following the methodology of cognitive computing. Finally, the property-composition correlation established previously was applied for the cognitive derivative compositions of the alternative standard and some non-standard alloys of the base alloy AA6110. These data are proprietary and beyond the scope of this publication.

The main advantage of the non-standard compositions predicted by the cognitive computing is in the higher upper concentrations of some of the main alloying elements (Fe, Si, Mg) and most of the trace elements, in this way enhancing the amount of scrap that could be involved in the pre-melting mixture. An additional advantage is the reduction of the minimal amount of the primary aluminium prerequisite for alloy production.

Table 1. Standard chemical composition of the alloy AA6110 and some cognitive-computed compositions

Alloy	Si	Fe	Cu	Mn	Mg	Cr	Zn	Ti	Zr	Others Each	Others Total
	wt%	wt%	wt%	wt%	wt%	wt%	wt%	wt%	wt%	wt%	wt%
6110	1.00-1.10	0.14-0.25	0.40-0.50	0.70-0.80	0.75-0.85	0.15-0.25	0.20	0.02-0.10	0.12-0.15	0.05	0.15
Com1	1.10-1.15	O.25-0.28	0.50-0.60	0.85-0.90	0.85-0.95	0.15-0.25	0.20	0.10-0.12	0.12-0.15	0.05	0.15
Com2	1.15-1.20	0.28-0.30	0.50-0.55	0.85-0.90	O.95-1.05	0.25-0.35	0.25	0.12-0.15	0.15-0.18	0.06	0.18
Com3	1.20-1-30	0.30-0.33	0.50-0.60	0.90-0.95	1.05-1.15	0.25-0.35	0.25	0.12-0.15	0.15-0.18	0.06	0.18

The collected results show that even slight differences in the individual processing paths cause, in the T1, T5 and T6 tempers, significant changes in the individual and the combined mechanical properties. A further validation of the algorithm will be carried out as part of a continuation of this work.

The so far existing validation of the proprietary property-composition correlation was performed by computing the properties of randomly selected samples (more than 30) taken from the 130 different technological paths of AA 6110A and vice-versa, by computing the chemical composition of the samples with known mechanical properties. In both cases the matching was better than 90%.
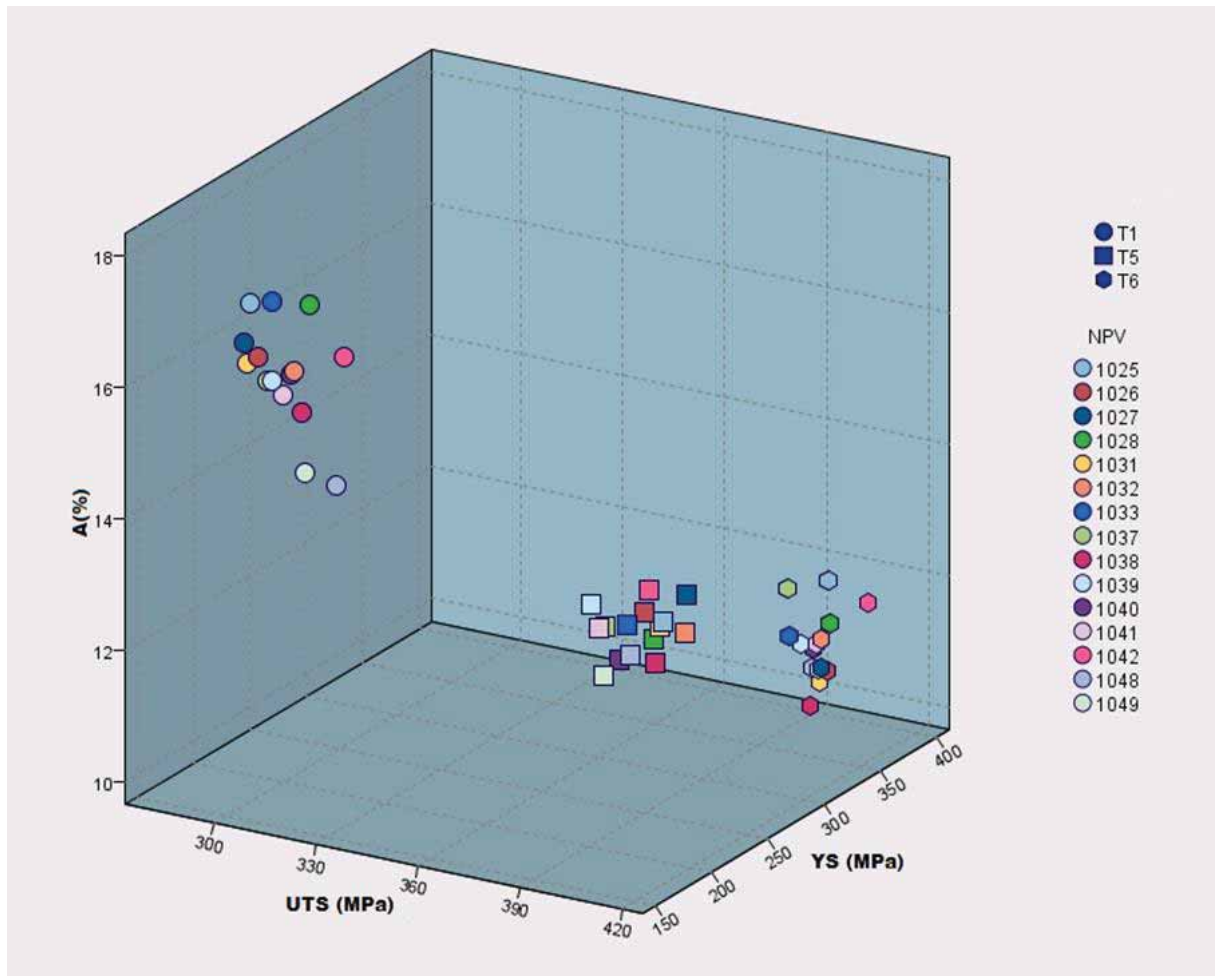
Figure 7. Experimentally determined tensile properties of the AA6110 extruded rod samples in T1, T5 and T6. The same production lots are marked with the same colour

The cognitive predicted relations between the technological paths and the mechanical properties indicate that both the chemical composition and the processing parameters have a considerable influence on the properties of the end-product. However, the influence of some of the alloying and trace elements in the non-standard alloy compositions was found to be stronger and, in some cases, even dominant, when compared with the main processing parameters of the extrusion and the heat treatment. In addition, the cognitive modelling clearly proved that, with the appropriate adoption and the optimization of the processing parameters, particularly the heat treatment, it is possible to compensate or, at least, significantly reduce the negative influences of the non-standard alloy composition on the mechanical properties. The result of such cognitive adopting is, *if it exists*, the proper technological path for achieving the required combination of properties. However, it is also important to note that at the same time, some other important properties that are out of the scope of those required (e.g., electrical conductivity, corrosion resistance, etc.) might be affected, which should be considered and improved, if necessary, by further modelling.
The reason for that is illustrated in Figure 8.

13
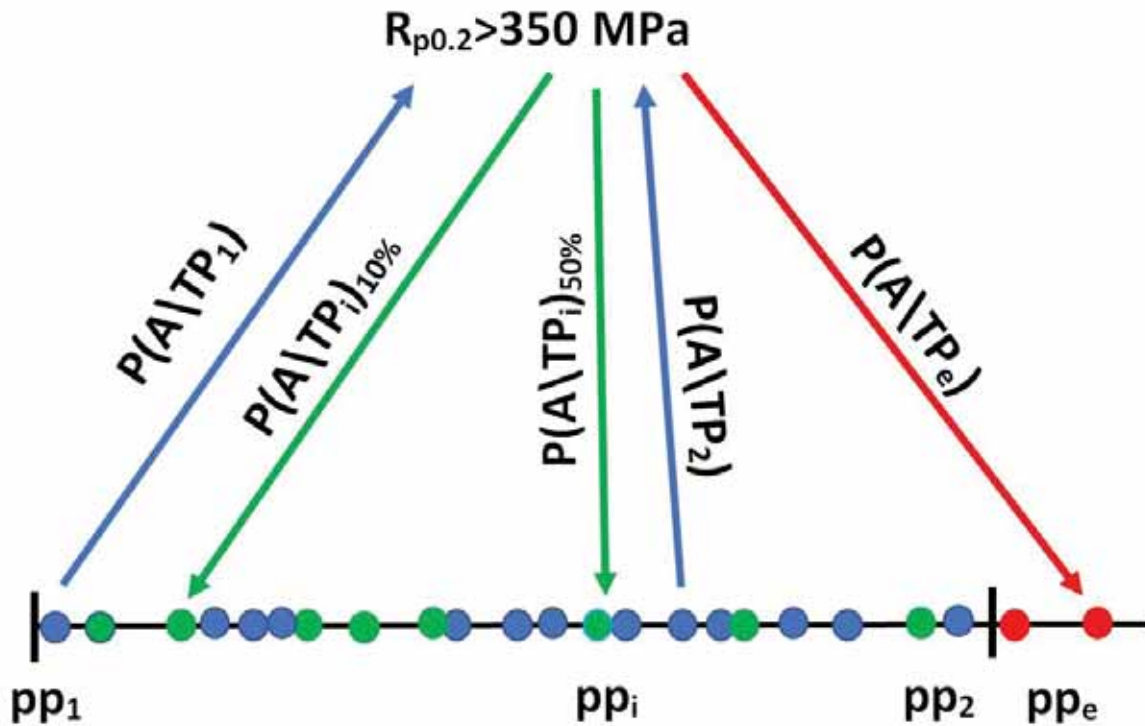
Figure 8. Interpolated and extrapolated technological paths, TP_i and TP_e, predicted by the cognitive computing

The learning process was based on the technological paths (TP_1, TP_2, …) obtained by data mining. The existing and the predicted technological paths resulted in the required mechanical properties – the event A that $R_{p0.2} > 350$ MPa. However, the accuracy of the prediction (the probability that event A will happen if the event TP_i or TP_e has already happened) is different and depends on the distance between the predicted and the base path. The accuracy of the prediction of the proper technological path, which differs from the initial by approximately 50%, is about 60%. This is insufficient for an industrial application, while the prediction of the technological path differs from the initial by approximately 10% and is higher than 90%. Therefore, from an industrial point of view, the cognitive adopting of the technological path (the chemical composition as well as the processing parameters) is only valuable if the predicted deviations from the initial standard alloy composition and the processing route are limited to less than 10–25%.

As illustrated in Figure 8, the accuracy of the prediction of an interpolated and an extrapolated processing path can be expressed as the probability that the predicted path will be the right one (i.e., that the predicted event will occur) for achieving the proper mechanical properties. Such a probability can be expressed as $e^{-\Delta}$, where $\Delta \in [0; 1]$ is the standardised difference between the initial and the predicted path.

The base alloy AA6110 is one of the commercial alloys of the 6xxx series, widely used for the structural parts in the transportation sector. One of the purposes of the study performed in this work was to predict, using cognitive computing, the effect of the alloying elements listed in Table 1 on the precipitates obtained using the various technological paths. The practical result was the controlling of the amount of β-AlFeSi phase, which is claimed to cause poor

14

ductility and severely reduces the hot workability during the extrusion process. It was also found that the addition of Mn and Cr will dramatically increase the amount of coarse α-Al(Fe, Mn, Cr)Si, which drastically deteriorates the mechanical properties. The processing conditions under which the unfavourable β-AlFeSi phase can be transformed into the less detrimental α-AlFeSi were predicted without influencing the production costs.

Even with higher concentrations, the alloying elements are still acting in the same way as in the standard alloy composition. For example, Mg and Si should be added in proportion to form Mg_2Si precipitates. However, in general, the excess of some of the alloying elements in the non-standard compositions allows the formation of some additional phases, ordinarily not present (or not present in that amount) in the base alloy 6110.

In addition, with 10–20% higher concentrations of some of the alloying elements, the cognitive derivative alloys remain heat treatable and with the same strengthening mechanism as the base alloy 6110.

Finally, based on the analytics of the big data, with the addition of the public data extracted from international patents and scientific articles, it was found that with the introduction of some of the alloying elements that are not usually present in the 6xxx series, valuable combinations of alloy properties can be created. These findings are opening up the prospects of further optimization and the development of new wrought alloys.

THE QUALITY OF BIG-DATA ELEMENTS AND ITS INFLUENCE ON THE EXTRACTING PROCESS

The prerequisite for a reliable correlation of the processing path and the mechanical properties of the end-product and vice versa, which is crucial for the successful learning of the algorithm, is big data with enough volume – the number of elements, and the sufficiently large data clusters – with the intervals of the individual variables being large enough for an adequate correlation. Usually, the data mining performed in an industrial environment is effective in providing sufficient data volume for the extraction and subsequent analytical evaluation. Conversely, providing sufficiently large data clusters is much more demanding and limited, since most of the industrial processes have high repeatability and are performed within the standard (and therefore narrow) processing paths.

The way of solving this problem, which could limit the potential of cognitive computing in some segments of industrial research and development, is in: (i) creating so-called "artificial big data", generated by the extrapolation of the existing big-data clusters and/or (ii) in involving the process of also extracting the public structured proprietary data sources (e.g., patents).

It is important to note that the cost of creating such big-data elements is considerable and represents an important part of the total investment in the so-called "digital transformation" of the production chain.

CONCLUSION
A cognitive algorithm for finding a correlation between the properties of wrought aluminium alloys, the chemical composition and the processing parameters was developed and validated on the AA 6110A alloy.

REFERENCES

[1] V. Kevorkijan, Modeling of Alternative Composition of Recycled Wrought Aluminum Alloys, JOM, 65(2013)8, pp. 973-981.

[2] V. Kevorkijan, Scrap-Intensive Wrought Aluminum Alloys of Standard Quality, Light Metals 2015, (ed. M. Hyland), TMS, 15.3, 2015, Orlando, USA, pp. 237-244.

[3] V. Kevorkijan, Light Metals 2017, (ed. A. P. Ratvik), TMS, 26.2, 2017, San Diego, USA, pp. 259-264.

MEASUREMENT OF RESIDUAL STRESSES IN STRESS LATICE BY THE HOLE DRILLING METHOD

MJERENJE ZAOSTALIH NAPREZANJA U REŠETKASTOJ PROBI METODOM BUŠENJA RUPE

Daniel Novoselović[1], Ivica Kladarić[1], Ivan Živković[2]

[1]Josip Juraj Strossmayer University of Osijek Mechanical Engineering Faculty
in Slavonski Brod, Slavonski Brod, Croatia
[2]Joze Ivakića 10, Bošnjaci, Croatia

<u>Invited lecture</u>
<u>Preliminary note</u>

Abstract

The residual stresses take place mainly due to unequal changes of volume and non-simultaneous phase and structural changes in different parts of the casting. To avoid casting defects, it is necessary to know how big the residual stresses are and if they surpass the allowed values. In this paper, measurements of residual stresses in stress lattices by hole drilling method are presented.

Keywords: *residual stresses, stress lattice, hole drilling method*

Corresponding author (e-mail address): daniel.novoselovic@sfsb.hr

Sažetak

Zaostala naprezanja uglavnom se pojavljuju zbog nejednakih volumenskih promjena i neistovremenih faznih i strukturnih promjena u različitim dijelovima odljevka. Da bi se izbjegle greške na odljevcima potrebno je znati kolika su zaostala naprezanja te da li ona prelaze dopuštena naprezanja. U radu su prikazana mjerenja zaostalih naprezanja u rešetkastim probama metodom bušenja rupe.

Ključne riječi: *zaostala naprezanja, rešetkasta proba, metoda bušenja rupe*

UVOD

Ako na neko tijelo djeluju vanjske sile, one nastoje razdvojiti ili približiti pojedine čestice

tijela. Tijelo se tome suprotstavlja unutarnjim silama koje djeluju među njegovim česticama. Unutarnja sila podijeljena s ploštinom površine presjeka na kojem djeluje, zove se naprezanje. Unutarnje sile u tijelu općenito ne djeluju okomito na presjek [1].

Prema načinu djelovanju razlikuju se normalna naprezanja i posmična naprezanja. Normalnim naprezanjem tijelo se opire međusobnom primicanju ili razmicanju čestica, a posmičnim naprezanjem tijelo se opire klizanju jednog sloja čestica tijela po drugom [2]. U tehničkoj praksi se normalne komponente označavaju oznakom σ s jednim indeksom, a posmične komponente oznakom τ s dva indeksa (sl. 1) [1].
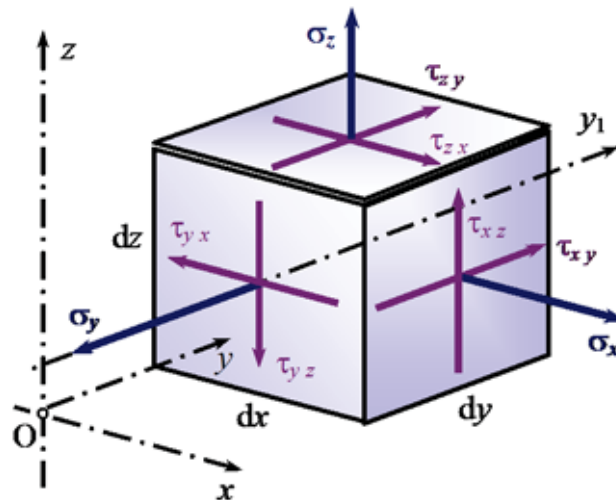
Slika 1. Oznake naprezanja u tehničkoj praksi [1]

Postoji orijentacija koordinatnih osi (1, 2, 3) u prostoru za koje su posmične komponente naprezanja jednake nuli, a normalna naprezanja imaju ekstremne vrijednosti i prikazana su na sl. 2 [1].
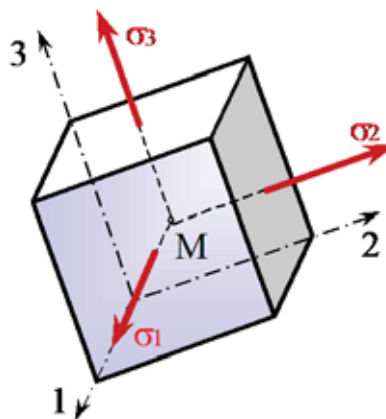
Slika 2. Ekstremne vrijednosti normalnih naprezanja [1]
1,2,3 – glavni pravci, naprezanja, $\sigma_1, \sigma_2, \sigma_3$ – glavna naprezanja

Ekstremne vrijednosti normalnih naprezanja nazivaju se glavna naprezanja, a međusobno okomiti presjeci na kojima normalne komponente naprezanja poprimaju ekstremne vrijednosti, nazivaju se glavni presjeci. Pripadne normale su glavni pravci naprezanja [1].

Postoje različita stanja naprezanja i to [1]:

- linearno (jednoosno) stanje naprezanja: $\sigma_1 \neq 0$, $\sigma_2 = \sigma_3 = 0$
- ravninsko (dvoosno) stanje naprezanja: $\sigma_1 > \sigma_2 \neq 0$, $\sigma_3 = 0$
- prostorno (troosno) stanje naprezanja: $\sigma_1 > \sigma_2 > \sigma_3 \neq 0$.

Slika 3 [1] prikazuje ravninsko (dvoosno) stanje naprezanja.
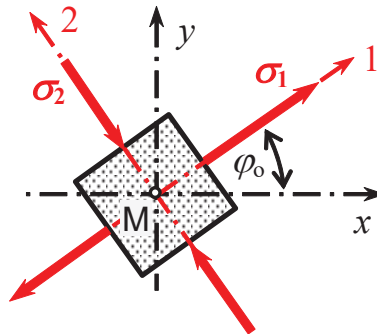
Slika 3. Ravninsko (dvoosno) stanje naprezanja [1]

Glavna naprezanja prikazana su izrazom (1):

$$\sigma_{1,2} = \frac{\sigma_x + \sigma_y}{2} \pm \sqrt{\left(\frac{\sigma_x - \sigma_y}{2}\right)^2 + \tau_{xy}^2} \ , \text{MPa} \qquad (1)$$

Pri čemu je uvijek $\sigma_1 > \sigma_2$, tj. vrijedi: $\sigma_1 = \sigma_{max}$ i $\sigma_2 = \sigma_{min}$.

ZAOSTALA NAPREZANJA

Zaostala naprezanja postoje u nekom konstrukcijskom elementu (odljevku) i kad nema vanjskog opterećenja ni temperaturnog gradijenta. Proizvodni procesi kao što su lijevanje, zavarivanje, strojna obrada, toplinska obrada unose naprezanja u odljevak što pogoduju stvaranju zaostalih naprezanja. Zaostala naprezanja smanjuju čvrstoću, uzrokuju trajne deformacije, smanjuju trajnost, a mogu prouzrokovati i lom konstrukcije (odljevka) [3].

Do pojave zaostalih naprezanja u odljevcima dolazi tijekom formiranja odljevka, a posebno od trenutka stvaranja dovoljno čvrste kore pa do sobne temperature. Zaostala naprezanja mogu nastati i zbog nejednakih dimenzijski promjena i neistovremenih faznih i strukovnih promjena u različitim dijelovima odljevka [4].

Zaostala naprezanja nakon potpunog hlađenja jednaka zbroju različitih naprezanja (mehaničkih, toplinskih, faznih, …). Ukoliko su zaostala naprezanja veća od vlačne čvrstoće, u proizvodnji ili uporabi, pojavit će se napukline ili deformacije na odljevcima (sl. 4) [5].

Napukline predstavljaju razdvajanje materijala, a uzrokovane su radnim opterećenjem odljevka. Deformacija je promjena oblika koja prelazi zadane granice tolerancije odljevka.

a-napukline   b-deformacije
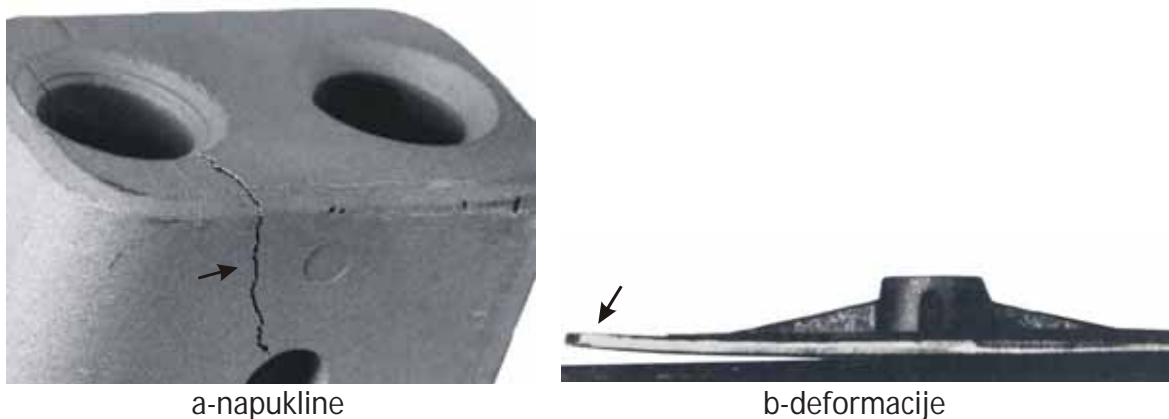
Slika 4. Greške na odljevcima uzrokovane zaostalim naprezanjima [5]

Jesu li zaostala naprezanja povoljna ili nepovoljna, ovisi o njihovom iznosu, predznaku i razdiobi. Poznavanje razdiobe i iznosa zaostalih naprezanja unutar odljevka vrlo je važno, jer ono daje smjernice za njihovo smanjenje ili uklanjanje. Uklanjanje ili smanjenje zaostalih naprezanja moguće je postići promjenom tehnološkog procesa ili uvođenjem određenih toplinskih postupaka (npr. postupak toplinske obrade).

Pouzdano određivanje zaostalih naprezanja zahtijeva mjerenje na odljevku i ne može se provesti na modelima, jer se pomoću modela može dobiti samo kvalitativna slika o razdiobi tih naprezanja. Uređaji za mjerenje moraju biti jednostavni kako bi se mogli primijeniti u pogonskim uvjetima i na nepristupačnim dijelovima odljevka. Mjerne metode moraju eliminirati utjecaje nastale promjenom temperature, vlažnosti itd. [6].

METODE MJERENJA ZAOSTALIH NAPREZANJA

U praksi često stojimo pred zadatkom kako odrediti iznos zaostalih naprezanja u odljevcima. Zbog složenosti konstrukcija i mnogo utjecajnih tehnoloških parametara, ne očekuje se skoro rješenje teorijskog određivanja, koje bi bilo prikladno za ljevačku praksu. Zbog navedenih razloga nastoji se razviti metoda za određivanje zaostalih naprezanja pri kontroli i proizvodnji odljevaka koja bi bila dovoljno pouzdana i što je najvažnije jednostavna i jeftina.

Dostupne tehnički primjenjive i praktički prikladne metode određivanja zaostalih naprezanja mogu se podijeliti s obzirom prema stupnju oštećenja konstrukcije/odljevka na:

- nerazarajuće,
- djelomično razarajuće,
- razarajuće.

Kod nerazarajućih metoda mjerenja konstrukcija/odljevka se ne oštećuje. Neke od metoda su: difrakcija rendgenskog zračenja, mjerenje ultrazvukom, mjerenje promjene magnetskih svojstava konstrukcijskog materijala nastalih zbog naprezanja i sl.

Djelomično razarajuće metode praktički se svode na nerazarajuće metode, jer je područje oštećenja konstrukcija/odljevaka vrlo malo. Kod odljevaka ta se područja razaranja mogu dimenzijama prilagoditi dodacima za obradu samog komada, a naknadnom obradom oštećena mjesta se uklanjaju. Dvije najraširenije metode djelomično razarajuće su metoda izrezivanja kružnog žlijeba i metoda bušenja rupe.

Razarajuće metode su one kod kojih se konstrukcija/odljevak potpuno uništi. Ove metode se još nazivaju i relaksacijske metode, jer ih prati rezanje i relaksacija. U ljevačkoj praksi za ove metode ispitivanja najčešće se primjenjuju tehnološke probe, konstruirane tako da se u odljevcima namjerno uzrokuju zaostala naprezanja. Tehnološke probe konstruirane su tako da sadrže tanki i masivni dio te se prilikom hlađenja, uslijed uzajamnog otpora skupljanju, pojavljuju naprezanja.

Imamo dvije najčešće tehnološke probe i to [6]:

- rešetkasta tehnološka proba (sl. 5a)
- tehnološka proba prema Thomasu (sl. 5b)
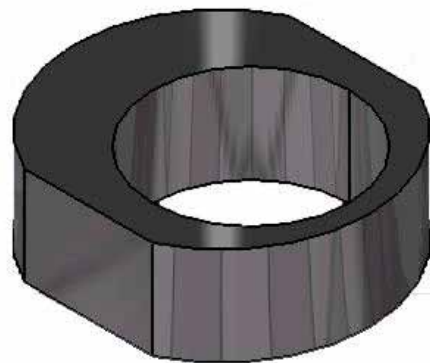
a-rešetkasta tehnološka proba   b- tehnološka proba prema Thomasu

Slika 5. Tehnološke probe

OPIS METODE MJERENJA

Mjerna metoda kojom se određuju zaostala naprezanja je metoda bušenja rupe, što spada u djelomično razarajuće metode. Međutim, metoda se može svrstati i u ne razarajuće metode (oštećenje zbog bušenja rupe je vrlo malo). Naime, mjesto bušenja može se dimenzijama prilagoditi dodacima za obradu, što znači da naknadnom obradom oštećena mjesta od bušenja nestaju.

Bušenjem rupe zaostala se naprezanja u materijalu i okolišu rupe djelomično relaksiraju. Deformacije koje pri tome nastaju mogu se izmjeriti i na temelju njih odrediti zaostala naprezanja. Deformacije se mjere rozetama. Rozete sadrže mjerne trake (tri ili više), postavljene pod raznim kutovima i na jednakim su udaljenostima od središta rozete [7]. Najčešće se koriste rozete s mjernim trakama postavljenim pod kutom 0°/45°/90°(sl. 6.) [7].
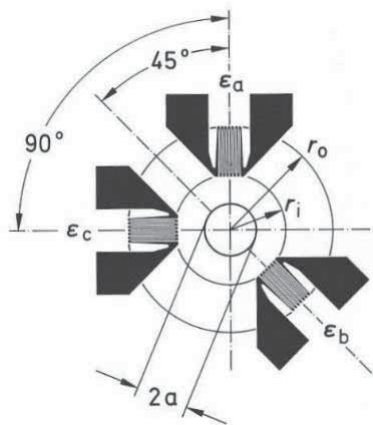
a - polumjer izbušene rupe
r_o - vanjski polumjer mjerne trake
r_i - unutarnji polumjer mjerne trake
ε_a, ε_b, ε_c - deformacije mjernog objekta u pravcima a, b, c mjernih traka na rozeti.

Slika 6. Mjerna rozeta HBM 1-RY61-1,5/120s [7]

Mjerenje deformacija provodi se na način da se prije početka bušenja izmjere deformacije ε_a, ε_b, ε_c na mjernim trakama a, b i c. Slijedi bušenje rupe te ponovno mjerenje deformacije na mjernim trakama a, b i c. Razlika izmjerenih vrijednosti deformacija prouzrokovana je relaksacijom materijala oko rupe ispitnog odljevka:

$$\Delta\varepsilon = \varepsilon_D - \varepsilon_R, \tag{2}$$

gdje je :

$\Delta\varepsilon$ - ukupna deformacija uslijed relaksacije ispitnog odljevka

ε_R - deformacija ispitnog odljevka prije bušenja

ε_D - deformacija ispitnog odljevka nakon bušenja.

Mjerenjem se dobivaju iznosi triju deformacija $\Delta\varepsilon_a$, $\Delta\varepsilon_b$ i $\Delta\varepsilon_c$ koje su kod dvoosnog stanja naprezanja prije i nakon bušenja rupe na ispitnom odljevku.

Glavna naprezanja računaju se prema izrazu [7]:

$$\sigma_{1,2} = -\frac{E}{4A}\left(\Delta\varepsilon_a + \Delta\varepsilon_c\right) \pm \frac{E}{4B}\sqrt{\left(\Delta\varepsilon_c - \Delta\varepsilon_a\right)^2 + \left(\Delta\varepsilon_a + \Delta\varepsilon_c - \Delta\varepsilon_b\right)^2} \ , \tag{3}$$

gdje je:

σ_1, σ_2 - vrijednosti glavnih naprezanja mjernog objekta, MPa
E - modul elastičnosti materijala mjernog objekta, MPa
A, B   - konstante (ovisne o vrsti rozete).

Za izračunavanje zaostalih naprezanja kod linearno elastičnih materijala, gdje se naprezanje ne mijenja po dubini bušenja, koristi se metoda opisana u standardu ASTM E837-08.

Izračunavanje zaostalih naprezanja pri neravnomjernoj razdiobi bazira sa na standardnoj metodi ASTM E837-08, ali se prilikom izračunavanja koriste drugi kalibracijski koeficijenti (matrice).

MJERENJE ZAOSTALIH NAPREZANJA NA REŠETKASTOJ PROBI

Rešetkaste probe prema dimenzijama sa slike 7 odlivene su od sivog lijeva EN-GJL-150 u jednom kalupu. Nakon hlađenja izvršena je priprema mjernih mjesta na probama. Priprema mjernih mjesta, kao i lijepljenje mjernih rozeta, obavljeno je prema uputama HBM (Hottinger Baldwin Masstechnik) [8].

Dimenzije rešetkaste probe   Odlivene rešetkaste probe
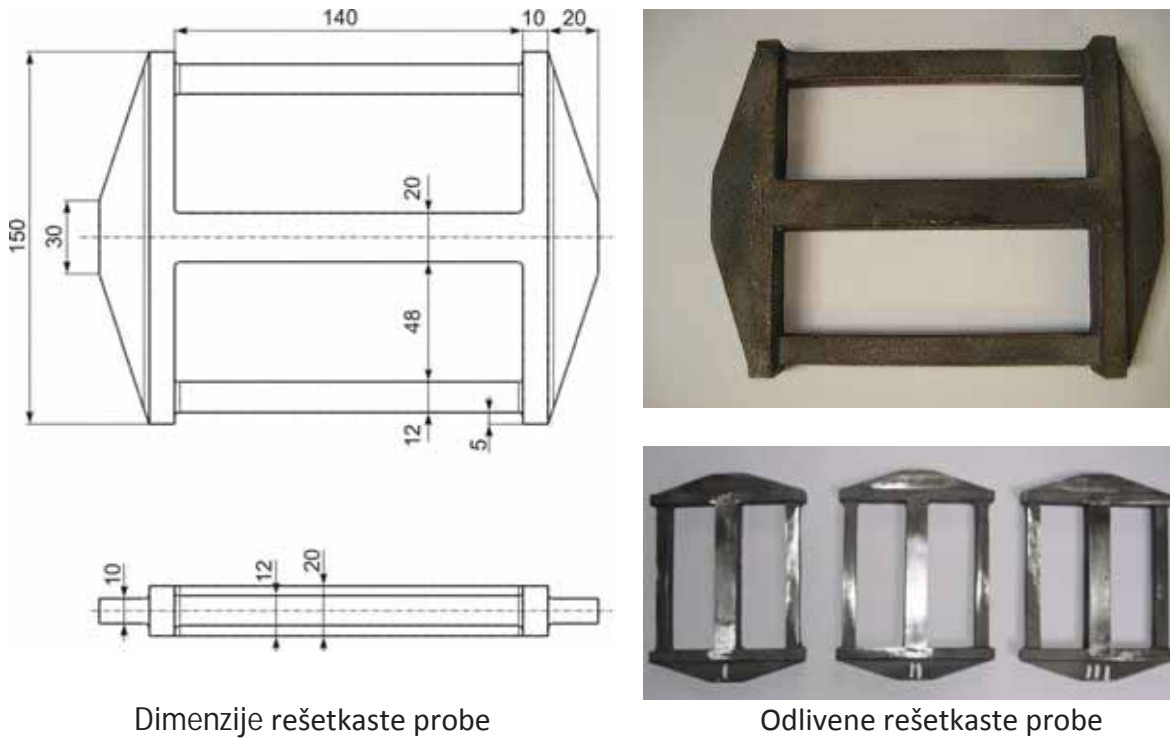
Slika 7. Rešetkaste probe

Površina na koju su lijepljene mjerne trake nisu sadržavale neravnine te su bile dovoljno velike za mjerne trake (rozete). Gruba kora odljevka izbrušena je brusnim kamenom nakon čega je izbrušena brusnim papirom (zrnatosti 180). Mjerna mjesta odmašćena su i očišćena sredstvom za čišćenje RMS1 (Aceton, Isopropanol) tvrtke HBM. Lijepljenje mjernih rozeta obavljeno je ljepilom Z 70. Nakon čega su zalemljeni kablovi na mjerne trake.

Za određivanje zaostalih naprezanja u rešetkastim probama korišten je uređaj MTS 3000 koji koristi djelomično razarajuću metodu bušenja rupe sl. 8.

Slika 8. Mjerenje zaostalih naprezanja na rešetkastoj probi uređajem MTS 3000

Sam proces bušenja kao i prikupljanje podataka mjerenja obavlja računalo pomoću programa „SINT_RSM.EXE". Nakon mjerenja dobiveni podaci se učitavaju u program "EVAL_RSM.EXE", gdje se na temelju izmjerenih deformacija izračunavaju zaostala naprezanja.

REZULTATI MJERENJA

Rezultati mjerenja zaostalih naprezanja za pojedine rešetkaste probe prikazani su na slikama 9-11. Na dijagramima su sa ''···'' označena naprezanja σ_1 odnosno σ_{max} , a sa ''---'' σ_2 odnosno σ_{min}. Dubina bušenja bila je 1 mm, a deformacije na mjernim trakama očitavane su svakih 0,1 mm s početnim pomakom od 0,05 mm.

Prosječan iznos zaostalih naprezanja uzima se za dubine od 0,25 do 0,85 mm. Na dijagramima se vidi se da je prosječan iznos zaostalih naprezanja manji od dopuštene granice vlačne čvrstoće (od 150 MPa). Također se vidi da u pojedinim probama tijekom ispitivanja naprezanja prelaze iz tlačnih u vlačna naprezanja.
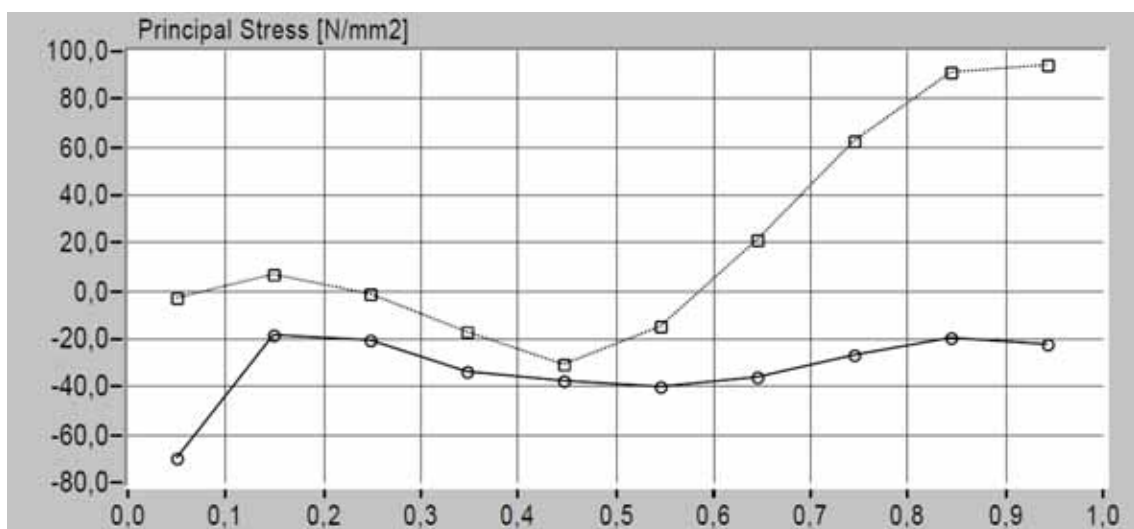
Slika 9. Glavna naprezanja na rešetkastoj probi br. 1 (··· σ_1 MPa , --- σ_2 MPa)

24
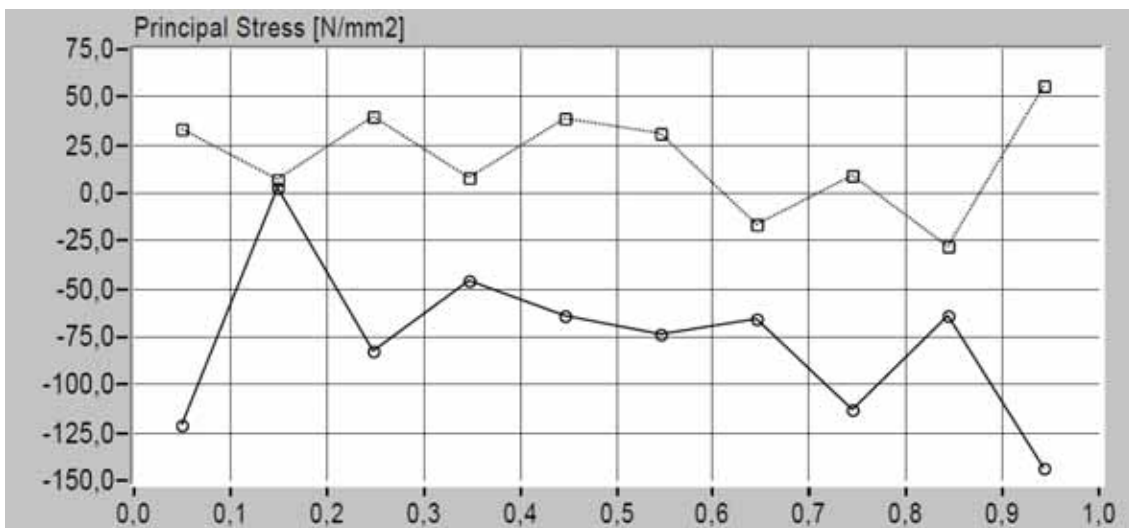
Slika 10. Glavna naprezanja na rešetkastoj probi br. 2 (⋯ σ_1 MPa , --- σ_2 MPa)
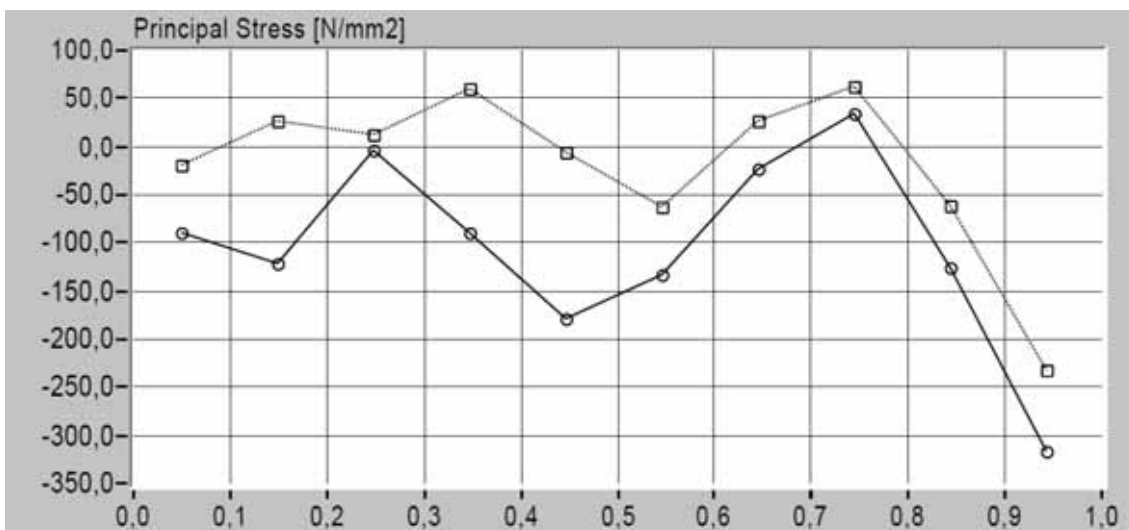
Slika 11. Glavna naprezanja na rešetkastoj probi br. 3 (⋯ σ_1 MPa , --- σ_2 MPa)

ZAKLJUČAK

Način na koji se mjere deformacije ovise o raspoloživoj opremi za mjerenje, gabaritima odljevka te o metodi ispitivanja. Pouzdano određivanje zaostalih naprezanja (na temelju izmjerenih deformacija) zahtijeva mjerenje na samoj konstrukciji i ne može se provesti na modelima, jer se pomoću modela može dodati samo kvalitativna slika o raspodjeli zaostalih naprezanja.

Nakon provedenih mjerenja može se zaključiti da je točan iznos i smjer naprezanja vrlo teško predvidjeti te da je za svaki odljevak potrebno izvršiti zasebno mjerenje. Obzirom da su rešetkaste probe lijevane u jednom kalupu, pretpostavka je bila da će iznos zaostalih naprezanja biti približno isti, što mjerenja nisu potvrdila. Razlog tome su različiti parametri

koji utječu na pojavu zaostalih naprezanja, u ovom slučaju brzina hlađena pojedinih rešetkastih proba u kalupu.

LITERATURA

[1] Z. Vnučec, On-line udžbenik: Nauka o čvrstoći: Dostupno na internetu: http://www.sfsb.hr/ksk/cvrstoca/web_cvrstoca/C_naprezanja/a_uvod/Frameset.htm (1.4.2017.)

[2] Nauka o čvrstoći, Tehnička enciklopedija, JLZ, Sv. 7. Zagreb, 1963-1997.

[3] Tenzometrija, Tehnička enciklopedija, JLZ,. Sv. 12., Zagreb, 1980.

[4] B. Kočovski, Teorija livarstva, Izdavačko grafički zavod, Beograd, 1972.

[5] Atlas ljevačkih pogrešaka, Knjiga 1. (sivi lijev), Metalbiro, 1965.

[6] B. Kočovski, Praktikum iz teorije livarstva, Naučna knjiga, Beograd, 1981.

[7] K. Hoffmann, An Introduction to measurements using strain gages, Hottinger Baldwin Messtechnik GmbH, Darmstadt, 1989.

[8] K. Hoffmann, Practical hints for the installation of strain gages, Hottinger Baldwin Messtechnik GmbH, Darmstadt, 1996.

INVESTIGATION OF SILAFONT 36 ALLOY MODIFIED WITH Zr

Jožef Medved[1], Stanislav Kores[2], Primož Mrvar[1], Maja Vončina[1]

[1]University of Ljubljana Faculty of Natural Sciences and Engineering,
Department for Materials and Metallurgy, Ljubljana, Slovenia
[2]TALUM d.d., Kidričevo, Slovenia

<u>Invited lecture</u>
<u>Subject review</u>

Abstract

The solidification process, microstructure features and mechanical properties of SILAFONT 36 die casting alloy with Zr addition were investigated. In the process of optimizing the mechanical properties of cast aluminium alloys the addition of the element Zr (0.1 – 0.25 wt.%) was suggested. Zr in Al-Zr alloys exist in four kinds of forms at different heat processing and heat-treatment stages, i.e., solid solution in matrix, coarse primary Al_3Zr phase, metastable Al_3Zr phase and equilibrium Al_3Zr phase. The alloy with 0.2 wt.% Zr was melted in a graphite crucible inside an induction furnace. The casting proces was made in a Crooning measuring cell at the temperature of 720 °C. As-cast alloys were then subjected to T6 heat treatment. The samples were analyzed by: using the program for calculations of thermodynamic equilibrium (Thermo-Calc), thermal analysis and for identifying the generated microstructures optical and scanning electron microscopy (SEM) were used. The solidification determined with simple thermal analysis and differential scanning calorimetric show that the solidification time is shorter and the temperature range of the solidification (ΔT_{solid}) is nearer when Zr is added to the investigated die casting alloy. The results revealed that the complex intermetallic phase based on Zr forms. Results also indicate that the hardness slightly increases in as-caste state and after T6 heat treatment.
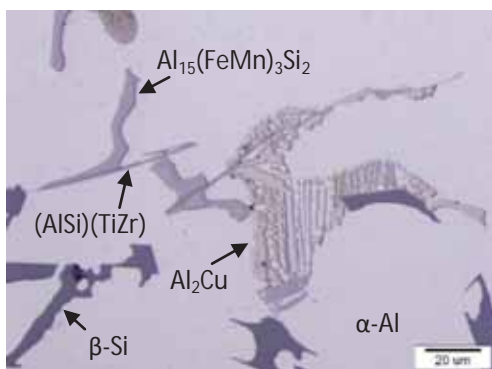
Micrograph of SILAFONT 36 alloy modified with Zr. SEM-EDS was used for phases identifications.

Keywords: aluminium cast alloys, solidification, thermal analysis, mechanical properties

Corresponding author (e-mail address): jozef.medved@omm.ntf.uni-lj.si

Univerza v Ljubljani

University of Ljubljana

Faculty of Natural Sciences and Engineering

Jožef MEDVED[1], Stanislav Kores[2], Primož MRVAR[1], Maja VONČINA[1]

[1]Department of Materials and Metallurgy
[2]TALUM d.d.

jozef.medved@omm.ntf.uni-lj.si

Investigation of SILAFONT 36 alloy modified with Zr

16th International Foundrymen Conference – May 15th – 17th, 2017
Opatija, Croatia

Outline

- Introduction   - Experimental

- Phase systems: Al-Zr, Al-Si-Cu-Zr   - Results
  -

- Thermodynamic simulation   - Conclusions
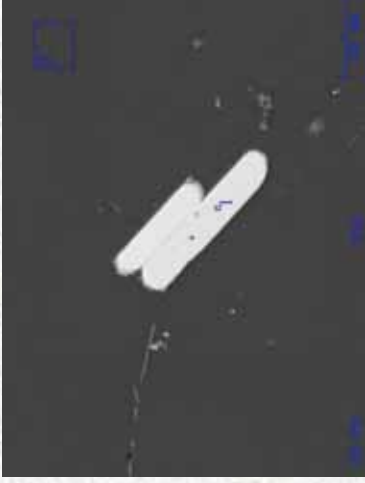
Aim

- Standard Al alloys do not satisfy the rigorous requirements for applications in different areas of technology.

- Alloying elements: Cr, Mn, and Zr
  - for the control of grain and subgrain structures,
  - contribute to the strengthening.

Phase system: Al-Zr
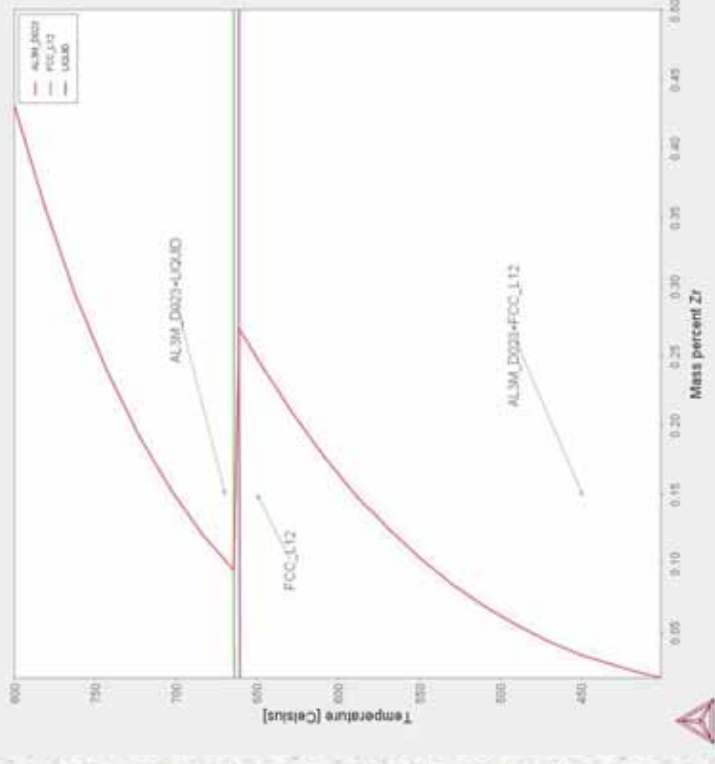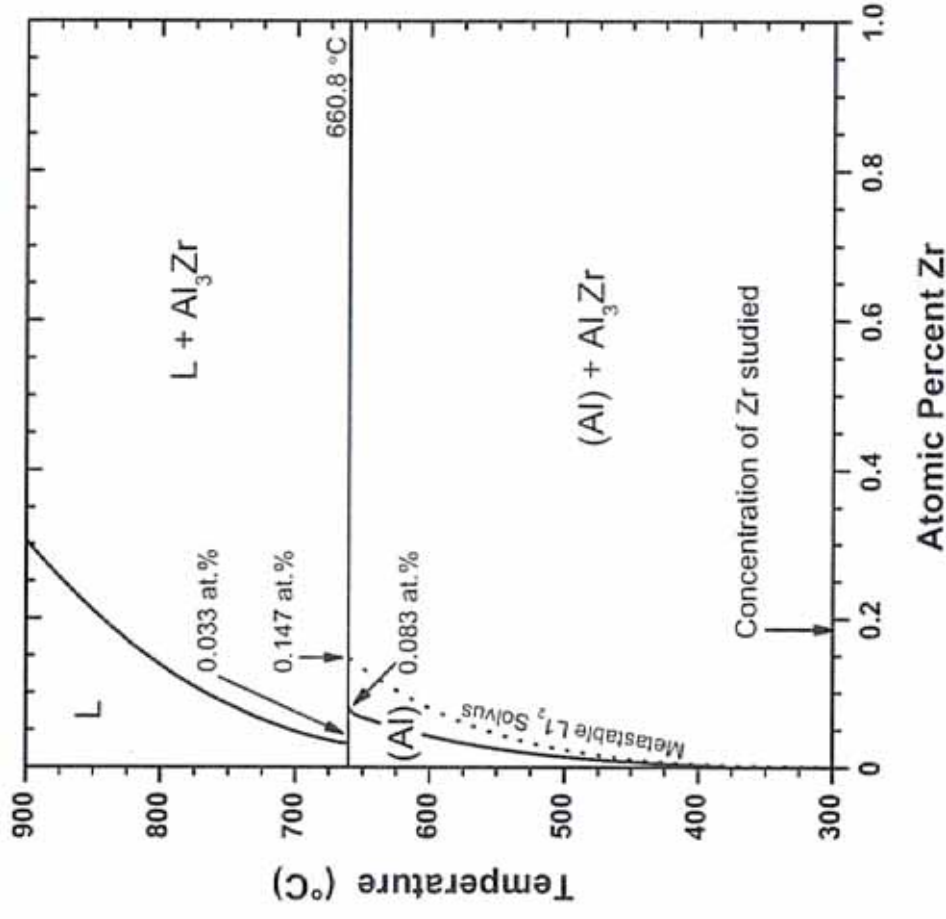
J.L.Murray,A.Peruzzi,andJ.P.Abriata,"TheAl-Zr(Aluminum-Zirconium)System,"JPhaseEquil, 13(3), pp. 277–291 (1992).

(a) Al atoms

39 nm

29 nm

Analysis direction
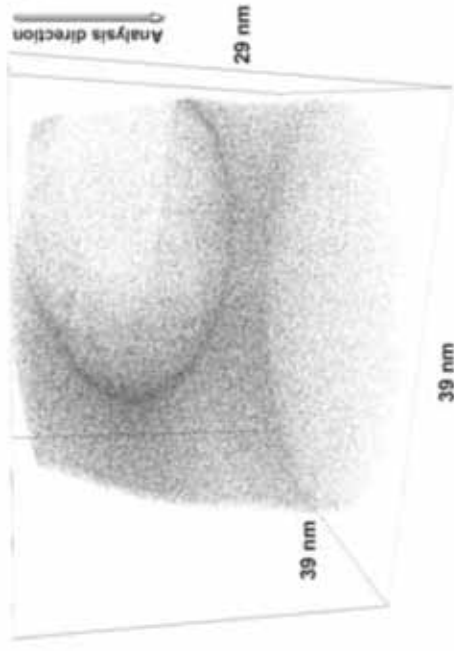
(b) Zr and Ti atoms

(c) Ti atoms

LEAP reconstruction of an $Al_3(Zr_{1-x}Ti_x)$ precipitate in alloy Al-0.1Zr-0.1Ti, (b) aged for 400 h at 425 °C. (a).

Vincent Rigaud, Bo Sundman, Dominique Daloz, Gérard Lesoult, **Thermodynamic assessment of the Fe–Al–Zr phase diagram,** Calphad, Volume 33, Issue 3, 2009, 442–449
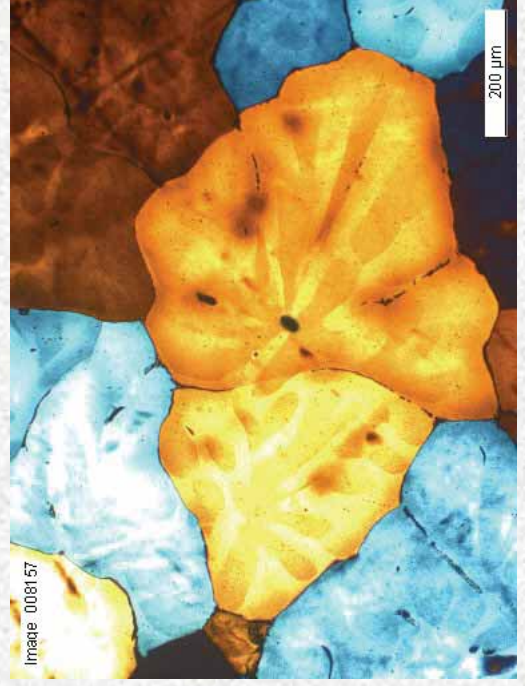
Image 0081 59

200 μm

Al-Ti-Zr:
0.25 Ti
0.3 Zr

Al-Ti-Zr:
0.O35 Ti
0.26 Zr
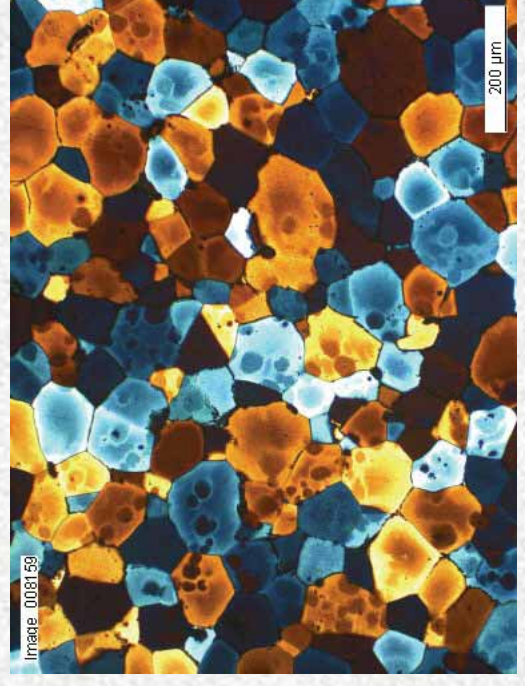
Image 0081 57

200 μm

System Al-Si-Cu-Zr

Elt.	Line	Intensity (c/s)	Error 2-sig	Atomic %	Conc	
Al	Ka	1,426.06	9.750	68.044	47.482	wt.%
Cu	Ka	569.47	6.161	31.956	52.518	wt.%
				100.000	100.000	wt.% Total

kV 20.0
Takeoff Angle 35.0°
Elapsed Livetime 60.0
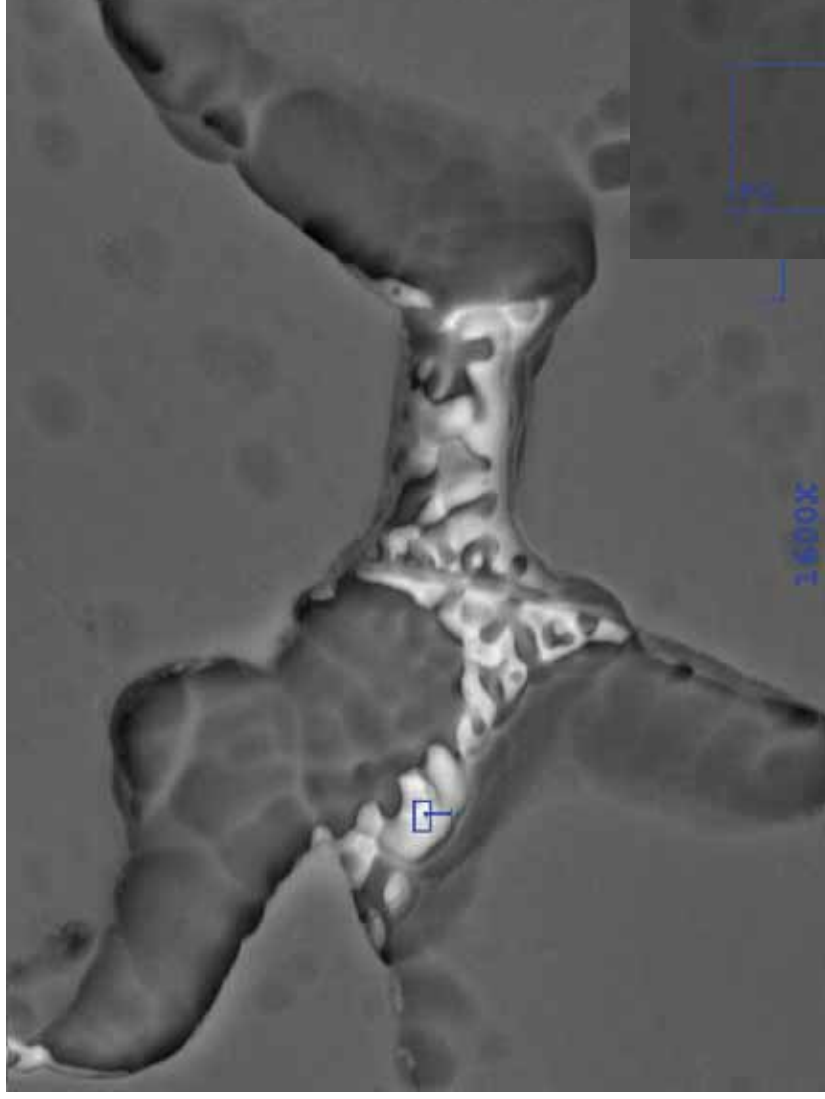
Elt.	Line	Intensity (c/s)	Error 2-sig	Atomic %	Conc	
Al	Ka	2,409.81	12.675	72.212	43.459	wt.%
Zr	La	1,028.26	8.279	27.788	56.541	wt.%
				100.000	100.000	wt.% Total

kV 20.0
Takeoff Angle 35.0°
Elapsed Livetime 60.0
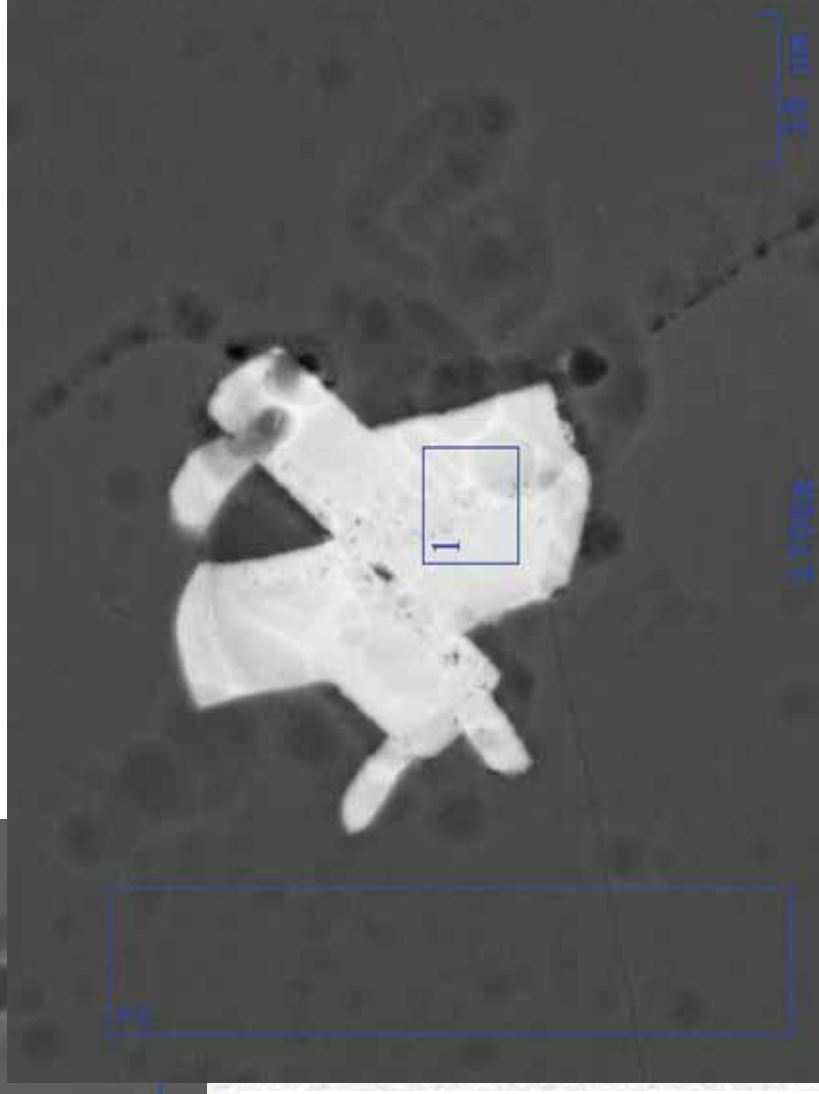
The microstructure of the alloy 356 in the as-cast state:

- **Microstructure of Alloy 1 (with Zr, V, Ti) (b) and 2 (a, c)**

- EDS analysis (d) of phase with Zr, Ti, and V:
  1- α –Al-Si eutectic,
  3-Al (ZrTiV)Si phase,
  4-Al_2Cu eutektik,
  5-Al-Al_2Cu-Si ternary eutectic and
  6-Al_{15}(FeCrMn)$_3$Si$_2$ phase.
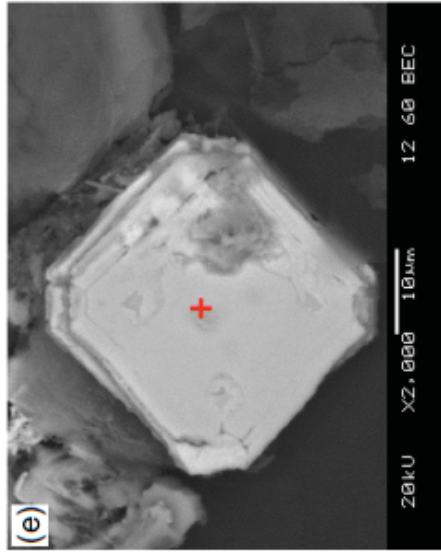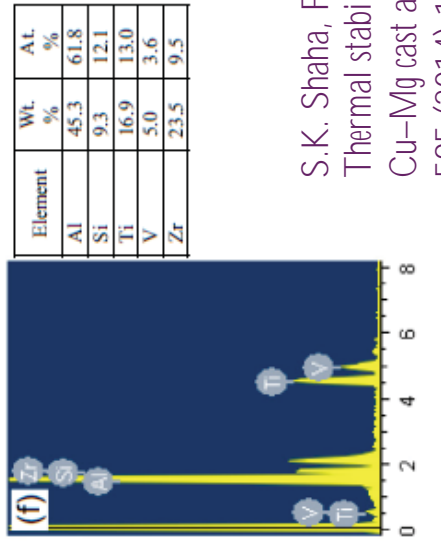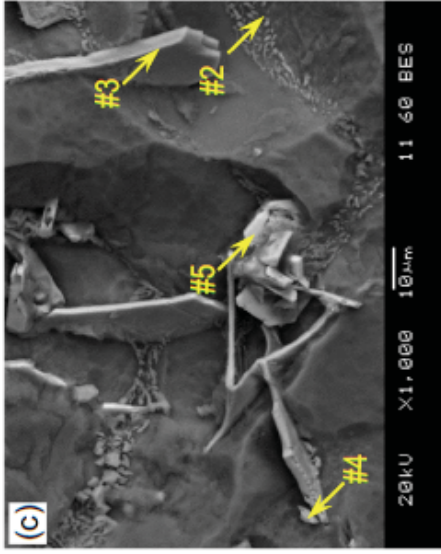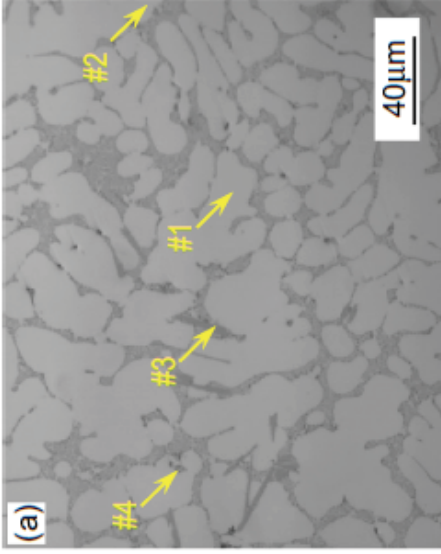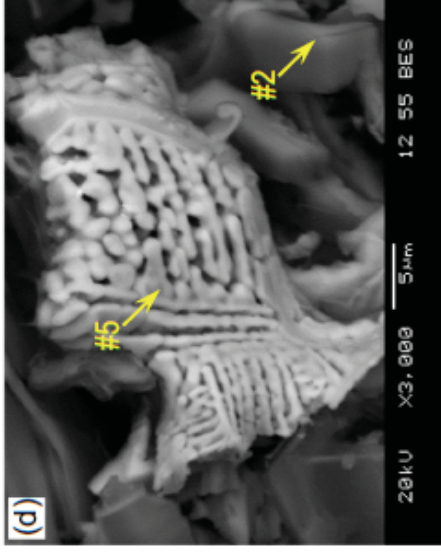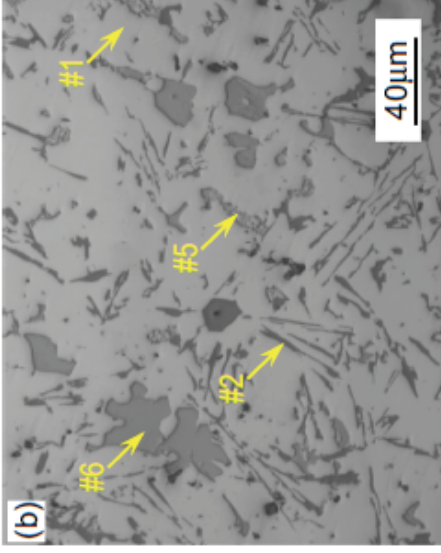
S.K. Shaha, F. Czerwinski, W. Kasprzak, J. Friedman, D.L. Chen, Thermal stability of (AlSi)$_x$(ZrVTi) intermetallic phases in the Al–Si–Cu–Mg cast alloy with additions of Ti, V, and Zr, Thermochimica Acta 595 (2014) 11–16

(b) #1 #5 #2 #6 40µm

(d) #2 #5 12 55 BES 20kU X3,000 5µm

Element	Wt. %	At. %
Al	45.3	61.8
Si	9.3	12.1
Ti	16.9	13.0
V	5.0	3.6
Zr	23.5	9.5

(f) Zr Si Al Ti V 0 2 4 6 8

(a) #2 #1 #3 #4 40µm

(c) #3 #2 #5 #4 11 60 BES 20kU X1,000 10µm

(e) 12 60 BEC 20kU X2,000 10µm
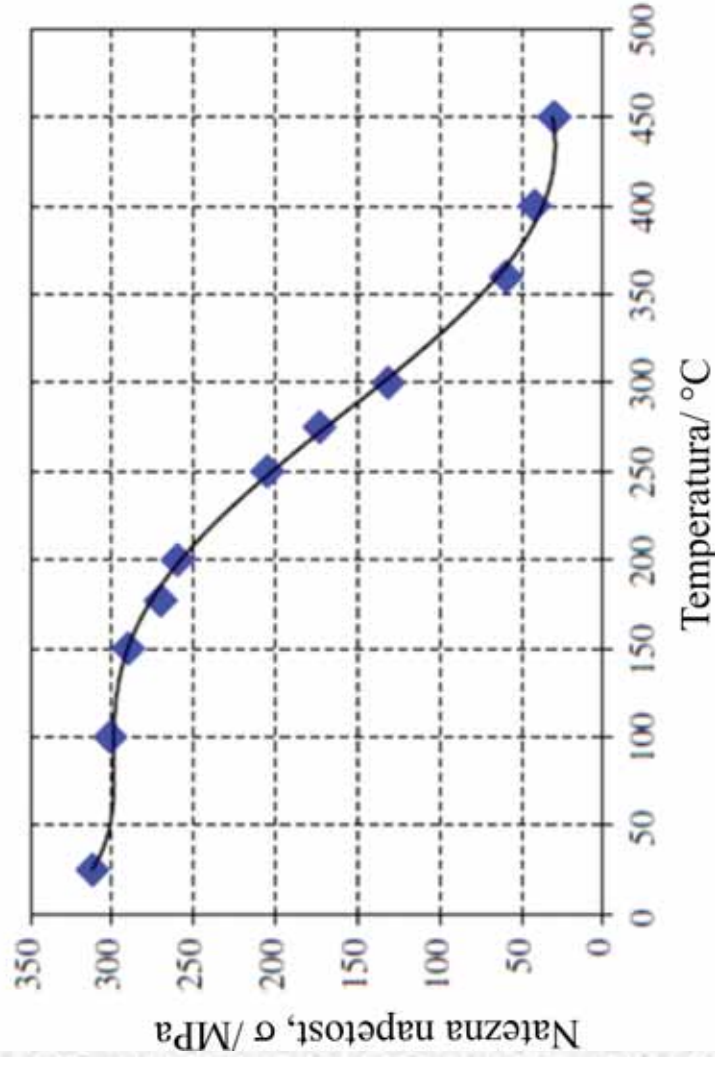
Influence of temperature on the tensile strength of the modified alloy AlSi7Cu1Mg0,5 after T6 heat treatment
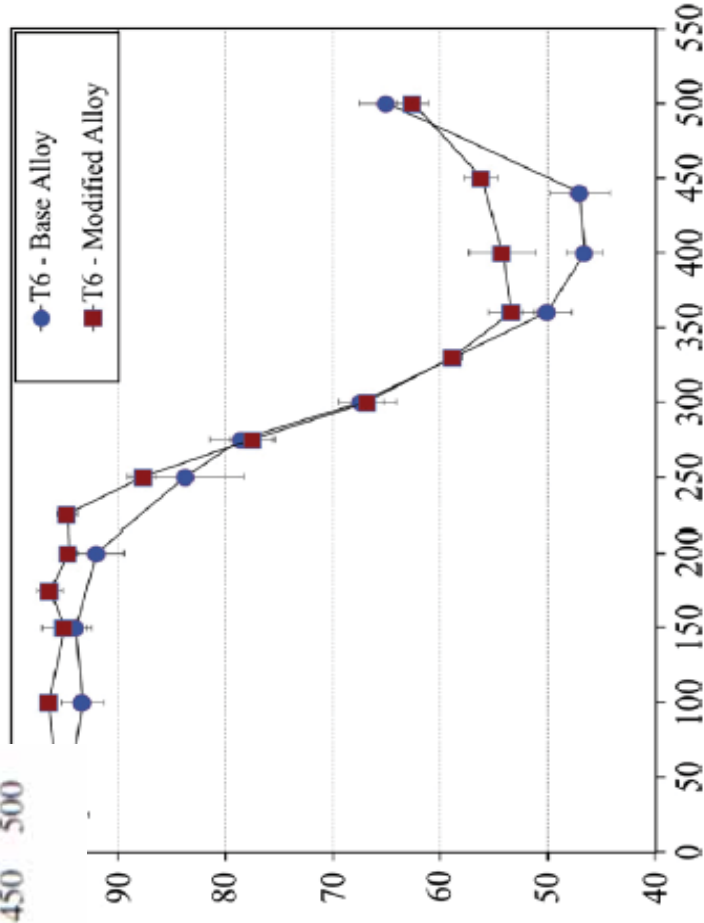
Wojciech Kasprzak, Babak Shalchi Amirkhiz, Marek Niewczas, Structure and properties of cast Al–Si based alloy with Zr–V–Ti additions and its evaluation of high temperature performance, Journal of Alloys and Compounds 595 (2014) 67–79

Alloys:
- SILAFONT 36   - S1
- SILAFONT 36 + 0,2 wt.%Zr   - S2

EXPERIMENTAL :

Thermodynamic calculations: ThermoCalc 2017a, TCAl3 and SSOL5 database.

The samples were meted in induction furnace in graphite crucibles.

Simple thermal analysis (ETA).
Diferential scaning calorimetry (DSC).

Metallographic examination:
- optical microscope Olympus BX 61
- scanning electron microscope JEOL JSM-5610,

Mechanical properties were performed on the Micro Hardness Tester Shimadzu

Chemical composition of **SILAFONT 36** diecasting alloys (wt.%).

Alloy	Sn	Zr	Zn	Cu	Fe	Mn	Cr	Ti	Mg	Si	Al
S1	0,122	0,0	0,45	2,47	0,73	0,30	0,35	0,05	0,27	11,7	Bal.
S2	0,124	0,20	0,34	2,11	0,76	0,33	0,23	0,06	0,76	11,7	Bal.

Thermodynamic calculations

with isopletic phase diagram and
equilibrium amount of phases
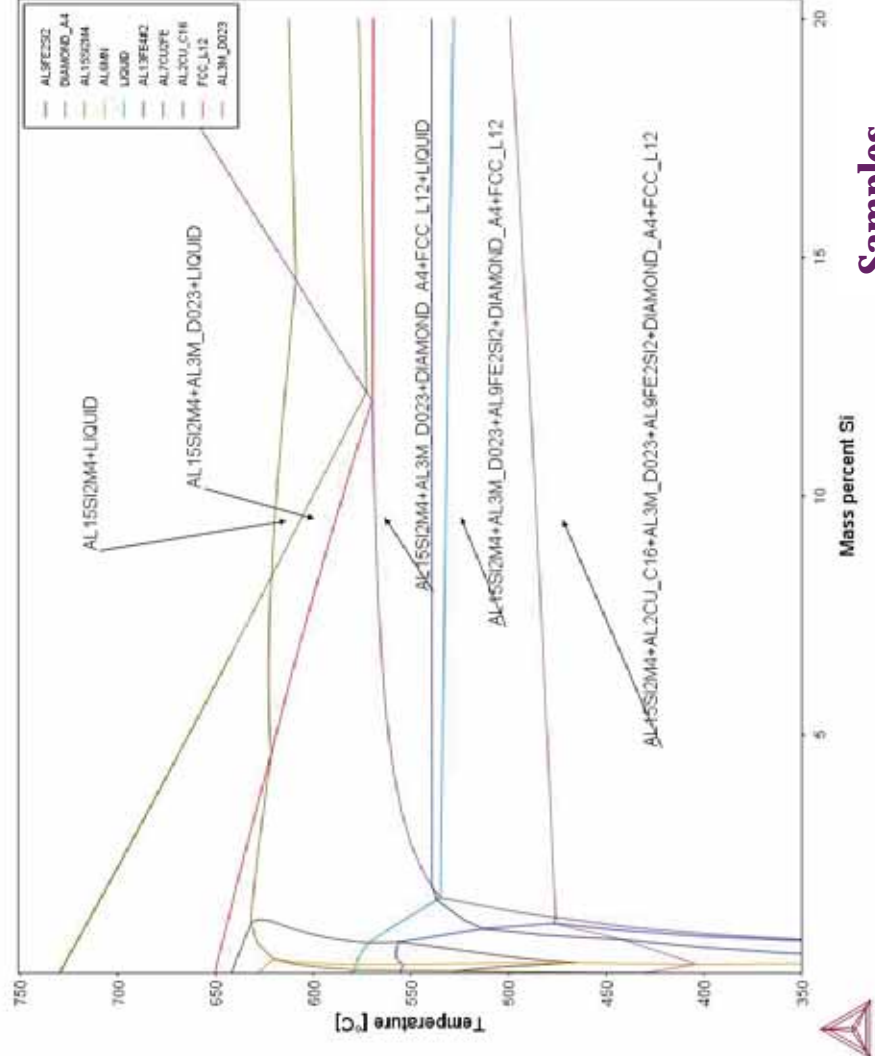
Samples	S1		S2	
Phases	**T**	**am.**	**T**	**am.**
Al3Cr4Si4	674,4	0,64	671,8	0,59
Al3Zr			614,0	0,43
Al14Si2Mn2	594,1	1,74	598,4	1,78
α -Al	586,8	86,13	591,5	86,42
β -Si	573,1	10,11	572,0	9,34
solidus	559,4		560,7	
Mg2Si	538,4	1	540,1	1
Al9Fe2Si2	0,38	327,8	0,42	320,2

ETA of samples S1 and S2

S1

$T_{L,min} = 583,8\ °C$
$T_{L,max} = 585,3\ °C$
$T_{E,min} = 570,6\ °C$
$T_{E,max} = 573,1\ °C$
$T_2 = 553,2\ °C$
$T_1 = 543,9\ °C$
$T_3 = 538,0\ °C$

$dT/dt\ /°C/s$
$T\ /°C$
$t\ /s$

S2

$T_{L,min} = 593,2\ °C$
$T_{L,max} = 593,4\ °C$
$T_{E,min} = 565,6\ °C$
$T_{E,max} = 569,4\ °C$
$T_2 = 553,7\ °C$
$T_3 = 547,3\ °C$
$T_5 = 536,5\ °C$

Derivative Y1
t
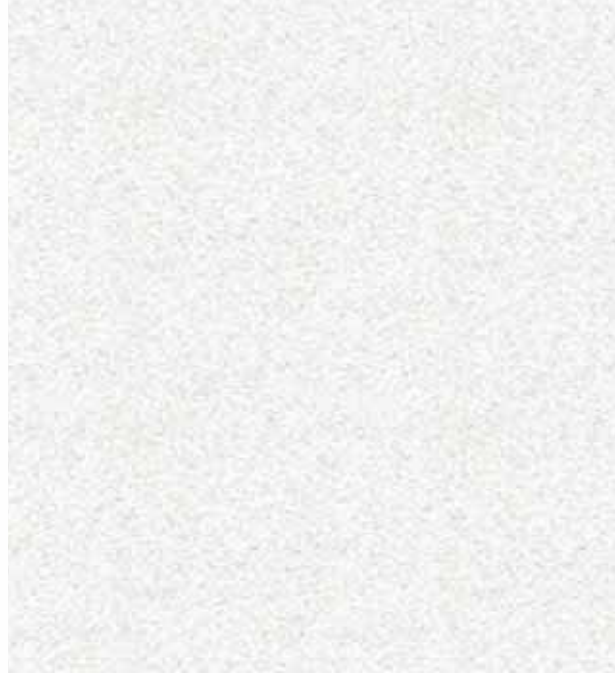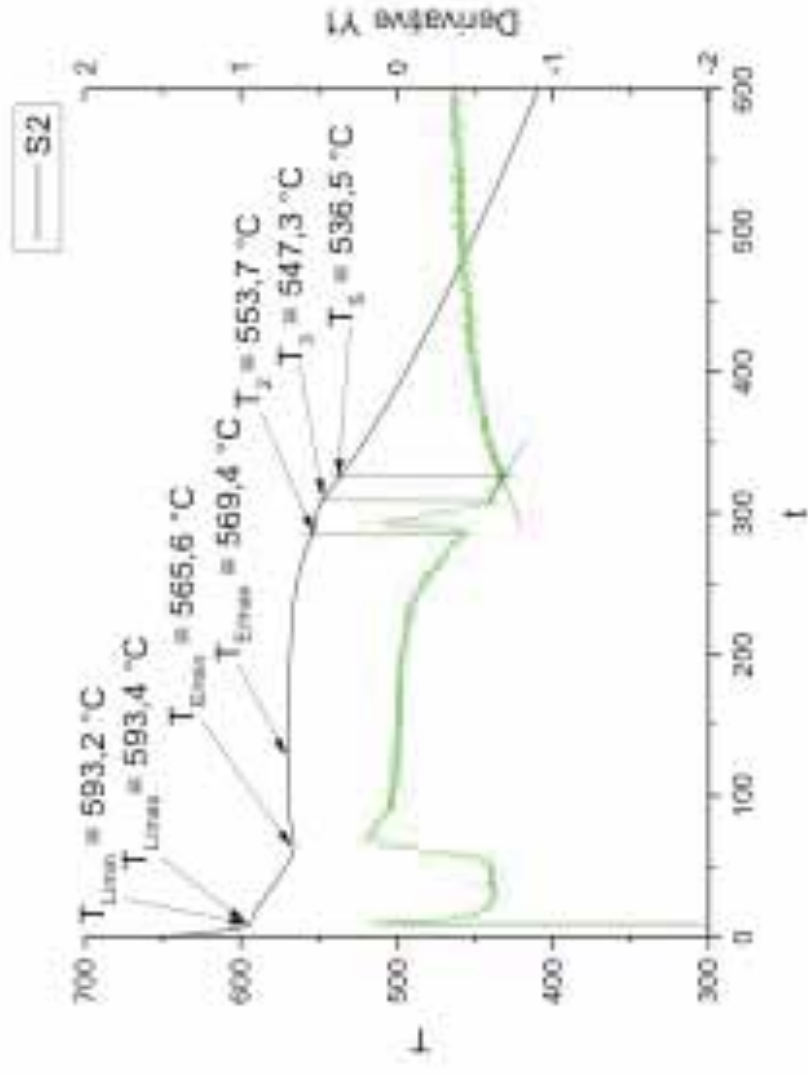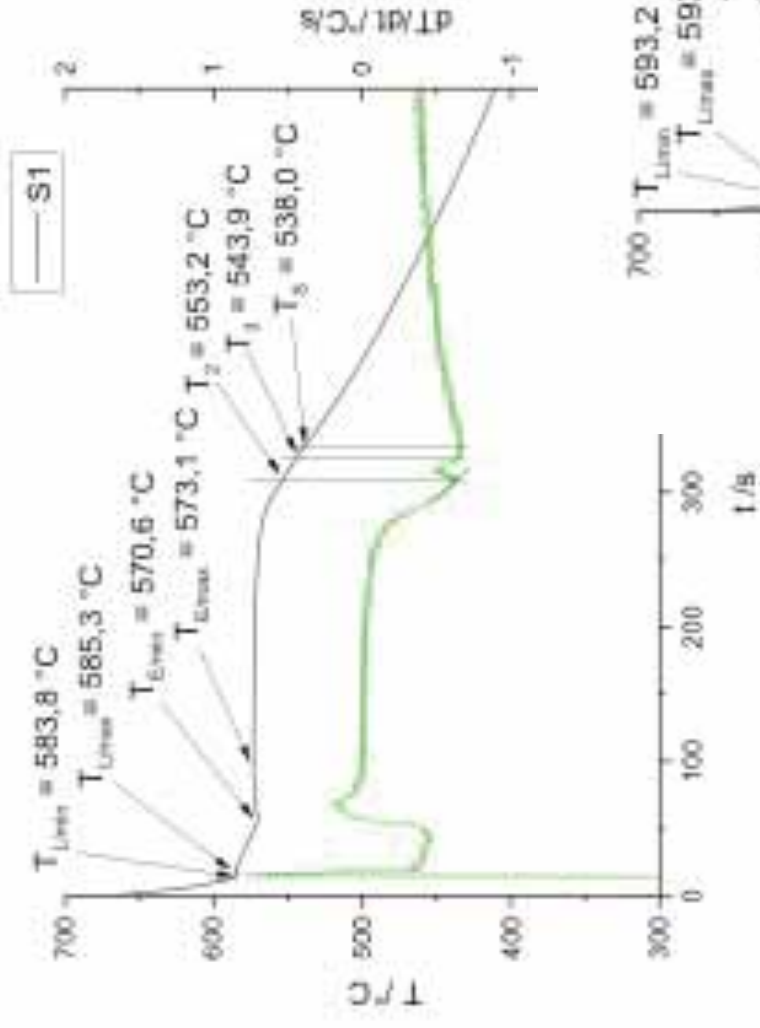
DSC heating and cooling curves of samples S1 and S2
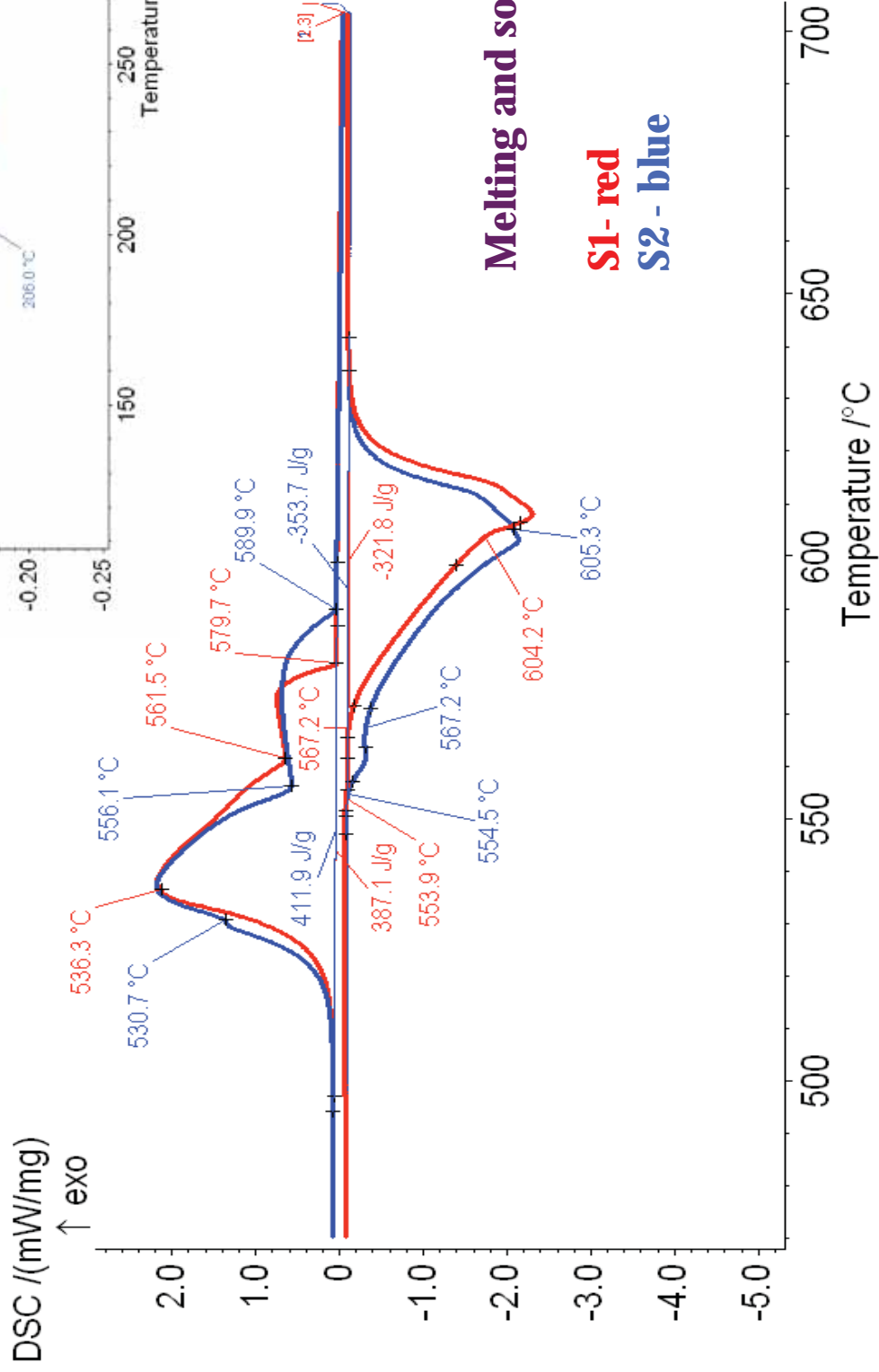
Precipitation Heating corves
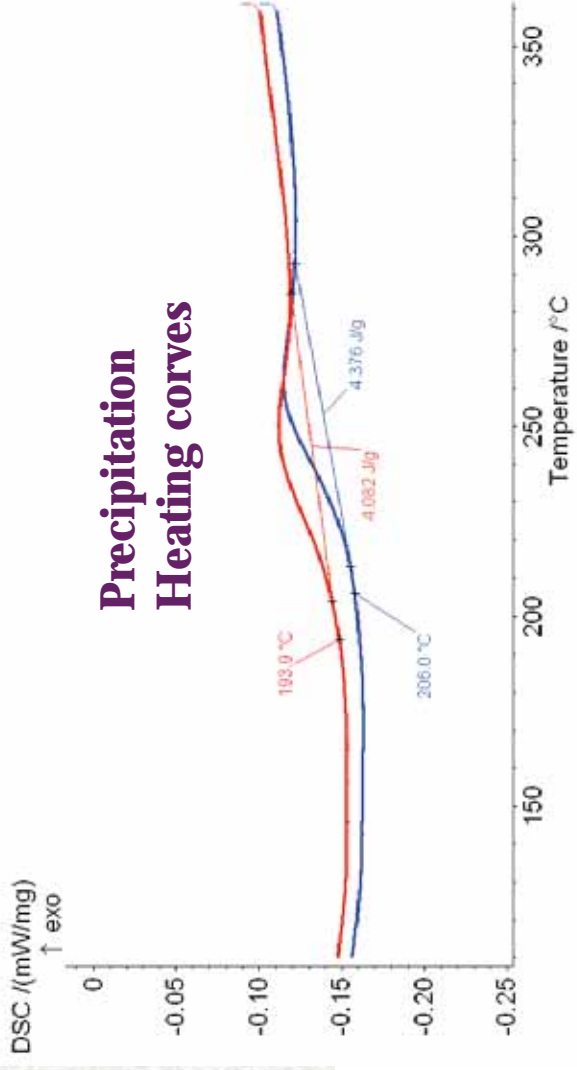
Melting and solidification

S1 - red
S2 - blue
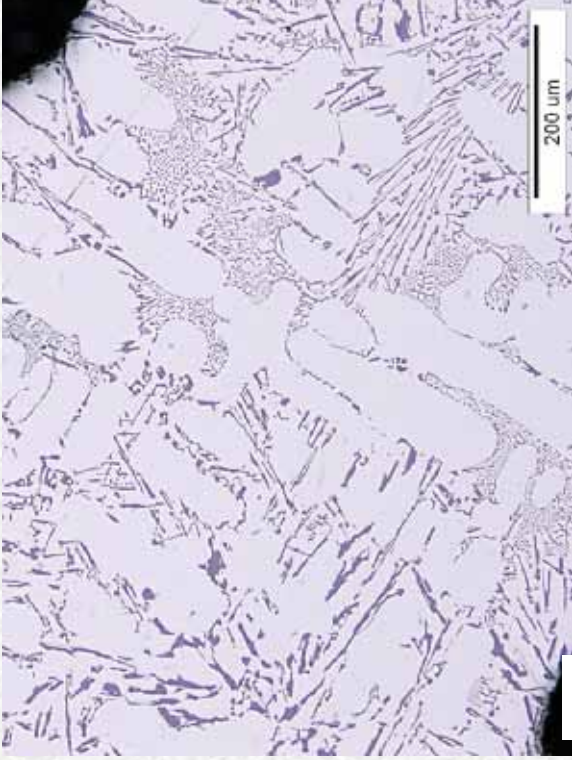
Micrographs obtained from AlSi9Cu3(Fe) base alloy (left) and alloy with Zr (right).
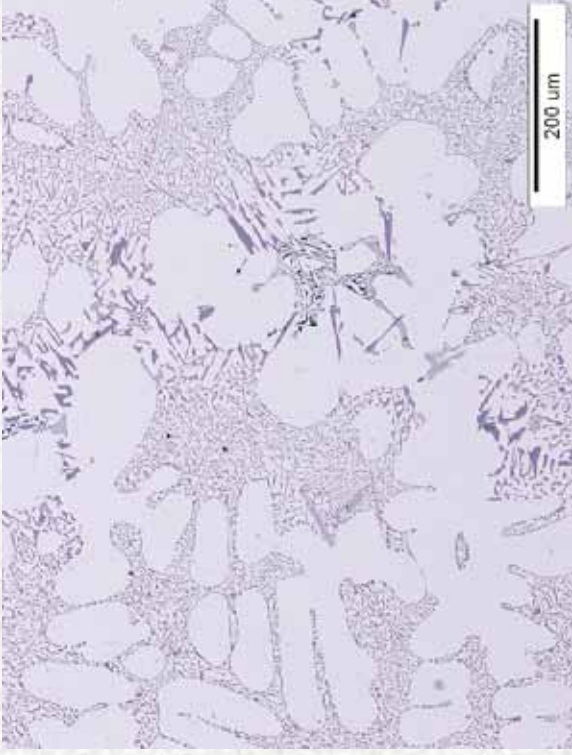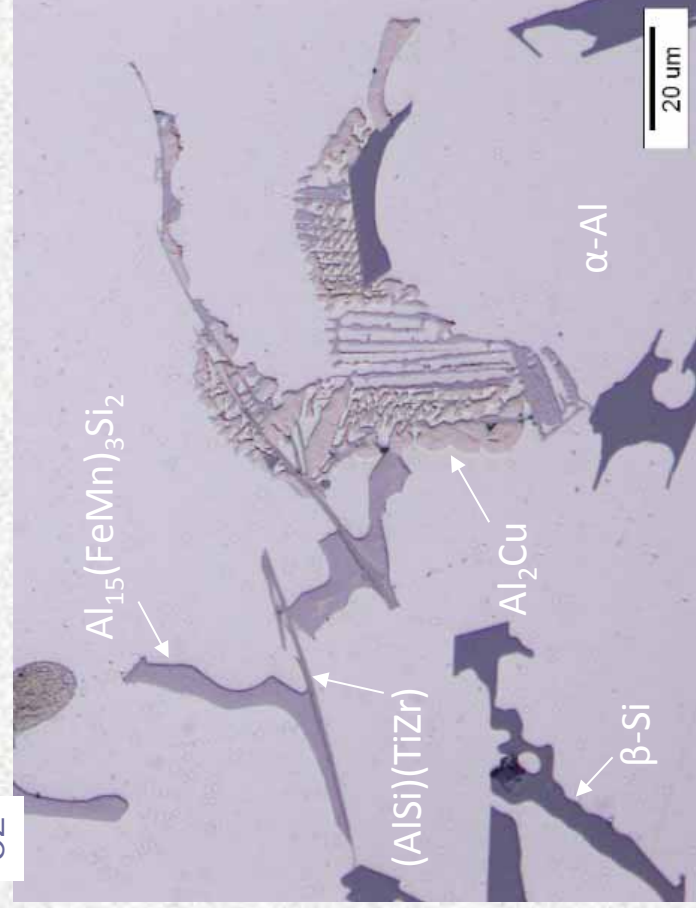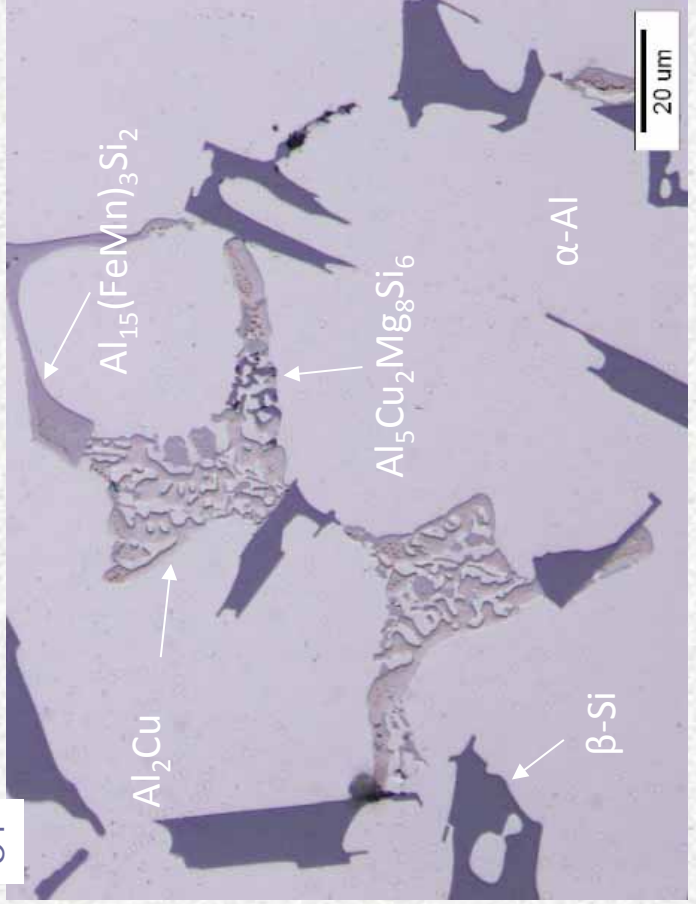
Micrographs obtained from AlSi9Cu3(Fe) alloy with Zr, in cast state (left) and in T6 state (right).
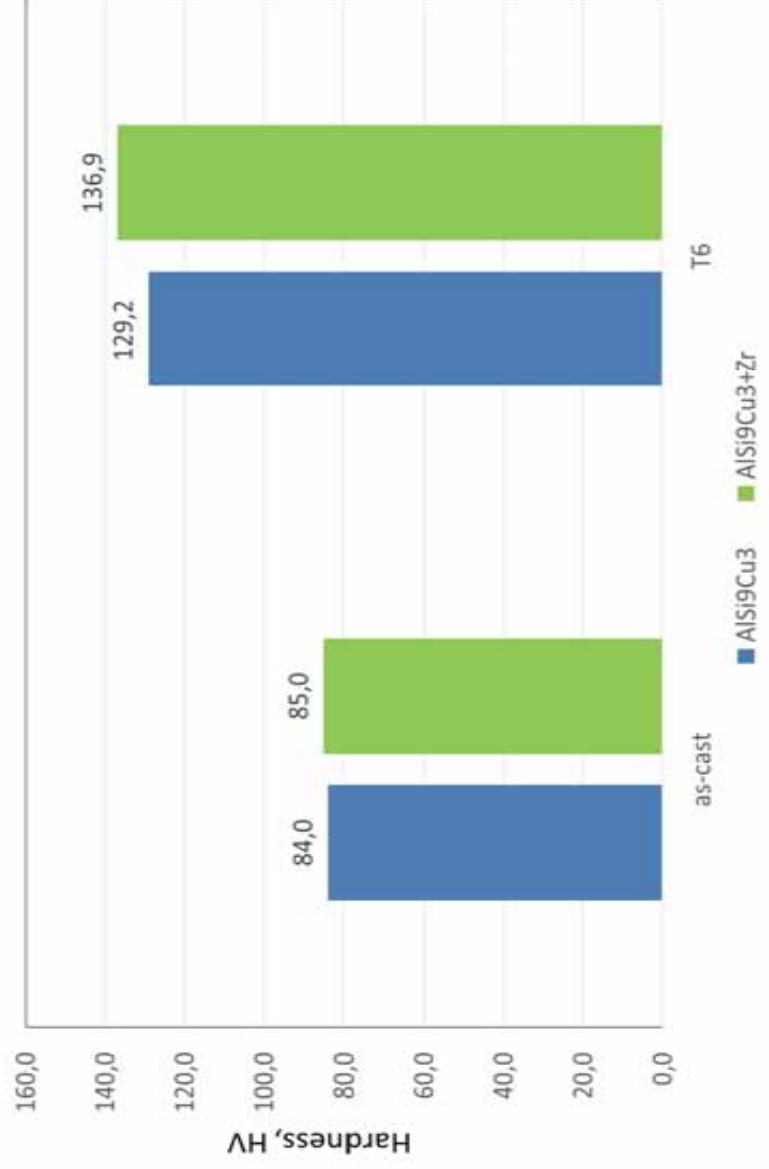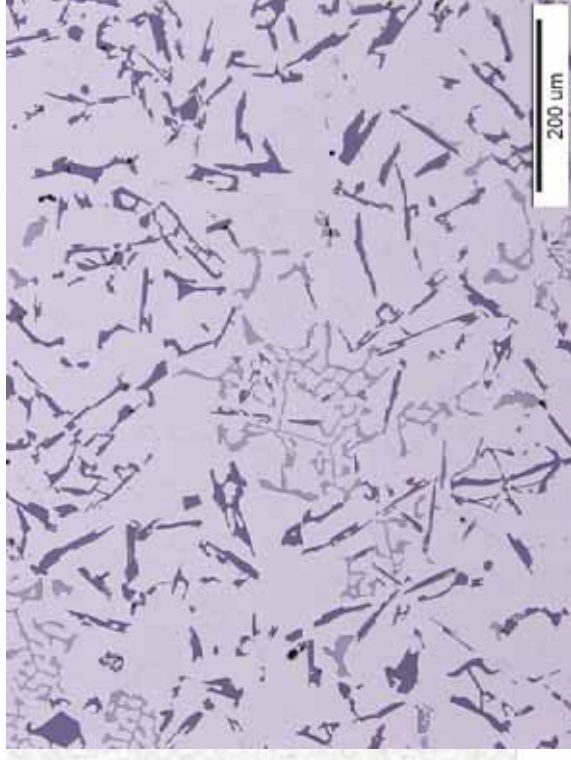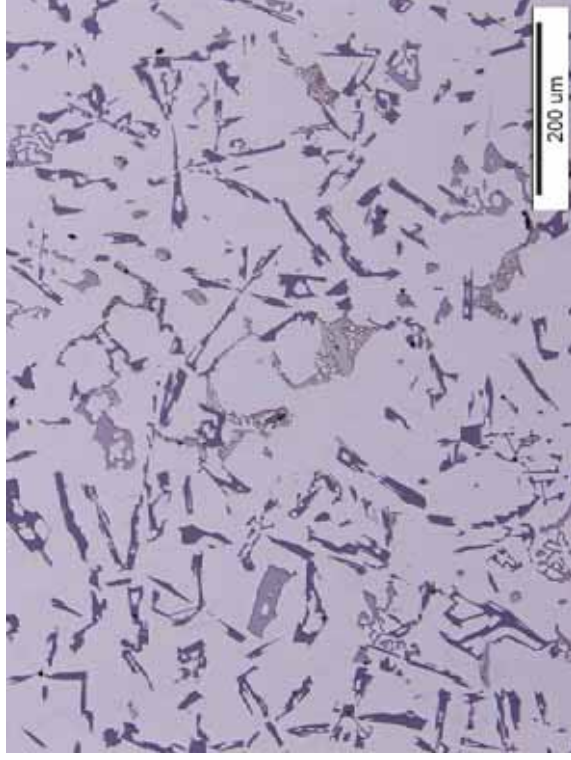
Vickers hardness of investigated samples in as-cast and T6 heat treated state

CONCLUSIONS

There are presented main phases in primary aluminium: α - Al and $Al_{13}Fe_4$ which solidified in the form of a eutectic and phase on the basis of Zr (Al_3Zr).

The results and the literature data show the addition of Zr of 0.1 to 0.25 wt.% improves the mechanical properties of the alloy, which may successfully be used by aluminium foundry alloys.

The solidification determined with simple thermal analyse and differential scanning calorimetric show that the solidification time is shorter and the temperature range of the solidification ($\Delta T_{solid.}$) is nearer when Zr is added to the investigated die casting alloy. .

The addition of Zr to AlSi9Cu3(Fe) alloy resulted in the formation of Zr-rich intermetallic phase, referred as a $(Al,Si)_3(Zr,Ti)$.

The hardness slightly increases in as-caste state and after T6 heat treatment.

COMPUTER SIMULATION OF CAST STEEL PROPERTIES

Božo Smoljan, **Dario Iljkić, Sunčana Smokvina Hanza, Lovro Štic, Andrej Borić**

University of Rijeka Faculty of Engineering, Department of Materials Science and Engineering, Rijeka, Croatia

Abstract

The mathematical model and computer simulation for prediction of mechanical properties of cast steel was developed. In addition, mathematical model for prediction of microstructure composition of cast steel was developed. Because of wide range of applicability and ease of use of finite volume method (FVM), this numerical method was suitable to create integrated computer program for simulation of transient temperature field in process of solidification and cooling of casting to the final temperature, mechanical properties and microstructure transformation.

The hardness of cast steel has been predicted by conversion of calculated cooling times from 800 to 500°C to the hardness. Also, distribution of microstructure of cast steel was found out based on calculated cooling times from 800 to 500°C. The established procedure was applied in computer simulation of cast steel properties.

Keywords: computer simulation, steel casting, hardness, microstructure

*Corresponding author (e-mail address): *dario.iljkic@riteh.hr*

INTRODUCTION

The numerical simulation of mechanical properties distribution in castings and ingots has one of the priorities in simulation of phenomena of casting. During the casting, many different physical processes, such as, solidification, solid state phase transformation, evolution of microstructure, diffusion, heat conduction, and mechanical stressing and distortion are at once taking place inside metal [1-7].

Many very useful software are exist for the calculation of grain structure, porosity, hot tearing, and solid-state transformation. For example there are coupled modules MAGMASOFT, ProCAST, NovaCast, PowerCAST, CalcoSOFT, SOLIDCast, PAM-CASTSIMULOR, ConiferCAST, MAVIS2000, FLOW-3D, CAPCAST, SUTCAST, dieCAS, ADSTEFAN, MICRESS that

can be used for computer simulation of casting. But, there are still questions on which answers should be given to satisfy all industry needs in mathematical modelling and simulation of casting [8-10]. Computer programs for simulation of the casting can be developed by considering the issues such as achievement of tolerable casting defects, desired hardness distribution, microstructure distribution and required workpiece shape [11].

Process simulation capabilities have been extended beyond thermal and flow modelling for casting. The input of the simulation is composed of the following categories: geometry of casting, physical characteristics of the alloy and the moulds, kinematic boundary conditions and thermal boundary conditions. Simulation of heat transfer is thermodynamical problem. It is necessary to establish the appropriate algorithm which describes cooling process and to involve appropriate input data in the model. Inverse heat transfer problems should be solved to determine thermal properties for casting based on experimentally evaluated cooling curve results [12].

Proposed numerical model of casting is based on finite volume method (FVM). The finite volume method (FVM) has been established as a very efficient way of solving fluid flow and heat transfer problems. Recently, FVM is used as a simple and effective tool for the solution of a large range of problems in the thermoplastic analysis [13,14]. The key feature of the FVM approach is that the FVM is based on flux integration over the control volume surfaces. The method is implemented in a manner that ensures local flux conservation, regardless of the grid structure [13].

COMPUTER MODELLING OF HEAT TRANSFER AND SOLIDIFICATION

Numerical simulation of solidification gives consideration to both the motions of molten metal during the mould cavity filing process and convective motions after pouring. Hot liquid is poured into colder mould and both, specific heat and heat of fusion of the solidifying metal pass through a series of thermal resistances to the cold mould until solidification is complete.

Complete process of solidification and cooling of casting is based on the following system of differential equations [2,3,15]:

- the Navier-Stokes equations

$$\mu\left(\frac{\partial^2 v_r}{\partial r^2} + \frac{1}{r}\frac{\partial v_r}{\partial r} + \frac{\partial^2 v_r}{\partial z^2} - \frac{v_r}{r^2}\right) - \frac{\partial p}{\partial r} + \rho g_r \beta(T - T_\infty) = \rho\frac{\mathrm{d}v_r}{\mathrm{d}t}$$

$$\mu\left(\frac{\partial^2 v_z}{\partial r^2} + \frac{1}{r}\frac{\partial v_z}{\partial r} + \frac{\partial^2 v_z}{\partial z^2}\right) - \frac{\partial p}{\partial z} + \rho g_z \beta(T - T_\infty) = \rho\frac{\mathrm{d}v_z}{\mathrm{d}t}$$

(1)

- the continuity equation

$$\frac{\partial v_r}{\partial r} + \frac{v_r}{r} + \frac{\partial v_z}{\partial z} = 0$$

(2)

- the Fourier's heat conduction equation including the convection term

$$\frac{\lambda}{r}\frac{\partial T}{\partial r}+\frac{\partial}{\partial r}\left(\lambda\frac{\partial T}{\partial r}\right)+\frac{\partial}{\partial z}\left(\lambda\frac{\partial T}{\partial z}\right)=\rho c_{\text{ef}}\left(\frac{\partial T}{\partial t}+v_r\frac{\partial T}{\partial r}+v_z\frac{\partial T}{\partial r}\right) \tag{3}$$

Characteristic boundary condition is:

$$-\lambda\frac{\delta T}{\delta n}\bigg|_s=\alpha(T_s-T_a) \tag{4}$$

where T/K is the temperature, t/s is the time, $\rho = \rho(T)$/kgm^{-3} is the density, λ/Wm^{-1}K^{-1} is the thermal conductivity coefficient, T_s/K is surface temperature, T_a/K is air temperature, α/Wm^{-2}K^{-1} is heat transfer coefficient, v_r, v_z/ms^{-1} are the r- and z-component of velocity, respectively, $\mu(T)$/Nsm^{-2} is dynamical viscosity coefficient, $c_{\text{ef}} = c + L/(T_6-T_\alpha)$/Jkg^{-1}K^{-1} is the effective specific heat of a mushy zone, L/Jkg^{-1} is the latent heat of solidification, c/Jkg^{-1}K^{-1} is the specific heat, p/Nm^{-2} is the pressure, g_r, g_z/ms^{-2} are the r- and z-component of gravitational acceleration, respectively, β/K^{-1} is the volume coefficient of thermal expansion, r, z/m are the coordinates of the vector of the considered node's position, T_∞/K is the reference temperature $T_\infty = T_{\text{in}}$, r/m is the radius.

Increment of solidified part in control volume can be calculated by:

$$f_i=\frac{m_i}{m_{\text{vol}}}=\frac{c_m(T_1-T_2)}{L} \tag{5}$$

where m_i/kg is mass quantity increase of solidified part in control volume, m_{vol}/kg is mass quantity of control volume, c_m/Jkg^{-1}K^{-1} is heat capacity of liquid and solid mixture, T_1/K is the temperature at the beginning and T_2/K is the temperature at the end of time step Δt. In proposed model it was presumed that convection term has no relevant role and that liquid metal flow could be neglected after pouring [16]. Equations (1) to (3) was found out using the finite volume method, but physical properties included in equations (1) to (5) should be defined [11,13,14]. Accuracy of the heat transfer prediction directly influences to the accuracy of both, calculations of phase transformation kinetics and calculations of mechanical properties of steel. Involved variables in model were additionally adjusted.

Quantity of growth of solidified part of casting was predicted by calculation of solidification rate in control volume. When $\Sigma f_i = 1$, the mass of solidified part of casting will grow up for mass of control volume.

COMPUTER MODELLING OF HARDNESS AND MICROSTRUCTURE COMPOSITION

Hardness and microstructure properties can be estimated based on isothermal transformation (IT) diagrams, continuous cooling transformation (CCT) diagrams and characteristic cooling times from 800 to 500 °C.

When using isothermal transformation (IT) diagrams, in accordance to the Scheil's additivity rule, characteristic microstructure transformation is completed when transformed part of microstructure, X is equal to one [17,18]:

$$\int_0^t \frac{dt}{\tau(X_0, T)} = 1 \tag{6}$$

where $\tau(X_0, T)$ represents the isothermal transformation time for $X = X_0$ at a temperature T, and t is the total transformation time. Time of isothermal transformation could be calculated by thermo-kinetic equations or could be found out by using IT diagram [18].

Transformed part of microstructure, X can be calculated by Avrami's isothermal equation:

$$X = 1 - \exp(-k \cdot t^n) \tag{7}$$

For purpose of numerical analysis by computer, it is convenient when kinetics of austenite decomposition is defined in an incremental form of Avrami's isothermal equation. By differentiating the Avrami's equation it follows that

$$\frac{dX}{dt} = \exp(-k \cdot t^n) \cdot n \cdot k \cdot t^{n-1} \tag{8}$$

and by extracting the time component from Eq. 8 it follows that

$$\frac{dX}{dt} = n \cdot k^{\frac{1}{n}} \cdot \left(\ln \frac{1}{1-X} \right)^{1-\frac{1}{n}} \cdot (1-X). \tag{9}$$

Eq. 9 can be written in an incremental form and the volume fraction ΔX of austenite transformed in the time interval Δt_i at temperature T_i can be calculated as follows:

$$\Delta X_{(N)} = n \cdot k^{\frac{1}{n}} \cdot \left(\ln \frac{1}{1-X_{(N-1)}} \right)^{1-\frac{1}{n}} \cdot \left(1 - X_{(N-1)} \right) \cdot \Delta t_{(N)}. \tag{10}$$

Kinetic parameters k and n from Eq. 10 can be determined inversely by using data from IT diagrams.

According to additivity rule, the non-isothermal transformation kinetics can be described as the sum of a series of the small isothermal transformations.

Figure 1 shows the scheme for microstructure prediction based on cooling curve and IT diagram. In Fig. 1, the temperature range is divided into a series of small finite steps. Maintaining the time interval, Δt_i to sufficiently short times permits the assumption that the conditions are isothermal over each time step. It was assumed that each time step produces such a transformation as occurs in the IT diagram at the same temperature and microstructure composition.

After calculation of microstructure composition at different location of cast steel, hardness can be estimated by:

$$HRC = X_P HRC_P + X_F HRC_F + X_B HRC_B + X_M HRC_M \tag{11}$$

where X_P, X_F, X_B, X_M are contents of ferrite, pearlite, bainite, martensite respectively, and HRC_P, HRC_F, HRC_B, HRC_M are HRC hardness of ferrite, pearlite, bainite, martensite

respectively.
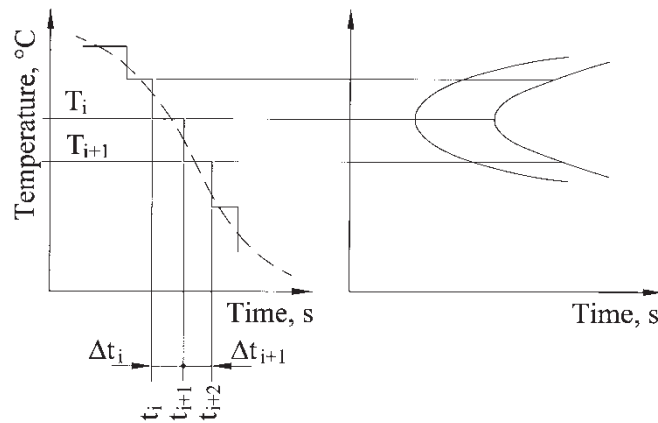
Figure 1. Prediction of microstructure composition from cooling curve and IT diagram

When using continuous cooling transformation (CCT) diagrams, hardness and microstructure composition at different location of cast steel can be estimated by drawing the cooling curves in the CCT diagram [17]. This is a very simple method which is often used.

Also, hardness at different location of cast steel can be estimated by the conversion of the calculated characteristic cooling times from 800 to 500 °C, $t_{8/5}$ to the hardness by using both, the relation between cooling times, $t_{8/5}$ and Jominy distance and the Jominy hardenability curve (Fig. 2) [19].
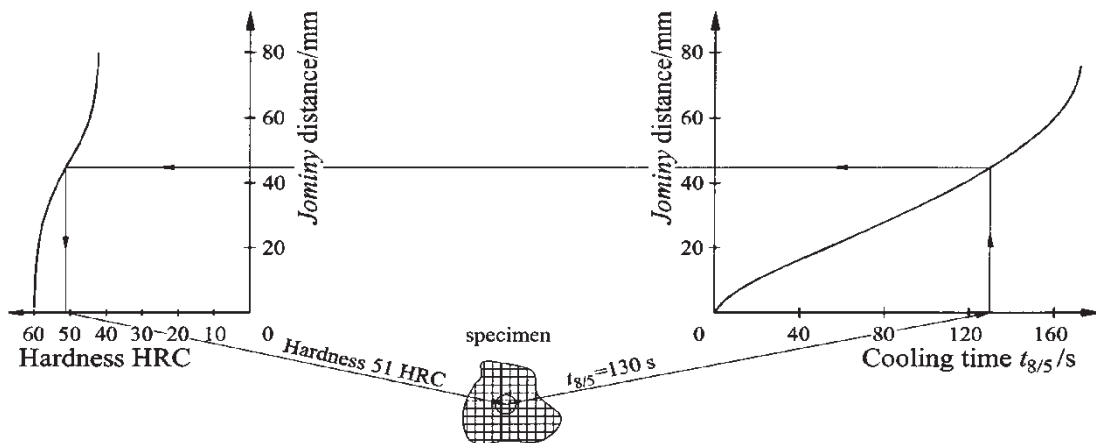
Figure 2. Conversion of the cooling time $t_{8/5}$ to the hardness

Cooling times, $t_{8/5}$ of characteristic microstructure composition can be calculated based on cooling times in characteristic points in Jominy specimen with 95 % of martensite, 50 % of martensite, 100 % of pearlite and 50 % of pearlite in microstructure. The microstructure composition in characteristic Jominy points can be calculated based on characteristic hardness. Hardness, microstructure composition of characteristic steel microstructure and characteristic temperature of austenite decomposition were calculated based on Jominy test results [20].

32

APPLICATION

The developed method for prediction of mechanical properties and microstructure distributions were applied in design of two different castings. Computer simulation of mechanical properties and microstructure distribution of cast steel was done using the computer software BS-CASTING. The castings were made of steel EN 42CrMo4 and steel EN 100Cr6. The chemical composition of castings is shown in Table 1.

Table 1. Specific heat capacity of different microstructural compositions of steel

Steel	Chemical composition/wt.%									
	C	Si	Mn	P	S	Cr	Ni	Mo	Cu	V
EN 42CrMo4	0.44	0.14	0.62	0.011	0.025	1.19	-	0.23	-	0.16
EN 100Cr6	1.05	0.25	0.33	0.030	0.020	1.53	0.31	0.01	0.20	0.01

The geometry of the mould and castings is shown in Figure 3. Pouring temperature during the casting was 1580 °C and the temperature of the mould was 105 °C. The steel castings are poured from the open top of the mould. The hardness distribution of the castings is shown in Figure 4 and 5. The distributions of ferrite, pearlite, bainite and martensite of cast steel are shown in Figure 6 and 7.
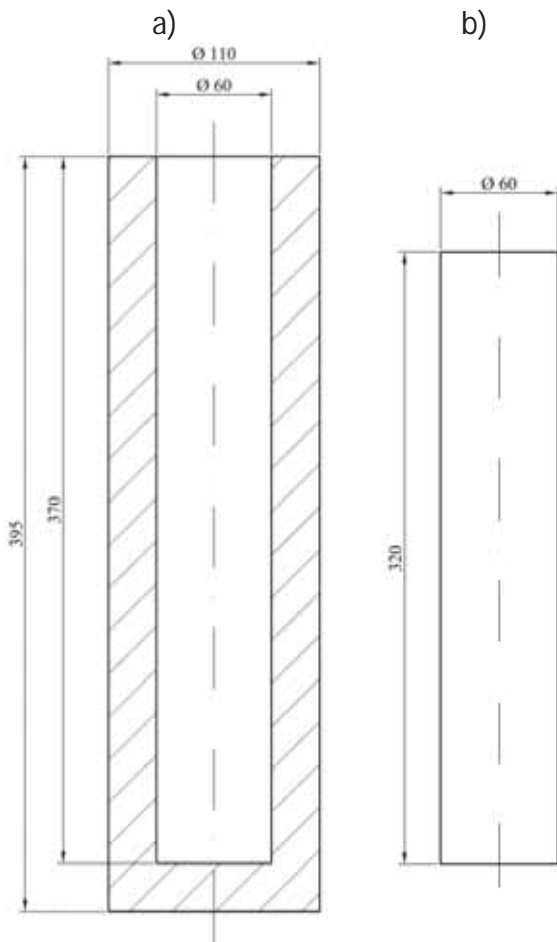
Figure 3. Geometry, a) mould, b) steel casting
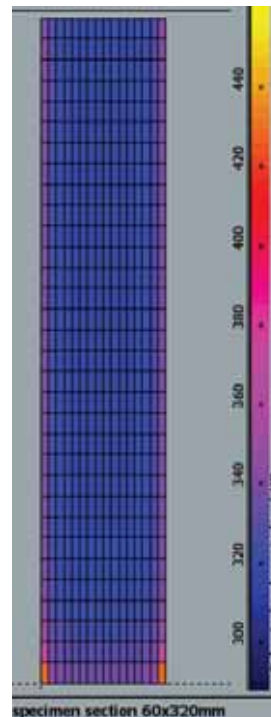
Figure 4. Distribution of hardness of EN 42CrMo4 steel
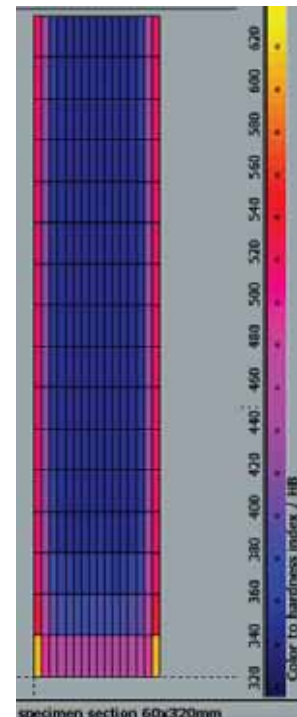
Figure 5. Distribution of hardness of EN 100Cr6 steel

33

Figure 6. Distributions of: a) ferrite, b) pearlite, c) bainite, d) martensite
of EN 42CrMo4 steel casting
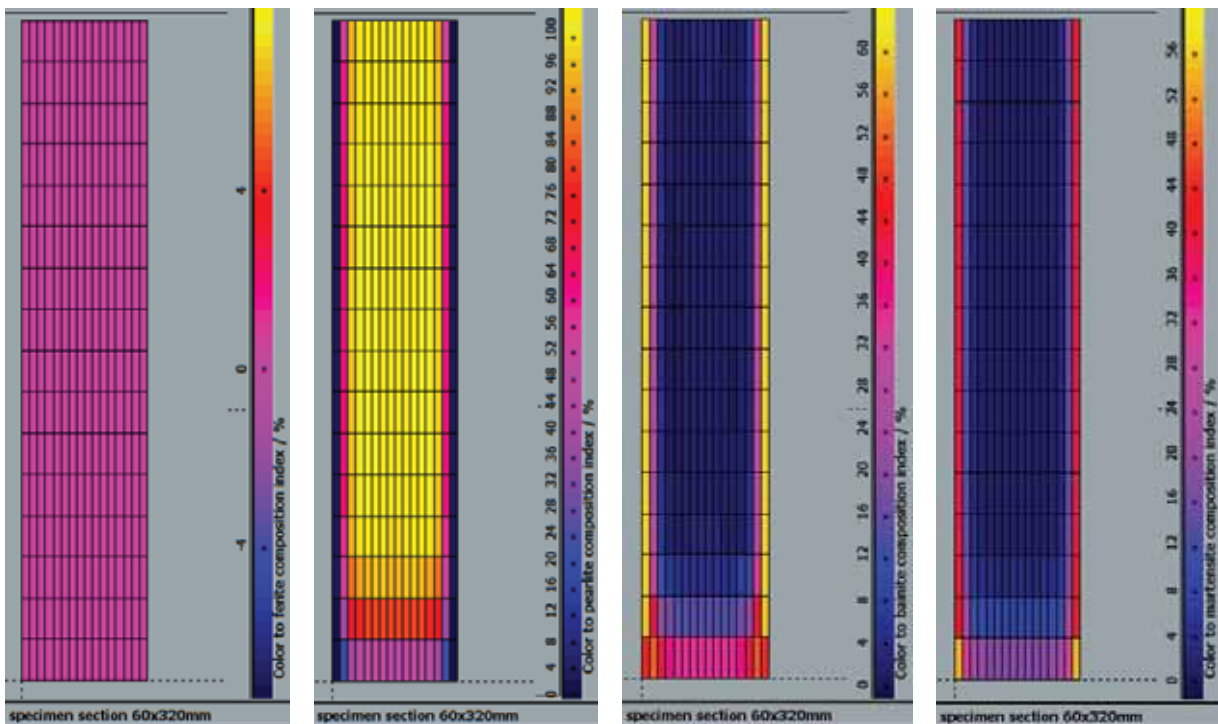
Figure 7. Distributions of: a) ferrite, b) pearlite, c) bainite, d) martensite
of EN 100Cr6 steel casting

CONCLUSIONS

The mathematical model of steel casting has been developed to predict the hardness and microstructure distribution in a cast steel specimen. The numerical model of casting is based on the finite volume method and is consisted of:

- numerical modelling of solidification,
- numerical modelling of transient temperature field,
- microstructure transformation in solid state,
- numerical modelling of hardness.

Input material properties involved in mathematical model of casting are additionally adjusted with experimental work by inversion method.

Hardness and microstructure composition in cast steel specimen points was calculated by the conversion of calculated cooling times from 800 to 500 °C to hardness and microstructure composition.

A developed mathematical model has been applied in computer simulation of casting of two ingots made of steel EN 42CrMo4 and steel EN 100Cr6. It can be concluded, that hardness and microstructure composition in cast steel can be successfully calculated by proposed method.

REFERENCES

[1] N. M. Vanaparthy, M. N. Srinivasan, Modelling of solidification structure of continuous cast steel, Modell. Simul. Mater. Sci. Eng., 6(1998), pp. 237–249.

[2] T. C. Tszeng, S. Kobayashi, Stress analysis in solidification process: Application to continuous casting, Int. J. Mach. Tools Manuf., 29(1989), pp. 121-140.

[3] M. Rosso, Modelling of Casting, in Handbook of thermal process modelling steels, eds. C.H. Gur, J. Pan, CRC Press, 2008.

[4] G. Golański, Effect of the heat treatment on the structure and properties of GX12CrMoVNbN9-1 cast steel, Archives of Materials Science and Engineering, 46/2 (2010), pp. 88-97.

[5] J. Falkus, K. Miłkowska-Piszczek, M. Rywotycki, E. Wielgosz, The influence of the selected parameters of the mathematical model of steel continuous casting on the distribution of the solidifying strand temperature, Journal of Achievements in Materials and Manufacturing Engineering, 55/2(2012), pp. 668-672.

[6] I. Telejko, H. Adrian, K. Skalny, M. Pakiet, R. Staśko, The investigation of hardenability of low alloy structural cast steel, Journal of Achievements in Materials and Manufacturing Engineering, 37/2(2009), pp. 480-485.

[7] A. Zieliěski, J. Dobrzaěski, G. Golaěski, Estimation of the residual life of L17HMF cast steel elements after long-term service, Journal of Achievements in Materials and Manufacturing Engineering, 34/2(2009), pp. 137-144.

[8] M. Schneider, C. Beckermann, Formation of macrosegregation by multicomponent thermosolutal convection during the solidification of steel, Metallurgical and Materials Transactions A, 26(1995)9, pp. 2373-2388.

[9] A. Sommerfeld, B. Böttger, B. Tonn, Graphite nucleation in cast iron melts based on solidification experiments and microstructure simulation, J. Mater. Sci. Technol., 24(2008), pp. 321-324.

[10] L. A. Dobrzański, A. Śliwa, T. Tański , Finite element method application for modelling of mechanical properties, Archives of Computational Materials Science and Surface Engineering, 1/1 (2009), pp. 25-28.

[11] B. Smoljan, D. Iljkić, L. Štic, Computer simulation of microstructure and mechanical properties of cast steel, Proceedings of the 15th International Foundrymen Conference, 11-13 May, 2016, Opatija, Croatia.

[12] C. H. Gur, J. Pan, Handbook of thermal process modelling steels, CRC Press, 2008.

[13] S. Patankar, Numerical heat transfer and fluid flow, McGraw Hill Book Company, New York, 1980.

[14] B. Smoljan, D. Iljkić, H. Novak, Estimation of coefficient of heat conductivity and heat transfer coefficient in the numerical model of the steel quenching, Proceedings of the 2nd Mediterranean Conference on Heat Treatment and Surface Engineering, 11-14 June, 2013, Dubrovnik - Cavtat, Croatia.

[15] L. Sowa, Mathematical model of solidification of the axisymmetric casting while taking into account its shrinkage, Journal of Applied Mathematics and Computational Mechanics, 13(2014)4, pp. 123-130.

[16] M. Flemings, Solidification processing, McGraw-Hill Book Company, 1984.

[17] Heat Treating, Vol. 4, ASM Handbook, ASM International, 1991.

[18] S. Smokvina Hanza, Mathematical modelling and computer simulation of microstructure transformations and mechanical properties during steel quenching, Doctoral Thesis, Department of Materials Science and Engineering, Faculty of Engineering, University of Rijeka, (2011) (in Croatian).

[19] A. Rose, F. Wever, Atlas zur Wärmebehandlung der Stähle I, Verlag Stahleisen, Düsseldorf, 1954.

[20] B. Smoljan, D. Iljkić, Computer modelling of mechanical properties and microstructure of quenched steel specimen, Proceedings of the 5th International Conference on Thermal Process Modeling and Computer Simulation, 16-18 June 2014, Orlando, FL USA.

Acknowledgements

QUO VADIS SLOVAK FOUNDRY INDUSTRY

Iveta Vasková[1], **Ján Cibuľa**[2], **Martin Conev**[1]

[1]Technical University of Košice Faculty of Metallurgy, Institute of Metallurgy,
Košice, Slovakia
[2]Cibula Consultant, Žiar nad Hronom, Slovakia

Abstract

Production of castings on Slovak ground has a longtime tradition and went through a different phases of development. Slovakia was a heart of industry in Hungarian part of Austria-Hungary until 1918 and in the beginning of 20th century it was studded by iron mills, which among the pig iron spread also the casting production. Creation of Czechoslovakia had a negative influence on castings production. Competition of more developed foundry industry of Czech lands led to reduction of industry in Slovakia. It has changed in 30ties when the military production was replaced away from the western borders of Czechoslovakia from a strategic reason. At the time of WW2 an industry boom had shown, naturally with a dominance of military industry and castings production began to increase. After the year 1948 many of plants were built in Slovakia, but most of them for production of raw materials and semi-finished product, which were then finished in Czech. It took almost 20 years after the Federation creation since the foundry production was on expansion in Slovakia again. Significantly helpful was the moving of production of die pressure machines to Snina, also a start of aluminium castings production with export to Czech, but mainly the military industry. Although a decreased production at the beginning of nineties they were able to stabilize the production by the end of the century. The beginning of 21th century was for Slovak foundries guided by a surprisingly high increase of production. Development of automotive production in Slovakia became such a strong customer, that in recent years, more foreign producers are incoming to Slovakia.

Keywords: *slovak foundry industry, development in 21st century, military industry, automotive industry*

*Corresponding author (e-mail address): *iveta.vaskova@tuke.sk*

INTRODUCTION

Castings production on Slovak land has a long-time tradition and went through a many phases. If we are not thinking about bronze castings from a renaissance time, then the first

industrially produced castings at the beginning of 19th century were mainly art-decorated castings from cast iron made in Prakovce, or later industrial castings in Krompachy or Cinobaňa. Slovakia was a heart of industry in Hungarian part of Austria-Hungary until 1918 and in the beginning of 20th century it was studded by iron mills, which among the pig iron spread the casting production too, foundries in Trnava and Fiľakovo. Creation of Czechoslovakia had a negative influence on castings production, compared to Czech lands, which were the industrial base of the Austrian part of monarchy. Slovakia (although in Hungarian greatly advanced) was much more behind. Competition of more developed foundry industry of Czech lands led to reduction of industry in Slovakia. It changed in 30ties when the military production was replaced away from the western borders of Czechoslovakia (Škoda Plzeň to Dubnica nad Váhom, Zbrojovka Brno to Považská Bystrica) from a strategic reason. At the time of WW2 an industry boom has shown, naturally with a dominance of military industry and castings production began to increase. After the year 1948 many of plants were built in Slovakia, but most of them for production of raw materials and semi-finished products, which were then finished in Czech. If there was a higher demand for castings, it was not covered by expanding of existing foundries, but by import - e.g. from Český Liberec to Brezno, even when in near Hronec was a foundry. It took almost 20 years after the Federation creation since the foundry production was on expansion in Slovakia again. The moving of production of die pressure machines to Snina, also a start of greater production of aluminium castings with export to Czech (for Avia, Tatra or Zetor), but mainly military industry (in Prakovce there were a special moulding lines for a tank treads segments) significantly helped.

Development until year 2000

In the 80ties, in the former Czechoslovakia 800 000 tons of castings was poured, more than 70% was made of grey cast iron. Crushing majority of production was for a military industry, in 1989 we were even one of the world greatest producers of weapons. For illustration in 1989 Závody ťažkého strojárstva (ZTS) made a products for cost of 8,4 billion euro and were employing a little over 87 thousand people. If we were producing these volumes of weapons today, Slovakia could theoretically compete even with Russia, which in 2014 officially exported weapons in cost of 13 billion euro to the world.

Figure 1. Military industry took a significant place in Slovak foundry development

Almost 4 thousand tanks T-55 (Figure 1) were exported to countries like Hungary, Romania, India, Morocco, Syria, Egypt and today not anymore existing German democratic republic and Yugoslavia (therefore into lands of today´s Croatia). In times when Slovakia was falling apart with Czech (in 1993) from the military industry only torso was left and most of Slovak foundries had to find a different customer. It also came to a significant restriction of export to civil sector of Czech Republic and a loss of these two large sales outlets had reflected very negatively. It came to a sudden decrease of production, stop of investing into foundry industry and almost third of foundries were even closed. A significant moment in 90ties was privatizing of most plants producing castings, mostly by their own management. Despite of initial decrease of production, until the end of last century a production of castings was stabilized and even progressively increased through the export into the West European countries. Gray cast iron and ductile iron castings were exported mainly into the Italy and Germany, aluminium castings were exported to the markets in Germany, France, Denmark etc. Slovak owners were successfully developing foundries by themselves and through the increasing production volumes were investing into the modern and efficient equipment, which further granted them a good competitive pros needed for export. Despite all of this the production at the end of century started to stagnate (see Table 1. and Figure 2.), because competition from Germany and other West European countries started to produce a part of castings in countries of Eastern Europe and simple product from grey cast iron were imported from China. Until 2000 these negative aspects caused a decrease of castings production in all technologies the aluminium castings including.

Table 1. Production of castings in ton/year between years 1993 and 2000 [1]

	1993	1994	1995	1996	1997	1998	1999	2000
Grey cast iron castings	34 765	37 938	42 224	44 678	38 683	37 260	39 000	39 447
Ductile cast iron castings	1 834	1 437	3 034	3 926	3 836	3 594	2 375	2 147
Steel castings	7 546	7 146	9 588	9 700	8 241	7 140	5 125	2 024
Investment casting							95	98
Non-ferrous castings	22 776	21 243	21 363	21 350	15 269	13 398	14 517	13 925
Casting in all	66 921	67 764	76 209	79 654	66 029	61 392	61 112	57 641
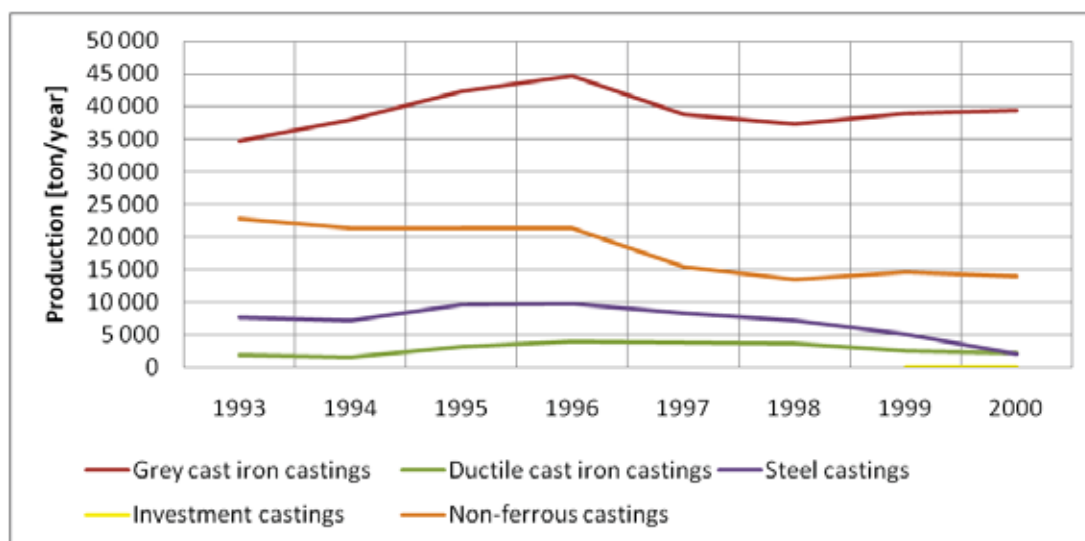
Figure 2. Graph of production development in 1993 - 2000
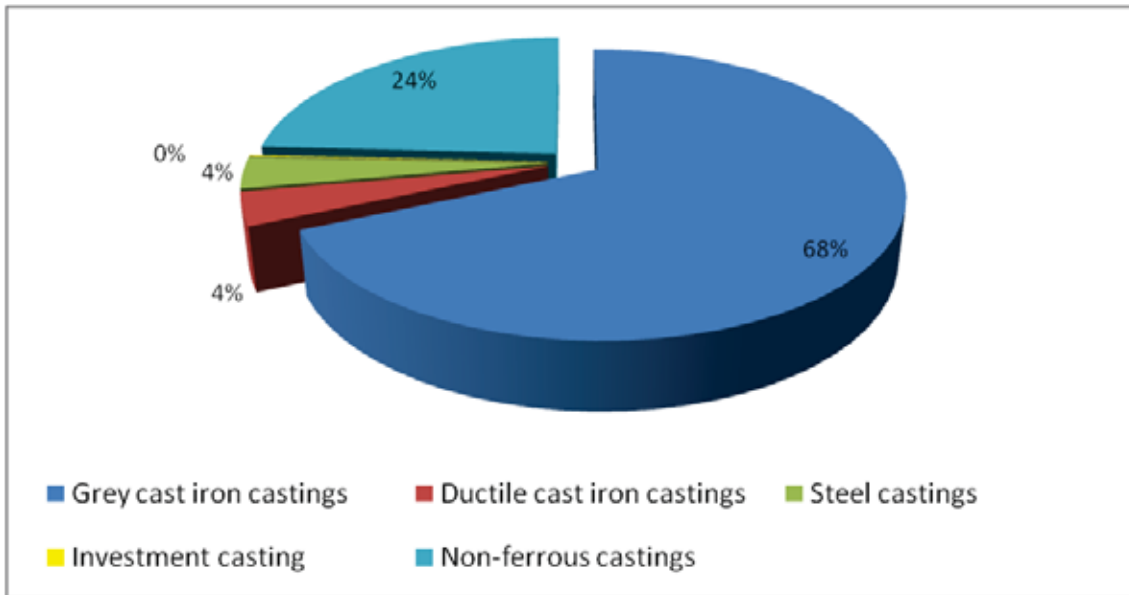
Figure 3. Graph of production in year 2000

Situation in 21st century

The beginning of 21st century was for Slovak foundries guided by a surprisingly high increase of production. After year 2000 an expanding industry of European countries became an acquisitive customer of Slovak castings. In first five years of this century practically 70-90% of produced castings were exported from Slovak foundries. Development of automotive production in Slovakia became such a strong customer, that in recent years, more foreign producers are incoming to Slovakia. Conditions of trade co-operation in the export were improved by Slovakia entering the EU and later Eurozone! It wasn´t a technology of grey cast iron though, but the Slovak foundries succeeded to get a ductile iron cast markets. In first five years of new century the increase of this commodity was over 600%! (Table 2 and Figure 4).

Table 2. Production of castings in ton/year after 2000 [1]

	2000	2004	2008	2009	2010	2012	2014	2015
Grey cast iron castings	39 447	40 850	34 852	22 450	24 500	25 310	25 200	24 950
Ductile cast iron castings	2 147	14 010	16 230	10 480	13 120	14 800	15 400	17 520
Steel castings	2 024	5 820	6 450	3 200	3 510	3 840	3 920	4 050
Investment casting	98	102	98	100	110	118	115	124
Non-ferrous castings	13 925	34 260	36 500	38 250	43 580	43 880	44 850	48 560
Casting in all	**57 641**	**95 042**	**94 130**	**74 480**	**84 820**	**87 948**	**89 485**	**95 204**

It managed to obtain also foreign markets for steel castings and double their production. Excellent outcome had managed also in production of aluminium alloy castings, where almost tripled production compared to the end of 20th century was achieved. However, this production segment was not about new foreign markets, but about the coming of multinational corporations producing castings to the Slovak foundries. Their ownership of Slovak foundries was initiated mainly by development of automotive industry in Slovak ground. Besides the Volkswagen assembly plant, other car factories were opened - Peugeot

40

and later KIA. Practically the whole volume of growing production of castings from aluminium alloys, made by both pressure die casting and mould casting, is already not exported, but stays in Slovakia and is supplying directly Slovak automobile plant branches. Automotive production development (last year more than million cars was made in Slovakia) in Slovakia became such a strong customer, that in recent years, other foreign producers are coming and building new and modern plants (latest Spain company Funderia Condals). Recently the British car factory Jaguar Land Rover has started building a new car assembling plant in Slovakia.
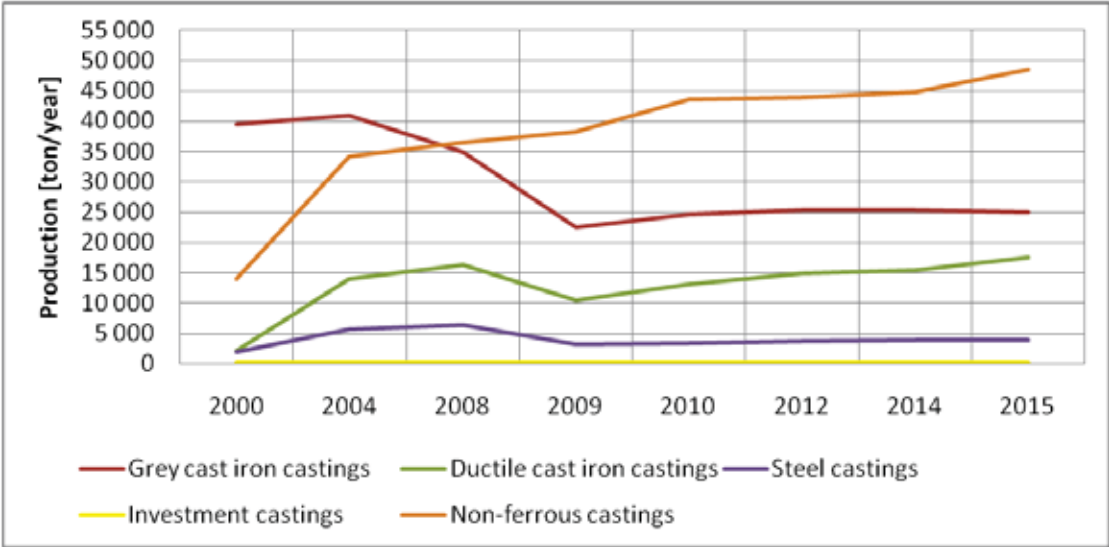
Figure 4. Graph of production development since 2000

Promising start of castings production increase was disrupted by year of crisis 2009 in Slovakia too, which had a significant impact on production. Mainly the production of iron alloys castings was decreased. Production of castings from aluminium was kept in mild increase, considering minimal impact of crisis on automotive industry.
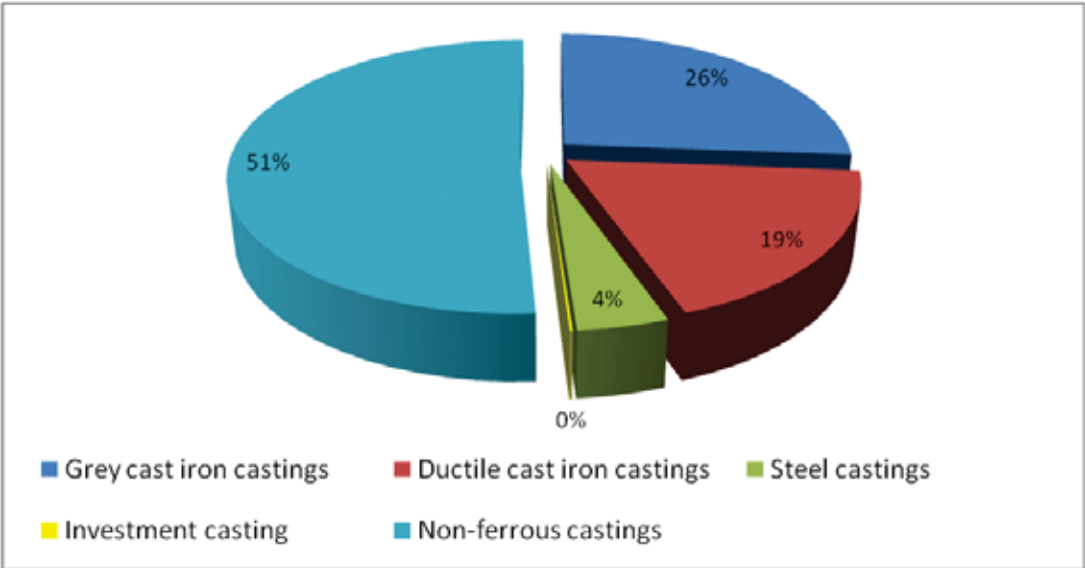
Figure 5. Graph of production in year 2015

41

CONCLUSIONS

Nowadays, there are 16 foundries producing castings from iron alloys, 27 foundries producing castings from aluminium alloys and 7 foundries producing castings from other non-ferrous metals. In the range of product composition the importance of gray cast iron had decreased and more than 50% of castings are made from aluminium alloys. Foundries in Slovakia are on a different level, regarding a technology of production and also a volume of production. They are able to manufacture castings from small-scaled castings from zinc or brass (100 grams) to castings over 500 kg from gray cast iron. In total, foundries were mostly greatly upgraded or more precisely automated and they are able to achieve high productivity with a small amount of employees. On average foundries are employing 126 of employees, but it depends on the volume of production from 10 to more than 300 people. Salaries in the sector are significantly varying and depend on a size of foundry, a nature of work and the differences can be in hundreds of euro. The average salary is around 880 €. Production of castings in Slovakia, if there will be no decrease in automotive industry or another crisis, is growing and perspective. Also foundries started developing of machining castings to a final shape and dimensions and are delivering them straight to assembling in machinery.

REFERENCES

[1] Association of Foundries and Forges of Slovakia.

DILATOMETRIC ANALASYIS OF THE AUSTEMPERED DUCTILE IRON SAMPLES

Hasan Avdušinović[1], Almaida Gigović-Gekić[1], Šehzudin Dervišić[2]

[1]University of Zenica Faculty of Metallurgy and Materials Science,
Zenica, Bosnia and Herzegovina
[2]Livnica Turbe, Travnik, Bosnia and Herzegovina

Abstract

Dilatometry is a thermoanalytical technique used to measure the expansion or shrinkage of solids, powders, pastes and liquids under negligible load when subjected to a controlled temperature/time program. Dilatometry is a type of investigation that is very often used for studying the phase transformation of the metals and alloys. In this paper, the dilatometric curves of the austempered ductile iron samples are used as a tool for studying microstructure change versus temperature or time, while the sample undergoes a controlled temperature program.

Keywords: dilatometry, austempered ductile iron, phase transformation

*Corresponding author (e-mail address): <u>hasan.avdusinovic@famm.unze.ba</u>

INTRODUCTION

Austempered ductile iron (ADI) is a heat-treated ductile iron. ADI has many good properties such as a very favorable combination of high strength and ductility, good wear resistance and high fatigue strength. Its increased mechanical properties compared with ductile iron are related to the specific microstructure of ADI called "ausferrite" that consists of acicular ferrite (α) and high carbon (retained) austenite (γHC). Austempering is a heat treatment process applied to ductile iron in order to improve its properties. A precondition for a successful heat treatment process is the high quality of the base ductile iron. Good quality base ductile iron means following: a minimum nodule count (higher than 120 / mm^2), a minimum nodularity of 85 % and consistent chemistry. ADI was first commercialized in the early 1970s but serious research in the field of ADI application was carried out at the end of the 20th and beginning of the 21st century [1,2].

ADI is often used where high strength is needed and where excellent wear resistance and fatigue strength are required, such as gears and other similar products. Due to the lower modulus of ADI better face to face contact can be achieved reducing contact stress on the teeth surfaces. Also austempered ductile iron will work harden improving the contact fatigue strength. The superior tribological properties of ADI will allow the gears to run temporarily without lubrication. Another common application of austempered ductile iron castings has been crankshafts and axles. Some applications of ADI include: timing gears, CV joints, steering knuckles sprockets, rollers, idlers, suspension housings and brackets, wear plates, wheel hubs, crankshafts, flanged shafts, etc. [3,4].

Generally, some Benefits of Austempered Ductile Iron Castings are:

- Up to 40% less cost than hardened steel forgings,
- Lower operating noise levels,
- 10% less weight than steel,
- Better wear than case hardened steel,
- Excellent resistance to crack propagation,
- Good impact strength to -80°C,
- Work hardening.

Having in mind above mentioned very good properties of the ADI material questions about its behavior after being exposed to elevated temperatures have been raised. This information is critical to the design engineers since it may determine the maximum allowable operating temperature for a component. Furthermore, heat treated materials would be expected to be less likely to maintain their mechanical properties if the elevated temperature exposure met or exceeded the heat treatment temperature.

It is already known that the Austenite in the Ausferrite structure is thermally stable to very low temperatures. However, the Austenite can break down into ferrite and carbide if exposed to elevated temperatures, resulting in a gradual degradation of mechanical and ductile properties [5].

Breaking down of the Austenite (Austenite transformation) into a ferrite and carbides is connected with some volume changes. For better understanding of volume changing of the material due to microstructure transformation dilatometry can be used. Dilatometry is a method for determining dimensional changes versus temperature or time while the sample undergoes a controlled temperature program. It is a thermoanalytical technique used to measure the expansion or shrinkage of solids, powders, pastes and liquids under negligible load when subjected to a controlled temperature/time program. A precise understanding of dilatometric behavior of the material can provide insight into microstructure transformation processes, the temperature range of the transformations etc. [6].

In a study performed with dilatometer, Nadkarni and Gokhale observed volumetric changes associated to decomposition of the ausferritic microstructure [7]. They reported the stable austenite transformation (volumetric changes) occurring in the range of 450-550°C.

MATERIALS AND METHODS

The objective of this study was to determine the microstructure stability under elevated temperature conditions of two types of Austempered Ductile Irons. Questions have been

raised as to how ADI will change its microstructure after being exposed to elevated temperatures and on which temperature range the microstructure change is going to happen.

Material selection

Two types of ADI material were chosen for this study, ASTM 897 ADI (grade 1 and 3) [4]. Chemical composition of the initial nodular iron is given in the Table 1. Microstructure of the initial nodular iron used for ADI production is presented in Figures 1 and 2.

Table 1. Chemical composition of the initial nodular iron

Chemical composition (wt. %)						
C	Si	Mn	P	S	Mg	Ceqv
3,48	2,10	0,40	0,027	0,012	0,045	4,18
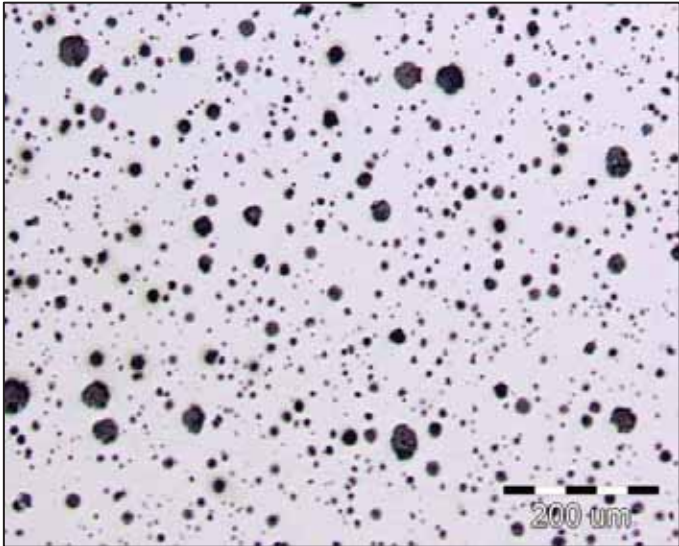
Figure 1. Microstructure of the Ductile Iron (after polishing)
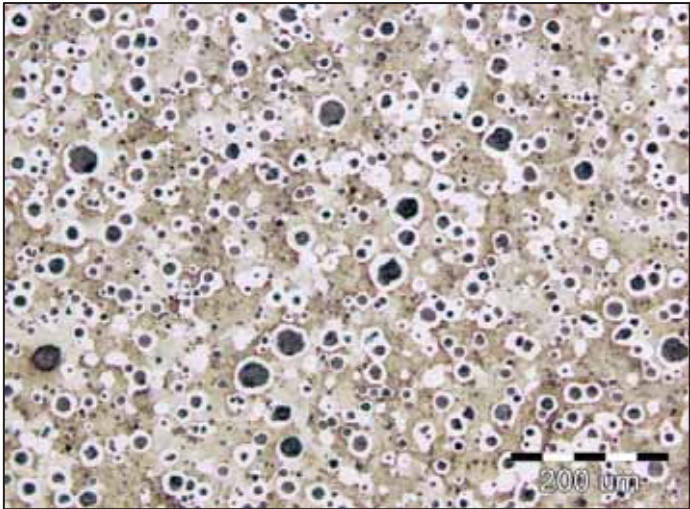
Figure 2. Microstructure of the Ductile Iron (3% Nital etched)

45

Initial material was heat treated in a heat treat furnaces. Austenitizing was completed at an 870°C in the air atmosphere for the both grades of ADI samples. Austempering was done in a potassium nitrate salt bath. The temperature of the salt bath for the Grade 1 ADI was 400°C and for the Grade 3 ADI was 340°C. Austenitization time for both ADI grades was 1.0 hour and austempering time was 1.5 hours. The heat treat cycle for production of ADI samples is presented in Figure 3.
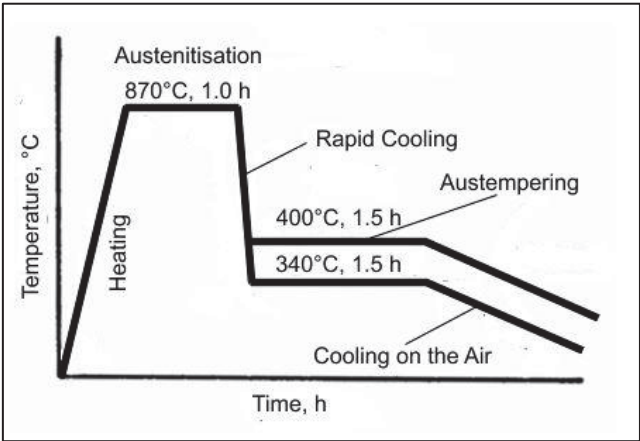
Figure 3. Heat treatment cycle for production of ADI samples (Grade 1 and Grade 3)

RESULTS AND DISCUSSION

After experimental procedure metallographic investigation of the treated material was carried out. For microstructure observation optical microscopy (Olympus) were used. The microstructure of the Grade 1 ADI and Grade 3 ADI are shown in Figures 4 and 5, respectively. Microstructure consists of well-formed graphite nodules in ausferrite matrix.
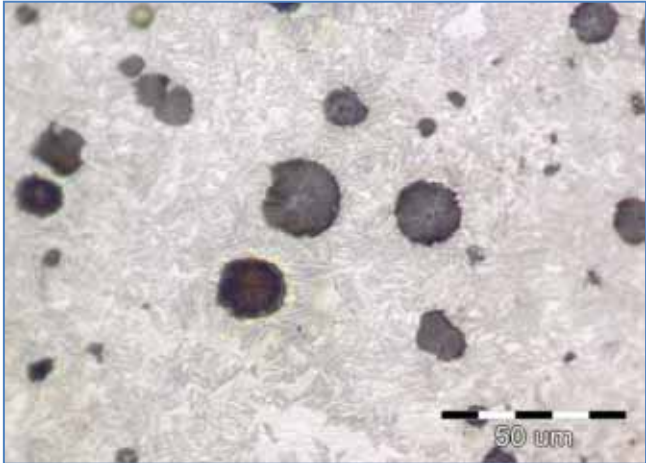
Figure 4. Microstructure of Grade 1 ADI sample (3% Nital etched)
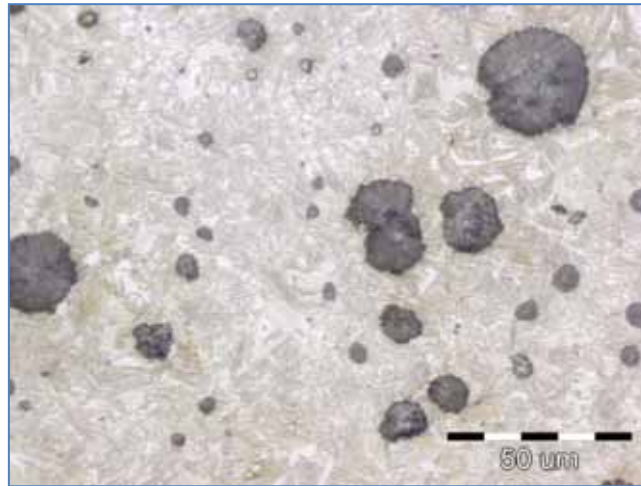
Figure 5. Microstructure of Grade 3 ADI sample (3% Nital etched)

Dilatometric behavior of the ADI grades was investigated using Netzsch 402/C/7 dilatometer (heating/cooling rate: 5 / K/min). The dilatometric curves are presented in Figure 6.
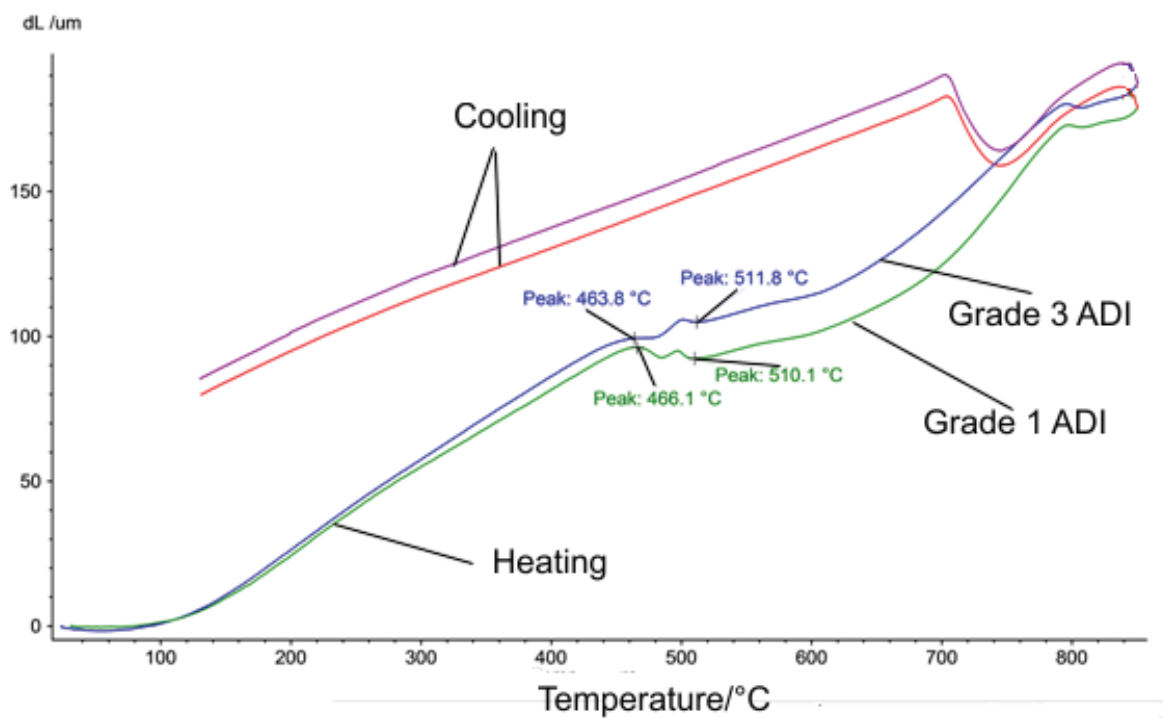
Figure 6. Dilatometric curves of ADI samples (Grade 1 and Grade 3)

The microstructure of the Grade 1 ADI and Grade 3 ADI after dilatometric behavior investigation is shown in Figures 7 and 8, respectively. Microstructure consists of well-formed graphite nodules in ferrite and globular pearlite metallic matrix.
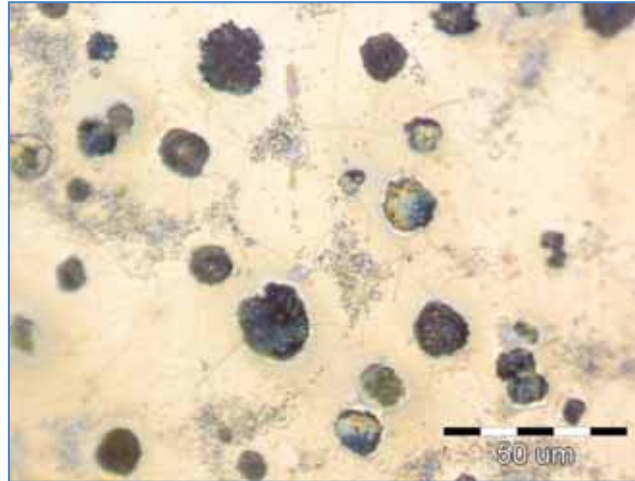
Figure 7. Microstructure of Grade 1 ADI sample after dilatometric behavior investigation (3% Nital etched)
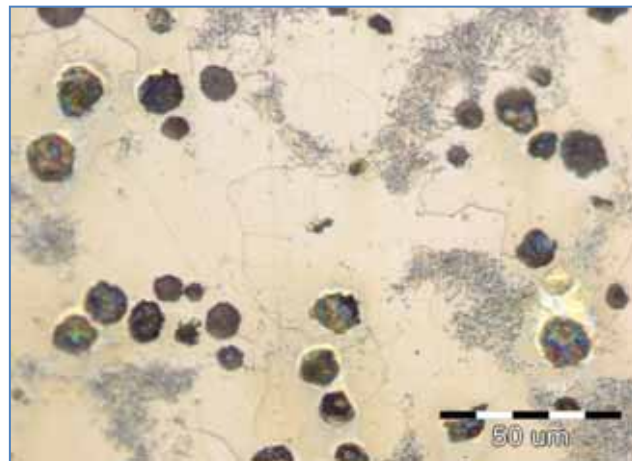
Figure 8. Microstructure of Grade 3 ADI sample after dilatometric behavior investigation (3% Nital etched)

CONCLUSIONS

The aim of this paper was to present the current possibilities of determining the microstructure changes for the real-ADI grades using dilatometric method. After analyzing of the experimental results following can be concluded:

- heating parts of the dilatometric curves for ADI Grade 1 and ADI Grade 3 from the diagram 2 clearly shows some volume changes in the temperature range of 460-510°C,
- the volume changes in the temperature range of 460-510°C indicate decomposition of the high carbon austenite,
- temperature regime of the high carbon austenite decomposition corresponds to the literature data for that phenomenon,
- comparing with the cooling parts of the same dilatometric curves volume changes in the temperature range of 460-510°C were not observed,

☐

- cooling parts of the dilatometric curves show typically behavior of cast iron samples with eutectoid transformation without any changes to room temperature.

REFERENCES

[1] M. Janjić, H. Avdušinović, Z. Jurković, F. Bikić, S. Savićević, Influence of austempering heat treatment on mechanical and corrosion properties of ductile iron samples, Metalurgija, 55(2016)3, pp. 325-328.

[2] S. Savićević, H. Avdušinović, A. Gigović-Gekić, Z. Jurković, M. Vukičević, M. Janjić, Influence of the austempering temperature on the tensile strength of the austempered ductile iron (ADI) samples, Metalurgija, 56(2017)1-2, pp. 149-152.

[3] J. R. Keough, K. L. Hayrynen, Automotive applications of austempered ductile iron (ADI): A critical review, Society of Automotive Engineers, Livonia, MI, USA, 2000.

[4] ASTM 897(M) Austempered Ductile Iron Specification, 1990.

[5] J. R. Keough, K. L. Hayrynen, G. L. Pioszak, Designing with austempered ductile iron (ADI), AFS Proceedings, American Foundry Society, 2010, Schaumburg, USA.

[6] http://thermalanalysislabs.com/dilatometry/(04-17-2017)

[7] G. Nadkarni, S. Gokhale, J. D. Boyd, Elevated temperature microstructural stability of austempered ductile irons, AFS Transactions, 104(1996), pp. 985-994.

16th INTERNATIONAL FOUNDRYMEN CONFERENCE
Global Foundry Industry – Perspectives for the Future
Opatija, May 15th-17th, 2017

EFFECT OF GATING SYSTEM DESIGN PARAMETERS ON MOLD FILLING PROPERTIES

UTJECAJ PARAMETARA ULJEVNOG SUSTAVA NA PUNJENJE KALUPA

Branko Bauer, Miran Milaković, Ivana Mihalic Pokopec

University of Zagreb Faculty of Mechanical Engineering and Naval Architecture,
Zagreb, Croatia

Abstract

Gating system should allow filling of the mould cavity, fast enough to prevent premature solidification of the melt, and yet slow enough to avoid inclusions in the casting. The shape, size and position of the gating system are critical process parameters for pouring of the melt into a mould cavity. For a given plate shaped casting, unpressurized gating systems with a gating ratio of 1:2:2 and 1:4:4 were modelled. Then the cross-sectional area of the bottom of the sprue was increased by seventy percent, while sections of runner and gates remained constant. For all four variants simulations were made in the simulation software QuikCAST. Wooden patterns of the gating system components were made and green sand moulds were produced. Aluminium alloy AlSi10Mg was casted. The results obtained by the simulations and experiments were compared.

Keywords: aluminium alloys, gating system, casting simulation

*Corresponding author (e-mail address): branko.bauer@fsb.hr

Sažetak

Oblik uljevnog sustava mora omogućiti dovoljno brzo punjenje kalupne šupljine kako ne bi došlo do preranog skrućivanja taljevine prije potpunog popunjavanja kalupne šupljine, a opet dovoljno sporo da se izbjegnu greške u odljevku uslijed turbulentnog strujanja taljevine. Oblik, veličina i položaj uljevnog sustava su kritični parametri procesa ulijevanja taljevine u kalupnu šupljinu. Za zadani odljevak u obliku ploče modelirani su semitlačni uljevni sustavi s omjerom presjeka kanala 1:2:2 i 1:4:4. Zatim je površina dna spusta povećana sedamdeset posto, a presjeci razvodnika i ušća ostali su konstantni. Za sve četiri varijante napravljene su simulacije u programskom paketu QuikCAST. Izrađeni su drveni modeli uljevnih sustava i jednokratni kalupi u koje je lijevana aluminijeva legura AlSi10Mg. Uspoređeni su rezultati dobiveni simulacijom i probnim lijevanjem.

Ključne riječi: aluminijeve legure, uljevni sustav, simulacija lijevanja

UVOD

Lijevanje metala je vrlo kompleksan proces i često može rezultirati neočekivanim rezultatima jer obuhvaća vrlo velik broj varijabli koje se moraju strogo kontrolirati. Iz prakse je poznato da većina grešaka na odljevcima potječe od nepravilno konstruiranog i postavljenog uljevnog sustava i sustava napajanja. Turbulentno strujanje taljevine, erozija kalupa i uključci u odljevku, deformacija odljevka, nepovoljni temperaturni gradijenti u kalupu itd. samo su neki od problema koji nastaju uslijed neadekvatnog uljevnog sustava [1]. Oblik uljevnog sustava mora omogućiti dovoljno brzo punjenje kalupne šupljine kako ne bi došlo do preranog skrućivanja taljevine prije potpunog popunjavanja kalupne šupljine, a opet dovoljno sporo da se izbjegnu uključci u odljevku uslijed turbulentnog strujanja taljevine. Oblik, veličina i položaj uljevnog sustava su kritični parametri procesa ulijevanja taljevine u kalupnu šupljinu [1-9].

MATERIJALI I METODE

Za zadani AlSi10Mg odljevak u obliku ploče dimenzija 150x100x20mm, modelirani su semitlačni uljevni sustavi sa omjerom presjeka kanala 1:2:2 i 1:4:4, slika 1. Proračun je izrađen prema literaturi [1]. Površina kritičnog presjeka na dnu spusta As iznosila je 116 mm^2, a promjer dna spusta ds iznosio je 12,2 mm. Zatim je površina kritičnog presjeka povećana sedamdeset posto, što je odgovaralo trideset posto većem promjeru dna spusta ds (1,3ds). Presjeci razvodnika i ušća ostali su konstantni. Za sve četiri varijante izvedene su simulacije lijevanja i skrućivanja odljevka u programskom paketu QuikCAST, s legurom AlSi10Mg. Vrijeme lijevanja iznosilo je 6 sekundi kod sve četiri varijante. Izrađeni su drveni modeli uljevnih sustava i jednokratni kalupi u koje je lijevana aluminijeva legura, s temperature 680 ⁰C. Dimenzije su za donjak: 300x200x65mm i za gornjak: 300x200x90mm.
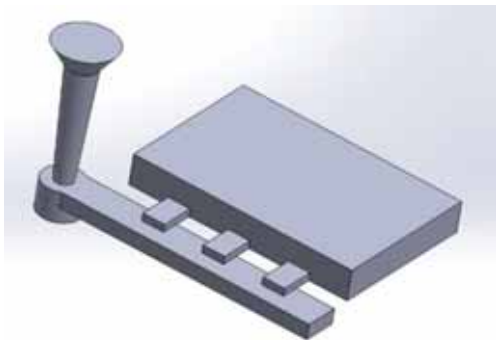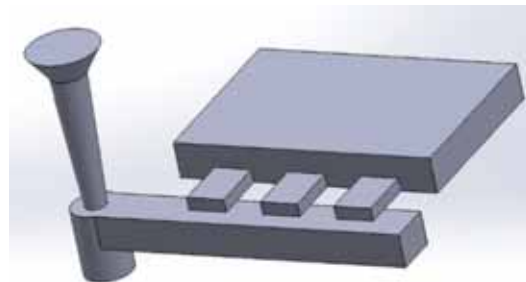
a) sustav 1:2:2   b) sustav 1:4:4

Slika 1. Modeli semitlačnih uljevnih sustava za lijevanje AlSi10Mg ploče

Brzine strujanja određene su prilikom simulacije punjenja kalupa u razvodniku i ušćima u trenutku kad je brzina taljevine kroz pojedino ušće postala konstantna, slika 2.
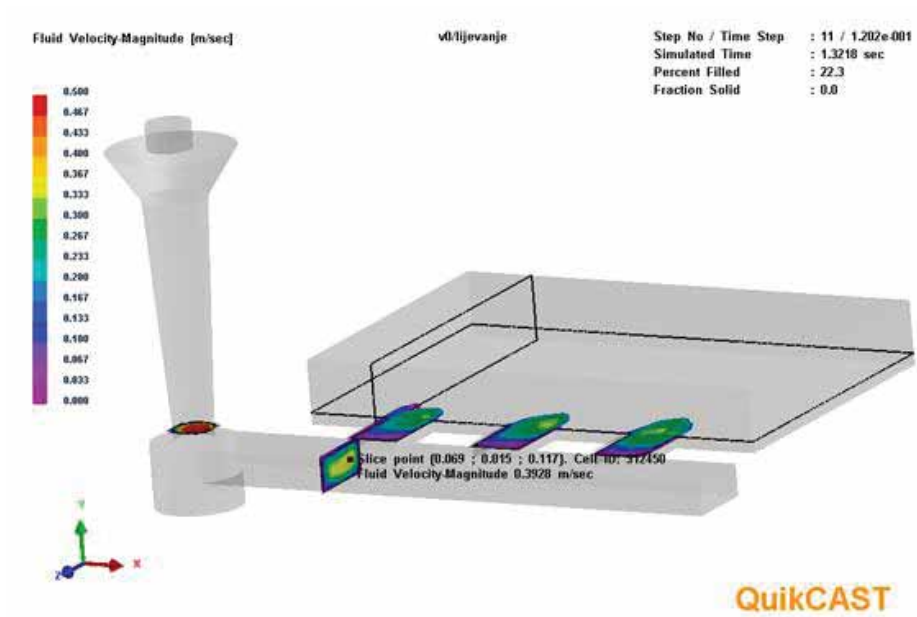
Slika 2. Mjesta mjerenja brzina strujanja u simulaciji

REZULTATI I DISKUSIJA

Na slici 3. Prikazano je popunjavanje razvodnika u semitlačnom sustavu 1:2:2.
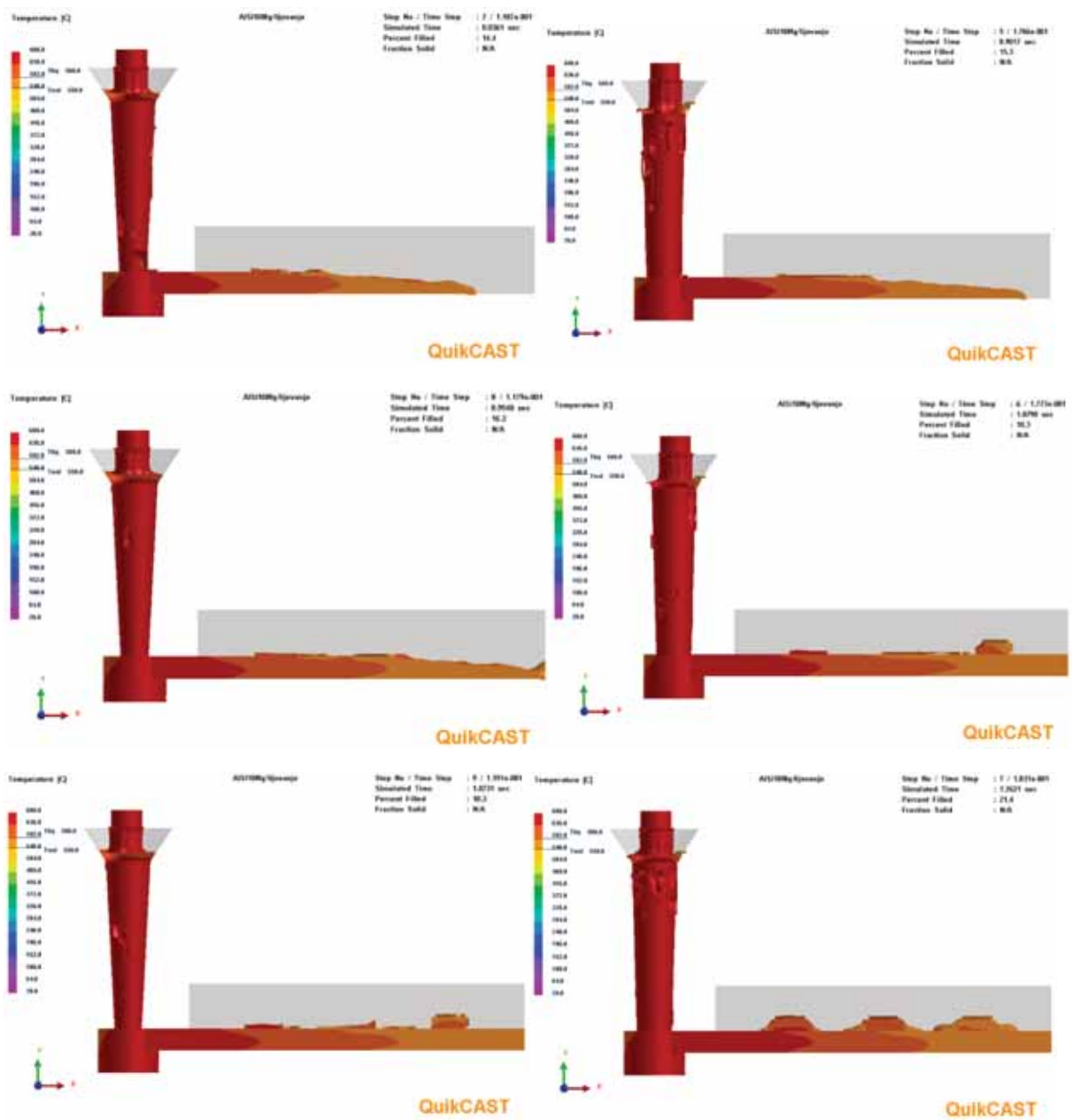
Slika 3. Popunjavanje razvodnika uljevnog sustava 1:2:2 (promjer dna spusta 12 mm u stupcu lijevo i 15 mm u stupcu desno)

Na slici 4. prikazano je popunjavanje razvodnika u semitlačnom sustavu 1:4:4.
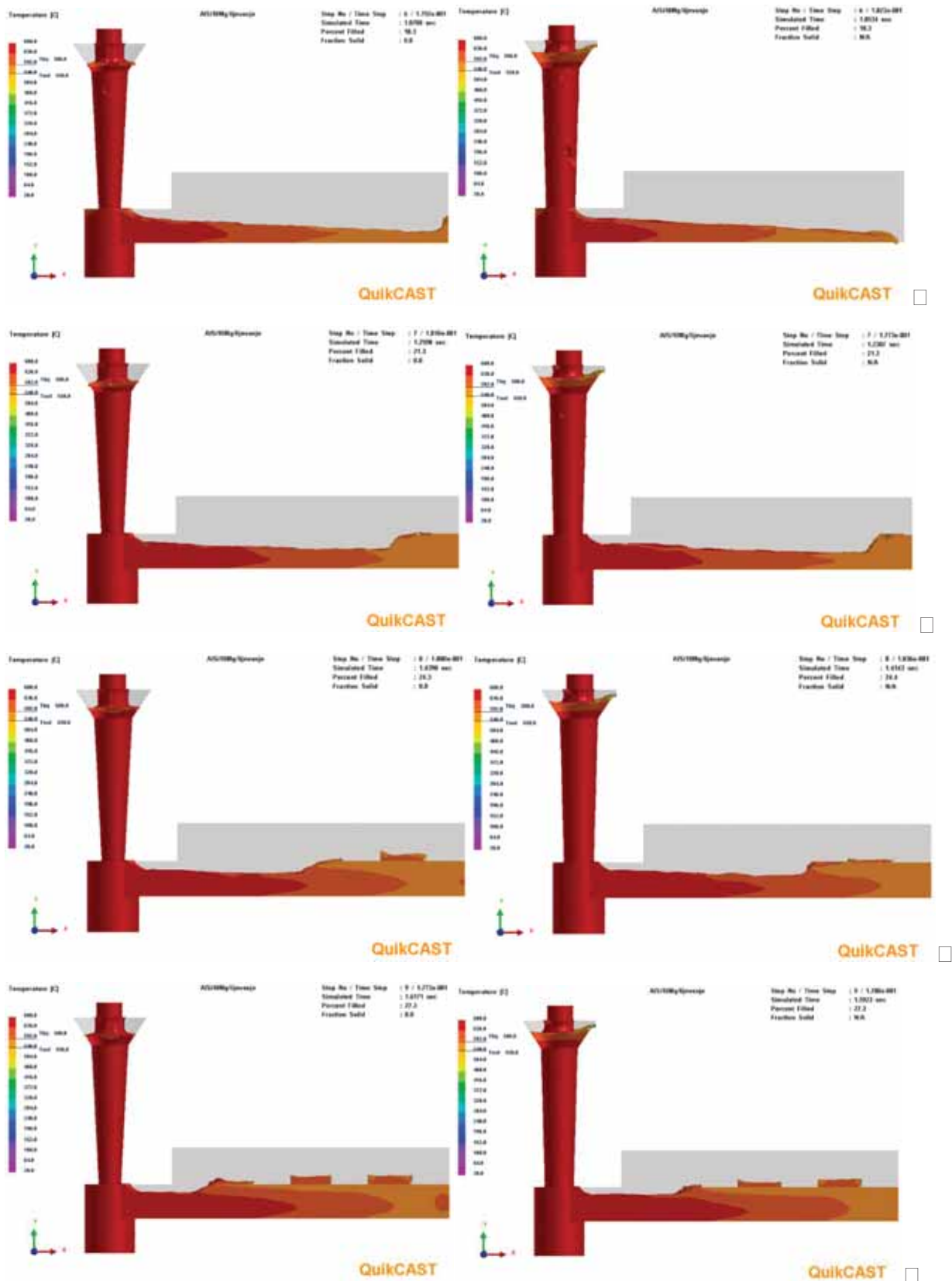
Slika 4. Popunjavanje razvodnika uljevnog sustava 1:4:4 (promjer dna spusta 12 mm u stupcu lijevo i 15 mm u stupcu desno)

Iz slika 3 i 4 može se uočiti jednak način popunjavanja razvodnika taljevinom bez obzira na površinu kritičnog presjeka. Prilikom popunjavanja razvodnika uljevnog sustava 1:2:2 taljevina teče cijelim presjekom razvodnika i zbog zakona inercije prvo počinje popunjavati treće, pa drugo i na kraju prvo ušće, slika 5. Prilikom popunjavanja razvodnika uljevnog sustava 1:4:4 taljevina teče do kraja razvodnika donjom polovicom, vraća se nazad u obliku povratnog vala i na kraju ulazi u ušća približno jednakim redoslijedom, slika 6.
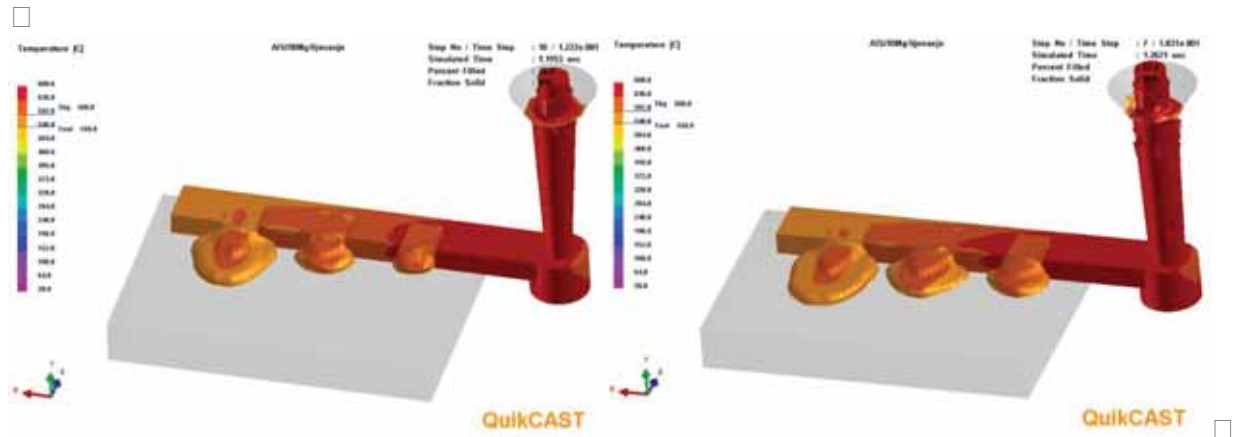
Slika 5. Ulaz taljevine u kalupnu šupljinu sustava 1:2:2 (promjer dna spusta 12 mm lijevo i 15 mm desno)
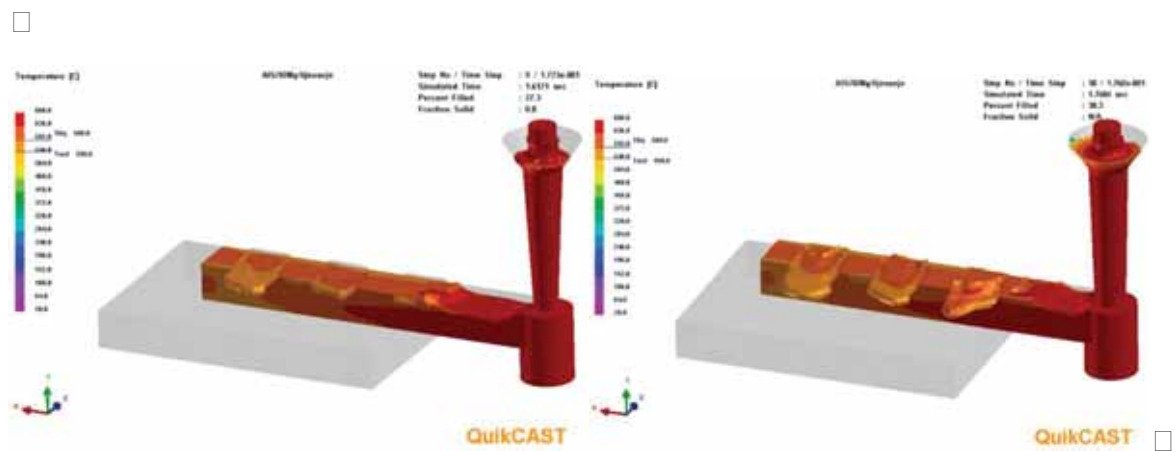
Slika 6. Ulaz taljevine u kalupnu šupljinu sustava 1:4:4 (promjer dna spusta 12 mm lijevo i 15 mm desno)

Razdioba brzina po presjeku ušća prikazana je slikama 7 i 8. Tok taljevine je s desna na lijevo. Uočava se veća brzina strujanja u sredini poprečnog presjeka ušća te povećanje područja većih brzina u smjeru toka taljevine. Brzine taljevine u ušću mjerene su u sredini područja s najvećom brzinom. Na slici 9 prikazan je dijagram brzina na ušćima tijekom punjenja kalupa u trajanju od 0 do 6 sekundi, za sustav 1:2:2.
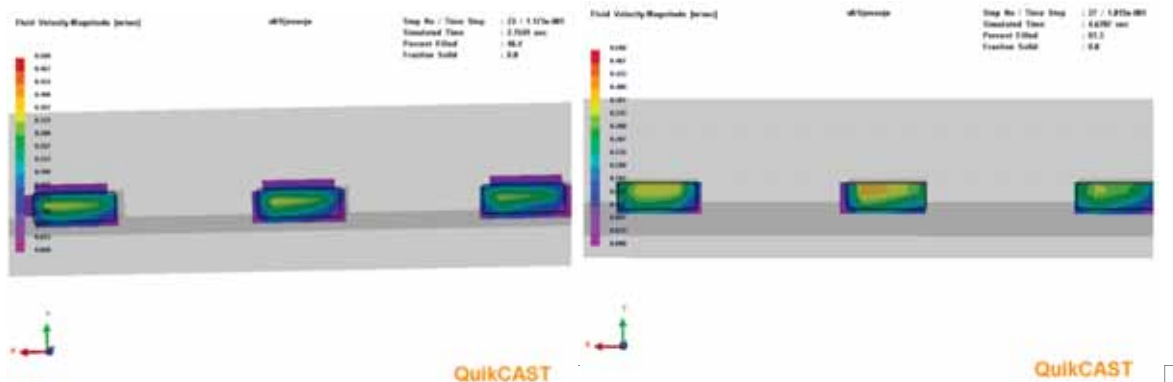
Slika 7. Razdioba brzina po poprečnom presjeku ušća sustava 1:2:2 (promjer dna spusta 12 mm lijevo i 15 mm desno)
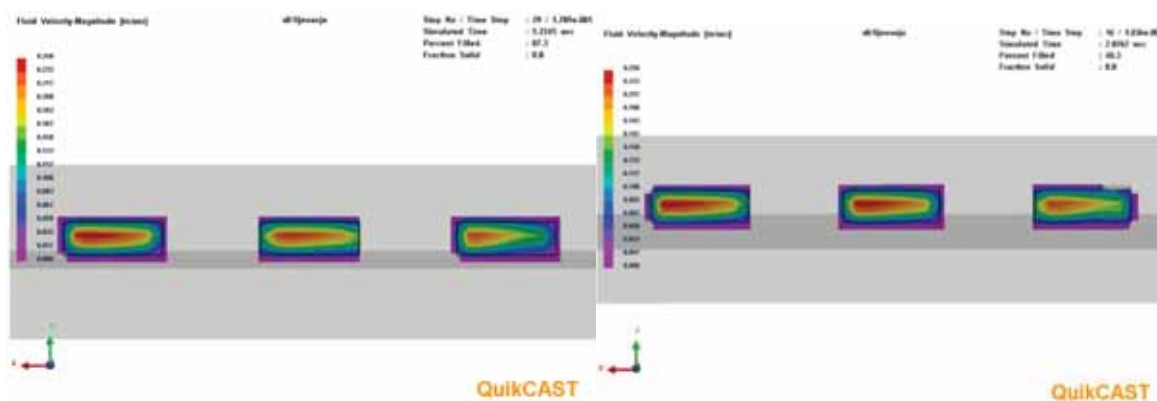
Slika 8. Razdioba brzina po poprečnom presjeku ušća sustava 1:4:4 (promjer dna spusta 12 mm lijevo i 15 mm desno)
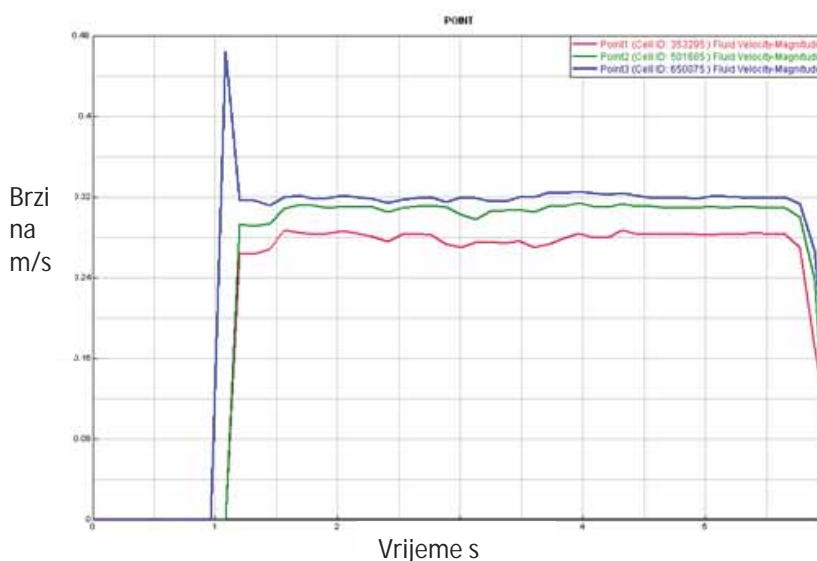
Slika 9. Brzine u ušćima, semitlačni uljevni sustav 1:2:2.
(crveno-brzina na prvom ušću, zeleno-brzina na drugom ušću, plavo-brzina na trećem ušću)

Na slici 10 dijagramski su prikazane brzine taljevine na ušćima uljevnih sustava 1:2:2 i 1:4:4, očitane iz simulacije. Kod uljevnog sustava 1:2:2 povećanje kritičnog presjeka djelovalo je na značajan porast brzina u ušćima, za razliku od sustava 1:4:4 gdje je taj porast minimalan. Može se uočiti značajno smanjenje brzina u ušćima u sustavu 1:4:4 u usporedbi sa sustavom 1:2:2, što doprinosi smanjenju turbulencija.
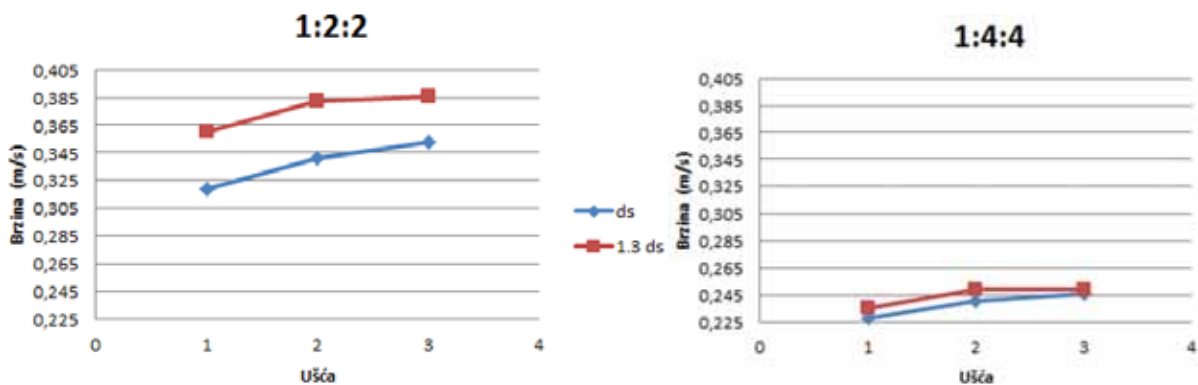
Slika 10. Brzina taljevine u ušćima uljevnih sustava 1:2:2 i 1:4:4 (ds-promjer dna spusta)

Rezultati mjerenja brzine u razvodniku prikazani su u tablici 1. Kod uljevnog sustava 1:2:2 povećanje kritičnog presjeka nije djelovalo na porast brzine u razvodniku, za razliku od sustava 1:4:4 gdje je porast brzine vidljiv. Može se uočiti značajno smanjenje brzina u razvodniku u sustavu 1:4:4 u usporedbi sa sustavom 1:2:2, što doprinosi smanjenju turbulencija.

Tablica 1. Brzine u razvodniku (ds-promjer dna spusta)

Uljevni sustav	1:2:2	1:2:2 (1,3ds)	1:4:4	1:4:4 (1,3ds)
Brzina strujanja u razvodniku m/s	0,39	0,40	0,24	0,28

Na slici 11. prikazano je lijevanje u stvarne kalupe u trenutku prodora taljevine u kalupnu šupljinu. Kod sustava 1:2:2 može se uočiti najveći protok kroz treće ušće kao što je dobiveno simulacijom, slika 5. Kod sustava 1:4:4 najveći je protok kroz prvo ušće, a zatim kroz drugo i treće, što se ne poklapa s rezultatima simulacije, slika 6. Kod sustava 1:4:4, slika 11 c) taljevina krene kroz prvo ušće, zatim kroz treće i na kraju kroz drugo. Kod sustava 1:4:4 s povećanim kritičnim presjekom, slika 11 d) taljevina krene kroz prvo ušće, zatim kroz drugo i na kraju kroz treće. Kod uljevnog sustava 1:4:4 na simulaciji se pojavljuje povratni val, što je mogući uzrok ne poklapanja rezultata simulacije i stvarnog lijevanja. Na ovaj način, ručnim lijevanjem teško je bilo postići vrijeme stvarnog lijevanja točno 6 sekundi.

57

a) sustav 1:2:2

b) sustav 1:2:2 (1,3ds)
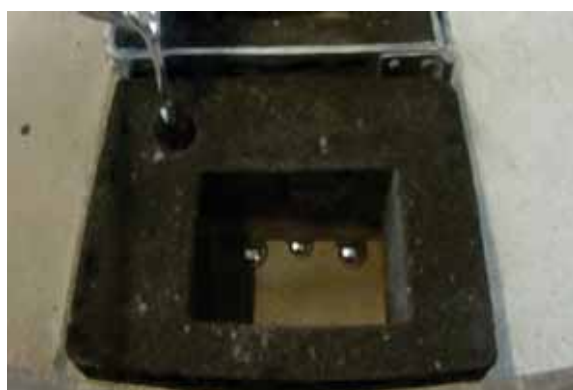
c) sustav 1:4:4

d) sustav 1:4:4 (1,3ds)

Slika 11. Početak punjenja kalupne šupljine (ds-promjer dna spusta)

ZAKLJUČAK

Za odljevak u obliku ploče konstruirane su dvije varijante semitlačnog uljevnog sustava s omjerom 1:2:2 i dvije varijante s omjerom 1:4:4. U drugoj varijanti kritični presjek povećan je 70%, dok su ostale dimenzije ostale nepromijenjene. Napravljene su simulacije i probno lijevanje aluminijeve legure AlSi10Mg. Iz simulacija su određene brzine u ušćima i razvodniku.

Za zadano vrijeme lijevanja 6 sekundi popunjavanje je mirnije kod uljevnog sustava 1:2:2, ali su brzine u ušćima veće. Kod uljevnog sustava 1:4:4 na simulaciji se pojavio povratni val taljevine u razvodniku, što povlači za sobom povećanje turbulencije i unošenje oksida. Povećanje površine kritičnog presjeka 70% rezultiralo je većom brzinom na ušćima i razvodniku, čime je dobiveno brže popunjavanje kalupne šupljine, ali i veće turbulencije. Na temelju rezultata simulacije, najbolji se pokazao uljevni sustav 1:2:2 s proračunom dobivenim kritičnim presjekom.

REFERENCES

[1] F. Unkić, Z. Glavaš, Osnove lijevanja metala, Metalurški fakultet, Sisak, 2009.

[2] V. Anjo, R. Khan, Gating system design for casting thin aluminium alloy (Al-Si) plates, Leonardo Electronic Journal of Practices and Technologies, Issue 23, July-December (2013), pp. 51-62.

[3] M. Masoumi, H. Hu, J. Hedjazi, M. A. Boutorabi, Effect of gating design on mold filling, AFS Transactions, (2005), pp. 1-12.

[4] V. Jaiganesh, K. Prakasan, Hydraulics, Dimensional analysis and visualization of flow through unpressurized gating systems using water models, Engineering Journal, 20 (2016)1, pp. 165-185.

[5] V. Jaiganesh, K. Prakasan, Influence of hydraulic and geometric variables on the performance of gating systems, Indian Foundry Journal, 61(2015)2, pp. 25-30.

[6] W. J. Chen, C. X. Lin, Y. T. Chen, J. R. Lin, Optimization design of a gating system for sand casting aluminium A356 using a Taguchi method and multi-objective culture-based QPSO algorithm, Advances in Mechanical Engineering, 8(2016)4, pp. 1–14.

[7] N. Jayakumar, S. Mohanamurugan, R. Rajavel, Design and analysis of gating system for pump casing, International Journal of Engineering and Technology, 6(2014)5, pp. 2421-2425.

[8] M. Swamy H M, J. R. Nataraj, C. S. Prasad, Design optimization of gating system by fluid flow and solidification simulation for front axle housing, International Journal of Engineering Research and Development, 4(2012)6, pp. 83-88.

[9] M. Iqbal, S. Patel, G. Vidyarthee, Simulation of casting and its validation by experiments, International Journal Of Engineering Sciences & Research Technology, 3(2014)8, pp. 555-565.

COMPUTATION OF CO_2 EMISSION FROM THE STEEL PRODUCTION BY ELECTRIC ARC FURNACE PROCESS

IZRAČUN EMISIJE CO_2 IZ PROCESA PROIZVODNJE ČELIKA ELEKTROPEĆNIM POSTUPKOM

Ivan Brnardić[1], Mario **Ćosić**[2]**, Mario Grd, Tamara Holjevac Grgurić**[1]

[1]University of Zagreb Faculty of Metallurgy, Sisak, Croatia
[2]ABS Sisak Ltd., Sisak, Croatia

Poster presentation
Professional paper

Abstract

All industries which have in their manufacturing process greenhouse gas emissions (defined by the Regulation on greenhouse gas emission units trading, Official gazette 69/12, Annex I), such as CO_2, N_2O, PFC, etc. must submit a "Report on annual emissions from plant". In report emission sources and materials should be exactly identified and the amount of emitted CO_2 calculated. Since the industries of steel production requires a high temperature, which is obtained from a variety of fuels (primarily fossil fuel or electricity), they have obligation to submit "Report on the annual emissions from the plant."

In this paper, the electric arc furnace process for producing the steel in plant ABS Ltd. Sisak has been described and the annual CO_2 emission for Year 2015 has been calculated. For calculation of CO_2 emission, all raw materials containing carbon, their carbon content and amount of spent raw materials were shown. Calculated CO_2 emission for year 2015 was 18382 t CO_2. To ensure the credibility of the data, the report has to undergo verification procedure by an authorized verifier for verification and approval (according to Regulation EU no. 600/2012).

Keywords: *steelwork, steel scrap, electric arc furnace process*, CO_2 *emission*

Corresponding author (e-mail address): brnardic@simet.hr

SAŽETAK

Sve djelatnosti koje u proizvodnim procesima emitiraju stakleničke plinove (definirano Uredbom o načinu trgovanja emisijskim jedinicama stakleničkih plinova, NN69/12, Prilog I), kao što su CO_2, N_2O, PFC, itd. moraju podnijeti "Izvješće o godišnjim emisijama iz postrojenja". U izvješću izvori emisija i materijali trebaju biti točno identificirani te količina ispuštenog CO_2 izračunata. Budući da industrija

proizvodnje čelika zahtijeva visoku temperaturu, koja se dobiva pomoću raznih goriva (prvenstveno fosilnih goriva i električne energije), oni imaju obvezu podnošenja "Izvješća o godišnjim emisijama iz postrojenja."

U ovom radu opisan je elektropećni postupak za proizvodnju čelika u čeličani ABS SISAK d.o.o. te je izračunata godišnja emisija CO_2 za 2015. godinu. Za potrebe izračuna emisije CO_2 dan je prikaz svih sirovina koje sadrže ugljik, njihov sadržaj ugljika i iznos utrošenih sirovina. Izračunata je emisija od 18.382 t CO_2 za 2015. godinu. Da bi se osigurala vjerodostojnost podataka, izvješće obavezno prolazi postupak verifikacije od strane ovlaštenog verifikatora koji isto provjerava i odobrava (sukladno Uredbi EU br. 600/2012).

Ključne riječi: *čeličana, čelični otpad, elektropećni postupak, emisija CO_2*

UVOD

Čovjek u svojoj težnji za napretkom kroz povijest nije davao previše pažnje na utjecaj posljedica na okoliš nastalih razvitkom. Jedan od glavnih pokretača napretka je energija koja se u velikim količinama dobivala i dobiva korištenjem fosilnih goriva. Danas je opće poznato da se korištenje fosilnih goriva može direktno povezati s nastajanjem i porastom stakleničkih plinova u atmosferi naše planete. Utjecaj stakleničkih plinova je opće poznat i naziva se „efekt staklenika". Staklenički plinovi su plinovi koji apsorbiraju infracrveno zračenje odbijeno od planete Zemlje te ga re-emitiraju natrag na njenu površinu povećavajući temperaturu planete Zemlje, a najpoznatiji/najzastupljeniji plin je CO_2. Znanstvenici su uspjeli osvijestiti političare kroz ukazivanje na štetne posljedice do kojih bi došlo daljnjim povećanjem temperature planete Zemlje te je iz toga uslijedio poznati Kyoto protoklol [1] kojima se države potpisnice obvezuju smanjiti emisije stakleničkih plinova. Jedan od mehanizama Kyoto protokola je međunarodno trgovanje emisijama koji kaže „*Tržište emisijom dozvoljava zemljama koje imaju višak jedinica, te ako su ispod granice emisija koje im zadaje Kyoto Protokol, prodavanje tih jedinica zemljama koje su prekoračile svoj limit*". S obzirom na dodijeljene kvote, svakome tko je obvezan predati „Izvještaj o godišnjim emisijama iz postrojenja" je u interesu da smanji svoje emisije stakleničkih plinova što direktno rezultira smanjenjem troška ili ostvarenjem dodatne dobiti tvrtke, i u konačnici, smanjenjem emisija se smanjuje utjecaj na klimatske promjene.

Sve djelatnosti koje u proizvodnim procesima emitiraju stakleničke plinove, kao što su CO_2, N_2O, PFC, itd., a zbog vrijednosti instaliranih proizvodnih kapaciteta, prema *Uredbi o načinu trgovanja emisijskim jedinicama stakleničkih plinova* [2] obveznici su podnošenja "Izvješća o godišnjim emisijama iz postrojenja". U izvješću izvori emisija i materijali trebaju biti točno identificirani te količina ispuštenog CO_2 izračunata. Budući da industrija proizvodnje čelika zahtijeva visoku temperaturu, koja se dobiva pomoću raznih goriva (prvenstveno fosilnih goriva i električne energije), oni imaju obvezu podnošenja "Izvješća o godišnjim emisijama iz postrojenja."

U ovom radu dan je izračun emisije CO_2 za 2015. godinu iz čeličane ABS Sisak d.o.o. (dalje u tekstu: ABS) koje za proizvodnju čelika koristi elektrolučni postupak. U elektrolučnom postupku najznačajnije mjesto zauzima elektrolučna peć koja umjesto izgaranja fosilnih goriva, za taljenje čelika koristi električni luk te je osnovni izvor energije za ovaj proces

električna energija. Naravno, uz električnu energiju je moguće dodatno zagrijavanje fosilnim gorivima.

OPIS ČELIČANE [3]

S ciljem što točnije izrade ovog rada i izračuna emisije CO_2 potrebno je točno identificirati sve izvore emisija, materijale koji emitiraju te količine emitiranih stakleničkih plinova. Da bi se to što bolje uradilo potrebno je dobro poznavati postupak proizvodnje čelika u čeličani ABS-a. Čeličana je postrojenje čiji je primarni cilj dobivanje čeličnog proizvoda traženog sastava. Proces proizvodnje čelika u čeličani ABS Sisak d.o.o. prikazan je na slici 1 (ELP – elektrolučna peć, LP – lonac peć, KL – kokila, V – vaga, MI – mjerni instrument). Proces je podijeljen na 3 organizacijsko – procesne cjeline:

1. Priprema uloška,
2. Pretaljivanje u elektrolučnoj peći i dorada taline,
3. Kontinuirano lijevanje taline.
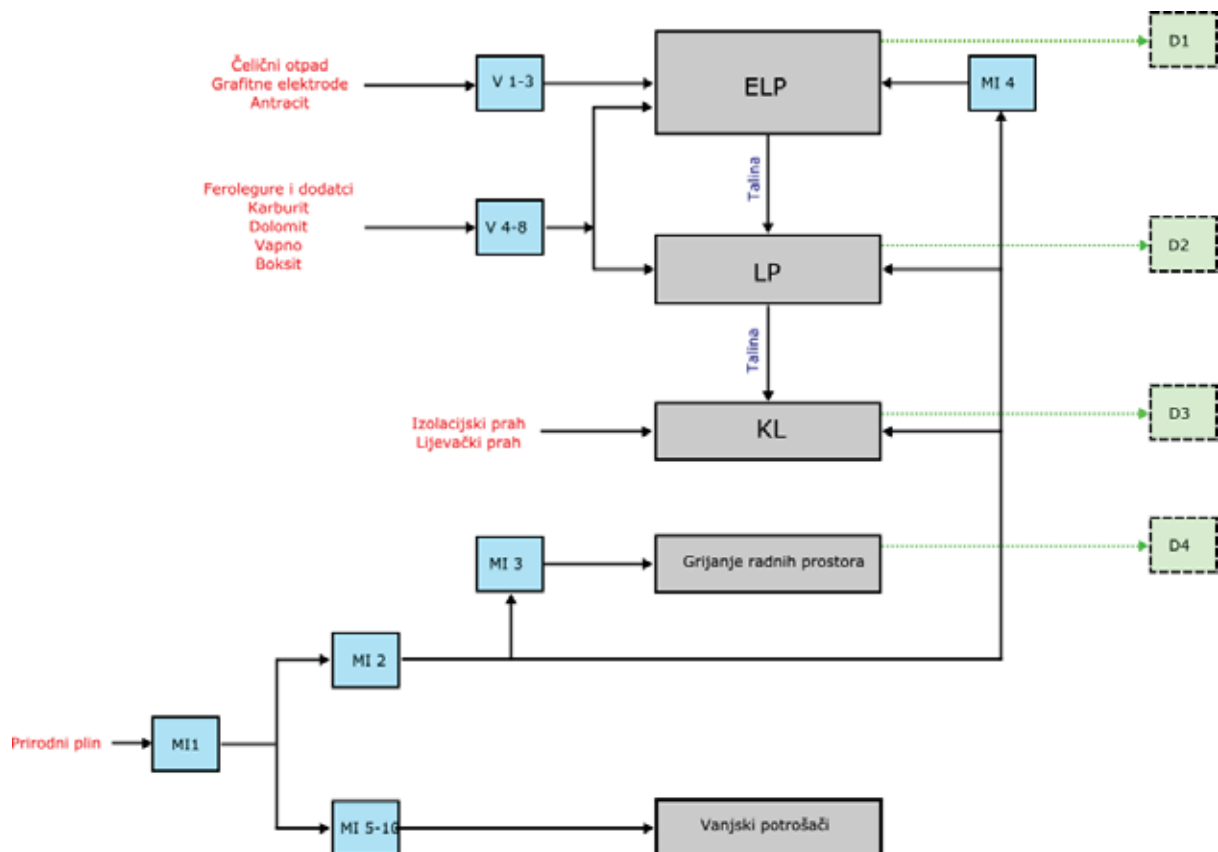
Slika 1. Shematski prikaz čeličane [3]

Priprema uloška

Osnovna sirovina za proizvodnju čelika u čeličani ABS Sisak d.o.o. je čelični otpad. Priprema uloška započinje rezanjem čeličnog otpada na komade odgovarajućih veličina, te punjenjem uložnih košara u lomari kapaciteta 40 m^3 (27,5 t) čeličnog otpada. U lomari se također obavlja uzorkovanje čeličnog otpada te se prosječni sadržaj ugljika u čeličnom otpadu

određuje sukladno Planu analiza sirovine prema pristiglim klasama čeličnog otpada. Košare se prvo pune vapnom i koksom te nakon toga se ulaže čelični otpad uz dodatnu kontrolu prisutnosti radioaktivnih tvari.

Pretaljivanje u elektrolučnoj peći i dorada taline

Za pretaljivanje čeličnog otpada koristi se 60 tonska elektrolučna peć, ukupne visine bez poklopca otprilike 2700 mm i unutarnjeg promjera peći od 4817 mm. U pomoćnoj zgradi se nalazi kontrolna soba, hidraulična oprema, transformator za napajanje peći, oprema za dovod prirodnog plina i kisika, garderoba i sanitarni čvor.

Do taljenja dolazi uspostavljanjem električnog luka između čeličnog otpada i grafitnih elektroda, koje napaja transformator kapaciteta 60.000 kVA. Toplina oslobođena kemijskim reakcijama u talini dodatno zagrijava peć što se postiže injektiranjem plinovitog kisika, prirodnog plina ili ugljika u talinu. Naginjanjem se, nakon završetka taljenja, izlijeva troska koja se odmah uklanja iz pogona i hladi raspršenim vodenim mlazom [4]. Nakon toga se iz peći izljeva talina u predgrijan lonac peć uz moguće dodavanje legirnih elemenata te se transportira do dijela za doradu taline.

Kontinuirano lijevanje taline

Lijevanje čelične taline se vrši pomoću trožilnog radijalnog uređaja. Lonac s talinom se diže u položaj iznad zagrijanog razdjelnika koji je spojen s vodom hlađenim bakrenim kokilama. Rastaljeni čelik se uvodi u bakrene kokile kontinuiranim lijevanjem te odljevak prolazi kroz komoru za sekundarno hlađenje. Nakon što odljevci dosegnu određenu duljinu, automatski se režu i transportiraju dalje na hladnjak.

SIROVINE U PROCESU PROIZVODNJE ČELIKA

Za izračun emisija CO_2 u elektrolučnom postupku proizvodnje čelika, identificirane su sirovine i dodaci koji sadrže ugljik te su pomoću standardne masene bilance izračunate količine emitiranog CO_2 za svaku sirovinu/dodatak posebno. Identificirane su sljedeće sirovine i dodatci: grafitne elektrode (elektrode φ350 mm i φ450 mm), talitelji (boksit i vapno), antracit, ferolegure i dodatci (FeSiMn, FeSi, FeMn MC, FeMn HC, FeV, FeMo, FeNb, FeCr LC, FeCr HC, CaSi – žica, C-žica, FeTi – žica), karburiti (3 – 6 mm i 1 – 3 mm), ljevački prahovi (SPH – C 176/ALS 9, ST – SP/512 – 21 – 3, SPH – C 411 – 81E, SPH – C 189 E1), izolacijski prahovi (Proteem MX 84 i 441 AT), sirovo željezo, čelični otpad te prirodni plin kao energent.

Grafitne elektrode dobivene iz petrol koksa služe za uspostavu električnog luka sa čeličnim otpadom. U Čeličani Sisak koriste se dvije vrste elektroda: φ350 i φ450 mm, a emisija CO_2 se računa po formuli:

$$(emisija)CO_2 = Efi * w(C) * m \tag{1}$$

gdje je: - E_{fi} - emisijski faktor,
     - *w(C)* - udio ugljika i
     - *m* - masa (t).

Talitelj služi za dobivanja reaktivne i fluidne troske sposobne za vezanje nepoželjnih primjesa, a kao talitelji se koriste vapno i boksit.

Antracit služi kao dodatno gorivo koje je nekada potrebno dodati ako nije moguće postići odgovarajuću temperaturu električnim lukom uslijed problema sustava.

Ferolegure i dodatci služe za legiranje čelika tj. kada se želi postići određeni udio elemenata u čeliku ovisno o zahtjevima kupca. Emisija CO_2 se računa se po formuli (1).

Karburiti se koriste kao „nosioci" ugljika s ciljem prilagodbe sadržaja ugljika u metalnoj talini, a emisija CO_2 se računa se po formuli (1).

Ljevački prahovi sastavljeni od talitelja i ugljika se koriste za zaštitu rastaljenog čelika kod kontinuiranog lijevanja čelika i osiguravanje kvalitetne površine metalne taline, a njihova emisija CO_2 se računa po formuli (1).

Izolacijski prahovi se koriste za bolju izolaciju metalne taline te se dodaju u procesu kontinuiranog lijevanja kako bi se čelični proizvodi pravilnije, tj. sporije hladili. Pravilnijim hlađenjem dobivamo kvalitetniju površinu te smanjujemo mogućnost nastanka zaostalih naprezanja uslijed prebrzog hlađenja površine proizvoda u odnosu na jezgru proizvoda. Emisija CO_2 se računa po formuli (1).

U tablici 1 je prikazana količina materijala i emisije CO_2 za grafitne elektrode, talitelje, antracit, ferolegure i dodatke, karburit, ljevačke prahove i izolacijske prahove za siječanj 2015. godinu (podatci za ostatak godine nisu prikazani).

U svrhu osiguravanja uvjeta za proizvodnju čelika viših kvalitetnih razreda dodaje se sirovo željezo, a emisija CO_2 se računa po formuli (1).

Čelični otpad je osnovna sirovina pri proizvodnji čelika elektrolučnim procesom, a najveći problem kod čeličnog otpada su primjese. Općenito primjese možemo podijeliti u tri skupine [4]:

a) anorganske primjese pomiješane sa željeznim komponentama čeličnog otpada koje se mehanički mogu odvojiti (beton, zemlja…),
b) primjese metala nanesenih na čelik u čeličnom otpadu (Zn, Ni, Cr…) i
c) dijelovi iz visoko legiranih čelika u čeličnom otpadu (Mn čelici, CrNi čelici…).

Tablica 1. Količina materijala i emisije CO_2 za siječanj 2015. godine

Emisije iz postrojenja	$\frac{CO_2}{C}$	Sječanj										
		Masa materijala [kg]					Emisija CO_2 [t]					
		ELP	LP	LL	KL	Ukupno	w(C)	ELP	LP	LL	KL	Ukupno
Boksit	3,664	4420	13475	0	0	17895	0					
Dolomit	3,664	3000	0	0	0	3000	0					
Vapno	3,664	393950	10304	0	0	404254	0,01348	5,31	0,14	0,00	0,00	5,45
Karburit 3-6 mm	3,664	7787	505	0	0	8292	0,9137	26,07	1,69	0,00	0,00	27,76
Karburit 1-3 mm	3,664	124060	0	0	0	124060	0,9139	415,42	0,00	0,00	0,00	415,42
Antracit	3,664	129000	0	0	0	129000	0,8854	418,49	0,00	0,00	0,00	418,49
FeSiMn	3,664	72025	14181	0	0	86206	0,0196	5,17	1,02	0,00	0,00	6,19
FeSi	3,664	8760	3555	0	0	12315	0,0008	0,03	0,01	0,00	0,00	0,04
FeMn MC	3,664	2570	12006	0	0	14576	0,0137	0,13	0,60	0,00	0,00	0,73
FeMn HC	3,664	24760	17732	0	0	42492	0,0784	7,11	5,09	0,00	0,00	12,21
FeV	3,664	0	2117	0	0	2117	0,0022	0,00	0,02	0,00	0,00	0,02
FeMo	3,664	0	3529,5	0	0	3529,5	0,0003	0,00	0,00	0,00	0,00	0,00
FeNb	3,664	0	0	0	0	0	0	0,00	0,00	0,00	0,00	0,00
FeCr LC	3,664	2725	3822	0	0	6547	0,0008	0,01	0,01	0,00	0,00	0,02
FeCr HC	3,664	21190	5662	0	0	26852	0,0787	6,11	1,63	0,00	0,00	7,74
CaSi-žica	3,664	0	2625	0	0	2625	0,0072	0,00	0,07	0,00	0,00	0,07
C-žica	3,664	0	807	0	0	807	0,98	0,00	2,90	0,00	0,00	2,90
FeTi-žica	3,664	0	565	0	0	565	0,0016	0,00	0,00	0,00	0,00	0,00
SPH-C 176/ALS 9	3,664	0	0	0	1581	1581	0,209	0,00	0,00	0,00	1,21	1,21
ST-SP/512-21-3	3,664	0	0	0	2455	2455	0,205	0,00	0,00	0,00	1,84	1,84
SPH-C 411-81E	3,664	0	0	0	1635	1635	0,195	0,00	0,00	0,00	1,17	1,17
SPH-C 189 E1	3,664	0	0	0	775	775	0,165	0,00	0,00	0,00	0,47	0,47
Proteem MX 84	3,664	0	0	0	8685	8685	0,028	0,00	0,00	0,00	0,89	0,89
Proteem 441 AT	3,664	0	0	0	8990	8990	0,089	0,00	0,00	0,00	2,93	2,93
Elektrode Ø450	3,664	25420	0	0	0	25420	0,99	92,21	0,00	0,00	0,00	92,21
Elektrode Ø350	3,664	0	7130	0	0	7130	0,99	0,00	25,86	0,00	0,00	25,86
Sirovo željezo	3,664	2040	0	0	0	2040	0,0425	0,32	0,00	0,00	0,00	0,32
HBI Briketi	3,664	0	0	0	0	0	0	0,00	0,00	0,00	0,00	0,00
SUMA [t]		821,71	98,02	0,00	24,12	925,95	6,82	976,37	39,05	0,00	8,51	1023,94

U tablici 2 su prikazane količine otpada i emisija CO_2 za I. polugodište 2015. godine koje su računate po formuli (1) (podatci za II. polugodište nisu prikazani).

Prirodni plin se koristi za grijanje radnih prostora, za potrebe lonac peći, kontinuiranog lijevanja te također za dodatno zagrijavanje elektrolučne peći. Emisija CO_2 se računa prema sljedećoj formuli (2):

$$(emisija)CO_2 = DOV * V_{ukupno} / 1000000 \qquad (2)$$

gdje je: - DOV - donja ogrjevna vrijednost MJ/m^3 i
 - V - volumen utrošenog plina izražen u Sm^3.

65

ČELIK	Siječanj			Veljača			Ožujak			Travanj			Svibanj			Lipanj		
Uloženo	9323,372			19797,51			20956,95			15870,37			21130,3			10782,53		
Liquid	-8567			-17985			-18890			-14512			-19533			-9973		
Casted	-8001			-16991			-18089			-13795			-18569			-9355		
PROIZVODNJA OTPADA	Masa	w(C)	Emisija CO_2	Masa	w(C)	Emisija CO_2	Masa	w(C)	Emisija CO_2	Masa	w(C)	Emisija CO_2	Masa	w(C)	Emisija CO_2	Masa	w(C)	Emisija CO_2
Troska	-800,1348	0,0033	-9,67	-1699,1473	0,0033	-20,54	-1808,8764	0,0033	-21,87	-1379,4652	0,0033	-16,68	-1953,3255	0,0033	-23,62	-997,26	0,0033	-12,06
Cunder	-8,8014828	0,00008	0,00	-18,69062	0,00008	-0,01	-19,89764	0,00008	-0,01	-15,174117	0,00008	0,00	-21,486581	0,00008	-0,01	-10,96986	0,00008	0,00
EAF prašina	-112,01887	0,015	-6,16	-237,88062	0,015	-13,07	-253,2427	0,015	-13,92	-193,12513	0,015	-10,61	-273,46557	0,015	-15,03	-139,6164	0,015	-7,67
Efi		3,664			3,664			3,664			3,664			3,664			3,664	

Količina potrošenog plina i emisije CO_2 za I. polugodište 2015. godine su prikazane u Tablici 3 (podatci za II. polugodište nisu prikazani).

Tablica 3. Količina potrošenog plina i emisije CO_2 za I polugodište 2015. godine

POTROŠNJA PLINA	Siječanj		Veljača		Ožujak		Travanj		Svibanj		Lipanj	
	Nm^3	Sm^3	Nm^3	Sm^3	Nm^3	Sm^3	Nm^3	Sm^3	Nm^3	Sm^3	Nm^3	Sm^3
Kotlovnica Čeličana	11371	11996,41	11885	12538,68	9513	10036,22	5172	5456,46	1615	1703,825	1109	1169,995
EAF	63838	67349,09	135175	142609,6	132084	139348,6	98828	104263,5	130469	137644,8	72860	76867,3
CCM	55028	58054,54	69344	73157,92	53469	56409,8	31974	33732,57	40375	42595,63	25033	26409,82
Čistionica	9711	10245,11	12237	12910,04	9436	9954,98	5643	5953,365	7125	7516,875	4418	4660,99
LL	131284	138504,6	136322	143819,7	131877	139130,2	146294	154340,2	156735	165355,4	196876	207704,2
Kotlovnica SO	7906	8340,83	8299	8755,445	7071	7459,905	4527	4775,985	910	960,05	0	0
Grijanje radnih prostora	10622	11206,21	13443	14182,37	10231	10793,71	5545	5849,975	1100	1160,5	19113	20164,22
Ukupno ABS	289760	305696,8	386705	407973,8	353681	373133,5	297983	314372,1	338329	356937,1	319409	336976,5
DOV (MJ/m3)	34,105		34,535		34,5		34,165		34,855		34,52	
Emisija (tCO_2)	584,89		790,41		722,18		602,54		697,94		652,58	

PRORAČUN EMISIJA IZ POSTROJENJA

Nadležna tijela za postrojenje ABS su Ministarstvo zaštite okoliša i prirode i Hrvatska agencija za okoliš i prirodu koja dodjeljuju predložak za izračun emisije prirodnih plinova. Operater je ovaj obrazac dužan ispuniti te ga predati do 01. ožujka tekuće godine za proteklu kalendarsku godinu. Nakon što smo odredili djelatnost (proizvodnja sirovog željeza i čelika), identificirali smo sve relevantne tokove izvora u postrojenju te uporabom metodologije na temelju standardne bilance mase izračunali njihovu emisiju.

Kako bi bio jasniji sljedeći dio proračuna potrebno je objasniti kratice koje će se koristiti u sljedećem dijelu (tablica 4).

Tablica 4. Značenje kratica korištenih u Tablici 5

PA	Podatci o aktivnostima – količina goriva/ materijala potrošena u proces
Početak	Količina goriva/materijala na početku izvještajnog razdoblja
Završetak	Količina goriva/materijala na zalihi na kraju izvještajnog razdoblja
Uvoz	Količina goriva/materijala kupljenog tijekom izvještajnog razdoblja
Izvoz	Količina goriva/materijala izvezenog iz postrojenja
(prelim) EF	„Preliminarni" emisijski faktor – ukupni faktor emisije miješanog goriva ili materijala na temelju ukupnog sadržaja ugljika koji se sastoji od udjela biomase i fosilnog udjela prije nego što se pomnoži s fosilnim udjelom kako bi se dobio emisijski faktor.
DOV	Donja ogrjevna vrijednost znači određena količina energije koja se ispušta u obliku topline pri potpunom izgaranju goriva ili materijala s kisikom u standardnim uvjetima, umanjena za toplinu isparavanja eventualno nastale vode
OF	Oksidacijski faktor
PretvF	Pretvorbeni faktor
Udio_C	Sadržaj ugljika
Bio_C	Udio biomase
Neodrživ	Udio „neodržive" biomase je udio ugljika koji potječe iz neodržive biomase

U Tablici 5 dani su izračuni emisija CO_2 na temelju standardne bilance mase za prirodni plin i grafitne elektrode. U radu su izračunate emisije i za sve druge navedene izvore ali nisu prikazane.

Tablica 5. Izračun emisija CO_2 za prirodni plin i grafitne elektrode

Nakon unesenih potrebnih podataka, izračunata je godišnja emisija stakleničkih plinova (tablica 6) koja za 2015. godinu iznosi 18.382 t CO_2.

Tablica 6. Emisija stakleničkih plinova za 2015. godinu

Sažetak Godišnjeg izvješće o emisijama stakleničkih plinova sukladno Direktivi 2003/87/EZ		
	Godina izvještavanja:	**2015**
Naziv operatera:	Acciaierie Bertoli Safau d.o.o. Sisak	
Naziv postrojenja:	ABS Sisak d.o.o Pogon Čeličana	
Jedinstveni ID postrojenja:	HR - 321	

Djelatnost iz Priloga I.	Ukupni kapacitet djelatnosti	Jedinice kapaciteta	Emitirani staklenički plin
A1 Proizvodnja sirovog željeza ili čelika (primarno ili sekundarno), uključujući	1200	tona po danu	CO2
A2			
A3			
A4			
A5			

	Emisije (fosilne) t CO$_{2e}$	Sadržaj energije (fosilni) TJ	*Emisije (biomasa)* t CO$_2$	*Sadržaj energije (biomasa)* TJ	*Emisije (neodrživa biomasa)* t CO$_2$
			Bilješke:		
Tokovi izvora	18.382	101,72	0	0,00	0
Izgaranje	5.707	101,72	0	0,00	0
Procesne emisije					
Masena bilanca	12.675	0,00	0	0,00	0
Emisije PFC					
MJERENJE					
CO2					
N2O					
preneseni CO2					
Nadomjesni pristup					
Ukupno	18.382	101,72	0	0,00	0

Ukupne emisije iz postrojenja:	18.382 t CO$_{2e}$

Ovo je ukupna količina emisijskih jedinica koje operater mora predati na račun.

ZAKLJUČAK

Čeličana Sisak za proizvodnju čelika koristi elektrolučni postupak kojim u elektrolučnoj peći, putem električnog luka, tali uložak. Osnovna sirovina je čelični otpad, a proces proizvodnje čelika možemo podijeliti na: pripremu uloška, pretaljivanje u elektrolučnoj peći i dorada taline te kontinuirano lijevanje taline.

Za potrebe izračuna emisije i izrade „Izvješća o godišnjim emisijama iz postrojenja" identificirani su svi materijali koji se koriste: grafitne elektrode, talitelji, antracit, ferolegure i dodatci, karburiti, ljevački prahovi, izolacijski prahovi, sirovo željezo, čelični otpad i prirodni plin.

Prikazan je njihov udio ugljika te potrošene količine. Nakon ispunjavanja formulara izračunata je godišnja emisija CO$_2$ za postrojenje ABS d.o.o. Sisak koja za 2015. godinu iznosi 18.382 t CO$_{2e}$. izvješće je predano u roku, te da bi se osigurala vjerodostojnost podataka izvješće obavezno prolazi postupak verifikacije od strane ovlaštenog verifikatora koji isto provjerava i odobrava, sukladno Uredbi EU br. 600/2012 [5].

LITERATURA

[1] Kyoto Protocol to the United Nations Framework Convention on Climate Chang, United Nations, 1998.
[2] Uredba o načinu trgovanja emisijskim jedinicama stakleničkih plinova, NN69/12.

[3] M. Ćosić, Plan praćenja emisije CO_2 u postrojenju ABS Sisak 2014., ABS Sisak, Sisak, 2014.

[4] M. Gojić, Metalurgija čelika, Sveučilište u Zagrebu, Sisak, 2005.

[5] Uredba Komisije (EU) br. 600/2012 o verifikaciji izvješća o emisijama stakleničkih plinova i izvješća o tonskim kilometrima te o akreditaciji verifikatora u skladu s Direktivom 2003/87/EZ Europskog parlamenta i Vijeća, SL L 181, 12. 7. 2012.

SLIP CASTING OF ALUMINA CERAMICS

Lidija Ćurković, Marijana Majić Renjo, Danko Ćorić, Zrinka Šokčević, Vera Rede

University of Zagreb Faculty of Mechanical Engineering and Naval Architecture,
Department of Materials, Zagreb, Croatia

<u>Oral presentation</u>
<u>*Original scientific paper*</u>

Abstract

Slip casting as a colloidal shaping method is one of the most common forming techniques, used in commercial production of different advanced ceramics. Colloidal shaping methods enable to achieve high microstructural homogeneity in green and sintered parts and offer near net shaping capabilities that reduce post-sintering machining and production costs. Slip casting is the process of filling a porous mold, usually a gypsum mold, with ceramic slurry. The first step in the slip casting process is the preparation of stable concentrated aqueous suspensions of the ceramic powders. At high solid loading, relatively low slip viscosity can only be achieved in the presence of an optimum dispersion state of particles.

In this paper highly concentrated (70 wt. %) aqueous suspensions of alumina (Al_2O_3) were prepared with different amount of dispersant DOLAPIX CE 64. Stability of highly concentrated aqueous suspensions of alumina ceramics suitable for slip casting was monitored by rheological properties measurements (flow curves and rheological parameters). Recorded flow curves were fitted to the power law, Herschel-Bulkley and Bingham models. Minimal viscosity was determined for each prepared suspension, in order to determine optimal slip casting parameters. Power law, Herschel-Bulkley model and Bingham plastic model were used in order to explain, characterize and predict the flow and pseudo-plastic behavior of highly concentrated alumina suspensions.

Keywords: *slip casting, alumina ceramics, rheological properties*

*Corresponding author (e-mail address): lcurkov@fsb.hr

INTRODUCTION

Ceramic materials are, in general, divided into conventional ceramics and advanced ceramics. Conventional ceramics are growing at a slow rate and some of their branches even show a decreasing tendency, i.e. refractory materials. In contradiction to the conventional ceramics, the market for advanced ceramics is large and growing continuously. Production of

advanced ceramics is very significant as one of the most economically potential branches in the developed countries and has received a great deal of attention from many fields of industry. Forming technology for green bodies is important to manufacture advanced ceramics. Slip casting is an old forming technique in ceramics industry, and is a method for the preparation of homogeneous large green bodies with fairly complex shape. Conventionally, plaster and resin are used for slip casting moulds. Improvement in slip properties and forming technologies is the way to improve the reliability of advanced ceramics and to lower their cost. Therefore, a lot of effort is put into the development of low cost technologies for complex ceramic components. The near-net-shape forming of advanced ceramics excite the greatest interest. The following forming processes are actually in the stage of commercialization or development: pressure slip casting, freeze casting, powder injection molding, tape casting/lamination, rapid prototyping, and colloidal processing of powders. The technologies based on the colloidal processing, such as slip casting, gel casting, electrophoretic casting, hydrolysis-assisted solidification, direct coagulation casting etc. are of great interest due to their ability to reduce the critical defects which can occur during the manufacturing process [1-8].

Slip casting as colloidal processing is the most adequate technology for the production of complex ceramic components. It is a simple, reliable, flexible, cost-effective and pollution-free procedure, but it requires an adequate understanding of colloid suspensions and their behavior. This knowledge is crucial for the optimization of technologies for the production of improved ceramic products, e.g. slip, gel, and centrifugal casting, injection molding, and coating. Properties of ceramic products depend on the size of powder particles. When particles are smaller (nanosize), the sintering is better and, consequently, product properties are better, too. On the other hand, particles smaller than 1 μm, in a combination with high suspension concentration, increase the suspension viscosity. It is a consequence of greater interactions among particles, which can lead to agglomeration or flocculation [1-8]. This interaction can be controlled with chemical additives in three different ways: electrostatic, steric, and electrosteric (a combination of the first two) stabilization. The influence of additives (different dispersants) on the ceramic suspension stability has been extensively researched [1-6]. Despite that, the worldwide ceramic industry requires new, better additives in order to improve the slip casting process and, consequently, ceramic products. In the past decade, a number of studies on rheological properties of binary systems, such as Al_2O_3-ZrO_2 composites, have been performed [9-14].

The selection of dispersant becomes more critical because it might be difficult to find a dispersant that is optimal for all components. Slip casting of advanced ceramics based on alumina requires the use of a dispersant, a binder and an agent for preventing the excessive grain growth. There are many commercially available dispersants and binders that can be used for the advanced ceramics slip casting process. However, the determination of a suitable combination and the quantification of optimal additions of the dispersant/binder pair for slip casting alumina ceramics with the starting particle size at the nano- and micro-levels can be time consuming. The suspension stability must be well achieved in order to establish complete control over suspension rheological properties. Sedimentation tests and viscosity measurements are often used for the suspension stability estimation, but they are rather limited when evaluating the stability of concentrated suspensions.

Therefore, in this paper rheological flow curves are used instead. Flow curves show the dependence of shear stress on viscosity as well as on shear rate, and can be used for

predicting the nature of interactions among particles in the suspension. Power law, Herschel-Bulkley model and Bingham plastic model were used in order to describe non-Newtonian systems. These models are effectively used to explain, characterize, and predict the flow and pseudo-plastic behavior of various systems, such as high concentrated alumina suspensions [5,6].

MATERIALS AND METHODS

Suspension preparation

For preparation of highly concentrated aqueous suspension following components were used:

- high purity Al_2O_3 powder; average particle size 300-400 nm (according to manufacturer specification),
- DOLAPIX CE 64 (Zschimmer & Schwarz GmbH &Co KG, Chemische Fabriken) – 70 wt. % aqueous solution of the ammonium salt of polymethacrylic acid (PMAA-NH4) as a dispersant,
- deionised water.

Alumina suspensions with solid loading of 70 wt. % were prepared. The amount of DOLAPIX CE 64 was varied in order to determine its optimal content, which is reflected in obtained minimal viscosity. The dispersant content was: 0.15, 0.2, 0.4, 0.6, 0.8 and 1.0 wt. %, calculated on the applied dry ceramic powder.

All suspensions were prepared by adding deionised water, containing dissolved DOLAPIX CE 64, into the grinding jar of planetary ball mill, after which ceramic powder was added. The grinding jar and ten balls used for homogenization were made of alumina ceramics in order to prevent the contamination of suspensions. Each of the prepared suspensions was homogenized for 90 minutes at a rate of 300 rpm in the planetary ball mill (PM 100, Retsch, Germany). In order to remove air bubbles and to achieve better homogeneity of prepared suspensions, each of them was treated in the ultrasonic bath, so the results of rheological measurements would be as reliable as possible.

Determination of rheological properties

Rheological characterization includes recording of the flow curves and describing obtained results by the appropriate model. The flow curves show dependence of the shear stress and viscosity on the shear rate.

After the homogenization, all suspensions were subjected to rheological measurements, one at the time. About 8 ml of each prepared suspension was used to measure the rheological properties on the rotational viscometer Brookfield DV-III Ultra, USA, with accompanying software Rheocalc. The testing temperature was held constant at 25 ± 1°C. In order to avoid influence of all previous occurrences ("sample history") on the results, each suspension was subjected to pre-shearing at the shear rate of 100 s^{-1} for 2 minutes. Subsequently, flow curves were recorded. The shear rate, γ, was increased from 0 s^{-1} to 180 s^{-1} with 50 equal intervals, which lasted for 3 seconds. Measurements were made just before each rate

change.

This study was focused on the influence of the DOLAPIX CE 64 on alumina suspensions prepared for slip casting. Three rheological models were used: Power law, Herschel-Bulkley model and Bingham plastic model. Obtained rheological curves show the dependence of the shear stress and viscosity on the shear rate.

The shear rate, γ, of 50 s^{-1} is the exact shear rate achieved during the gravity slip casting. One of the goals of this investigation was also to determine which amount of the DOLAPIX CE 64 will enable minimal viscosity at this shear rate.

All experiments were carried out under ambient laboratory conditions.

RESULTS AND DISCUSSION

The aim of this research was to investigate how the concentration of the dispersant DOLAPIX CE 64 influences the viscosity of prepared Al_2O_3 ceramic suspensions. Prepared suspensions contained 70 wt. % of ceramic powder and variable amount of dispersant DOLAPIX CE 64 (0.15, 0.2, 0.4, 0.6, 0.8 and 1.0 wt. %, calculated on the applied dry ceramic powder).

Rheological measurements were used to determine the optimal dispersant amount, which is in correlation with the lowest achieved viscosity at the shear rate of 50 s^{-1}. It is the exact shear rate of the gravity slip casting. Dependence of the obtained viscosity on the dispersant amount is given in Figure 1. It can be observed that the lowest viscosity is not joined to the highest amount of the dispersant, but for the "optimal" amount, which is 0.2 wt. % of the dry powder content. Average dynamic viscosity for that composition was 7.06 mPas.
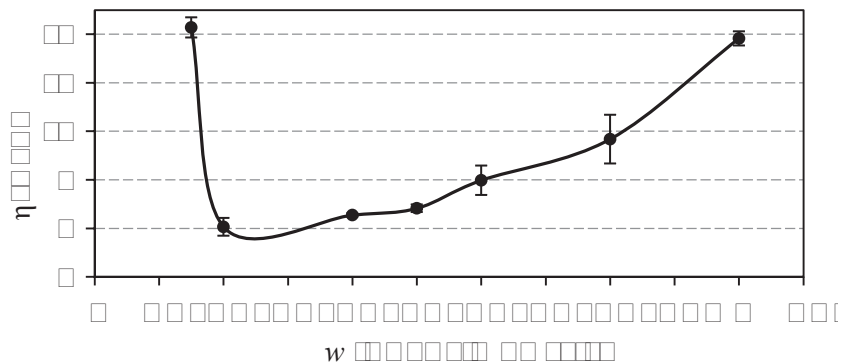
Figure 1. The dependence of viscosity on the concentration of DOLAPIX CE 64 for the investigated Al_2O_3 suspensions

The optimal amount of dispersant was chosen for further analysis: aqueous suspension containing 70 wt. % of alumina and 0.2 wt. % of DOLAPIX CE 64 was prepared again (3 samples in total) and their rheological properties were determined. The results of the rheological characterization are summarized in the Figure 2. It shows the dependence of the dynamic viscosity on the shear rate (Figure 2A) and the dependence of the shear stress on the shear rate (Figure 2B). It can be seen that the suspension viscosity decreases with the increasing shear rate, which confirms this suspension is non-Newtonian fluid.

73

In order to evaluate this experimental data, three different flow models were used:

- Power law, presented with: $\tau = k\gamma^n$,   (1)
- Herschel-Bulkley model: $\tau = \tau_0 + k\gamma^n$,   (2)
- Bingham plastic model: $\tau = \tau_0 + \rho\gamma$,   (3)

Where:

τ – shear stress, Pa,
τ_0 – yield stress, Pa,
k – consistency index,
γ – shear rate, s^{-1},
n – flow index,
ρ – plastic viscosity, Pa.

Obtained values of all parameters are represented in Table 1.
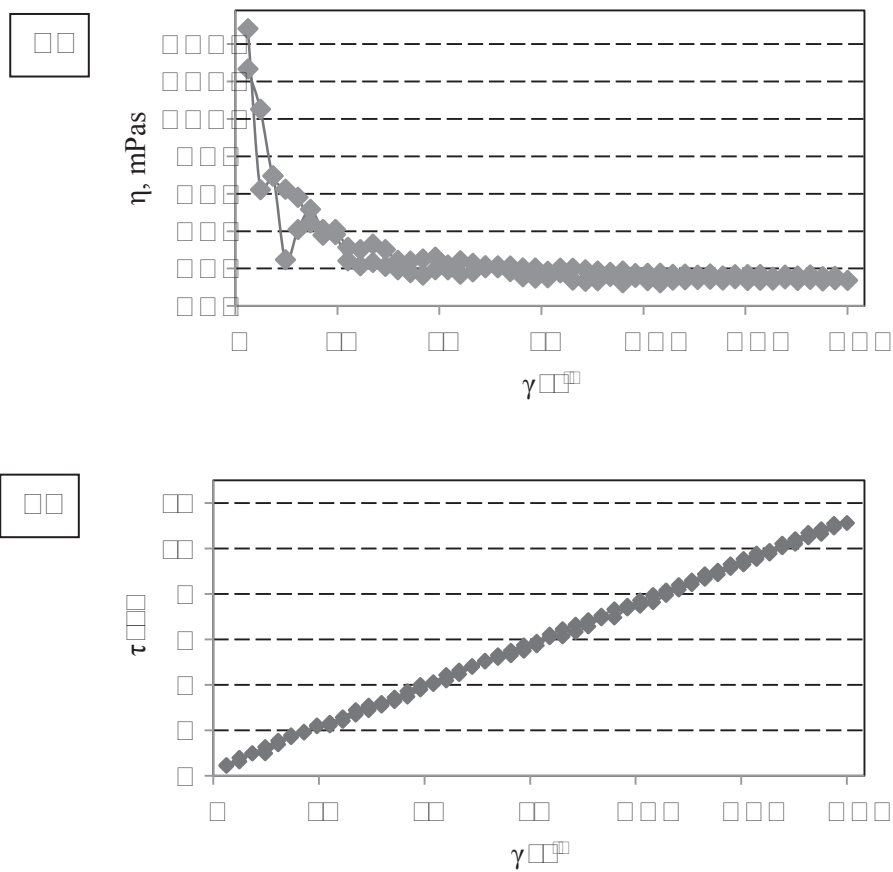
Figure 2.The flow curves of prepared suspensions: a) the dependence of the viscosity on the shear rate; b) the dependence of the shear stress on the shear rate

Table 1. Rheological parameters of prepared suspensions, according to used mathematical models

Sample	Power law model			Herschel-Bulkley model				Bingham plastic model		
	k	n	R^2	τ_0	k	n	R^2	τ_0	ρ	R^2
1	8.35	0.94	96.9	0.02	5.95	1.01	99.9	0.01	6.16	96.9
2	10.9	0.89	96.3	0.03	6.01	1.01	99.9	0.02	6.45	97.9
3	7.75	0.95	96.8	0.01	5.72	1.01	99.9	0.01	6.02	97.5
$\bar{x}$	9.00	0.93	96.7	0.02	5.89	1.01	99.9	0.01	6.21	97.4
s	1.67	0.03	0.32	0.01	0.15	0.00	0.00	0.01	0.22	0.50

According to obtained correlation coefficients R^2 (Table 1), the best results gives the Herschel-Bulkley model, with its correlation coefficient of 99.9 %. For all fluids that behave according to the Herschel-Bulkley law, the yield stress τ_0, the consistency index k and the flow index n obtain values larger than zero. This model is sometimes referred to as pseudoplastic model with yield stress. This means that a certain stress is required for the beginning of flowing and when the flowing occurs, the suspension behaves like a pseudoplastic fluid (the viscosity decreases with the increasing shear rate).

CONCLUSIONS

In this investigation highly concentrated suspensions (70 wt. %) of alumina ceramics were prepared. In order to stabilize them, the commercial dispersant DOLAPIX CE 64 was used. The optimal amount of this dispersant was determined by rheological measurements – the optimal amount is shown with the lowest viscosity. For the alumina suspension containing the optimal dispersant amount (0.2 wt. %), rheological characterization was conducted. Three models were used to describe the suspension's behavior. The Herschel-Bulkley model, with its correlation coefficient of 99.9 %, gives the best results. This means that a certain stress is required for the beginning of the suspension's flowing and when the flowing occurs, the suspension behaves like a pseudoplastic fluid (the viscosity decreases with the increasing shear rate).

REFERENCES

[1] L. Wu, Y. Huang, L. Liu, L. Meng, Interaction and stabilization of DMF-based alumina suspensions with citric acid, Powder Technol., 203(2010), pp.477-481.
[2] S. Zurcher, T. Graule, Influence of dispersant structure on the rheological properties of highly-concentrated zirconia dispersions, J. Eur. Ceram. Soc., 25(2005), pp. 863-873.
[3] A. P. Tinke, R. Govoreanu, I. Weuts, K. Vanhoutte, D. De Smaele, A review of underlying fundamentals in a wet dispersion size analysis of powders, Powder Technol., 196(2009), pp. 102-114.

[4] L. Wu, Y. Huang, Z. Wang, L. Liu, Interaction and dispersion stability of alumina suspension with PAA in N,N'-dimethylformamide, J. Eur. Ceram. Soc., 30(2010), pp. 1327-1333.

[5] A. U. Khan, A. U. Haq, N. Mahmood, Z. Ali, Rheological studies of aqueous stabilised nano-zirconia particle suspensions, Mat. Res., 15(2012), pp. 21-26.

[6] M. Majić Renjo, M. Lalić, L. Ćurković, G. Matijašić, Rheological properties of aqueous alumina suspensions, Materialwissenschaft und Werkstofftechnik, 43(2012), pp. 979-983.

[7] C. Tallon, M. Limacher, G. V. Franks, Effect of particle size on the shaping of ceramics by slip casting, J. Eur. Ceram. Soc., 30(2010), pp. 2819-2826.

[8] T. Hottaa, H. Abeb, M. Naitob, M. Takahashic, K. Uematsud, Z. Kato, Effect of coarse particles on the strength of alumina made by slip casting, Powder Technol., 149(2005), pp. 106-111.

[9] M. León-Carriedo, C. A. Gutiérrez-Chavarría, J. L. Rodríguez-Galicia, Multilayered Zircon-Alumina Components Fabricated by Slip Casting, Materials Science Forum, 755(2013), pp. 145-151.

[10] H. Sarraf, J. Havrda, Rheological behavior of concentrated alumina suspension: effect of electrosteric stabilization, Ceramics – Silikáty, 51(2007), pp. 147-152.

[11] F. F. A. T. Guimaraes, K. L. Silva, V. Trombini, J. J. Pierri, J. A. Rodrigues, R. Tomasi, E. M. J. A. Pallone, Correlation between microstructure and mechanical properties of Al_2O_3/ZrO_2 nanocomposites, Ceram. Int., 35(2009), pp. 741-745.

[12] H. Wakily, M. Mehrali, H. S. C. Metselaar, Preparation of Homogeneous Dense Composite of Zirconia and Alumina (ZTA) using Colloidal Filtration, World Academy of Science, Engineering and Technology, 46(2010), pp. 140-145.

[13] L. Sun, A. Sneller, P. Kwon, Fabrication of alumina/zirconia functionally graded material: From optimization of processing parameters to phenomenological constitutive models, Materials Science and Engineering A, 488(2008), pp. 31-38.

[14] Y. Zhang, M. J. Sun, D. Zhang, Designing functionally graded materials with superior load-bearing properties, Acta Biomaterialia, 8(2012), pp. 1101-1108.

Acknowledgements

INFLUENCE OF MEDIUM ON CORROSION PROPERTIES AND MICROSTRUCTURE OF COPPER AND BRASS

UTJECAJ MEDIJA NA KOROZIJSKA SVOJSTVA I MIKROSTRUKTURU BAKRA I MESINGA

Natalija Dolić[1], Anita Begić Hadžipašić[1], Barbara Tubić

[1]University of Zagreb Faculty of Metallurgy, Sisak, Croatia

<u>Oral presentation</u>
Original scientific paper

Abstract

In this paper the corrosion resistance of copper and brass in water-pipe and 3.5% NaCl solution at room temperature was examined by electrochemical measurements. Changes in the surface of the samples was followed by light microscope. The test results showed that the corrosion rate both copper and brass were higher in 3.5% NaCl solution than in the water. Brass showed a higher corrosion rate in both media, ie the copper as a more noble metal showed more resistance to corrosion. Metalographic investigations have found that on copper surface during the electrochemical process in 3.5% NaCl solution creates a copper chloride layer which is insufficiently stable to completely prevent the penetration of aggressive ions from the solution. Also, by exposing the brass to the 3.5% NaCl solution resulted in the formation of a layer which, due to its porosity, has no protective role in the corrosion process.

Key words: copper, brass, electrochemical examinations, metalographic investigations, corrosion rate

Corresponding author (e-mail address): *ndolic@simet.hr*

SAŽETAK

U ovom je radu elektrokemijskim mjerenjima ispitana korozijska otpornost bakra i mesinga u vodovodnoj vodi i 3.5% otopini NaCl pri sobnoj temperaturi. Svjetlosnim mikroskopom praćene su promjene na površini uzoraka. Rezultati ispitivanja pokazali su da je brzina korozije i bakra i mesinga u 3.5 % NaCl veća nego u vodi. Veću brzinu korozije u oba medija pokazao je mesing, odnosno bakar se kao plemenitiji metal pokazao korozijski otpornijim. Metalografskim ispitivanjima je ustanovljeno da se na površini bakra za vrijeme elektrokemijskog procesa u 3.5 % otopini NaCl stvara sloj bakrovog klorida, koji je nedovoljno postojan da u potpunosti spriječi prodiranje agresivnih iona iz otopine. Također, izlaganjem mesinga 3.5 % otopini NaCl rezultiralo je nastankom sloja koji zbog svoje poroznosti nema zaštitnu ulogu u korozijskom procesu.

UVOD

Zahvaljujući visokoj električnoj i toplinskoj vodljivosti, dobroj mehaničkoj obradivosti, otpornosti na trošenje i udare, bakar je materijal koji se primjenjuje za cjevovode za dovod vode u industriji i kućanstvima, uključujući morsku vodu, provodnike topline i toplinske izmjenjivače [1,2]. Bakar i njegove legure imaju široko područje primjene u industriji i tehnologiji jer su lako dostupni i ekonomski prihvatljivi obzirom da se nalaze prilično visoko na ljestvici konstrukcijskih materijala s visokom otpornošću na koroziju. Bakar i njegove legure također se i dobro lijevaju, lako obrađuju na toplo i hladno te se koriste za proizvodnju limova, traka, cijevi, šipki, profila, žice i raznih odljevaka.

Mesing je dvokomponentna legura bakra s cinkom [3,4]. Da bi se poboljšala svojstva mesinga, npr. obradivost, čvrstoća, otpornost na trošenje i otpornost na koroziju dodaju se u manjim količinama drugi kemijski elementi (kao što su Pb, Sn, Si, As, Ni itd.), čime se dobivaju takozvani specijalni mesinzi. Dodavanjem cinka povećava se vlačna čvrstoća mesinga, a smanjuje električna i toplinska vodljivost i otpornost na koroziju. Najbolja mehanička svojstva imaju mesinzi sa sadržajem cinka 33 – 40 %, što i objašnjava njihovu najveću upotrebu. Jedna od takvih legura je i mesing CuZn37 sa sadržajem bakra od 63 % i cinka od 37 %, s granicom razvlačenja 350 MPa i izduženjem 45 % [5]. Cu-legure sa sadržajem cinka 35 – 45 % sastoje se od smjese α i β faza, a poznati su pod nazivom alfa-beta ili duplex mesinzi (ili Muntz metal) [6]. Odnos α / β faza ovisi o sadržaju cinka. Uključivanje određenih trećih elemenata, osobito aluminija, silicija ili kositra, ima za učinak povećanje sadržaja β faze pri bilo kojem sadržaju cinka [6,7].

Korozija je razaranje materijala elektrokemijskim reakcijama s okolinom. Nedostatak mogućnosti i načina potpunog sprječavanja tog procesa predstavlja ozbiljnu prijetnju kako ekonomiji tako i ljudima [8]. Dosadašnja istraživanja pokazala su da se u neutralnim (svježoj vodi) i približno neutralnim pH uvjetima na površini bakra formira zaštitni sloj bakrenog oksida ili hidroksida, poput Cu_2O i $Cu(OH)_2$ [1,2,8]. Ti su slojevi značajni iz više razloga: korisni su zbog svojih svojstava zaštite od korozije i utječu na elektrokemijski proces na bakrenoj elektrodi. Nastanak ovih slojeva i proces korozije su kompleksniji u prisutnosti kloridnih iona i u morskoj vodi.

Korozija bakra i njegovih legura ovisi o širokom rasponu svojstava elektrolita koji je u kontaktu s površinom metala [2]. U oksidacijskim uvjetima, korozijski mehanizam uključuje otapanje bakra na lokalnim područjima, koja se ponašaju kao anodna mjesta i elektrokemijsku redukciju kisika i vode na katodnim mjestima [7]. Ta površina može se ponašati kao anoda ili kao katoda i rezultirati jednolikom površinskom korozijom. Nastanak oksida i hidroksida će u konačnici usporiti otapanje i reakcije redukcije. Nekoliko studija je pokazalo da je brzina tih reakcija proporcionalna brzini difuzije bakrovih kloridnih iona u kloridnu otopinu [3].

Općenito je prihvaćeno da je anodno otapanje bakra u kloridnom mediju uzrokovano djelovanjem značajnije koncentracije kloridnih iona. Kod koncentracija klorida nižih od 1M otapanje bakra se na početku manifestira kao nastanak CuCl, koji ne štiti metal dovoljno i prelazi u topljivi $CuCl_2^-$ prilikom reakcije s prisutnim klorom [1]. Prisutnost oksidnih ili

hidroksidnih netopljivih produkata korozije na površini metala ne sprječava difuziju i redukciju korozijskog medija poput kisika [1-4].

U kloridnim otopinama prvi korak anodnog otapanja jest nastanak kompleksa $CuCl_2^-$ [2]. Osim toga, utvrđeno je da tijekom anodne polarizacije uvijek postoji ravnoteža između tankog sloja CuCl i gustog sloja otopljenog $CuCl_2^-$.

Reakcije otapanja bakra u kloridnoj otopini mogu biti prikazane reakcijama [2]:

$$Cu + Cl^- \leftrightarrow CuCl_{ads} + e^- \tag{1}$$

$$CuCl_{ads} + Cl^- \leftrightarrow CuCl_2^- \tag{2}$$

$$Cu + 2Cl^- \leftrightarrow CuCl_2^- + e^- \text{ (spora)} \tag{3}$$

U međuvremenu mogu nastati bakreni oksid i hidroksid. Katodna reakcija se sastoji od redukcije kisika prema reakciji:

$$O_2 + 2H_2O + 4e^- \leftrightarrow 4OH^- \tag{4}$$

Bough je ustanovio da je sloj oksida koji se stvara na površini mesinga u području pH = 3.8 – 5.8 porozan i nepasivirajući. Cinkov oksid nije stabilan u kiselom mediju i disocira prema reakcijama [9]:

$$ZnO + 2H^+ \leftrightarrow Zn^{2+} + H_2O \tag{5}$$

Reakcija mesinga u kiseloj otopini može se opisati jednadžbama:

$$2Zn_{(CuZn)} + O_2 + 4H^+ \leftrightarrow 2Zn^{2+} + 2H_2O \tag{6}$$

$$4Cu_{(CuZn)} + O_2 + 4H^+ \leftrightarrow 4Cu^+ + 2H_2O \tag{7}$$

Smatra se da bakrov kloridni ion ubrzava decinfikaciju mesinga u kiselim medijima zbog katalizirajućeg djelovanja otapanja bakra, koji se naknadno nataložio kao posljedica otapanja cinka.

Navodi se da je negativna osobina legura bakra s cinkom njihova slabija korozijska otpornost u usporedbi s bakrom, iako se kaže da su u atmosferskim uvjetima te legure korozijski postojane. Ovo istraživanje pokazalo je da je na sobnoj temperature i u vodovodnoj vodi i u kloridnom mediju brzina korozije za mesing veća nego za bakar.

MATERIJALI I METODE

Otpornost općoj koroziji procijenjena je na osnovi elektrokemijskih značajki uzoraka bakra (99.9 % Cu) i mesinga (CuZn37) u dva različita medija. Uzorci su ispitivani u sisačkoj vodovodnoj vodi i 3.5 % otopini NaCl (0.6 M, pH = 4.74) pri temperaturi od 20 °C. Slobodna površina uzoraka, odnosno elektroda koje su bile u kontaktu s elektrolitom iznosila je 0,1 cm^2.

Prije svakog mjerenja površine uzoraka su mehanički obrađene. Brušene su pod mlazom vode na uređaju za automatsku pripremu uzoraka (Vector LC, Buehler) brusnim papirom gradacije 400, 600, 800 i 1000. Na svakoj gradaciji brusnog papira uzorak je brušen 10 minuta kod sile opterećenja od 10 N i brzine okretanja rotacijskog diska 150 o/min. Nakon brušenja uzorci su polirani na platnu za poliranje Microcloth vodenom otopinom glinice granulacije 0.3 μm. Brušenje i poliranje je provedeno na istom uređaju, pri istim uvjetima.

Nakon poliranja, površina uzoraka se temeljito ispire vodom, potom odmašćuje u etanolu i suši. Nakon toga su uzorci kao radne elektrode postavljene u standardnu troelektrodnu elektrokemijsku ćeliju zajedno s protuelektrodom od platine i zasićenom kalomel elektrodom (SCE) kao referentnom elektrodom, slika 1.

Slika 1. Troelektrodna staklena ćelija

U ovom radu izvedena je potenciodinamička polarizacija u području potencijala od -250 mV do +250 mV vs E_{corr}, uz brzinu promjene potencijala od 1 mV/s, a korozijski parametri su određeni pomoću softvera PowerCorrTM primjenom Tafelove metode ekstrapolacije i Faradayevih zakona [10]. Prije svakog mjerenja potenciodinamičke polarizacije pokrenuta je stabilizacija potencijala kod otvorenog strujnog kruga E_{ocp}, pomoću računalom upravljanog potenciostata/galvanostata ("Parstat 2273") u trajanju od 30 minuta. Za svaki uzorak i svaki medij ponovljena su po dva mjerenja te su za obradu rezultata uzete srednje vrijednosti.

Metalografska analiza provedena je na svjetlosnom mikroskopu Olympus GX51 opremljenim digitalnom kamerom i programskom podrškom za analizu slike Analysis® Materials Research Lab.

Sva ispitivanja provedena su na Metalurškom fakultetu Sveučilišta u Zagrebu u Laboratoriju za kemiju i Laboratoriju za željezo, čelik i ljevarstvo.

REZULTATI I RASPRAVA

Prije elektrokemijskih ispitivanja uzorci bakra i mesinga nagriženi su u HNO_3 da bi se istakla njihova mikrostruktura, slika 2. Kao što je prikazano na slici 2a, mikrostruktura uzorka bakra sastoji se od finih usmjerenih zrna iz kojih proizlazi izotropno ponašanje materijala. Iz slike 2b jasno se vidi mikrostruktura CuZn37 mesinga koja se sastoji od α + β faza.

|a) Cu, 200x | b) CuZn37, 500x|

Slika 2. Mikrostrukturne snimke uzoraka Cu i CuZn37 nagriženih s HNO_3

Nakon snimanja mikrostrukturi uzorci bakra i mesinga su ponovo strojno brušeni i polirani u svrhu provođenja elektrokemijskih mjerenja. Nakon mjerenja potencijala otvorenog strujnog kruga E_{ocp}, u svrhu određivanja sljedećih korozijskih parametara: korozijskog potencijala E_{corr}, anodnog nagiba b_a, katodnog nagiba b_c i brzine korozije v_{corr} izvedena je potenciodinamička polarizacija u području potencijala od −250 mV do +250 mV vs E_{corr} u mediju 3.5 % otopini NaCl i vodovodnoj vodi pri sobnoj temperaturi. Ovisnosti potencijala kod otvorenog strujnog kruga o vremenu za ispitane materijale prikazane su na slici 3, a polarizacijske krivulje bakra i mesinga u vodi i 3.5 % otopini NaCl prikazane su na slici 4.
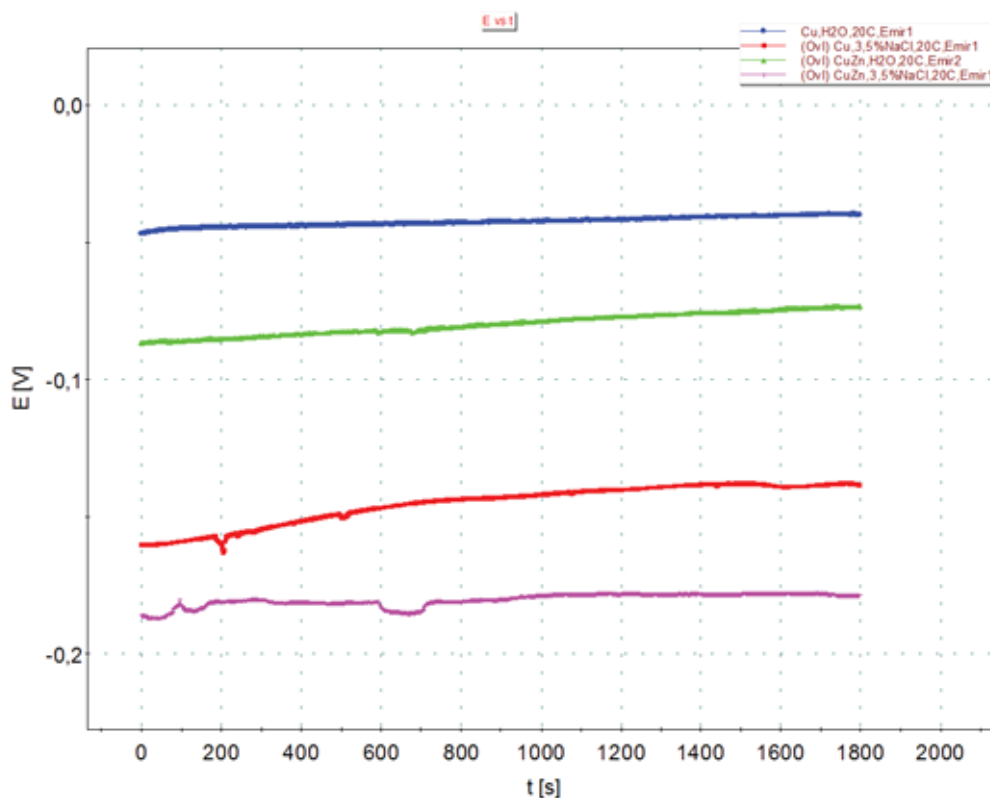
Slika 3. Ovisnost mirujućeg potencijala uzoraka Cu i CuZn37 o vremenu u H_2O i 3.5 % otopini NaCl

Iz prikazanih krivulja vidljivo je da bakar i mesing u vodi imaju nešto „plemenitiji" karakter od onog u otopini NaCl, što potvrđuje pomak vrijednosti za korozijski potencijal u pozitivnom (anodnom) smjeru. Također, vidljivo je da oba ispitana materijala i u vodi i u 3.5 % otopini NaCl brzo postižu svoj mirujući potencijal, tj. potencijal kod otvorenog strujnog kruga.
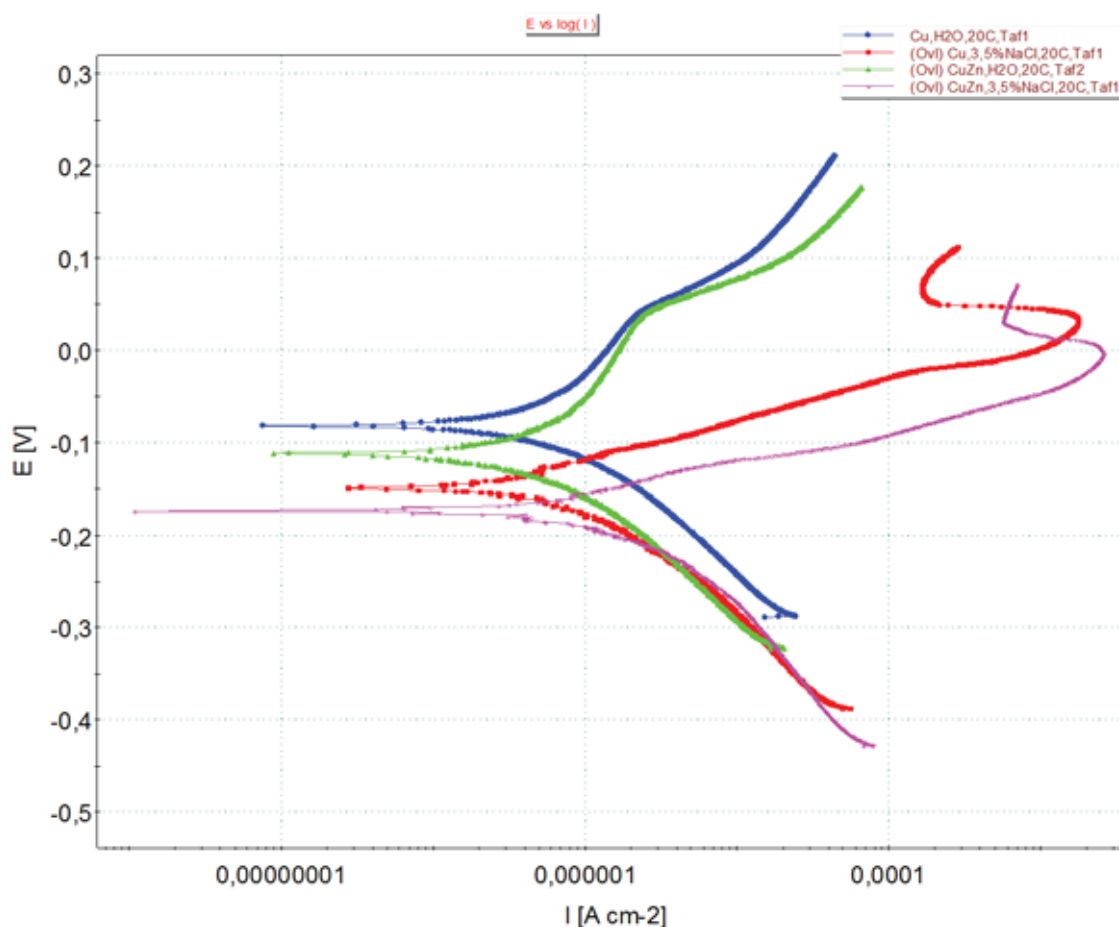
Slika 4. Polarizacijske krivulje za Cu i CuZn37 u H_2O i 3.5 % otopini NaCl

Iz linearnog dijela polarizacijskih krivulja, odnosno ekstrapolacijom Tafelovih pravaca određene su vrijednosti elektrokemijskih parametara koje su navedene u tablici 1. U tablici su navedene srednje vrijednosti dvaju mjerenja.

Tablica 1. Korozijski parametri ispitanih materijala u H_2O i 3.5 % otopini NaCl

Materijal	Medij	E_{corr} vs SCE (mV)	b_a (mV dec^{-1})	b_c (mV dec^{-1})	v_{corr} (mm god^{-1})
Cu	voda	-80.83	128.00	80.41	0.064
Cu	NaCl	-148.76	102.50	147.40	0.252
CuZn	voda	-108.70	150.90	152.70	0.076
CuZn	NaCl	-174.52	55.30	185.40	0.335

Iz tablice 1 se uočava da je brzina korozije bakra koji je izložen djelovanju kiselo kloridnog medija (v_{corr}(Cu, NaCl)) = 0.252 mm god^{-1}) veća nego u vodi (v_{corr}(Cu, H$_2$O)) = 0.064 mm god^{-1}). Za vrijeme elektrokemijske korozije bakra u 3.5 % otopini NaCl pretpostavlja se da dolazi do nastanka sloja bakrovog klorida (slike 5a i b), koji je nedovoljno postojan da spriječi prodiranje agresivnih iona iz kisele otopine NaCl na površinu bakra. Relativno mala brzina korozije bakra u vodi se objašnjava stvaranjem pasivnog filma oksida ili hidroksida na površini bakra.
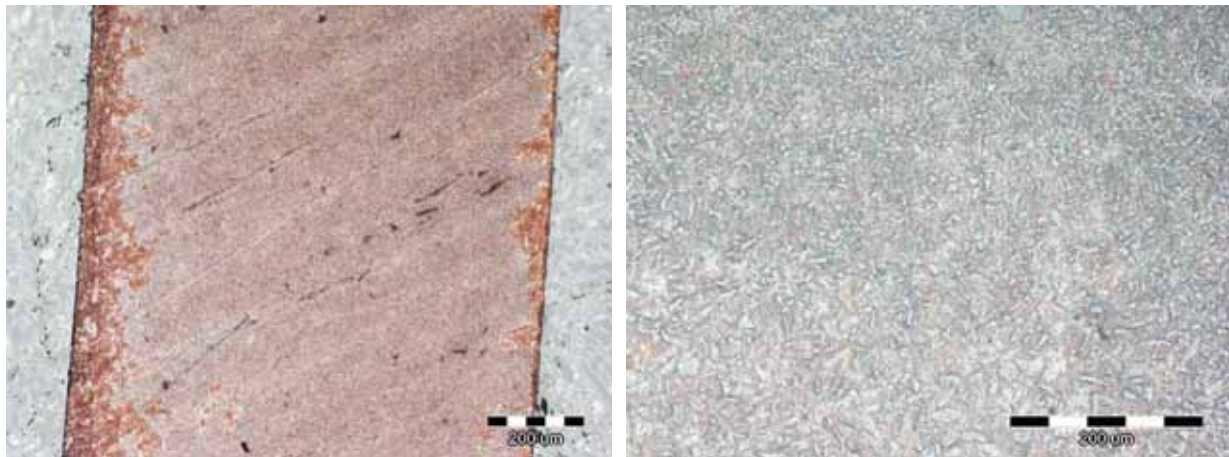
| a) Cu, 3.5 % NaCl, 100x | b) Cu, 3.5 % NaCl, 200x |

Slika 5. Metalografski snimci bakra nakon elektrokemijskih mjerenja u 3.5 % otopini NaCl

Iz tablice 1 se također uočava da je brzina korozije mesinga koji je izložen djelovanju kiselo kloridnog medija (v_{corr}(CuZn37, NaCl)) = 0.335 mm god^{-1}) veća nego u vodi (v_{corr}(CuZn37, H$_2$O)) = 0.076 mm god^{-1}). To se može objasniti činjenicom da pri pH < 5 teško dolazi do nastanka zaštitnog sloja na površini mesinga jer je taj sloj nepostojan i porozan te se brzo rastvara [9]. Sa slike 6 uočava se prisustvo nastalog sloja korozijskih produkata na površini mesinga, koji prema literaturnim navodima [11] odgovaraju oksidima, oksikloridima i/ili kloridima bakra i cinka. Koja vrsta korozijskog produkta će nastati na površini mesinga ovisi o sadržaju bakra i cinka u samoj leguri.
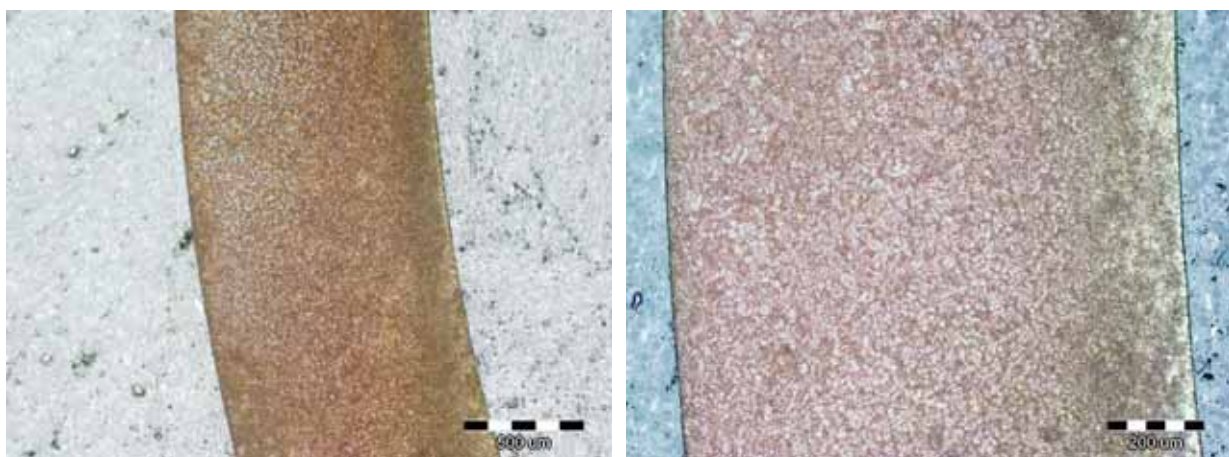
| a) CuZn37, 3.5 % NaCl, 50x | b) CuZn37, 3.5 % NaCl, 100x |

Slika 6. Metalografski snimci mesinga nakon elektrokemijskih mjerenja u 3.5 % otopini NaCl

Iz dobivenih rezultata prikazanih u tablici 1 također se može uočiti da su oba ispitana materijala pokazali manju korozijsku otpornost u 3.5 % otopini NaCl nego u vodovodnoj vodi, o čemu svjedoče veći iznosi za brzinu korozije. Iz rezultata je vidljivo da je u oba medija veću brzinu korozije pokazao mesing, tj. bakar se pokazao korozijski otpornijim materijalom. Međutim, razlika u brzinama korozije bakra i mesinga u vodi je zanemariva, dok je mesing u 3.5 % NaCl pokazao veću brzinu korozije od bakra za 25 %.

ZAKLJUČAK

Elektrokemijskim ispitivanjima proučavana je korozijska otpornost materijala bakra i mesinga u vodovodnoj vodi i 3.5 % otopini NaCl pri temperaturi od 20 °C. Utvrđeno je da je brzina korozije bakra koji je izložen djelovanju kiselo kloridnog medija veća nego u vodi. To dovodi do zaključka da za vrijeme elektrokemijskog procesa dolazi do nastanka sloja bakrovog klorida koji je nedovoljno postojan da spriječi prodiranje agresivnih iona iz kisele otopine NaCl na površinu bakra. Također se može zaključiti da je brzina korozije mesinga koji je izložen djelovanju kiselo kloridnog medija veća nego u vodi što se objašnjava nastankom poroznog zaštitnog sloja na površini mesinga koji bi mogao odgovarati oksidima, oksikloridima i/ili kloridima bakra i cinka. Veću brzinu korozije u oba medija pokazao je mesing, odnosno bakar se pokazao korozijski otpornijim materijalom.
Ovo istraživanje daje rezultate korozijskog ponašanja bakra i mesinga u čistoj vodovodnoj vodi i 3.5 % otopini NaCl na sobnoj temperaturi. Daljnja istraživanja usmjerit će se ispitivanju korozijskog ponašanja pri povišenim temperaturama te uz dodatak određenih inhibitora. Također je daljnjim istraživanjima potrebno utvrditi točan sastav dobivenih slojeva na oba materijala.

LITERATURA

[1] K. Rhattas, M. Benmessaoud, M. Doubi, N. Hajjaji, A. Srhiri, Corrosion inhibition of copper in 3% NaCl solution by derivative of aminotriazole, Materials Sciences and Applications, 2(2011)4, pp. 220-225.
[2] K. F. Khaled, Studies of the corrosion inhibition of copper in sodium chloride solutions using chemical and electrochemical measurements, Materials Chemistry and Physics, 125 (2011), pp. 427-433.
[3] Z. Avramović, M. Antonijević, Korozija mesinga, Zaštita materijala, 47(2006)3, pp. 49-60.
[4]https://books.google.hr/books?id=y1eTDQRdI2wC&pg=PA377&lpg=PA377&dq=microstructure+of+copper+and+CuZn37&source=bl&ots=IAqZ597mPq&sig=Cc6wXJXmkxtw4VxX1Q6oiUcUc7A&hl=hr&sa=X&ved=0ahUKEwjghprA3MfTAhXHISwKHYv7B0UQ6AEIJDAA#v=onepage&q=microstructure%20of%20copper%20and%20CuZn37&f=false (10.03.2017.)
[5] R. Konečná, S. Fintová, Copper and copper alloys: Casting, classification and characteristic microstructures, University of Žilina, Slovak Republic.
http://cdn.intechopen.com/pdfs/30472/InTech-Copper_and_copper_alloys_casting_classification_and_characteristic_microstructures.pdf (20.03.2017.)
[6]http://www.walcownia.com.pl/index.php?option=com_content&view=article&id=71&Itemid=226&lang=en (20.03.2017.)

[7] https://www.thebalance.com/brass-types-3959219 (12.02.2017.)

[8] H. Alhumade, A. Abdala, A. Yu, A. Elkamel, Leonardo Simon, Corrosion inhibition of copper in sodium chloride solution using polyetherimide/graphene composites, The Canadian Journal of Chemical Engineering, 94(2016), pp. 896-904.

[9] A. Gamal, El-Mahdy, Electrochemical impedance study on brass corrosion in NaCl and $(NH_4)_2SO_4$ solutions during cyclic wet – dry conditions, Journal of Applied Electrochemistry 35(2005), pp. 347-353.

[10] E. Stupnišek-Lisac, Korozija i zaštita konstrukcijskih materijala, Sveučilište u Zagrebu Fakultet kemijskog inženjerstva i tehnologije, Zagreb, 2007.

[11] M. B. Radovanović, Uticaj organskih inhibitora na koroziono ponašanje mesinga u rastvoru natrijum-sulfata, Doktorska disertacija, Univerzitet u Beogradu Tehnički fakultet u Boru, Bor, 2012.

Zahvala

INFLUENCE OF HEAT INPUT ON DIFFUSIBLE HYDROGEN CONTENT AND MECHANICAL PROPERTIES IN UNDERWATER WET WELDING

Ivica Garašić, **Zoran Kožuh**, **Slobodan Kralj**

University of Zagreb Faculty of Mechanical Engineering and Naval Architecture, Zagreb, Croatia

<u>Poster presentation</u>
<u>*Original scientific paper*</u>

Abstract

The rapidly increasing development of the laying of high-strength steel underwater pipelines for the transportation of gas and oil requires adequate welding technology for maintenance and repair. As FCAW is suitable for automation and appropriate for application at greater depths it represents a welding process capable of replacing MMAW underwater wet welding. Moreover, the complexity of underwater wet welding on high strength steels up to grade X70 requires precise welding parameters and heat input control. This paper presents the basic issues of FCAW underwater wet welding. Measurement of diffusible hydrogen was made with the glycerine method for different welding parameters and levels of heat input for FCAW welding of API 5L X70 pipeline steel. In addition, hardness HV10 was also determined in order to define the effect of heat input on steel microstructure. This work was done as part of the scientific project "Improvement of underwater welding and inspection" which is being conducted at the Faculty of Mechanical Engineering and Naval Architecture, University of Zagreb.

Keywords: *underwater wet welding, hydrogen, API 5L X70, FCAW*

*Corresponding author (e-mail address): *zoran.kozuh@fsb.hr*

INTRODUCTION

Underwater MMA wet welding is the oldest technique for joining metals underwater. It is applicable for the repair of both ship hulls and underwater structures but is considered a second-rate technology because of the poor mechanical characteristics of the welded joint. Today, wet underwater welding has an important industrial, commercial and economic potential in the development and maintenance of underwater structures and because of the much lower costs and better flexibility has an advantage over dry underwater welding techniques, high quality welds also being achieved. However, further development of the

basic materials, the large number of installed and planned underwater structures and pipelines and increasing depth require further development of the procedure of underwater wet welding. Clearly in this the MMAW technology is facing the major barrier of automation solutions, which restricts it to use at lower depths, down to 60 m, while other welding techniques like FCAW are becoming of primary importance for further research.

Wet underwater welding with the MMAW is characterised by the following [1-5]:

- Electric arc instability, which produces irregular welded joint geometry, the inclusion of slag, porosity and insufficient penetration.
- Rapid cooling produces high hardness in the heat affected zone, low toughness of the welded joint and the appearance of porosity because of gas bubble capture.
- High hydrogen content in the electric arc column, melted metal drops in the transfer and the weld pool, leading to the capture of hydrogen in the weld metal and in the heat affected zone. This increases sensitivity to the occurrence of cold cracks, produces porosity and degrades the mechanical properties of the joint.
- The high oxygen content in the electric arc column, melted metal drops in the transfer and weld pool, which leads to oxidation, reduction of the percentage of alloying elements and degradation of the mechanical properties.
- Dissolution and melting of the coating of the electrodes, which results in instability in the electric arc and the occurrence of porosity.

Direct access of water to the arc and molten metal has several negative consequences for the properties of the welded joint. Because of the rapid cooling, the creation of a locally hardened structure of great hardness in the joint appears, the hardness of which quite often exceeds 350 HV10 in the heat affected zone. In addition the high percentage of diffusible hydrogen that ranges from 30 to 80 ml H_2/100g of the weld [6,7], makes the structure sensitive to the appearance of hydrogen brittleness, i.e., leads to the occurrence of cracks caused by hydrogen. The sequence of micropores that arises because of the rapid solidification and the impossibility of degassing the metal of the weld contributes to such a situation.

The advantage of welding with FCAW relates primarily to an increase in productivity, better mechanical properties in the weld, together with the possibility of automation and with a reduced share of hydrogen in the weld. Today's systems can be applied for welding with self-shielding flux cored wire. In addition, wire feeders that are completely immersed in the water and can be used down to 40 m have been developed. The power source and the control panel are situated on the surface. For the sake of the elimination of the influence of hydrostatic pressure the feeder is filled with water, with only the housing of the electric motor for the drive of the wire being sealed and filled with a dielectric current for the sake of insulation. Coils of wire of a weight of 3.5 kg are used, and can be changed underwater. Welding power source of electricity with a constant voltage CV characteristic of 400A capacity at 60% intermittence is used. The welding parameters are measured and adjusted on the surface on control panel [8,9]. A comparative investigation of the MMAW and the FCAW procedures has shown that in the welding of plates 14 mm thick it is possible to achieve a cost reduction of about 40% [8,9]. The employment of flux cored wire in wet underwater welding significantly raises demands for equipment and electricity sources for the welding, which implies the need for further research. The supply of filler materials and also perhaps of shielding gas is considerably hampered at greater depths. However, precisely the greater possibility of varying the filler material and shielding gas in conjunction with

optimisation of the parameters can have a great impact on the quality of the welded joints. It has been shown that the employment of such shielding gases as Freon in wet underwater welding with a metal electrode in gas shielding reduces the quantity of hydrogen in the weld [10]. However, the employment of such gases is not permitted, for well-known reasons. Along with systems for automatic underwater welding already developed, which nevertheless require considerable financial investment, it is apparent that there is a need for the optimisation of parameters, filler materials and shielding gases, so as to be able to make full use of these actually highly productive systems. The problem of optimising parameters is more complex if it is a matter of high strength steels that are much more sensitive to weld parameters.

Research carried out with a double metal coating showed that with flux cored wire quantities of diffusible hydrogen up to 50% lower were achieved [11]. In addition, the area of parameter regulation for a certain diameter of flux cored wire is much wider with respect to a certain electrode diameter, which improves the operational area of the work. Also, it has been stated that a combined application of shielding gas and electrode does not provide the best conditions in the shielding of the process, which is explained by the collision of shielding mechanisms, during which they cancel each other out [11].

Welding with flux cored wire enables the application of sophisticated sources of electricity, which can have a considerable influence on the transfer of melted metal and the stability of the process.

Steels of group X70 according to API 5L have good mechanical properties and good weldability. This is the result of development in the area of metallurgy and thermomechanical treatment. Reduction of the percentage of carbon below 0.1%, microalloying with Nb, V or Al in correlation with the parameters of TMCP have resulted in a fine-grained structure of excellent mechanical characteristics. X70 steels are used every day in the construction of pipelines and to a lesser extent in off-shore plant. However, because of the microstructure it is necessary to define the welding parameters in narrow borders in order to make it possible to obtain welded joints of satisfactory mechanical properties [17].

Because the length and operating pressure of pipelines is constantly on the rise, the development of high strength steel considerably contributes to the reduction of development costs. For underwater off-shore pipelines, the working pressure is the most important design factor. A much greater impact derives from the hydrostatic pressure of the environment, i.e., much more important than the strength of the material is the resistance of the pipeline to being flattened or squashed as a result of a pressure overload, which requires from the producers a much more qualitative geometry and shape for their pipes. With an increase in the percentage of H_2S in the transport gas, problems of the occurrence of hydrogen-induced cracks also rise.

From all of this it can be concluded that it is necessary to define the technology of wet underwater welding in order to minimize the quantity of diffusible hydrogen and thus to a reduction of the risk of hydrogen cracks in wet underwater welding. This paper is part of complex research that deals with this issue in the context of the scientific projects at the Faculty of Mechanical Engineering and Naval Architecture, University of Zagreb.

MATERIALS AND METHODS

Wet underwater welding was carried out in laboratory conditions in a small pool with dimensions of 1100 x 600 x 75 mm with a volume of 500 litres. Water temperature in the pool came to 22°C. Test tubes for the determination of diffusible hydrogen were machined from tubes of API 5L X70 diameter 700 mm and wall thickness 16 mm. For determination of the diffusible hydrogen, the glycerine method was employed. All samples were welded automatically with a speed of 30 cm/min. The chemical composition of the basic material is given in Table 1.

Table 1. Chemical composition of API 5L X70 steel

C	Si	Mn	Cr	Ni	Mo	Ti	Nb	V
0.091	0.30	1.72	0.03	0.03	0.12	0.025	0.05	0.06

Filler material was rutile flux cored self-shielding wire diameter 1.7 mm, classification AWS: A5.20-95: E 71T-8. Welding was carried out with the electrode on the negative polarity. The chemical composition of the metal of the weld is shown in Table 2, while the mechanical properties of the metal of the weld are shown in Table 3. Table 4 shows the welding parameters.

Table 2. Chemical composition of the metal of the weld with flux cored wire (welded in dry)

Chemical element	C	Mn	Si	S	P	Al
Mass percentage, %	0.18	0.65	0.27	0.004	0.006	0.55

Table 3. Mechanical properties of the flux cored wire weld metal

R_m N/mm^2	R_e N/mm^2	A %	K_v -20°C
590	490	26	65 J

Table 4. Welding parameters with self-shielding flux cored wire

Level	Welding current A	Wire feed speed m/min	Welding Voltage V	Heat input kJ/cm
1	290	4	27	12.5
2	350	6	27.9	15.6
3	390	7.16	30	18.7

Figure 1 shows a sample prepared for welding gripped in a copper fixture. It is particularly important to control the wire stickout because this affects the welding parameters and the drying of the flux cored wire brought about by the heat of electric resistance.

Figure 1. Sample prepared for welding
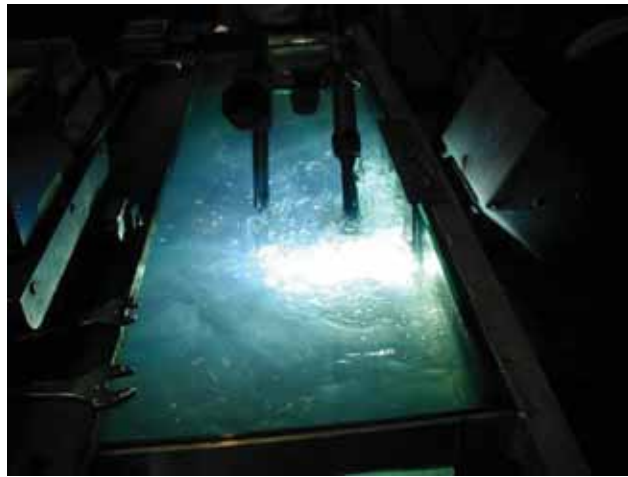
Figure 2. Underwater wet welding in the laboratory pool

Figure 3. Appearance of the welded sample

Figure 4. Collecting hydrogen in a measuring tube

RESULTS AND DISCUSSION

Results of diffusible hydrogen determination are given in Table 5. Quantities from 27.73 ml H_2/100 g for a heat input of 12 kJ/cm to 29.75 ml H_2/100 g for an input of 18 kJ/cm were measured.

Table 5. Results of diffusible hydrogen determination

Designation	Mass of weld deposition m, g	Read volume of Hydrogen V, ml	Diffusible hydrogen content H_D ml H_2/100 g
IB1	13.3	4.36	
IB1	13.0	4.32	
IB1	13.8	4.06	27.73
IB1	14.0	3.98	
IB2	22.8	6.91	
IB2	26.5	8.41	
IB2	25.5	8.11	28.34
IB2	24.2	7.61	
IB3	27.5	9.18	
IB3	30.4	9.24	
IB3	27.4	9.34	29.75
IB3	30.4	10.02	

Figure 5. Graph showing the results of diffusible hydrogen determination

The quantities of diffusible hydrogen measured for the flux cored wire without gas shielding welding technique correspond to the data from [11]. With an increase in heat input, only a small growth in the volume of diffusible hydrogen was observed, Figure 5. In this procedure electro-resistance preheating and drying of the wire is most vigorous because of the high welding currents, from 290 to 390 A, while the speeds of wire are relatively smaller and for the same stickout of the wire the preheating time is longer. The voltage range of the electric arc was from 27 V for 12 kJ/cm, 27.9 V for 15 kJ/cm to 30 V for 18 kJ/cm. For an increase in the voltage of the electric arc is connected with an increase in the height of the electric arc. For a higher voltage it holds that the drops of molten material will travel longer through the atmosphere of the electric arc in which the partial pressure of hydrogen is relatively high. The consequence is that the molten drops will be contaminated with hydrogen.

Values were measured that are lower than data for MMA welding in which the quantities of diffusible hydrogen range from 30 to 80 ml H_2/100 g of weld deposit [3,5,15,19]. This shows the lower likelihood of cold cracks appearing for underwater FCAW.

Measuring of the hardness HV 10 showed that the highest values for all three heat inputs were measured around 0.5 mm from the fusion line, which indicates the martensite microstructure in this zone. For a heat input of 12 kJ/cm a hardness of 409 HV10 was measured; for 15 kJ/cm of 380 HV10, and for 18 kJ/cm of 370 HV 10. This indicates a slower cooling with a rise in heat input and an elevation of the percentage of bainite.
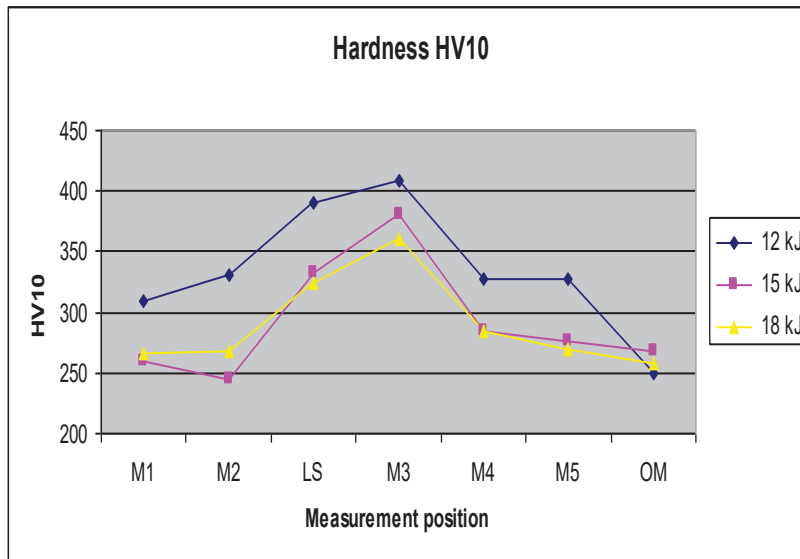
Figure 6. Hardness in the welded joint

In single pass wet underwater welding, martensite microstructures that are sensitive to the occurrence of cracks are common. According to [3] the width of this martensite belt comes to about 0.5 mm, depending on the heat input. From the hardness results it can be seen that as a rule maximum values were measured at a distance of 0.5 mm from the fusion line (LS marks fusion line). In the very next measuring point, about 1 mm distant from the melting line, the hardness begins to decline. It thus follows that the width of the martensite zone right by the melt line ranges around 0.5 mm.

Figure 7. Fusion line – sample IB21, magnification 200 x

Figure 7 shows the weld metal, the fusion line and the coarse grained martensite microstructure. In the coarse-grained part of HAZ along the melting line it is martensite that prevails, while with increasing distance from the line, a martensite-bainite structure is formed.

93

Figure 8. Inclusion in the weld metal close to the fusion line, magnification 100 x

A self-shielding flux cored wire of a diameter of 1.7 mm has a highly stable electric arc. The greatest problem with this wire is the relatively difficult cleaning of the slag that remains entrapped on the weld surface. In conjunction with the good mechanical properties and geometry of the weld, it is necessary to make some modifications to the composition of the flux in order to prevent slag inclusions, Figure 8.

CONCLUSIONS

In this work, an investigation was carried out into the diffusible hydrogen occurring in wet underwater welding with self-shielding flux cored wire on API 5L X70 basic material.

In addition, testing of hardness and a microstructural analysis were carried out on the same samples.

On the basis of the research carried out it is possible to make the following conclusions:

- the volume of diffusible hydrogen in wet underwater welding with self-shielding rutile flux cored wire depends on the heat input, although only a relatively small rise is involved (27.73 ml H_2/100g for 12 kJ/cm to 29,71 ml H_2/100g for 18 kJ/cm),
- the hardness values decline with a rise in the heat input, from 409 HV10 for 12 kJ/cm to 370 HV10 for 18 kJ/cm,
- for wet underwater welding of X70 steel with self-shielding flux cored wire heat input of 18 kJ/cm is better, for although this does result in a somewhat higher quantity of diffusible hydrogen, a better microstructure is nevertheless obtained.

Small changes in the quantity of diffusible hydrogen enable a better flexibility in the choice of working parameters of welding in the context of the risk of cold cracks occurrence.

REFERENCES

[1] K. Masubuchi, Underwater factors affecting welding metalurgy, Proceedings of Underwater welding of offshore platforms and pipelines, 1980., New Orleans, USA,

pp. 81-98,

[2] P. Szelagowski, Underwater wet welding part part I-wet SMA welding, IIW doc. SCUW, 1990.

[3] R. T. Brown, K. Masubuchi, Fundamental research on underwater welding, Welding Journal, June 1975.

[4] C. L. Tsai, Underwater welding, cutting and inspection, Welding Journal, February 1995., pp. 55-62,

[5] S. Anik, L. Dorn, Schweisseignung mettalischer Werkstoffe, Dt. Verlag für Schweisstechnik, DVS-Verlag, ISBN 3-87155-141-4, Düsseldorf, 1995.

[6] P. S. Maslennikov, V. L. Russo, Special features of the effect of hydrogen on the weldability of structural steels in underwater welding by the «wet» method, Welding International, 17(2003)3, pp. 221-225,

[7] S. Kralj, Z. Kožuh, I. Garašić, L. Dorn, Influence of the water environment on the parameters in underwater wet welding, Welding and Cutting, 55(2003)2, pp. 97-99.

[8] M. A. Cooper, Some aspects of underwater engineering-Ministry of Defence, 1995-2003, IIW-Doc. XII-1874-05, 2005.

[9] M. Cooper, W. Lucas, Underwater wet welding and cutting using the FCA process, IIW-Doc. SC-UW-178-99, 1999.

[10] D. Chandiramani, Hydrogen reduced in wet underwater GMA welds, Welding Journal, (1994), pp. 45-49,

[11] H. Haferkamp, F. W. Bach, J. H. Hamkens, Underwater wet welding of structural steels for the off-shore sector using «self-shielded» flux-cored electrodes, Welding and Cutting, pp. E71-E72, 5/1990.

[12] N. J. Woodward, D. Yapp, I. M. Richardson, D. Widgery, M. A. P. Armstrong, R. L. P. Verley, J. O. Berge, Subsea pipeline repair-diverless GMA welding using fillet welded sleeve, IIW-Doc. XII-1868-05.

[13] N. J. Woodward, D. Yapp, I. M. Richardson, D. Widgery, M. A. P. Armstrong, R. L. P. Verley, J. O. Berge, Retrofit Tee Hot Tapping using Diverless Underwater GMA Welding, IIW-Doc. XII-1898-06.

[14] M. Parvu, Welding technology to repair by socket welding an underwater gas pipeline, Sudura, XVI-2(2006), pp. 5-13,.

[15] S. Kralj, Z. Kožuh, I. Garašić, Electrodes for underwater wet welding, Proceedings of Welding and Joining 2000, Israel Society of Mechanical Engineering, 2000., Tel Aviv, pp. 161-168,

[16] P. Zimmer, T. Boellinghaus, T. Kannengiesser, Effects of hydrogen on weld microstructure mechanical properties of the high strength steels S690Q and S1100QL, IIW Doc. II-1525-04, 2004.

[17] H. G. Hillenbrand, M. Gräf, C. Kalva, Development and production of high-strength pipeline steels, Proceedings of the International Symposium Niobium, Orlando, USA, 2001.

[18] Y. Bai, Pipelines and risers-Elsevier Ocean Engineering Book Series Vol. 3, ISBN 0 08 0437125, Elsevier Science Ltd, Oxford, United Kingdom, 2001.

[19] I. Garašić, Susceptibilty of X70 steel on cold cracking during underwater wet welding, Doctoral thesis, University of Zagreb, 2008.

MODELLING OF INFLUENCE OF FOUNDRY SAND ON SOLIDIFICATION SIMULATION OF CASTINGS

MODELIRANJE UTJECAJA LJEVAONIČKOG PIJESKA NA SIMULACIJU SKRUĆIVANJA ODLJEVAKA

Vladimir Grozdanić

University of Zagreb Faculty of Metallurgy, Sisak, Croatia

Poster presentation

Original scientific paper

Abstract

Modelling of influence of zircon and olivine foundry sand on solidification simulation of middle carbon steel „L" shaped castings has been presented in the paper.

Keywords: modelling, solidification, foundry sand, steel casting

*Corresponding author (e-mail address): _grozdan@simet.hr_

Sažetak

U radu je modeliran utjecaj cirkonskog i olivinskog ljevaoničkog pijeska na simulaciju skrućivanja srednje ugljičnog čeličnog odljevka u obliku slova „L".

Ključne riječi: modeliranje, skrućivanje, ljevaonički pijesak, čelični odljevak

UVOD

Matematičko modeliranje kao suvremena znanstvena metoda omogućuje rješavanje i najkompleksnijih ljevaoničkih problema, kao što je skrućivanje odljevaka složene geometrije. To je potpomognuto brzim razvojem računala i numeričkih metoda rješavanja parcijalnih diferencijalnih jednadžbi.

Temelj matematičkog modela skrućivanja je Fourierova parcijalna diferencijalna jednadžba provođenja topline. Jednadžba se rješava po domeni odljevka i geometriji kalupa, s time da su inkorporirani početni i rubni uvjeti, što spada u kategoriju početno-rubnih problema. Pri operacionalizaciji matematičkog modela općenito se mogu koristiti dvije numeričke metode: metoda konačnih elemenata (MKE) i metoda konačnih razlika (MKR). MKE je kompliciranija od MKR, a posebno je pogodna za odljevke kompleksnog oblika, kao i za zakrivljene plohe. MKR je nešto jednostavnija, a temelji se na diferencijalnom pristupu.

U radu je korištena MKR – implicitna metoda promjenljivog smjera (eng. Implicit alternating direction – ADI), iz razloga što je bezuvjetno stabilna i drugog je reda s obzirom na aproksimaciju prostora i vremena. Budući da se temperatura u sustavu odljevak – kalup mijenja za cca 1600°C, u model su ugrađena temperaturno ovisna toplinska svojstva.

Na temelju matematičkog modela, odnosno provedene numeričke simulacije, moguće je zorno vidjeti skrućivanje čeličnog odljevka. Posebice brzine skrućivanja, pomicanje izosolidusa, pomicanje izolikvidusa, trajanje skrućivanja, kao i potencijalna mjesta za pojavu defekta, te konačno utjecaja vrste (cirkonskog i olivinskog) pijeska.

MATEMATIČKI MODEL

Numerička simulacija skrućivanja provedena je za srednje ugljični čelični odljevak u pješčanom cirkonskom i olivinskom kalupu, kao što je prikazano na slici 1.
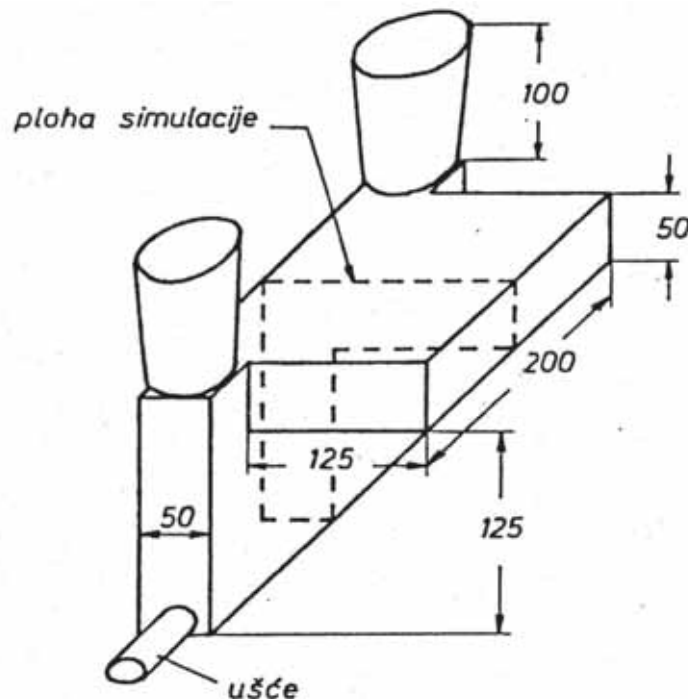
Slika 1. Shematski prikaz odljevka

Pri simulaciji procesa razmatra se presjek kroz kalup i odljevak kao na slici 2.
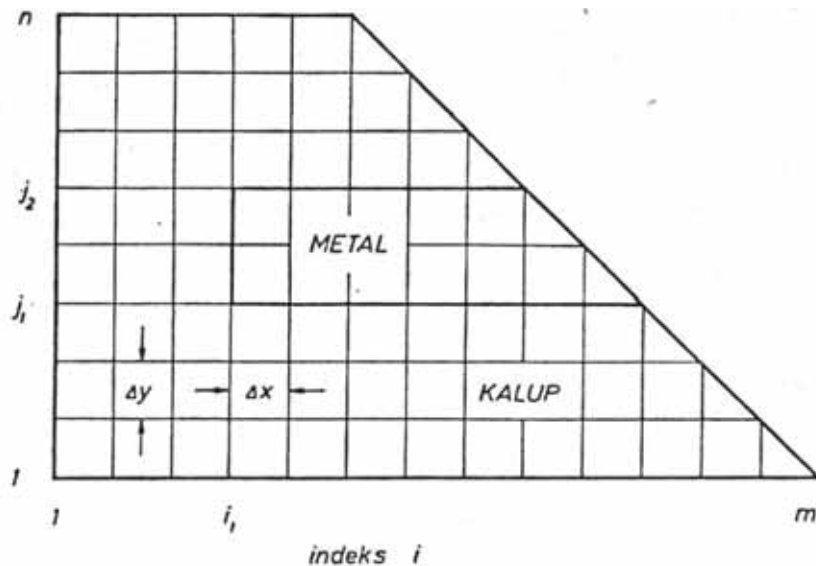
Slika 2. Dio presjeka kroz kalup i odljevak koji se razmatra pri simulaciji procesa

Matematički model skrućivanja odljevka sastoji se od Fourierove parcijalne diferencijalne jednadžbe provođenja topline i odgovarajućih početnih i rubnih uvjeta. Dvodimenzionalna parcijalna diferencijalna jednadžba provođenja topline u pravokutnom koordinatnom sustavu ima oblik [1]:

$$\frac{\partial T}{\partial t} = a\left(\frac{\partial^2 T}{\partial x^2} + \frac{\partial^2 T}{\partial y^2}\right) \tag{1}$$

Početni uvjet dobiven je na temelju toplinske bilance sustava [2]:
$$t = 0 \qquad T = T_s$$

$$T_i = \frac{\rho_m\, c_{pm}\, T_L + \rho_k c_{pk} T_s + \rho_m \Delta H_f}{\rho_m c_{pm} + \rho_k c_{pk}} \tag{2}$$

Pri čemu je: T_s — površinska temperatura kalupa, K

T_L — temperatura lijevanja, K

T_i — temperatura na graničnoj plohi kalup-metal, K

ρ_m — gustoća metala, kg/m^3

c_{pm} — specifični toplinski kapacitet metala pri konstantnom tlaku, J/kgK

ρ_k — gustoća kalupa, kg/m^3

c_{pk} — specifični toplinski kapacitet kalupa pri konstantnom tlaku, J/kgK

ΔH_f — entalpija taljenja, J/kg

Rubni uvjeti. Vanjska ploha kalupa je pri konstantnoj temperaturi T_s. U blizini plohe koja leži na dijagonali pod kutom od 45°C nema toplinskih razlika, tako da su toplinski tokovi jednaki. Iz Fourierovog zakona slijedi:

$$\frac{\partial T}{\partial n} = 0 \tag{3}$$

98

Na dodirnoj plohi kalup – metal kontinuitet je toplinskog toka, tako da vrijede rubni uvjeti četvrte vrste [3]:

$$k_m \frac{\partial T_m}{\partial n} = k_k \frac{\partial T_k}{\partial n}$$ (4)

U jednadžbama (3) i (4) n je normala na promatranu plohu.

TOPLINSKA SVOJSTVA ČELIČNOG LIJEVA I KALUPNOG MATERIJALA

Budući da se pri skrućivanju i hlađenju čeličnog odljevka u pješčanom kalupu temperatura mijenja u rasponu od gotovo 1600 °C da bi se što bolje opisao realni proces u matematičkom je modelu potrebno uzeti temperaturnu ovisnost toplinskih svojstava materijala. Na slikama 3. i 4. prikazana temperaturna ovisnost toplinske vodljivosti i specifičnog toplinskog kapaciteta pri konstantnom tlaku za srednje ugljični čelični lijev, na temelju podataka iz literature [4,5]. Temperatura likvidusa i solidusa za srednje ugljični čelični lijev je 1482°C, odnosno 1427°C. Latentna toplina kristalizacije iznosi 271 kJ/kg, a inkorporirana je u specifični toplinski kapacitet čelika.
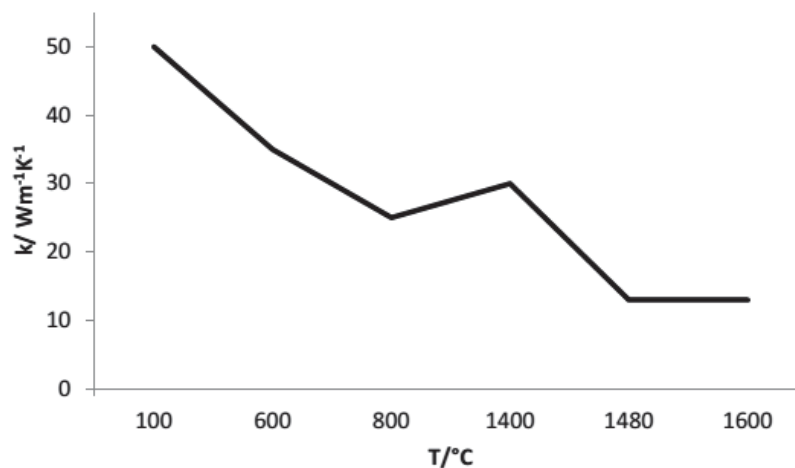
Slika 3. Temperaturne ovisnost toplinske vodljivosti srednje ugljičnog čeličnog lijeva
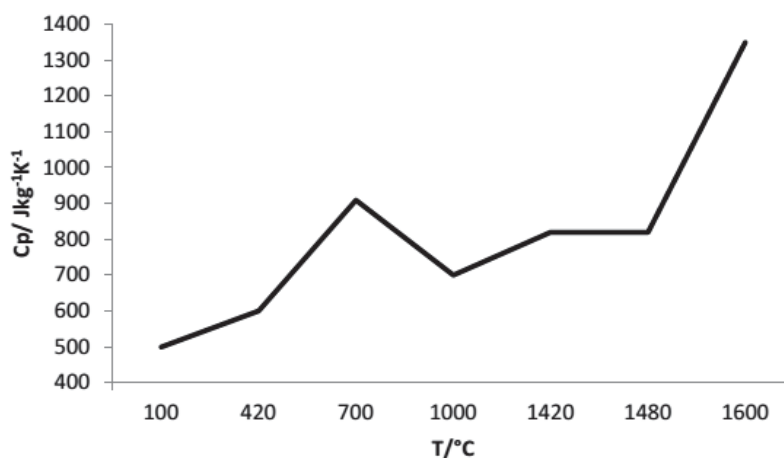
Slika 4. Temperaturna ovisnost specifične topline srednje ugljičnog čeličnog lijeva

Na slikama 5. do 8. prikazana je ovisnost prividne toplinske vodljivosti i specifične topline za cirkonski i olivinski pijesak. Gustoća cirkonskog pijeska iznosi 4400 kg/m^3 , a olivinskog 3200 kg/m^3 .
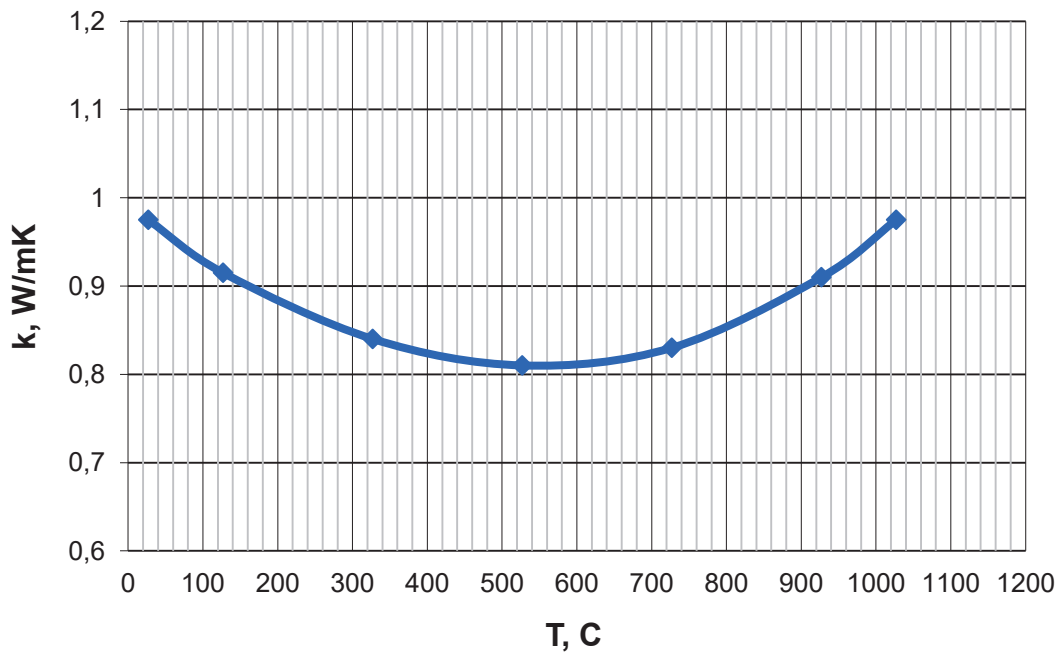
Slika 5. Temperaturna ovisnost toplinske vodljivosti cirkonskog pijeska
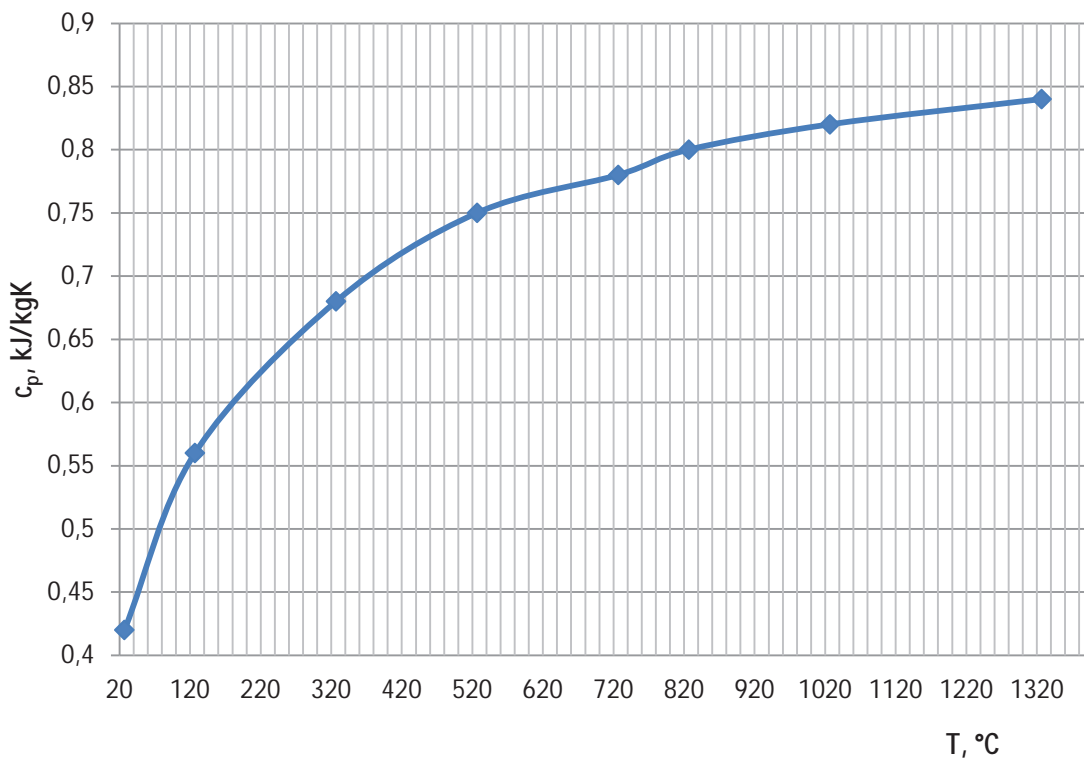
Slika 6. Temperaturna ovisnost specifične topline cirkonskog pijeska
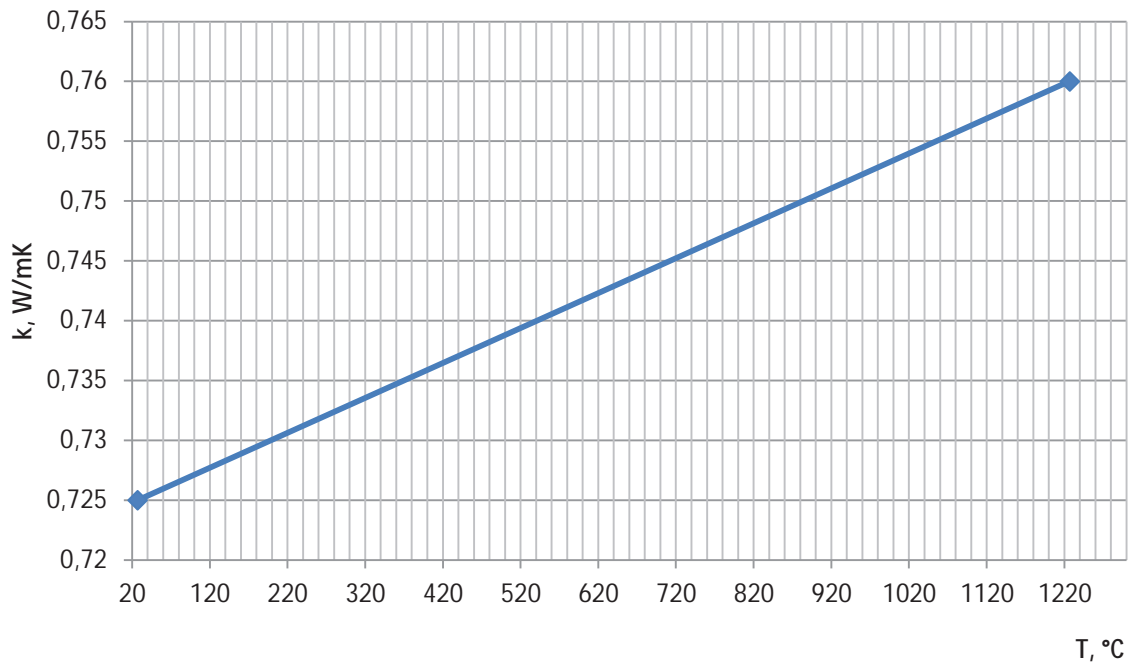
Slika 7. Temperaturna ovisnost toplinske vodljivosti olivinskog pijeska
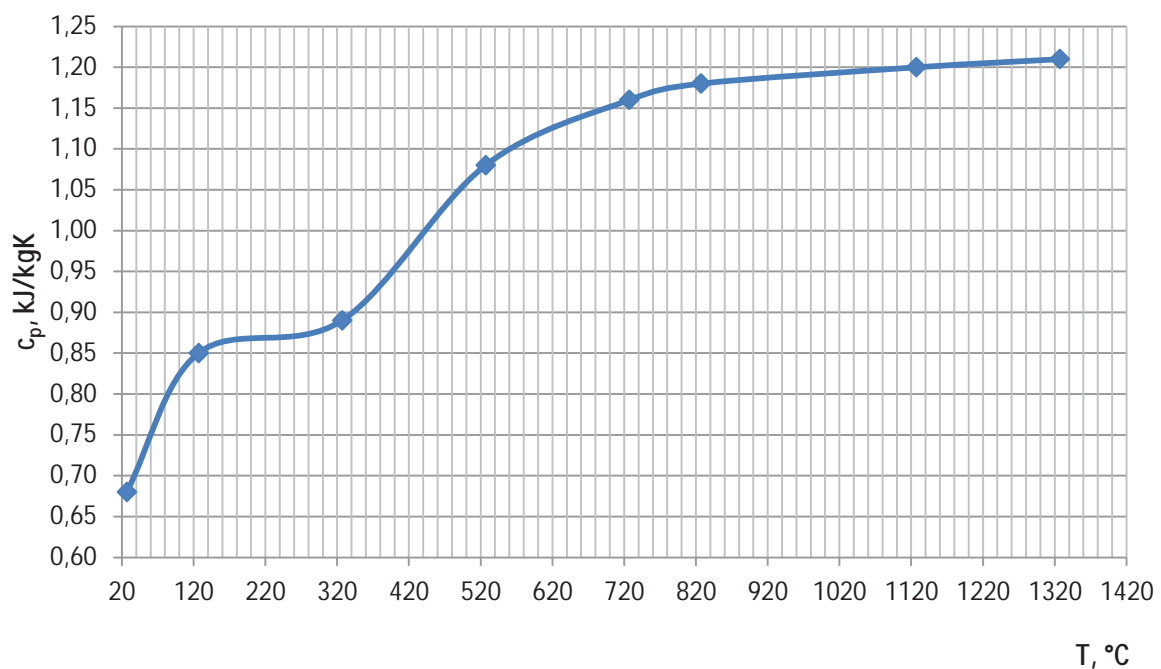
Slika 8. Temperaturna ovisnost specifične topline olivinskog pijeska

IMPLICITNA METODA PROMJENLJIVOG SMJERA (ADI)

Kod ADI metode vremenski interval Δt dijeli se na dva vremenska koraka, od kojih svaki traje $\Delta t/2$. Prostorna derivacija u jednadžbi (1) aproksimira se implicitno u x smjeru i eksplicitno u y smjeru tokom prvog $\Delta t/2$; postupak je obrnut tokom drugog $\Delta t/2$ - eksplicitno u x smjeru i implicitno u y smjeru. Neka je $T_{i,j}^*$ temperatura u točki (i,j) na kraju prve polovine vremenskog koraka, neposredno između t_n i t_{n+1}. Razmotrimo općenitu točku (i,j), koja ne

101

leži na granici kao i na međuplohi kalup/metal. Tokom dvaju sukcesivnih vremenskih koraka, od kojih svaki traje $\Delta t/2$, odgovarajuće ADI aproksimacije jednadžbe (1) su:

$$\delta_x^2 T_{i,j}^* + \delta_y^2 T_{i,j}^n = \frac{1}{a_{i,j,n}} \frac{T_{i,j}^* - T_{i,j}^n}{\Delta t/2} \tag{5}$$

$$\delta_x^2 T_{i,j}^* + \delta_y^2 T_{i,j}^{n+1} = \frac{1}{a_{i,j,n}} \frac{T_{i,j}^{n+1} - T_{i,j}^*}{\Delta t/2} \tag{6}$$

Pri čemu $a_{i,j,n}$ označava temperaturnu vodljivost u točki (i,j) pri temperaturi $T_{i,j}^n$ na početku vremenskog koraka za kalup ili metal. Neka je recipročna vrijednost Fourierove značajke

$$z_{i,j,n} = \frac{(\Delta x)^2}{a_{i,j,n}\Delta t} \tag{7}$$

Odaberemo li pravokutnu mrežu ($\Delta x = \Delta y$), jednadžbe (5) i (6) mogu se pisati kao:

$$-T_{i-1,j}^* + 2(z_{i,j,n} + 1)T_{i,j}^* - T_{i+1,j}^* = T_{i,j-1}^n + 2(z_{i,j,n} - 1)T_{i,j}^n + T_{i,j+1}^n \tag{8}$$

$$-T_{i,j-1}^{n+1} + 2(z_{i,j,n} + 1)T_{i,j}^{n+1} - T_{i,j+1}^{n+1} = T_{i-1,j}^* + 2(z_{i,j,n} - 1)T_{i,j}^* + T_{i+1,j}^* \tag{9}$$

U slučaju vertikalne granične plohe između kalupa i metala dobiju se ADI aproksimacije, i to za prvi $\Delta t/2$:

$$-\frac{2k_k}{k_k+k_m}T_{i-1,j}^* + 2(z_{i,j,n} + 1)T_{i,j}^* - \frac{2k_m}{k_k+k_m}T_{i+1,j}^* = T_{i,j-1}^n + 2(z_{i,j,n} - 1)T_{i,j}^n + T_{i,j+1}^n \tag{10}$$

gdje je:

$$z_{i,j,n} = \frac{c_1}{k_k+k_m}\left(\frac{k_k}{a_k} + \frac{k_m}{a_m}\right) \tag{11}$$

$$c_1 = \frac{(\Delta x)^2}{\Delta t} \tag{12}$$

Za drugi $\Delta t/2$ dobije se:

$$-T_{i,j-1}^{n+1} + 2(z_{i,j,n} + 1)T_{i,j}^{n+1} - T_{i,j+1}^{n+1} = \frac{2k_k}{k_k+k_m}T_{i-1,j}^* + 2(z_{i,j,n} - 1)T_{i,j}^* + \frac{2k_m}{k_k+k_m}T_{i+1,j}^* \tag{13}$$

U slučaju horizontalne granične plohe između kalupa i metala dobiju se slične ADI aproksimacije.

Za plohu koja leži na dijagonali pod kutom 45°C, odgovarajuće ADI aproksimacije su:

Prvi $\Delta t/2$:
$$-T_{l-1,j}^* + (z_{l,j,n} + 1)T_{l,j}^* = T_{l,j-1}^n + (z_{l,j,n} - 1)T_{l,j}^n \tag{14}$$

Drugi $\Delta t/2$:
$$-T_{l,j-1}^{n+1} + (z_{l,j,n} + 1)T_{l,j}^{n+1} = T_{l-1,j}^* + (z_{l,j,n} - 1)T_{l,j}^* \tag{15}$$

Pri čemu je $z_{l,j,n}$ kao u jednadžbi (7).

ADI metoda vodi do sustava linearnih simultanih algebarskih jednadžbi koje imaju tridijagonalni oblik, a za koji postoji posebno efikasan algoritam [6].

Prednosti ADI metode su:

a) Vrlo je efikasna zbog algoritma za brzo rješavanje tridijagonalnog sustava jednadžbi,
b) Bezuvjetno je stabilna i konvergira bez obzira na vrijednost Fourierove značajke,
c) Greška diskretizacije je $O[(\Delta x)^2 + (\Delta t)^2]$, te je prema tome drugog reda s obzirom na aproksimaciju prostora i vremena.

Na temelju danog algoritma može se napisati program u programskom jeziku FORTRAN za osobno računalo. Osnovna karakteristika programa je da se za pohranjivanje temperature koriste dvije matrice. Matrica T koristi se za pohranjivanje temperatura na početku i na kraju cijelog vremenskog koraka, dok se matrica T^* koristi za pohranjivanje temperatura na kraju prvog $\Delta t/2$. Korištenje matrica ponavlja se tokom sukcesivnih vremenskih koraka, pa je na taj način izbjegnuta primjena trostruko indeksiranih matrica. Naravno, temperature treba periodički ispisati kako se ne bi izgubile njihove vrijednosti. Glavni program sastoji se od četiri potprograma i dviju funkcija.

REZULTATI NUMERIČKE SIMULACIJE

U vremenu $t = 0$ kalup i metal su pri početnoj temperaturi 25°C, odnosno 1580°C. Odgovarajuće temperature na graničnoj plohi kalup – metal su 1500°C za srednje ugljični čelik lijevan u cirkonski i olivinski pijesak. Toplina tokom vremena postupno prelazi iz odljevka u kalup. Odljevci progresivno skrućuju u intervalu temperatura od 1482°C do 1427°C.

Točnost simulacije uz pomoć računala je ograničena u nekim aspektima zbog potrebe uvođenja pretpostavki pri opisu procesa lijevanja i skrućivanja odljevaka. Međutim, ta ograničenja nisu tako izražena kao npr. ograničeno poznavanje toplinskih svojstava materijala, osobito kalupne mješavine, te utjecaj granične plohe na mehanizam prijelaza topline.

Ograničavajući je faktor simulacije uz pomoć računala točnost podatak za svojstva čeličnog lijeva, a posebno kalupnog materijala. Toplinska svojstva pijeska funkcija su sastava, sadržaja vlage, metode kalupljenja, tvrdoće i njezine jednolikosti, granulometrijskog sastava, kao i temperature. Iz tog razloga podaci za temperaturnu ovisnost toplinskih svojstava pijeska, naročito toplinske vodljivosti, pokazuju širok raspon rasipanja. Sljedeći ograničavajući faktor je promjenljivost toplinskog toka tokom skrućivanja na granicama odljevaka uslijed stezanja metala i pomicanja stjenke kalupa. Nastajanje zračnog raspora, kao i odgovarajuće smanjenje prijelaza topline čak i kod pješčanih kalupa ograničuje točnost simulacije procesa skrućivanja i hlađenja odljevka.

Na slikama 9. i 10. prikazano je progresivno skrućivanje promatranih odljevaka u dvije vrste kalupnog materijala.
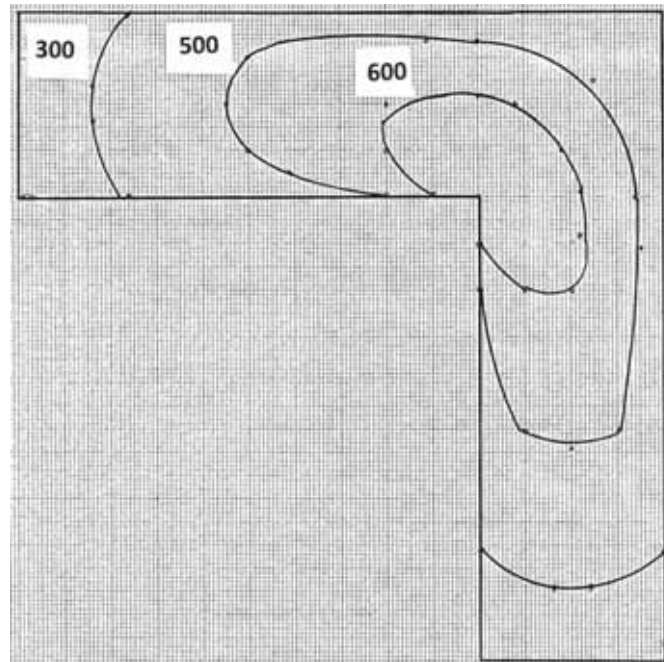
Slika 9. Napredovanje izosolidusa (1427°C) u odljevku od srednje ugljičnog čelika lijevanog u cirkonski pijesak za vremena 300, 500 i 600 s
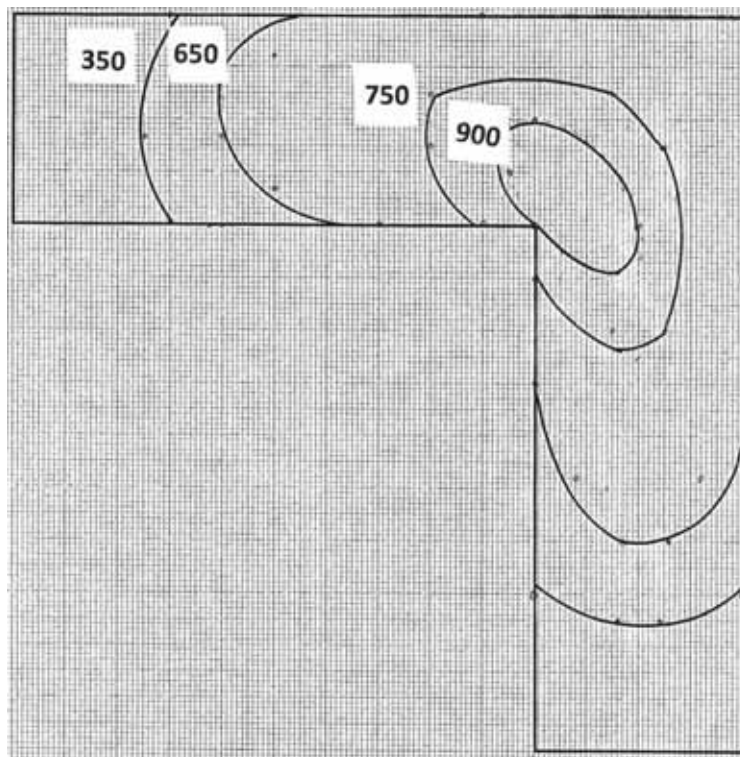
Slika 10. Napredovanje izosolidusa (1427°C) za odljevak od srednje ugljičnog čelika lijevanog u olivinski pijesak za vremena 350, 650,750 i 900 s

Iz slika se uočava da vanjski ugao i ekstremiteti odljevka skrućuju prvi, a toplina se relativno sporo uklanja iz unutarnjeg ugla. Skrućivanje završava blizu unutarnjeg ugla, što predstavlja mjesto moguće pojave defekta u odljevku.

Na temelju predloženog matematičkog modela i numeričke simulacije za vrijeme skrućivanja odljevka od srednje ugljičnog čelika u slučaju lijevanja u cirkonski pijesak dobije se 800 s, a u slučaju lijevanja u olivinski pijesak 1000 s. Prema tome, čelični odljevci lijevani u cirkonski pijesak brže skrućuju nego oni lijevani u olivinski pijesak.

ZAKLJUČAK

U radu je formuliran i istražen matematički model skrućivanja i hlađenja čeličnih odljevaka u pješčanim kalupima koji se temelji na prijelazu topline provođenjem. U model su ugrađeni početni i rubni uvjeti, kao i temperaturno ovisna toplinska svojstva materijala (toplinska vodljivost i specifični toplinski kapacitet), a u intervalu skrućivanja, tj. između likvidusa i solidusa, ugrađena je entalpija skrućivanja. Numerička analiza provedena je korištenjem implicitne metode promjenljivog smjera (engl. ADI), koja je odabrana zbog velike preciznosti pri aproksimaciji prostora i vremena. Naime, metoda je bezuvjetno stabilna, jer konvergira bez obzira na vrijednost Fourierove značajke. Simulacija je provedena za srednje ugljični čelik lijevan u cirkonski i olivinski pijesak. Na temelju pomicanja izosolidusa moguće je vidjeti točke u kojima se javlja defekt (točke koje zadnje skrućuju), u blizini unutarnjeg ugla odljevka. Također je definirano trajanje skrućivanja od 800 s za čelik lijevan u cirkonski pijesak, te 1000 s za čelik lijevan u olivinski pijesak. Dobiveni rezultati omogućuju da se na moderan i znanstveni način vidi kako odabir pojedine vrste kalupnog materijala utječe na tijek skrućivanja i hlađenja odljevka.

LITERATURA

[1] E. R. G. Eckert, R. M. Drake, Analysis of Heat and Mass Transfer, McGraw-Hill Kogakusha, Tokyo, 1972.
[2] V. Grozdanić, V. Novosel-Radović, R. Dmitrović, AFS Transactions, 100(1992), pp. 265-271.
[3] V. Grozdanić, J. Črnko, Železarski zbornik, 25(1991)4, pp. 149-158.
[4] R. D. Phelke, A. Jeyarajan, H. Wada, Summary of Thermal Properties for Casting Alloys and Mold Materials, University of Michigan, Ann Arbor, 1982.
[5] P. R. Sahm, P. N. Hansen, Numerical simulation and modelling of casting and solidification processes for foundry and cast-house, CIATF, Zurich, 1984.
[6] B. Carnahan, H. A. Luther, J. O. Wilkes, Applied Numerical Methods, John Wiley, New York, 1969.

MEASURING OF WAX PROPERTIES FOR SIMULATION INJECTION OF WAX PATTERNS AND THEIR DEFORMATION PREDICTION

Aleš Herman, Ondřej Vrátný, Bohumír Bednář

Czech Technical University in Prague Faculty of Mechanical Engineering, Department of Manufacturing Technology, Prague, Czech Republic

Abstract

The paper deals with problem of measuring wax input data for process simulation of injection wax pattern for investment casting technology. The process of material data acquisition (heat conductivity, viscosity and modulus of elasticity) for 2 types of wax mixtures, filled by micro granules of polystyrene, is described. The output data of wax material properties are used as input for wax data to database of simulation software for simulation of polymers injection.

Keywords: wax properties, investment casting, numeric simulation SW

*Corresponding author (e-mail address): ales.herman@fs.cvut.cz

INTRODUCTION

These days there exist a requirement from manufacturing companies to prepare production by using numerical simulation software. These programs are very useful tools and they can effectively save costs associated with the optimization of production processes. However companies using these software must own certainly knowledge about principle of operation of simulations. Wrong input data can lead to an incorrect understanding of the results. The simulation works without any problem but the results do not correlate with reality – and this is very dangerous.

Waxes used in the investment casting industry are used to manufacture complex patterns with tightly specified dimensions. They are complex blend of various additives such as resins, fillers, microcrystalline waxes, paraffin waxes, and other additives. All the above ingredients that create final wax blend play a role in determining the resulting properties. It is important that the manufacturer of the wax fully characterizes the properties. These properties will be

useful in the recommendation or selection of a wax. Also the mechanical properties of casting waxes play a vital part in the investment casting process. Patterns must be sufficiently tough to resist breakage during assembly and must not distort if dimensional tolerances are to be maintained. Equally, runner bars must not fracture or sag when assemblies are handled by robots on automated dipping lines.

A lot of information from suppliers of wax materials are limited in the thermo-physical and mechanical property definitions. It usually contains information on the melting of the wax and some basic data related to the fluidity of the wax. However, this data is not detailed enough to provide accurate simulation results and fully characterize the material. Additionally, mechanical information is not typically provided to characterize the viscoelastic nature of wax. This paper will detail and discuss some of the various properties that are evaluated on wax blend [1,2,5,6].

Viscoelasticity

When stress is applied on some kind of materials (e.g. waxes, polymers, asphalts) and they are deformed, they exhibit elastic and viscous characteristic at the same time. This is called viscoelasticity. A viscoelastic material does not meet the characteristics of elastic and viscous materials. Considering harmonic stress, certain amount of the input mechanical energy is used during following unload of material. The rest of energy is dissipated, it changes into thermal energy. The amount of energy, which is changed from mechanical into thermal is proportional to the area under the hysteresis curve. This curve is a dependence between stress and strain and because this curve has not linear character, we cannot use Hooke´s law [3-6].
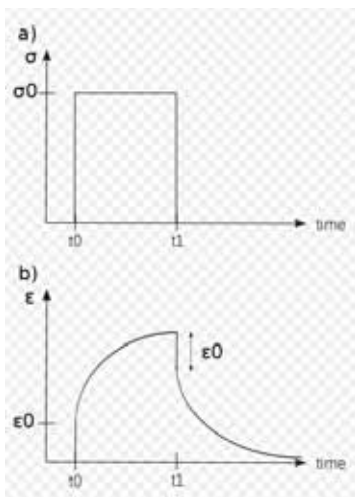
Figure 1. Viscoelastic creep [3]   Figure 2. Dependence stress and strain on time [3]
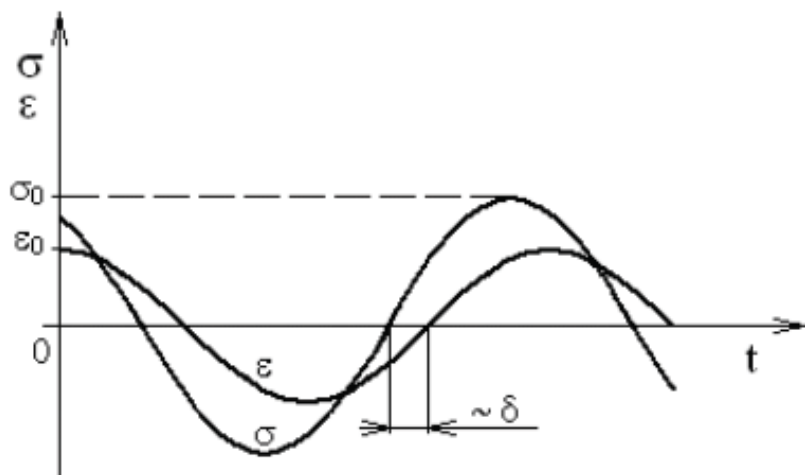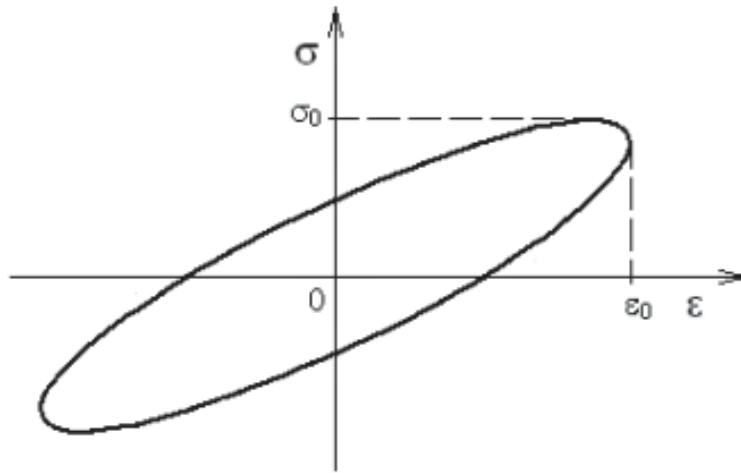
Figure 3. Stress-Strain curve for viscoelastic material [3]

For viscoelasticity model to simulation software is needed to define next material properties [5,6]:

- ➢ Elastic modulus
- ➢ Thermal conductivity as function of temperature
- ➢ Viscosity as function of temperature
- ➢ Specific heat as function of temperature
- ➢ Enthalpy as function of temperature
- ➢ PVT diagram

MATERIALS AND METHODS

In this section, there will be described two tested wax materials and methods, which lead to obtain required wax properties. We performed experiments for two waxes, green wax – Remet virgin wax (HYFILL-478) and brown wax – Remet recycled wax (B-478).
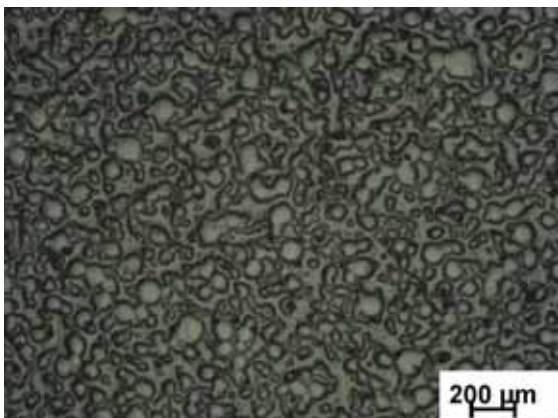
Figure 4. Structure of brown wax

Figure 5. Structure of green wax

As it is seen from Figure 4 and 5 the structure of both are very similar. Waxes used in investment casting industry are complex blend of various additives such as resins, fillers,

microcrystalline waxes, paraffin waxes, and other additives. In the figures we can see polystyrene as a filler in wax matrix. Filler is used especially because of dimensional stability. At the first glance we may say, that the green wax has a bit greater difference in the size of filler. On the other hand, the polystyrene in the brown wax is similar size.

Measurement of elastic modulus

In the pictures, there is shown which method was needed to obtain elastic modulus and which kind of samples we used. The principal is to find out elastic modulus by bending samples using three points. For this purpose, we prepared several samples with square and round cross-section.

A bit problem was to find out where consider the right part of curve which describe the elastic area. In the end, we decided to evaluate stress-strain dependences for each sample according to the standard ČSN EN ISO 178. The procedure is indicated in Figure 8 and 9.
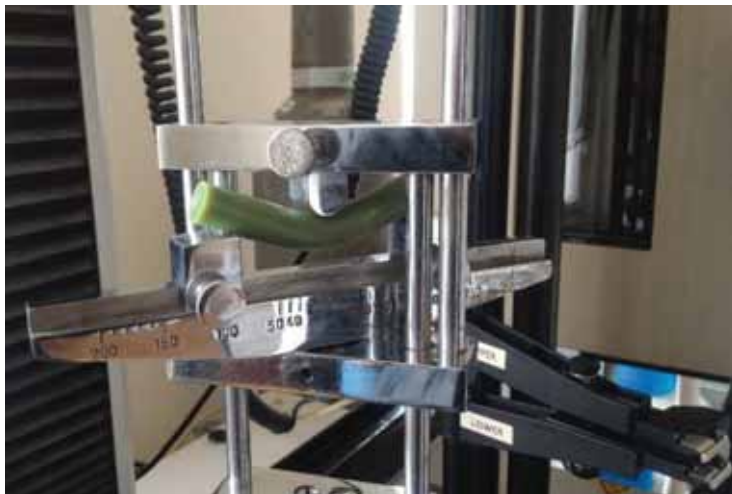
Figure 6. Bending of samples   Figure 7. Samples for measurement
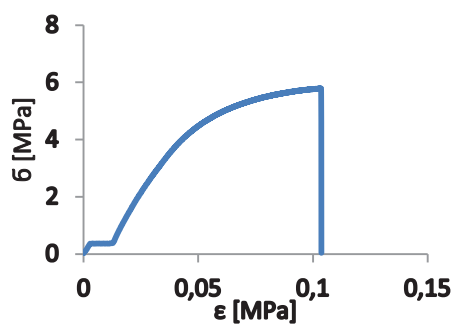
Figure 8. Ideal stress-strain dependence
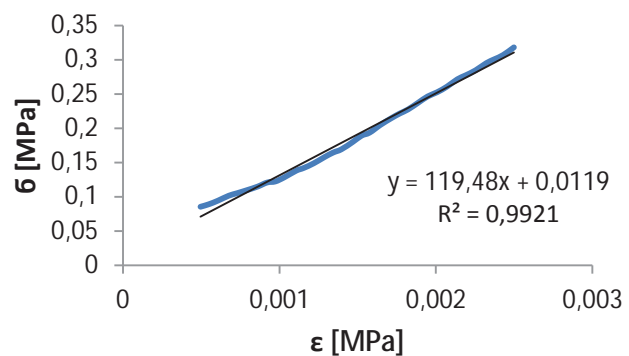
Figure 9. The area of measurement according to ČSN EN ISO 178

Measurement of thermal conductivity

The task was to measure thermal conductivity of our samples of two different waxes (brown and green) for two temperature level. Standard method of heated wire was used. This apparatus ordinarily works till 50°C. Five samples made of green wax and 12 samples of brown wax were prepared.
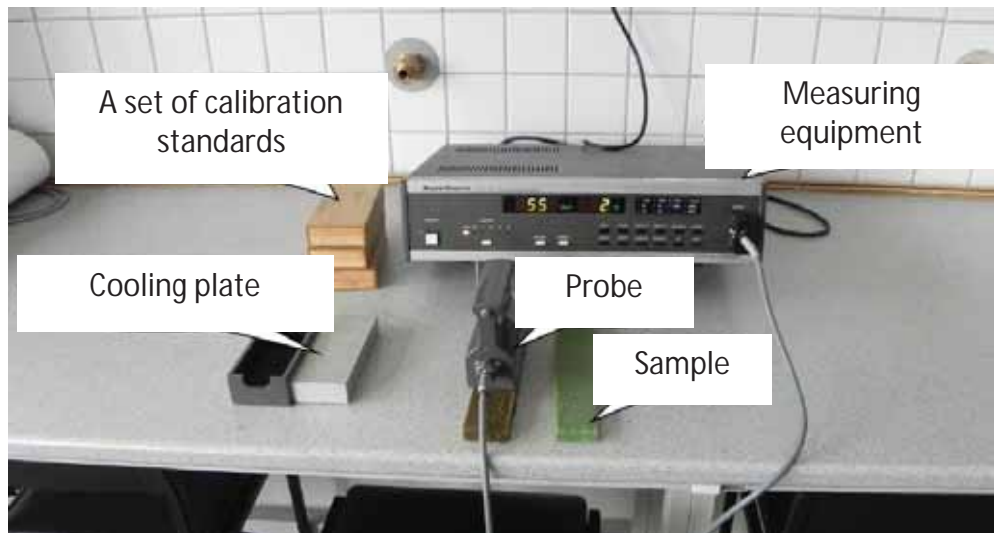
Figure 10. The measuring assembly for thermal conductivity

Measurement of viscosity

Again, we were testing both wax materials (green and brown wax). For measurement, there was used rheometer Rheotec RC 20 with system of parallel plates P25 and ME-CP/PP with the bottom heated plate by external thermostat Julabo F 25 EH (the upper plate is not heated). The distance between both surfaces was in the range 0.5 to 0.8 mm.

Measurement of specific heat

Specific heat capacity was measured by measuring the total heat flux, which has been integrated and the enthalpy determined. For this measurement, a differential scanning calorimeter DSC Diamond (Perkin Elmer). Wax samples were first sliced with a knife into small pieces in a way to fit into the capsule. The sample was then inserted into a measurement aluminium capsule (nominal volume 40 ml) and closed (sample weight was about 10 to 20 mg). Before the measurement, the sample was heated in the apparatus at 90°C with a holding time of about 20 seconds to melt the sample in the capsule to achieve good contact of the sample with the wall of the capsule. Following measurement started at 2°C and continued to 100°C with a holding time of 1 minute at initial and a final temperature. The heating rate was about 10°C/minute. This procedure was repeated for each type of wax 5 times.

RESULTS AND DISCUSSION

Elastic modulus

As it is obvious in the Table 1, there was prepared overall 40 samples (10x brown prisms, 10x brown cylinders, 10x green prisms, 10x green cylinders).

Table 1. Results of measurement of elastic modulus

Modulus of elasticity [MPa]				
	BROWN PRISM	BROWN CYLINDER	GREEN PRISM	GREEN CYLINDER
eps %	0.05-0.25	0.05-0.25	0.05-0.25	0.05-0.25
	103.6	90.0	116.3	**112.2**
	93.2	20.6	83.9	**90.2**
	95.9	98.6	111.1	**92.2**
	91.4	106.1	109.0	110.5
	109.6	6,4	113.7	93.1
	126.8	108.9	111.1	110.4
	110.9	14.0	101.2	98.6
	102.5	100.3	96.9	105.6
	70.8	110.2	110.8	96.6
	75.6	75.7	113.7	17.4
Average	98.0	79.3	106.8	92.7
Median	96.965	88.94	109.9	94.85

Viscosity

First tested sample was made of green wax and the measurement was done at the temperature of 70°C. Immediately was found out, that wax exhibits rheological behaviour, that can be described by Ostwald-de Waele model

$$\tau = K.\gamma^n \tag{1}$$

The value of flow index was close to 1, what leads to apply linear step when changing the shear deformation rate by each measurement of values of share rate. The measurement was several times repeated at the temperature of 70°C (72°C). Then was done the measurement for lower temperatures and soon after the measurement for samples made of brown wax. In following graphs you can compare obtained data.
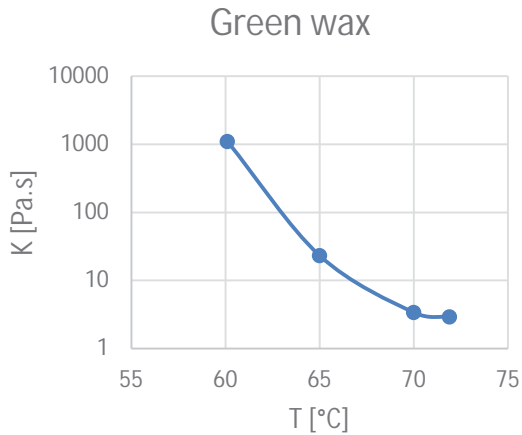
Figure 11. Dependence of Coefficient of consistency on temperature for green wax
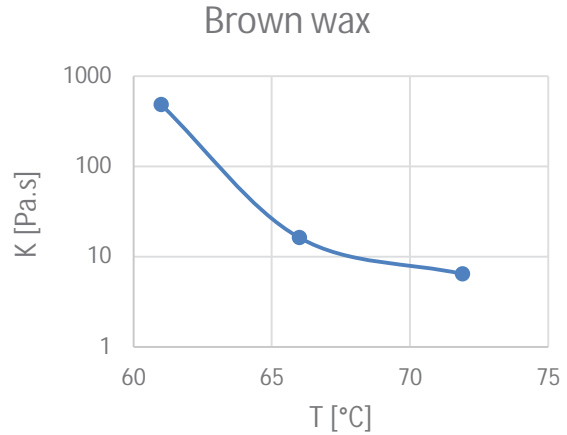
Figure 12. Dependence of Coefficient of consistency on temperature for brown wax

Thermal conductivity

Measurement of thermal conductivity for two temperature level of prepared samples was successfully done. Conclusion is that in the chosen temperature range is not able to statistically validate dependence between thermal conductivity and temperature.

Table 2. Results of measurement of thermal conductivity at different temperatures

Sample	Temperature of samples [°C]	Thermal conductivity [W.m^{-1}.K^{-1}]	Standard deviation
Remet virgin Hyfill-478 (green)	22	0.1858	0.0037
	39	0.1889	0.0069
Remet recycled B-478 (brown)	22	0.1935	0.0033
	39	0.1951	0.0062

Specific heat

In the Figures 13 and 14 there is a dependence of specific heat on temperature.
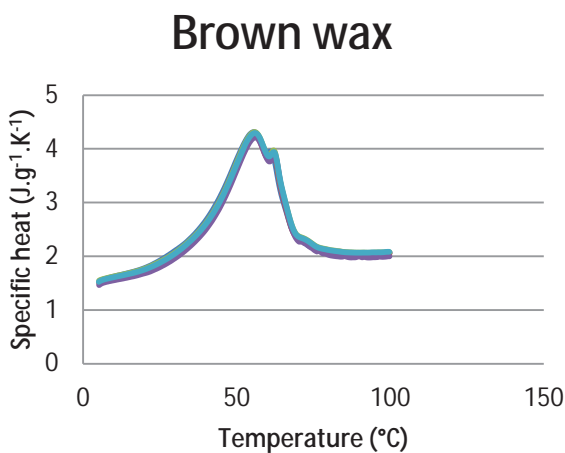
Figure 13. Dependence of Specific heat on temperature for brown wax
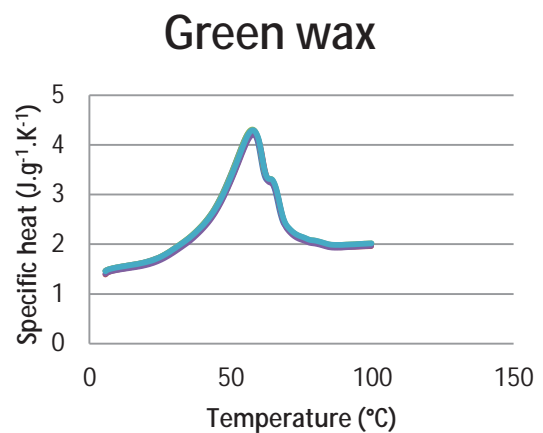
Figure 14. Dependence of Specific heat on temperature for green wax

We may say that the graphs of functions are very similar.

THE CONCEPTUAL DESIGN FOR PVT DIAGRAM TEST
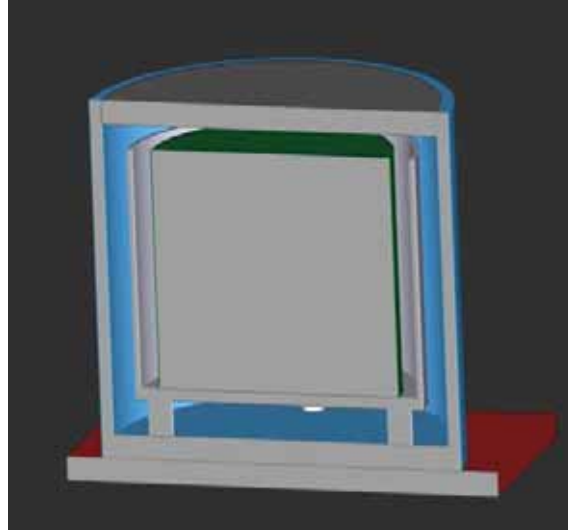
Figure 15. The suggested apparatus for measurement of PVT

The conceptual design for PVT diagram is based on small change of volume. The prepared experiment consists of heating plate, glass beaker, glass bowl and floating cover. We use the exact volume of wax sample and water. We plan to measure the movement of cover in Z axis by a gauge with the resolution of 0.1 μm. Because of the change of gauge scale, we are able to calculate the dependence volume change on temperature for atmospherically pressure. The temperature in wax sample will be checked by thermocouple.

CONCLUSIONS

This paper described the problems of obtaining data on composite materials for making wax models, which are used as a matrix mixture of technical wax and wax filler granules made of polystyrene. For simulation of injection wax models, their behaviour during deformation is needed to expand the database of properties of these moulded materials. Given the fact that the suppliers of these waxes are limited and inaccurate in data information, we had to make the findings of the data of our experiments.

Due to the number of experiments and their statistical evaluation we can say that the data show a large coefficient of reliability. The simulation of the behaviour of viscoelastic model gives an accurate picture of the behaviour of wax mixtures from the perspective of deformations.

REFERENCES

[1] Remet, Wax characterisation [online]. [cit. 2017-04-17]. Accessible on internet: http://www.remet.com/uk/technicalpaper/wax-characterisation/

[2] Remet, The mechanical properties of investment casting waxes [online]. [cit. 2017-04-17]. Accessible on internet: Remet, Wax characterisation [online]. [cit. 2017-04-17]. Accessible on internet: http://www.remet.com/uk/technicalpaper/wax-characterisation/

[3] Viskoelasticita matariálů [online]. [cit. 2017-04-17]. Accessible on internet: http://ufmi.ft.utb.cz/texty/env_fyzika/EF_06.pdf

[4] S. Shiromoto, Y. Masutani, M. Tsutsubuchi, Y. Togawa, T. Kajiwara, The effect of viscoelasticity on the extrusion drawing in film-casting process, Rheologica Acta, 49(2010)7, pp. 757-767 [cit. 2017-04-17]. DOI: 10.1007/s00397-010-0454-9. ISSN 0035-4511. Accessible on Internet: http://link.springer.com/10.1007/s00397-010-0454-9

[5] R. Biernacki, R. Haratym, A. Bałkowiec, P. Wawulska-Marek, H. Matysiak, J. Zdunek, K. J. Kurzydłowski, Evaluation of Physical Properties of Wax Mixtures Obtained From Recycling of Patterns Used in Precision Casting, Archives of Metallurgy and Materials: The Journal of Institute of Metallurgy and Materials Science and Commitee on Metallurgy of Polish Academy of Sciences 2015, 60(2015)1, 5 [cit. 2017-04-17]. Accessible on Internet: http://www.imim.pl/files/archiwum/Vol1_2015/56.pdf

[6] A. S. Sabau, S. Viswanathan, Material properties for predicting wax pattern dimensions in investment casting, Materials Science and Engineering A, 362(2003)1-2, pp. 125-134 [cit. 2017-04-17]. DOI: 10.1016/S0921-5093(03)00569-0. ISSN 09215093. Accessible on Internet:
http://linkinghub.elsevier.com/retrieve/pii/S0921509303005690

INVESTIGATION OF DEFORMATION BY
DIGITAL IMAGE CORRELATION

Ivan Jandrlić[1], Stoja Rešković[1], Tin Brlić[1], Ladislav Lazić[1], Tamara Aleksandrov Fabijanić[2]

[1]University of Zagreb Faculty of Metallurgy, Sisak, Croatia
[2]University of Zagreb Faculty of Mechanical Engineering and Naval Architecture,
Zagreb, Croatia

Abstract

Conventional methods for investigation of metallic materials during elastic and plastic deformation cannot provide the full insight into materials behaviour during deformation. Lately new methods for investigation of deformation are being intensively used. Digital Image Correlation (DIC) has proven to be very suitable method for exploring of deformation zone. It is a non-contact method that allows detailed analysis of the deformation zone. Along the qualitative values, this method provides also the quantitative values of deformation that can be applied for construction and/or validation of various mathematical models. By analysis of the actual deformation, it is possible to obtain so-called deformation maps, which clearly illustrate the amounts of deformation in different parts of the deformation zone. In order to test the method of digital image correlation, static tensile testing was conducted on samples from low carbon steel. During static tensile testing surface of samples were continuously recorded with a digital camera. Subsequent analysis of acquired deformation images was done using digital image correlation, in order to determine deformation maps in deformation zone. Results of digital image correlation were compared with the results of the static tensile tests.

INTRODUCTION

Significant part of metallurgical production of semi-finished and finished products refers to the cold plastic deformation, using various technological processes of plastic deformation. Depending on type of technological process and the alloy which is being deformed, there is a different material flow during plastic deformation. Research of the material plastic flow has always been a challenge for researchers [1-3]. By using the conventional methods of research it was not possible to obtain all informations on processes that are taking place in

deformation zone. Method of visioplasticity is commonly used for investigation of material plastic flow [1,2]. These methods require a special preparation of samples and detailed analysis of the obtained measurement results. Another very common method of determining strain in deformation zone includes the usage of so cold strain gages [3,4]. Strain gages have shown to be sensitive on the temperature changes and are not suitable for accurate for strain measurement in case of large amounts of deformation [4].

Developments in technology led to development of new methods for investigation of elastic and plastic deformations [4-7]. Digital image correlation (DIC) is one of them and today it is the most commonly used method of research of strain during deformation. It has been proven to be a very useful method for investigation of deformation zone during cold plastic deformation. This is no-contact method by which it is possible to observe the material flow over the whole deformation zone during the entire period of deformation.

Method is based on monitoring of changes on surface of samples which are deformed, precisely on the measuring of changes in position of markers that were applied on samples before the deformation. Due to the deformation there is a change in the markers location in relation to their initial position [6-8]. Therefore, it is of great importance that before the testing of the samples there is adequate sample preparation, in the form of the applying the stochastic markers of different shape and size on the samples surface. Recording of changes in position of markers during deformation is performed by using a high resolution digital video camera or photo camera. Displacements of markers, due to achieved deformation, are measured by using analysis software package that compares pictures of samples taken before and after deformation. Subsequently, by using appropriate mathematical algorithms the achieved strain is determined from measured displacements [7,8]. Digital image correlation has found its application in various laboratory studies, due to its simplicity in application and possibilities of rapid determination of strains in the entire deformation zone, [4,6-10]. By comparing results of measured strains obtained using digital image correlation and strain gages, it is shown that digital image correlation can determine the reliable values of deformation, and unlike strain gages, digital image correlation method is not sensitive to temperature changes [9]. It can be measured from very small up to the significantly large amount of deformation, with high accuracy of readings [4,9].

Method of digital image correlation, along with deformation values, has the ability of displaying deformation maps [9,10]. As example is research in which researchers investigated the absence of neck during static tensile testing, and by using deformation maps obtained with DIC they were able to link it with continuous hardening of steel [10]. Using stereo cameras for recording of deformation, it is possible carry out 3D correlation and thus to determine the deformation of irregular shaped body's and measure deformation on side surfaces of body, for example when testing deformation of welded pipe [9]. Its application for strain measurement digital image correlation has found even for determination of residual stress, as measured from the displacement it can be determined residual stresses which occur in material during fatigue [11,12]. In this way it not necessary to perform classical methods of measuring the crack progression, that often cannot be measured. In this way DIC becomes indispensable when researches are done in order to develop or validate various models of plastic flow for metals and alloys [13,14].

The aim of this study is to determine the deformation zone on samples during the static tensile tests of steel by using digital image correlation. Results of digital image correlation

116

and static tensile experiments will be compared in the order to determine the material flow in deformation zone during necking of samples.

MATERIALS AND METHODS

Studies were conducted on samples of rectangular cross section. Samples were taken from the hot rolled low-carbon steel strip. Since a thin layer of oxide was present, that forms during hot rolling of strip, and who peels off samples during deformation, samples were first cleaned. After cleaning, the samples had a shiny surface. As for digital image correlation it needs to be a good contrast between the background and the random markers, a thin layer of black coating was first applied on samples. After that random markers were sprayed with white paint.

Deformation of samples was carried out by static tensile stretching on tensile testing machine Zwick 50kN, during which the force - elongation diagrams were recorded. Samples were stretch until fracturing. The whole process of sample deformation was recorded with a digital camera. Used digital camera has a CCD sensor and 25 frames per second rate of taking pictures. Images of samples deformation were taken from recorded videos after the end of the experiment. Afterwards they were analyzed using MatchID 2D software for digital image correlation. The deformation maps were determined from analysis, and strains were measured. In the results and discussion is given the comparison of results obtained by digital image correlation and static tensile testing.

RESULTS AND DISCUSSION

Samples deformation recorded during the static tensile testing was analyzed using digital image correlation. Deformation zone was analyzed during the whole period of tensile testing, Figure 1.
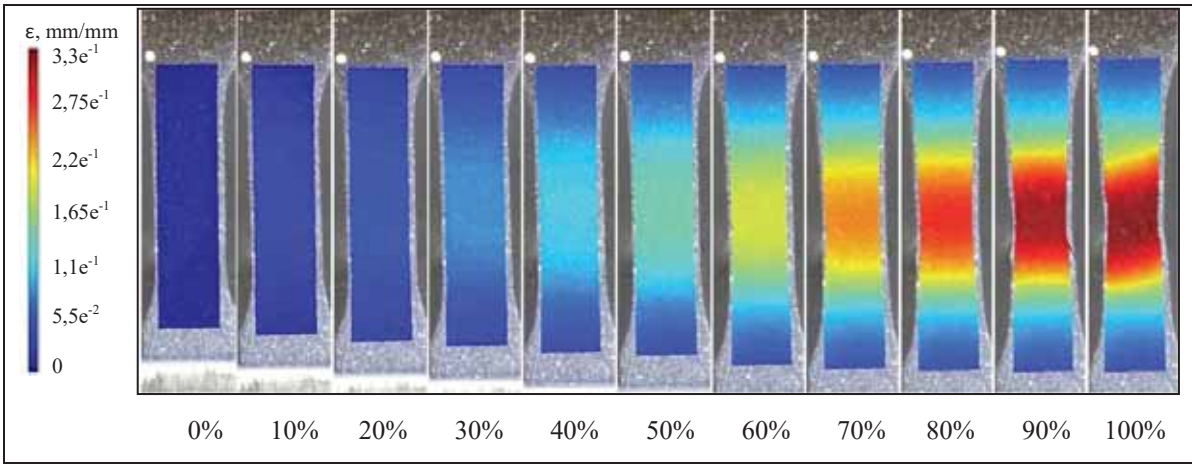
Figure 1. Deformation zone for every 10% of total strain of tested sample

Different values of achieved deformation are presented on Figure 1 with the change in the colour intensity. In order to show changes in samples deformation zone during the whole

period of tensile stretching, pictures were taken for every 10% of total strain. It can be seen that after reaching the proportionality limit deformation of samples starts at the centre, Figure 1. Recorded force – elongation diagrams during tensile testing show that tested steel does not have expressed transition from elastic into plastic deformation, Figure 2 a) (point 1). At the same time on deformation diagram obtained by DIC on can see the sharp increase in the deformation change, Figure 2 b) (point 1). This confirms that by the method of digital image correlation it is possible to determine the beginning of plastic flow even for metals that do not have a clearly expressed proportionality limit.
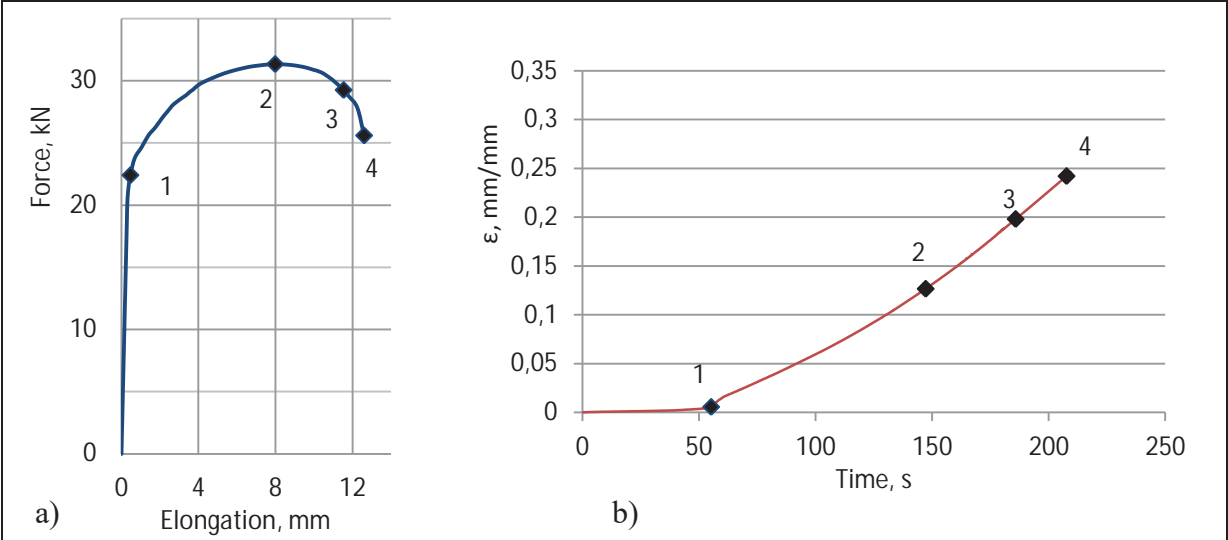
Figure 2. Comparison of test results:
a) Force – elongation diagram
b) Diagram of deformation changes during the experiment

Upon reaching the proportionality limit, results of digital image correlation show a continuous increase of deformation of the tested specimen, Figure 2 b). Results of tensile test during this period show continuous hardening of steel, Figure 2 a). At the point of reaching the tensile strength it comes to the occurrence of necking, and Figure 2 a) (point 2). The view of the deformation zone during the necking and up until fracturing of samples was observed by digital image correlation, and the recordings are shown on Figure 3.
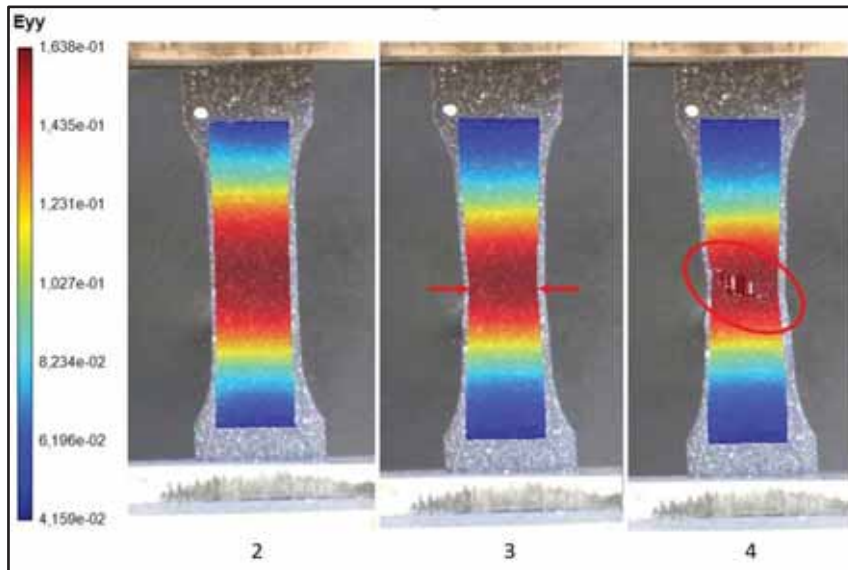
Figure 3. Localization of deformation during necking

From recorded deformation maps using DIC it can be seen that after forming of neck on samples further deformation takes place in that narrow area of sample, Figure 3 (point 2). This results in a significant elongation of sample in that area, along with the simultaneous occurrence of higher contractions of side-walls to the centre of sample, as shown by the arrows in Figure 3 (Section 3) and expressed with darker colour.

With the further deformation this becomes more expressed, and one can predict the place of samples fracture before the fracture occurs, Figure 3 (point 4). Because the significant deformation and contraction in the narrow part of the sample, and the appearance of reduction in the samples thickness there is a loss of correlation in this narrow area, Figure 4 (point 4). In this way it is possible to predict the location of crack formation and predict the place of fracture of samples during static tensile testing.

CONCLUSIONS

Conducted studies of the deformation zone confirm that by using digital image correlation method, one can clearly follow the development of the deformation zone. It was also confirmed that with this method is easy to determine the beginning of plastic flow of steels, even if one does not have a pronounced transition from elastic to plastic deformation on force - elongation diagram.

Results indicate that after necking of samples, deformation measured on whole gauge length show continuous increase. From deformation maps generated by digital image correlation it is possible to see that after necking further deformation takes place in a narrow area of the sample, that is only in the neck area. Thereby the rest of the sample is not deformed, and deformation zone is concentrated in the narrow neck area. The same is accompanied by a significant amount of contraction and due to that it may come to loss of correlation before the fracture.

REFERENCES

[1] A. Shabaik, E. G. Thomsen, Investigation of the application of visioplasticity methods of analysis to metal deformation processing, Final Report prepared for the U. S. Navy, Bureau of Naval Weapons, 1967.

[2] L. Gusel, R. Rudolf, B. Kosec, Analysis of a strain rate field in cold formed material using the visioplasticity method, Metallurgy 48(2009)2, pp. 103-107.

[3] K. Hoffmann, An introduction to measurements using strain gages, Hottinger Baldwin Messtechnik GmbH 1989, Darmstadt, Accessible on Internet: http://www.kk-group.ru/help/Strain_Gauge_Measurements_Book_2012_01.pdf, date: August 20th 2014.

[4] H. Lu, P. D. Cary Deformation measurements by digital image correlation: implementation of a second-order displacement gradient, Experimental Mechanics, 40(2000)4, pp. 393-400.

[5] Digital Image Correlation: Overview of Principles and Software, University of South Carolina, Correlated Solutions, Inc., Accessible on Internet: www.correlatedsolutions.com/digital-image-correlation, date: August 25th 2014.

[6] I. Jandrlić., The stress distribution in the deformation zone of niobium microalloyed steel, doctoral thesis, University of Zagreb Faculty of Metallurgy, 2015.

[7] P. Lava, Practical considerations in DIC measurements, DIC course, Cambridge, UK, 1st July, 2014.

[8] Shun-Fa Hwang, Yi-Jie Ho, Wei-Jie Wu, Deformation measurement by a digital image correlation with a hybrid genetic algorithm, Proceedings of the XIth International Congress and Exposition June 2-5, 2008 Orlando, Florida USA.

[9] M. De Strycker, P. Lava, W. Van Paepegem, L. Schueremans, D. Debruyne, Measuring welding deformations with the Digital Image Correlation technique Welding Journal, 90(2011)6, pp. 107-112.

[10] M. Eskandari, A. Zarei-Hanzaki, M. Yadegari, N. Soltani, A. Asghari, In situ identification of elastic-plastic strain distribution in a microalloyed transformation induced plasticity steel using digital image correlation, Optics and Lasers in Engineering, 54(2014), pp. 79-87.

[11] D. Nowell, O. F. P de Matos, Application of digital image correlation to the investigation of crack closure following overloads, Procedia Engineering, 2(2010)1, pp. 1035-1043.

[12] Y. Xu, R. Bao, Residual stress determination in friction stir butt welded joints using a digital image correlation-aided slitting technique, Chinese Journal of Aeronautics, Accessible on internet: http://doi.org/10.1016/j.cja.2016.11.003, date: December 21st 2016.

[13] R. Kopp, C. Wiedner, E. El-Magd, J. Gebhard, Comparison between visioplasticity measurements and finite element computations for tensile tests on cold rolled perforated ferritic chromium steel P92, Computational Materials Science, 31(2004), pp. 439-447.

[14] P. Lava, S. Coppieters, R. Van Hecke, P. Van Houtte and D. Debruyne, Digital Image Correlation in the classroom: determining stress concentration factors with webcams, Accessible on Internet: http://www.matchid.org/pascal/Articles/plava_classroomfinal2.pdf, date: May 25th 2015.

Acknowledgements

ADVANCE USAGE OF NUMERICAL SIMULATIONS IN FOUNDRY

Sebastjan Kastelic[1,2]**, Almir Mahmutović**[1]**, Mitja Petrič**[2]**, Primož Mrvar**[2]

[1]TC Livarstvo d.o.o., Ljubljana, Slovenia
[2]University of Ljubljana Faculty of Natural Sciences and Engineering,
Department of Materials and Metallurgy, Ljubljana, Slovenia

<u>Oral presentation</u>
Professional paper

Abstract

In foundry, the numerical simulation as a helping tool to foundrymen and technologist is indispensable. In some foundries, the work without the use of numerical simulation is unthinkable. Foundrymen use numerical simulation for fast evaluation of the casting complexity to prepare fast and accurate offer. Also, they use the calculations to develop best foundry technology possible base on their resources for new castings, they optimize the foundry technology for the castings that they have problems with. With the mass usage of software for numerical simulations of foundry processes the development of these software rapidly expanded. Software development follows the foundry demands to cover all the new technologies to be able to cover these new technologies in simulations. ProCAST software covers all the foundry technologies and most of the special variants like local squeezing or jet cooling in HPDC. With proper module, also rheocasting is possible to simulate.

In the article, some of these special modules or variants of foundry technology will be presented as an example on a real case.

Keywords: *numerical simulations, ProCAST, HPDC, investment casting, spin casting, material database*

*Corresponding author (e-mail address): sebastjan.kastelic@omm.ntf.uni-lj.si

INTRODUCTION

Using numerical simulations for some foundries is an imperative in nowadays. Some foundries that are just starting to use numerical simulations realize that the benefits from using numerical simulations is not a competitor's advantage but it is a must to produce quality parts for a reasonable price. To cover all foundry technologies software producers

must be in constant development and cover all new features to stay in touch with industry demands. Software that covers all the foundry technologies and most of the special variants is ProCAST. ProCAST, based on Finite Element technology, in addition to the basics results like gas and shrinkage porosity, flow analysis, temperature field in the casting and in mold, is able to predict deformations and residual stresses. Software covers all the basic foundry technologies like gravity casting in unique and permanent mold, low pressure die casting, high pressure die casting and also more specific processes like investment casting, semi-solid modeling, core blowing, centrifugal casting, lost foam and the continuous casting process. Useful for all castable alloys, the metal casting simulation software helps to address defect detection, residual stresses, part distortion, microstructure and mechanical properties prediction.

NUMERICAL SIMULATIONS STANDARD USAGE

Standard using of numerical simulations in foundry is to help produce quality parts. With the help of analyzing numerical results during development phase of foundry technology for a new part we can get most benefits from numerical simulation. Using results from numerical simulations we can plan and avoid possible problems of casting productions and quality of casting. The standard usage is based on the analysis of the melt flow using different gating system including, temperature field analysis and porosity prediction. Example of casting quality optimization based on changing ingate system to reduce porosity is presented on Figure 1 and 2 [1].
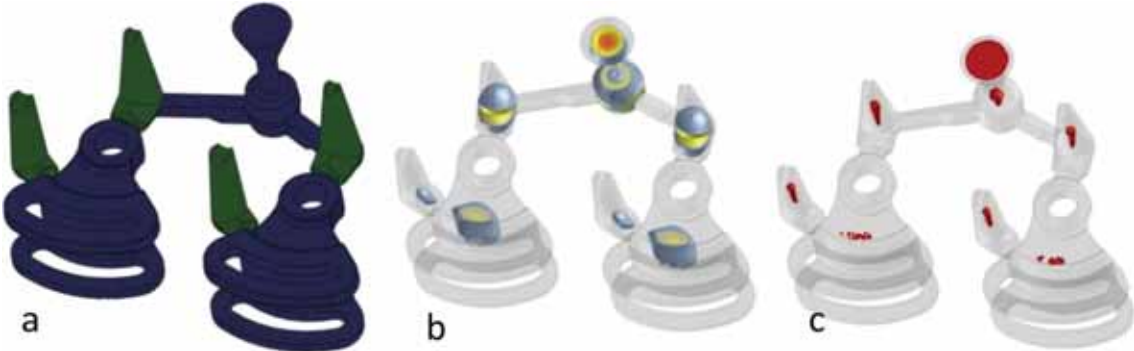
Figure 1. Geometry before optimization: a) geometry, b) last solidification area, c) shrinkage porosity
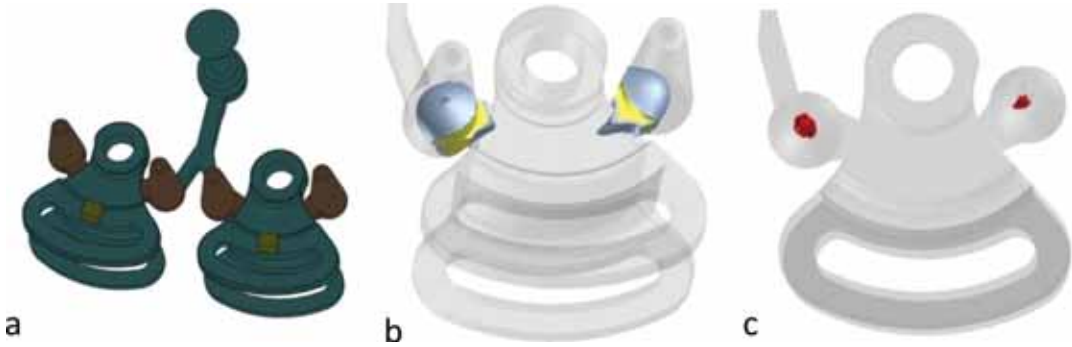
Figure 2. Geometry after optimization: a) geometry, b) last solidification area, c) shrinkage porosity

Basic usage in HPDC also includes the optimization of piston movement during the shot in the casting chamber. With optimal parameters we can avoid air entrapment in the casting chamber due to inaccurate piston movement. Optimal piston movement and start of the second phase can be determine. On Figure 3 it is shown the influence of piston velocity on the melt wave and air entrapment in the casting chamber. On Figure 3c is presented optimal length and time for start of the second phase – shoat [2].
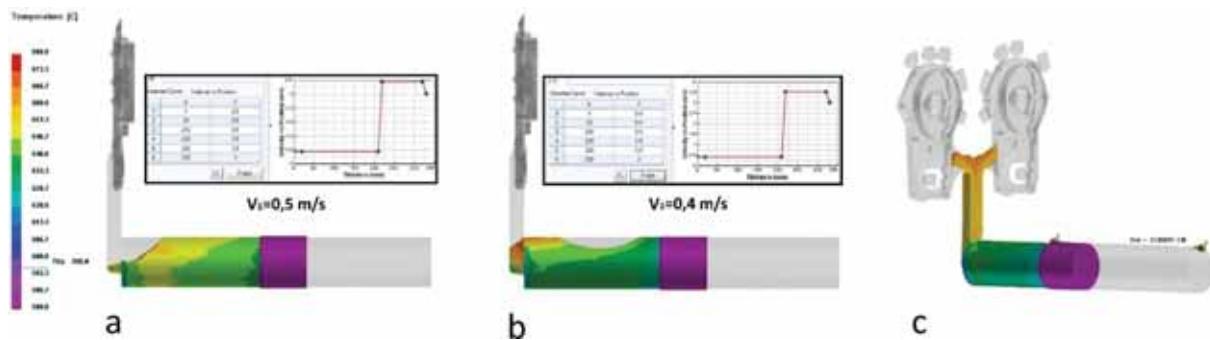
Figure 3. Optimization of piston movement; a) optimal piston velocity during phase 1, b) slow piston velocity during phase 1, c) optimal time for start of 2nd phase - shoat

NUMERICAL SIMULATIONS ADVANCE USAGE

First upgrade to advance user in using numerical simulations in casting development and/or optimization is to analyze stresses and deformation of casting and/or mold. Analyzing stresses we can predict critical areas for product quality or even prediction of the lifetime of the produced part. On Figure 4a are presented calculated critical area for crack prediction base on the stress analyze, on Figure 4b is the crack on the mold that accrued in reality [3].
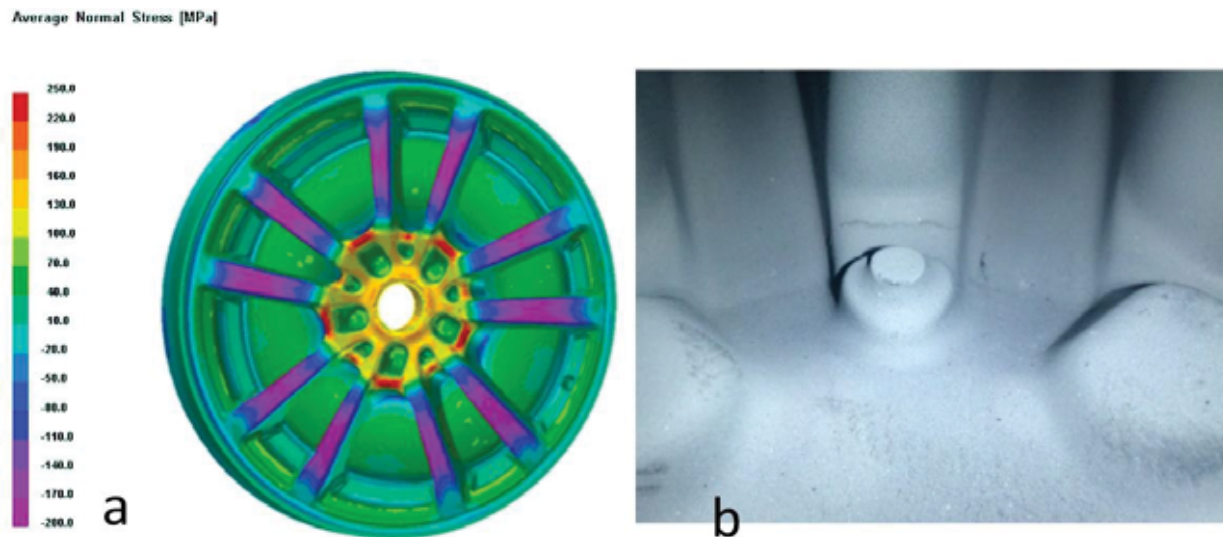
Figure 4. a) calculated stresses with critical areas, b) crack on the real mold

The advance using of special variants is most common in use in HPDC. One of these advance features is local squeeze simulation or jet cooling. Shrinkage porosity in the casting is the consequence of material shrinkage during solidification and cooling of the casting. The filling

of the casting during solidification to completely compensate shrinkage porosity is still unsolvable problem in the foundry. With ProCAST software we can simulate local squeeze in the high pressure die casting. With the calculation, we can very fast determine the optimal time to start the squeeze and the optimal squeeze length. These parameters are needed to reduce the shrinkage to minimum. For accurate simulation results all high pressure die casting parameters must be applied and the precise calculation of steady state temperature in the die must be calculated. The effect on porosity in the casting with and without using local squeeze can be seen on Figure 5.
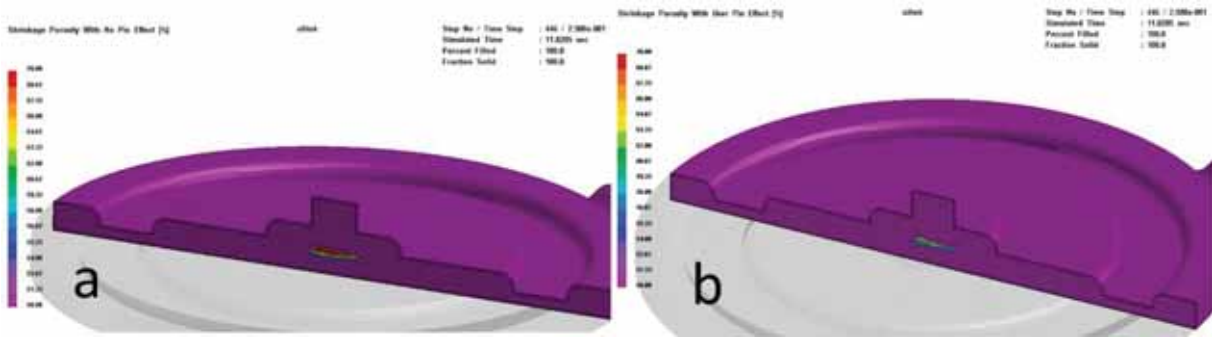
Figure 5. Porosity with (a) and without (b) using local squeeze

To simulate semi solid technology like rheocasting ProCAST uses special flow model to accurate calculate the flow of the semi solid alloy. The comparison of cavity filling using standard HPDC flow model and flow model for semi solid technology is presented on Figure 6.
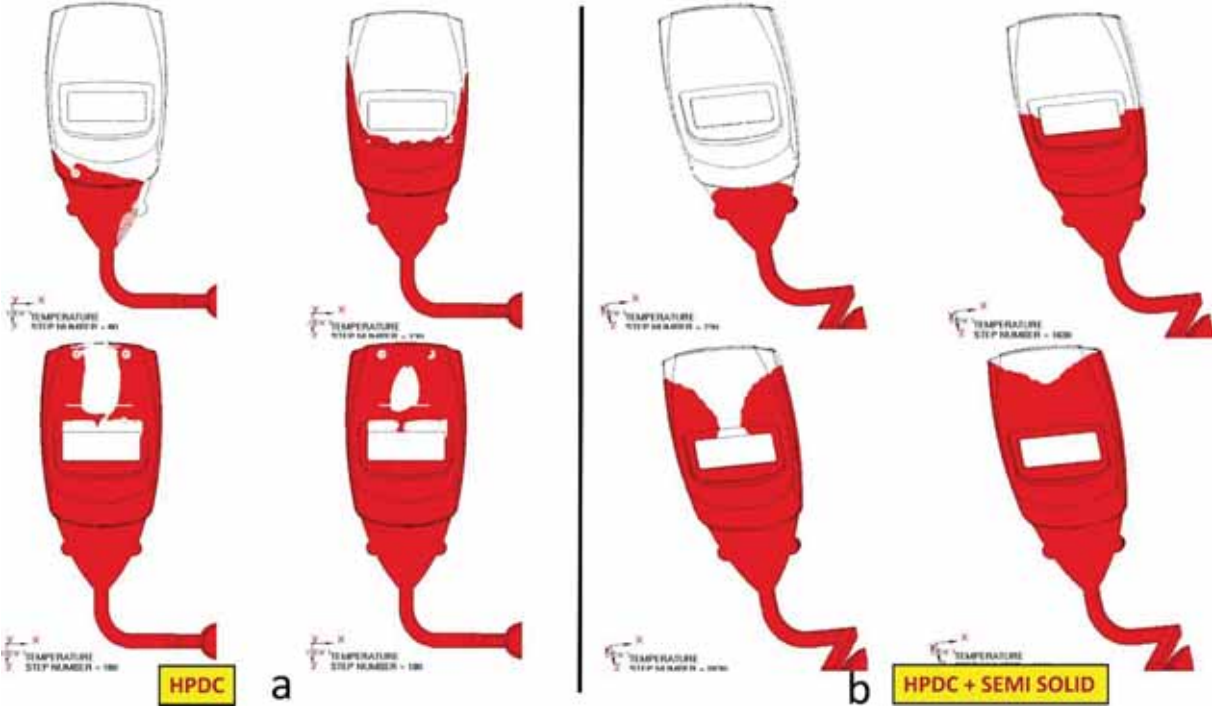
Figure 6. Filling of the casting using HPDC (a) and HPDC + semisolid (b) using rheocasting technology

Salsa 3D is additional module for ProCAST which helps to calculate the size of gating and running systems for the High Pressure Die Casting process. It assists in designing gates, runners and overflows that are constructed from lines in 3D space and by controlling the maximum gate velocity and thickness based on the available pressure machine we obtain geometry of gating system that can be used to make first simulations very fast. This potentially delivers significantly increased yield and reduced die development time and the filling system can be validated using ProCAST or QuikCAST. The workflow is presented on Figure 7.
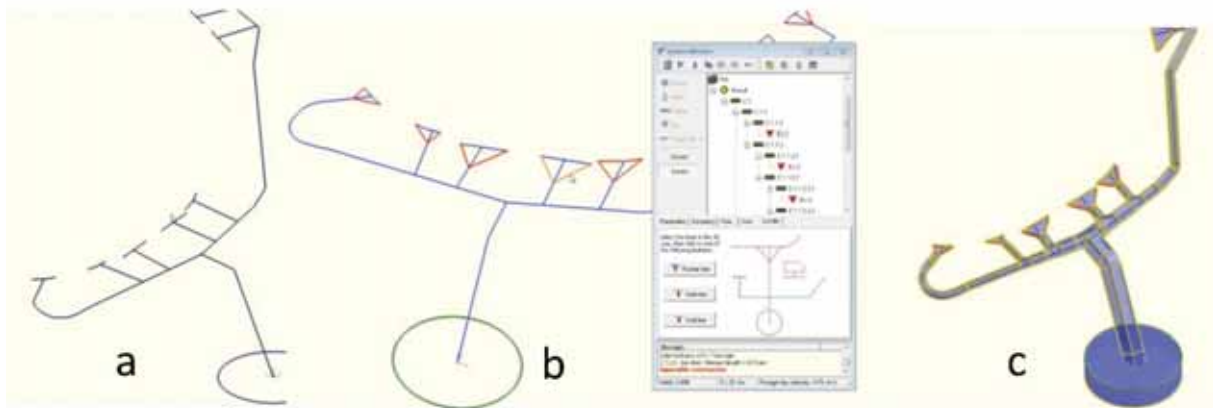
Figure 7. Salsa 3D workflow; a) lines sketched in 3D workspace, b) definition of segments and connections, c) automatically generated 3D model of gating system based on maximum gate velocity and gate thickness

Special features are also available for investment casting and continuous casting. In investment casting technology ProCAST is able to automatically generate a mesh representing the shell mold suitable for Investment Castings & Shell Molding processes. Software also has dedicated features to address the specific needs of investment casting foundries like allowing for non-uniform shell thickness to be blended and multiple shell layers to be created. Also taking into account radiation with view factors, including shadowing effects, which are critical for high temperature alloys.

ProCAST provides a complete solution for continuous and semi-continuous casting process. The software can simulate steady-state conditions as well as the initial and final stages of continuous casting processes. ProCAST also offers a unique capability to use user functions which allow even more advanced users to program their specific process requirements. For example, user functions allow you to define boundary conditions as time, temperature and space-dependent variables in order to accurately model any specific casting process.

CONCLUSIONS

Using numerical simulations in foundry technology is an imperative in nowadays. With increasing the demands on quality castings and with castings that are more and more complex and has implemented even more functions. For some castings the development of foundry technology without the usage of numerical simulations would be practically impossible. Foundries that are at the beginning of using numerical simulations are using

basic functions to optimize the ongoing processes to obtain better quality and to reduce the scrap. Expert users are using all the special features of numerical simulations at the start of casting development path to get the parts with desired quality and with lowest development costs possible.

REFERENCES

[1] A. Mahmutović, D. Krmpotić, M. Petrič, P. Mrvar, Influence of local cooling rate on directional solidification of nodular graphite cast iron, Zbornik referatov 53. mednarodnega livarskega posvetovanja, (ur. KRIŽMAN Alojz et al), Društvo livarjev Slovenije, 2013, Portorož, Slovenia.

[2] A. Mahmutovič, S. Kastelic, M. Petrič, P. Mrvar, High pressure die casting optimization using numerical simulation, Abstracts proceedings, Društvo livarjev Slovenije, 2016, Ljubljana, Slovenia, pp. 76-77.

[3] A. Mahmutovič, J. Potočnik, V. Petrović, P. Mrvar, Optimization of low pressure die-casting process of alloy wheel by casting simulation program, *Abstracts book: development and optimization of the casting production processes*, 14th International Foundrymen Conference, University of Zagreb Faculty of Metallurgy, May 15th-16th, 2014, Opatija, Croatia, pp. 21.

MICROSTRUCTURAL EVALUATION OF Al - 2.5wt.%Mg – 0.7wt.%Li ALLOY IN AS CAST CONDITION

Franjo Kozina[1], Zdenka Zovko Brodarac[1], Mitja Petrič[2]

[1]University of Zagreb Faculty of Metallurgy, Sisak, Croatia
[2]University of Ljubljana Faculty of Natural Sciences and Engineering, Ljubljana, Slovenia

<u>Oral presentation</u>
<u>*Original scientific paper*</u>

Abstract

The intention of designing of innovative engineering materials with advanced properties found its role in special purposes, such as aerospace application. The main issue has been recognized as a weight savings, stiffness development and mechanical properties. Lithium, in Al-Mg-Li alloys, plays a significant role through stimulation of precipitation hardening, increasing of Young's modulus, stiffness, fracture toughness and enhancing corrosion resistance. Other significant alloying element such as magnesium influences strengthening effect by enhancing the precipitation of metastable δ' (Al$_3$Li) phase. This indirect strengthening effect is possible due to fact that magnesium reduces solubility of lithium in aluminium. While the mechanism of this indirect strengthening seems to be simple, it is not fully understood if presence of magnesium merely changes the phase stability, interfacial energy or diffusion coefficient. In order to understand magnesium role in Al-Mg-Li ternary system, Al-2.5wt.%Mg–0.7wt.%Li was produced under laboratory conditions. Obtained results of Thermo-Calc calculations and microstructural investigation enabled valuation of solidification sequence and micro constituent's development and/or transformation.

Keywords: *Al-Mg-Li alloy, lithium, magnesium, density, phase precipitation*

*Corresponding author (e-mail address): *fkozin@simet.hr*

INTRODUCTION

The interest in the aluminium-lithium alloys is fuelled by three important considerations: reduction of density, increase in elastic modulus and introduction of precipitation hardening by the formation of metastable δ' (Al$_3$Li) phase [1]. Because the unique combination of properties provided by aluminium (Al) and Al based alloys [2], it is not surprising that they have been utilized in the aircraft construction since 1930., manly those of 2XXX and 7XXX series [3]. However, despite their low specific density, wide interval of strength properties,

good workability, corrosion resistance and electrical and thermal conductivity, stiffness represents a problem when using Al and Al based alloys, due to their low Young's modulus [4]. Onwards, the need for further weight reduction and higher stiffness indicated a need for chemical composition redesign [5]. The key alloying elements contributing to the reduction in density of Al based alloys are lithium (Li), calcium (Ca), magnesium (Mg) and beryllium (Be) [6]. But from the aforementioned elements, Li has been found the most effective addition to reduce density of commercial Al alloys as well as to stimulate the precipitation hardening, increase stiffness, fracture toughness and enhance corrosion resistance [7]. Besides Be, associated with health and manufacturing problems, Li is the only metal that significantly improves elastic modulus, as illustrated in Figure 1 [8]. Namely, every 1% of Li added to Al alloys increases elastic modulus roughly for 3 GPa and decreases density by approximately 80 kg/m^3 [9] for the addition up to 4% [10]. As a consequence Al-Li based alloys have high specific modulus and specific strength, allowing large weight savings in aircraft structures. Just to illustrate, direct substitution of traditional Al based alloys for Al-Li alloys can yield to ~11% weight savings, while complete redesign of aircraft utilizing their full potential up to ~17% of weight savings [11]. Furthermore, Li has a high solubility in Al reaching up to 14% at 600°C which respectively decreases with temperature decrease, consequently opening the possibility for modelling mechanical properties by artificial aging [12].
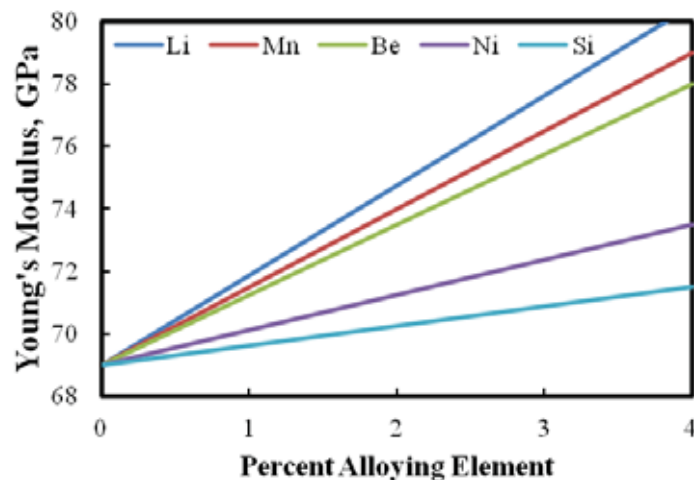
Figure 1. Impact of alloying elements on Young's modulus of Al based alloys [13]

Consequently, a several microstructural features are found to be unique for these alloys: nature and volume fraction of strengthening precipitates, amount of co-precipitates that alter the planar slip deformation behaviour, width of the precipitate free zone (PFZ) and the content, size and distribution of coarse and angular equilibrium precipitates [14]. The nature, structure, size and distribution of the precipitates are influenced by chemical composition and heat treatment parameters [15]. This microstructural features have pronounced effect on the mechanical behaviour of these alloys [16]. While the PFZ contribute to the formation of cracks at the grain boundaries leading to the fatigue and corrosion resistance decrease [17], the precipitates can interact with dislocations therefore significantly increasing anisotropy originating from microstructural texture [18], as well as increase of sensitivity to long term low temperature exposure [19]. Onwards, insoluble

constituents of second-phase particles (often aided by trace elements, such as sodium (Na) and potassium (K) lead to low ductility and fracture toughness [20].

Alloying additions of copper (Cu), zirconium (Zr), silver (Ag) or Mg, minimize those problems by interdicting new precipitates and changing the nucleation characteristic of existing metastable δ' phase [16]. Besides solid solution and precipitation strengthening, Mg leads to further density reductions as well.

Based on this, several Al-Li-Mg alloys have been developed and utilized. They are represented by grades 1420, 1421 and 1423. Initially, it was established that alloying Al-Mg alloys with Li has a little effect on their mechanical properties and that it does not results with improvements during heat treatment. However, this claim was disputed after development of 1420 alloy in 1965, which was 10-12% lighter than any other Al-Li-X alloys used at that time. The chemical composition and density of commercially used Al-Li-Mg alloy is given in Table 1. Relatively higher concentrations of Li and Mg are required to compensate for the presence of much heavier elements such as zirconium (Zr) and scandium (Sc). Besides, 1420 alloy had a high corrosion resistance, good weldability, high elastic modulus and static tensile strength [21]. On the other hand, Mg additions can cause small decrease in elastic modulus [18].

Table 1. Chemical composition and density of commercially used Al-Li-Mg alloys[1]

Alloy	Li, wt.%	Mg, wt.%	Zr, wt.%	Sc, wt.%	Al, wt.%	ρ, g/cm^3
1420	2.1	5.2	0.11	-	Bal.	2.47
1421	2.1	5.2	0.11	0.17	Bal.	2.47
1423	1.9	3.5	-	-	Bal.	-

Although, precipitation in Al-Li-Mg and Al-Li system seem to be similar, it is suspected that Mg decreases solubility of Li in α_{Al} matrix enhancing the precipitation of metastable δ' phase [22]. During that time, parameters of α_{Al} lattice become enhanced due to the Mg enrichment. Onwards, at higher temperatures, metastable δ' phase transforms into ternary phase T (Al_2MgLi) with a complex cubic lattice. Mg from the enriched α_{Al} precipitates to the ternary T phase consequently decreasing its lattice parameters and increasing ductility [23]. Although this system seems quite simple, the precise distribution of Mg atoms between matrix and metastable δ' phase is not fully understood. Onwards, it is not clear if the precipitation enhancement, due to Mg addition, is mainly controlled by the phase stability, changes in interfacial energy or changes in diffusion coefficient [24].

In order to understand mechanism of phase precipitations and Mg distribution in Al-Mg-Li ternary system, Al-2.5wt%Mg–0.7wt%Li was produced under laboratory conditions. Computer aided thermodynamic diagram calculation (CALPHAD) enabled the extrapolation of particular multicomponent alloy and prediction of corresponded solidification sequence. Correlation of obtained results with microstructural analysis reveals identification of present constituents and theirs behaviour.

MATERIALS AND METHODS

Due to high reactivity of Li with molten alloy, crucible materials and open atmosphere,

melting and casting of Al-Li based alloys represents a challenge. To minimize Li reactivity and a following loss, three different melting procedures have been developed: alloying with Al-Li master alloy (containing up to 20 % of Li), melting under a flux cover and Li addition under vacuum or inert atmosphere [6].

The Al block (technical purity), placed into a graphite crucible coated with boron-nitrite has been deposited into induction melting furnace. Controlled atmosphere was maintained by Ar introduction and crucible cover, Figure 2a. The Al block was melted at 720 °C, followed by Mg addition. A steel bell coated with boron-nitrite was used for introduction of Li, wrapped in Al-foil (commercial purity) into a molten alloy, and stirring to ensure a homogeneous distribution of Li in the melt. Casting was performed into a steel mould at 700 °C without protective atmosphere (Figure 2b).

a)   b)
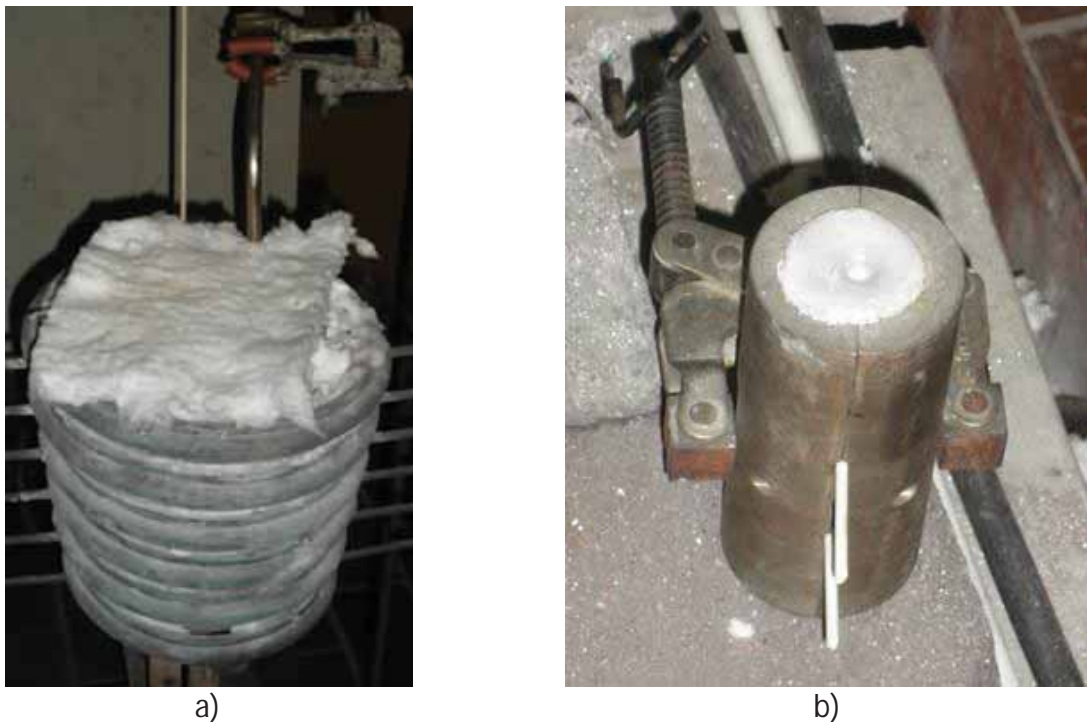
Figure 2. Induction furnace and steel mould:
a) Melting process of Al-2.5wt%Mg–0.7wt%Li alloy
b) Steel mold after casting of Al-2.5wt%Mg–0.7wt%Li alloy

In order to establish a loss of Li and Mg during melting and casting, the sample for chemical analysis was taken. The analysis was done using ARL™ 4460 Optical Mass Spectroscope.
In order to calculate density, weight and volume of a whole sample were measured, first. Casting shape and geometry indicates different solidification conditions in corresponding zones. Afterwards, sample was cut into characteristic sections (Figure 3b). The weight and volume of each section were measured as well. Finally, samples for metallographic analysis were taken.

Samples for metallographic analysis were prepared semi-automatically on grinding/polishing machine Pheonix Beta Biller SAD. In order to observe grain size and microstructure, samples were etched. The solution containing 2 parts of hydrofluoric acid, 1 part of nitric acid and 3 parts of glycerine was used to reveal the grain boundaries. Grain boundaries and

microstructure were observed by electrolytic etching using Barker etching solution (5 ml HBF_4 in 200 ml distilled H_2O). Images were taken under polarized light. And finally, Weck's reagent, consisting of 100 ml of water, 4 g of potassium permanganate and 1 g of sodium hydroxide, was used to obtain microstructure. Polarized light was necessary for imaging too.

While Olympus GX51 microscope was used to perform the optical microscopy, electron microscopy was done on Tescan, Vega TS 5136 MM in combination with energy dispersal spectrometer (EDS) Bruker Dispersive Spectrometer.

a)   b)
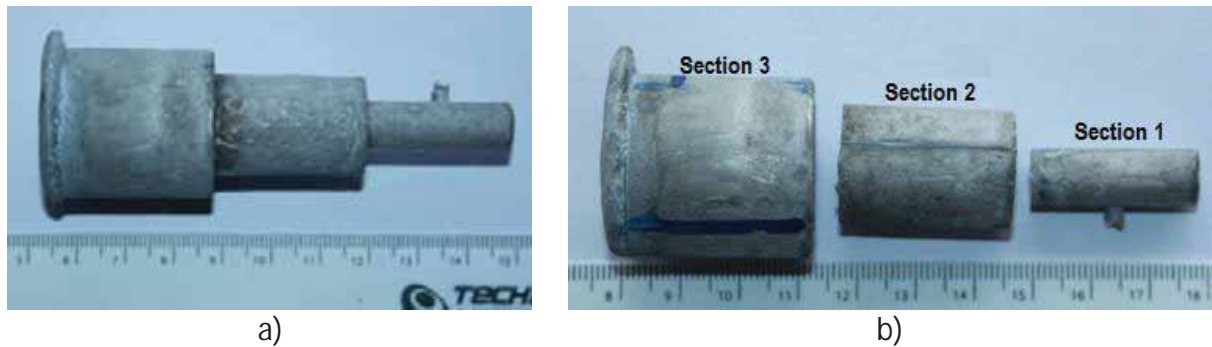
Figure 3. The sample of Al-2.wt.Mg-0.7wt.%Li alloy: a) After casting,
b) After sampling for density calculations

RESULTS AND DISCUSSION

According to the results of chemical analysis, given in Table 1, 74 wt% of Li added has been lost during melting and casting. Low vapour pressure of Li comprehends its significant loss. Beside this, higher mobility and atomic fraction of Li allows early formation of Li_2O. Although MgO is thermodynamically more stable, Li_2O will start to appear at temperatures slightly above 100°C, much earlier than any other compound in Al-Li-Mg ternary system. Supporting this fact, only 13 wt% of Mg added was lost.

Table 2. Addition of particular element and chemical composition of Al-2.5Mg-0.7Li alloy

Element	Al	Mg	Li
Addition	Bal.	2.8	2.9
wt.%	Bal.	2.480	0.726

Density (ρ) of individual sections and a whole sample is given in Table 3. The lack of deviation in density between individual sections means that all absorbed Li is equally distributed among them. Since the last section is closest to the open atmosphere, and has a lowest cooling rate, somewhat higher density is not surprising.

Table 3. Density value of sample and individual sections

Section	m, g	V, cm^3	ρ, g/cm^3
1	5.432	2.200	2.469
2	22.074	9.0	2.453
3	56.301	22.0	2.559
Sample	84.623	34.0	2.489

Compared to the other commercially used Al based alloys, especially those of 2XXX (2.78 g/cm^3) and 7XXX (2.81-2.86 g/cm^3) series, Al-2.5wt%Mg–0.7wt%Li alloy has a lower density. It can even parry to other commercially used Al-Li-Mg alloys with much higher Li and Mg content (Table 1).

Based on achieved chemical composition, computer aided thermodynamic diagram calculation (CALPHAD) was used to obtain solidification sequence and to see precipitation of stabile phases.

Equilibrium phase diagram obtained by Thermo-Calc software support reveals phase transformation and precipitation, as shown in Figure 4□
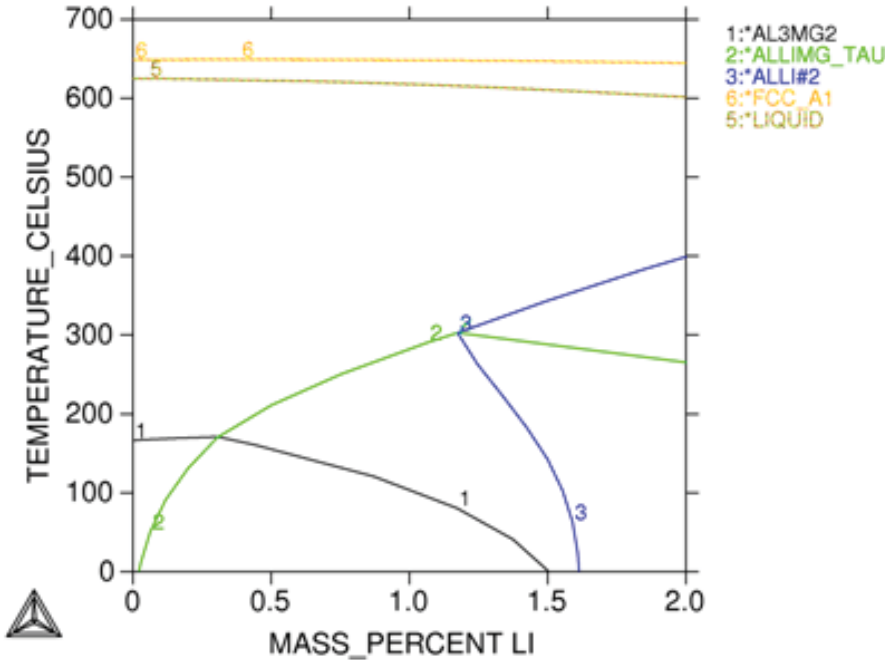
Figure 4. The Al-rich corner of Al-Mg-Li diagram in respect to Li

Solidification sequence according to the equilibrium phase diagram is given in Table 4.

Table 4. Solidification sequence according to Thermo-Calc calculations

Reaction	Temperature, °C
L → α_{Al}	622
L + α_{Al} → α_{Al}' + AlLi	368
α_{Al}' + AlLi → α_{Al}'' + Al$_2$LiMg	257
α_{Al}'' → α_{Al}''' + Al$_3$Mg$_2$	138

According to the diagram in Figure 4, the equilibrium solidification involves formation of primary Al dendrite development at **622°C**, followed by stabile δ (AlLi) phase precipitation. In real solidification conditions for high Li/Mg ratio, metastable δ' phase becomes stabile as δ. In chase that the Li/Mg ratio is low, metastable δ' phase transforms into T phase [1]. In non-equilibrium condition, Mg reduces the solubility of Li in α_{Al}, encouraging metastable δ' phase to develop first. Precipitation of the δ' causes the extraction of Al from the solid solution

leading to the increase in the lattice parameters of α_{Al}. Consequently, Mg content in solid solution increases [23].

The incoherent equilibrium T phase has a complex cubic lattice (a=2.02 nm) [24], and tends to precipitate at high angle grain boundaries [25] (Figure 5a and 5b). Since the Mg contain in solid solution decreases, a decrease in lattice parameters of α_{Al} is expected as well [22].

a)   b)
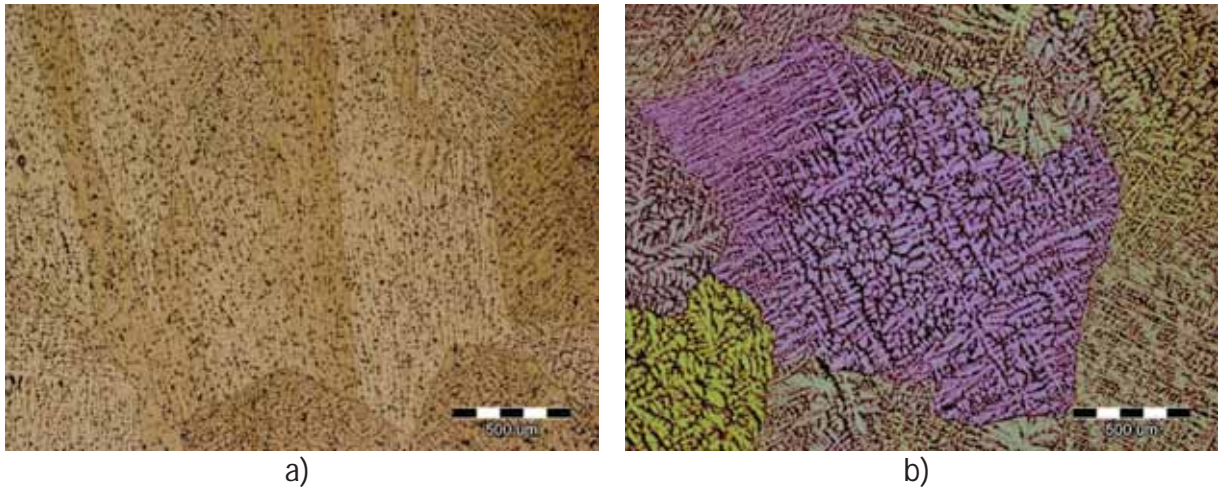
Figure 5. Micrograph showing phase precipitations (predicted T phase) on the grain boundaries: a) between columnar and equiaxed zone, magnification 50X
b) in equiaxed zone, magnification 50X

Figure 5a and 5b shows regular spherical precipitates at the grain boundaries located between columnar and equiaxed zone. The quantitative line analysis is given in Figure 6.
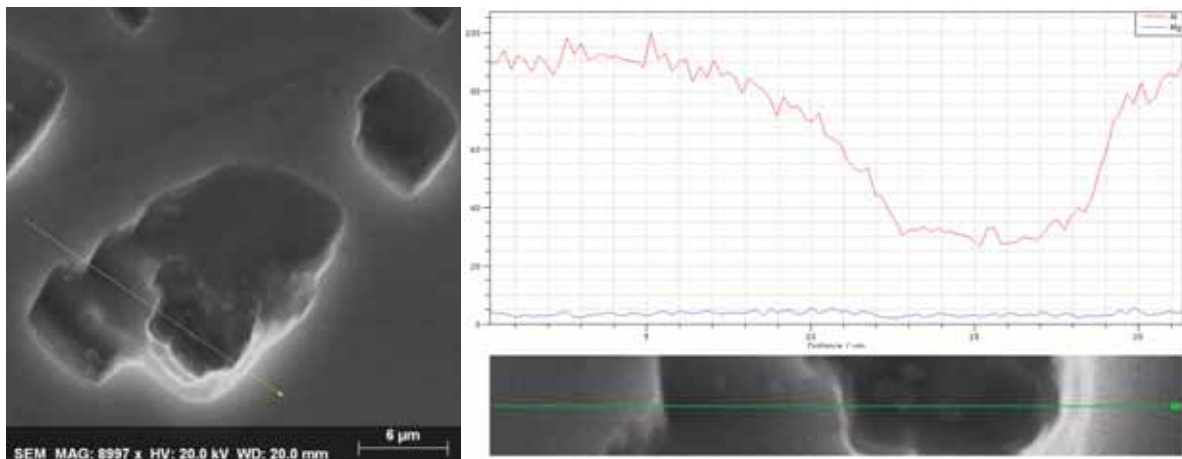
Figure 6. Quantitative microstructural analysis

However, results of line analysis, given in Figure 6, indicate no significant change in the Mg content between solid solution and phase precipitated at grain boundaries. Although, the α_{Al} becomes enriched in Mg, the following interaction with δ' will result in precipitation of T phase. Consequently, the parameters of α_{Al} lattice stay increased until eutectic reaction ($\alpha_{Al}'' \rightarrow \alpha_{Al}''' + Al_3Mg_2$) causes significant precipitation of Mg from the bulk α_{Al}''. Since Al_3Mg_2,

also known as Al_8Mg_5 [14] is the last solidifying phase, it will precipitate at the grain boundaries. The precipitates located at the grain boundaries are given in Figure 7a and 7b.
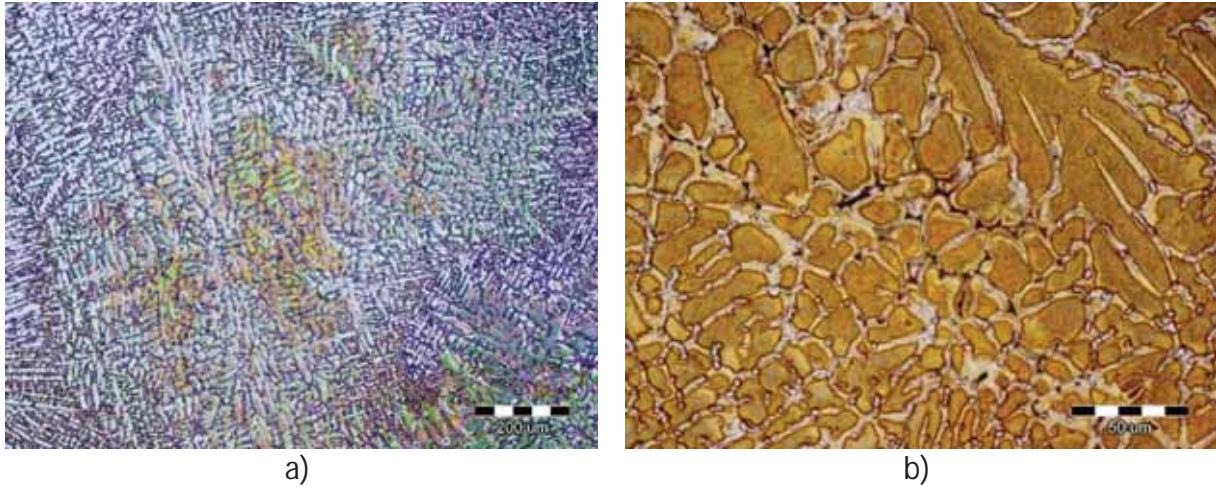
Figure 7. Micrograph showing precipitations in interdendritic spaces of:
a) Fully formed dendrites at magnification 100X
b) Last solidifying area at magnification 200X

The areas between fragmented and fully formed dendrites represent the potential locations for precipitation of δ' (Figure 7a). Grain boundaries at the last solidifying areas are potential areas for Al_3Mg_2 precipitation, as shown in Figure 7b. The SEI and following mapping analysis is given if Figure 8a and 8b.
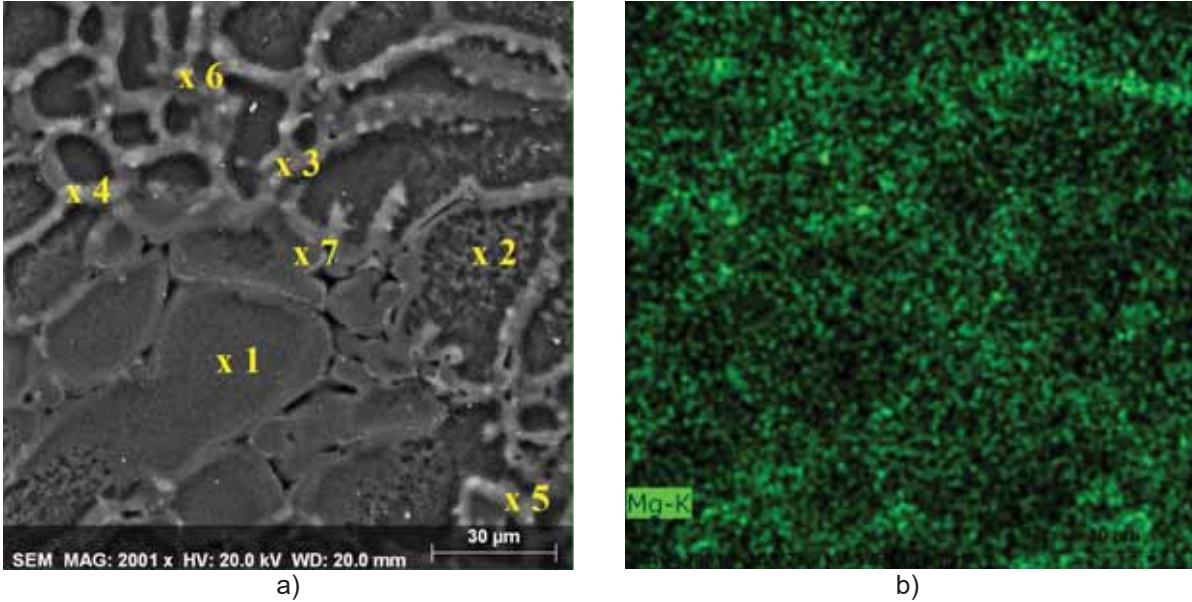
Figure 8. SEI of:
a) Al - 2.5wt.%Mg – 0.7wt.%Li alloy with marked EDS analysis position
b) Mapping analysis of Mg content

Figure 8a shows SEI of densely distributed phases in both fragmented and fully developed dendrite areas, respectively. Since the results of mapping analysis have shown significant variations in colour intensity concerning Mg contains (Figure 8b), additional EDS quantitative microstructural analysis was done. The locations of EDS analysis are given in Figure 8a followed by chemical composition in Table 5.

Table 5. Results of EDS quantitative microstructural analysis

Location	Al, wt.%	Mg,wt.%
1	75.89	1.87
2	75.46	1.96
3	65.65	4.32
4	69.47	4.52
5	76.65	3.45
6	92.77	7.23
7	96.06	3.94

While the measurements taken at the location 1 and 2 confirm the existence of residual Mg in bulk α_{Al}, difference between measurements 3, 4, 5, 6 and 7 indicate the occurrence of different phases as well. Since EDS did not possess a possibility of light elements identification, prediction of present phases has been calculated from Al:Mg ratio. Comparison of Al:Mg ratio indicates presence of characteristic T phase.

Since the strengthening in Al-Li-Mg alloys is mainly done by metastable δ' precipitation, mechanical properties in as cast condition should be considered. Ultimately, in the as cast condition, Al_3Mg_2 and Al_2LiMg are the only identified secondary phases in α_{Al} matrix. Ternary T phase causes material softening because of Li deployment from δ' phase [25]. Since the Al_3Mg_2 precipitates as an irregular coarse particle at the grain boundaries, it cannot contribute to the strengthening effect [26]. However, since the stoichiometry of Al_3Mg_2 changes pending on Mg segregation and cooling rate, the amount of Mg left to increase the lattice parameters of α_{Al} lattice changes as well, consequently influencing strengthening potential of the alloy.

CONCLUSIONS

Correlation of predicted solidification sequence with microstructural analysis reveals identification of present constituents and theirs behaviour.

- Alloying with Mg and Li enable a significant decrease of casting density (ρ=2.489 g/cm^3) when compared to any commercial one.
- Lack of significant deviations in density between characteristic casting sections indicates no loss of Li during solidification neither by oxidation nor flotation processes.
- Mg addition decreases Li solubility in α_{Al} forcing the precipitation of metastable δ' phase, despite of low Li contents. Low Li/Mg ratio forces metastable δ' phase to decompose producing ternary T phase. During this peritectic reaction Li is first to deplete while the Mg contents in bulk α_{Al} stays unchanged.

136

- As the concentration of Mg increases in the bulk α_{Al}, the final eutectic reaction resulted in evolution of secondary eutectic Al_3Mg_2 phase.

So, even though, significant density reduction can be obtained by lower addition of Li – 0,7 wt.% and Mg – 2,5wt.%. Microstructure development and constituent's features are expected to have a significant influence on mechanical properties development.

REFERENCES

[1] N. Prasad, A. Eswara, A. Gokhale, R. J. H. Wanhill, Aluminium–lithium alloys, Aerospace Materials and Material Technologies Butterworth-Heinemann, Oxford, 2013.

[2] J. R. Santos, C. Mário, Machining of aluminum alloys: a review, The International Journal of Advanced Manufacturing Technology, 89(2016)9, pp. 3067-3080.

[3] R. Rajan, P. Kah, B. Mvola, J. Martikainen, Trends in Aluminium alloys development and their joining methods, Reviews on Advanced Materials Science, 44(2016)4, pp. 383-397.

[4] H. Buhl, Advanced aerospace materials, Springer Science & Business Media, Köln, 2012.

[5] M. Peters, C. Leyens, Aerospace and Space Materials, Material Science and Engineering, 3(2016)1, pp. 1-11.

[6] A. Akhtar, E. W. Akthar, S. J. Wu, Melting and casting of lithium containing aluminium alloys, International Jurnal of Cast Materials Research, 28(2015)1, pp. 1-8.

[7] C. Huang, A. J. Ardell, Determining the effect of microstructure and heat treatment on the mechanical strengthening behavior o fan aluminum alloy containing lithium precipitation hardened with the δ' Al3Li intermetallic phase, Journal of Materials Engineering and Performance, 9(2000)4, pp. 428-440.

[8] J. W. Martin, Aluminium-Lithium alloys, Ann. Rev. Mater. Sci, 18(1988)1, pp. 101-119

[9] C. J. Peel, B. Evans, R. Grimes, W. S. Miller, 9th Eur. Rotorcraft Forum, September 13-15, 1983, Stresa, Italy.

[10] K. K. Sankaran, N. J. Grant, The structure and properties of splat-quenched aluminium alloy 2024 containing lithium additions, Materials Science and Engineering, 44(1980)2, pp. 213-227.

[11] K. T. V. Rao, R. O. Ritchie, Fatigue of aluminium lithium alloys, International Materials Reviews 37(1992)4, pp. 153-185.

[12] J. Augustyn-Pieniążek, H. Adrian, S. Rzadkosz, M. Choroszyński, Structure and Mechanical Properties of Al-Li Alloys as Cast, Archives of Foundry Engineering, 13(2013)2, pp. 5-10.

[13] W. F. Hosford, Physical Metallurgy, CRC Press, New York, 2010.

[14] N. A. Belov, D. G. Eskin, A. A. Aksenov, Multicomponent phase diagrams: applications for commercial aluminum alloys Elsevier, 2006.

[15] R. K. Gupta, N. Nayan, G. Nagasireesha, S. C. Sharma, Development and characterization of Al-Li alloys, Materials Science and Engineering - Structural Materials Properties Microstructure and Processing, 420(2006)2, pp. 228-234.

[16] N. E. Prasad, S. V. Kamat, K.S. Prasad, G. Malakondaiah, V.V. Kutumbarao, Inplane anisotropy in the fracture-toughness of an Al-Li 8090-alloy plate, Engineering Fracture Mechanics, 46(1993)2, pp. 209-223.

[17] R. J. Rioja, Fabrication methods to manufacture isotropic Al-Li alloys and products for space and aerospace applications, Materials Science and Engineering A - Structural Materials Properties Microstructure and Processing, 257(1998)1, pp. 100-107.

[18] R. J. Rioja, J. Liu, The Evolution of Al-Li Base Products for Aerospace and Space Applications, Metallurgical and Materials Transactions A -Physical Metallurgy and Materials Science, 43(2012)9, pp. 3325-3337.

[19] M. Trinca, A. Avalino, H. Garmestani, J. Foyos, E. W. Lee, O. S. Es-Said, Effect of rolling orientation on the mechanical properties and crystallographic texture of 2195 aluminum-lithium alloy, 331(2000)1, pp. 849-854.

[20] N. E. Prasad, A. A. Gokhale, P. R. Rao, Mechanical behavior of aluminium-lithium alloys Sadhana, 28(2003)1, pp. 209-246.

[21] I. N. Fridlyander, N. I. Kolobnev, A. L. Berezina, K. V. Chuistov, The effect of scandium on decomposition kinetics in aluminium-lithium alloys, Aluminium-Lithium, 1-2(1992)1, pp. 107-112.

[22] S. Betsofen, M. Chizhikov, Quantitative Phase Analysis of Al-Mg-Li and Al-Cu-Li Alloys, Aluminium Alloys, 794(2014)1, pp. 915-920.

[23] S. Betsofen, V. Ya, V. Antipov, M.I. Knyazev, Al–Cu–Li and Al–Mg–Li alloys: Phase composition, texture, and anisotropy of mechanical properties (Review), Russian Metallurgy (Metally), 4(2016), pp. 326-341.

[24] A. Deschamps, C. Sigli, T. Mourey, F. de Geuser, W. Lefebvre, B. Davo, Experimental and modelling assessment of precipitation kinetics in an Al-Li-Mg alloy, Acta Materialia 60(2012)5, pp. 1917-1928.

[25] A. Mogucheva, R. Kaibyshev, Microstructure and Mechanical Properties of an Al-Li-Mg-Sc-Zr Alloy Subjected to ECAP, Metals, 6(2016)11, pp. 254.

[26] Z. Z. Brodarac, F. Unkic, J. Medved, P. Mrvar, Determination of solidification sequence of the AlMg9 alloy, Kovove Materialy-Metallic Materials, 50(2012)1, pp. 59-67.

Acknowledgements

MICROSTRUCTURE AND HARDNESS OF Cu-Al-Mn-Ni SMA INGOT BEFORE AND AFTER HEAT TREATMENT

Stjepan Kožuh[1], Tomislav Vuković, Ivana Ivanić[1], Tamara Holjevac Grgurić[1], Borut Kosec[2], Mirko Gojić[1]

[1]University of Zagreb Faculty of Metallurgy, Sisak, Croatia
[2]University of Ljubljana Faculty of Natural Sciences and Engineering, Ljubljana, Slovenia

Abstract

In this work the effect of heat treatment on microstructure and hardness of Cu-Al-Mn-Ni shape memory alloy was determined. Ingots (8 mm in diameter and 15 mm in length) were produced by melting and casting process. Melting was performed using the heat produced by electric arc and by a water-cooled, specially constructed copper anode that also served as a casting mould. The samples were analysed in as-cast state and in as-quenched state (900 °C/15 min/H_2O). Microstructural analysis was performed by optical microscopy (OM), scanning electron microscopy (SEM) equipped by device for energy dispersive spectroscopy (EDS) and using differential scanning calorimeter (DSC). Preliminary metallographic analysis of investigated ingot confirmed that microstructure was consisted from martensite in both, as-cast and as-quenched state. A microhardness measurement was performed by Vickers method. Microhardness of Cu-Al-Ni-Mn shape memory alloy ingot was 260.8 HV10, and after heat treatment 285.6 HV10. By DSC analysis the phase transformation temperatures (A_s, A_f, M_s and M_f) were determined.

Keywords: Cu-Al-Mn-Ni, shape memory alloy, microstructure, hardness, heat treatment

*Corresponding author (e-mail address): kozuh@simet.hr

INTRODUCTION

The shape memory alloys (SMAs) are alloys which belong to the group of metallic materials that demonstrate the ability to return to some previously defined shape. Return of shape occurs when the alloys are exposed to the appropriate thermal process. This irregular behaviour is called the shape memory effect (SME). The only two alloy systems that have achieved any level of commercial exploitation are alloys on the basis of Ni-Ti (Nitinol) and alloys based on copper. The Ni-Ti alloys have greater shape memory strain, tend to much

more thermally stability, have excellent corrosion resistance etc., but the copper based alloys are much less expensive, can be melted and extruded in air with ease, and have a wider range of potential transformation temperatures. The shape memory effect of alloys on the copper basis is based on the properties of the high temperature β phase (Cu-Al phase) [1].

In the recent years, for improving the properties of Cu-Al systems, addition of other elements such as manganese and nickel is used [2]. Commercial shape memory alloys on the copper basis are mostly available in form of ternary Cu-Al-Ni and Cu-Zn-Al alloys, or in their quaternary modification with manganese. Manganese in combination with copper, aluminium, and nickel has been proved to enhance the thermoelastic and pseudoelastic behaviours [1]. Addition of manganese in Cu-Al-Ni system depresses transformation temperatures and shifts the eutectoid transformation to higher aluminium content. Therefore, it often replaces aluminium for better ductility. Also, by the combination of grain size and the texture control Cu-Al-Mn alloys exhibit a superelastic strain of about 7% which is comparable to that of Nitinol alloy [3]. Micro-alloying elements, like boron, cerium, cobalt, iron, titanium, vanadium, and zirconium can be also added to achieve a grain refining effect. These elements produce second phase precipitates. This precipitates then control the grain growth during the heat treatment [4].

Usual composition of Cu-Al-Ni alloys is 11-14.5% Al and 3-5 %Ni (in wt.%). However, these Cu-Al-Ni alloys are quite brittle at low temperatures and can only be hot finished. This adverse property is thought to be caused by the coarse grains and brittle γ_2 precipitates [5]. To suppress the formation of γ_2 precipitates (i.e. eutectoid $\beta_1 \rightarrow \alpha + \gamma_2$ decomposition process) and thus increase ductility, manganese is a well-known alloying element [6]. For this reason, the Cu-Al-Mn-Ni system is selected in this study.

In the present paper, the effect of heat treatment (quenching) on microstructure and microhardness of Cu-Al-Mn-Ni SMA have been investigated.

MATERIALS AND METHODS

The investigated Cu-Al-Mn-Ni alloy was prepared by arc melting of pure elements. Purity of used elements was: copper (99.9%), aluminium (99.5%), manganese (99.8%) and nickel (99.8%). The aim in this work was to produce SMA alloy with nominal composition of Cu-13Al-2.5Mn-2Ni (in wt.%). In order to achieve homogeneity in chemical composition, the samples were remelted three times using electric arc, and button-like ingots weighting approximately 6 g were obtained. The melting and casting of ingots was done using the same device (Fig. 1a) in a water-cooled, specially constructed copper anode that also served as casting mould. Cylindrical samples (ingots) with 8 mm in diameter and 15 mm in length were produced by casting process (Fig. 1b). These ingots were sectioned using a Buehler Isomet low-speed diamond saw to produce specimens for various examinations. The heat treatment was carried out at 900 °C held for a short period of time (15 minutes) and water quenched (WQ) immediately after heating.

<div align="center">(a)   (b)</div>

Figure 1. Photographs of the device for melting and casting (a) and casted ingots (b)

For microstructural characterization the samples were prepared using the standard metallographic techniques, i.e. grinding from 400 to 1200 grit paper (SiC) followed by polishing with 0.3 μm alumina powder (5 minutes) to mirror finishing and etching with a solution of 2.5 g $FeCl_3$, 10 mL HCl and 48 mL methanol (5 sec). The microstructure analysis of investigated SMA alloy was examined using optical microscope (OM) OLYMPUS GX and the Tescan Vega TS 5136 MM scanning electron microscope (SEM) equipped with the device for energy dispersive X-ray spectroscopy (EDS). After microstructural analysis all samples were exposed to microhardness testing. Microhardness was tested by Vickers method (HV10).

Thermal analysis was carried out using differential scanning calorimeter (DSC) Mettler Toledo DSC882e, in the temperature range from -50 °C to 250 °C, in the inert atmosphere of nitrogen. DSC investigations were done through two cycles of heating and cooling, with heating/cooling rate of 10 °C/min.

RESULTS AND DISCUSSION

To get the information about the possible effect of heat treatment on the microstructure, OM and SEM observations were carried out. Results of optical and scanning electron microscopy of as-cast state and heat treated sample (as-quenched state) are presented in Figs. 2-4. As can be seen from optical micrographs (Figs. 2 and 3) microstructure was consisted of martensite in both states of investigated alloy (before and after heat treatment). A more detailed SEM analysis confirmed the existence of martensitic microstructure at room temperature (Fig. 4).

(a)

(b)

(c)

(d)

Figure 2. Optical micrographs of Cu-Al-Mn-Ni SMA in as-cast state at different magnifications and positions (a,b – middle of the sample; c,d – edge of the sample)

The grains appear clearly and the martensite plates have different orientation in different grains. According to literature [1] in the case of Cu-Al-Mn-Ni alloy after quenching only $\beta_1`$ martensite can exists. While $\gamma_1`$ martensite mainly appears as coarse variants, the $\beta_1`$ martensite forms in the typical zig-zag morphology. Sari [1] also observed that $\beta_1`$ plates are small and have a highly thermoelastic behaviour due to their controlled growth in self-accommodating groups. It is known that martensite groups nucleate at numerous sites in the grain and the martensite growth process involves the accommodation of local stress field. This process requires the formation of other plate groups [7].
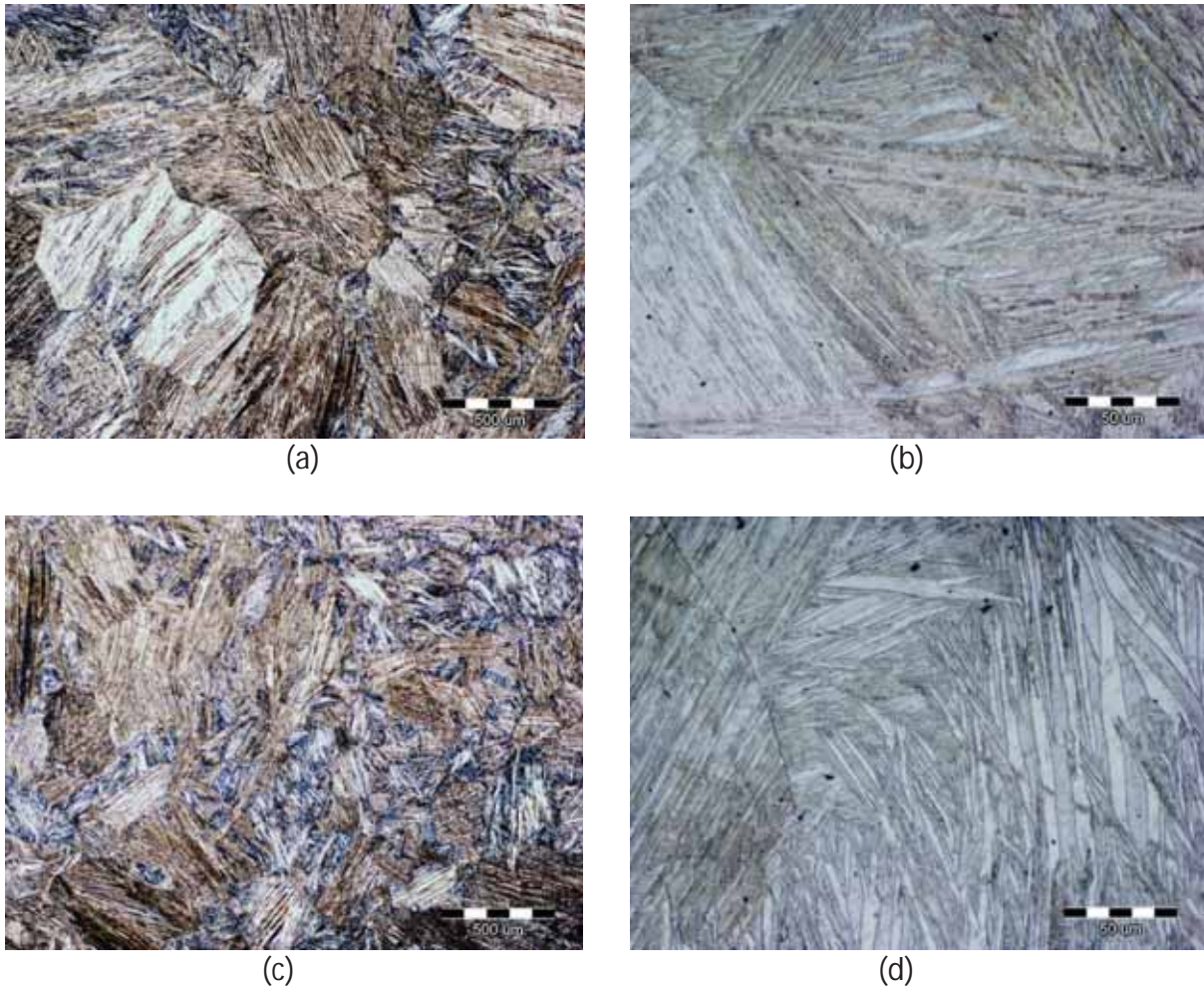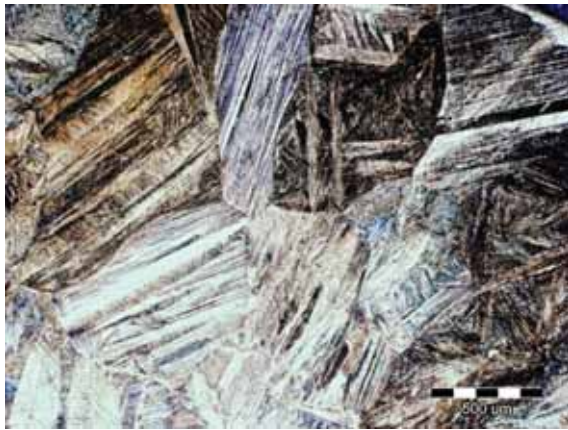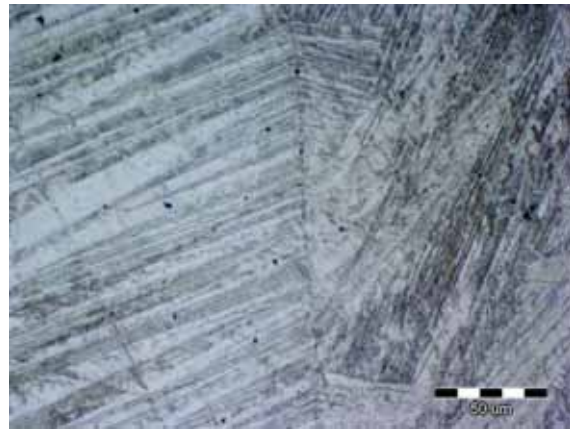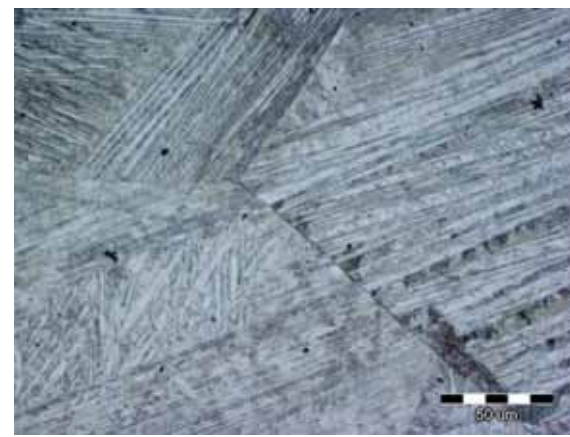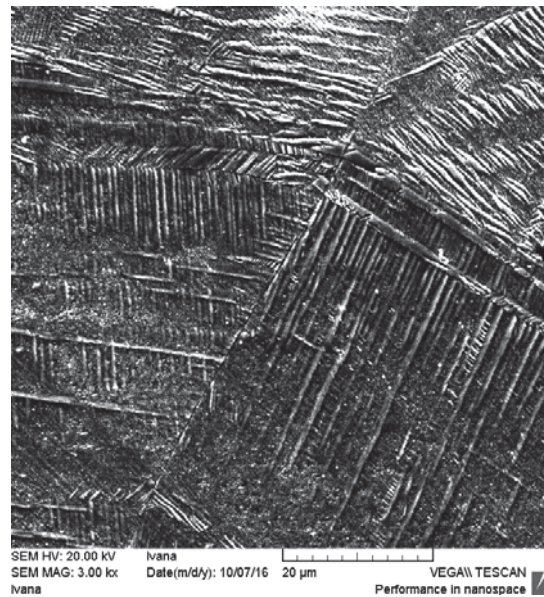
Figure 3. Optical micrographs of Cu-Al-Mn-Ni SMA in as-quenched state at different magnifications and positions (a,b – middle of the sample; c,d – edge of the sample)

Figure 4. SEM micrographs of Cu-Al-Mn-Ni SMA in as-cast state (a) and as-quenched state (b)

It is known that the martensitic transformation is a diffusionless phase transition in the solid state [2]. During this transformation the atoms keep on moving comparatively in regard to their neighbours. SME is related with transformation from an ordered austenite phase (i.e. β-phase) to the martensite. Nickel in the ternary alloy slows down the diffusion of copper and aluminium. In this way nickel efficiently helps to suppress the decomposition of the parent phase β during cooling. Sari [1] investigated the influence of 2.5 wt.% addition of manganese on the microstructure Cu-Al-Ni SMA and mentioned that β-phase in Cu-based SMAs have A2 type disordered structures at high temperatures and undergo the ordered structures with B2, DO_3 or L2 type superlattices during quenching. During quenching or rapid solidification, the β phase undergoes to order-disorder transitions: $β(A2) → β_2(A2) → β_1(L2_1)$. After that the thermoelastic martensitic transformation has occurred as $β_1(L2_1) → β_1`$ (9R or 18R). According to literature [3], similar alloy Cu-17Al-8.7Mn-3Ni (in at %) shows the α+β two-phase structure and the final shape memory treatment to obtain the β single phase can be performed at temperatures over 800 °C. It can be assumed that in our case the cooling rate during casting was high enough and this is the reason for forming of martensite already in as-cast state.

The EDS analysis confirms some small differences in the chemical composition for all analyzed positions (Figs. 5 and 6, Tables 1 and 2). In as-cast state the amount of copper is in the range between 84.05-85.05, aluminium 9.15-10.44, manganese 2.74-2.91 and nickel in the range between 2.60-2.89 (in wt.%). These values confirm that alloy with homogenous chemical compositions was produced. Similar values of alloying elements contents were obtained in the as-quenched state (Table 2).

(a)   (b)
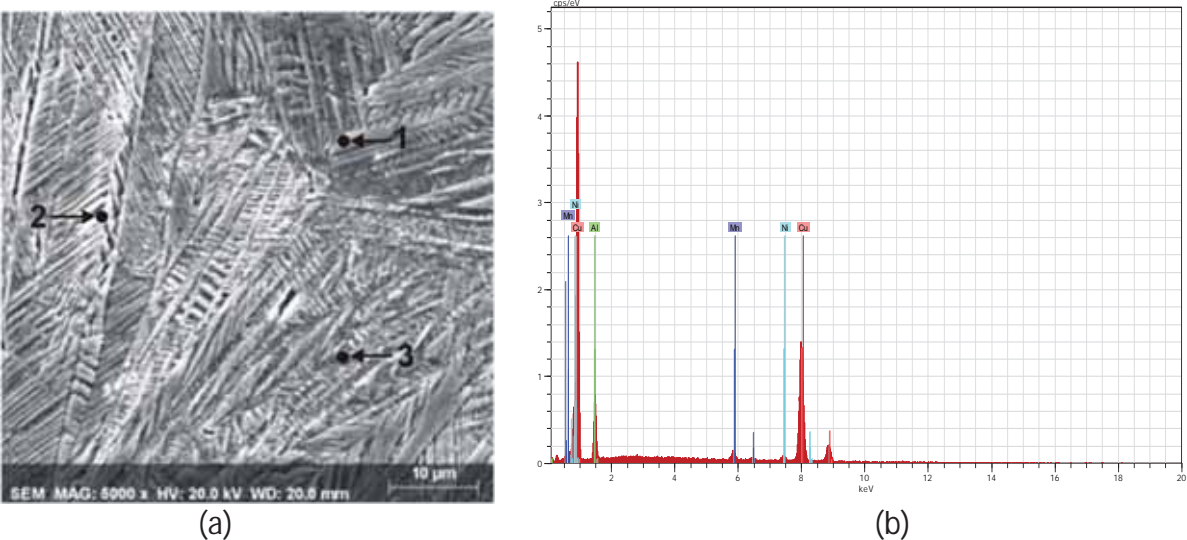
Figure 5. SEM micrograph (a) and energy dispersive spectrum – Position 1 (b) of Cu-Al-Mn-Ni SMA sample in as-cast state

Table 1. The chemical composition of the Cu-Al-Mn-Ni SMA in as-cast state (positions marked at the Fig. 5a), wt.%

	Cu	Al	Mn	Ni
Position 1	85.05	9.15	2.91	2.89
Position 2	84.06	10.29	2.74	2.91
Position 3	84.05	10.44	2.75	2.60

(a)   (b)
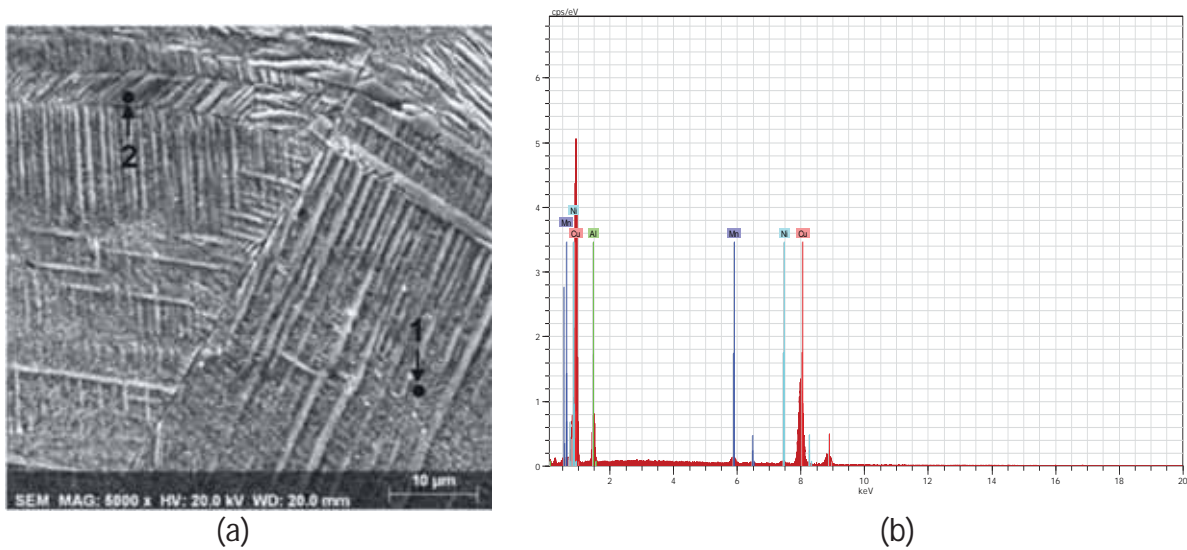
Figure 6. SEM micrograph (a) and energy dispersive spectrum – Position 1 (b) of Cu-Al-Mn-Ni SMA after quenching (900 °C/15`/H$_2$O)

Table 2. The chemical composition of the Cu-Al-Mn-Ni SMA in as-quenched state (positions marked at the Fig. 6a), wt.%

	Cu	Al	Mn	Ni
Position 1	84.32	10.26	2.81	2.61
Position 2	82.59	12.21	2.73	2.47

The results of microhardness testing obtained before and after heat treatment are given on Fig. 7. The highest value of hardness can be observed in as-quenched sample (285.6 HV10). The hardness value of as-cast state was 260 HV10.
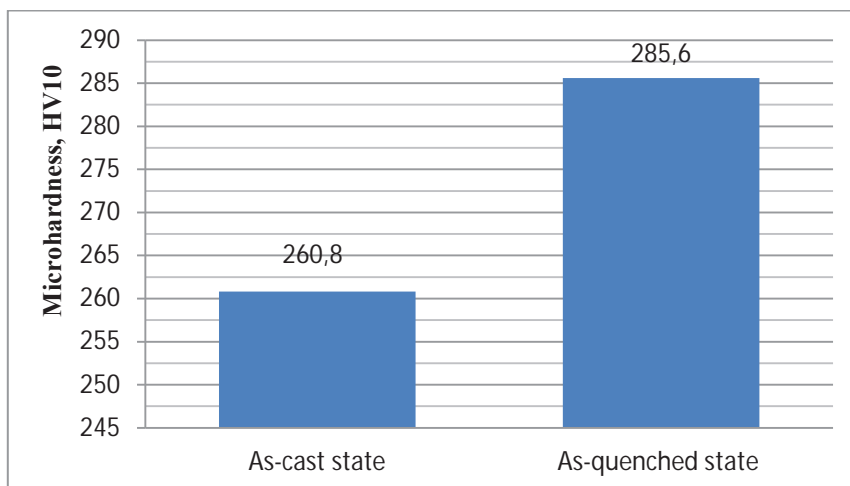
Figure 7. Microhardness (HV10) of investigated Cu-Al-Mn-Ni SMA

The differential scanning calorimetry measurements were made with heating/cooling rate of 10 °C/min, and are shown in Fig. 8. The characteristic austenite and martensite

temperatures (A_s, A_f, M_s and M_f) were determined by the tangent method, and the obtained data is given in Table 3.
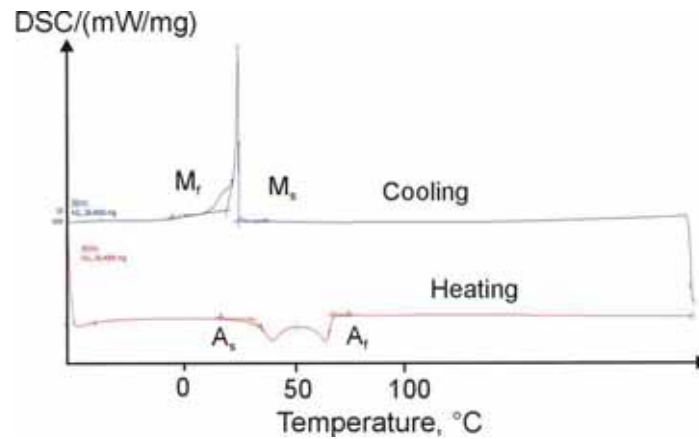
(a)
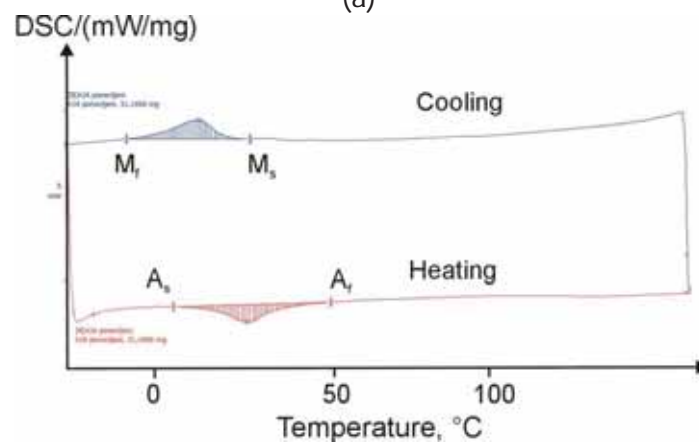
(b)

Figure 8. DSC diagrams of Cu-Al-Mn-Ni SMA in as-cast state (a) and as-quenched state (b)

Table 3. Phase transformation temperature values and temperature hysteresis of the investigated Cu-Al-Mn-Ni SMA

| State of alloy	Phase transformation temperatures / °C				ΔT_H / °C
	A_s	A_f	M_s	M_f	
As-cast	38.50	77.27	32.25	26.54	45.02
As-quenched	18.07	52.23	24.31	-8.82	27.92

The endothermic peak on DSC heating curve is associated with transformation of austenite. In contrast, the exothermic peak on the cooling curve indicates the martensite transformation. The martensitic transformation occurred in the thermal range between 32.25 °C and 26.54 °C for as-cast state and between 24.31 °C and -8.82 °C for as-quenched state. The value A_f-M_s represents temperature hysteresis ΔT_H. The reverse and forward transformation exhibit a typical thermoelastic feature with temperature hysteresis 45.02 °C for as-cast state, and 27.92 °C for as-quenched state. Canbay et al. [2] concluded that Cu-Al-Mn-Ni has the lowest transformation hysteresis value in comparison with Cu-Al-Mn alloy.

They mentioned that this behaviour can be explained with the effect of nickel. Nickel has a high solubility and decreases the M_S temperature when added in Cu-Al-Mn system.

CONCLUSIONS

The microstructural analysis with microhardness measurement was carried out on ingots of Cu-Al-Mn-Ni shape memory alloy in as-cast state and as-quenched state (900 °C/15`/H$_2$O). From the obtained results we can draw the following conclusions:

- Optical microscopy established the presence of martensite in investigated alloy in both investigated states, before and after heat treatment. Detailed SEM analysis confirmed the existence of martensitic microstructure at room temperature in both samples.

- In the microstructure the grains appear clearly and the martensite plates have different orientation in different grains. It can be assumed that in the case of investigated Cu-Al-Mn-Ni ingots after quenching only β_1` martensite exists and that this $\beta_1$` martensite forms the typical zig-zag morphology.

- The EDX analysis noted some small differences in the chemical composition in both investigated samples and analyzed positions. This suggests that high homogeneity of alloy composition was achieved successfully.

- After the heat treatment the microhardness value was increased. The microhardness value of as-cast state was 260.8 HV10 while in as-quenched state was 285.6 HV10.

- DSC analysis showed that the martensite transformation occurred in region between 32.25 °C and 26.54 °C for as-cast state and between 24.31 °C and -8.82 °C for as-quenched state. Temperature hysteresis for as-cast state was 45.02 °C, and for as-quenched state 27.92 °C.

REFERENCES

[1] U. Sari, Influence of 2.5 wt% Mn addition on the microstructure and mechanical properties of Cu-Al-Ni shape memory alloys, International Journal of Minerals, Metallurgy and Materials, 17(2010)2, pp. 192-198.
[2] C. Aksu Canbay, Z. Karagoz Genc, M. Sekerci, Thermal and structural characterization of Cu-Al-Mn-X (Ti, Ni) shape memory alloys, Applied Physics A, 115(2014), pp. 371-377.
[3] T. Omori, N. Koeda, Y. Sutou, R. Kainuma, K. Ishida, Superplasticity of Cu-Al-Mn-Ni shape memory alloy, Materials Transactions, 48(2007)11, pp. 2914-2918.
[4] H. Y. Peng, Y. D. Yu, D. X. Li, High resolution electron microscopy studies of martensite around X_s precipitates in a Cu-Al-Ni-Mn-Ti shape memory alloy, Acta Materialia, 45(1997)12, pp. 5153-5161.
[5] J. Gui, W. H. Zou, R. Wang, D. Zhang, C. H. Tang, M. Z. Xiang, D. Z. Yang, X-ray diffraction study of the reverse martensitic transformation in Cu-Al-Ni-Mn-Ti shape memory alloy, Scripta Materialia, 35(1996)3, pp. 435-440.
[6] M. Benke, V. Meringer, P. Pekker, Investigation of the bainitic reaction in CuAlNiMnFe shape memory alloy, J. Min. Metall. Sect. B – Metall., 49B(2013)1, pp. 43-47.
[7] U. Sari, I. Aksoy, Micro-structural analysis of self-accommodating martensites in Cu-11.92 wt% Al-3.78wt% Ni shape memory alloy, J. Mater. Process. Technol., 195(2008),

pp. 72-76.

Acknowledgements

INFLUENCE OF RIBS ON STRENGTH OF CIRCULAR MANHOLE COVER

Martina Lovrenić-Jugović[1], Ivica Skozrit[2]**, Ladislav Lazić**[1]**, Ivona Borošić**

[1]University of Zagreb Faculty of Metallurgy, Sisak, Croatia
[2]University of Zagreb Faculty of Mechanical Engineering and Naval Architecture, Zagreb, Croatia

Abstract

In this paper the displacement and stresses in the sections of circular manhole cover caused by bending load was analysed for chosen type of material. Using the software package Autodesk Simulation Mechanical, the three-dimensional linear static analysis, based on the finite element method, was performed to investigate the size of the bending stresses in the casted circular manhole cover. The analysis of the three different cover constructions was conducted. Since the circular cover with circular and radial ribs is circularly symmetrical, only one part of the geometry of the cover was analysed. Because analytical solutions are only applicable for simple geometric problems such as bending of thin circular plate, the numerical simulation of the thin circular plate was carried out. Results of the deflections and radial and circular stresses, obtained by the numerical simulation were compared with analytical solution. In the numerical simulations the equivalent stresses based on the energy theory of strength were monitored. After the verification of numerical results of the bending of thin circular plate, the increased stresses were detected on plate. For that reason the circular ribs were added on the bottom of the plate and the numerical simulation was carried out and for thus shaped cover. Due to the existence of a large equivalent stress another simulation with the addition of radial ribs was carried out. By analysing the results, it was concluded that the maximum equivalent stress passes into the circular and radial ribs at the bottom of the cover. Described numerical analysis was applied onto the covers made of ductile or gray iron.

Keywords: *circular manhole cover, linear analysis, finite element method, strength, ductile and gray iron*

Corresponding author (e-mail address): mlovrenic@simet.hr

INTRODUCTION

Modern civilization cannot be imagined without a system of drainage of waste and precipitation water. Manhole covers are essential functional and safety parts of the system.

They must allow access to the system, i.e. to be mobile, but also must have the required strength.

Manhole covers are circular or square plates, which are generally located on pavements or roads. They must be very strong and durable to be able to withstand the load and impact of pedestrians and/or vehicles' constant weight upon them. They are generally made out of cast iron. The circular shape for the manhole cover allows easier transporting by rolling as well as manufacturing, installing and maintaining [1,2]. Figure 2 presents schematic representation of installation place of sewage gratings and manhole cover sat typical cross-section of one road according to the classes (EN124).
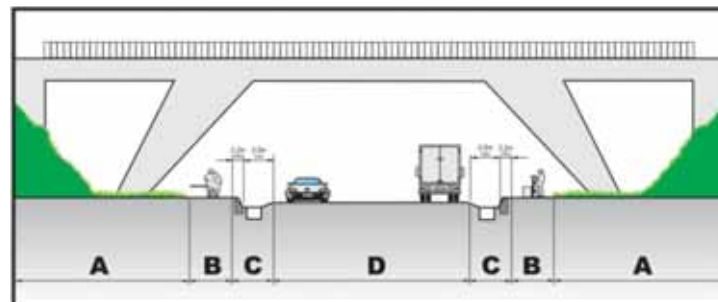
Figure 1. Typical cross-section of one road with representation of associated range in the installation place [2]

In the paper the influence of vertical ribs on the strength of the circular manhole cover class D 400 according to HRN M.J6.210 was researched. Covers class D 400, placed on the roads and parking lots for cars and for heavy goods vehicles, should endure a load of 400 kN (Figure 2).
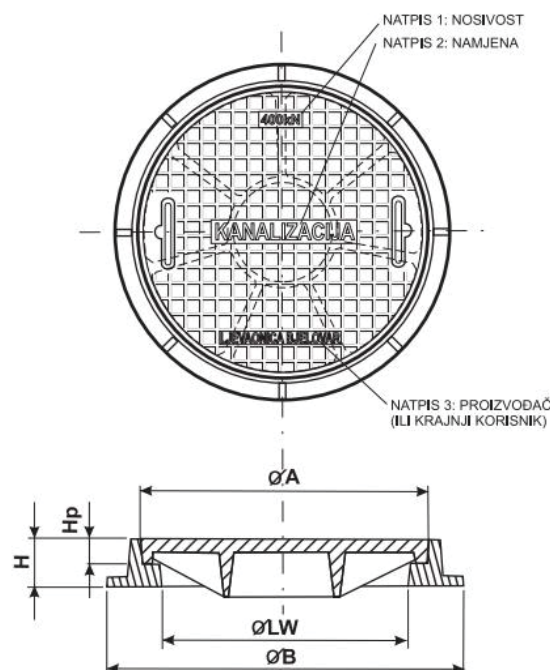

Figure 2. Circular manhole cover Class D 400 [2]

150

In this paper cover made of ductile iron with following dimensions was analyzed: diameter $A=\phi600$ mm, height $Hp=50$ mm, thickness 22 mm.

Firstly, the analytical analysis for bending of thin circular plate was conducted. Then, the same analysis was performed numerically using the software package Autodesk Simulation Mechanical [3] based on the finite element method. Results of the vertical displacement and radial and circular stresses, obtained by the numerical simulation were compared with analytical solution. After the verification of numerical results of the bending of thin circular plate with analytical solution, the ribs on the bottom side of plate were gradually added.

ANALYTICAL SOLUTION

Analytical solutions are only applicable for simple geometric problems such as bending of thin circular plate. A thin circular cover with a radius of $R=300$ mm by simply supported edge and loaded by uniformly continuous load q is presented in Figure 3a.
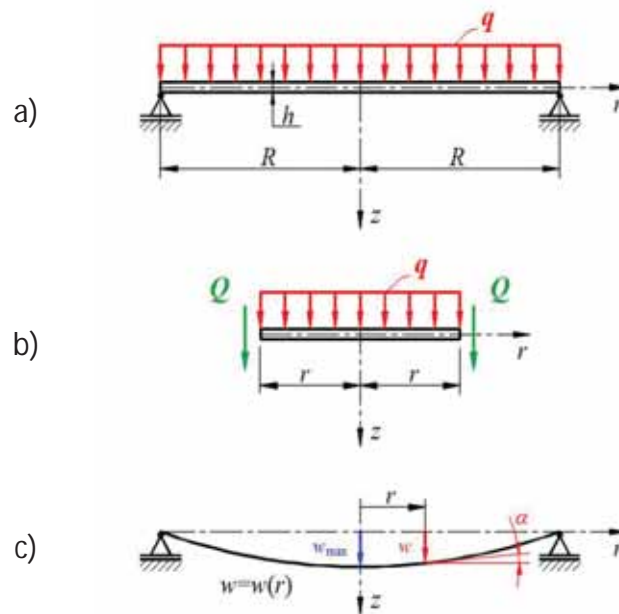
Figure 3. Bending of thin circular plate [4]: a) simply supported on the edge, b) internal transverse forces and c) elastic bending lines

Internal transverse force Q will be determined from the equilibrium condition for the radius r of the plate element according to Figure 3b

$$\sum F_z = 2r\pi Q + r^2\pi q = 0,$$ (1)

where follows

$$Q = -\frac{1}{2}qr.$$ (2)

The differential equation of bending the thin circular plate [4] is as follows

151

$$\frac{\Box}{\Box r}\left[\frac{1}{r}\frac{\Box}{\Box r}\left(\alpha\cdot r\right)\right]=\frac{Q}{\ },\qquad\qquad(3)$$

where D is flexural stiffness of the thin plate expressed by expression

$$=\frac{\Box}{12\left(1-v^2\right)}.\qquad\qquad(4)$$

Rotation of the normal to the elastic line is represented by an angle α, which is variable in the radial direction [4] determined by the following expression

$$\alpha=-\frac{\Box}{\Box r}\qquad\qquad(5)$$

and represents the slope of the tangent to the elastic line (Figure 3c).

Inserting equations (2) and (4) into the equation (3), followed by its integration, and inserting two boundary conditions bring the expression for angle α: (i) complete plate (for $r=0 \to \alpha=0$) and (ii) there is no the bending moment on the outer edge (for $r=R \to M_r =0$).

The necessary information about vertical displacement (deflection) w could be define by rearranging equations (5) and by including the boundary condition of inability of deflection on the outer plate edge (for $r=R \to w=0$). It is known that on the center of the plate the vertical displacement is maximal, as shown by the following expression

$$_{\mathbf{max}}=\frac{\Box+v}{1+v}\cdot\frac{q\cdot\ ^{\Box}}{\Box\cdot}.\qquad\qquad(6)$$

Incorporating all known values for the material (E, v), the load ($q=F/(R^2\pi)$) and the geometry of the plate (D and h), the analytical solution of the maximal vertical displacement is achieved. The material used in this analysis is a ductile cast iron of the following characteristics: $E=158579.412$ N/mm^2, $v=0.275$.

Terms of normal stresses [4] in the radial (σ_r) and circular (σ_φ) direction are expressed with the following expressions:

$$\sigma_r=\frac{\ }{1-v^2}\left(\frac{\Box\alpha}{\Box r}+v\frac{\alpha}{r}\right)z,\qquad \sigma_\varphi=\frac{\ }{1-v^2}\left(\frac{\alpha}{r}+v\frac{\Box\alpha}{\Box r}\right)z.\qquad(7)$$

NUMERICAL SIMULATION

The analysis of the circular manhole covers was being conducted by software package Autodesk Simulation Mechanical [3] based on the finite element method.
The task of this paper was to analyse the influence of ribs on strength of circular manhole cover in three variants of circular plates:

    (I) thin circular plate without ribs (Figure 4a),

(II) thin circular plate with two circular ribs added on the bottom side: lower on the outer circumference and higher on one third of radius (Figure 4b),

(III) thin circular plate with seven radial ribs connected with the circular ribs on the bottom side (Figure 4c).

Figure 4. Circular manhole cover: a) Variant I, b) Variant II, c) Variant III

In numerical analysis it is not necessary to model the entire manhole covers in all three variants. Variants I and II of the covers are axially symmetric and the analysis can be conducted by the axisymmetric elements [5]. Because of the seven radial ribs in Variant III, this model cover is only axisymmetric on 1/7 of the cover surface. Taking this into account, all numerical analysis was carried out on 1/7 of the model.

All geometries of circular covers was being modeled by the software package Autodesk Inventor Professional [6], and imported to the software package Autodesk Simulation Mechanical [3] to be performed the preprocessing. Imported geometric domain is divided into a network of finite elements on which are associated material properties, natural boundary conditions (q) and geometric boundary conditions shown in Figure 5. Before defining the boundary conditions, it is necessary to set up a cylindrical coordinate system.

$$q = \frac{F}{A} = \frac{F}{R^2 \pi} = 1,4147 \frac{\text{N}}{\text{mm}^2}$$

φ-SYM
$T_\varphi = 0$
$R_r = 0$
$R_z = 0$

φ-SYM
$T_\varphi = 0$
$R_r = 0$
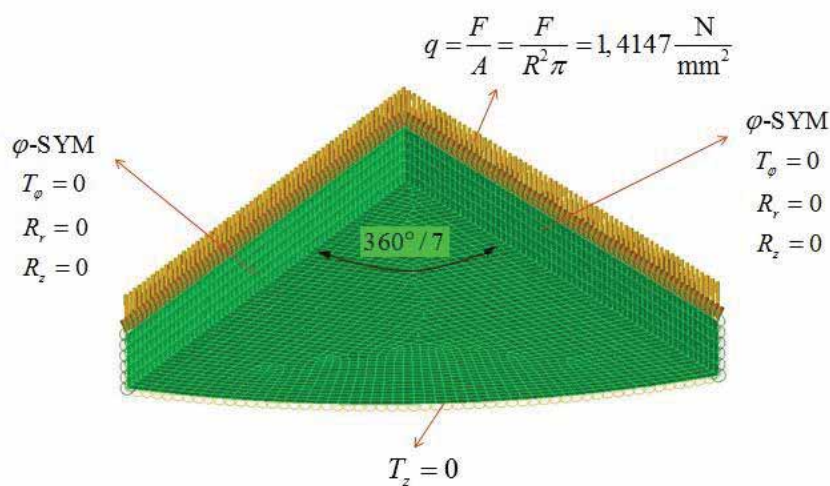$R_z = 0$

$360°/7$

$T_z = 0$

Figure 5. Natural and geometric boundary condition applied on thin circular plate (Variant I)

Load of F=400 kN in the form of pressure q over the entire upper surface of circular manhole cover is added (Figure 5) and the following boundary conditions are defined as follows: (i) at the outer bottom periphery edge the condition of prevented displacement in z direction (T_z=0) and (ii) based on a cylindrical coordinate system at the radial sections the boundary conditions of φ-symmetry (T_φ=0, R_r=0 and R_z=0).

The program offers to the user the choice of variety of materials. Selected material used in present analysis is the ductile cast iron (60-41-18 ductile iron quality according to ASTM A-536) of the following mechanical properties: E=158579.412 N/mm^2, v=0.275, R_m=414 N/mm^2 and $R_{p0.2}$=276 N/mm^2.

In the numerical simulations the equivalent stresses based on the energy theory of strength were monitored [7]. After preprocessing, the three-dimensional linear static analyses of all three variants of cover are performed. The results of these analyses in the next section are presented.

The design process has to ensure that the maximum calculated stress is less than the allowable stress. In this paper the allowed stress is calculated according to Ref. [8], taking into account the safety factor of f_s=1.5.

RESULTS AND DISCUSSION

Results of numerical analysis of bending of thin circular plate (Variant I) of displacement in the z direction (deflection) and equivalent stress are shown in Figure 6a and 6b, respectively.

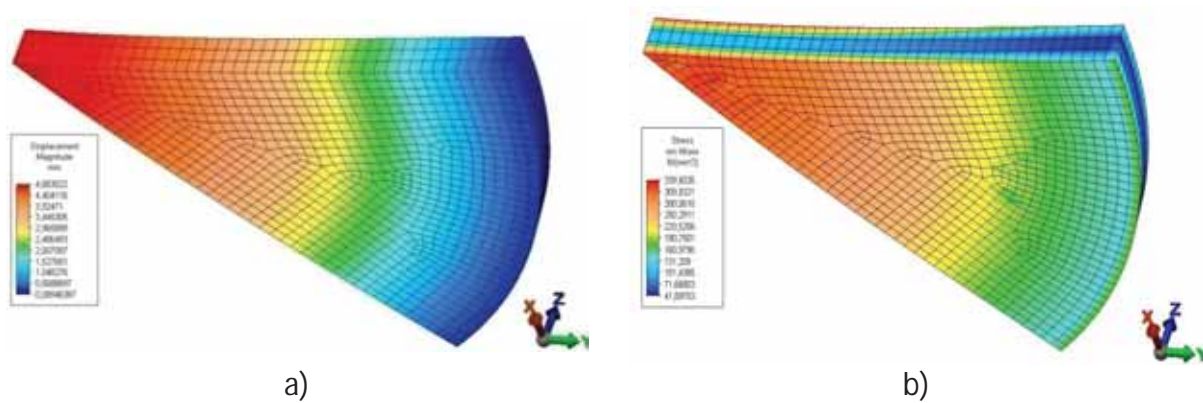a)   b)

Figure 6. Results of vertical displacement (a) and equivalent stress (b) for bending of thin circular plate (Variant I)

It is apparent that deflection and equivalent stress are greatest in the center of the plate. Results of radial and circular stresses are presented in Figure 7a and 7b, respectively.
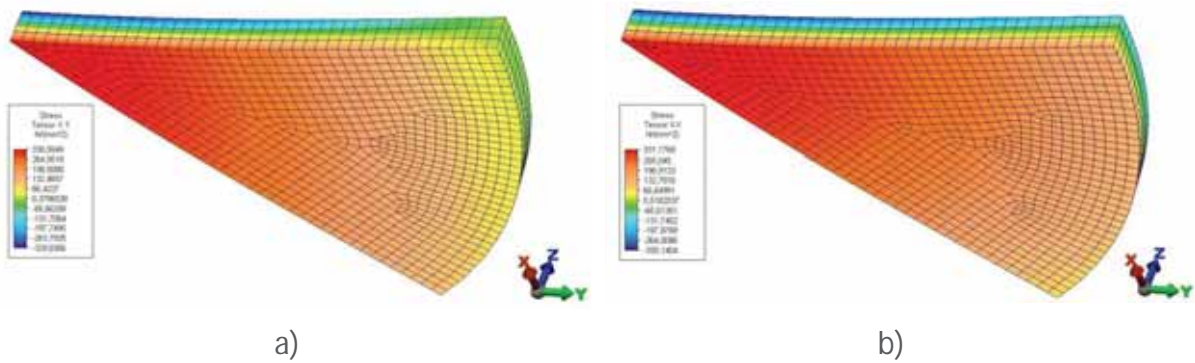
Figure 7. Results of radial (a) and circular (b) stresses for bending of thin circular plate (Variant I)

Analytical and numerical solutions for maximal deflection and maximal radial and circular stresses are compared in Table 1. Numerical analysis was verified by analytical solution.

Table 1. Comparison of analytical and numerical solutions for bending the thin circular plates

	Analytical solution	Numerical solution
w_{max}, mm	4.87	4.88
σ_r, N/mm^2	±323.08	+330.60 -329.84
σ_φ, N/mm^2	±323.08	+331.18 -330.14

The maximal equivalent stress, obtained numerically using the energy theory of strength (von Mises), is 339.60 N/mm^2 (Figure 6b). It could be seen that in case of the analysis of Variant I (Figure 4a) the condition of strength is not achieved. For this reason, two circular ribs are added on the bottom side of existing thin circular plate (Figure 4b, Variant II).

Results of numerical analysis of bending of circular manhole cover with two circular ribs (Variant II) of displacement in the z direction and equivalent stress are shown in Figure 8a and 8b, respectively.
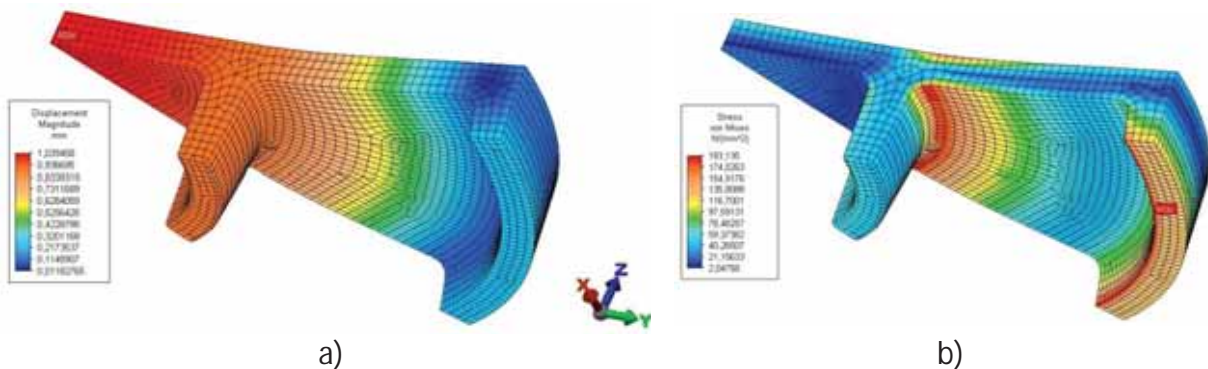

Figure 8. Results of vertical displacement (a) and equivalent stress (b) for bending of circular manhole cover with two circular ribs (Variant II)

As can be seen, the maximal equivalent stresses are lower in comparison to the thin circular plate without ribs and they are moved closer to the center of the plate, but their values are still above the allowable stress.

As the results of the previous two cover designs (Variant I and II) did not satisfy the requirements of strength, i.e., the obtained results of equivalent stresses were greater than the allowable stress in both cases of covers, the structure with seven radial ribs was reinforced.

Results of numerical analysis of bending of circular manhole cover with two circular and seven radial ribs (Variant III) of deflection and equivalent stress are shown in Figure 9a and 9b, respectively.

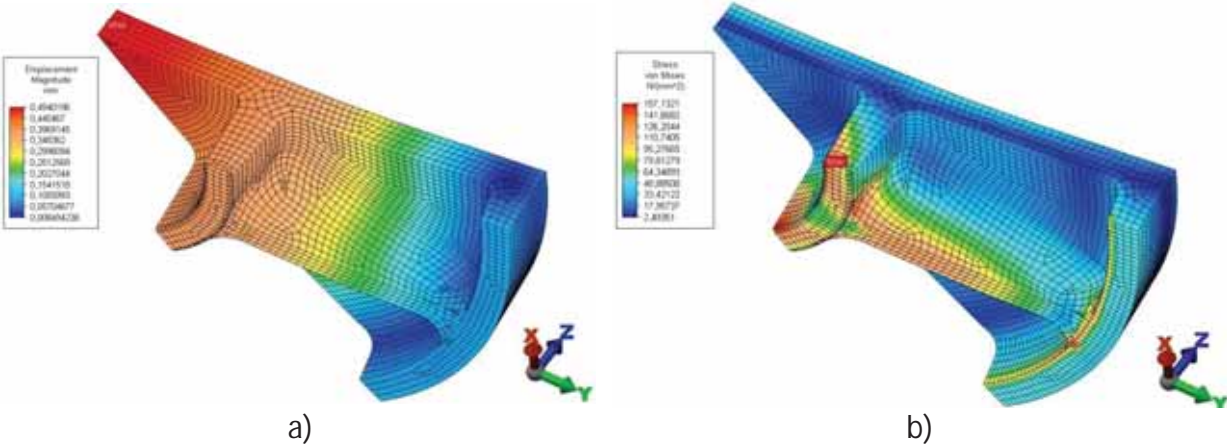a)   b)

Figure 9. Results of vertical displacement (a) and equivalent stress (b) for bending of circular manhole cover with two circular and seven radial ribs (Variant III)

All numerical values of the maximal deflection w_{max} and the maximal equivalent stress σ_{max} for bending three variants of circular covers are presented in Table 2.

Table 2. Comparison of results of the maximal deflection and the maximal equivalent stress for bending three variants of circular covers

	w_{max}, mm	σ_{ekv}, N/mm^2
Variant I	4.88	339.60
Variant II	1.04	193.14
Variant III	0.49	157.1

Based on the presented results in Table 2 a significant reduction of the maximal deflection at variants of circular covers with ribs in relation to the Variant I are achieved. Maximal deflection of Variant II is 78% lower in comparison to the Variant I, and maximal deflection at Variant III is about 90% lower in comparison to Variant I. Maximal deflection of Variant III is about 53% lower in relation to Variant II.

Based on the Table 2, the same analysis can be applied for equivalent stress. As can be seen, a significant reduction of the maximal equivalent stress at variants of circular covers with ribs in relation to the Variant I. This reduction in the case of circular ribs (Variant II) is 43% lower compared to the circular plate (Variant I), while the reduction in the equivalent

stresses of the circular and radial ribs (Variant III) is 54% lower compared to the circular plate without ribs (Variant I) and 19% lower in relation to the circular plate with circular ribs (Variant II). It is important to note that the equivalent stresses in the plate of Variant I exist in the center of the plate, in Variant II are moved closer to the internal circular rib, and in variant III lower to the top of the circular rib. According to Table 2 and allowed stress of 184 N/mm^2, the condition of strength for Variants I and II is not satisfied, while the condition of strength in Variant III is achieved.

Manhole covers are more often made from gray cast iron as they have lower price than ductile cast iron. For this reason, a numerical analysis was performed for the third design of the manhole cast (Variant III) of gray cast iron. The selected material for numerical simulation is gray cast iron ASTM A-48 Grade 30, which has according to Autodesk Simulation Mechanical [1] material database the following mechanical properties: E=101490.827 N/mm^2, v=0.253, R_m=275 N/mm^2 , $R_{p0.2}$ = 214 N/mm^2.
After performed analysis, the numerical solutions of the maximum deflection of 0.85 mm and equivalent stress of 163.75 N/mm^2 were obtained. These results satisfy the strength conditions, i.e. the resulting equivalent stress is lower than the permitted.

By comparing the results of the numerical analysis for Variant III of cover obtained by casting the different irons (gray and ductile), it could be notice the following: there is no difference in the result of equivalent stresses, while the increase of the deflection of the gray cast cover is 73% larger than at the ductile cover. Although the ductile casting shows better results due to the materials properties in relation to gray casting, it could be concluded that the cover design itself has stronger effects on stresses and deflection.

CONCLUSIONS

The task of this paper was to analyse the influence of ribs on strength of circular manhole cover in three variants of thin circular plate:

- thin circular plate without ribs (Variant I),
- thin circular plate with two circular ribs added on the bottom side: lower on the outer circumference and higher on one third of radius (Variant II).
- thin circular plate with seven radial ribs connected with the circular ribs on the bottom side (Variant III).

Numerical solution for bending thin circular plate (Variant I) is compared with analytical solution. For Variant II and III of manhole cover numerical simulation of bending are conducted.

It is important to note that the equivalent stresses in the plate of Variant I exist in the center of the plate, in Variant II are moved closer to the internal circular rib, and in variant III lower to the top of the circular rib. By incrementally adding the ribs on the bottom side of the thin circular plate, the maximum deflection at the centre of the plate is smaller ($w_{max,I}$ > $w_{max,II}$ > $w_{max,III}$).

For the same constructional design of circular manhole cover in Variant III, the same numerical analysis for differently selected materials ductile cast iron (quality 60-41-18 to ASTM A-536) and gray cast iron (grade Grade 30 according to ASTM A-48) was performed. The circular manhole cover made in Variant III from the different cast iron meets the

condition of the strength, but better results with regard to the deflection shows the ductile cast.

REFERENCES

[1] S. El Haggar, L. El Hotow, Reinforcement of thermoplastic reject in the production of manhole covers, Journal of Cleaner Production, 17(2009), pp. 440-446.

[2] Kanalska galanterija (HRN EN-124:2005), Accessible on Internet: http://www.aqua-invest.hr/images/stories/down/kanalska_galanterija.pdf, March 30th 2017.

[3] Autodesk Simulation Mechanical: Tutorial, Accessible on Internet: https://knowledge.autodesk.com/support/simulation-mechanical, March 30th 2017.

[4] I. Alfirević, Nauka o čvrstoći II, Golden marketing, Zagreb, 1999.

[5] J. Sorić, Metoda konačnih elemenata, Golden marketing–Tehnička knjiga, Zagreb, 2004.

[6] Autodesk Inventor Professional: Tools and Design, Accessible on Internet: http://www.sdcpublications.com/pdfsample/978-1-58503-958-6-7.pdf, March 30th 2017.

[7] I. Alfirević, Nauka o čvrstoći I, Tehnička knjiga, Zagreb, 1989.

[8] I. Vitez, Ispitivanje mehaničkih svojstava metalnih materijala, Sveučilište J. J. Strossmayera u Osijeku, Strojarski fakultet u Slavonskom Brodu, Slavonski Brod, 2006.

ANALYSIS OF THE MICROSTRUCTURE OF THE PISTON MADE OF ALUMINUM PISTON ALLOYS

Srećko Manasijević[1], Zdenka Zovko **Brodarac**[2], Natalija **Dolić**[2],
Mile **Djurdjević**[3], Radomir **Radiša**[1]

[1]LOLA-Institute, Belgrade, Serbia
[2]University of Zagreb Faculty of Metallurgy, Sisak, Croatia
[3]Nemak Europe, Linz, Austria

Abstract

This paper presents the results of testing the microstructure of pistons made of aluminum piston alloys. The phase stoichiometry was identified by comparing the results of EDS analysis with the results reported in the studied literature. The results show that different intermetallic phases can appear depending on the chemical composition of the microstructure of aluminum piston alloys.

Keywords: _piston, aluminum piston alloys, aluminum multicomponent alloys, intermetallic phases_

*Corresponding author (e-mail address): _srecko.manasijevic@li.rs_

INTRODUCTION

Piston alloys are a special group of industrial aluminum alloys that have good mechanical properties at elevated temperatures (approximately up to 350 °C) [1], and are resistant to sudden temperature changes [1]. During exploitation, these alloys are exposed to the aggressiveness of the environment in which they are used [1]. Typical aluminum piston alloys are very complex with respect to their chemical composition and the obtained structures. Different piston alloys have various contents of major and minor alloying elements. The usual ranges for some of the alloying elements used by the well-known manufacturers of pistons KS Kolbenschmidt GmbH and MAHLE GmbH from Germany and the local Concern PDM Mladenovac, Serbia are: 11–23 wt. % Si; 0.5–3 wt. % Ni; 0.5–5.5 wt. % Cu; 0.6–1.3 wt. % Mg; up to 1.0 wt. % Fe and up to 1 wt. % Mn [1–4].

Piston alloy microstructure can be very different. It is not accidental, but rather caused by the strictly defined rules. The microstructure is caused, on the one hand, by the chemical

composition of the alloy and solidification method and, on the other hand, by heat treatment. In the piston alloys there are at least six elements (Al, Si, Cu, Ni, Mg and Fe), which have a significant impact on the solidification path of these alloys. Interactions among them create different phases and intermetallics, the shape and distribution of which in the as-cast and heat-treated alloys depend on the corresponding process parameters. Al–Si piston alloys have different structure depending on the content of silicon and other alloying elements. The results of previous tests show dependence between the combination of alloying elements, casting conditions and heat treatment given to different microstructures [1–5]. The structural composition of material has a direct impact on the physical and mechanical properties of the casting.

The shape, distribution and dispersion of microconstituents in the microstructure is not the same in all sections of the piston casting and piston casting manufacturers strive to create the necessary conditions for forming the needed microstructure in the desired section that provides optimal properties. The zones subjected to greater strain during exploitation (piston pin boss and rings groove) need to have greater resistance to plastic deformation. This requires a fine grain structure in these zones. A fine grain structure can accumulate a larger quantity of energy [4,6].

The structure of the material directly affects the physical and mechanical properties of a casting. The main goal of the paper is, it is necessary to define and describe the macro and microstructure, both in terms of quality and quantity.

MATERIALS AND METHODS

The tests were performed on an Ø89 mm piston used for OM604 diesel engine with turbocharger. The mass of the tested piston casting with a pouring system and feeder is 1275 g and the mass of the casting is 868 g (Fig. 1).
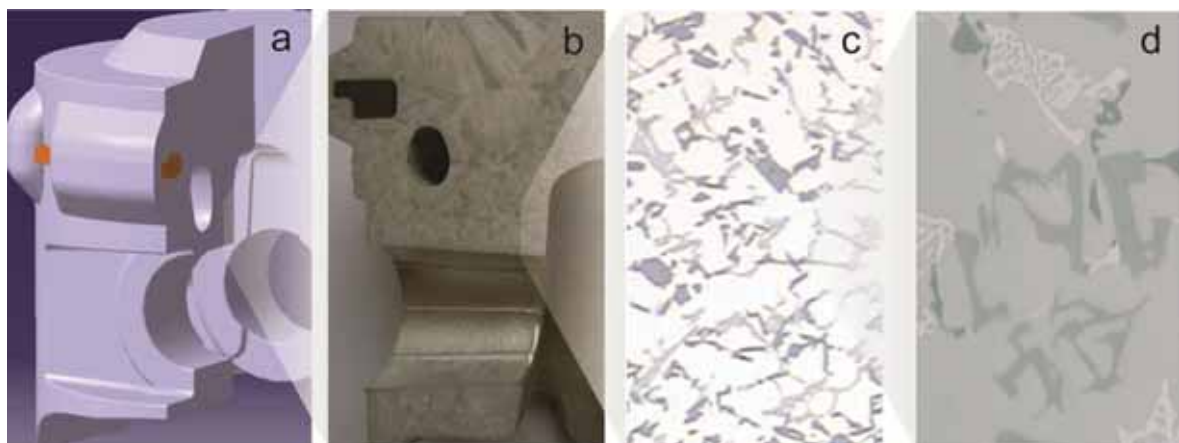

Figure 1. The piston casting: a) CAD model, b) macrostructure, c) microstructure and d) SEM

The experiment was conducted by producing a sample piston made of aluminum alloys of the chemical composition given in Table 1.

160

Table 1. Nominal chemical composition of the experimental alloy

Alloys	Chemical composition (wt. %)										
	Si	Cu	Ni	Mg	Fe	Mn	Cr	Ti	Zr	V	Al
A	13.12	1.11	0.89	0.85	0.59	0.18	0.09	0.07			
B	13.05	3.58	1.01	0.90	0.52	0.19	0.09	0.07	≈0.03	≈0.01	residual
C	11.20	5.41	2.09	0.53	0.37	0.25	0.09	0.07			

In order to improve its mechanical properties, the piston casting was subjected to certain treatments (refining, modification and degasification processes) during its preparation. All three operations were performed at 725±5 °C. The temperature of liquid casting was measured using a Ni–Cr–Ni digital pyrometer.

The investigated pistons were cast in the semi-automatic machines under industrial conditions in Concern PDM, Serbia. The casting was done in a metal mold within the defined internal procedures of the piston manufacturer.

An optical microscope (Olympus GX51) with magnification up to 1000x was used for visualizating and collecting data for determining the material microstructure. Sample micrographs were acquired by an Olympus DP70 color digital camera (12.5 mega-pixel resolution). Metallographic samples were cut out from the piston, polished and electrolytically etched in a HF reagent for 15 sec. The samples were observed under a scanning electron microscope (SEM) TESKAN VEGA TS5136LS using magnifications between 200x and 5000x. Qualitative and quantitative assessments of the chemical compositions of phases were done using an energy dispersive spectrometer (EDS, Bruker).

RESULTS AND DISCUSSION

The following can be observed in the microstructure of all investigated aluminum piston alloys by using the light optical micrographs: an Al-matrix (white), primary Si (blue) and different gray tones: multicomponent phases containing Al, Mg, Cu, Ni, Si, Fe and Mn (Fig. 2). Primary silicon crystals are clearly visible under an optical microscope in all 3 investigated alloys.
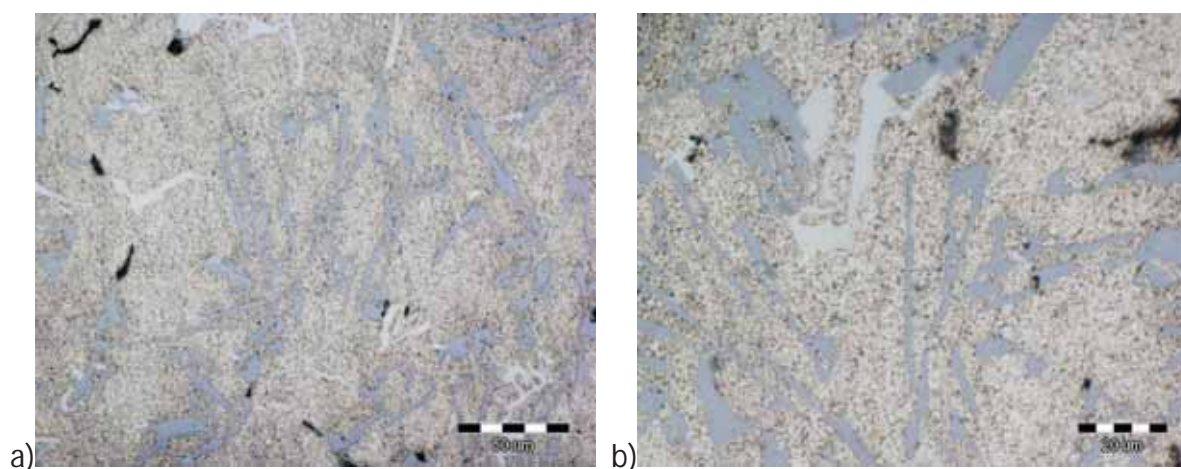

a)   b)

Figure 2. Microstructure of alloy B, a) 200x and b) 500x

The investigated alloys are of approximately eutectic composition. The identification of possible intermetallic phases as well as the solidification process has been defined by Belov [3], Manasijevic [1] and other authors [11] in their published papers.

Primary silicon crystals are clearly visible under an optical microscope. Identification of other complex intermetallic phases present is not possible using optical microscopy, so a SEM was used in this case, which is capable of identifying other phases in combination with EDS. Each phase has its own key elements, as given in Table 2. Additionally, EDS mapping also provides useful information to predict the possible phases where the key elements show higher contrast.

Table 2. Key elements in various intermetallic phases

□□□□□□	□ □□□	□□□□	□ □□□	□□□□-□□	□□□□□□	□□□□₂□ □-□□
□□□ □□□□ □□□ □□□□□□, □□□ □,□□	□2 □□	□2.□□□	□□2 □□ □□.□□□□	38.5–50.7 Cu 11.8–22.2 Ni	4.5–14.0 Fe 18–28 Ni	20.□□□, □1.1 □□ □2.□□□
□□□ □□□ □□□□□,10□	□□	□□	□ □	□□,□□□	□□	□ □, □□

In the previous papers available, the authors have shown that, at approximately 554–530 °C, the Mg_2Si and $Al_8Mg_3FeSi_6$ phases begin to precipitate in Al–Si alloys. At approximately 530–503 °C, a "massive" or "blocky" Al_2Cu phase (containing approximately 52.5 wt.% Cu) forms together with β-Al_5FeSi platelets, while at approximately 515–503 °C, a fine Al-Al_2Cu eutectic phase forms (containing approximately 24 wt. % Cu). If the melt contains more than 0.5 wt. % Mg, an ultra-fine $Al_5Mg_8Cu_2Si_6$ eutectic phase also forms at this temperature. This phase grows from either of the two previously mentioned Al_2Cu phases [1–3]. These phases have been identified in the microstructure of all of the investigated the piston alloys. Fig. 3a shows a SEM analysis of the alloy A, where 3 phases are visible: primary crystals of Si (1), Al_2Cu (2) and Mg_2Si (3). The Fig. 3b shows EDS spectra for the phase identified. The EDS results were used to identify the stoichiometry for the particular phases based on the data reported in the literature.
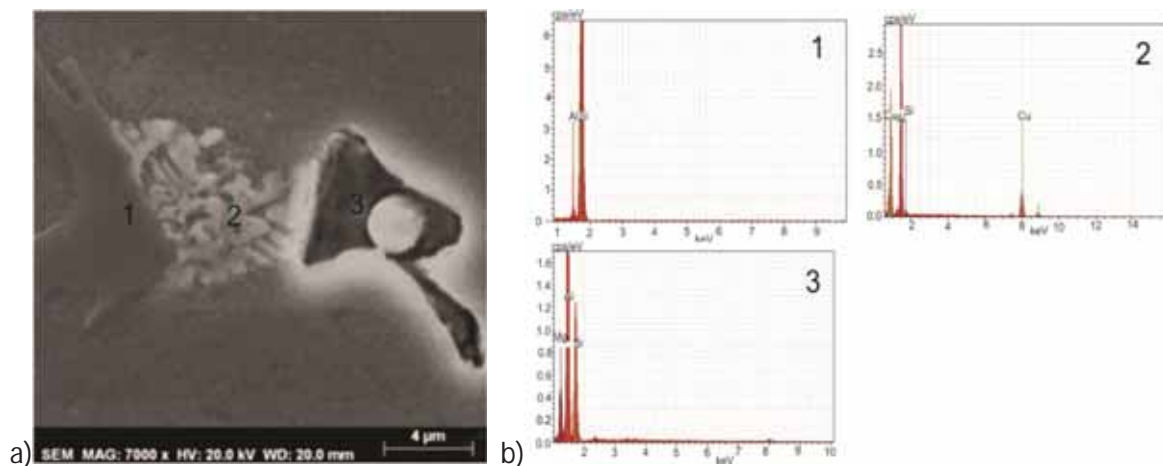

Figure 3. The alloy A: a) SEM and b) EDS

In addition to the presented phases in the microstructure of Al-Si piston alloys, phases formed by Cu and Ni have been identified. The Fig. 4a shows the microstructure of alloy C,

where EDS mapping was done in addition to characterization by SEM microscopy in order to better identify the phases. The Figure shows the SEM analysis of the microstructure of alloy C from Table 1 and EDS mapping of all elements.

Fig. 4b shows a qualitative analysis of the phases conducted by EDX scanning electron microscopy of the marked zone (I) in Fig. 4a. Based on the conducted analysis (the results are given in Fig. 4 and in Table 3) and using key elements (Table 2), the phases present in the microstructure were identified as follows: Al_3Ni (1), Al_9FeNi (2), Al_9FeNi (3) and Al_5FeSi (4).
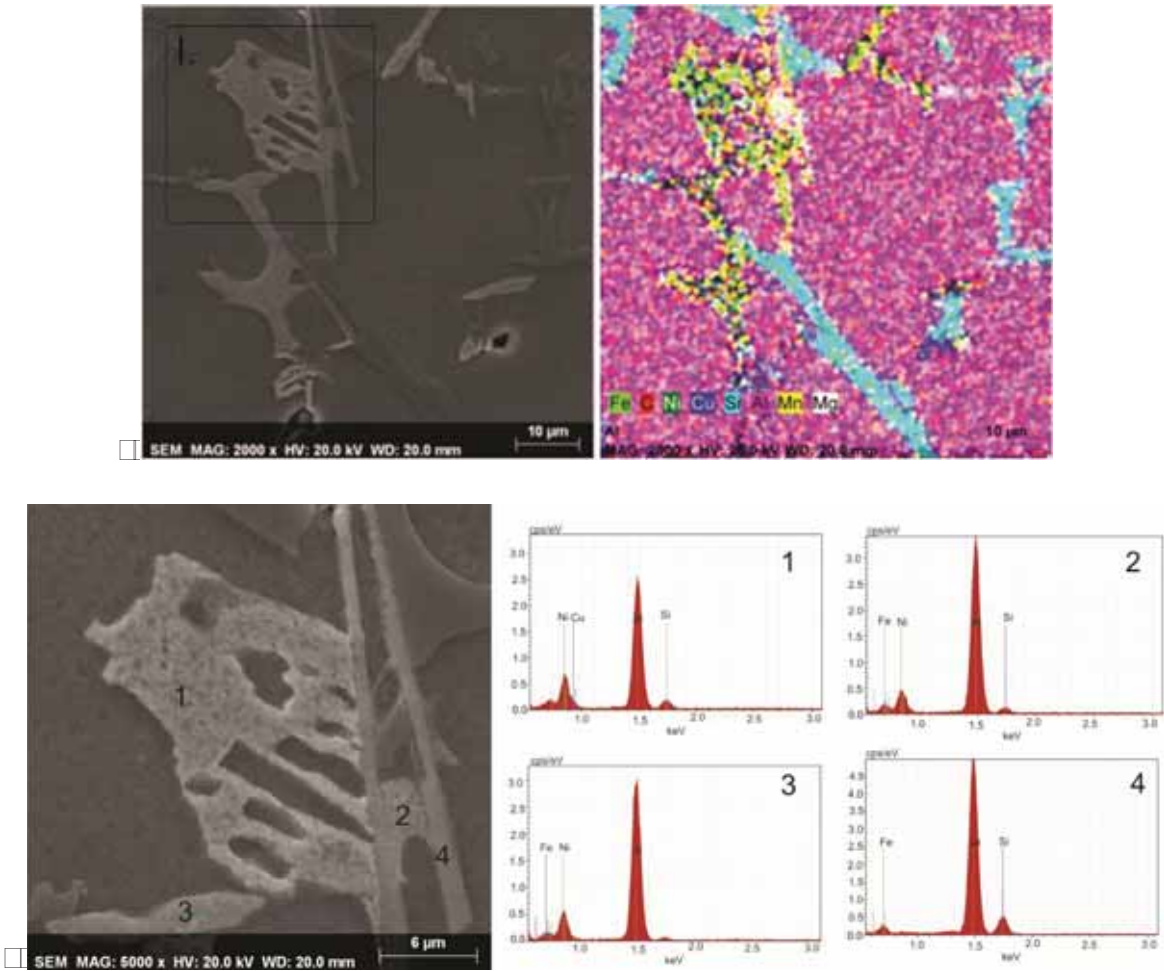

Figure 4. The alloy C: a) SEM with EDS mapping of all elements and b) SEM of the marked zone (I) with EDS

An additional SEM observation combined with X-ray spot microanalysis for the investigated alloy was performed to identify the morphology and stoichiometry of the observed Cu enriched phases. This analysis confirmed the earlier assertion that Cu enriched phases appear in three main morphologies: blocky, eutectic type and fine eutectic type. The Fig. 5 shows the microstructure of piston alloy B, where EDS mapping was done in addition to characterization by SEM microscopy.
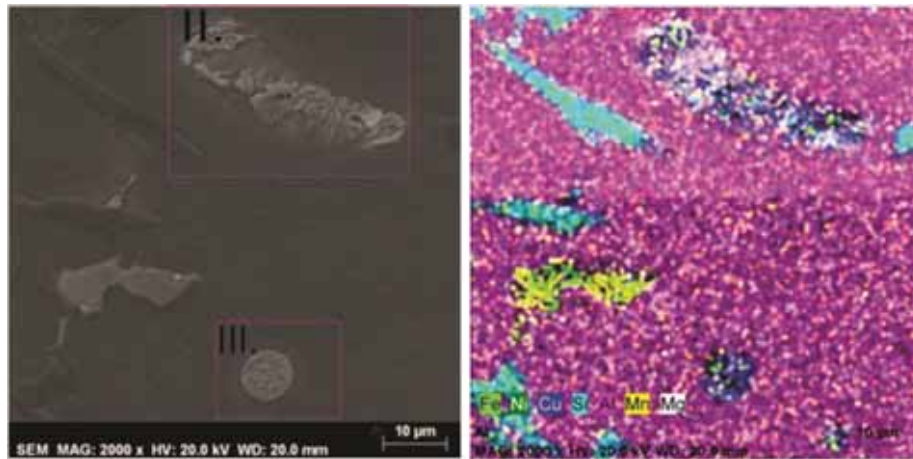
Figure 5. SEM micrographs with characteristic morphology of Cu enriched phases and EDS mapping [12]

Fig. 5 shows a SEM microstructure analysis, and EDS mapping of other key elements. The following are SEM micrographs with characteristic morphology of Cu enriched phases found in the investigated alloys: eutectic type (II, phase Al_7Cu_4Ni.) and fine eutectic type (III, phase Al_2Cu).

Fig. 6a shows fine eutectic type Al_2Cu phase, whose EDS analysis is given in Fig. 6b. The results of the EDS analysis of the Al_2Cu phase are given in Table 3.
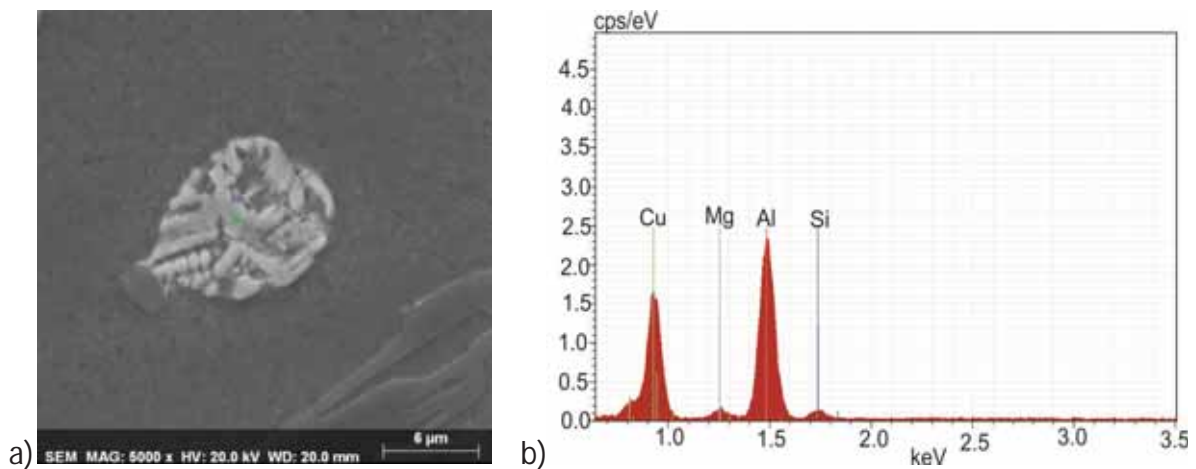

Figure 6. Al_2Cu phase: a) SEM and b) EDS analysis [12]

The typical composition of the Al_2Cu phase given in Table 3 contains higher Cu and extremely low Ni contents. This phase is largely different in crystal structure and chemical composition compared with the Al_3Ni_2 and Al_7Cu_4Ni phases, making the identification easier. The next phase that appears is Al_9FeNi.

Table 3. Typical composition of various intermetallic phases observed in the alloy [12]

Phase	Composition, wt.%						Figs.
	Al	Si	Cu	Ni	Mg	Fe	
Si	3.86		95.99				Fig. 1. Fig.2.
Al_2Cu	46.55		48.32				Fig.3. Fig. 6.
Mg_2Si		34.51			62.24		Fig.3.
		33.07			61.78		
Al_9FeNi	73.39			13.58		8.33	Fig.4.
	59.79			25.78		12.16	
Al_5FeSi	9.73	9.73				23.24	Fig.4.
Al_3Ni_2	40.96		32.96	23.16			
	32.76		32.32	33.79			
Al_3Ni	52.42			36.56			Fig.4.
Al_7Cu_4Ni	43.24		44.08	11.55			
	44.37		41.13	17.50			
$Al_5Cu_2Mg_8Si_6$		31.82	20.00		31.32		
		30.51	21.98		31.79		

It is characterized by high chemical content of Ni and key element Fe (Table 2), as can be seen in Table 3. The Al_7Cu_4Ni phase forms in equilibrium with aluminum, and some copper can replace nickel in Al_3Ni_2 [2,5–8]. The ternary phase has a range of existence, with a structure that varies with composition and the dissolved copper controls the lattice parameter; nickel has little or no effect [2,5].

Taking into account that the Si crystals are a primary phase in eutectic and hypereutectic piston alloys, the sequence of solidification is: L→(Si), L→(Al)+(Si), L→(Al)+(Si)+Y and L+Y→(Al)+(Si)+Y, where Y is: (ε-Al_3Ni, θ-Al_2Cu, M-Mg_2Si, δ-Al_3CuNi(Al_3Ni_2), γ-Al_7Cu_4Ni, T-Al_9FeSi, β-Al_5FeSi, π-$Al_8FeMg_3Si_6$ and Q-$Al_5Cu_2Mg_8Si_6$) [1–5]. Based on the previous studies of all authors, it has been shown that only these phases may be present in the casting made of Al–Si piston alloys. Based on the presented analysis of investigated aluminum piston alloys from Table 1, the phases present in the investigated alloys were defined (Table 4).

Table 4. The phases present in investigated alloys

Alloys		
A	B	C
(Si), (Si)+(Al), γ, θ	(Si), (Si)+(Al), δ, M, γ, Q, θ	(Si), (Si)+(Al), ε, δ, γ, Q, θ

CONCLUSIONS

This paper presents the results of research on multiphase aluminum alloys in the vicinity of eutectic contents, the microstructure of which consists of a larger number of complex phases.

Based on the analysis of the experimental test results presented in this paper and the available data from the literature, it could be concluded that it depends on the Ni/Cu ratio which of the above phases (Al_3Ni_2, Al_7Cu_4Ni and Al_2Cu) will be formed. By increasing the Ni content at the expense of Cu, the phase formation goes in the direction of $Al_3Ni_2 \rightarrow Al_7Cu_4Ni \rightarrow Al_2Cu$ (or in reverse) [12].

The results presented in this paper are only an introduction to further ongoing research.

REFERENCES

[1]   S. Manasijevic, R. Radisa, S. Markovic, Z. Acimovic-Pavlovic, K. Raic, Thermal analysis and microscopic characterization of the piston alloy AlSi13Cu4Ni2Mg, Intermetallics, 19(2011)2, pp. 486-492.

[2]   R. Gholizadeh, S. G. Shabestar, Investigation of the effects of Ni, Fe, and Mn on the formation of complex intermetallic compounds in Al–Si–Cu–Mg–Ni alloys, Metallurgical and Materials Transactions A, 42(2011), pp. 3447-3458.

[3]   N. Belov, D. Eskin, N. Avxenieva, Constituent phase diagrams of the Al–Cu–Fe–Mg–Ni–Si system and their application to the analysis of aluminum piston alloys, Acta Materialica, 58(2005), pp. 4709-4722.

[4]   M. Zeren, The effect of heat treatment on aluminum-based piston alloys, Materials and design, 28(2007) pp. 2511-2517.

[5]   S. Manasijevic, Aluminum Piston Alloys, Monograph ISBN 978-86-912177-1-6, print: Development Research Center of Graphic Engineering of the Faculty of Technology and Metallurgy, University of Belgrade, published by LOLA Institute Belgrade, 2012.

[6]   C. L. Chen, R. C. Thomson, Study on thermal expansion of intermetallics in multicomponent Al–Si alloys by high temperature X-ray diffraction, Intermetallics, 18(2010), pp. 1750-1757.

[7]   C. L. Chen, R. C. Thomson, The combined use of EBSD and EDX analyses for the identification of complex intermetallic phases in multi-component Al–Si piston alloys, Journal of Alloys and Compounds, 490(2010), pp. 293-300.

[8]   C. L. Chen, A. Richter, R. C. Thomson, Mechanical properties of intermetallic phases in multicomponent Al–Si alloys using nanoindentation, Intermetallics, 17(2009) pp. 634-651.

[9]   Y. Yang, K. Yu, Y. Li, D. Zhao, X. Liu, Evolution of nickel-rich phases in Al–Si–Cu–Ni–Mg piston alloys with different Cu additions, Materials and Design, 33(2012), pp. 220–225.

[10] Y. Yang, Y. Li, W. Wu, D. Zhao, X. Liu, Effect of existing form of alloying elements on the microhardness of Al–Si–Cu–Ni–Mg piston alloy, Materials Science and Engineering A, 528(2011), pp. 5723-5728.

[11] R. C. Hernández, J. H. Sokolowski, Thermal analysis and microscopic characterization of Al–Si hypereutectic alloys, Journal of Alloys and Compounds, 419(2006), pp. 180–190.

[12] S. Manasijević, N. Dolić, K. Raić, R. Radiša, Identification of Phases Formed by Cu and Ni in Al–Si Piston Alloys, Metallurgia Italiana, 106(2014)3, pp. 13-19.

INFLUENCE OF PRE-DEFORMATION DEGREE ON PROPERTIES OF PM COPPER-PLATINUM ALLOY DURING ISOCHRONAL ANNEALING

Ivana Marković, **Desimir Marković, Dragoslav Gusković, Ljubiša Balanović, Marko Banković**

University of Belgrade Technical Faculty in Bor, Bor, Serbia

<u>Poster presentation</u>
Preliminary note

Abstract

The influence of pre-deformation degree on properties of PM copper-platinum alloy during isothermal annealing has been studied in this paper. Copper based alloy with 6 wt.% platinum was prepared using powder metallurgy (PM) process. PM samples were cold deformed by rolling using 25 % and 60 % deformation degrees. Cold rolled samples were isochronally annealed up to the 450 ^{o}C. During the annealing hardness, microhardness and electrical conductivity were measured; while the microstructure was examined using SEM. Results in this paper presented that PM Cu-6wt.%Pt alloy can be hardened after cold deformation by a suitable low temperature annealing. The amount of hardening during the isochronal annealing increases with increasing the pre-deformation degree.

Keywords: copper-platinum alloy, pre-deformation degree, isochronal annealing, hardening

*Corresponding author (e-mail address): *imarkovic@tf.bor.ac.rs

INTRODUCTION

The Cu-Pt alloys are widely used in industry, especially for hydrocarbon reactions and oxidation of CO to CO_2 [1,2]. According to Cu-Pt phase diagram, these two metals form continuous series of solid solutions [1]. In some concentration areas at lower temperatures, these alloys subject to the order-disorder transformations forming the superstructures of the types: Cu_3Pt, $PtCu_3$ or CuPt [2]. Because of that, the Cu-Pt system has been primarily studied in relations of ordered superstructures [3-5]. There is no study on dilute Cu-Pt alloys or alloys of this system obtained by powder metallurgy (PM) technique. For these reasons, the subject of this paper is a dilute Cu-Pt alloy with 6 wt. % platinum obtained using the PM process. The present investigation gives results of study the influence of pre-deformation degree on properties of PM copper-platinum alloy during an isochronal annealing.

MATERIALS AND METHODS

The starting materials are an electrolytic copper powder and a platinum elemental powder. The powders were mixed using the 3-dimensional mixer Turbula T2F for 2 h. The mixed powders were cold uniaxially pressed with 700 MPa. No lubricant was added during the mixing to prevent eventually uncleanness of the powder mixture [6]. The green compacts were sintered in a tube furnace T-40/600 under the flowing hydrogen atmosphere. The processing parameters of the sintering were: sintering temperature 810 °C, dwell time at sintering temperature 90 min and cooling rate of 5 °C/min. The sintered Cu-Pt samples were multi-pass cold-rolled using a Cavallin Eco 120 rolling mill with the deformation degree for each pass less than 5 %. The final deformation degrees were 25 % and 60 %. After cold rolling with selected deformation degrees, the samples were isochronally annealed for 0.5 h at different temperatures from the temperature interval 100 °C – 450 °C.

The examination of cold rolled microstructures was carried out using a scanning electron microscope (SEM) Tescan Vega 3LMU. The samples were grinded, polished and etched according to the usual metallographic procedure for copper based samples. Vickers hardness/microhardness tests were carried out in deformed and isochronally annealed samples using a WPM-Leipzig/PMT 3 hardness/microhardness tester with a load of 10 kg and 100 g, respectively. Electrical conductivity measurements were completed on polished samples using a Sigmatest 2.063 instrument at frequencies of 60 kHz.

RESULTS AND DISCUSSION

Figures 1a and 1b show the microstructure of the PM Cu-Pt alloy after deformation with 25 % and 60 %, respectively. The fine, equi-axed grains obtained by PM technique were elongated in the rolling direction. Also, it is eminent that the pores are no longer spherical, but stretched in the rolling direction, too.
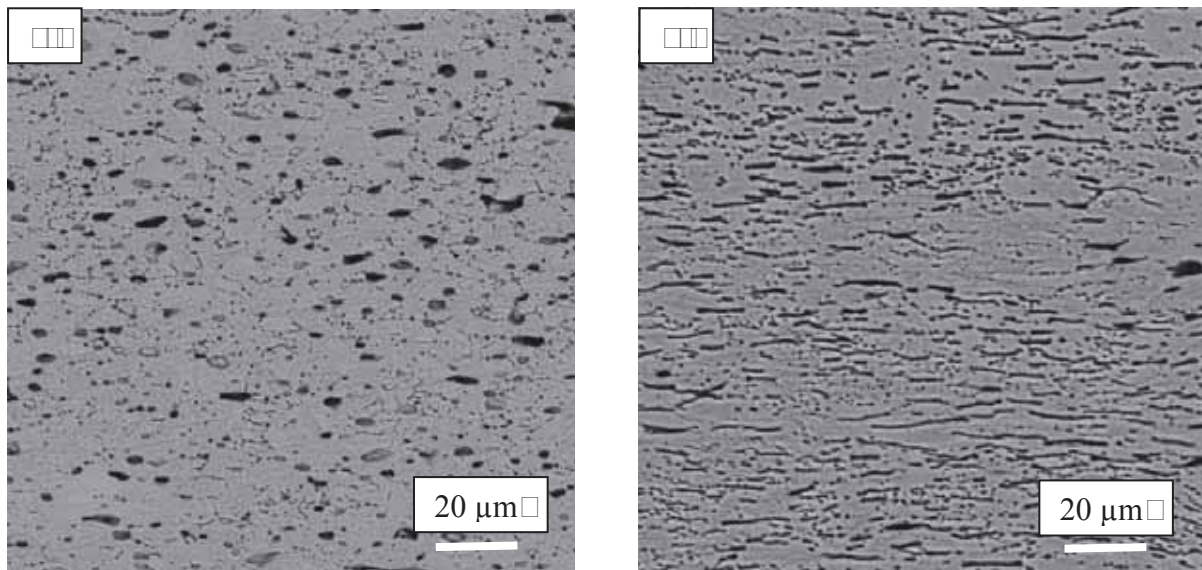

Figure 1. SEM images of PM Cu-Pt alloy after (a) deformation with 25 % and (b) deformation with 60 %

Figure 2 shows the influence of annealing temperature on the hardness values of PM Cu-Pt alloy pre-deformed with 25 % and 60 % degrees, during the isochronal annealing.
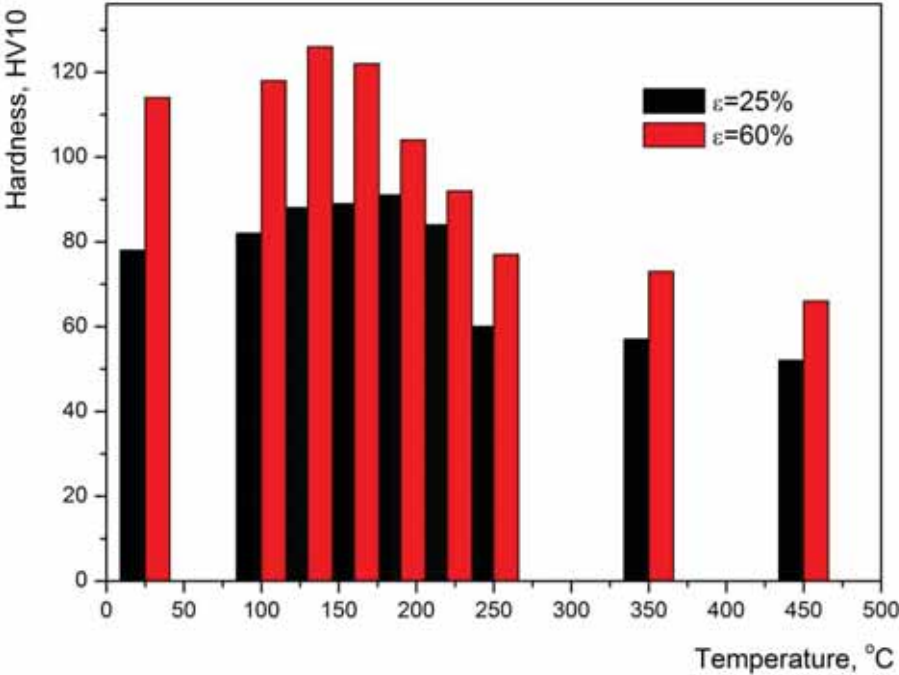

Figure 2. Influence of annealing temperature on the hardness values of PM Cu-Pt alloy pre-deformed with 25 % and 60 % degrees, during the isochronal annealing
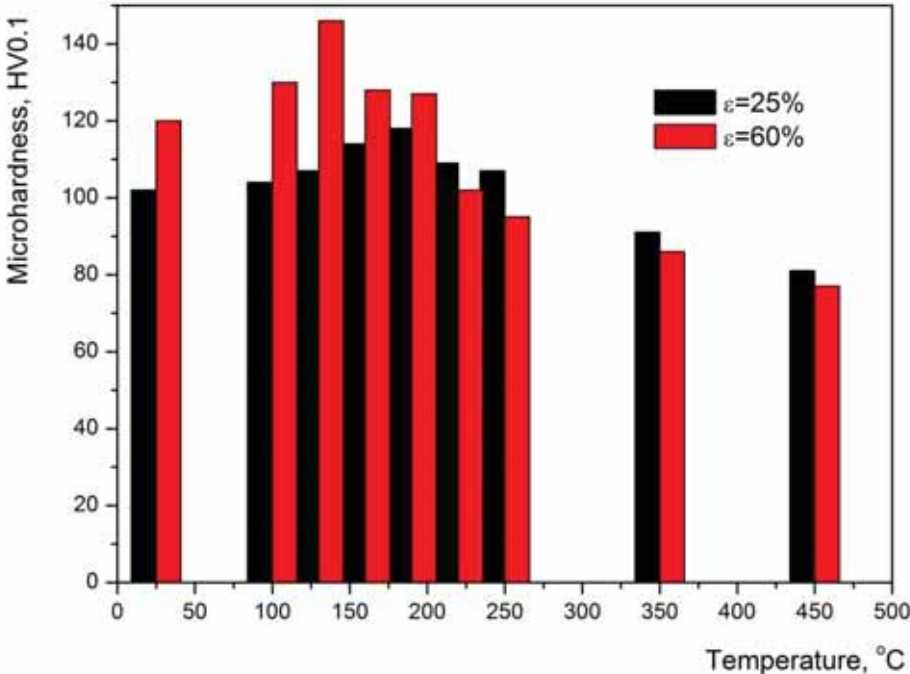

Figure 3. Influence of annealing temperature on the microhardness values of PM Cu-Pt alloy pre-deformed with 25 % and 60 % degrees, during the isochronal annealing

When the pre-deformed PM Cu-Pt alloy is annealed at temperatures in the range of 100 to 200 °C, it harden as a result of the anneal hardening effect [7-9]. The hardness value of the pre-deformed PM Cu-Pt alloy with 25 % reduction is 78 HV10, and during the annealing at 190 °C it increases to 89 HV10. The hardness value of the pre-deformed PM Cu-Pt alloy with 60 % reduction is 114 HV10, and during the annealing at 130 °C it increases to 128 HV10. Hardness of pre-deformed PM Cu-Pt alloy with 25 % and 60 % reductions after isochronal annealing increased for 11 HV10 and 14 HV10 respectively. This approves that the amount of anneal hardening increases with an increase in the reduction of pre-deformation, as some other investigations showed [10,11].

Figure 3 shows the influence of annealing temperature on the microhardness values of PM Cu-Pt alloy pre-deformed with 25 % and 60 % degrees, during the isochronal annealing. It is noticeable from Figure 3 that the relation between the microhardness and the annealing temperature during the isochronal annealing is similar as relation between the hardness and the annealing temperature (Figure 2). The microhardness value of pre-deformed PM Cu-Pt alloy with 25 % reduction was 102 HV0.1 and it increased to 118 HV0.1 after annealing at 190 °C. The microhardness value of pre-deformed PM Cu-Pt alloy with 60 % reduction is 120 HV0.1 and it increases to 146 HV0.1 after annealing at 130 °C. This means that the rolled samples with 25 % and 60 % reduction reach the absolute increase in microhardness of 16 HV0.1 and 26 HV0.1, respectively.

Figure 4 shows the influence of annealing temperature on the electrical conductivity values of PM Cu-Pt alloy pre-deformed with 25 % and 60 % degrees, during the isochronal annealing.
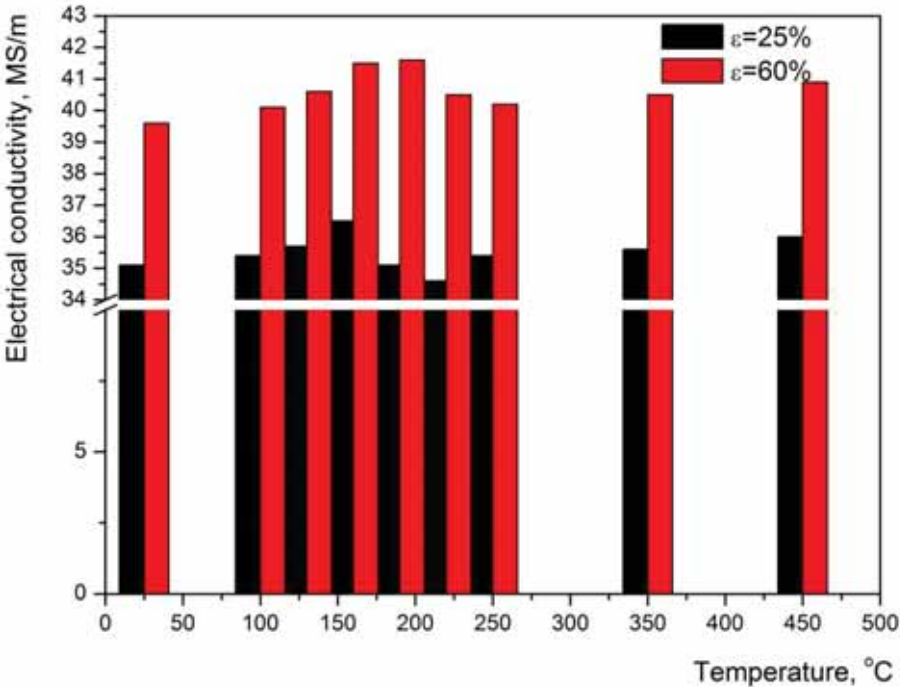

Figure 4. Influence of annealing temperature on the electrical conductivity values of PM Cu-Pt alloy pre-deformed with 25 % and 60 % degrees, during the isochronal annealing

The electrical conductivity of pre-deformed PM Cu-Pt alloy with 25 % reduction increases from 35.1 to 36.5 MS/m after annealing at 160 °C, and then decreases slightly. The electrical

conductivity of the pre-deformed PM Cu-Pt alloy with 60 % reduction is 39.6 MS/m, and during the annealing at 190 $^{\circ}$C it increases to 41.6 MS/m. According to Bader [12], this increase in electrical conductivity indicates a decrease in a number of dissolved platinum atoms in copper based solid solution due to the segregation of platinum atoms at lattice defects.

CONCLUSIONS

Influence of pre-deformation degree on properties of PM copper-platinum alloy during isochronal annealing was described using hardness, microhardness and electrical conductivity measurements, as well as SEM microscopy. The following conclusions can be drawn from this investigation:

- Isochronally annealed alloy showed enhanced all measured properties compared to the pre-deformed alloy.

- The hardness, microhardness and electrical conductivity of pre-deformed alloy continually increased with increasing annealing temperature up to the recrystallization occurrence.

- Increase in properties during the isochronal annealing was more intensive in samples pre-deformed with higher deformation degree.

REFERENCES

[1] E. Arola, C. J. Barnes, R. S. Rao, A. Bansil, M. Pessa, Electronic structure of a Cu75Pt25 disordered alloy, Surface Science, 249(1991), pp. 281-288.

[2] Y. G. Shen, D. J. O'Connor, K. Wandelt, R. J. MacDonald, Studies of surface composition and structure of $Cu_3Pt(111)$ by low energy alkali ion scattering, Surface Science, 328(1995), pp. 21-31.

[3] K. Hisatsune, T. Shiraishi, Y. Takuma, Y. Tanaka, E. Miura, Effect of cold working on ordering of an equiatomic CuPt alloy, Journal of Alloys and Compounds, 391(2005), pp. 38-41.

[4] A. Senhaji, G. Trkglia, B. Legrand, On the various terminations occurring in CuPt-ordered alloys: the TBIM approach, Surface Science, 307-309(1994), pp. 440-444.

[5] S. R. Haines, A. W. Newton, P. Weightman, Evaluation of the surface contribution to disorder broadened core level XPS spectra in CuPd alloys, Journal of Electron Spectroscopy and Related Phenomena, 137–140(2004), pp. 429-434.

[6] L. Bolzonia, E. M. Ruiz-Navasb, E. Gordo, Evaluation of the mechanical properties of powder metallurgy Ti-6Al-7Nb alloy, Journal of the Mechanical Behavior of Biomedical Materials, 67(2017), pp. 110-116.

[7] A. Varschavsky, E. Donoso, Modeling the kinetics of solute segregation to partial dislocations in cold-rolled copper-alloys, Materials Latters, 31(1997), pp. 239-245.

[8] A. Varschavsky, E. Donoso, A calorimetric investigation on the kinetics of solute segregation topartial dislocations in Cu-3.34at%Sn, Materials Science and Engineering A, 251(1998), pp. 208-215.

[9]   A. Varschavsky, E. Donoso, Kinetics of solute flow to partial dislocation in Cu-3.4at.%Sb, Journal of Thermal Analysis and Calorimetry, 57(1999), pp. 607-622.

[10] S. Nestorovic, I. Rangelov, D. Markovic, Improvements in properties of sintered and cast Cu-Ag alloys by anneal hardening effect, Powder Metallurgy, 54(2011)1, pp. 36-39.

[11] S. Nestorovic, Influence of alloying and secondary annealing on anneal hardening effect at sintered copper alloys, Bulletin of Materials Science, 28(2005)5, pp. 401-403.

[12] M. Bader, G. T. Eldis, H. Warlimont, The mechanisms of anneal hardening in Cu-Al alloys, Metallurgical Transactions A, 7(1976), pp. 249-254.

Acknowledgements

INFLUENCE OF MEDIUM AND MICROSTRUCTURE ON CORROSION BEHAVIOR OF NODULAR CAST IRON

UTJECAJ MEDIJA I MIKROSTRUKTURE NA KOROZIJSKO PONAŠANJE NODULARNOG LIJEVA

Sandra Mitić[1], **Anita Begić Hadžipašić**[1], **Gordana Gojsević Marić**[2], Zdenka Zovko Brodarac[1]

[1]University of Zagreb Faculty of Metallurgy, Sisak, Croatia
[2]ELKEM AS, Sisak, Croatia

<u>**Oral presentation**</u>
<u>*Original scientific paper*</u>

Abstract

Due to its high dynamic endurance, tensile strength and high modulus of elasticity, the nodular cast iron is applied in production of parts for agricultural machines. Therefore, in this paper the corrosion resistance of nodular cast irons in the medium of artificial rain and 0.5 M H_2SO_4 medium and the influence of micostructure and number of nodules on their corrosion behavior in the mentioned media was investigated. By Tafel's extrapolation of the polarization curves, it was found that the examined samples show approximately the same values for the corrosion rate in the medium of artificial rain, which means that the number of nodules per unit area has no influence on their corrosion behavior in the artificial rain medium. In opposite of that, in the acidic medium, the nodular cast with a larger number of nodules showed a triple lower corrosion rate in the acidic medium, indicating that the nodules do not represent potential corrosion centres that lead to degradation of corrosion resistance. This is also confirmed by charge transfer resistance values obtained by the electrochemical impedance spectroscopy. Namely, in artificial rain medium, no significant difference was observed in these values, while in the acid medium there was a triple higher value of charge transfer resistance for nodular cast iron with more nodules per unit of surface, which means better corrosion resistance. However, despite all the above, due to the extremely high corrosion rates in the acid medium, the examined nodular cast irons are not recommended for use in a very acidic conditions.

Keywords: nodular cast iron, corrosion rate, impedance, artificial rain, microstructure.

*Corresponding author (e-mail address): *begic@simet.hr*

Sažetak

Nodularni lijev se zbog svoje visoke dinamičke izdržljivosti i vlačne čvrstoće te visokog modula elastičnosti primjenjuje u izradi dijelova za poljoprivredne strojeve. Stoga, u ovom radu je ispitana korozijska otpornost nodularnih lijevova u mediju umjetne kiše i mediju 0.5 M H_2SO_4 te utjecaj mikostrukture i broja nodula na njihovo korozijsko ponašanje u navedenim medijima. Tafelovom ekstrapolacijom polarizacijskih krivulja je ustanovljeno da ispitani uzorci pokazuju približno iste vrijednosti za brzinu korozije u mediju umjetne kiše, što znači da broj nodula po jedinici površine nema utjecaja na njihovo korozijsko ponašanje u mediju umjetne kiše. Nasuprot tome, u kiselom mediju nodularni lijev s većim brojem nodula je pokazao trostruko manju brzinu korozije u kiselom mediju, što ukazuje na činjenicu da nodule ne predstavljaju potencijalne korozijske centre koji dovode do degradacije korozijske otpornosti. To potvrđuju i vrijednosti otpora prijenosu naboja dobivene metodom elektrokemijske impedancijske spektroskopije. Naime, u mediju umjetne kiše nije zamijećena bitna razlika u tim vrijednostima, dok je u kiselom mediju registriran trostruko veći otpor prijenosu naboja za nodularni lijev s više nodula po jedinici površine, što znači i bolju korozijsku otpornost. Međutim, bez obzira na sve navedeno, zbog izrazito visokih vrijednosti brzina korozije u kiselom mediju, ispitani nodularni lijevovi se ne preporučuju za primjenu u jako kiselim uvjetima.

Ključne riječi: nodularni lijev, brzina korozije, impedancija, umjetna kiša, mikrostruktura.

UVOD

Korozija je proces razaranja materijala, koji ima značajan utjecaj na čovjeka i okoliš. Kao jedna od posljedica korozije metala može se istaknuti degradacija mehaničkih svojstava koja dovodi do loma metalnog proizvoda, a time i do velikih gubitaka u industrijskim sektorima [1,2]. Budući da su metali i njihove legure našli vrlo široku primjenu u svijetu, potrebno je konstantno proučavanje njihove korozijske otpornosti, kako bi se ljudske nesreće i materijalni gubici sveli na najmanju moguću razinu.

Metali po svojoj prirodi teže reakciji s drugim tvarima čime odgovarajućim oslobađanjem energije prelaze u stanje niže energije, što dovodi do nastanka pokretačke sile korozije [3]. Korozijski procesi reakcije metala s okolišem mogu se odvijati mehanizmom kemijske ili elektrokemijske korozije [4]. Kemijska korozija metala odvija se u mediju u kojem nije prisutan elektrolit, a elektrokemijska korozija metala zbiva se u elektrolitima, tj. u medijima s ionskom vodljivošću. Najčešće je elektrolit voda koja sadrži otopljeni kisik, soli, kiseline ili baze [1-4].

Elektrokemijska korozija je vrlo raširena, jer je velik broj metalnih strojeva izložen vodi ili otopinama, vlažnom tlu ili vlažnoj atmosferi. Atmosferska korozija nastaje uz oborine, odnosno u vodenom adsorbatu ili kondenzatu koji zbog vlažnosti zraka nastaju na površini metala te na taj način imaju osobine elektrolita [3]. Zbog toga, u mnogim industrijskim postrojenjima koji mogu biti izloženi atmosferskim uvjetima, odnosno medijima različite pH vrijednosti, nastanak korozije stvara veliku štetu u gospodarstvu. Atmosferski utjecaji negativno djeluju na razne strojeve i konstrukcijske elemente koji su u doticaju s oborinama i vlažnim tlom [5]. Naročito su tome izloženi dijelovi poljoprivrednih strojeva kod kojih se skraćuje vijek trajanja, dolazi do zastoja u radu i proizvodnji te se poskupljuje njihovo održavanje.

174

Nodularni lijev se zbog povoljne kombinacije svojstava učestalo primjenjuje u izradi dijelova poljoprivrednih strojeva. Nodularni lijev (eng. Spheroidal graphite cast iron; Ductile iron) je vrsta lijevanog željeza kod kojeg je grafit izlučen u obliku kuglica (nodula) [5,6]. Proizvodnja nodularnog lijeva zasniva se na postupku obrade s Mg osnovne ili bazne taline, odnosno predlegurama, uz naknadno cijepljenje po potrebi ovisno o vrsti nodularnog lijeva. Uloga magnezija je da dezoksidira (MgO) i odsumporava (MgS) talinu pri čemu se mijenja smjer rasta grafita i nastaje grafit kuglastog oblika [6]. Svojstva nodularnog lijeva ovise o mikrostrukturi (obliku, veličini i raspodjeli izlučenog grafita, te strukturi metalne osnove). Zbog nodularnog (kuglastog) oblika grafita, nodularni lijev ima vrlo dobra svojstva, kao što su: visoka dinamička izdržljivost i vlačna čvrstoća, visok modul elastičnosti, može se zavarivati, dobro se obrađuje odvajanjem čestica itd. [6,7]. Također se može potpuno reciklirati. Upravo zbog povoljnih svojstava, proizvodnja nodularnog lijeva u posljednjih nekoliko godina je znatno porasla.

Budući se nodularni lijev koristi za proizvodnju dijelova poljoprivrednih strojeva u ovom radu je proučavan utjecaj različitih medija i mikrostrukture na korozijsko ponašanje tog materijala. Primjenom elektrokemijskih ispitivanja u mediju koji simulira umjetnu kišu i mediju 0,5 M H_2SO_4, kao i primjenom metalografske analize ispitanih materijala prije i nakon korozije dobiveni su korozijski parametri koji daju uvid u korozijsko ponašanje ispitanih vrsta nodularnog lijeva.

MATERIJALI I METODE

Materijali

Za ispitivanje utjecaja medija i mikrostrukture na korozijsku otpornost nodularnog lijeva korišteni su uzorci kvalitete EN-GJS-400-18-LT, čiji kemijski sastav je prikazan u tablici 1 [8]. Za usporedbu su korištena dva uzorka navedene kvalitete s različitim udjelom nodula: uzorak broj 2 = 360 nodula/mm^2 i uzorak broj 6 = 213 nodula/mm^2.

Tablica 1. Kemijski sastav ispitanih uzoraka nodularnog lijeva (mas. %) [8]

Oznaka uzorka	C	S	Si	Mn	P	Cr	Cu	Mg	CE	$T_{lijevanja}$/ °C
2	3.39	0.004	2.22	0.130	0.025	0.035	0.10	0.044	4.34	1369
6	3.71	0.008	2.24	0.131	0.028	0.018	0.11	0.039	4.47	1367

U oba slučaja kemijski sastavi u potpunosti zadovoljavaju zahtjeve propisane normom. S obzirom na prisutni sadržaj Si i P te izračunati ekvivalent ugljika (CE) radi se o nadeutektičkom nodularnom lijevu. Za navedenu kvalitetu nodularnog lijeva EN-GJS-400-18-LT očekuje se postizanje visoke nodularnosti i feritne osnove, bez karbida po granicama zrna koji će omogućiti razvoj mehaničkih svojstava i duktilnost.

Metode ispitivanja

Elektrokemijska ispitivanja (E_{corr}, EIS, Tafel)

Određivanje korozijskog potencijala E_{corr}

Pri svakom elektrokemijskom ispitivanju obično se prvo mjeri vremenska promjena potencijala između elektroda galvanskog članka pomoću voltmetra kroz koji prolazi slaba električna struja. Da bi se odredio elektrodni potencijal nekog uzorka u određenom mediju, potrebno je mjeriti elektromotornu silu između tog uzorka (radne elektrode) i referentne elektrode poznatog i konstantnog potencijala, koja služi kao standard prema kojem se mjeri potencijal radne elektrode. U svrhu određivanja potencijala kod otvorenog strujnog kruga E_{ocp} ispitanih uzoraka nodularnog lijeva kao funkcije vremena uzorci su pripremljeni prešanjem u konduktivnu masu pomoću uređaja za vruće prešanje uzoraka (SimpliMet® 1000), strojnim brušenjem (gradacije No. 600, 800 i 1000) i poliranjem (suspenzija Al_2O_3 u vodi) na automatskom uređaju za brušenje i poliranje (Büehler), nakon čega su isprani u destiliranoj vodi i odmašćeni u etanolu [9,10]. Uzorak se kao radna elektroda uranjao u radni medij u troelektrodnoj staklenoj ćeliji koja se još sastojala od protuelektrode (Pt) i referentne elektrode (zasićene kalomel elektrode-SCE). Kao radni medij u elektrokemijskim eksperimentima korištene su dvije otopine: 0.5 M H_2SO_4 (pH = 0,83) i umjetna kiša (pH = 7.2). Otopina umjetne kiše pripremljena je od 0.2 g/l Na_2SO_4 i 0.2 g/l $NaHNO_3$. Stabilizacija potencijala kod otvorenog strujnog kruga E_{ocp} je izvedena pri (19±2) °C uz pomoć računalom upravljanog potenciostata/galvanostata (Parstat 2273) i u trajanju od 30 minuta. Nakon toga izvedena su elektrokemijska mjerenja metodom elektrokemijske impedancijske spektroskopije (EIS).

Određivanje korozijskih parametara primjenom elektrokemijske impedancijske spektroskopije (EIS)

Elektrokemijska impedancijska spektroskopija (EIS) je jedna od metoda mjerenja korozijskih parametara koja se temelji na primjeni izmjenične struje, a zasniva se na odzivu strujnog kruga na izmjenični napon ili struju kao funkciju frekvencije [3,11]. U svrhu istraživanja granice faza elektroda/elektrolit, izvedeno je mjerenje impedancije u području frekvencija od 100 kHz do 10 mHz s amplitudom sinusoidnog napona u iznosu od 5 mV. Parametri impedancije analizirani su pomoću softvera ZSIMPWin 3.21. primjenom odgovarajućih modela električnog kruga [3,11]. Nakon elektrokemijske impedancijske spektroskopije izvedena je potenciodinamička polarizacija ispitanih uzoraka nodularnog lijeva.

Određivanje korozijskih parametara primjenom metode Tafelove ekstrapolacije

U svrhu dobivanja korozijskih parametara (korozijski potencijal E_{corr}, brzina korozije v_{corr}, anodni nagib b_a i katodni nagib b_c) Tafelovom metodom ekstrapolacije nakon elektrokemijske impedancijske spektroskopije izvedena je potenciodinamička polarizacija u području potencijala od -250 mV do +250 mV vs E_{corr}, uz brzinu promjene potencijala od 1 mV/s, a korozijski parametri su određeni pomoću softvera PowerCorr™ primjenom Tafelove metode ekstrapolacije i Faradayevih zakona [1,3,12].

Važno je napomenuti da su uzorci prije svake serije elektrokemijskih mjerenja metalografski pripremljeni strojnim brušenjem i poliranjem, koje je prethodno opisano.

Metalografska ispitivanja

U svrhu metalografskih ispitivanja, izrezani uzorci su sprešani u konduktivnu masu pomoću uređaja za vruće prešanje uzoraka [9,10]. Potom su strojno brušeni (gradacije No. 600, 800 i 1000) i polirani suspenzijom Al_2O_3 u vodi na automatskom uređaju za brušenje i poliranje, te isprani u destiliranoj vodi i odmašćeni u etanolu. Tako pripremljeni uzorci promatrani su na optičkom mikroskopu s digitalnom kamerom (Olympus GX 51) i sustavom za automatsku obradu slike (AnalySIS® Materials Research Lab) prije i poslije korozije u ispitanom mediju. U svrhu snimanja mikrostrukture ispitanih uzoraka nodularnog lijeva uzorci su nakon metalografske pripreme nagrizani u nitalu (5 %-tna HNO_3 u etanolu) te su snimane njihove mikrostrukture.

REZULTATI I RASPRAVA

Ovisnosti potencijala kod otvorenog strujnog kruga o vremenu za ispitane vrste nodularnog lijeva u oba medija prikazane su na slici 1. Dobiveni Nyquistovi EIS-spektri za ispitane uzorke i njihove analize provedene su primjenom odgovarajućeg modela električnog kruga, što je prikazano na slikama 2-7. Modeliranjem EIS spektara dobiveni su parametri impedancije otpor elektrolita R_{el}, konstantno fazni element dvosloja Q_{dl}, mjera heterogenosti površine n i otpor prijenosu naboja R_{ct} te su navedeni u tablicama 2 i 3.
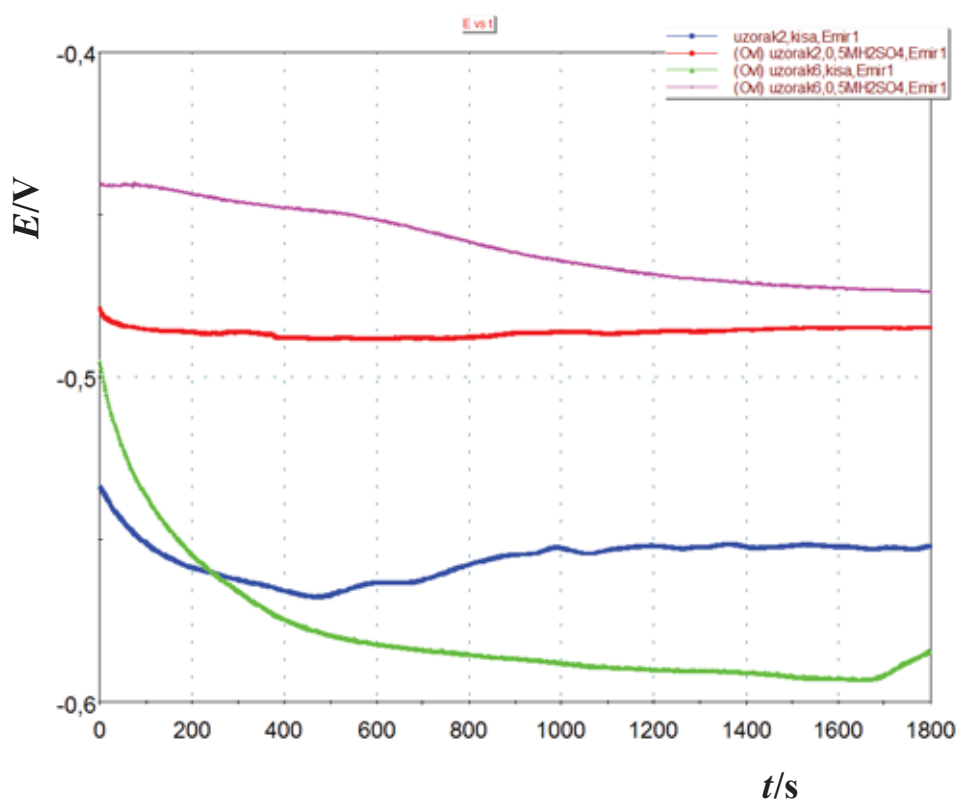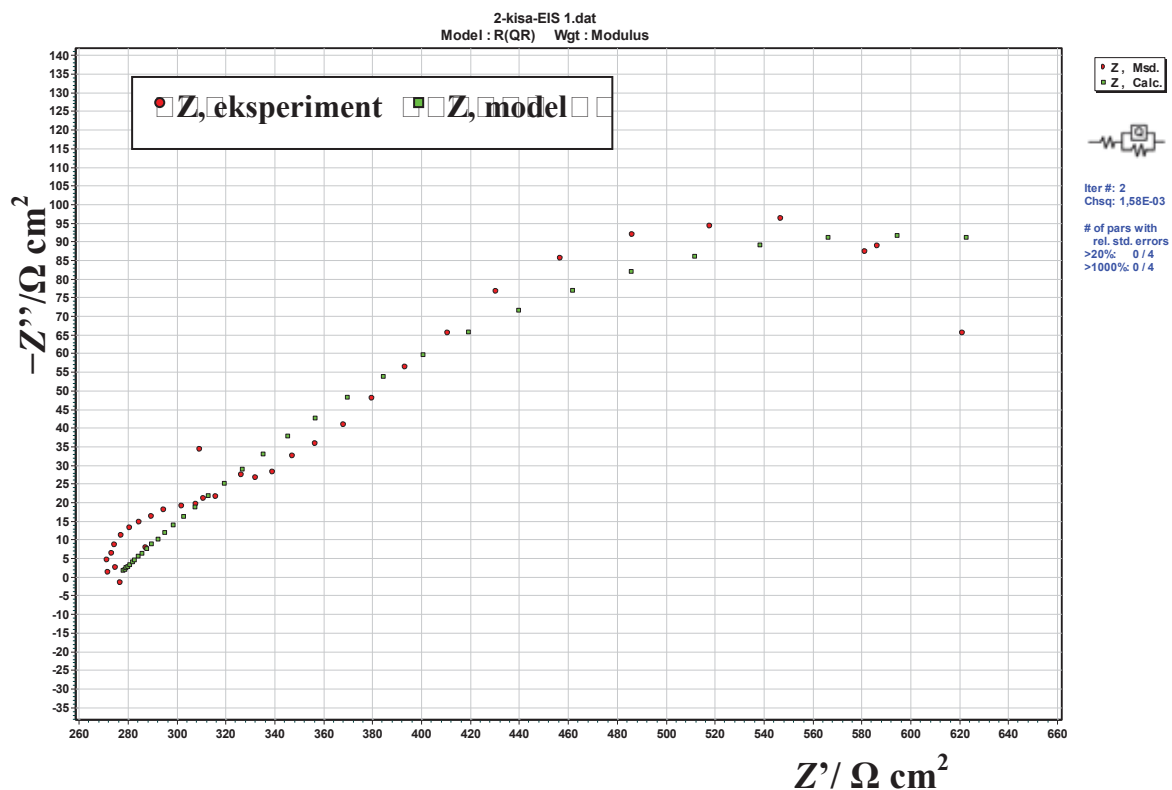

Slika 1. Ovisnost mirujućeg potencijala o vremenu za ispitane uzorke nodularnog lijeva u mediju umjetne kiše i mediju 0.5 M H_2SO_4
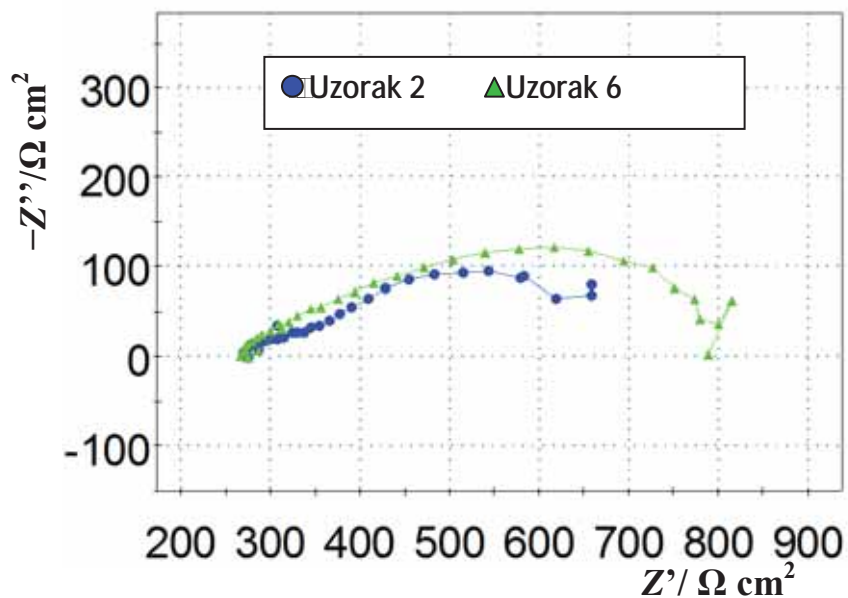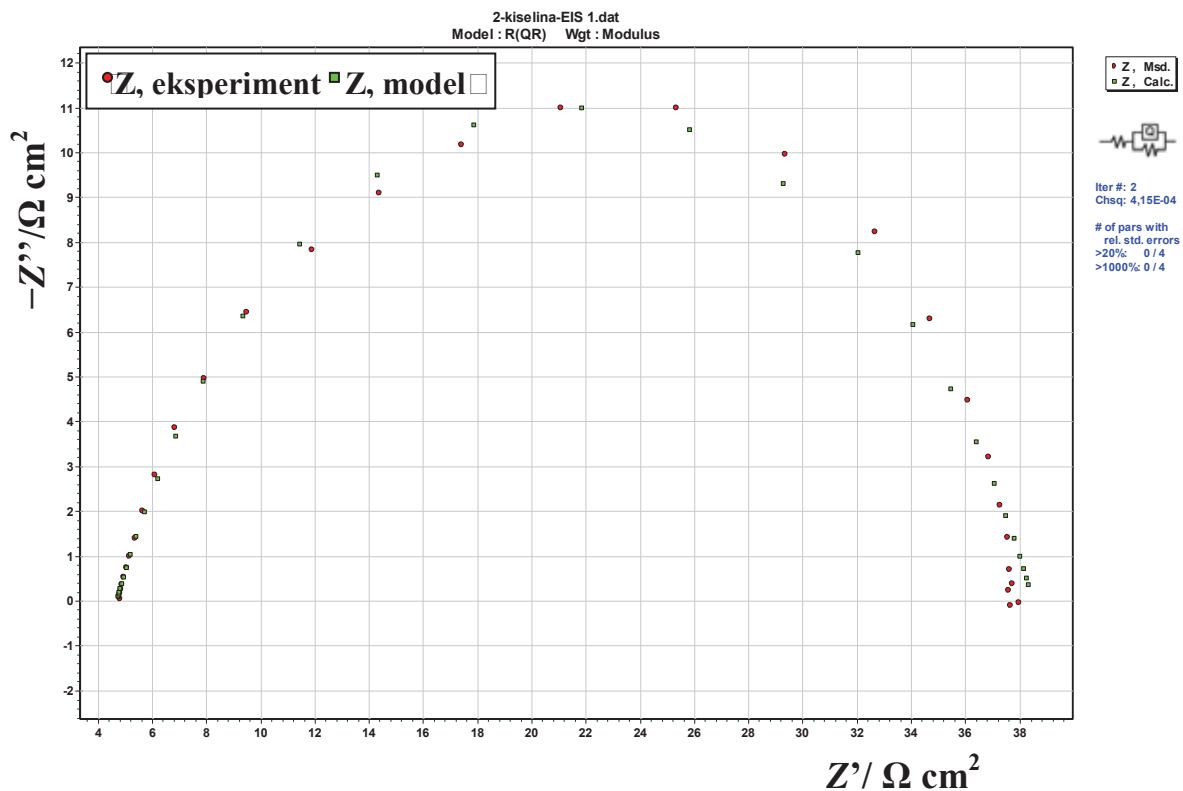
Slika 2. Nyquistov impedancijski prikaz ispitanih uzoraka nodularnog lijeva u mediju umjetne kiše
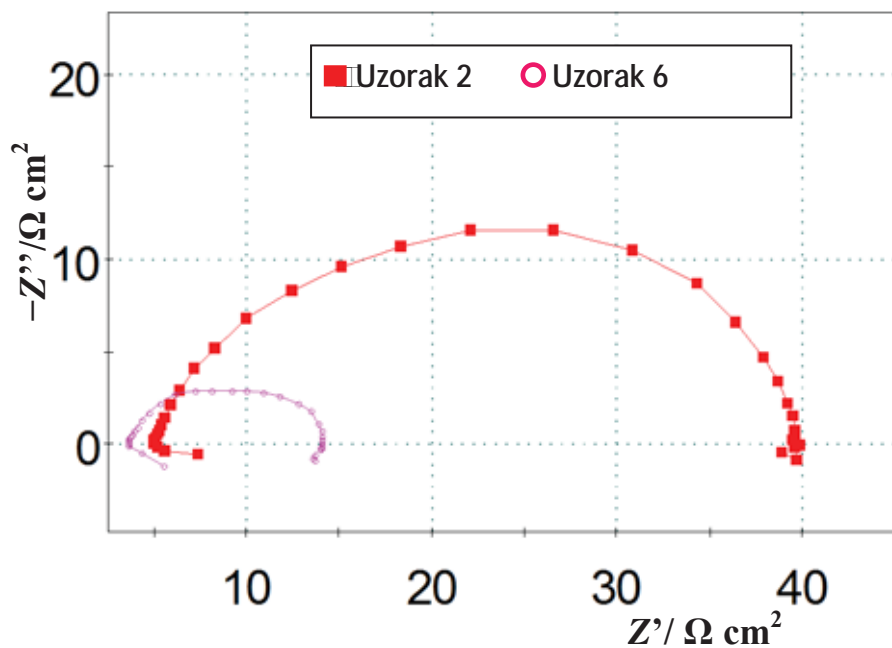
Slika 3. Nyquistov impedancijski prikaz ispitanih uzoraka nodularnog lijeva u mediju 0.5 M H_2SO_4
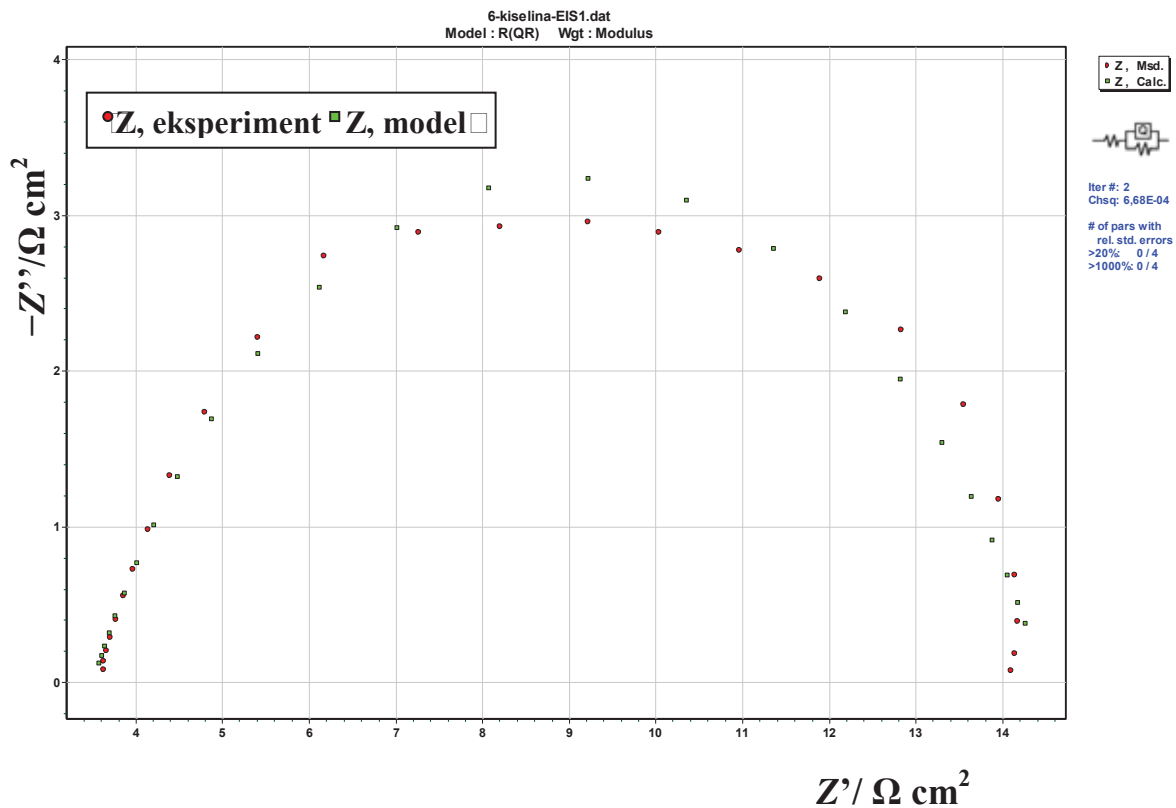
Slika 4. Modeliranje dobivenog Nyquistovog EIS spektra za nodularni lijev oznake 2
u mediju umjetne kiše

Slika 5. Modeliranje dobivenog Nyquistovog EIS spektra za nodularni lijev oznake 2
u mediju 0.5 M H$_2$SO$_4$
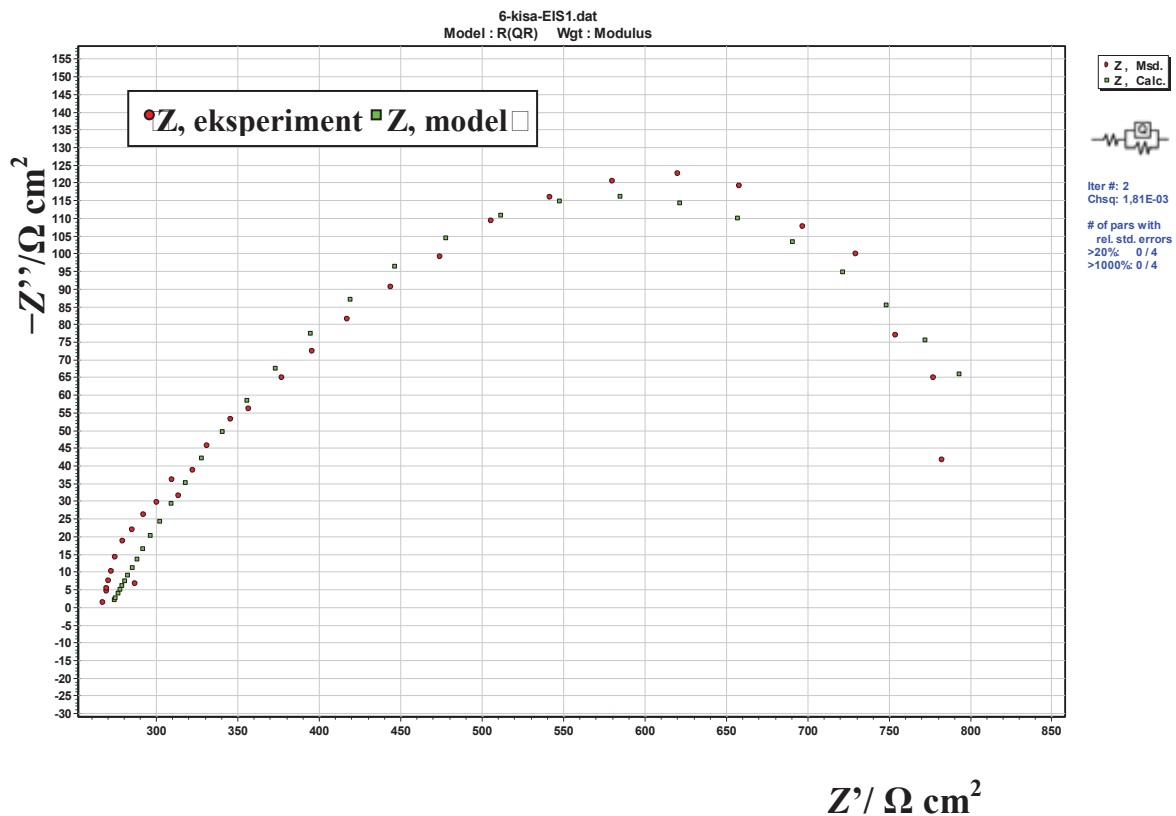
Slika 6. Modeliranje dobivenog Nyquistovog EIS spektra za nodularni lijev oznake 6 u mediju umjetne kiše

Slika 7. Modeliranje dobivenog Nyquistovog EIS spektra za nodularni lijev oznake 6 u mediju 0.5 M H_2SO_4

180

Tablica 2. Parametri impedancije ispitanog nodularnog lijeva oznake 2 u oba medija

Medij	P	E_{corr} vs. SCE	R_{el}	$Q_{dl} \times 10^6$	n	R_{ct}
	cm^2	mV	Ωcm^2	$\Omega^{-1}s^n cm^{-2}$		$\Omega\ cm^2$
Umjetna kiša	0.952	−570.1	261.2	2708.0	0.36	602.4
0.5 M H_2SO_4		−468.0	4.7	1383.0	0.73	33.8

☐

Tablica 3. Parametri impedancije ispitanog nodularnog lijeva oznake 6 u oba medija

Medij	P	E_{corr} vs. SCE	R_{el}	$Q_{dl} \times 10^6$	n	R_{ct}
	cm^2	mV	Ωcm^2	$\Omega^{-1}s^n cm^{-2}$		$\Omega\ cm^2$
Umjetna kiša	1.005	−580.5	272.3	685.3	0.46	618.9
0.5 M H_2SO_4		−459.3	3.51	2759.0	0.68	11.0

☐

Promatrajući sliku 1 može se uočiti da ispitani uzorci nodularnog lijeva oznake 2 i 6 brzo postižu svoj mirujući potencijal (potencijal otvorenog strujnog kruga) u oba ispitana medija. Na slikama 2 i 3 vidljivo je da se kod oba uzorka širina Nyquistovog polukruga smanjuje u mediju 0.5 M H_2SO_4, što znači da se u tom mediju očekuju manji otpori prijenosu naboja R_{ct}, a time i manja korozijska otpornost u odnosu na medij umjetne kiše. Ove činjenice potvrđuju impedancijski parametri dobiveni modeliranjem Nyquistovih prikaza za oba uzorka u oba ispitana medija (tablica 2 i 3). Modeliranje EIS spektara izvedeno je u oba medija pomoću modela najjednostavnijeg ekvivalentnog električnog kruga R(QR). Iz slika 4-7 vidljivo je da se simulirane krivulje dobro podudaraju s eksperimentalnim s registriranim odstupanjem reda veličine 10^{-3}. Također je vidljivo da oba ispitana uzorka u oba medija pokazuju samo jednu kapacitivnu petlju depresivnog oblika, što je karakteristično za čvrste elektrode [13].

Iz podataka u tablicama 2 i 3 vidljivo je da su uzorci pokazali vrlo malen otpor prijenosu naboja u mediju 0.5 M H_2SO_4, što dovodi do zaključka da se u kiselom mediju stvara vrlo tanak oksidni sloj koji nema zaštitnu ulogu u borbi protiv korozije. Iako je uzorak 2 pokazao trostruko veću vrijednost otpora prijenosa naboju u odnosu na uzorak 6, ovi ljevovi su izrazito podložni koroziji u kiselom mediju i neprihvatljivi za takvu primjenu. U mediju umjetne kiše koji je približno neutralan po pH vrijednosti, uzorci su pokazali velik otpor prijenosu naboja, što znači da se na njima u kontaktu s takvim medijima stvara izrazito debeo oksidni sloj, koji dalje štiti materijal od napredovanja korozije. Međutim, ne može se sa sigurnošću tvrditi koji je prema ovim podacima iz tablica 2 i 3 korozijski otporniji, jer su dobivene vrijednosti otpora prijenosu naboja vrlo bliske za oba ispitana uzorka u mediju umjetne kiše. Što se tiče otpora elektrolita, R_{el} se smanjuje kod oba ispitana uzorka u kiselom mediju. Također, može se uočiti da su oba uzorka nodularnog lijeva pokazala vrlo visoke vrijednosti konstantno faznog elementa dvosloja Q_{dl} u oba ispitana medija, što ukazuje na činjenicu da pasivni sloj koji raste na površini ispitanih uzoraka nije dovoljno kompaktan, zbog čega onda i dolazi do porasta kapaciteta na međupovršini metal/oksidni sloj ili unutar pasivnog sloja [14].

Saznanja dobivena metodom elektrokemijske impedancijske spektroskopije podudaraju se i s korozijskim parametrima dobivenim metodom Tafelove ekstrapolacije. Naime, potenciodinamička polarizacija u području potencijala od −250 mV do +250 mV vs. E_{corr} izvedena je u svrhu određivanja korozijskih parametara, koji su navedeni u tablicama 4 i 5.

☐

Polarizacijske krivulje ispitanih uzoraka nodularnog lijeva u oba ispitana medija prikazane su na slici 8.

Tablica 4. Korozijski parametri ispitanog nodularnog lijeva oznake 2 u oba ispitana medija

Medij	P	E_{corr} vs. SCE	b_a	b_c	v_{corr}
	cm^2	mV	mV dec^{-1}	mV dec^{-1}	mm god^{-1}
Umjetna kiša	0.952	−569.7	222.4	233.1	0.50
0.5 M H$_2$SO$_4$		−468.4	103.1	171.0	7.60

Tablica 5. Korozijski parametri ispitanog nodularnog lijeva oznake 6 u oba ispitana medija

Medij	P	E_{corr} vs. SCE	b_a	b_c	v_{corr}
	cm^2	mV	mV dec^{-1}	mV dec^{-1}	mm god^{-1}
Umjetna kiša	1.005	−581.8	246.8	279.2	0.52
0.5 M H$_2$SO$_4$		−458.4	117.1	207.3	24.5
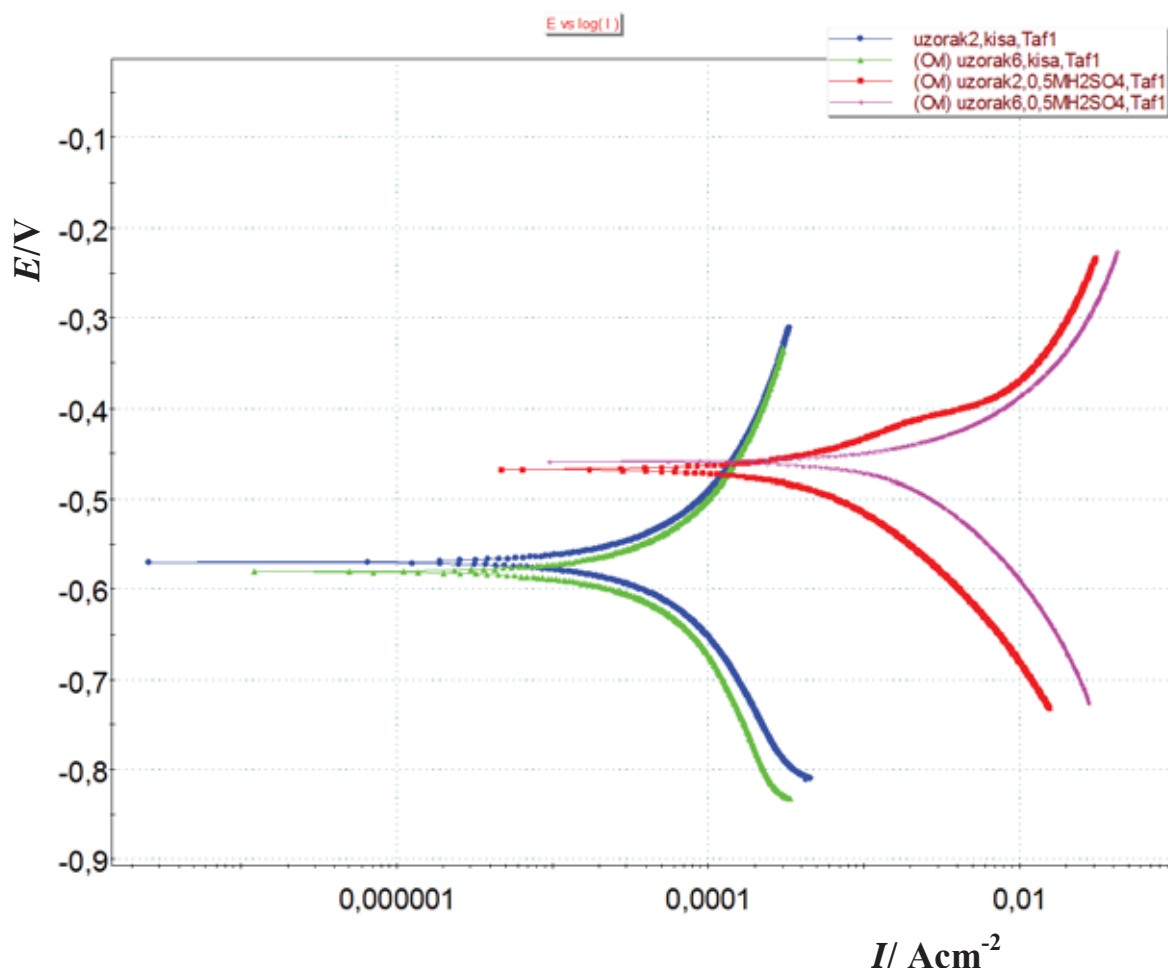
Slika 8. Polarizacijske krivulje ispitanih uzoraka nodularnog lijeva u oba ispitana medija

Iz dobivenih rezultata prikazanih na slici 8 i u tablicama 4 i 5 može se uočiti da su oba ispitana uzorka nodularnog lijeva pokazala približno sličnu vrijednost brzine korozije u

mediju umjetne kiše (oko 0.5 mm god^{-1}), što dovodi do zaključka da su oba ova materijala podjednako korozijski otporna u mediju umjetne kiše. Međutim, kod kiselog medija ustanovljeno je da je uzorak oznake 2 korozijski otporniji, budući je pokazao trostruko manju brzinu korozije od uzorka oznake 6. To dovodi do zaljučka da broj nodula po jedinici površine izrazito ima utjecaj na korozijsku otpornost ispitanih ljevova. Naime, veći broj nodula po jedinici površine znači i veću pokrivenost površine nodulama, koje zapravo imaju ulogu izolatora, zbog oksidnog sloja koji se stvara između grafita i metalne osnove. Zbog uloge nodula kao izolatora, uzorak 2 je i pokazao veći otpor prijenosu naboja te stoga i bolju korozijsku otpornost. Drugim riječima, nastali oksidni sloj između nodula i metalne osnove predstavlja zapreku agresivnim ionima iz medija pa medij djeluje korozijski samo na metalnu osnovu u mikrostrukturi ispitanih uzoraka.

Također, vidljivo je da su oba uzorka pokazala veće anodne i katodne nagibe u mediju umjetne kiše, što znači da su u tom mediju dominantnije reakcije na anodi i katodi, nego u kiselom mediju.

Iz literature je poznato da se proces elektrokemijske korozije željeza i negovih legura u kiselom mediju odvija na slijedeći način [4,13,15-17]:

$$\text{Anodna reakcija (otapanje željeza): Fe} - 2e^- \rightarrow Fe^{2+} \tag{1}$$

$$\text{Katodna reakcija (izlučivanje vodika): } 2H^+ + 2e^- \rightarrow H_2 \tag{2}$$
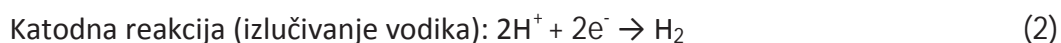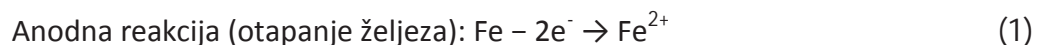
S obzirom na sve navedeno, može se zaključiti da budući se dobivene vrijednosti brzine korozije u ispitanom jako kiselom mediju kreću oko 7 do 25 mm god^{-1}, ovi nodularni ljevovi su vrlo podložni koroziji u jako kiselom mediju te se stoga ne preporučuje primjenjivati ih u takvim agresivnim uvjetima [16,17]. Što se tiče njihove primjene za poljoprivredne strojeve u uvjetima izlaganja atmosferilijama, oba ispitana nodularna lijeva pokazuju sličnu korozijsku otpornost iako se razlikuju prema mikrostrukturi, tj. po broju i veličini nodula po jedinici površine [17].

Za potrebe dobivanja mikrostrukture ispitanih nodularnih lijevova, uzorci 2 i 6 su pripremljeni strojnim brušenjem i poliranjem te nagrizanjem u nitalu u trajanju od 4-7 sekundi. Slika 9 prikazuje mikrostrukturu ispitanih uzoraka nodularnog lijeva prije i nakon nagrizanja u nitalu, a u tablici 6 su dani rezultati analize grafita te rezultati ispitivanja udjela ferita i perlita u metalnoj osnovi.

Nodularni lijev se općenito upotrebljava za dinamički opterećene konstrukcije, a materijali iz kojeg su dobiveni uzorci namjenjeni su za proizvodnju dijelova poljoprivrednih strojeva koji su izloženi nepovoljnim vremenskim uvjetima [8].
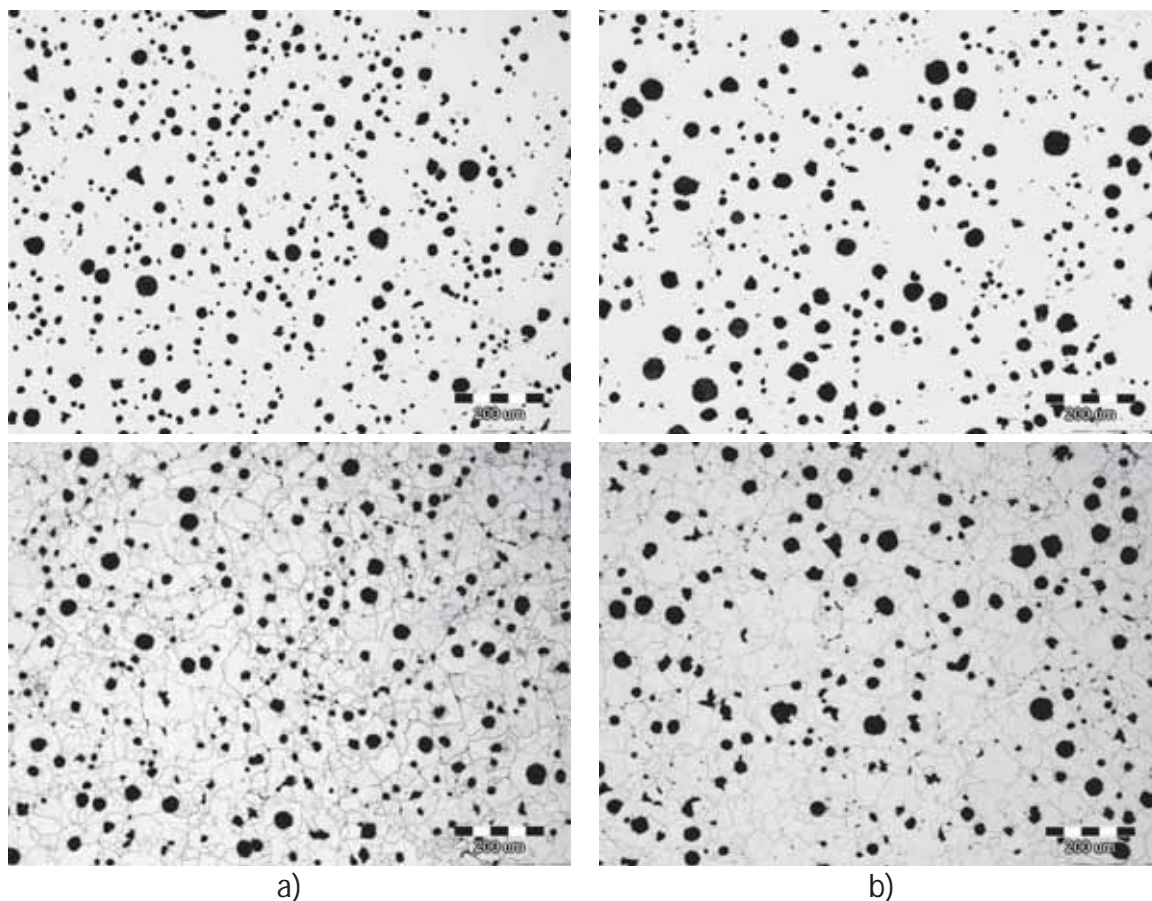
Slika 9. Mikrostruktura nodularnog lijeva prije i nakon nagrizanja u nitalu:
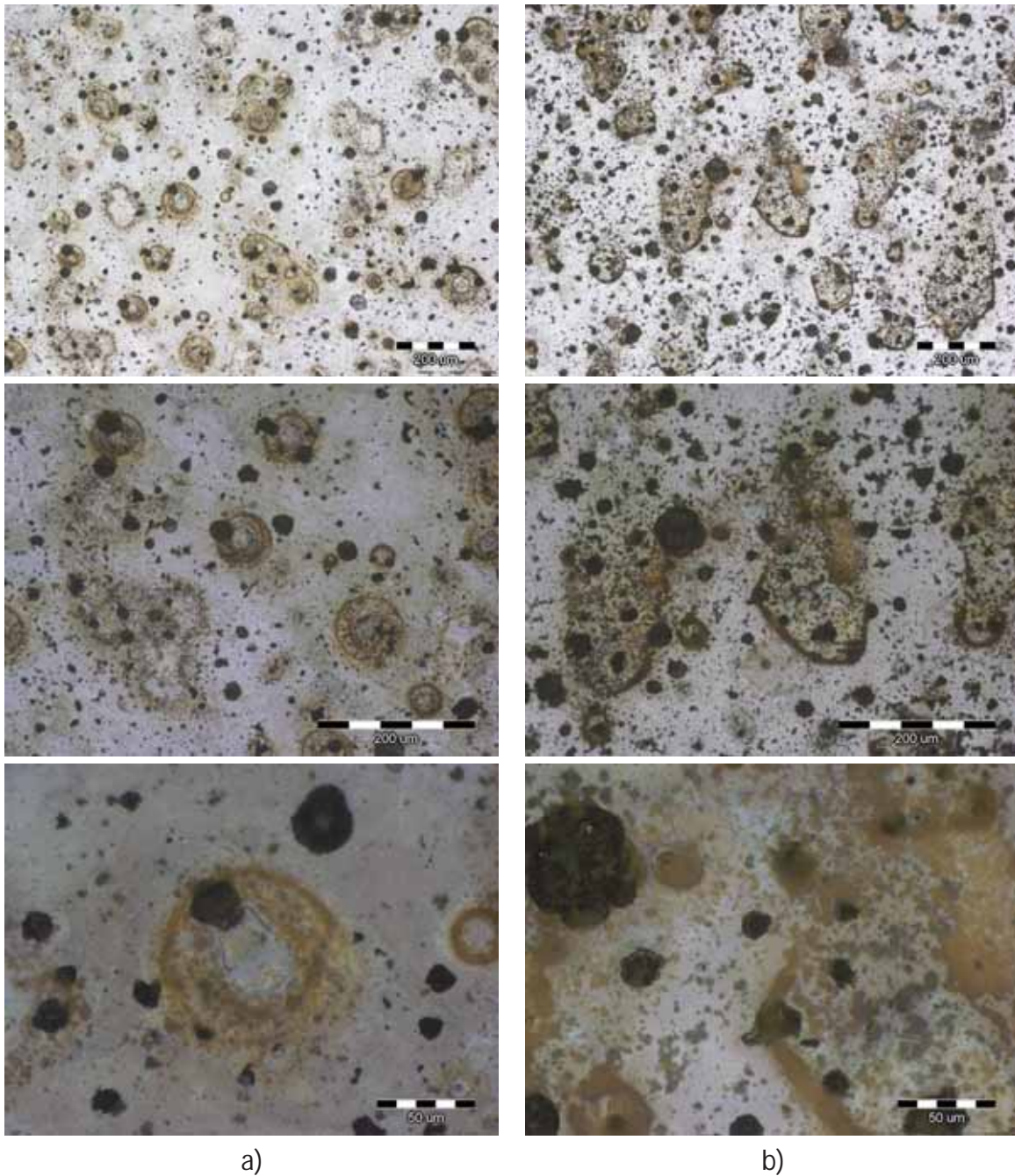a) uzorak 2,
b) uzorak 6

Tablica 6. Rezultati ispitivanja mikrostrukture u uzorcima [8]

Oznaka uzorka	Oblik	Veličina	Nodularnost	Udio grafita %	Broj nodula/mm^2	Udio ferita %	Udio perlita %
2	VI	7	0.75	9.72	360	100	0
6	VI	6	0.74	10.06	213	100	0

Kao što je vidljivo iz podataka iz tablice 6 mikrostrukura metalne osnove uzoraka 2 i 6 je 100 % feritna [8]. Za feritnu mikrostrukturu nodularnog lijeva karakteristična je niža čvrstoća i veća istezljivost.

Kod oba uzorka grafit je izlučen u obliku nodula (oblik VI), veličine 7 za uzorak 2, te veličine 6 za uzorak 6 [8]. Broj nodula predstavlja prosječnu vrijednost tri mjerenja. Kod uzorka 2 ustanovljen je veći broj nodula (360 nodula/mm^2), dok kod uzorka 6 broj nodula iznosi 213 nodula/mm^2 [8]. Povećanje broja nodula djeluje nepovoljno na razvoj vlačne čvrstoće. Važno je napomenuti da se broj nodula u oba slučaja nalazi u granicama prema postavljenim zahtjevima proizvodnje.

Na slici 10 prikazane su mikrostrukture nodularnog lijeva prije i nakon korozije u mediju umjetne kiše, a na slici 11 su prikazane mikrostrukture nodularnog lijeva prije i nakon korozije u 0.5 M H_2SO_4.

a)   b)

Slika 10. Mikrostruktura nodularnog lijeva nakon korozije u mediju umjetne kiše pri različitim povećanjima: a) uzorak 2 i b) uzorak 6
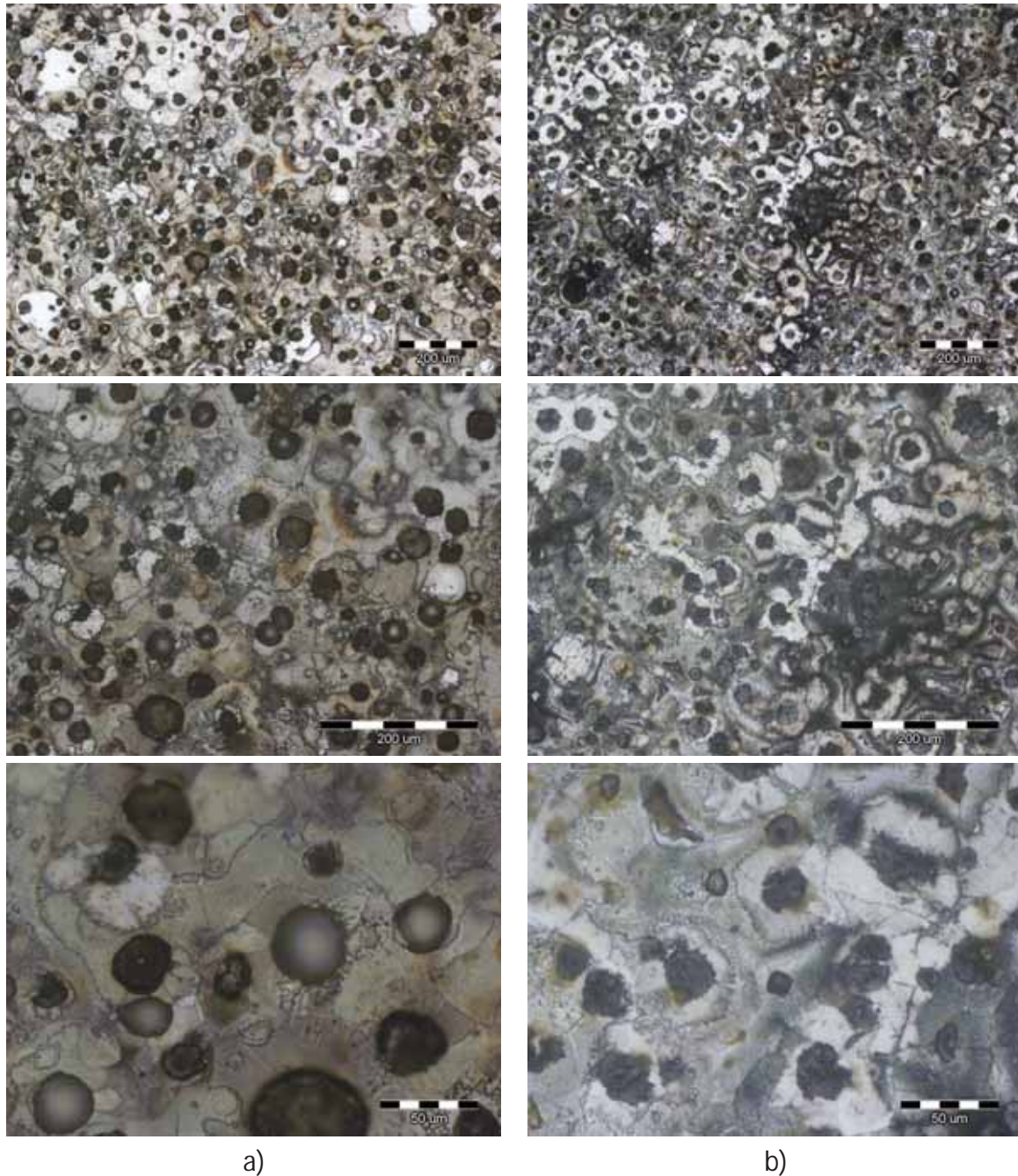
Slika 11. Mikrostruktura nodularnog lijeva nakon korozije u u 0.5 M H_2SO_4 pri različitim povećanjima: a) uzorak 2 i b) uzorak 6

Kao što je ranije spomenuto, nema velike razlike u brzinama korozije između ispitanih uzoraka u mediju umjetne kiše, ali se zato iz slike 10 može uočiti da se u mediju umjetne kiše vidi veći utjecaj medija na mikrostrukturu kod uzorka 6 s manjim brojem nodula. To samo potvrđuje činjenicu da primijenjeni medij djeluje na metalnu osnovu uzorka i više napada onaj uzorak s manjom prekrivenosti nodulama.

Međutim, u kiselom mediju (slika 11) je vidljiva vrlo velika agresivnost kiseline koja također napada mikrostukturu oba ispitana uzorka, ali ipak se vidi jača izraženost utjecaja kiseline kod nodularnog lijeva oznake 6, koji je imao manje nodula po jedinici površine.

S obzirom na sve navedeno, iako se uzorak oznake 2 pokazao korozijski otpornijim u jako kiselom mediju, zbog vrlo velikih vrijednosti brzine korozije, nodularni lijevovi ovakve kvalitete se ne preporučuju za primjenu u jako kiselim uvjetima.

ZAKLJUČAK

1. Elektrokemijskim mjerenjima ispitana je korozijska otpornost nodularnog lijeva kvalitete EN-GJS-400-18-LT u mediju umjetne kiše i mediju 0,5 M H_2SO_4 .

2. Metalografska analiza ispitanih lijevova je pokazala da se radi o 100 %-tnoj strukturi ferita, gdje je grafit izlučen u obliku nodula (oblik VI), s razlikom u broju nodula po jedinici površine.

3. Ispitani uzorci nisu pokazali znatnu razliku u brzini korozije u mediju umjetne kiše, dok je u kiselom mediju registrirana trostruko veća brzina korozije nodularnog lijeva oznake 6 sa skoro dvostruko manjim brojem nodula po jedinici površine u odnosu na uzorak oznake 2.

4. Elektrokemijska impedancijska spektroskopija je zabilježila trostruko veći otpor prijenosu naboja kod uzorka 2 u kiselom mediju što znači i veću korozijsku otpornost, dok u mediju umjetne kiše nije bilo znatne razlike u ispitanim uzorcima.

5. Mikrostrukturna analiza ispitanih uzoraka u oba medija upućuje na činjenicu da oba medija imaju utjecaj na mikrosturkturu, pri čemu je utjecaj izraženiji kod uzorka 6 s manjim brojem nodula. Naime, nodule imaju ulogu izolatora, zbog oksidnog sloja koji se stvara između grafita i metalne osnove te je manja korozijska otpornost registrirana kod uzorka 6, gdje je manja prekrivenost površine nodulama.

6. Uzorak oznake 2 se pokazao korozijski otpornijim u kiselom mediju. Međutim, zbog velikih iznosa brzine korozije, nodularni lijevovi ispitane kvalitete nisu preporučljivi za primjenu u jako kiselom okolišu.

7. S obzirom na korozijske parametre dobivene u mediju umjetne kiše, oba ispitana lijeva mogu se primjenjivati za izradu dijelova poljoprivrednih strojeva koji će možda biti izloženi atmosferilijama i atmosferskoj koroziji.

LITERATURA

[1]   I. Esih, Z. Dugi, Tehnologija zaštite od korozije I, Školska knjiga, Zagreb, 1990.
[2]   I. Esih, Z. Dugi, Tehnologija zaštite od korozije II, Fakultet strojarstva i brodogradnje, Zagreb, 1992.
[3]   E. Stupnišek-Lisac, Korozija i zaštita konstrukcijskih materijala, Fakultet kemijskog inženjerstva I tehnologije, Zagreb, 2007.
[4]   C. D. Fernández-Solis, Fundamentals of Electrochemistry, Corrosion and Corrosion Protection, Accessible on Internet: https://www.google.hr/search?q=google+prevoditelj&oq=google+prevoditelj&aqs=chrome.0.69i59j0l3j69i64j69i60.4644j0j8&sourceid=chrome&ie=UTF-8#q=www.springer.com/cda/content/.../9783319245003-c2.pdf, dostupno 20.04.2017.

[5]   K. J. Naughton, Controling Corrosion in Process Equipment, Mc.Graw-Hill Book Comp., New York, 1980.

[6]   F. Unkić, Z. Glavaš, Lijevanje željeznih metala, Sveučilište u Zagrebu Metalurški fakultet, Sisak, 2008.

[7]   M. Novosel, D. Krumes, Željezni materijali (metalografske osnove i tehnička primjena željeznih ljevova), Sveučilište u Osijeku, Strojarski fakultet, Slavonski Brod, 1997.

[8]   L. Voloder, Utjecaj kemijskog sastava i cjepljenja na mikrostrukturne značajke i mehanička svojstva nodularnog lijeva, diplomski rad, Sveučilište u Zagrebu Metalurški fakultet, Sisak, 1996.

[9]   A. Begić Hadžipašić, J. Malina, M. Malina, The influence of microstructure on hydrogen diffusion and embrittlement of multiphase fine-grained steels with increased plasticity and strength, Chem. Biochem. Eng. Q., 25(2011)2, pp. 159-169.

[10]   A. Begić Hadžipašić, J. Malina, Š. Nižnik, The influence of microstructure on hydrogen diffusion in dual phase steel, Acta Metallurgica Slovaca, 17(2011)2, pp. 129-137.

[11]   D. Petrović, Inhibicija korozije konstrukcijskog čelika u kiselom mediju primjenom *Aloe vere* kao "zelenog" inhibitora, rad nagrađen Rektorovom nagradom, Sveučilište u Zagrebu Metalurški fakultet, Zagreb, 2012.

[12]   K. Jarić, A. Rešetić, Korozija, Korexpert d.o.o., Zagreb, 2003.

[13]   M. A. Quraishi, A. Singh, V. K. Singh, D. K. Yadav, A. K. Singh, Green approach to corrosion inhibition of mild steel in hydrochloric acid and sulphuric acid solutions by the extract of Murraya koenigii leaves, Materials Chemistry and Physics, 122(2010), pp. 114-122.

[14]   S. Kožuh, M. Gojić, M. Kraljić Roković, The effect of PWHT on electrochemical behaviour of AISI 316L weld metal, Chemical and Biochemical Engineering Quarterly, 22(2008)4, pp. 421-431.

[15]   P. P. Sarkar, P. Kumar, M. K. Manna, P. C. Chakraborti, Microstructural influence on the electrochemical corrosion behavior of dual-phase steels in 3.5 % NaCl solution, Materials Letters, 59(2005), pp. 2488-2491.

[16]   T. Filetin, Izbor materijala pri razvoju proizvoda, Fakultet strojarstva i brodogradnje, Zagreb, 2000.

[17]   E. Stupnišek-Lisac, H. Otmačić Ćurković, Korozija i okoliš, skripta, Fakultet kemijskog inženjerstva i tehnologije, Zagreb, 2015.

Zahvala

☐

HEATING – COOLING SYSTEMS IN HPDC TOOLS

Mitja Petrič[1], Lejla Lavtar[2]**, Boštjan Taljat**[2], Sebastjan Kastelic[1]**, Primož Mrvar**[1]

[1]University of Ljubljana Faculty of Natural Sciences and Engineering,
Department for Materials and Metallurgy, Ljubljana, Slovenia
[2]STEEL d.o.o., Ljubljana, Slovenia

<u>Oral presentation</u>
<u>Preliminary note</u>

Abstract

High pressure die-casting process (HPDC) is a permanent mould casting technology. During one cycle the heat from melt is transported into a steel tool which is a reason for heating of a tool. In order to prevent overheating the heating-cooling system is positioned in the tool. Cooling-heating system heats up the tool at the beginning of the casting process and cools the tool in further production of castings. Paper describes the problems at conventional tool with defect analysis of a tool as a result of thermal loading. On basis of analysis of existing tool made by ProCAST software the change of heating-cooling system in a tool was prepared and verified. In further the new tool was produced.

Key words: heating-cooling system, high pressure die casting, numerical simulation

*Corresponding author (e-mail address): *[*mitja.petric@omm.ntf.uni-lj.si*](mailto:mitja.petric@omm.ntf.uni-lj.si)

INTRODUCTION

High Pressure die-casting process (HPDC) is highly interesting for technological and scientific practice. HPDC process is used for production of parts for automotive industry, aeronautics etc. HPDC process is cyclic process appropriate for mass production and is one of the most important casting technologies. Recently the research is done on HPDC casting alloys [1-3], die materials [4] and most important on regulation of different parameters of the process [5-7] such as melt injection important for gas porosity and shrinkage porosity. Research from the field of thermal loading of the tool [8,9] and chemical reactions on the interface melt/die are still important questions since they influence the die lifetime. In order to reduce costs for die production the development of software for simulation of the HPDC process is supported.

Important process in a HPDC technology is heating-cooling system of the tool conducted by several loops of cooling channels through the tool. Cooling channels are usually produced by drilling [10] and in recent publications there is no evidence of different technologies used for production of cooling channels. There are some papers describing adjusted cooling channels at production of polymers [11-16] where they can be also produced by 3D printing [17]. Findings are showing that cooling channels are not effective if they are positioned away from die cavity so they should be positioned closer to the die cavity surface in order to extract the heat from the die more effectively [18].

Paper describes the investigation and production of new innovative heating-cooling system for the tool in order to improve directional solidification of castings and to extend the lifetime of the die.

MATERIALS AND METHODS

The case of research was a HPDC tool with two casting cavities as is presented on Fig. 1a and the distributor presented in Fig. 1b. The tool was produced from tool steel UTOPMO2 with chemical composition presented in Table 1. The tool was hardened, tempered and nitride. Both parts of a tool have same dimensions 300 × 300 × 100 mm. Water was used as a cooling agent for a tool. The casting produced by this tool was a carburettor from AlSi9Cu3 alloy presented in Fig. 1c. Chemical composition of an alloy is presented in a Table 2.

In order to analyse the casting cycle and to correlate measured and calculated results the thermal imaging was used. Results of thermos imaging were used to correlate and verify the calculated results made by numerical simulation programme ProCAST. Calculated results gave information about heating and cooling of a tool during process of casting and predicted stress results in a tool as a result of cyclic thermal loading. The analysis of defects on destructed tool was made in order to analyse the critical spots in a tool.

According to numerical calculations the new heating-cooling system was made in a new tool and new distributor and verified in practise.

| (a) | (b) | (c) |
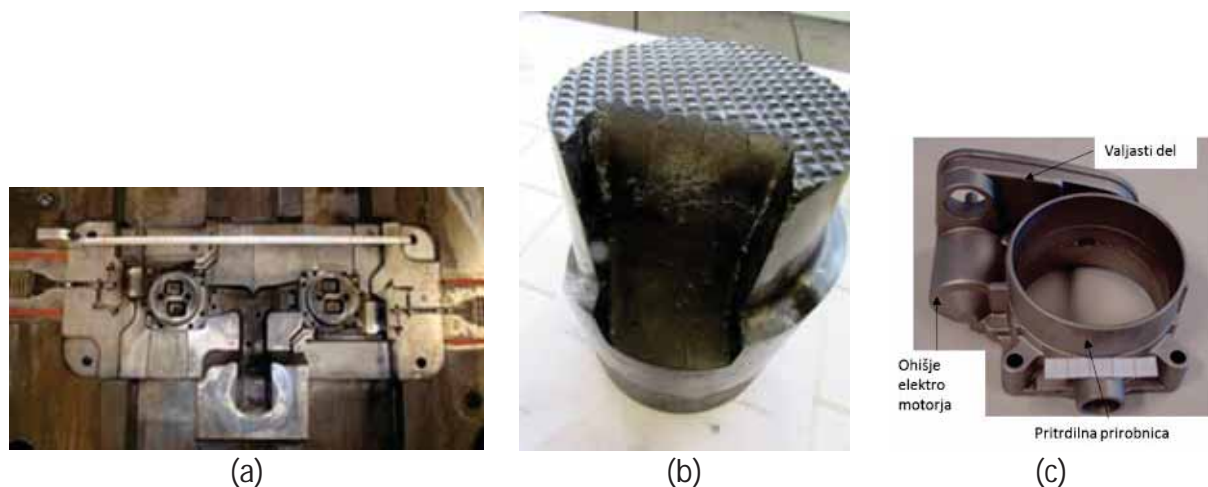
Figure 1. Two casting cavity HPDC tool (a), distributor (b) and the casting (c)

Table 1. Chemical composition of tool steel

C	Si	Mn	Cr	Mo	V
0.40	1.05	0.40	5.15	1.35	1.00

Table 2. Chemical composition of AlSi9Cu3 alloy in mass. %

Si	Fe	Mg	Cu	Mn	Zn	Sn
9.15	0.66	0.18	2.25	0.26	0.47	0.10

RESULTS AND DISCUSSION

Analysis of cyclic thermal loading of a tool showed that the stable part of a tool has 130 °C higher temperature than moving part of a tool at the position shown on Figs. 2 and 3. The picture is taken before spraying of a tool. The lifetime of a stable part of a tool was 73070 cycles while the lifetime of a moving part of a tool was 95332 cycles which confirms that higher temperatures has negative effect on lifetime. A new stable part of a tool was produced with newly positioned heating-cooling channels nearer to the casting cavity (Fig. 4). Analysis of thermal loadings showed the difference in temperature for old and new tool where temperature of old tool was 297 °C and temperature of a new tool was 285 °C shown on Fig. 5. The lower temperatures brought also changes in stress formation during cycles. Fig. 6 is presenting most critical spot of a moving part of a tool and is showing that amplitude of average normal stresses is lowered from 1080 N/mm^2 to 700 N/mm^2 which means 36 % lower loadings. According to calculations the lifetime of a tool should increase. The new tool made only 9474 cycles due to end of production of casting.

The stable part of an old tool was analysed for defects caused by cyclic thermal loading. Fig. 7 is showing thermal fatigue cracks and wear at spot f where the tool was loaded by the melt and on spot n where there were no loadings. Also other defects are presented such as adhesion, wear and cracks on the same places as calculated by ProCAST software (Fig. 6). Profile of Vickers hardness is presented on Fig. 8 is presenting the lowered hardness on the spot f where the wear occurred. The hardness is lowered form 1050 HV0.1 to 940 HV0.1.

As mentioned also the distributer was analysed and according to calculated results and changed cooling system the new distributer was produced. Analysis of thermal loadings presented on Fig. 9 is showing differences in temperatures and average normal stresses for old and new distributer. One can see that better and more effective cooling system affects the temperatures where the temperature in a new distributer is only 94.7 °C while in old one is 235.3 °C. In this manner the temperature is 60 % lower. The lowered temperature is leading also to lowered induced stresses where stresses are lowered for 47 % from 109 N/mm^2 to 58.5 N/mm^2 in most critical spot. The lifetime of an old distributer was 74928 cycles while the lifetime of a new one is at least 102246 cycles since it is still tested. In this way the lifetime is increased for more than 36 %.
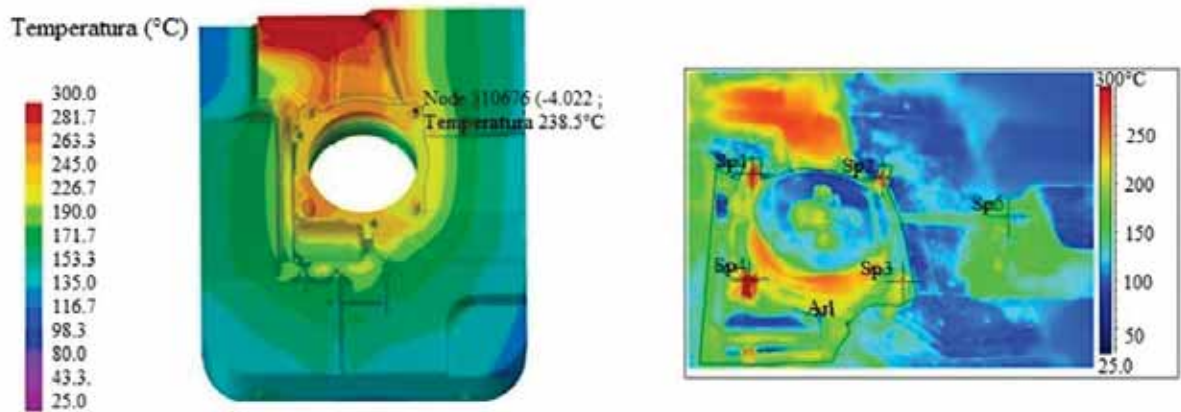
Figure 2. Calculated temperature field of movable part of a tool (a) and thermal imaging of a surface of same part before spraying
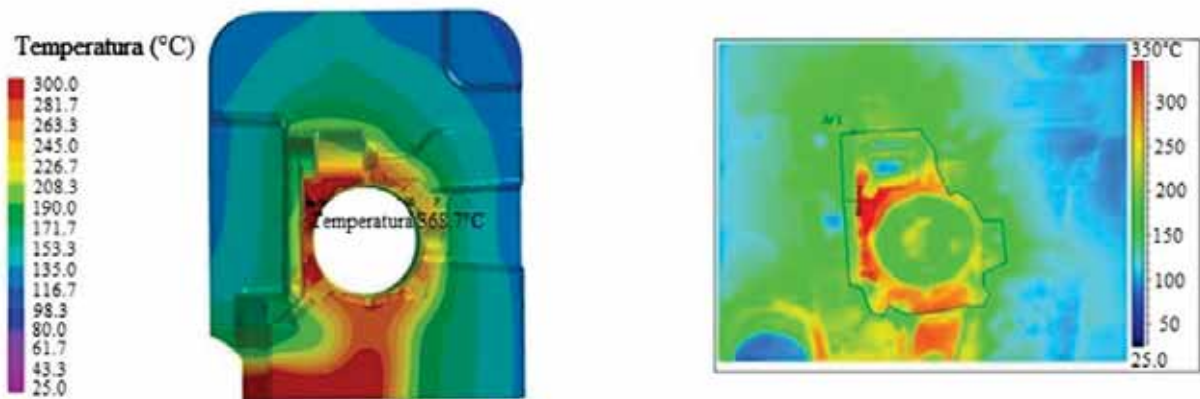

Figure 3. Calculated temperature field of stable part of a tool (a) and thermal imaging of a surface of same part before spraying
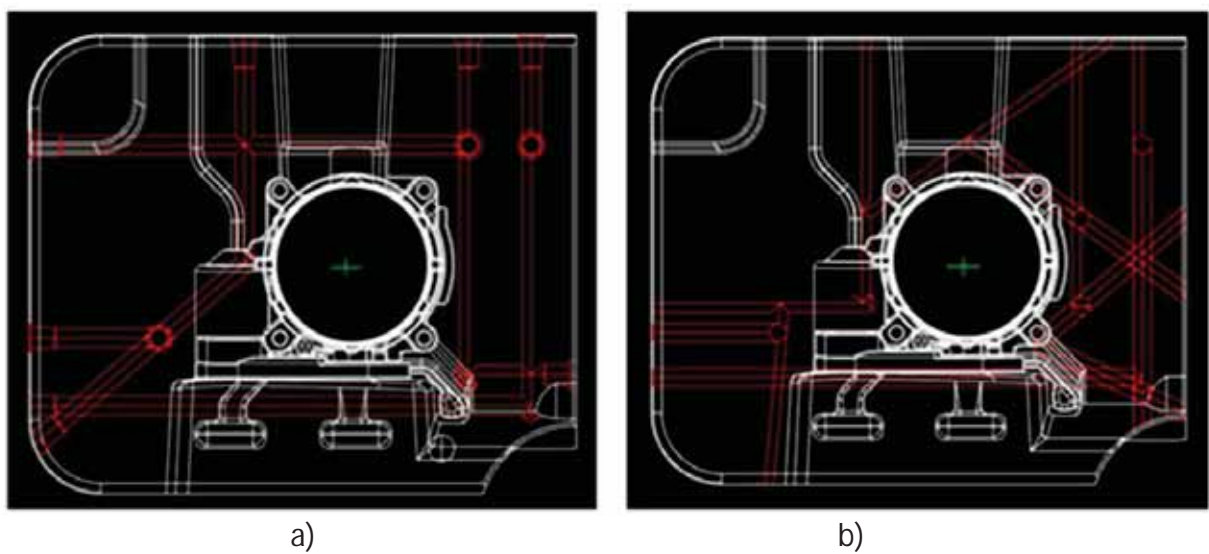

a)   b)

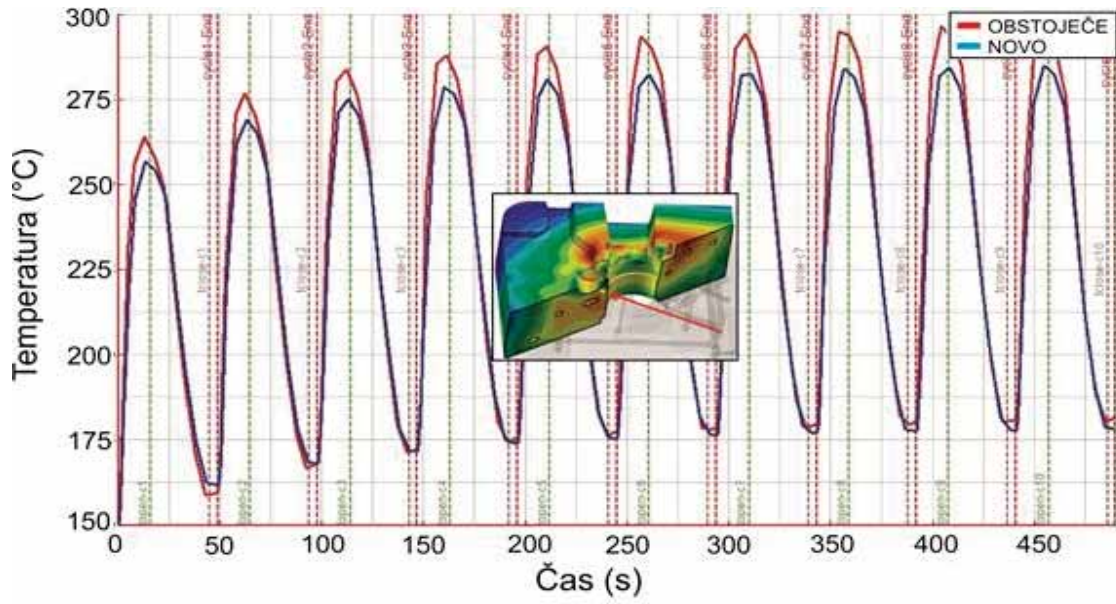Figure 4. Positioning of heating-cooling system in a stable part of a tool: a) old tool and b) new tool

Figure 5. Temperature during cycling in an old (red) and new tool (blue)
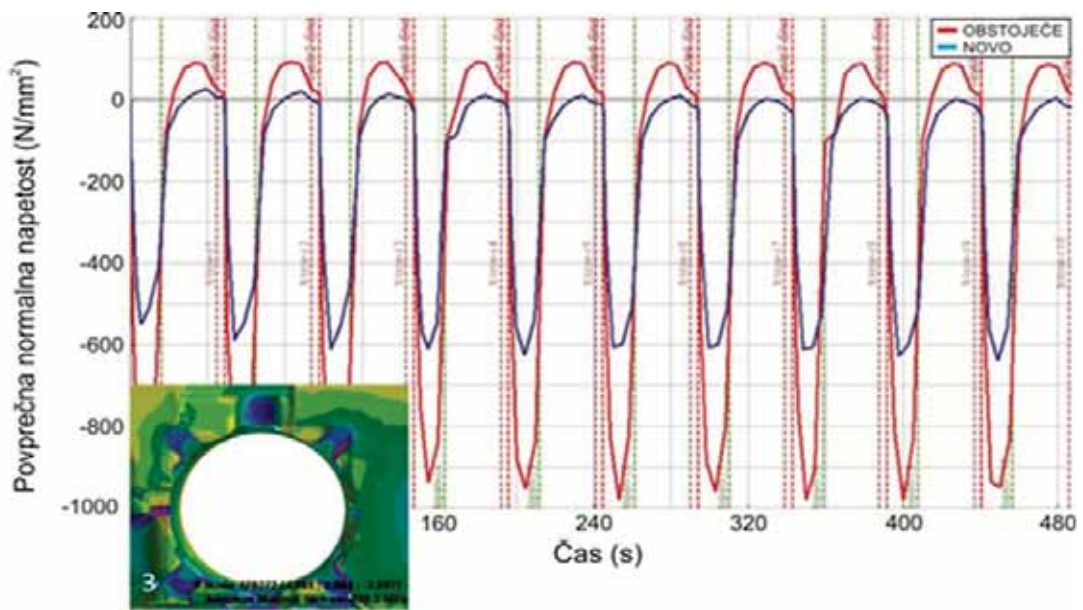
Figure 6. Calculated average normal stresses during cycling in an old (red)
and new tool (blue)
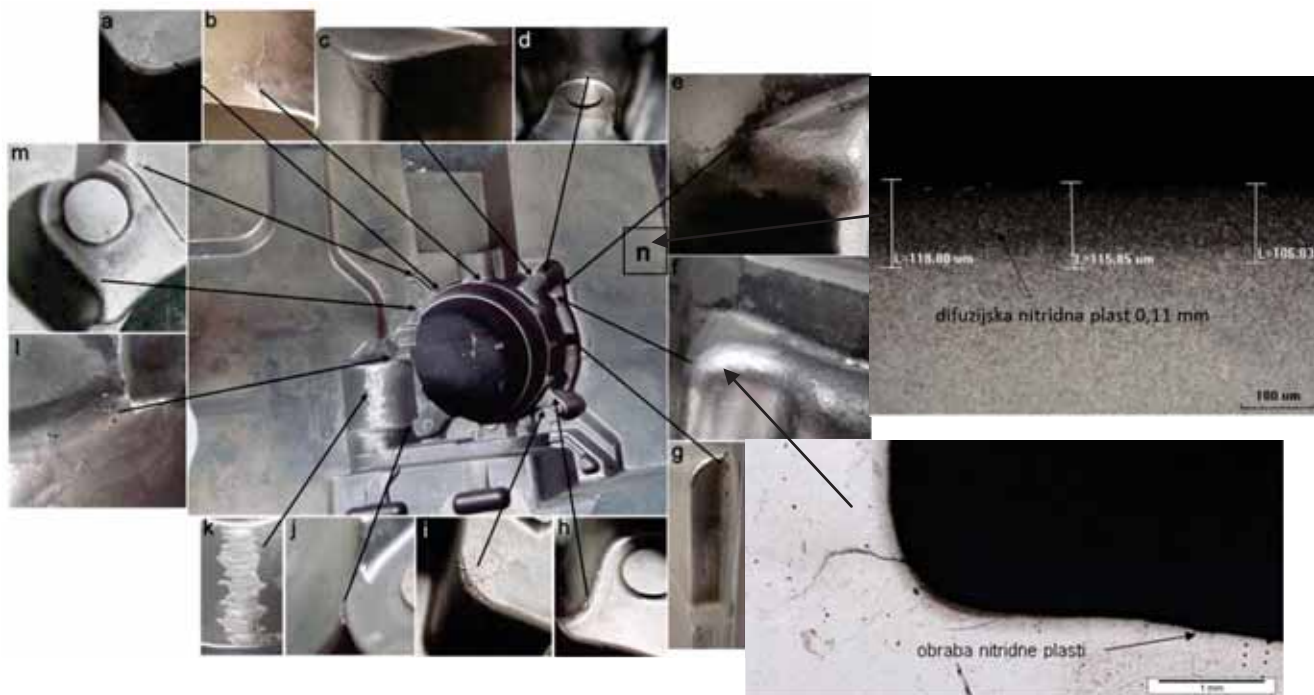
Figure 7. Defects in a tool with thickness and wear of nitrided surface
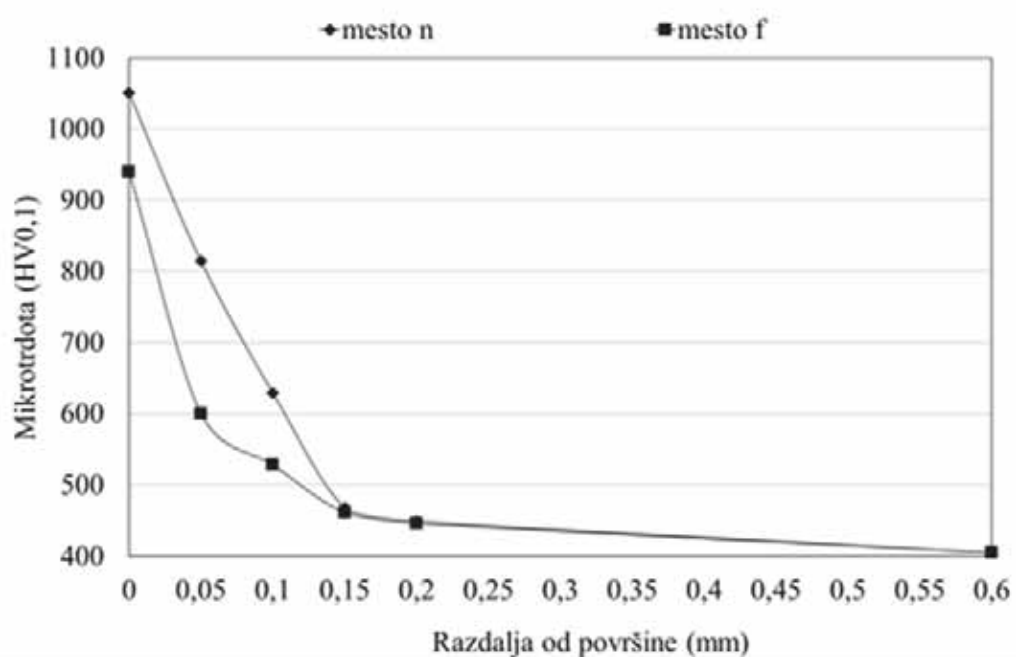
Figure 8. Vickers hardness profiles on spots n and f
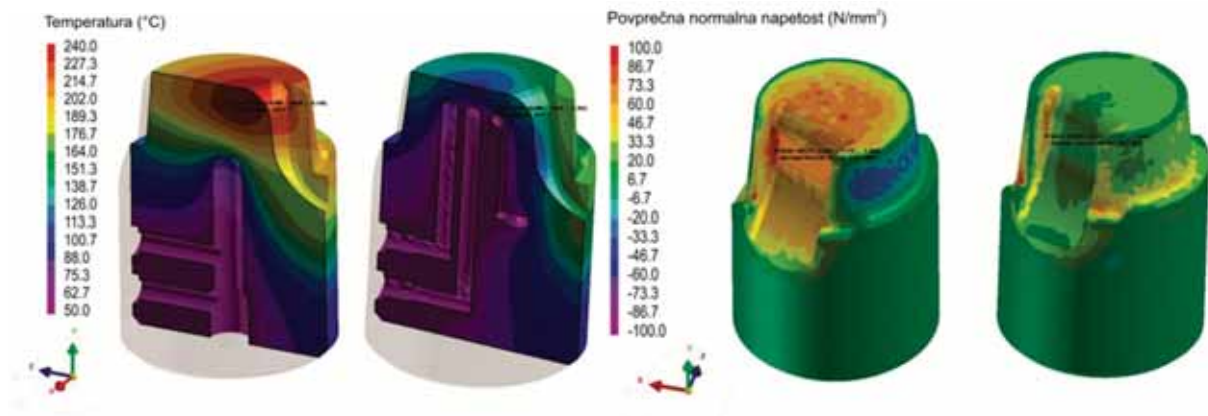
Figure 9. Old (left) and new (right) cooling system of a distributor: thermal field (a), average normal stress field (b)

CONCLUSIONS

Analyses of a tool made by ProCAST software and by thermal imaging showed that the stable part of a tool has approximately 130 °C higher temperature which leads to a shorter lifetime of a tool. The stable part of a tool had a lifetime of 72070 cycles while movable part of a tool had lifetime of 95332 cycles. Based on calculations the new position of heating-cooling system has been made and tool produced. This has resulted in lowered temperatures and lowered stresses in the tool. Calculation showed that the amplitude of average normal stresses in an old tool was 1080 N/mm^2 but in new tool it was decreased to 700 N/mm^2. The lifetime of a new tool should increase but the tool was not tested to the end since the production of a casting was stopped.

Similar analyses were done for the distributor and same trend of results was observed. The distributor with new more effective cooling system reached about 60 % lower temperatures then in an old one. Maximum temperature in new distributor was 94.7 °C. Lowered temperatures caused for 47 % lower stresses and average normal stresses reached only 58.4 N/mm^2. This leads to increased lifetime for over 36 %. An old distributor made 74928 cycles and new one made over 102246 cycles and still running.

REFERENCES

[1] M. Trbižan, Livarstvo, interna skripta, Naravoslovnotehniška fakulteta, Katedra za livarstvo, Ljubljana, 1996.

[2] ASM Metals Handbook, Volume 15, Casting, ASM International, 1988.

[3] ASM Specialty Handbook – Aluminium and Aluminium Alloys, Edited by J. R. Davis, ASM International, 1993.

[4] A. C. Street, The diecasting book, Second edition, Portcullis press ltd, Surrey, 1990.

[5] G. Lojen, I. Anžel, A. Križman, Vpliv pogojev strjevanja na mikrostrukturo zlitin in kompozitov s sestavo AlSi17Cu5, Materiali in tehnologije, 35(2001)37, pp. 1-2.

[6] M. Petrič, J. Medved, P. Mrvar, Vpliv udrobnjevanja, modificiranja in ohlajevalne hitrosti na mikrostrukturo zlitine AlSi10Mg, RMZ–Material and Geoenvironment, 53 (2006)3, pp. 385-401.

[7] M. Petrič, J. Medved, P. Mrvar, Effect of grain refinement, modification and cooling rate on the microstructure of alloy 239 and 226, Giessereiforschung, 60(2008)2, pp. 26-37.

[8] D. Klobčar, J. Tušek, M. Pleterski, L. Kosec, M. Muhič, Analiza toplotnih razpok na orodjih za tlačno litje aluminija, Materiali in tehnologije, 42(2008)5, pp. 203-210.

[9] B. Kosec, L. Kosec, J. Kopač, Analysis of casting die failures, Engineering Failure Analysis, 8(2001)8, pp. 355-359.

[10] E. Brunhuber, Praxis der Druckguβfertigung, Schiele & Schön, Berlin, 1991.

[11] X. P. Dang, H. S. Park, Design of U-shape Milled Groove Conformal Cooling Channels for Plastic Injection Mold, International Journal of precision engineering and manufacturing, 12(2011)1, pp. 73-84.

[12] C. L. Li, C. G. Li, A. C. K. Mok, Automatic layout design of plastic injection mould cooling system, Computer-Aided Design, 37(2005)7, pp. 645-662.

[13] C. G. Li, C. L. Li, Y. Liu, Y. Huang, A new C-space method to automate the layout design of injection mould cooling system. Computer-Aided Design, 44(2012)9, pp. 811-823.

[14] H. S. Park, X. P. Dang, Optimization of conformal cooling channels with array of baffles for plastic injection mould, International Journal of Precision Engineering and Manufacturing, 11(2010)6, pp. 879-890.

[15] Y. F. Sun, K. S. Lee, A. Y. C. Nee, Design and FEM analysis of the milled groove insert method for cooling of plastic injection moulds, International Journal of Advanced Manufacturing Technology, 24(2004)9, pp. 715-726.

[16] C. G. Li, C. L. Li, Plastic injection mould cooling system design by the configuration space method, Computer-Aided Design, 40(2008)4, pp. 334-349.

[17] L. Frick, The Difference Between Machined and 3D Printed Metal Injection Molds, Accesible on internet: http://machinedesign.com/3d-printing/difference-between-machined-and-3d-printed-metal-injection-molds

[18] B. Kosec, G. Kosec, M. Soković, Temperature field and failure analysis of die-casting die, Archives of Materials Science and Engineering, 28(2007)3, pp. 182-187.

SOL-GEL SYNTHESIS OF NANOSTRUCTURE TiO$_2$ ON EGGSHELL MEMBRANE AS BIO-TEMPLATE

SINTEZA NANOSTRUKTURIRANOG TiO$_2$ DOBIVENOG SOL-GEL METODOM NA BIO-PREDLOŠKU MEMBRANE LJUSKE JAJA

Jelena **Petruša**[1], **Lidija Ćurković**[1], **Ivana Bačić**[2], Davor Ljubas[1], Stanislav Kurajica[3]

[1]University of Zagreb Faculty of Mechanical Engineering and Naval Architecture, Zagreb, Croatia
[2]Forensic Science Centre "Ivan Vučetić", Zagreb, Croatia
[3]Faculty of Chemical Engineering and Technology, Zagreb, Croatia

<u>Poster presentation</u>
Original scientific paper

Abstract

Biomimicry is a new branch of science with the help of which people try to imitate sustainable solutions from nature to create materials of improved properties. The eggshell membrane represents a unique biomaterial that can be used as a bio-template for the synthesis of hierarchically structured nanomaterials because of its fiber and porous microstructure.

In this research the nanostructured titanium dioxide was synthetized by sol-gel/sonochemical synthesis using the eggshell membrane as a bio-template. For the preparation of sol, titanium isopropoxide was used as a precursor, 2-propanol as a solvent and acetyl acetone as a chelating agent with the addition of nitric acid as a catalyst. The egg shell membranes as bio-template were added to the prepared sol. After the infiltration, gelation and drying, the heat treatment of sample was performed at 500 °C. Characterization of nanostructured TiO$_2$ on bio-template was performed by field emission scanning electron microscopy (FE-SEM), XRD analysis as well FT-IR and micro-Raman spectroscopy. It was found that anatase phase of nanostructured TiO$_2$ was obtained with crystallite size of 29 nm.

Keywords: *TiO$_2$, bio-template, XRD, FE-SEM, FT-IR, Raman*

*Corresponding author (e-mail address): lcurkov@fsb.hr

Sažetak

Biomimikrija je nova grana znanosti uz pomoć koje se nastoje oponašati održiva rješenja iz prirode kako bi se stvorili materijali poboljšanih svojstava. Membrana ljuske jaja predstavlja jedinstveni

biomaterijal koji se zbog svoje vlaknaste i porozne mikrostrukture može koristiti kao bio-predložak za sintezu hijerarhijski strukturiranih nanomaterijala.

U ovom radu sintetiziran je nanostrukturirani titanijev dioksid sol-gel/sonokemijskom sintezom pomoću membrane ljuske jaja kao bio-predloška. Za pripravu sola korišten je titanov izopropoksid kao prekursor, 2-propanol kao otapalo, acetilaceton kao kelirajući reagens uz dodatak nitratne kiseline kao katalizatora. U pripremljenu sol dodane su membrane ljuske jaja kao bio-predložak. Nakon infiltriranja, geliranja i sušenja uzorak je toplinski obrađen na temperaturi od 500 °C. Karakterizacija nanostrukturiranog TiO_2 sintetiziranog na bio-predlošku provedena je pretražnim elektronskim mikroskopom s emisijom polja (FE-SEM), XRD analizom te FT-IR i mikro-Raman spektroskopijom. Dobiveni rezultati pokazuju da je sintetizirani nanostrukturirani TiO_2 na bio-predlošku u kristalnoj formi anatasa s veličinom kristalita od 29 nm.

Ključne riječi: TiO_2 na bio-predlošku, FE-SEM, XRD, FT-IR, Raman

UVOD

Sinteza nanomaterijala može se podijeliti u dvije osnovne grupe: odozgo prema dolje (engl. *top down*) i odozdo prema gore (engl. *bottom up*) (slika 1).
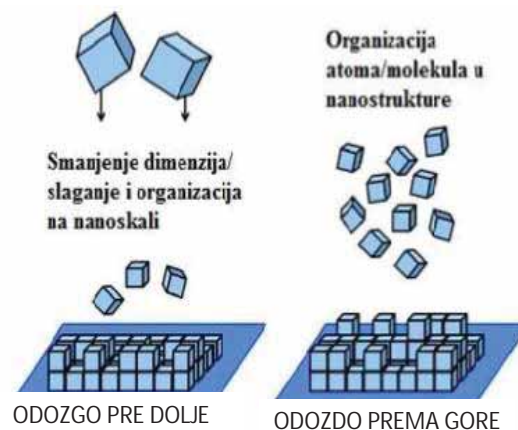
Slika 1. Shematski prikaz dvije osnovne metode nastanka nanomaterijala [1]

Posljednjih desetljeća razvija se interes inženjera kemije i materijala za istraživanjem i razvojem novih metoda sinteze nanomaterijala. Sve se više teži za pronalaskom sinteze uz pomoć koje se može kontrolirati oblik, veličina i morfologija nanočestica.

U prirodi se nalazi široki spektar bioloških materijala s različitim funkcijama i odgovarajućim strukturama. Na taj je način priroda riješila i osigurala svoj održivi razvoj u uvjetima koji su prisutni na Zemlji. Upravo takve prirodne strukture služe kao inspiracija mnogim inženjerima i znanstvenicima za rješavanjem problema u tehničkom svijetu. Za uspješno oponašanje prirodnih struktura potrebno je znanje i razumijevanje odnosa između strukture i funkcije bioloških materijala. Zbog sve većeg interesa za ovom vrstom bioinspiracije razvija se nova grana znanosti, biomimikrija. Nanotehnologija koristi biomimikriju kako bi uz pomoć

oponašanja prirodnih struktura imitirala održiva rješenja iz prirode te stvorila materijale poboljšanih svojstava.

Prilikom sinteze nanomaterijala najčešće se koristi metoda odozdo prema gore, gdje se materijali sastavljaju od nanoskale prema makroskali osiguravajući jedinstvena svojstva (slika 1). Stoga se što više nastoji koristiti bioinspirirana porozna struktura materijala. U prirodi se nalaze različiti biološki sustavi koje možemo oponašati poput listova biljka (slika 2a), guštera (slika 2b), morskih spužva (slika 2c), koralja, peluda, krila leptira, membrane ljuske jaja, membrane bambusa, papira, drva, pa i DNA, proteina te virusa. Korištenjem bio-predložaka (engl. *bio-template*) kao podloga za rast nanočestica moguće je proizvesti anorganske materijale s kontroliranim oblikom i poroznošću.
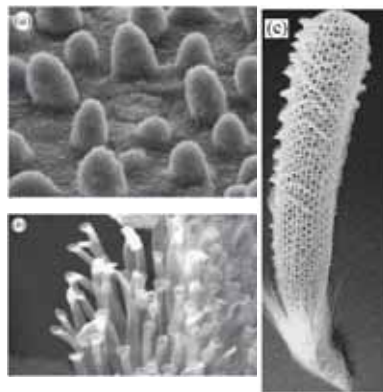
Slika 2. Različiti biološki sustavi: a) list lotosovog cvijeta, b) stopala guštera macaklina i c) morska spužva Euplectelli aspergillum [2]

Tako nastale nanočestice imaju poroznu unutarnju strukturu te se one mogu slagati u sklopove višeg reda kako bi se stvorili hijerarhijski strukturirani materijali. To su materijali u kojima su kristaliti minerala mikrometarske veličine, određenog oblika i orijentacije posloženi u veći, određeni uzorak [3]. Trenutno se ulaže puno znanja u istraživanja sinteza hijerarhijski strukturiranih nanomaterijala s bioporoznošću zbog toga što se time mogu definirati kristalne faze, stupanj kristalitičnosti, dimenzije, oblici i raspodjela pora [4]. Time privlače sve više pozornosti te im se širi potencijalna primjena u katalizi, sorpciji, separaciji i optici. U usporedbi s umjetnim predlošcima, bio-predlošci su kompleksni i hijerarhijski, općenito jeftini te ekološki prihvatljiviji [5].

Membrana ljuske jaja (engl. *eggshell membrane ESM*) je jedinstveni biomaterijal koji pronalazimo kao otpadni materijal u obiteljskim domovima, mrijestilištima i prehrambenoj industriji, gdje se koriste u velikim količinama te obično završavaju u otpadu. Međutim, membrane imaju izvanredna svojstva zahvaljujući svojoj jedinstvenoj strukturi. Iz tog razloga mnogi ih znanstvenici sve više istražuju i primjenjuju u različitim područjima poput medicine, biotehnologije, biokemije, farmacije, prehrambene industrije, te elektronike. Ljuske jaja zajedno s membranama možemo prikupiti u velikim količinama i iskoristiti ih kao izvor za nastanak novih materijala. Ljuske i membrane jaja možemo iskoristiti kao gnojivo biljkama za dobavu kalcija, kao stabilizator tla, kao lijek za osteoporozu i oboljenje pokretljivosti zglobova, kao pomoć za liječenje u ortopediji i stomatologiji, kao pomoć pri liječenju pacijenata oboljelih od raka, u sportskoj prehrani za povećanje performansi sportaša, u industriji hrane kao pojačivač okusa, u umjetnosti za proizvodnju mozaika, kao lijepilo za

glazbene instrumente, u kozmetici i plastičnim operacijama za poboljšavanje izgleda kože [7]. Znanstveno-istraživačka djelatnost koncentrirana je uglavnom na tri područja [8]: (i) iskorištavanje membrane ljuske jaja kao bio-predloška za sintezu različitih nanomaterijala, (ii) upotreba membrane ljuske jaja kao sorbensa za uklanjanje iona teških metala i organskih bojila, (iii) primjena membrane ljuske jaja kao biosenzora.

Uz pomoću bio-predložaka možemo proizvesti novi hijerarhijski keramički materijal s jedinstvenom i kompleksnom strukturom. Tehnika pripreme keramičkih materijala uz pomoću bio-predloška je jeftina, lako dostupna i jednostavna, ekološki prihvatljiva te na učinkovit način kontrolira morfologiju, posebna funkcionalna svojstva i strukturu. Prema literaturi [5], sol-gel proces membrane ljuske jaja predstavlja prilagodljiv postupak za sintezu bioinspiriranih hijerarhijskih uređenih metalnih oksida. Princip upotrebe bio-predložak tehnike sastoji se od toga da se najprije u prirodnu membranu ljuske jaja infiltrira koloidna otopina, te se zatim kalcinira na višim temperaturama kako bi nastala biomorfna funkcionalna keramika [9]. Sinteza uz pomoću bio-predloška u sustavu sol-gel procesa pokazuje idealan pristup dizajnu i konstrukciji naprednih materijala s unaprijed određenim fizičkim i kemijskim svojstvima.

U ovom radu sintetiziran je nanostrukturirani TiO_2 sol-gel/sonokemijskom metodom na bio-predlošku membrane ljuske jaja. Karakterizacija TiO_2 na bio-predlošku membrane ljuske jaja provedena je pretražnim elektronskim mikroskopom s emisijom polja (FE-SEM), XRD, FT-IR i Raman analizom.


MATERIJALI I METODE

Priprema membrane ljuske jaja

U ovome radu za sintezu TiO_2 nanočestica korišten je bio-predložak membrane ljuske jaja. Korištena su komercijalno lako dostupna kokošja jaja, odnosno ljuske i membrane iz komunalnog otpada. Prije same sinteze membrane je bilo potrebno pripremiti.

Tijek pripreme membrana:

- kokošja jaja se nježno slome i isprazne,
- ljuske se zajedno s membranom operu destiliranom vodom,
- membrane se od ljuske odvajaju ručno,
- membrane se stavljaju u razrijeđenu octenu kiselinu, 20% CH_3COOH na jedan dan da se otopi kalcijev karbonat $CaCO_3$ koji potječe iz ljusaka jaja,
- membrane se ispiru destiliranom vodom,
- membrane se suše na sobnoj temperaturi (25 °C).

Priprema sola (koloidne otopine) TiO_2

Za sintezu TiO_2 nanočestica pripremljena je sol (koloidna otopina) za čiju su pripravu korištene sljedeće komponente: titanov izopropoksid (TIP) kao prekursor, 2-propanol (PrOH) kao otapalo, HNO_3 (HN) kao katalizator i acetilaceton kao kompleksirajući agens.
Molarni omjer rektanata bio je [10]: TIP:PrOH:AcAc:HN = 1:35:0.63:0.015.
Navedene komponente dodavane su u staklenu Erlenmayerovu tikvicu redoslijedom kojim su gore navedeni uz konstantno miješanje na magnetnoj miješalici.

Infiltracija TiO$_2$ sola na membrane ljuske jaja i toplinska obrada

TiO$_2$ sol prikazana je na slici 3a. Otopina TiO$_2$ sol ostavljena je na magnetskoj miješalici jedan dan da se homogenizira. Nakon toga u sol se dodaje 10 grama membrane ljuske jaja (slika 3b). Tako pripremljena koloidna otopina (sol) TiO$_2$ ostavljena je tri dana da se infiltrira na membranu ljuske jaja. Otopina TiO$_2$ sola zajedno s membranama ljuske jaja sonokemijski je tretirana uređajem Hielscher UP400S snage 400 W, pri frekvenciji 24 kHz, sa sondom (sonotrodom) ϕ14 mm. Postupak je trajao 15 minuta, s početnom temperaturom 25 °C koja je postepeno rasla do 70 °C (slika 3c). Nakon sonokemijskog tretiranja (slika 3d) slijedi geliranje TiO$_2$ na bio-predlošku membrane ljuske jaja te sušenje i toplinska obrada. Toplinska obrada sastoji se od zagrijavanja uzorka u električnoj peći na temperaturu od 500 °C brzinom grijanja od 3 °C/min te izotermnog držanja na temperaturi od 500 °C tijekom 60 minuta. Nakon toga slijedi hlađenje na zraku do sobne temperature, 25 °C.

Slika 3. a) TiO$_2$ sol, b) infiltracija TiO$_2$ sola na membrane ljuske jaja, c) sonokemijsko tretiranje sonotrodom, d) nakon tretiranja sonotrodom

Karakterizacija TiO$_2$ na bio-predlošku membrane ljuske jaja

U svrhu karakterizacije uzoraka membrane ljuske jaja i sintetiziranog nanostrukturiranog TiO$_2$ na bio-predlošku membrane ljuske jaja provedena su sljedeća ispitivanja i analize:

- analiza morfologije uzoraka provedena je uporabom pretražnog elektronskog mikroskopa s emisijom polja (FE-SEM) na uređaju model MIRA3, Tescan Co,
- fazni sastav i veličina kristalita sintetiziranog nanostrukturiranog TiO$_2$ na bio-predlošku membrane ljuske jaja određen je rendgenskom difrakcijskom analizom na uređaju rendgenski difraktometar Shimadzu XRD-6000 (Shimadzu Corporation, Japan),
- karakterizacija uzoraka provedena je i primjenom spektroskopskih metoda (i) infracrvene spektroskopije s Fourierovom transformacijom (FTIR) na spektrometru Bruker Alpha FT-IR te (ii) Ramanovom spektroskopijom uporabom Ramanovog disperzivnog spektrometra SENTERRA II (Bruker Corp., SAD) u konfiguraciji s mikroskopom Olympus (Olympus Imaging Corp., Japan).

REZULTATI I DISKUSIJA

Morfologija membrane ljuske jaja, te nanostrukturiranog TiO$_2$ na bio-predlošku membrane ljuske jaja analizirana je pretražnim elektronskim mikroskopom s emisijom polja (FE-SEM) i

prikazana je na slici 4. Na slici 4a može se uočiti porozna struktura membrane ljuske jaja, koja se sastoji od mnogo isprepletenih i spojenih vlakana; na slikama 4b i 4c može se vidjeti porozna struktura TiO$_2$ nanočestica sintetiziranih na bio-predlošku membrane ljuske jaja promatrana FE-SEM-om pri povećanju od 66700x.
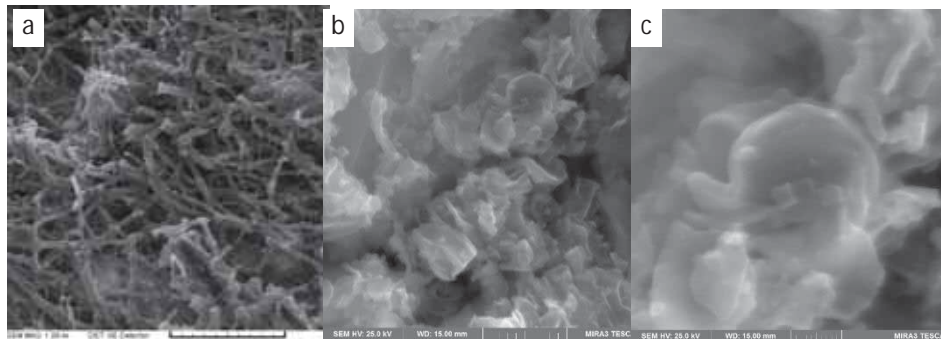
Slika 4. FE-SEM snimka: a) membrana ljuske jaja, b) TiO$_2$ nanočestica na bio-predlošku membrane ljuske jaja pri povećanju od 66700x i c) TiO$_2$ nanočestica pri povećanju od 200000x

Mogu se uočiti čestice štapićastog, kružnog, kvadratnog i pločastog oblika uz povećanje 200000x (slika 4c).

Na slici 5a prikazan je difraktogram titanijevog dioksida sintetiziran na bio-predlošku membrane ljuske jaja, a na slici 5b prikazan je samo refleks (101) za koji je korišten za određivanje veličine kristalita pomoću Scherrerove metode.
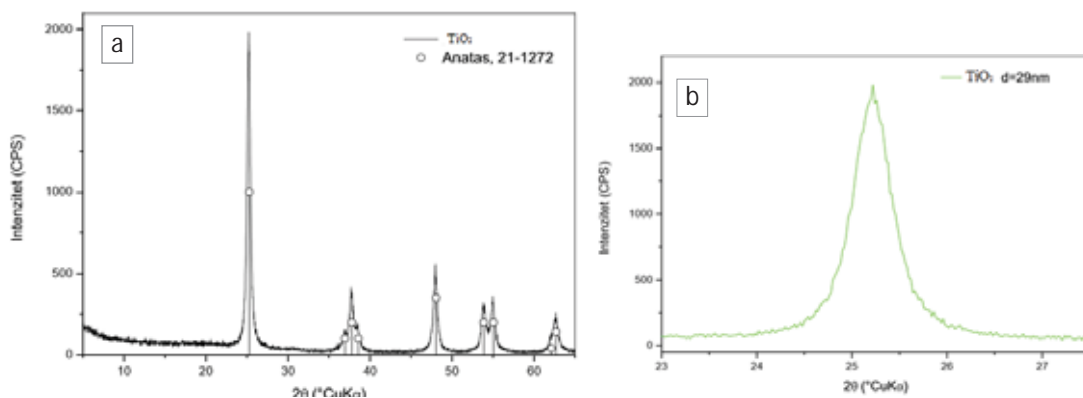
Slika 5. a) Difraktogram titanijevog dioksida sintetiziran na bio-predlošku membrane ljuske jaja, b) refleks (101) koji je korišten za određivanje veličine kristalita pomoću Scherrerove metode

Rendgenskom difrakcijskom analizom utvrđeno je da je u sinteriranom nanostrukturiranom TiO$_2$ na bio-predlošku membrane ljuske jaja prisutan čisti anatas s veličinom kristalita u iznosu od oko 29 nm.

Infracrvena spektroskopija pogodna je tehnika za određivanje strukture proteina. Položaji vrpci uočenih u spektru membrane ljuske jaja (slika 6, tablica 1) dobro se slažu s literaturnim podacima o karakterističnim vrpcama peptidne veze [8,11-13]. Spektar membrane ljuske jaja karakterizira Fermijev rezonantni dublet vrpci u području ~3600-3000 cm^{-1} s maksimumima

pri 3272 cm^{-1} odnosno 3071 cm^{-1}. Navedene vrpce, označene kao amid A odnosno amid B posljedica su istezanja N-H veze u rezonanciji s prvim višim tonom amida II [12].
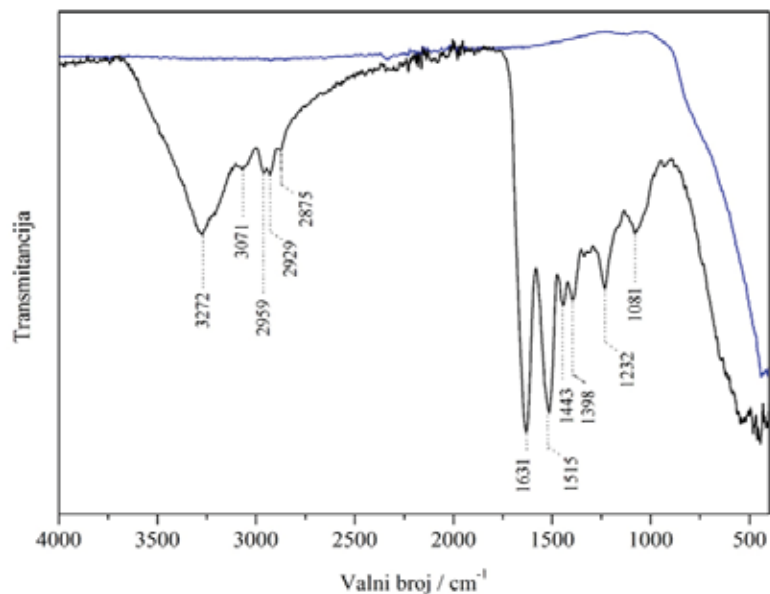
Slika 6. FTIR spektri membrane ljuske jaja (crno) i TiO_2 na bio-predlošku membrani ljuske jaja (plavo)

Tablica 1. Vibracijske vrpce u FTIR i Ramanovom spektru membrane ljuske jaja

Valni broj / cm⁻¹		Vibracija
FTIR	Raman	
3272		rezonancija ν N–H i viših tonova amida II (amid A)
3071		rezonancija ν N–H i viših tonova amida II (amid B)
2959		ν_{as} CH_3
2929		ν_{as} CH_2
2875		ν_s CH_3
1631	1670	većinom ν C=O (amid I)
1515	1548	δ_{ip} N–H i ν C–N (amid II)
1443	1445	ν –C=C
1398		ν C=O karboksilne skupine
1232	1233	δ_{ip} N–H i ν C–N (amid III)
1081		ν C–O
	1003	ν benzene ("disanje" prstena)
	510	ν S–S

Vibracijske vrpce pri 2959, 2929 i 2875 cm^{-1} pripisane su antisimetričnom i simetričnom istezanju C-H veza metilenskih i metilnih skupina. Karakteristične vibracijske vrpce u IR spektrima proteina odnosno membrani ljuske jaja nalaze se pri 1631 cm^{-1}, 1515 cm^{-1} i 1232 cm^{-1} i u literaturi se označavaju kao amid I, amid II i amid III vibracije [12,13].

Amid I vibracija potječe većinom od istezanja C=O veze amidne skupine (70-85 %) koja je u manjoj mjeri združena sa svijanjem N-H veze u ravnini i istezanjem C-N veze. Vrpce amida II odnosno amida III kombinacija su svijanja N–H veze u ravnini i istezanja C-N veze s malim doprinosom vibracija svijanja C=O veze u ravnini te istezanja C-C veze. Preostale vrpce pri 1443, 1398 i 1081 cm^{-1} odnose se na istezne vibracije -C=C veze, C=O veze karboksilne skupine te C-O veze. Za razliku od spektra same membrane ljuske jaja, spektar TiO$_2$ nanočestica sintetiziranih na bio-predlošku nakon toplinske obrade na 500 °C je veoma jednostavan, a u njemu je najznačajnija široka apsorpcija u području ~800–400 cm^{-1} koja ukazuje na nastanak titanijevog dioksida.

Ramanov spektar membrane ljuske jaja (slika 7, crno) potvrdio je rezultate dobivene FTIR spektroskopijom. U spektru se nalaze već opisane karakteristične vrpce amida I, amida II i amida III (tablica 1), kao i dvije dodatne vrpce pri 1003 i 510 cm^{-1}. Vrpca pri višem valnom broju pripisana je ''disanju'' aromatskog prstena aminokiseline fenilalanin (Phe), dok je ona pri nižem valnom broju posljedica istezanja S-S veze što ukazuje na prisutnost disulfidnog mosta [14]. Toplinskom obradom membrane ljuske jaja i TiO$_2$ u Ramanovom spektru dobivene su dobro definirane vrpce čiji se položaji pri 143 (E$_g$), 195 (E$_g$), 396 (B$_{1g}$), 516 (A$_{1g}$+B$_{1g}$) i 638 cm^{-1} (E$_g$) podudaraju s literaturnim vrijednostima za TiO$_2$ u kristalnoj formi anatasa [15,16].
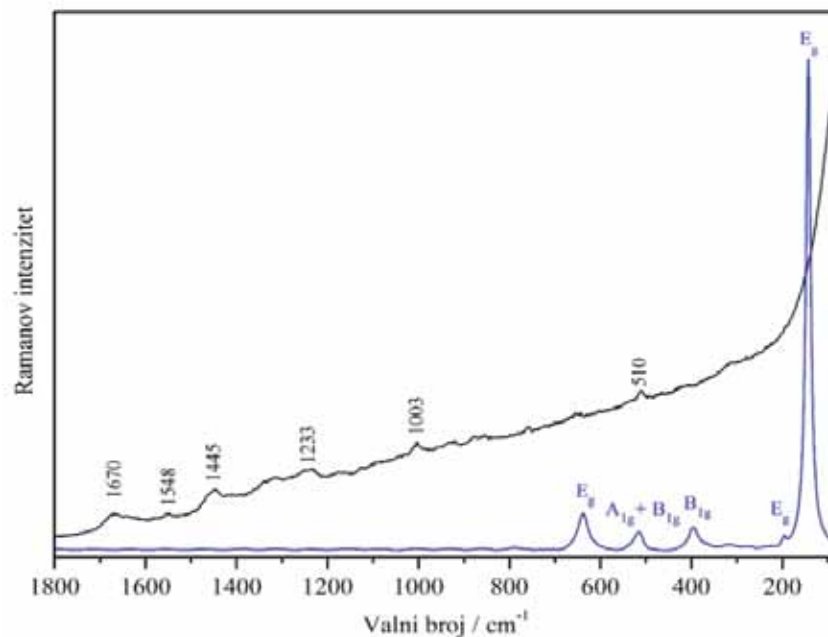
Slika 7. Ramanovi spektri membrane ljuske jaja (crno) i TiO$_2$ nanočestice sintetiziranie na bio-predlošku (plavo), s naznačenim vibracijskim modovima titanijevog dioksida u kristalnoj formi anatasa

204

ZAKLJUČCI

Iz dobivenih rezultata može se zaključiti sljedeće:

- Membrana ljuske jaja predstavlja jedinstveni biomaterijal koji se zbog svoje morfologije, vlaknaste i porozne mikrostrukture može iskoristiti kao bio-predložak za sintezu hijerarhijski strukturiranih nanomaterijala.

- Sinteza sol-gel procesom potpomognuta sonokemijskom metodom predstavlja prilagodljiv postupak za sintezu bioinspiriranih hijerarhijskih uređenih metalnih oksida s unaprijed određenim fizičkim i kemijskim svojstvima.

- FE-SEM analizom potvrđena je vlaknasta i porozna struktura membrane ljuske jaja, te porozna nanostruktura različite morfologije TiO_2 nanočestica sintetiziranih na bio-predlošku membrane ljuske jaja.

- XRD analizom određena je veličina kristalita TiO_2 nanočestica na bio-predlošku membrane ljuske jaja u iznosu od oko 29 nm. Također, analizom je potvrđena prisutnost čistog anatasa u sinteriranom TiO_2 na bio-predlošku.

- FTIR i Ramanovom spektroskopijom potvrđeno je da je uzorak TiO_2 sintetiziran na bio-predlošku nakon toplinske obrade pri 500 °C u kristalnom obliku, u polimorfnoj modifikaciji anatas što je u skladu s rezultatima XRD analize.
- U sljedećim istraživanjima ispitat će se fotokatalitička razgradnja famaceutika uz korištenje sintetiziranog nanostrukturiranog TiO_2 na bio-predlošku membrane ljuske jaja primjenom Sunčevog zračenja.

LITERATURA

[1] M. Plodinec, Fizikalna i kemijska svojstva funkcionaliziranih titanatnih nanostruktura, doktorski rad, Sveučilište u Zagrebu, Prirodoslovno-matematički fakultet, 2014.

[2] L. Eadie, T. Ghosh, Biomimicry in textiles: past, present and potential. An overview, Journal of The Royal Society Interface, 59(2011)8, pp. 761-775.

[3] I. Žmak, T. Filetin, H. Ivanković, Biomimetički materijali i proizvodi, (ur. Tomislav Filetin), Croatian society for materials and tribology, 2005, pp. 141-166.

[4] S. Bao, C. Lei, M. Xu, C. Cai, D. Jia, Environment-friendly biomimetic synthesis of TiO_2 nanomaterials for photocatalytic application, Nanotechnology, 23(2012)20, pp. 205601.

[5] D. Yang, L. Qi, J. Ma, Hierarchically ordered networks comprising crystalline ZrO_2 tubes through sol–gel mineralization of eggshell membranes, Journal of Materials Chemistry, 13(2003)5, pp. 1119-1123.

[6] D. Ramimoghadam, S. Bagheri, S. Abd Hamid, Biotemplated Synthesis of Anatase Titanium Dioxide Nanoparticles via Lignocellulosic Waste Material, BioMed Research International, 2014 (2014), pp. 1-7.

[7] A. Kingori, A Review of the Uses of Poultry Eggshells and Shell Membranes, International Journal of Poultry Science, 10(2011)11, pp. 908-912.

[8] M. Baláž, Eggshell membrane biomaterial as a platform for applications in materials science, Acta Biomaterialia, 10 (2014)11, pp. 3827-3843.

[9] Q. Dong, H. Su, J. Xu, D. Zhang, R. Wang, Synthesis of biomorphic ZnO interwoven microfibers using eggshell membrane as the biotemplate, Materials Letters, 61(2007)13, pp. 2714-2717.

[10] L. Ćurković, D. Ljubas, S. Šegota, I. Bačić, Photocatalytic degradation of Lissamine Green B dye by using nanostructured sol-gel TiO_2 films, Journal of Alloys and Compounds, 604(2014), pp. 309-316.

[11] A. Barth, Review Infrared spectroscopy of proteins, Biochimica et Biophysica Acta, 1767 (2007), pp. 1073–1101.

[12] P. Garidel, S. Heidrun, Fourier-transform midinfrared spectroscopy for analysis and screening of liquid protein formulations, BioProcess International, 4 (2006), pp. 48-55.

[13] M. K. Rath, B. H. Choi, M. J. Ji, K. T. Lee, Eggshell-membrane-templated synthesis of hierarchically-ordered $NiO–C_{0.8}Gd_{0.2}O_{1.9}$ composite powders and their electrochemical performances as SOFC anodes, Ceramics International, 40(2014), pp. 3295–3304.

[14] A. Rygula, et al., Raman spectroscopy of proteins: a review, Journal of Raman Spectroscopy, 44(2013), pp. 1061-1076.

[15] S. Saja Al-Taweel, H. R. Saud, New route for synthesis of pure anatase TiO_2 nanoparticles via utrasoundassisted sol-gel method, Journal of Chemical and Pharmaceutical Research, 8(2016)2, pp. 620-626.

[16] H. C. Choi, M. J. Young, B. K. Seung, Size effects in the Raman spectra of TiO_2 nanoparticles, Vibrational Spectroscopy, 37(2005), pp. 33-38.

Zahvala

PREDICTION OF THE Ge-In AND Ge-Pb NANOALLOY PHASE DIAGRAM

Milena Premović[1,2], Yong Du[2], **Duško Minić**[1]**, Aleksandar Đorđević**[1], **Dušan Milisavljević**[1], **Aleksandar Marković**[1], **Milica Tomović**[1]

[1]University of Priština Faculty of Technical Science, Kosovska Mitrovica, Serbia,
[2]Central South University State Key Laboratory of Powder Metallurgy, Changsha, Hunan, China

Abstract

Investigations of the nano-system are in focus of many researchers due to unique physical and chemical properties of nanomaterials. Investigation of nanoalloys significantly increasing with years but in another hand, experimental investigation of nanoalloys is difficult to perform. Due to experimental difficulty, prediction of the nanophase diagram is strongly encouraged. By using extended powerful CALPHAD technique calculation of nano-phase diagram can be carried. For calculation of nano diagrams, additional parameters need to be added to the excess Gibbs energies which are related to the surface. The surface effect which needs to be added is particle size and shape factor. Calculations of these two factors were done in present paper for the binary Ge-In and Ge-Pb system. Size and shape dependent contributions have been added to the description of the Ge-In and Ge-Pb system. Chemical potentials and the excess Gibbs energies in the Ge-In and Ge-Pb system were reassessed as a function of composition, temperature, particle size and shape factor.

Keywords: CALPHAD, nanophase diagram, binary alloys, Ge-In, Ge-Pb, surface effect, particle size and shape factor

*Corresponding author (e-mail address): *milena.premovic@gmail.com

INTRODUCTION

Preparation and examination of nanoparticles are complex and time-consuming tasks for researchers. Sometimes it is impossible to prepare wanted size of particles and shape, usually at the real experiment, as a result, appears a mixture of nanoparticles with different size and shapes. According to the reality, it is important to predict how nanoparticles behave with changing of composition and temperature. Chosen binary systems are important due to the possible application as a phase-change memory (PCM) materials [1-4]. At a first stage as

a basis for future investigations of PCMs, knowledge of phase diagram is important. Alloys which consist germanium have a special application in the modern technology for making optical discs, DVD, Blue-Ray discs, flash memories [5,6]. Due to the importance of binary systems based on Ge, calculation of nanophase Ge-In and Ge-Pb diagram was done. The calculation was performed using extended CALPHAD method for nanoparticles [7-9].

MATERIALS AND METHODS

Calculation of nanophase diagram performed using the CALPHAD method described by Park and Lee [10] which is based on the minimization of the molar Gibbs energy of the phases present. The total Gibbs energy of nanoparticles is written as equation (1).

$$G^{Total} = G^{Bulk} + G^{Surface} \tag{1}$$

Equation (1) is a standard expression of total Gibbs energy for every other A-B system. In equation (1), G^{Bulk} is the Gibbs energies of the bulk binary system and $G^{Surface}$ is the Gibbs energy of the surface. G^{Bulk} of the bulk, the binary system is expressed as following

$$G^{Bulk} = x_A G_A^o + x_B G_B^o + RT\left(x_A \ln x_A + x_B \ln x_B\right) + G^{Ex\,Bulk} \tag{2}$$

where x_A and x_B are mole fraction of A=Ge and B=In, Pb, G_A^o and G_B^o are the standard Gibbs energy of A=Ge and B=In, Pb, R is the universal gas constant, T is the temperature and $G^{Ex\,Bulk}$ is the excess Gibbs energy of the bulk which is given by equation (3).

$$G^{Ex\,Bulk} = x_A x_B \sum_{\upsilon} L^{\upsilon}(T)\left(x_B - x_A\right)^{\upsilon} \text{ and } \upsilon = \square\square\square \ \square\square\square \tag{3}$$

$$L^{\upsilon}(T) = a_{\upsilon} + b_{\upsilon} \cdot T + c_{\upsilon} \cdot T \cdot \square(T) \tag{4}$$

where υ and $L^{\upsilon}(T)$ are temperature dependent. The second parameter from equation (1) $G^{Surface}$ is expressed in equation (5).

$$G^{Surface} = \frac{\square C\sigma V}{r} \tag{5}$$

C is a correction factor considering the effects from the shape, σ is the surface tension, r is the radius of the particle, V is the molar volume. The molar volume for the binary A-B system is expressed as the sum of fractions of each constituent (equation 6).

$$V = x_A V_A + x_B V_B \tag{6}$$

Lee et al. [10] have been estimated correction factor (C) for the liquid to be 1.00 and for solid 1.05. Equation (5) can be extended with an important factor for nanosystem, shape factor. The extended equation is follow

$$G^{Surface} = \frac{\Box C \sigma V \alpha}{r}$$

(7)

The shape factor α are defined by Qi et al. [11] and in Table 1 are listed defined shape factors.

Table 1. The shape factors for nanoparticles of various shapes

Shape	
Particle	Factor - α
Nanofilm	0.333
Spherical	1
Regular octahedral	1.18
Regular hexahedral	1.24
Regular tetrahedral	1.49

The surface tension (σ) of pure A and B in liquid and solid state are defined in the literature [12,13] but for calculation of the surface tension of binary A-B liquid alloy Butler equation [14] need to be used. Butler equation is expressed by equation (8).

$$\sigma = \sigma_A + \frac{\Box}{A_A}\left(G_A^{Surface} - G_A^{Ex\,\Box Bulk}\right) + \frac{RT}{A_A}\,\Box\left(\frac{\Box - x_B^S}{\Box - x_B}\right)$$

$$\sigma = \sigma_B + \frac{\Box}{A_B}\left(G_B^{Surface} - G_B^{Ex\,\Box Bulk}\right) + \frac{RT}{A_B}\,\Box\left(\frac{x_B^S}{x_B}\right)$$

(8)

where σ_A and σ_B are the surface tension of A and B, A_A and A_B are the superficial area occupied by the liquid component A and B, $G_A^{Surface}$ and $G_B^{Surface}$ are the partial excess Gibbs energy of component A and B in the surface and $G_A^{Ex\,\Box Bulk}$, $G_B^{Ex\,\Box Bulk}$ are the partial Gibbs energy of component A and B in bulk. The superficial area A_A and A_B are expressed as following

$$A_A = kN_\Box^{\Box\Box\Box} V_A^{\Box\Box\Box}$$

$$A_B = kN_\Box^{\Box\Box\Box} V_B^{\Box\Box\Box}$$

(9)

where k is a geometrical factor and for liquid alloys is 1.091 [15] and $N_\Box$ is an Avogadro's number (6.02214199(47)·10^{23} mol^{-1}). The partial excess Gibbs energy $G_A^{Surface}$ and $G_B^{Surface}$ of component Ag and Ge have been calculated using equation (10).

$$G_A^{Surface} = \beta^{mix} G_A^{Ex\,\Box Bulk}$$

$$G_B^{Surface} = \beta^{mix} G_B^{Ex\,\Box Bulk}$$

(10)

where β^{mix} is a parameter corresponding to the ratio of the coordination number in the surface in the bulk. Tanaka et al. [15] showed that the surface tension of various liquid alloys

was obtained by assuming that β^{mix} is equal to β^{Pure}. The β^{mix} is estimated to be 0.83 for liquid. The parameter β^{Pure} is defined as following

$$\sigma_A A_A = \left(\square - \beta^{Pure}\right)\Delta H_{LG\square A}$$
$$\sigma_B A_B = \left(\square - \beta^{Pure}\right)\Delta H_{LG\square B}$$

(11)

where $\Delta H_{LG\square A}$ and $\Delta H_{LG\square B}$ are the heat for the liquid-gas transformation of A and B. A similar equation is given for solid β^{Pure}

$$\sigma_A A_A = \left(\square - \beta^{Pure}\right)\Delta H_{SG\square A}$$
$$\sigma_B A_B = \left(\square - \beta^{Pure}\right)\Delta H_{SG\square B}$$

(12)

where $\Delta H_{SG\square A}$ and $\Delta H_{SG\square B}$ are the heat for solid–gas transformation of A and B. The parameter β^{Pure} for solid state was estimated to be 0.84 [10] which is close to liquid metals. According to this conclusion, the surface tension of solid alloys can be predicted also by the Butler equation [14]. Then the standard Gibbs energy should be redefined as a function of the particle size in a way to the assessment of the nanoparticles phase diagram. The chemical potential of pure A and B of radius $G_A^{\square\square Nano}$ and $G_B^{\square Nano}$ are given

$$G_A^{\square\square Nano} = G_A^{\square} + \frac{\square C\sigma_A V_A \alpha}{r}$$
$$G_B^{\square\square Nano} = G_B^{\square} + \frac{\square C\sigma_B V_B \alpha}{r}$$

(13)

Then, the excess Gibbs energy of constituents in the nanoparticles is obtained by equation (14).

$$G^{Ex\square Nano} = G^{Total} - x_A G_A^{\square\square Nano} - x_B G_B^{\square\square Nano} - RT\left(x_A \square x_A + x_B \square x_B\right)$$

(14)

where G^{Total} is calculated by using equations from 1 to 8 and $G_A^{\square\square Nano}$, $G_B^{\square\square Nano}$ by using equation (13). That the excess Gibbs energy of nanoparticles has a Redlich–Kister dependency on composition, temperature and particle radius.

$$G^{Ex\square Nano} = x_A x_B \sum_{\upsilon} L_\upsilon^{Nano}(T)\left(x_B - x_A\right)^{\upsilon} \quad \text{and} \quad \upsilon = \square\square\square\ \square\square\square\square\square$$

(15)

where L_υ^{Nano} is expressed as

$$L_\upsilon^{Nano} = L_\upsilon^{Bulk} + L_\upsilon^{Surface} = \left(a + \frac{a^{\square}}{r}\right) + \left(b + \frac{b^{\square}}{r}\right)T + \left(c + \frac{c^{\square}}{r}\right)T\square(T) + \square\square$$

(16)

where the parameters a, b, and c are the same as those for the bulk phase and $a^{\square}$, $b^{\square}$, $c^{\square}$ are empirical constants (calculated correction for nanoparticles).

RESULTS AND DISCUSSION

The eutectic binary systems Ge-In and Ge-Pb have been selected for the thermodynamic assessment. The assessment was done using CALPHAD method described above. Necessary data for the calculation are summarized in Table 2 [12,13,16].

Table 2. Physical properties of Ge, In, and Pb pure elements
(L – liquid, S – solid phase)

Variables	Equations
Surface tension	$\sigma_{In}^{L}\left(N\cdot m\right)=\square\square\square\square-\square\square\square\cdot\square\square^{\square}T$
	$\sigma_{In}^{S}\left(N\cdot m\right)=\square\square\square\square\square-\square\square\square\cdot\square\square^{\square}T$
	$\sigma_{Pb}^{L}\left(N\cdot m\right)=\square\square\square\square-\square\square\square\cdot\square\square^{\square}T$
	$\sigma_{Pb}^{S}\left(N\cdot m\right)=\square\square\square\square\square-\square\square\square\cdot\square\square^{\square}T$
	$\sigma_{Ge}^{L}\left(N\cdot m\right)=\square\square\square\square-\square\square\square\cdot\square\square^{\square}T$
	$\sigma_{Ge}^{S}\left(N\cdot m\right)=\square\square\square\square\square-\square\square\square\cdot\square\square^{\square}T$
Molar volume	$V_{In}^{L}\left(m^{\square}\cdot mol\right)=\square\square\square\cdot\square\square^{\square}+\square\square\square\cdot\square\square^{\square}T$
	$V_{In}^{S}\left(m^{\square}\cdot mol\right)=\square\square\square\cdot\square\square^{\square}$
	$V_{Pb}^{L}\left(m^{\square}\cdot mol\right)=\square\square\square\cdot\square\square^{\square}+\square\square\square\cdot\square\square^{\square}T$
	$V_{Pb}^{S}\left(m^{\square}\cdot mol\right)=\square\square\square\cdot\square\square^{\square}$
	$V_{Ge}^{L}\left(m^{\square}\cdot mol\right)=\square\square\square\cdot\square\square^{\square}+\square\square\square\cdot\square\square^{\square\square}T$
	$V_{Ge}^{S}\left(m^{\square}\cdot mol\right)=\square\square\square\square\cdot\square\square^{\square}$

The excess Gibbs energy of bulk Ge-In and Ge-Pb are used from Chevalier [17]. The surface Gibbs energy parameters were calculated using equation (7) and added to the Gibbs energy of bulk Ge-In and Ge-Pb systems. Surface tension needed for calculation of the surface Gibbs energy of binary alloys for the Liquid phase is calculated by using a Butler equation (8). Some software is implemented Butler equation (8) for easier calculation of the surface tension. Software used in this calculation was stxs-xbt.exe [18]. Concentration dependence of surface tension for liquid phase at 1300 K, 1400 K and 1500 K are present in Figure 1.
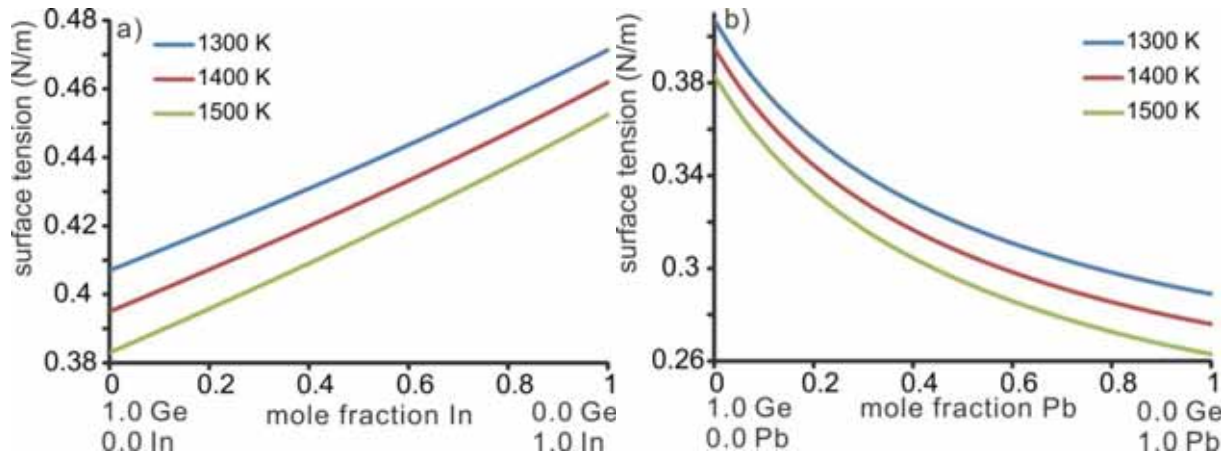
Figure 1. Calculated surfaces tension of liquid phases at 1300 K, 1400 K and 1500 K of the a) binary Ge-In and b) Ge-Pb system.

Calculated concentration dependence of the surface tension of liquid phase multiplied by the (linear) concentration dependence of molar volume (equation 6) makes it possible to express the concentration dependence of the excess surface Gibbs energy for nano-alloys in the liquid phase. Based on the above-given description the thermodynamic parameters for the binary Ge-In and Ge-Pb nano-system are calculated and presented in Table 3. Reciprocal radius is introduced as a function (1/r), and shape factors as a function SF.

Table 3. Thermodynamic parameters for the binary Ge-In and Ge-Pb nanophase diagram

Bulk
Indium
Between $\left(\Box\Box\Box\Box\Box\ T\ \Box\Box\Box\Box\Box\right)$
$\Box G_{In}^{L\,\Box Bulk} = -\Box\Box\Box\Box\Box + \Box\Box\Box\Box\Box\Box\cdot T - \Box\Box\Box\Box\Box\Box\cdot T \cdot \Box\Box T\ \Box-$ $\Box\Box\Box\Box\Box\Box\Box\Box\Box\cdot T^{\Box} - \Box\Box\Box\Box\Box\Box\cdot\Box\Box^{\Box}\cdot T^{\Box} - \Box\Box\Box\Box\Box\cdot T^{-\Box} - \Box\Box\Box\Box\Box\Box\cdot\Box\Box^{\Box\Box}\cdot T^{\Box}$
$\Box G_{In}^{Tetrag\,\Box A\,\Box Bulk} = -\Box\Box\Box\Box\Box\Box + \Box\Box\Box\Box\Box\Box\cdot T - \Box\Box\Box\Box\Box\Box\cdot T \cdot \Box\Box T\ \Box-$ $\Box\Box\Box\Box\Box\Box\Box\Box\Box\cdot T^{\Box} - \Box\Box\Box\Box\Box\Box\cdot\Box\Box^{\Box}\cdot T^{\Box} - \Box\Box\Box\Box\Box\cdot T^{-\Box}$
Between $\left(\Box\Box\Box\Box\Box\ T\ \Box\Box\Box\Box\right)$
$\Box G_{In}^{L\,\Box Bulk} = -\Box\Box\Box\Box\Box + \Box\Box\Box\Box\Box\Box\cdot T - \Box\Box\Box\Box\Box\Box\cdot T \cdot \Box\Box T\ \Box+ \Box\Box\Box\Box\Box\Box\Box\Box\Box\cdot T^{\Box} - \Box\Box\Box\Box\Box\cdot\Box\Box^{\Box}\cdot T^{\Box} - \Box\Box\Box\Box\Box\Box\cdot T^{-\Box}$
$\Box G_{In}^{Tetrag\,\Box A\,\Box Bulk} = -\Box\Box\Box\Box\Box\Box + \Box\Box\Box\Box\Box\Box\cdot T - \Box\Box\Box\Box\Box\Box\cdot T \cdot \Box\Box T\ \Box+ \Box\Box\Box\Box\Box\Box\Box\Box\Box\cdot T^{\Box} - \Box\Box\Box\Box\cdot\Box\Box^{\Box}\cdot T^{\Box} - \Box\Box\Box\Box\Box\cdot T^{-\Box} + \Box\Box\Box\Box\Box\Box\cdot\Box\Box^{\Box\Box}\cdot T^{-\Box}$
Lead
Between $\left(\Box\Box\Box\Box\Box\ T\ \Box\Box\Box\Box\Box\right)$
$\Box G_{Pb}^{L\,\Box Bulk} = -\Box\Box\Box\Box\Box\Box + \Box\Box\Box\Box\Box\Box\Box\cdot T - \Box\Box\Box\Box\Box\Box\Box\cdot T \cdot \Box\Box T\ \Box-$ $\Box\Box\Box\Box\Box\Box\Box\Box\Box\cdot T^{\Box} - \Box\Box\Box\Box\Box\Box\cdot\Box\Box^{\Box}\cdot T^{\Box} - \Box\Box\Box\Box\cdot\Box\Box^{\Box\Box}\cdot T^{\Box}$
$\Box G_{Pb}^{Fcc\,\Box A\,\Box Bulk} = -\Box\Box\Box\Box\Box\Box + \Box\Box\Box\Box\Box\Box\Box\Box\cdot T - \Box\Box\Box\Box\Box\Box\Box\Box\cdot T \cdot \Box\Box T\ \Box-$ $\Box\Box\Box\Box\Box\Box\Box\Box\Box\cdot T^{\Box} - \Box\Box\Box\Box\Box\Box\cdot\Box\Box^{\Box}\cdot T^{\Box}$
Between $\left(600.61 < T < 1200\right)$

$$^{0}G_{Pb}^{Bulk} = -\square 6\square,\square\square\square + 1\square6.1\square60\square6 \cdot \square - \square2.\square1\square\square\square\square \cdot \square \cdot \square\square\square \square +$$
$$.001\square\square61\square \cdot \square^{2}$$

$$^{0}G_{Pb}^{Fcc\,\square A1\square Bulk} = -10\square\square1.0\square\square + 1\square\square2\square\square1\square2 \cdot \square - \square2.\square1\square\square\square\square \cdot \square \cdot \square\square\square \square +$$
$$0.001\square\square61\square \cdot \square^{2} - 0.0\square\square1\square\square \cdot 10^{-6} \cdot \square^{\square}$$

Between $(1200 < T < 2100)$

$$^{0}G_{Pb}^{Bulk} = \square010.\square\square\square + \square\square0\square1\square\square\square \cdot \square - 1\square\square6\square06\square\square \cdot \square \cdot \square\square\square \square -$$
$$.002\square\square2\square\square \cdot \square^{2} + 0.0\square\square1\square\square \cdot 10^{-6} \cdot \square^{\square} - 26\square6\square\square\square \cdot \square^{-1}$$

$$^{0}G_{Pb}^{Fcc\,\square A1\square Bulk} = \square1\square\square616 + \square\square1\square\square0\square2 \cdot \square - 1\square\square6\square06\square\square \cdot \square \cdot \square\square\square \square -$$
$$0.002\square\square2\square\square\square \cdot \square^{2} + 0.0\square\square1\square\square \cdot 10^{-6} \cdot \square^{\square} - 26\square6\square\square\square \cdot \square^{-1} + \square0\square\square\square\square \cdot 10^{2\square} \cdot \square^{-\square}$$

Germanium

Between $(2\square\square1\square < T < \square00)$

$$^{0}G^{Bulk} = +2\square6\square\square,\square\square\square + 1\square\square,\square\square\square\square\square\square \cdot \square - 2\square\square\square\square6\square2 \cdot \square \cdot \square\square\square \square +$$
$$.00\square6\square2\square\square \cdot \square^{2} - 1.\square\square6\square\square \cdot 10^{-6} \cdot \square^{\square} + 16\square2\square\square \cdot \square^{-1} + \square6.6\square2 \cdot 10^{-2\square} \cdot \square^{\square}$$

$$^{0}G^{Fcc\,\square A1\square Bulk} = 26\square1\square\square,\square\square\square + 1\square\square,\square\square\square\square\square\square \cdot \square - 2\square\square\square\square6\square2 \cdot \square \cdot \square\square\square \square +$$
$$0.00\square6\square2\square\square \cdot \square^{2} - 1.\square\square6\square\square \cdot 10^{-6} \cdot \square^{\square} + 16\square2\square\square \cdot \square^{-1}$$

$$^{0}G^{\square A\square Bulk} = -\square\square6.1\square\square + 16\square6\square\square\square\square\square \cdot \square - 2\square\square\square\square6\square2 \cdot \square \cdot \square\square\square \square +$$
$$0.00\square6\square2\square\square \cdot \square^{2} - 1.\square\square6\square\square \cdot 10^{-6} \cdot \square^{\square} + 16\square2\square\square \cdot \square^{-1}$$

Between $(\square00 < T < 1211.\square0)$

$$^{0}G^{Bulk} = +\square1\square\square2.2\square + \square2.1\square\square\square26 \cdot \square - 1\square\square\square\square62\square\square \cdot \square \cdot \square\square\square \square -$$
$$.00\square6\square2\square2\square \cdot \square^{2} + \square\square6.6\square2 \cdot 10^{-2\square} \cdot \square^{\square}$$

$$^{0}G^{Fcc\,\square A1\square Bulk} = +\square0\square10.\square61 + \square0.\square60\square\square \cdot \square - 1\square\square\square\square62\square\square \cdot \square \cdot \square\square\square \square -$$
$$.00\square6\square2\square2\square \cdot \square^{2}$$

$$^{0}G^{A\square Bulk} = -\square6\square\square2\square\square + 102.\square60\square\square \cdot \square - 1\square\square\square\square62\square\square \cdot \square \cdot \square\square\square \square -$$
$$.00\square6\square2\square2\square \cdot \square^{2}$$

Between $(1211.\square0 < T < \square200)$

$$^{0}G^{Bulk} = +2\square2\square\square,\square\square\square + 126.\square2\square1\square6 \cdot \square - 2\square61\square\square \cdot \square \cdot \square\square\square \square$$

$$^{0}G^{Fcc\,\square A1\square Bulk} = +26\square\square1.\square6 + 1\square\square.\square0\square02\square \cdot \square - 2\square61\square\square \cdot \square \cdot \square\square\square \square -$$
$$\square\square\square.\square0\square \cdot 10^{26} \cdot \square^{-\square}$$

$$^{0}G^{\square A\square Bulk} = -\square\square\square\square20\square + 1\square6.\square0\square02\square \cdot \square - 2\square61\square\square \cdot \square \cdot \square\square\square \square -$$
$$\square\square\square.\square0\square \cdot 10^{26} \cdot \square^{-\square}$$

Alloys

$$^{0}L_{\square}^{\square Bulk} = 1\square\square\square2 + 0.\square\square\square0\square \cdot \square$$

$$^{1}L_{\square}^{\square Bulk} = -\square\square\square\square - 1.\square10\square2 \cdot \square$$

$$^{0}L_{\square Pb}^{\square Bulk} = 1\square2\square\square1 + 1.\square\square20\square \cdot \square$$

$$^{1}L_{\square Pb}^{\square Bulk} = -\square\square\square.\square$$

$$^{0}L_{\square Pb}^{Fcc\,\square A1\square Bulk} = \square0 \cdot \square$$

Nanosystem

$\square$

Indium		
Liquid		

$$^0\square^\square = {}^0\square^{\square Bulk} + \frac{1.\square\square\cdot10^{-\square}}{\square}\cdot F - \frac{1.1\square\cdot10^{-\square}}{\square}\cdot F\cdot\square -$$

$$\frac{2.\square\square\cdot10^{-1\square}}{\square}\cdot F\cdot\square^2$$

Tetrag_A6

$$^0\square^\square_{\square A6} = {}^0\square^{\square A6\square Bulk} + \frac{2.\square6\cdot10^{-\square}}{\square}\cdot F - \frac{\square12\cdot10^{-\square}}{\square}\cdot F\cdot\square$$

Lead		
Liquid		

$$^0\square^\square_{Pb} = {}^0\square^{\square Bulk}_{Pb} + \frac{1.\square\square\cdot10^{-\square}}{\square}\cdot F - \frac{2.\square\square\cdot10^{-\square}}{\square}\cdot F\cdot\square -$$

$$\frac{6.26\cdot10^{-1\square}}{\square}\cdot F\cdot\square^2$$

Fcc_A1

$$^0\square^\square_{Pb\square Fcc\square A1} = {}^0\square^{Fcc\square A1\square Bulk}_{Pb} + \frac{2.20\cdot10^{-\square}}{\square}\cdot F - \frac{\square\square\square\cdot10^{-\square}}{\square}\cdot F\cdot\square$$

Germanium		
Liquid		

$$^0\square^\square = {}^0\square^{\square Bulk} + \frac{1.\square6\cdot10^{-\square}}{\square}\cdot F - \frac{1.\square\square\cdot10^{-\square}}{\square}\cdot F\cdot\square - \frac{2.\square2\cdot10^{-1\square}}{\square}\cdot F\cdot\square^2$$

Fcc_A1

$$^0\square^\square_{\square F} = {}^0\square^{Fcc\square A1\square Bulk} + 0$$

Diamond_A4

$$^0\square^\square_{\square A\square} = {}^0\square^{\square A\square Bulk} + \frac{1.\square\square\square\cdot10^{-\square}}{\square}\cdot F - \frac{\square\square\cdot10^{-\square}}{\square}\cdot F\cdot\square$$

Alloys		
Liquid (Ge, In)		

$$^0\square^\square = {}^0\square^{\square Bulk}_{\square} - \frac{\square226\square0\cdot10^{-\square}}{\square}\cdot F + \frac{\square\square\square\square1\cdot10^{-11}}{\square}\cdot F\cdot\square$$

$$^1\square^\square = {}^1\square^{\square Bulk}_{\square} - \frac{2.2\square\square1\cdot10^{-\square}}{\square}\cdot F + \frac{1.\square\square\square6\cdot10^{-12}}{\square}\cdot F\cdot\square$$

$$^2\square^\square = {}^2\square^{\square Bulk}_{\square} - \frac{2.\square\square\square6\cdot10^{-\square}}{\square}\cdot F + \frac{\square\square\square\square\square\cdot10^{-12}}{\square}\cdot F\cdot\square$$

Liquid (Ge, Pb)

$$^0\square^\square_{\square Pb} = {}^0\square^{\square Bulk}_{\square Pb} - \frac{\square\square12\square\cdot10^{-6}}{\square}\cdot F + \frac{1.6\square6\square\cdot10^{-11}}{\square}\cdot F\cdot\square$$

$$^1\square^\square_{\square Pb} = {}^1\square^{\square Bulk}_{\square Pb} - \frac{\square6\square\square\cdot10^{-\square}}{\square}\cdot F + \frac{1.111\square\cdot10^{-10}}{\square}\cdot F\cdot\square$$

$$^2\square^\square_{\square Pb} = {}^2\square^{\square Bulk}_{\square Pb} - \frac{6.\square0\square\square\cdot10^{-\square}}{\square}\cdot F + \frac{1.6\square6\square\cdot10^{-11}}{\square}\cdot F\cdot\square$$

□

Using calculated data presented in Table 3, nanophase diagrams were calculated and presented in Figure 2 a) binary Ge-In and b) binary Ge-Pb system. Presented phase diagrams correspond to the nanoparticle of 20nm, (radius 10nm) with different shapes. Calculation of phase diagram was done by using Pandat software.
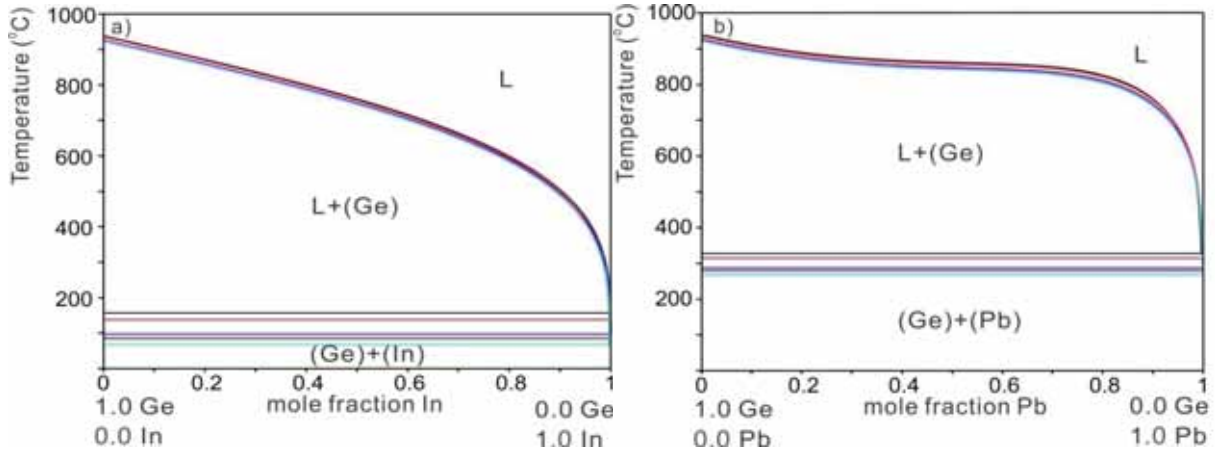
Figure 2. Predicted phase diagram of bulk (black lines), 20nm nanofilm (red lines) and 20 nm nanoparticles of different shapes (spherical (blue lines), regular octahedral (magenta lines), regular hexahedral (green lines), and regular tetrahedral (cyan lines)): a) Ge-In and b) Ge-Pb.

Based on predicted phase diagrams, the shape of nanoparticle has a significant influence on phase boundaries and temperature of the eutectic reaction. In Table 4 are presented temperature of three important points of the nanophase diagram compared with the bulk system.

Table 4. Comparison of the temperature of bulk and nanophase Ge-In and Ge-Pb diagram

different shape	Temperature in K			
	pure In	pure Pb	pure Ge	eutectic point Ge-In/Ge-Pb
Bulk system	429.75	600.6	1211.4	429.4/600.1
Nanofilm	410.3	587.9	1207.5	410.1/586.9
Spherical	370.5	560.2	1199.6	370.4/559.9
Regular octahedral	359.8	552.7	1197.5	359.5/552.5
Regular hexahedral	356.1	550.2	1196.8	355.8/550.0
Regular tetrahedral	340.7	539.7	1193.9	340.4/539.5

From Table 4 and Figure 2a) and 2b), is noticeable that nanoparticles with regular tetrahedral shape have lower temperatures in comparison with another shape of the particle.

215

CONCLUSIONS

Paper presents a description of nanophase diagrams of binary Ge-In and Ge-Pb system. Calculation of the phase diagram was done by using the extended CALPHAD method. The calculated surface Gibbs energy of binary alloys in the liquid phase and pure element in solid and liquid phase were added to Gibbs energy of the bulk system and together present parameters for nanosystem. Calculated data can be used for prediction of nanophase diagrams with different nanoparticles size from 5-100nm. As an illustration in presented paper phase diagram of binary Ge-In and Ge-Pb with the size of 20nm nanoparticles independence of different shape is presented. For visualization of diagrams, Pandat software was used. Besides Pandat presented calculated data of nanophase diagram can be used in different software such as Thermo-Calc, Pandat, MTData, FactSage and many others.

Presented results are useful for calculation of high order system, prediction of phase diagrams with different size of nanoparticles and for easier choosing of nanoalloys. Future experimental examination of this nanophase diagram is necessary for a way to confirm binary phase boundaries.

REFERENCES

[1] D. Ielmini, A. L. Lacaita, Phase change materials in non-volatile storage, Mater. Today., 14(2011)12, pp. 600-607.

[2] W. Wełnic, M. Wuttig, Reversible switching in phase-change materials, Mater. Today., 11(2008)6, pp. 20-27.

[3] S. Raoux, R. M. Shelby, J. Jordan-Sweet, B. Munoz, M. Salinga, Y. C. Chen, Y. H. Shih, E. K. Lai, M. H. Lee, Phase change materials and their application to random access memory technology, Microelectronic Eng., 85(2008), pp. 2330-2333.

[4] M. A. Caldwell, R. Gnana David Jeyasingh, H. S. Philip Wong, D. J. Milliron, Nanoscale phase change memory materials, Nanoscale, 4(2012), pp. 4382-4392.

[5] A. A. Bahgat, E. A. Mahmoud, A.S. Abd Rabo, I. A. Mahdy, Study of the ferroelectric properties of Ge–Sb–Te alloys. Physica B: Condensed Matter, 382(2006), pp. 271-278.

[6] M. A. Caldwell, R. Gnana David Jeyasingh, H. S. Philip Wong, D. J. Milliron, Nanoscale phase change memory materials, Nanoscale, 4(2012), pp. 4382-4392.

[7] T. Tanaka, S. Hara, Thermodynamic evaluation of binary phase diagrams of small particle systems. Zeitschrift für Metallkunde, 92(2001), pp. 467-472.

[8] T. Tanaka, S. Hara, Thermodynamic evaluation of nanoparticle binary alloy phase diagrams, Zeitschrift für Metallkunde, 92(2001), pp. 1236–1241.

[9] J. P. Hajra, T. Ray, S. Acharya, Thermodynamics and adsorption behavior of the nano phases in the Bi-Sn system, Journal of Computational and Theoretical Nanoscience, 2(2005)2, pp. 319-327.

[10] J. Park, J. Lee, Phase diagram reassessment of Ag–Au system including size effect, Computer Coupling of Phase Diagrams and Thermochemistry, 32(2008), pp. 135-141.

[11] W. H. Qi, M. P. Wang, Q. H. Liu, Shape factor of non-spherical nanoparticles, Journal of Material Science, 40(2005)9, pp. 2737-2739.

[12] S. Gruner, M. Köhler, W. Hoyer, Surface tension and mass density of liquid Cu–Ge alloys, Journal of Alloys and Compounds, 482(2009), pp. 335-338.

[13] T. Iida, R. I. L. Guthrie, The physical properties of liquid metals, Clarendon Press, Oxford, 1993.

[14] J. A. V. Butler, The thermodynamics of the surfaces of solutions, Proc. R. Soc. A, 135(1932), pp. 348-375.

[15] T. Tanaka, K. Hack, T. Iida, S. Hara, Application of thermodynamic databases to the evaluation of surface tensions of molten alloys, salt mixtures and oxide mixtures, Z. Metallkd., 87(1996), pp. 380-389.

[16] I. Sa, B. M. Lee, C. J. Kim, M. H. B. Jo, J. Lee, Thermodynamic analysis for the size-dependence of $Si_{1-x}Ge_x$ nanowire composition grown by a vapor-liquid-solid method, Computer Coupling of Phase Diagrams and Thermochemistry, 32(2008), pp. 669-674.

[17] P. Y. Chevalier, A thermodynamic evaluation of the Germanium-Indium, Germanium-Lead, Germanium-Antimony, Germanium-Thallium and Germanium Zinc systems Thermochimica Acta, 155(1989), pp. 227-240.

[18] R. Picha, J. Vrestal, A. Kroupa, Prediction of alloy surface tension using a thermodynamic database, Computer Coupling of Phase Diagrams and Thermochemistry, 28(2004), pp. 141-146.

Acknowledgments

CAST STAINLESS STEELS

Vera Rede, Zrinka Šokčević

University of Zagreb Faculty of Mechanical Engineering and Naval Architecture

<u>Poster presentation</u>
Preliminary note

Abstract

Cast stainless steels are different from other cast steels by a chromium content of at least 12% which makes them corrosion resistance to a variety of aggressive media. Except chromium, they contain other alloying elements that improve corrosion, mechanical and technological properties. According to the microstructure, they are divided into four groups: austenitic, martensitic, ferritic and duplex casts. According to the operating temperature, they are divided into casts for operation up to 650 °C and cast for operation at temperatures above 650 °C. Their corrosion resistance is similar to that of their wrougth equivalents. Due to microsegregation and localized contamination in the cast microstructure, their corrosion resistance can become lower. Mechanical properties of cast steinless steels are generally comparable to their wrought counterparts.

Keywords: cast stainless steels, microstructure, properties, designation

*Corresponding author (e-mail address): *vrede@fsb.hr*

Sažetak

Nehrđajući čelični ljevovi se razlikuju od drugih čeličnih ljevova po sadržaju kroma od minimalno 12 % što ih čini korozijski postojanim u različitim agresivnim medijima. Osim kroma sadrže i druge legirne elemente koji poboljšavaju korozijska, mehanička i tehnološka svojstva. Prema mikrostrukturi dijele se na četiri skupine: austenitne, martenzitne, feritne i dupleks ljevove. Prema temperaturi primjene dijele se na ljevove za rad do 650°C i ljevove za rad na temperaturi iznad 650°C. Korozijska postojanost im je ista kao kod gnječenih legura istog sastava ili nešto lošija zbog mogućih nepravilnosti i segregacija u lijevanoj mikrostrukturi. Mehanička svojstva su im podudarna s gnječenim legurama istog sastava.

Ključne riječi: nehrđajući čelični ljevovi, mikrostruktura, svojstva, označivanje.

UVOD

Nehrđajući čelični ljevovi pripadaju skupini visokolegiranih FeC-legura, a njihova osnovna značajka je izvrsna korozijska postojanost. Kao i nehrđajući čelici i ljevovi moraju sadržavati barem 12% Cr u krutoj otopini da bi se na površini formirao zaštitni sloj kromovog oksida. Ovaj pasivni film, debljine svega nekoliko nanometara, predstavlja mehaničku barijeru između potencijalno agresivnog medija i površine čeličnog lijeva te ima sposobnost samoobnavljanja u vrlo različitim medijima [1]. Većina čeličnih ljevova sadrži i više od minimalnog sadržaja kroma, neki čak oko 30%. Osim kroma u sastavu čeličnih ljevova nalaze se i drugi legirni elementi čiji je sadržaj pomno određen s ciljem da se dobije željena mikrostruktura i najbolja moguća kombinacija korozijske postojanosti, mehaničkih te drugih svojstava. Većina ljevova sadrži nikal, molibden i dušik što ih čini otpornijim na koroziju. Nikal također pozitivno djeluje na žilavost, a molibden, dušik, titanij, bakar i aluminij povisuju čvrstoću. Čvrstoća se može povisiti i dodavanjem ugljika (koji je osnovni, a ne legirni element), osobito kod ljevova koji su namijenjeni za rad na višim temperaturama. Za poboljšanje obradivosti odvajanjem čestica ljevovima se dodaje selen. Neki od navedenih elemenata promiču austenitnu, a neki feritnu mikrostrukturu. Osim kemijskog sastava na formiranje mikrostrukture bitno utječe i režim toplinske obrade pa se temperatura žarenja i brzina hlađenja moraju pomno kontrolirati da se postigne željena mikrostruktura [1-4]. Ako je poznat kemijski sastav, mikrostruktura lijeva može se odrediti iz Schaefflerovog dijagrama gdje se na x-osi nalaze vrijednosti Cr-ekvivalenta, a na y-osi vrijednosti Ni-ekvivalenta, slika 1 [5]. Ovaj dijagram nije ravnotežni dijagram, a prikazuje mikrostrukturu dobivenu naglim hlađenjem s temperature od 1050°C do sobne temperature.

Cr- i Ni-ekvivalenti određuju se prema sljedećim izrazima:

$$Cr_{ekv} = \%Cr + 2(\%Si) + 1{,}5(\%Mo) + 5(\%V) + 5{,}5(\%Al) + 1{,}75(\%Nb) + 1{,}5(\%Ti) + 0{,}75(\%W) \quad (1)$$

$$Ni_{ekv} = \%Ni + \%Co + 30(\%C) + 25(\%N) + 0{,}5(\%Mn) + 0{,}3(\%Cu) \quad (2)$$
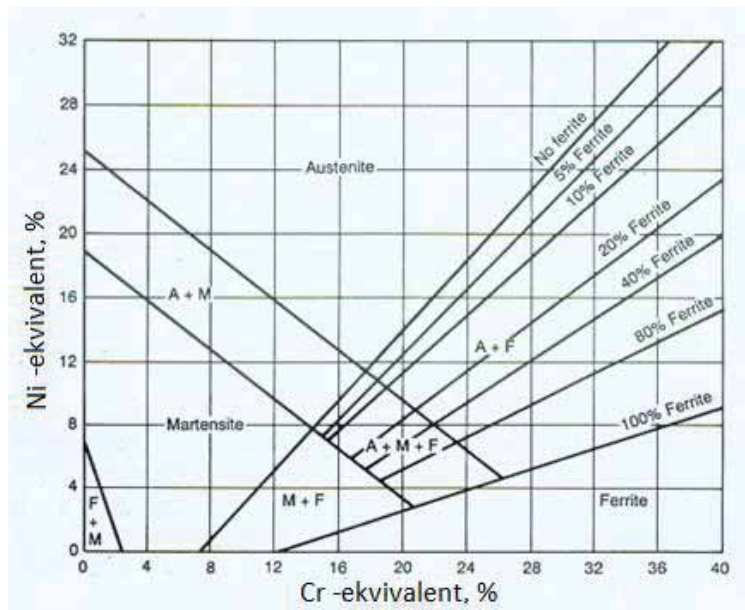
Slika 1. Schaefflerov dijagram [5]

OZNAČIVANJE

S obzirom da se radi o visokolegiranim čeličnim ljevovima, kod označivanja čelika prema kemijskom sastavu prema normi HRN EN 10027-1 [6], oznaka uvijek počinje sa znakom „X" iza kojeg slijedi sadržaj ugljika pomnožen sa 100 te kemijski simboli i maseni udjeli legirnih elemenata poredani po veličini masenih udjela.

Hrvatska norma HRN EN 10020 [7] svrstava nehrđajuće čelike i ljevove u skupinu legiranih čelika kojima, prema brojčanom sustavu označivanja i normi HRN EN 10027-2 [8], pripadaju znamenke 1.40 – 1.49 (Nehrđajući i vatrootporni čelici).

U tablici 1 navedene su oznake nekoliko korozijski postojanih čeličnih lijevova skupa s oznakama dizajniranim od High Alloy Product Group of the Steel Founders Society of America (bivši Alloy Casting Institute - ACI) i prihvaćenim od American Society for Testing and Materials (ASTM). Prema ovom sustavu označivanja oznaka počinje slovnim simbolom **C** za korozijski postojane ljevove za primjenu do 650°C, ili slovnim simbolom **H** za korozijski postojane ljevove za primjenu iznad 650°C. Na drugom mjestu u oznaci nalazi se slovni simbol koji ukazuje na kemijski sastav (udio kroma i nikla), prema slici 2, [4,6], iza čega slijedi broj koji ukazuje na sadržaj ugljika (%C x 100). Iza toga slijedi slovo koje ukazuje na ostale legirne elemente.
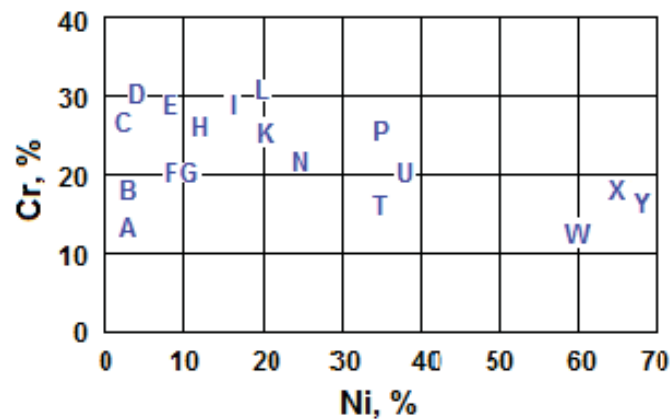
Slika 2. Sadržaj kroma i nikla u standardnim vrstama nehrđajućih čeličnih lijevova [9]

Tablica 1. Kemijski sastav i mehanička svojstva nehrđajućih čeličnih ljevova za primjenu do 650°C [2,11]

HRN EN 10027-1	HRN EN 10020	ACI	Kemijski sastav, %							Rm N/mm²	Rp$_{0,2}$ N/mm²	A %	HB
			C	Cr	Ni	Mn	Si	Mo	Ostalo				
Austenitni nehrđajući čelični ljevovi													
GX2CrNi19-11	1.4306	CF-3	0,03	17-21	8-12	1,5	2,0	-	-	531	248	60	140
GX5CrNi19-10	1.4308	CF-8	0,08	18-21	8-11	1,5	2,0	-	-	531	255	55	140
GX25CrNiSi18-9	1.4825	CF-20	0,20	18-21	8-11	1,5	2,0	-	-	531	248	50	163
GX2CrNiMo17-12-2	1.4404	CF-3M	0,03	17-21	9-13	1,5	1,5	2-3	-	552	262	55	150
GX5CrNiMo19-11-2	1.4408	CF-8M	0,08	18-21	9-12	1,5	2,0	2-3	-	552	290	50	170
GX8CrNi 19 10	1.4815	CF-8C	0,08	18-21	9-12	1,5	2,0	-	-	531	262	39	149
-	-	CF-16F	0,16	18-21	9-12	1,5	2,0	1,5	Se 0,2-0,35	531	276	52	150
GX6CrNiMo17-13	1.4448	CG-8M	0,08	18-21	9-13	1,5	1,5	3-4	-	565	303	45	176
-	-	CH-20	0,20	22-26	12-15	1,5	2,0	-	-	607	345	38	190
GX15CrNi25-20	1.4840	CK-20	0,20	23-27	19-22	1,5	2,0	-	-	524	262	37	144
(GX7NiCrMoCuNb25-20)	(1.4500)	CN-7M	0,07	19-22	27-30	1,5	1,5	2-3	Cu 3-4	476	214	48	130
Martenzitni nehrđajući čelični ljevovi													
-	-	CA-15	0,15	11,5-14	1,0	1,0	1,5	0,5	-	931	793	17	390
(GX20Cr14)	(1.4027)	CA-40	0,40	11,5-14	1,0	1,0	1,5	0,5	-	1034	862	10	470
(GX4CrNi13-4)	(1.4313)	CA-6NM	0,06	11,5-14	4,0	1,0	1,5	0,7	-	827	689	24	300
-	-	CA-6N	0,06	10,5-12,5	8,0	0,5	1,0	-	-	965	931	15	-
Feritni nehrđajući čelični ljevovi													
GX22CrNi17	1.□□	CB-30	0,30	18-22	2,0	1,0	1,5	-	-	655	414	15	195
G-X40CrSi29	1.4776	CC-50	0,50	26-30	4,0	1,0	1,5	-	-	669	448	18	210
Dupleks nehrđajući čelični ljevovi													
GX4CrNiMoN26-5-2	1.4474	CD-4MCu	0,04	26	5,0	1,0	1,0	2	Cu 3	745	558	25	260
-	-	255-3SC	0,05	25	6,0	1,5	1,0	3	Cu 2,2	725	450	20	245
-	-	Z5 20.8M	0,07	21-23	8,5	2,0	1,5	3	Cu 2, N 0,16	650	350	20	-
Precipitacijski očvrsnuti nehrđajući čelični ljevovi													
-	-	CB7-Cu1	0,05	16	4,0	-	-	-	Cu 3	1138	1089	14	400
X5CrNiCuNb16-4	1.4542	CB7-Cu2	0,05	15	5,0	-	-	-	Cu 3, Nb	1138	1089	14	400

KLASIFIKACIJA NEHRĐAJUĆIH ČELIČNIH LIJEVOVA

Nehrđajući čelični ljevovi se klasificiraju na tri načina – prema temperaturi primjene, prema kemijskom sastavu i prema tipu mikrostrukture.

Prema temperaturi primjene nehrđajući čelični ljevovi dijele se u dvije skupine:

- korozijski postojani ljevovi za primjenu do 650°C
- korozijski i toplinski postojani ljevovi za primjenu iznad 650°C

Osnovna razlika među njima je u sadržaju ugljika. Ljevovi za primjenu do 650°C sadrže znatno manju količinu ugljika (obično manje od 0,2, a ponekad manje i od 0,03%) i imaju bolju korozijsku postojanost. Ljevovi za primjenu na temperaturi iznad 650°C sadrže više ugljika zbog bolje otpornosti na puzanje i čvrstoće na višoj temperaturi, ali su zbog toga osjetljiviji na koroziju.

Prema kemijskom sastavu nehrđajući čelični ljevovi se dijele na:

- ljevove legirane kromom
- ljevove legirane kromom i niklom kod kojih je krom dominantni legirni element
- ljevove legirane niklom i kromom kod kojih je nikal dominantni legirni element.

Svi ljevovi sadrže više od 12 % kroma, a većina sadrži između 1 i 30 % Ni. Samo nekoliko vrsta sadrži manje od 1 % nikla. Legiranje niklom povisuje duktilnost i čvrstoću, a isto tako povećava otpornost na koroziju u neutralnim kloridnim otopinama i slabim oksidirajućim kiselinama. Legiranje molibdenom povisuje otpornost na rupičastu koroziju u kloridnim otopinama, a povisuje i otpornost u slabo oksidirajućim otopinama. Dodatak bakra u nekim ljevovima omogućava formiranje finih precipitata te povišenje čvrstoće i tvrdoće (precipitacijsko očvrsnuće) [10].

Prema mikrostrukturi nehrđajući čelični ljevovi dijele se, kao i gnječene FeC-legure, na:

- austenitne,
- feritne,
- martenzitne,
- dupleks i
- precipitacijski očvrsnute.

- Austenitni nehrđajući čelični ljevovi najzastupljeniji su i po vrstama i po proizvedenoj količini. Njihov sastav je podešen tako da u mikrostrukturi na sobnoj temperaturi osim austenita mogu sadržavati i značajnu količinu delta-ferita. Ferita može biti od 5 do 40 %, a raspoređen je u austenitnoj osnovi u manje ili više povezanim nakupinama i zbog njega su ovi ljevovi magnetični [4]. Zahvaljujući feritnoj fazi austenitni ljevovi imaju višu čvrstoću i bolju zavarljivost te bolju otpornost na napetosnu i interkristalnu koroziju. Korozijska postojanost ovih ljevova je optimalna kad je ugljik potpuno otopljen u kristalu mješancu. Ako se tijekom primjene ili pri zavarivanju, lijev zadrži dovoljno dugo u temperaturnom području između 425°C i 870°C na granicama kristalnih zrna može doći do precipitacije karbida što će ga učiniti osjetljivim na interkristalnu koroziju. Ovo se može spriječiti ili snižavanjem udjela ugljika ili legiranjem s karbidotvorcima koji imaju jači afinitet prema ugljiku od kroma (Nb, Ta, Ti) [2]. Otporni su na većinu organskih kiselina i primjenjuju se u farmaceutskoj i kemijskoj industriji, industriji hrane i mljekarama. U mirujućoj morskoj vodi postoji opasnost od pojave rupičaste korozije pa se takva primjena izbjegava. Također su relativno visoko otporni na eroziju kapljevinama, a neki od njih i na kavitaciju.

U tablici 1 prikazani su kemijski sastav i mehanička svojstva austenitnih nehrđajućih čeličnih ljevova (proizvedenih u SAD-u) s oznakama po ACI sustavu označivanja, a u prva dva stupca nalaze se ekvivalentne slovno brojčane i brojčane HRN EN oznake [11].
Obradivost odvajanjem čestica im je dobra.

Na slici 3 prikazana je mikrostruktura austenitnog čeličnog lijeva oznake GX5CrNi19-10 (1.4308) nakon otapajućeg žarenja. U mikrostrukturi je prisutno između 15 i 20 % delta ferita uglavnom homogeno raspoređenog u austenitnoj osnovi. Pri statičko vlačnom ispitivanju dobivena je vlačna čvrstoća od 580 N/mm^2, granica razvlačenja Rp$_{0,2}$ od 184 N/mm^2 i istezljivost 42%. Na Charpy-jevom batu izmjerena je žilavost KV od 66 J pri sobnoj temperaturi.
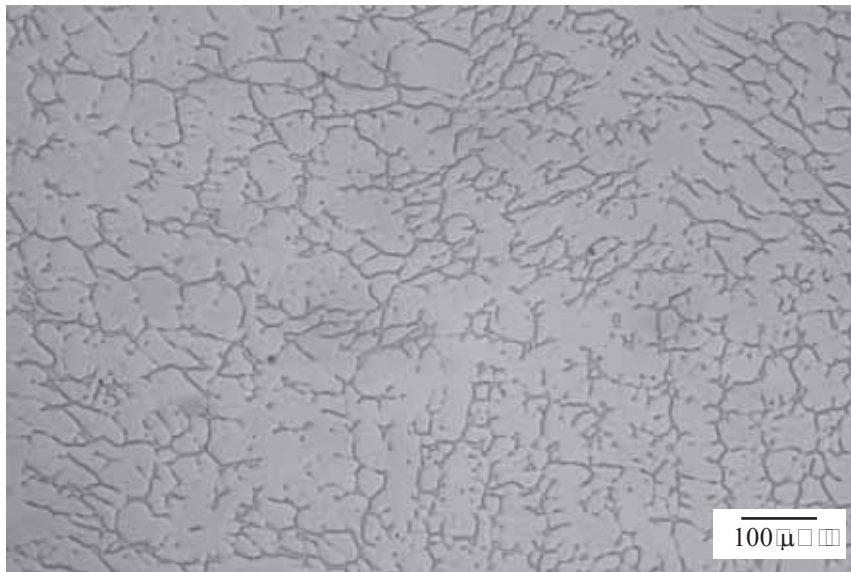
Slika 3. Mikrostruktura austenitnog nehrđajućeg čeličnog lijeva GX5CrNi19-10

- *Martenzitni nehrđajući čelični ljevovi* postižu željena svojstva, prije svega visoku čvrstoću, tvrdoću i otpornost na abraziju, toplinskom obradom. U tablici 1 predočen je kemijski sastav ovih ljevova i njihova mehanička svojstva. Korozijska postojanost martenzitnih nehrđajućih čeličnih ljevova slabija je od postojanosti drugih ljevova, ali su im bolja mehanička i tribološka svojstva. Skoro sve vrste ovih ljevova legiraju se molibdenom što im povisuje čvrstoću i otpornost na višim temperaturama, a dobro djeluje i na livljivost.

- *Feritni nehrđajući čelični ljevovi* se ne mogu očvrsnuti toplinskom obradom. Sadržaj kroma u ovim ljevovima je vrlo visok (% Ni je nizak) što im osigurava visoku otpornost na oksidirajuće kiseline.
U tablici 1 navedene su dvije vrste feritnih ljevova s pripadajućim kemijskim sastavom i mehaničkim svojstvima.

- *Dupleks nehrđajući čelični ljevovi* su najmlađa skupina nehrđajućih čeličnih ljevova. Njihov sastav je podešen tako da nakon gašenja s određene temperature, na sobnoj temperaturi imaju izbalansiran omjer ferita i austenita. Idealni omjer je 50:50, ali je dovoljno i 40 % ferita da bi svojstva ostala dobra. Zbog visokog udjela ferita imaju bolju otpornost na rupičastu i napetosnu koroziju u medijima koji sadrže kloride od austenitnih ljevova. Zbog visokog

udjela kroma i molibdena općenito imaju bolju otpornost na lokalne oblike korozije. Zavarivanje može narušiti izbalansirani omjer ferita i austenita te izazvati izlučivanje nekih štetnih faza u zoni oko zavara, što može znatno narušiti i korozijska i mehanička svojstva.

Dupleks ljevovi se ne primjenjuju na temperaturama višim od 315°C zbog pojave *krhkosti 475* u feritnoj fazi.

U tablici 1 prikazane su tri standardne vrste dupleks ljevova s propisanim kemijskim sastavom i mehaničkim svojstvima.

Na slici 4 prikazana je mikrostruktura dupleks čeličnog lijeva oznake GX2CrNiMoN25-6-3 (1.4468). Omjer ferita i austenita je oko 50:50.

Slika 4. Mikrostruktura dupleks nehrđajućeg čeličnog lijeva GX2CrNiMoN25-6-3

- *Precipitacijski očvrsnuti čelični ljevovi* su visokočvrsti ljevovi s niskim sadržajem ugljika. Visoka čvrstoća se postiže postupkom precipitacijskog očvrsnuća gdje se u fazi dozrijevanja izlučuju sitne, fino dispergirane čestice bogate bakrom, koje dodatno povećavaju čvrstoću martenzitne osnove. Zbog visoke tvrdoće i čvrstoće, obrada odvajanjem čestica provodi se prije precipitacijskog očvrsnuća. Korozijska postojanost im je nešto slabija od drugih skupina korozijski postojanih čeličnih ljevova.

Čelični nehrđajući ljevovi za primjenu iznad 650°C sadrže više ugljika od drugih čeličnih ljevova. Zbog toga imaju povišenu čvrstoću koja se znatnije ne smanjuje ni na višim temperaturama. Također imaju visoku otpornost na puzanje i nešto nižu duktilnost. Visoki udjeli kroma i nikla također djeluju pozitivno na korozijska i druga svojstva. Krom poboljšava otpornost na oksidaciju te otpornost u medijima koji sadrže sumpor, povisuje otpornost na puzanje i lomnu čvrstoću. Nikal povisuje otpornost na pouglijčavanje te smanjuje koeficijent toplinskog širenja čime doprinosi povećanju otpornosti prema toplinskom umoru. Mikrostruktura je uglavnom austenitna (uz manju količinu ferita) ili potpuno austenitna. U nekim ljevovima prisutni su u maloj količini i eutektički karbidi.

Na slici 5 prikazana je mikrostruktura nehrđajućeg čeličnog lijeva HT-44. Po granicama austenitnih zrna vide se nakupine karbida.
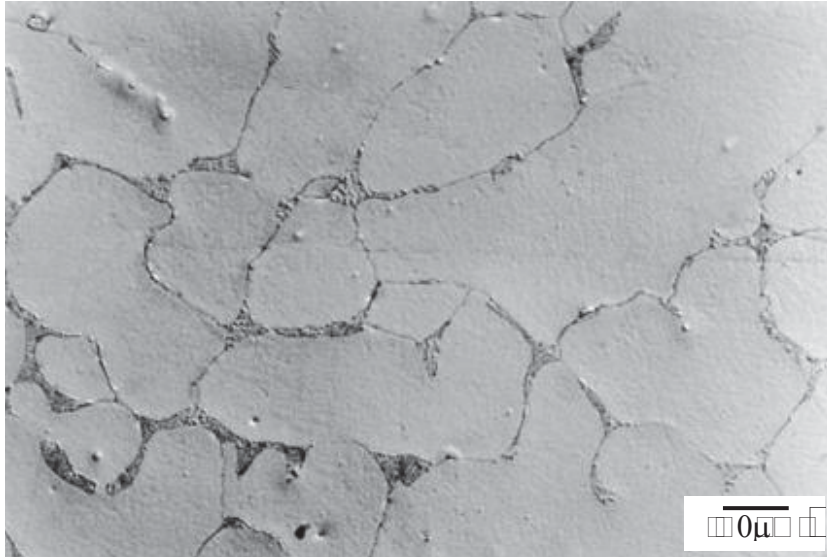
Slika 5. Mikrostruktura nehrđajućeg čeličnog lijeva HT-44 (austenit i karbid)

ZAKLJUČAK

Osnovno svojstvo nehrđajućih čeličnih ljevova je njihova izvrsna korozijska postojanost u različitim agresivnim medijima. Ovo svojstvo proizlazi iz njihovog kemijskog sastava u kojem nužno mora biti barem 12% kroma. Uz krom sadrže manji ili viši postotak nikla, a u nekima ima i molibdena te drugih legirnih elemenata. Osim dobre korozijske postojanosti neke vrste imaju i zavidna mehanička svojstva pa se mogu primjeniti na mjestima gdje se osim visoke korozijske postojanosti traži i visoka mehanička otpornost. Kod vrsta koje su namijenjene za rad na visokoj temperaturi, povišeni sadržaj ugljika osigurava dovoljnu čvrstoću i otpornost na puzanje, a visoki sadržaj nikla i kroma, visoku otpornost na oksidaciju, pouglijičavanje i sulfidizaciju. Većina vrsta, zbog niskog sadržaja ugljika ima dobru obradivost odvajanjem čestica i dobru zavarljivost.

LITERATURA

[1] J.R. Davis, Stainless Steels, ASM International, Materials Park, Ohio, 1994.
[2] A. J. Sedriks, Corrosion of stainless steels, Office of naval research, Arlington, Virginia, 1996.
[3] F. B. Pickering, International Metals Review, 21(1976), pp. 227.
[4] https://www.nickelinstitute.org, pristup 1.svibnja 2017.
[5] A. Schaeffler, Constitution diagram for stainless steel, Metal Progress, 56(1949)11, pp. 680-680B.
[6] HRN EN 10027-1: 2007. Sustavi označivanja za čelike -- 1. dio: Nazivi čelika, Hrvatski zavod za norme
[7] HRN EN 10020:2008. Definicija i razredba vrsta čelika, Hrvatski zavod za norme
[8] HRN EN 10027-2:2015. Sustavi označivanja čelika -- 2. dio: Brojčani sustav, Hrvatski zavod za norme

[9]   ASM Handbook, Volume 1, Properties and Selection: Irons, Steels and high Performans alloys, International, Park, Ohio, 2015.

[10] http://www.totalmateria.com, dostupno 1. svibnja 2017.

[11] https://www.grantadesign.com/resources/materials/designations/ferrous.caststainlessteel.htm, dostupno 1. svibnja 2017.

OVERVIEW OF CASTING DEFECTS IN DUCTILE CAST IRON

Tomislav **Rupčić**[1], Zdenka Zovko **Brodarac**[1], **Katarina Terzić**[1], Franjo Kozina[1], **Jovica Lošić**[2]

[1]University of Zagreb Faculty of Metallurgy, Sisak, Croatia
[2]Bentoproduct d.o.o., Šipovo, Bosnia and Hercegovina

<u>Oral presentation</u>
<u>Preliminary note</u>

Abstract

Objective of this article is to provide an overview of common casting defects occurred during production of ductile cast iron (DCI) and the influence of non-metallic inclusions in the DCI. These defects are referred to slag, sand mould or other foreign substances that are imbedded in the surface, or underneath. The research was investigated on ductile cast iron samples using optical microscopy and scanning electron microscope (SEM) with energy dispersive spectroscopy (EDS). With SEM image position, shape and type of inclusion could be defined while EDS analysis reveals chemical composition of particular formations. The investigation of casting defects indicates necessity of DCI production parameters control. This article deals with investigation of surface defects in DCI such as non-metallic inclusions (Al_2O_3, SiO_2, MgO, CaO, MnO, FeO, Fe_2O_3) which mostly originate from slag, melt oxidation, reactions with refractory materials, mould erosion, and melt treatment interactions.

Keywords: *ductile cast iron, casting defect, non-metallic inclusion, SEM, EDS.*

*Corresponding author (e-mail address): *trupcic@simet.hr

INTRODUCTION

Common foundry defects are sand and slag inclusions, pinholes, blowholes, shrinkage and cracks. Sand inclusion could be entrapped due to sand cut, wash or hole, mould erosion or drop, raised, broken or crushed sand core, damaged mould elements. Possible causes for these problems are related to gate, runner and riser design. On the other side, possible causes related to mould material are inferior quality of resin, insufficient cohesive strength of sand, low green strength, improper moisture content, defective mould and core drying, incorrect mould and core permeability, improper mould hardness and high compressive strength. The causes like improper alignment of mould halves, pattern and match plate, moulding boxes and machine, careless pattern removal, improper procedure and parameter control during moulding also cause defects [1].

Inclusions can be defined as non-metallic and sometimes intermetallic phases embedded in metal matrix. They are usually oxides, silicates, sulphides, nitrides or other complex forms. In most cases they are detrimental to the performance of the cast component. Mechanical properties can be adversely influenced by inclusions, which act as stress raisers. Some properties are more sensitive to the presence of inclusions than others. There are essentially two classifications for all inclusions: exogenous from external causes and indigenous which are native, innate, or inherent in the molten metal treatment process [2]. Slag, entrapped mould materials and refractories are examples of inclusions that would be classified as exogenous. In most cases these inclusions would be macroscopic and visible at the casting surface. When the casting in sectioned, they may also appear beneath the external casting surface if they have had insufficient time to float out or settle due to density differences with respect to the molten metal. Indigenous inclusions include oxides, silicates, sulphides and nitrides derived from the chemical reaction of the molten metal with the local environment. Such inclusions are usually small and require microscopic magnification for identification [2].

Ductile cast iron (DCI) is also known as spheroidal or nodular cast iron produced by melt treatment (preconditioning) of corresponded composition with magnesium (Mg) which promotes the precipitation of graphite in spheroidal form [3]. Melt treatment is important step in producing ductile cast iron and have influence on casting performance. Most elements in inoculants and nodularisers are highly reactive metals, such as magnesium (Mg), aluminium (Al), silicon (Si), titanium (Ti) and calcium (Ca). These elements are creating finely distributed oxides in reaction with oxygen (O) and sulphur (S) in the DCI melt forming inclusions [4-7].

In DCI production, reaction between oxygen (O) and the elements like magnesium (Mg), silicon (Si), calcium (Ca), manganese (Mn) and aluminium (Al) can result in long accumulated particle formations – slag. Slag, as a non-metallic inclusion can be found in ductile cast iron, containing elements such as Al, Ca, Mg, Si, Fe and O [8]. More complex oxide inclusions can contain strontium (Sr), barium (Ba) and other rare earths as constituent elements [9].

Sand inclusions are casting defects mostly developed as a result of turbulent mould cavity filling causing mould erosion. Turbulent mold filling causes thermo-mechanical stresses on mould and cores. According to Giesserei Lexikon *"The considerable compressive and shear stresses acting on the mould and core surface under the metallostatic pressure can lead to mould fracture followed by isolation and withdrawal of particular grains or their agglomerates."* Sand inclusion along with slag inclusion and other oxides it can cause defects on or under the casting surface once when they get in the mould cavity. If one part of the mould gets damaged, there is probability that casting will have outgrowth on surface [10].

Inclusions in DCI are separated in three categories. Square-shaped inclusions contain magnesium, calcium, sulphur and silicon as the main constituent elements. Rectangular-shaped inclusions appear mainly in iron matrix and they mostly contain elements such as Mg and Si. Irregularly-shaped inclusions are located in DCI interdendritic areas. Major elements are magnesium (Mg), phosphorus (P), and rare earth elements (Ba, La, Ce) [11].

This investigation represent an microstructural confirmation of common surface defects in DCI samples on the base of non-metallic inclusions occurred due to interaction in melt-mould system and refractory materials features, as well as melt oxidation and slag

formation. Also thickwall sections often indicate degeneration of graphite shape and require specialcare relating to heat and mass transport.

MATERIALS AND METHODS

The research was performed on ductile cast iron samples. Several types of surface defects were noticed. Figure 1a) shows an example of the casting section with defect. Figure 1b) shows prepared sample for metallographic analysis.

a)

b)
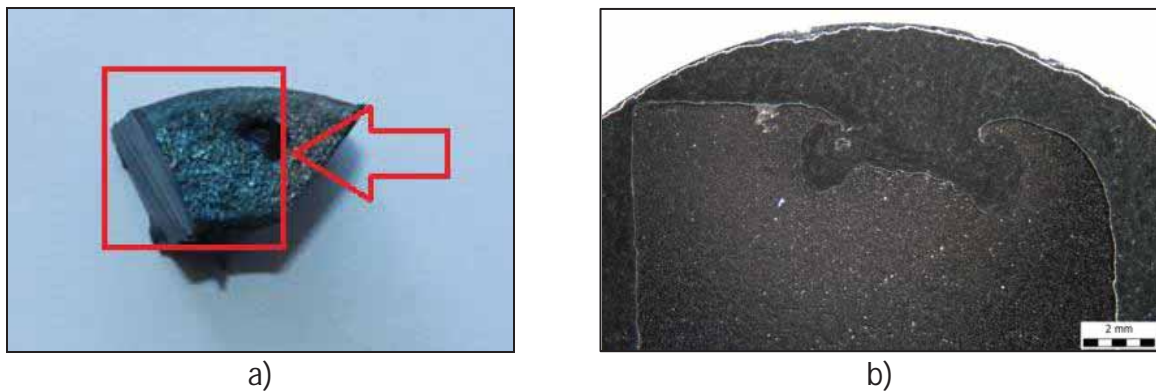
Figure 1. Overview of casting section with surface defect: a) photography of sample, b) sample prepared for metallographic analysis

Samples were submitted to metallographic analysis positioned vertically to the defect in order to define development of the defect. Microstructural analysis was performed in order to determine their main characteristic such as shape, size and dimension which could lead to determination of theirs origin.

The metallographic and microstructure analysis was performed by light microscopy using Olympus BX51 equipped with DP70 digital camera and AnalySIS Materials ResearchLab automatic image processing system. The sample for metallographic and microstructure analysis was prepared by standard grinding and polishing process and etching in 4% nital (solution of alcohol and nitric acid). Chemical composition of inclusions and other phenomena were established by scanning electron microscope (SEM) Tescan Vega TS 5136 MM equipped with Bruker energy dispersive spectrometer (EDS).

RESULTS AND DISCUSSION

Figures 2a) and 2c) represent an example of sample microstructure before etching, while 2b) and 2d) are corresponding micrographs after etching.

a)

b)

c)

d)
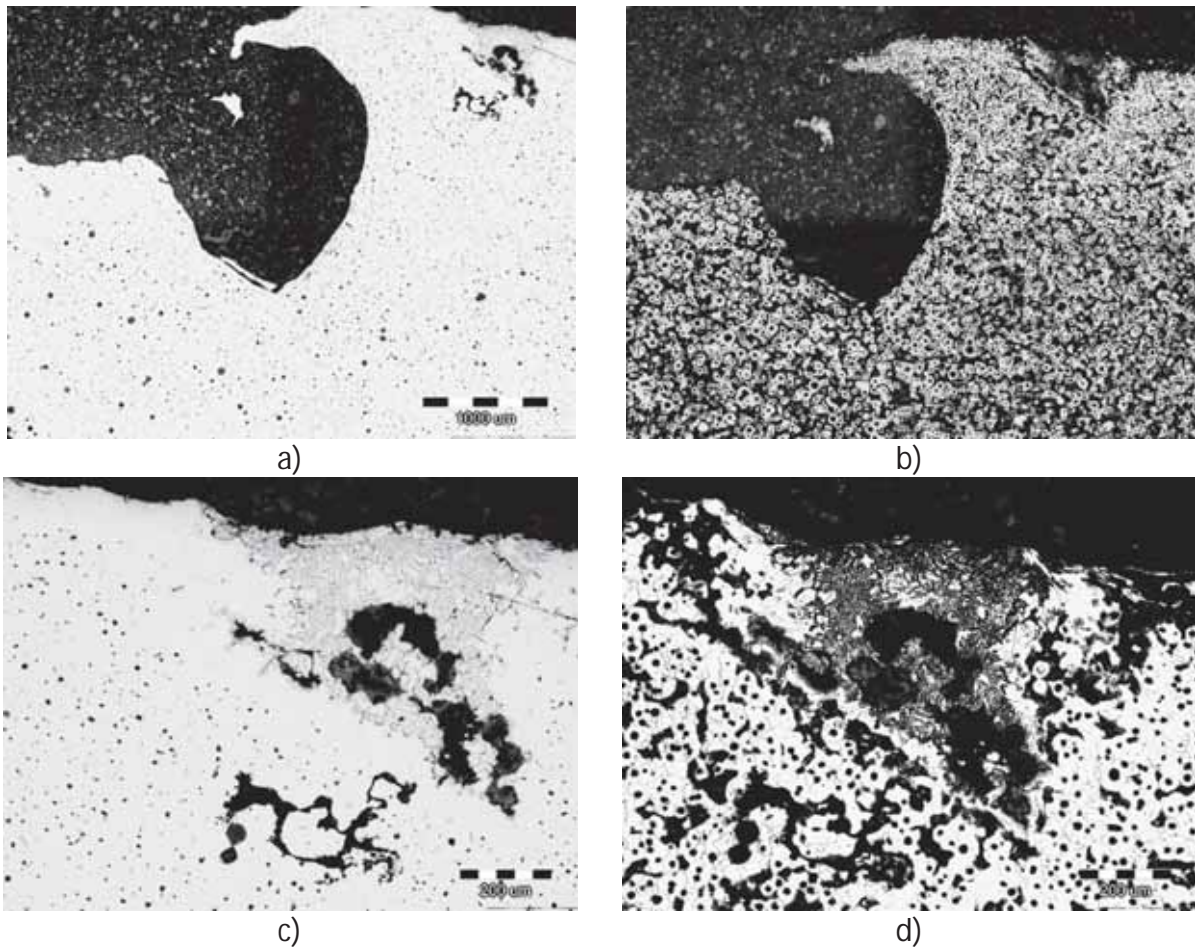
Figure 2. Microstructure of the sample in area of defect vertically to the sample surface

Figure 2 shows the gas porosity along the surface of the sample. Gas porosity often occurs in combination with heterogeneous non-metallic inclusions under the surface.

Comparison of inclusion morphology with literature survey indicates development of oxide and silicate inclusions. Presence and composition of these inclusions was investigated by SEM mapping and EDS analysis. SEM mapping analysis indicates intensity and distribution of chemical elements within the inclusion, and therefore enables identification of its type. Figure 3 represent a mapping analysis of inclusion under the surface of the casting.
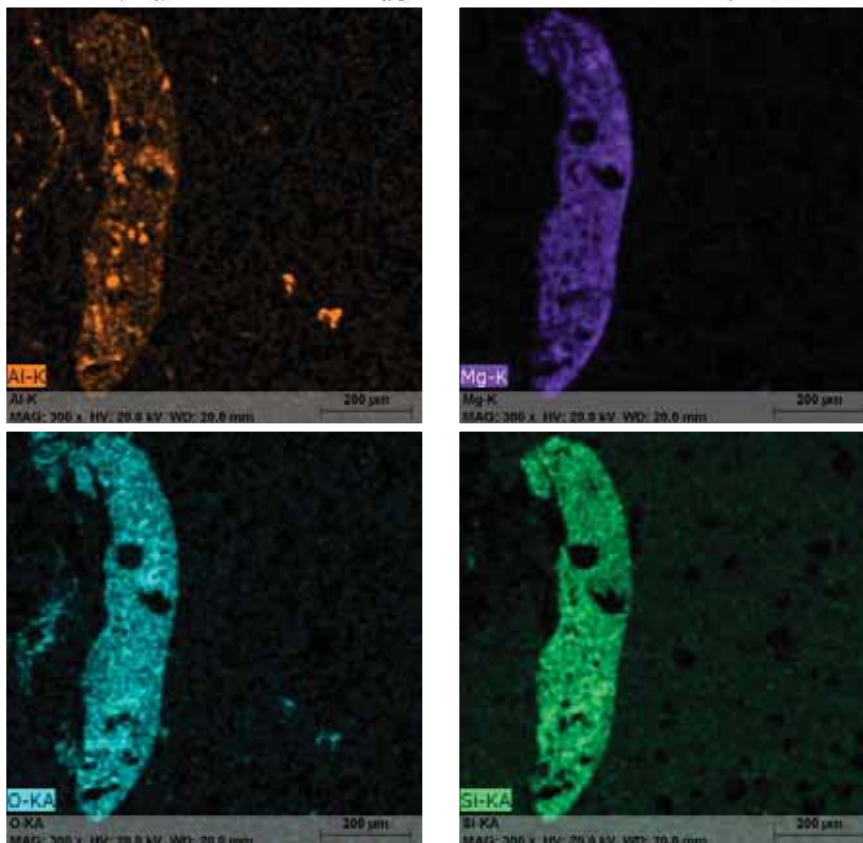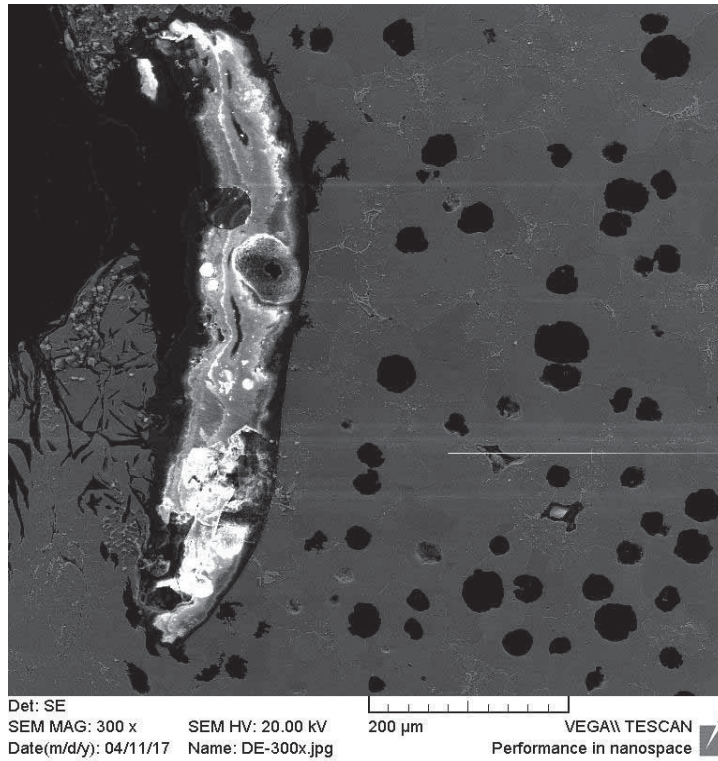
Figure 3. Mapping analysis of inclusion

Figure 3 shows an example of distributed elements and formed Al-, Mg- and Si oxide. Melt turbulence and low mould mechanical strength could result in mould erosion and sand

entrapping. Influencing factors on mould erosion are sand strength, hardness, wall thickness, feeding and gating system size and position.

Slag and sand inclusions reveal in mostly irregular shape as shown in Figure 4.
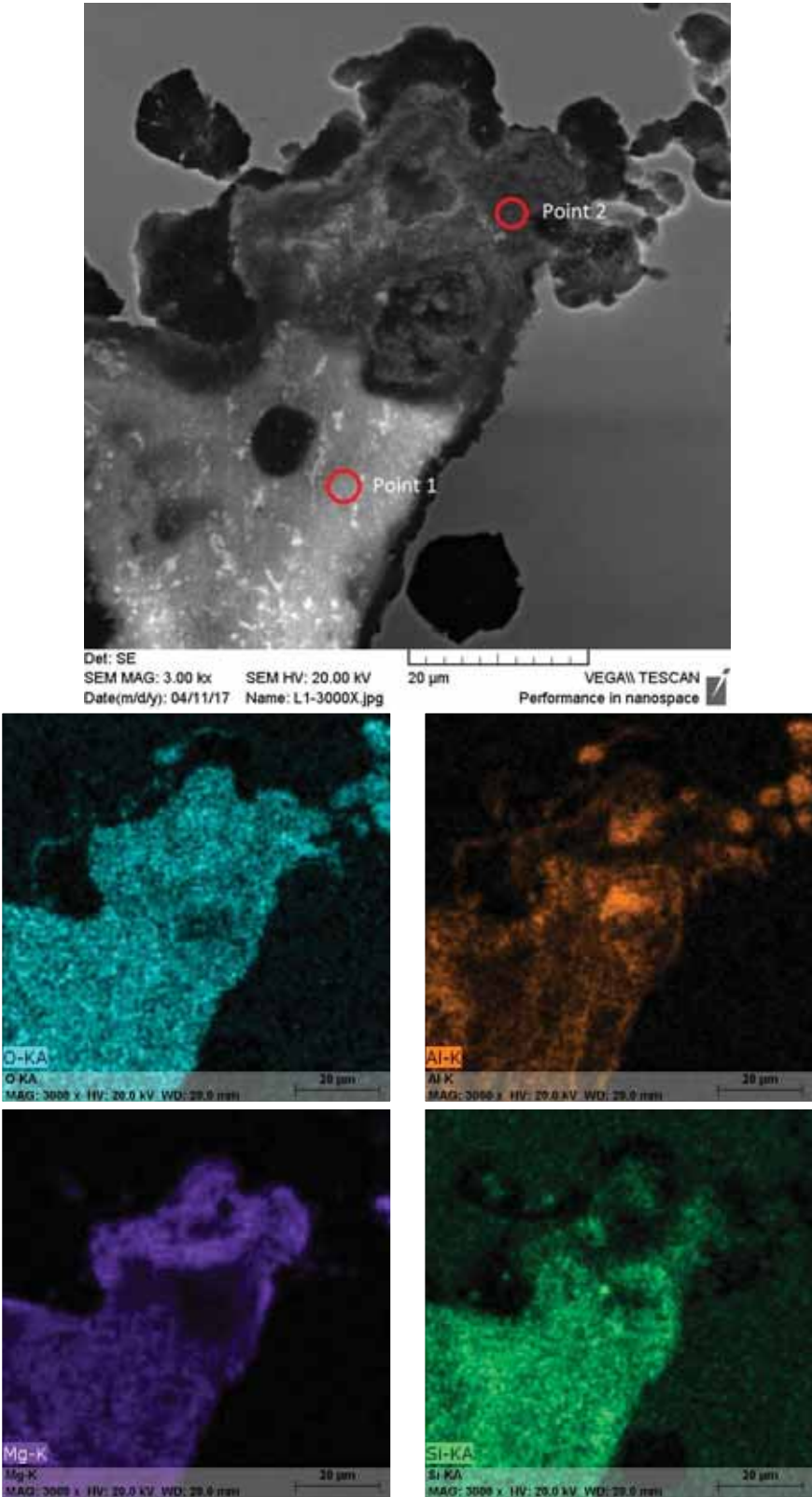
Figure 4. Distribution of elements using SEM image with mapping and EDS

Figure 4 shows an example of oxide inclusion entrapped beneath the casting surface. EDS investigation revealed that behind standard elements like aluminium (Al), magnesium (Mg) and silicon (Si), there is also calcium (Ca) as integral part of typical inoculation agent for DCI on FeSi base. Table 1 shows results of chemical composition in characteristic points indicated in Figure 4.

Table 1. Chemical composition of marked positions

Element	O	Mg	Al	Si	Ca
Point 1 (wt%)	48.42	14.24	6.45	11.08	17.20
Point 2 (wt%)	46.41	28.64	0.95	4.33	13.97

Obtained results indicate the oxidative atmosphere during DCI melt treatment.
Other example of non-metallic inclusion indicates entrapped oxide, as shown in Figure 5.
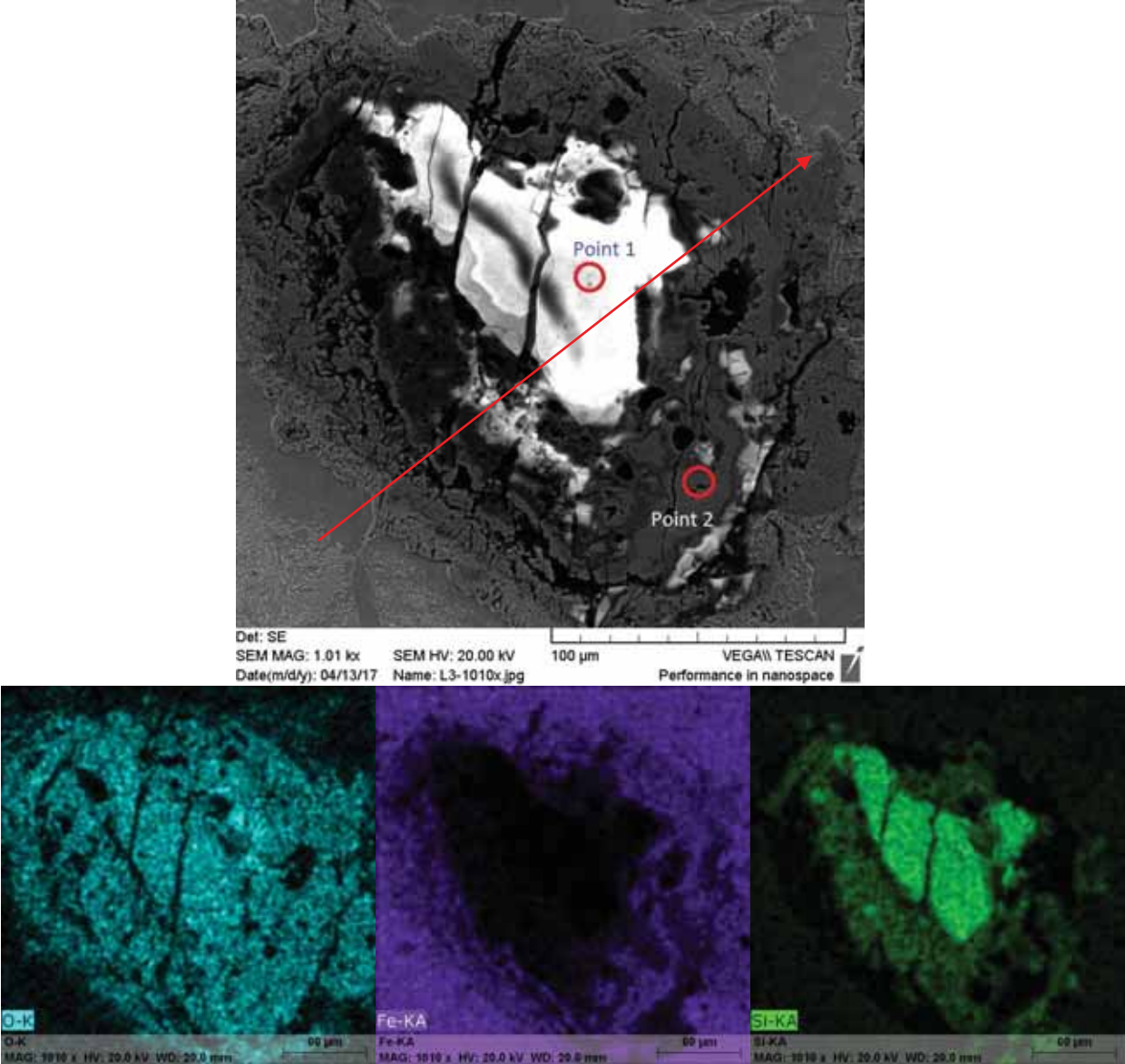
Figure 5. Mapping analysis of non-metallic inclusion with distribution of O, Fe and Si

Table 2 indicates chemical composition in corresponding positions marked in Figure 5 using EDS analysis.

Table 2. Chemical composition of marked positions in Figure 5.

Element	O	Si	Fe
Point 1 (wt%)	58.72	36.41	0.89
Point 2 (wt%)	20.00	-	77.53

SEM image reveals existence of non-metallic inclusion on the silica base surrounded by Fe-based oxide, which indicates the origin from metal reaction with sand. Turbulent mould filling induce mould erosion, segregation of particular sand grains or their agglomeration followed by oxide formations. Those phenomena resulted in Si- and Fe- oxide occurrence.

Figure 6 shows line analysis of inclusion indicated in marked direction on SEM image in Figure 5.
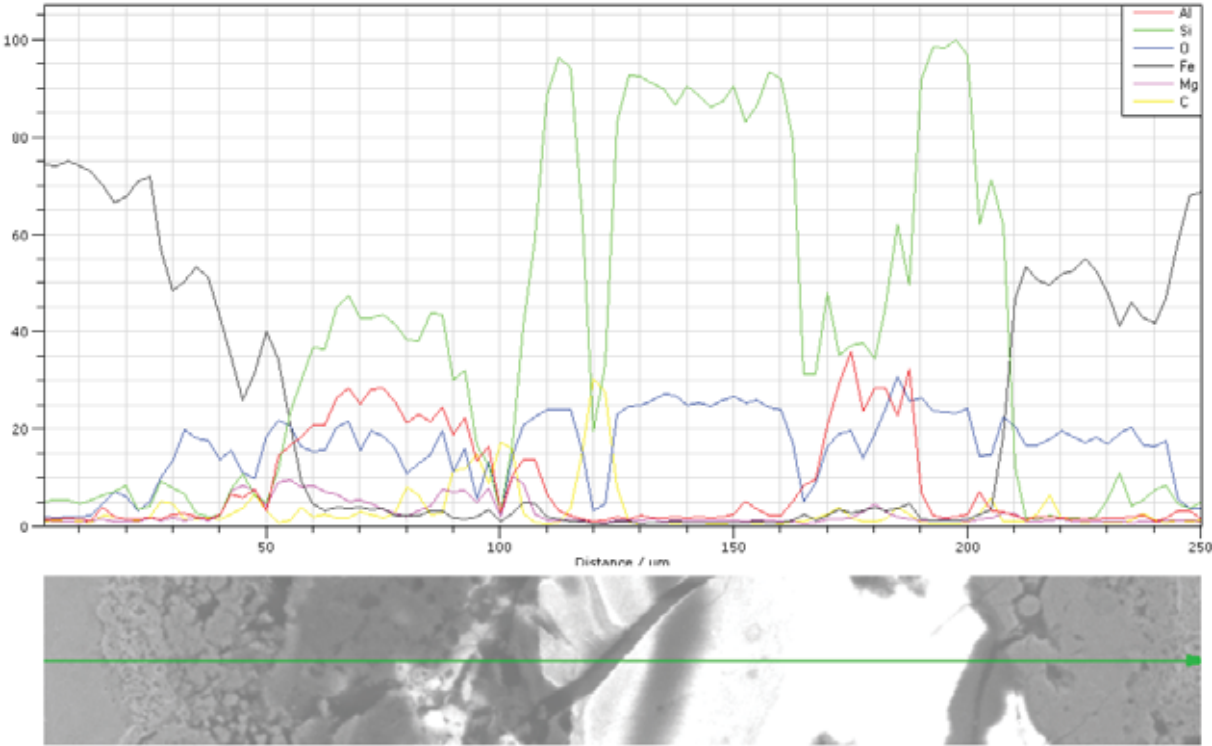
Figure 6. Line analysis of inclusion

Line analysis confirms the oxidation of silica sand. Surrounded area indicates higher amount of Si- and Al- oxide. Whole area is significantly poor in Fe content.

Next case represents an example of Fe-based oxide inclusion surrounded by graphite nodules, as shown in Figure 7.
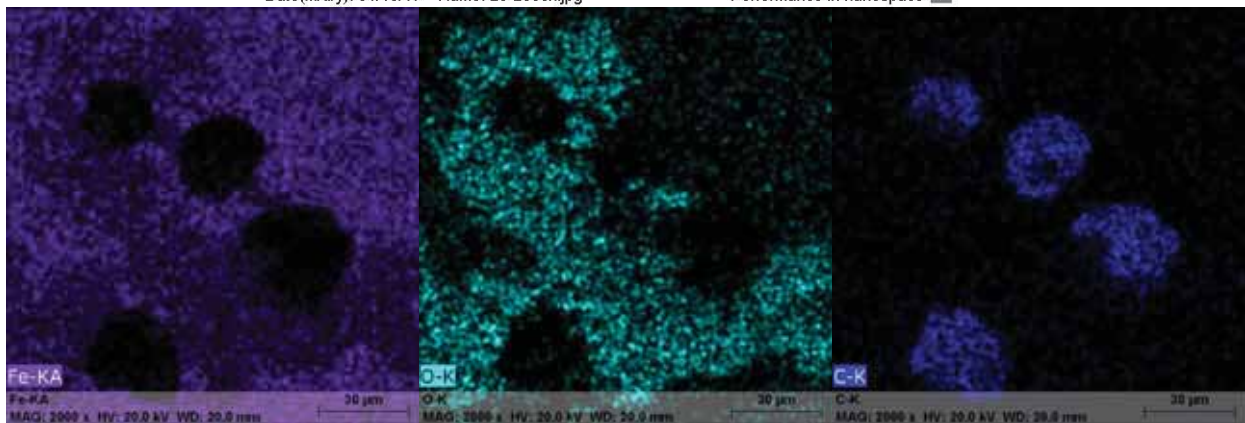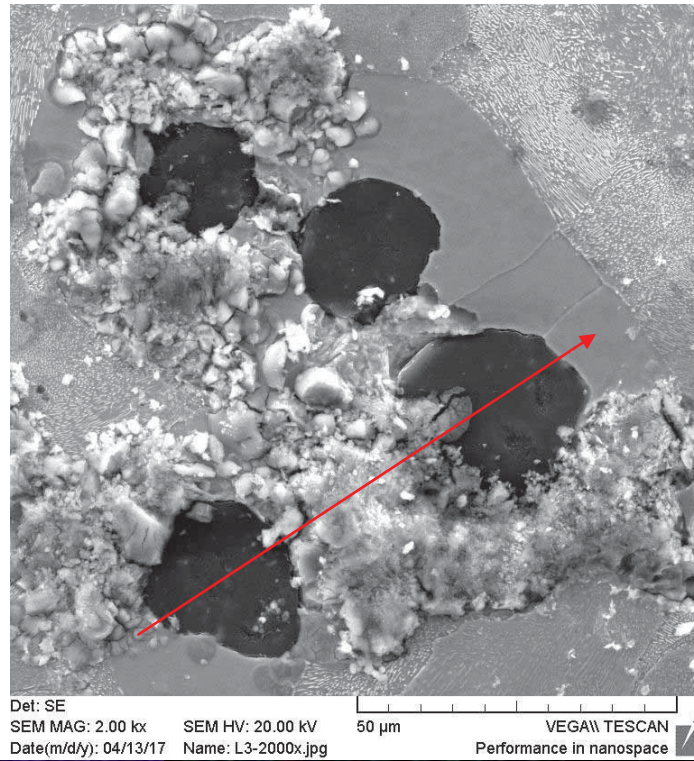
Figure 7. Distribution of chemical elements using SEM mapping analysis

Figure 7 reveals an example of Fe- oxide in metal matrix surrounded with graphite nodules. This defect occurred due to melt oxidation. In order to establish intensity changes in chemical composition line analysis was performed, as shown in Figure 8.
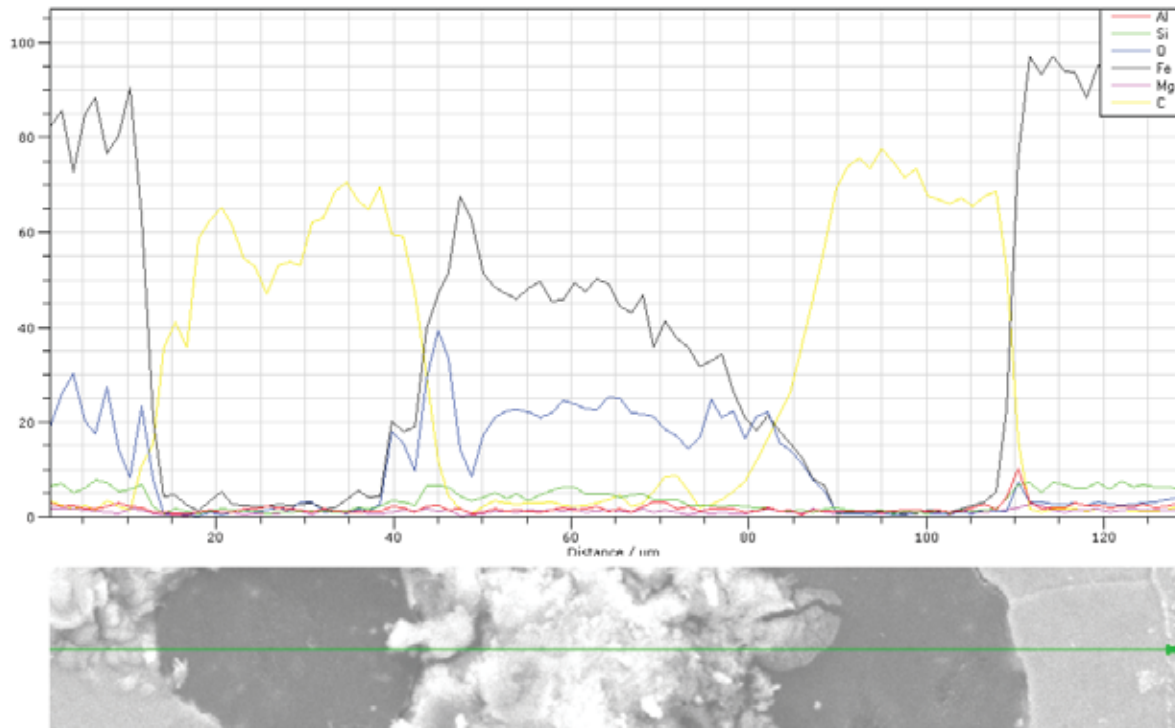
Figure 8. Line analysis of distributed elements on marked position in Figure 7.

Figure 8 shows line analysis indicating distribution of elements along the line with significant increase of Fe and O in the oxide area, and marked positions of graphite (C line). Other present elements do not reveal any significant change.

Figure 9 shows an example of entrapped Fe-oxide in the form of slag, followed by silicate inclusion under the surface of casting.
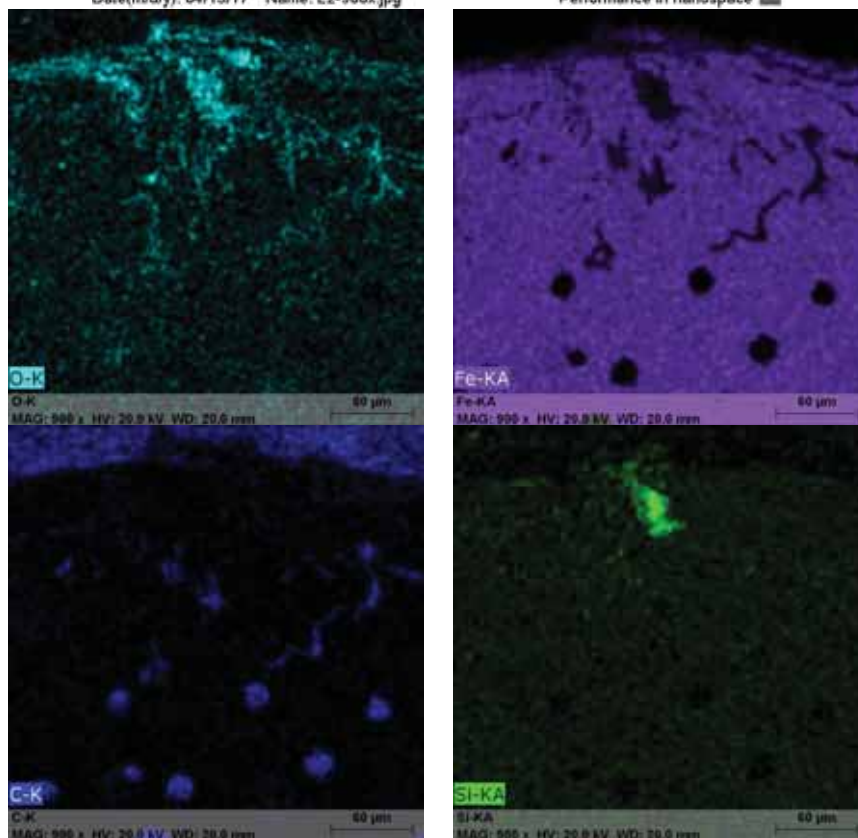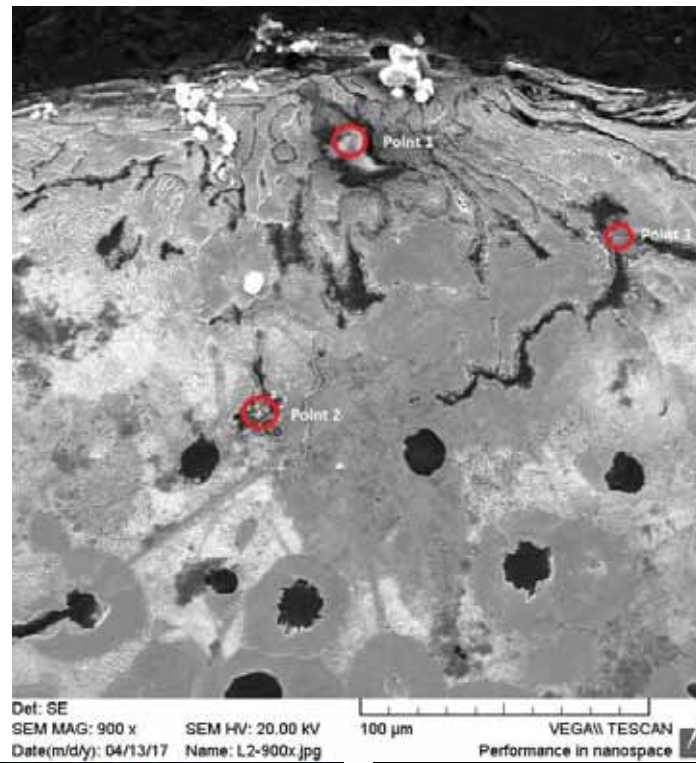
Figure 9. Distribution of chemical elements using SEM mapping analysis

Figure 9 reveals slag formation (Fe-O) in the form of stria followed by Si-O inclusion and degenerated graphite types in the area of defect. Presence of silicate inclusion indicates that erosion of sand mould also occurred during filling of mould cavity. Oxide formations were investigated using EDS. Analysis was performed on 3 points as shown in Figure 9 and Table 3.

237

Table 3. Chemical composition of corresponded positions in Figure 9.

Element	O	Si	Fe
Point 1 (wt%)	51.47	31.31	1.76
Point 2 (wt%)	16.67	1.69	74.53
Point 3 (wt%)	22.23	4.68	74.09

Chemical composition confirms the presence of Fe-based and Si-based oxides which all occur due to mould-melt interaction.

CONCLUSIONS

Casting defects represent a major problem in foundries, from technological to financial aspect, respectively. These defects causes scrap. It is very important to identify them and eliminate their origin. This investigation resulted in determination of following casting surface defects in DCI:

- Gas porosity due to melt treatment and inner reaction in mould-melt system
- Non-metallic oxide inclusions on the base of Al, Fe, Mg, Si
- Sand inclusions due to inadequate mould features
- Slag formation due to melt treatment

Melt quality and treatment, correct casting technology, mould features are significantly influencing parameters on defect occurrence. Establishing the defect nature, characterization is the first step to determine its origin. Follow-up of whole process parameters should lead to recognizing and avoiding defect occurrence.

REFERENCES

[1] V. S. Deshmukh, S. S. Sarda, the Critical Casting Defect in Cast Iron: Sand Inclusion – A Review, International Journal of Mechanical Engineering and Technology, 6(2015)9, pp. 30-42. http://www.iaeme.com/currentissue.asp?JType=IJMET&VType=6&IType=9

[2] D. M. Stefanescu, ASM Metals Handbook, Casting, Volume 15, ASM International, Ohio, 1988.

[3] J. R. Brown, Foseco Ferrous Foundryman's Handbook, Butterworth-Heinemann, Oxford, 2000.

[4] C. Z. Wu and T. S. Shih, Materials Transaction, 44(2003)5, pp. 995-1003.

[5] R. B. Gundlach, AFS Trans, 191(1997), pp. 219-228.

[6] T. S. Shih and J. Y. Wang: AFS Trans. 107, 1990, pp. 105-113.

[7] F. T. Shiao, T. S. Lui and L. H. Chen, Materials Transaction, JIM 39(1998), pp. 1033-1039.

[8] M. Gagné, M. Paquin, P. Cabanne, Dross in ductile iron: source, formation and explanation, 68th World Foundry Congress, 7-11 February 2008, India, Chennai, pp. 101–106.

[9] T. Skaland, Nucleation mechanisms in ductile iron, Proceedings of the AFS cast iron inoculation conference, 2005, Schaumburg, Illinois, USA, pp. 13–30.

[10] http://www.giessereilexikon.com/en/foundry-lexicon/Encyclopedia/show/sand-inclusion-2817/

[11] T. Skaland, Q. Grong, T. Grong, A Model for the Graphite Formation in Ductile Cast Iron, Part I. Inoculation Mechanisms, Metallurgical Transaction A, 24A(1993), pp. 2321-2345.

Acknowledgements

PHASE TRANSFORMATIONS UNDER CONTINUOUS COOLING CONDITIONS IN HIGH STRENGTH STEEL

FAZNE TRANSFORMACIJE U UVJETIMA KONTINUIRANOG HLAĐENJA KOD VISOKO-ČVRSTIH ČELIKA

Sanja Šolić[1], Bojan Podgornik[2], Matjaž Godec[2]

[1]University North University Centre Varaždin, Department of Mechanical Engineering, Varaždin, Croatia
[2]Institute for Metals and Technology, Ljubljana, Slovenia

<u>**Oral presentation**</u>
<u>Original scientific paper</u>

Abstract

Properties of high strength steels for automotive industry are highly dependent on their microstructure i.e. on different amounts of microstructural phases that are achieved by continuous cooling. The paper investigates the effect of cooling rate on phase changes and the fraction of excreted phases in the microstructure of continuously cooled high - strength steel. The microstructure and the measured hardness were analyzed on steel samples cooled with five different cooling speeds. Qualitative and quantitative results have shown that the optimal structure, ie the satisfactory bainite fraction in the mixed martensitic-bainite structure can be obtained by cooling to a rate of 0.5 ° C / s.

Keywords: high strength steels, continuous cooling, microstructure, bainite

*Corresponding author (e-mail address): ssolic@unin.hr

Sažetak

Svojstva visoko-čvrstih čelika za primjenu u automobilskoj industriji značajno ovise o njihovoj strukturi, tj. o vrstama i udjelima pojedinih strukturnih faza postignutih kontinuiranim ohlađivanjem. U radu se istražuje utjecaj brzine ohlađivanja na fazne promjene i udio izlučenih faza u mikrostrukturi kontinuirano hlađenog visoko čvrstog čelika. Analizirana je mikrostruktura i mjerena tvrdoća na uzorcima čelika hlađenih s pet različitih brzina. Kvalitativni i kvantitativni rezultati su pokazali da se optimalna struktura, tj. zadovoljavajući udio bainita u mješovitoj martenzitno – bainitnoj strukturi dobiva hlađenjima do brzina od 0,5 °C/s.

Ključne riječi: visoko-čvrsti čelici, kontinuirano ohlađivanje, mikrostruktura, bainit

UVOD

Srednje ugljični čelici s udjelom ugljika 0,3 % – 0,4 % upotrebljavaju se posljednjih desetljeća kao grupa visoko-čvrstih čelika za proizvodnju dijelova u automobilskoj industriji. Čelici iz te grupacije uobičajeno se upotrebljavaju u poboljšanom stanju (Q + T) s dobrim omjerom čvrstoće i žilavosti. Takva toplinska obrada daje finu martenzitnu strukturu čija duktilnost se optimira odabirom temperature popuštanja. Međutim, takva toplinska obrada dodaje proizvodnom procesu ekonomski i ekološki zahtjevan korak. Austenitizacija cjelovitog volumena je energetski vrlo zahtjevan postupak, a gašenje nakon austenitizacije može uzrokovati deformaciju strojnih dijelova koju je potrebno korigirati ili mehanički ili nekom naknadnom obradom odvajanjem čestica. Iz tih razloga bainitni čelici su se pojavili kao alternativa kaljenim i popuštenim čelicima s martenzitnom strukturom. Bainitni čelici su postali alternativa za čitav niz kovanih strojnih dijelova, ali i za velik broj toplo oblikovanih dijelova [1].

Za tu namjenu optimirani su kemijski sastavi čelika kojima se bainitna struktura postiže tijekom ohlađivanja na zraku nakon vrućeg kovanja ili vrućeg valjanja. Mnogi autori su obrađivali takve čelike kojima je zajedničko da imaju visoku granicu razvlačenja u rasponu 650 MPa – 850 MPa i vlačnu čvrstoću do 1300 MPa [2-10].

Današnja istraživanja na bainitnim čelicima obuhvaćaju čelike s rasponom udjela ugljika od manje od 0,1 % C do 1 % C [2]. Najviše istraživanja provodi se na srednje ugljičnim i visoko ugljičnim čelicima obzirom na mogućnost postizanja visokih vrijednosti čvrstoće, ali uz još uvijek relativno niske vrijednosti žilavosti. S tim ciljem provodi se niz istraživanja utjecaja toplinskih obrada (klasičnih izotermičkih te kontinuiranog ohlađivanja) na razvoj mikrostrukturnih oblika donjeg, gornjeg ili granularnog bainita radi postizanja viših iznosa žilavosti i što boljeg ponašanja u uvjetima loma [1].

Austenitno – bainitna transformacija je vrlo kompleksna, a i vrlo je teško postići monofaznu bainitnu strukturu obzirom da će prilikom ohlađivanja doći do izlučivanja i drugih mikrostrukturnih faza.

Kod proizvodnje kontinuirano hlađenih dijelova vrlo važan faktor je brzina hlađenja. Različite kovačnice proizvode identične strojne dijelove za određenu primjenu, ali nemaju identične uvjete ohlađivanja nakon kovanja obzirom da mogu koristiti zatvorene konvejere ili ventilatore za optimiranje brzine hlađenja. Uvjeti ohlađivanja mogu i u istoj tvornici varirati između proizvodnih linija. Obzirom na sve moguće utjecajne faktore, varijacije u uvjetima ohlađivanja potrebno je uzeti u obzir kao dio normalnog proizvodnog procesa kovanih strojnih dijelova. To je popuno prihvatljivo kod kaljenih i popuštenih dijelova obzirom da oni prolaze naknadne toplinske obrade te njihova svojstva ovise samo o točno odabranim i provedenim parametrima tih obrada. S druge strane, bainitni čelici postižu svoju konačnu mikrostrukturu i konačna mehanička svojstva tijekom faze kontinuiranog ohlađivanja. Osjetljivost na uvjete ohlađivanja može imati vrlo štetne posljedice kao što je pojava različitih vrsta mekših faza u strukturi materijala što utječe na konačna mehanička svojstva kao što su dinamička izdržljivost, čvrstoća itd. [2].

Iz tog razloga bainitni čelici moraju biti dizajnirani da postižu optimalna mehanička svojstva uz minimalnu osjetljivost na promjenu uvjeta ohlađivanja. U ovom radu prikazane su fazne transformacije pri različitim brzinama ohlađivanja visoko-čvrstog čelika s ciljem utvrđivanja raspona brzina ohlađivanja koje će dati okvir unutar kojeg će čelik postizati optimalna

tražena mehanička svojstva za koja se zahtjeva od 10 % do maksimalno 30 % bainita, morfologije donjeg bainita u mješovitoj martenzitno - bainitnoj strukturi.

MATERIJALI I METODE

Za potrebe ispitivanja izlivena je laboratorijska šarža čelika kemijskog sastava prikazanog u tablici 1.

Tablica 1. Kemijski sastav čelika

element	C	Si	Mn	S	Cr	Ni	Cu	Mo	V	N	Fe
% wt	0,41	0,97	1,33	0,008	1,57	0,19	0,23	0,21	0,29	0,0105	ostatak

Čelik je taljen u laboratorijskoj 50 kW indukcijskoj peći u kojoj je pretaljeno ukupno 9 kg čelika. Čelik je umiren aluminijem (Al killed) te uliven u ingot. Ingot dimenzija 60 mm x 60 mm valjan je u vrućem stanju (u području od 1150 °C do 1050 °C) do dimenzija 20 mm x 70 mm. Toplinska obrada uzoraka sastojala se od ugrijavanja na temperaturu od 1000 °C brzinom 0,33 °C/s progrijavanja u trajanju od 15 min te hlađenja na zraku brzinama ohlađivanja prikazanim u tablici 2. Brzine ugrijavanja i hlađenja praćene su pomoću termo-elementa smještenog u jezgri pomoćnog uzorka oblika CVN.

Tablica 2. Oznake uzoraka u ovisnosti o brzini hlađenja

Oznaka uzorka	v_{hl}, °C/s
U1	5
U2	1
U3	0,5
U4	0,1
U5	0,05

Za ispitivanje mikrostrukture uzorci su pripremljeni standardnim metalografskim postupkom pripreme uzorka. Mikrostruktura je ispitana na uzorcima za ispitivanje udarnog rada loma na field-emission skenirajućem elektronskom mikroskopu FE SEM JEOL JSM6500F. Za ispitivanje mikrostrukture uzorci su nagriženi u 3 % nitalu. Kvantitativna analiza udjela faza napravljena je na temelju analize cijele površine poprečnog presjeka uzorka na FE SEM mikroskopu uzimajući u obzir brzinu ohlađivanja i tvrdoću uzorka. Tvrdoća uzoraka izmjerena je Vickers metodom HV 1 na uređaju Instron, Tukon 2100 B. Na svakom uzorku napravljeno je deset mjerenja te rezultat predstavlja srednju vrijednost dobivenih rezultata.

REZULTATI I RASPRAVA

U tablici 3 prikazani su rezultati ispitivanja tvrdoće HV1.

Tablica 3. Tvrdoća HV 1 uzoraka

Oznaka uzorka	HV 1
U1	690
U2	662
U3	640
U4	550
U5	450

Na slici 1 prikazana je mikrostruktura uzorka U1 na različitim povećanjima. Vidljivo je da se struktura čelika sastoji od samopopuštenog martenzita u 100 % udjelu što je i u skladu s brzinom ohlađivanja te izmjerenom tvrdoćom.
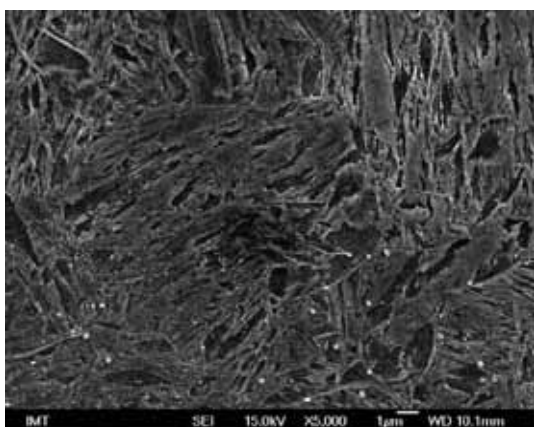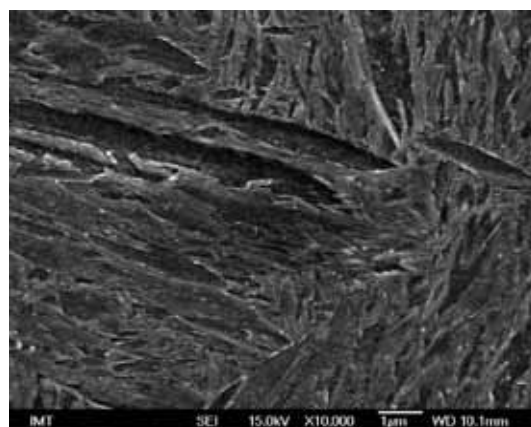
a)   b)

Slika 1. Mikrostruktura uzorka U1, v_{hl} = 5 °C/s: a) manje povećanje, b) veće povećanje

Na slici 2. prikazana je mikrostruktura uzorka U2 na različitim povećanjima.
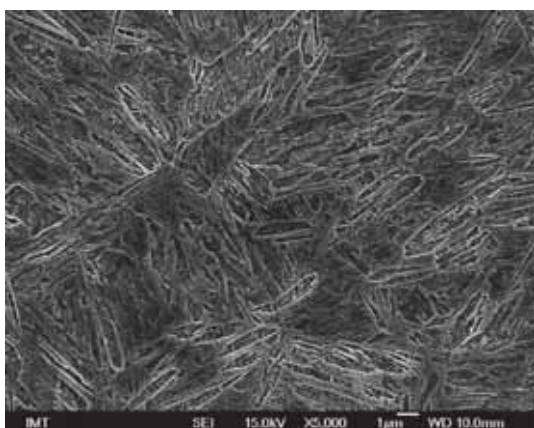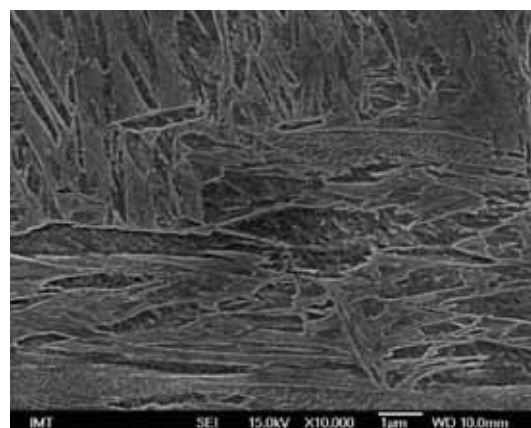
a)   b)

Slika 2. Mikrostruktura uzorka U2, v_{hl} = 1 °C/s: a) manje povećanje, b) veće povećanje

Uzorak hlađen manjom brzinom ima mješovitu martenzitno bainitnu mikrostrukturu s 10 % – 20 % bainita morfologije donjeg bainita. Jasno je vidljiva morfologija letvica (lath-like) karakteristična za donji bainit s karbidnim česticama postavljenim pod kutom 50° − 60° u

243

odnosu na granicu zrna. Također, vidljiv je mali udio pločastog donjeg bainita (plate-like). Pločasti (eng. plate-like) bainit se naziva još i srasli (eng. coalesced) bainit. Pločasti ili srasli bainit nastaje kada dolazi do srastanja individualno nastalih pločica tj. letvica bainitnog ferita koji imaju identičnu kristalografsku orijentaciju [11].

Predočena su dva uvjeta koja su nužna za nastanak pločastog bainita:

(1) kada pojedine pod-jedinice tj. letvice bainitnog ferita imaju jednaku kristalografsku orijentaciju one u principu mogu srasti neprimjetno, ali tanja pločica/letvica povezana je s većim naprezanjem uslijed deformacije oblika pri formiranju bainita tako da mora postojati dovoljna pokretačka sila (izmjena slobodne kemijske energije), koja će osigurati formiranje većih ploča bainitnog ferita;

(2) mora postojati dovoljno mjesta kako bi se osiguralo nesmetano srastanje i rast pločastog ferita. Ugljik ostaje zarobljen unutar feritnog zrna te kasnije precipitira unutar zrna u karbidne čestice ili djelomično odlazi u zaostali austenit. Prisutnost pločastog bainita u većim udjelima uglavnom se negativno odražava na žilavost čelika [12].

Na slici 3 prikazana je mikrostruktura uzorka U3 na različitim povećanjima.

a)   b)
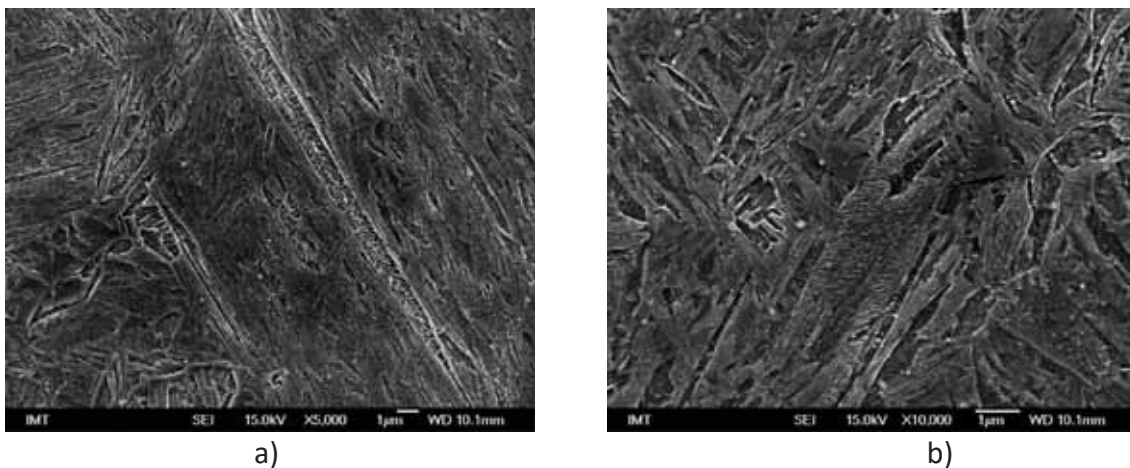
Slika 3. Mikrostruktura uzorka U3, v_{hl} = 0,5 °C/s: a) manje povećanje, b) veće povećanje

Iz slika je vidljivo da se mikrostruktura nije značajno promijenila u odnosu na uzorak U2 odnosno da smanjenje brzine ohlađivanja s 1 °C/s na 0,5 °C/s nije značajno promijenilo kinetiku transformacije austenita u martenzit i bainit. Mikrostruktura uzorka hlađenog s 0,5 °C/s također se sastoji pretežno od samopopuštenog martenzita i bainita morfologije letvica karakterističnog za donji bainit u udjelu 10 % − 20 %. Izmjerena tvrdoća također korelira udjelima mikrostrukturnih faza.

Na slici 4. prikazana je mikrostruktura uzorka U4 na različitim povećanjima.
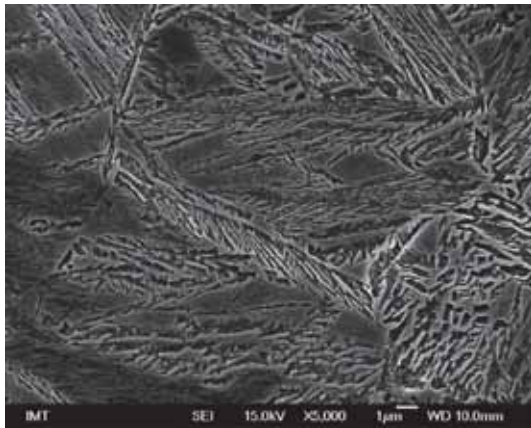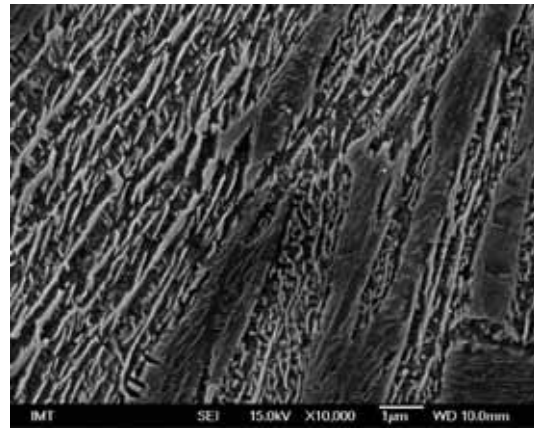
a)	b)

Slika 4. Mikrostruktura uzorka U4, v_{hl} = 0,1 °C/s: a) manje povećanje, b) veće povećanje

Na slikama je vidljiva mješovita bainitno martenzitna struktura uglavnom degeneriranog gornjeg bainita, bainitnog ferita prošaranog cementitom i visokougljičnim zaostalim austenitom te martenzitno/austenitnim blokovima. Udio bainita u ovom uzorku nešto je veći nego kod uzorka U2 i U3 te iznosi oko 70 %, u odnosu na 30 % martenzita. Iz mikrostrukture je jasno vidljivo da je pri ohlađivanju manjom brzinom došlo do nastanka mješovite bainitne strukture morfologije pretežno gornjeg bainita u udjelu oko 50 % te donjeg bainita oko 20 % i ostatak martenzita.

Na slici 5. prikazana je mikrostruktura uzorka U5 na različitim povećanjima.
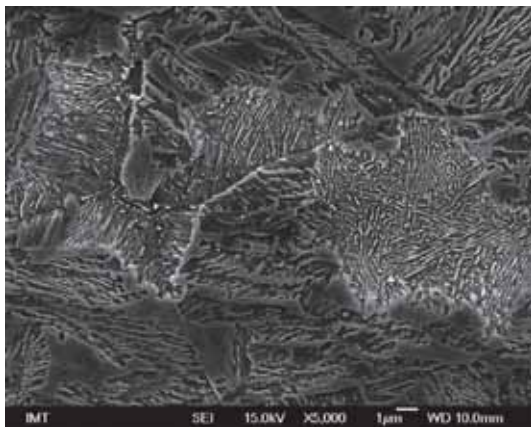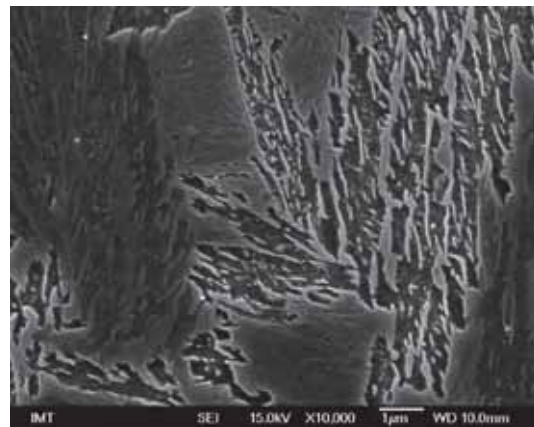
a)	b)

Slika 5. Mikrostruktura uzorka U5, v_{hl} = 0,05 °C/s: a) manje povećanje, b) veće povećanje

Na slikama je vidljiva mješovita mikrostruktura karakteristična za spore brzine ohlađivanja. Jasno je vidljivo da je došlo do izlučivanja perlita i to u udjelu 10 % – 15 %. Martenzit se također izlučio u nešto manjem udjelu, 10 % – 15 %, a prisutna je i značajna količina zaostalog austenita u morfološkom obliku degeneriranog gornjeg bainita što je jasno vidljivo na slici 5b. Tvrdoća ovog uzorka od 450 HV 1 odgovara analiziranoj mikrostrukturi te ukazuje da je brzina ohlađivanja od 0,05 °C/s premala za postizanje mješovite mikrostrukture koja se sastoji samo od martenzita i bainita.

ZAKLJUČAK

U radu je analiziran utjecaj brzine hlađenja na fazne promjene i udio izlučenih faza u mikrostrukturi kontinuirano hlađenog visoko-čvrstog čelika za upotrebu u automobilskoj industriji. Obzirom da kontinuirano hlađeni visoko čvrsti čelici svoja konačna mehanička svojstva postižu tijekom hlađenja nakon kovanja te ne prolaze naknadne toplinske obrade od ključne je važnosti za kvalitetu proizvoda odrediti raspon brzina ohlađivanja unutar kojeg će se osigurati izlučivanje određenih mikrostrukturnih oblika u točno određenim udjelima. Analiza je pokazala da se zadovoljavajući udio bainita u mješovitoj martenzitno – bainitnoj strukturi dobiva hlađenjima do brzinama od 0,5 °C/s. Obzirom da se pri toj brzini izlučuje do 20 % donjeg bainita može se očekivati da će minimalne moguće varijacije pri hlađenju u industrijskim uvjetima još uvijek zadovoljiti traženi raspon bainita od 10 % do maksimalno 30 % bainita (morfologije donjeg bainita) u strukturi strojnog dijela nakon hlađenja.

LITERATURA

[1]   M. Gomez, L. Rancel, E. Escudero, S. F. Medina, Phase Transformation under Continuous Cooling Conditions in Medium Carbon Microalloyed Steels, J. Mater. Sci. Technol., 30(2014)5, pp. 511-516.

[2]   T. Sourmail, V. Smanio, Optimisation of the mechanical properties of air cooled bainitic components through tailoring of the transformation kinetics, Materials Science & Engineering A, 582(2013), pp. 257-261.

[3]   H. S. Yang, H. K. D. H. Bhadeshia, Mater. Sci. Technol., 23(2007), pp. 556-560.

[4]   G. Gomez, T. Pérez, H. K. D. H. Bhadeshia, Mater. Sci. Technol., 25(2009), pp. 1502-1507.

[5]   G. Gomez, T. Pérez, H. K. D. H. Bhadeshia, Mater. Sci. Technol., 25(2009), pp. 1508-1512.

[6]   T. Sourmail, H. Michaud, E. d'Eramo, G. Baudry, in: Super High Strength Steels, Verona, 2010.

[7]   S. Engineer, H. Justinger, P. Janssen, M. Härtel, C. Hampel, F. Randelhoff, in: International Conference on Steel in Cars and Trucks, Salzburg, Austria.

[8]   K. Sugimoto, in: International Conference on Steel in Cars and Trucks, Salzburg, Austria.

[9]   H. Roelofs, S. Hasler, M. Lembke, F. Caballero, in: International Conference on Steel in Cars and Trucks, Salzburg, Austria.

[10]   C. Keul, L. Moseker, W. Bleck, T. Rekersdrees, C. Beyer, H. W. Raedt, A. Stuber, H. Schliephake, in: International Conference on Steel in Cars and Trucks, Salzburg, Austria.

[11]   H. K. D. H. Bhadeshia, E. Keenan, L. Karlsson, H. O. Andren, Coalesced Bainite, Transaction of the Indian Intstitute of Metals, 59(2006), pp. 689-694.

[12]   H. K. D. H. Bhadeshia, Bainite in Steel, The Institute of Materials, London, 1992.

INFLUENCE OF THE STEEL CHEMICAL COMPOSITION ON THE MECHANICAL PROPERTIES OF HOT ROLLED STEEL STRIPS

Irena Žmak[1]**, Stoja Rešković**[2]**, Darko Ević**

[1]University of Zagreb Faculty of Mechanical Engineering and Naval Architecture, Zagreb, Croatia
[2]University of Zagreb Faculty of Metallurgy, Sisak, Croatia

<u>Poster presentation</u>
<u>*Original scientific paper*</u>

Abstract

The paper presents the results of statistical analysis of experimental data from the hot rolling process of steel. The influence of carbon, manganese and the sum of carbon and manganese content onto the tensile strength, yield strength and elongation of hot rolled steel strips was determined. The correlation of some of the studied problems showed that the measured data dissipation is significant; therefore, a more powerful mathematical method is proposed for the determination of influence of the steel chemical composition on the mechanical properties of hot rolled steel strips.

Keywords: *steel, hot-rolling, mechanical properties, regression, chemical composition*

Corresponding author (e-mail address): irena.zmak@fsb.hr

INTRODUCTION

Rolling is a metalworking forming process, where metal stock passes through one or several pairs of rolls in order to reduce the thickness of the steel, and also to uniform the material thickness. The rolling process may be classified as to the temperature: when the metal temperature is over the metal's recrystallization temperature, the rolling process is called hot-rolling. When the metal temperature is below the recrystallization temperature, the rolling process is classified as cold rolling [1].

Roll stands that hold the roll pairs are typically grouped into the rolling mills, Figure 1. Rolling mills can easily process different metallic materials, although steel is the typically rolled metal. Typical products are structural steel components, bar stock, as well as rails. Steel mills usually have divisions which process the half-finished castings products into final products.

Plates and strips are rolled from cast steel in a warm state. They are divided into:

- thin strips, with thickens up to 2.5 mm,
- medium thick strips: 2.5 to 4.5 mm,
- thick strips: 4.5-7.0 mm and
- plates: thicker than 7.0 mm.

During hot deformation, the recrystallization and the recovery occur, so the hot-rolled plates and strips have a homogeneous structure, Figure 2.

After hot rolling, strips and plates may be rolled in the cold state. Cold deformation increases the mechanical properties and the surface quality.
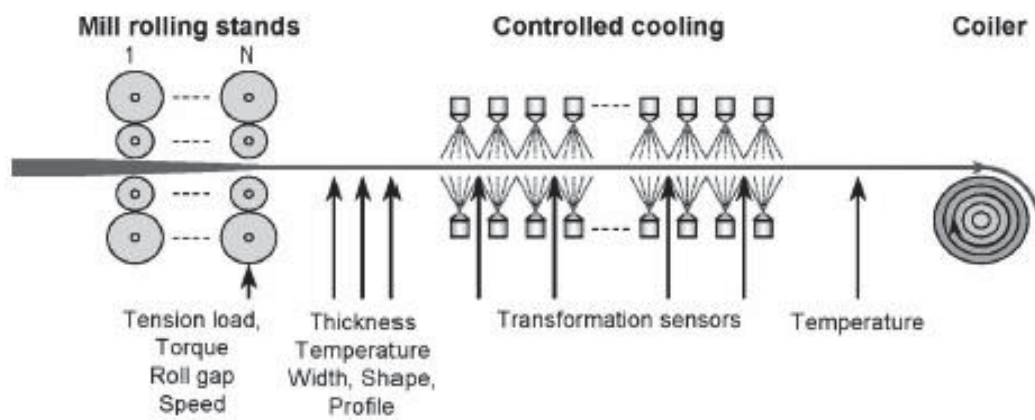
Figure 1. Schematic representation of the hot strip mill [2]

| a) | b) |
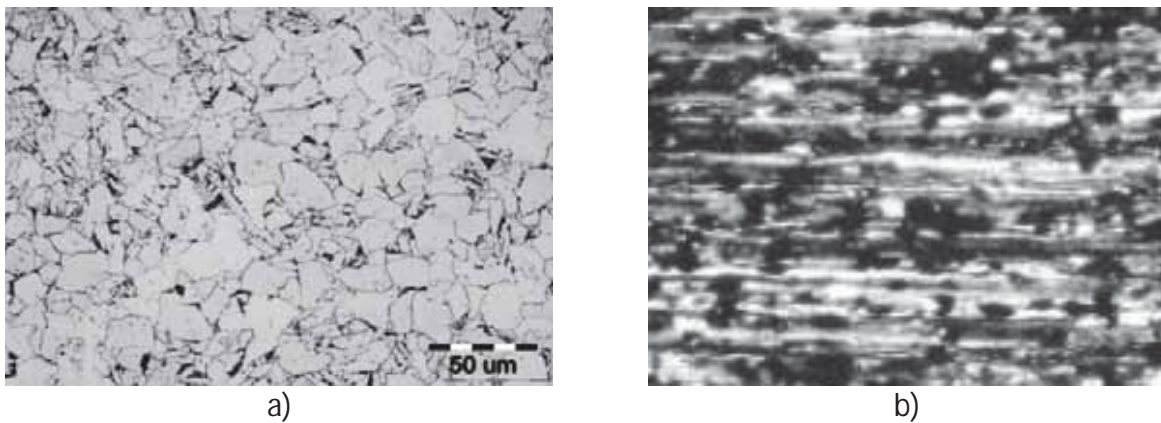
Figure 2. Microstructure of a) hot, b) cold rolled steel strip [3]

The study was conducted on 159 samples of hot-rolled strip, produced in Croatian ironworks. The detailed chemical composition was determined, and tensile mechanical properties were measured. The influence of the most important chemical elements on tensile mechanical properties was analyzed.

MATERIALS AND METHODS

The analysis of 15 different steel types, with a total of 159 datasets was done, as the testing was done on several strip rolls from each melt. The chemical composition and the following static tensile mechanical properties were determined: tensile strength, yield strength and elongation.

Chemical composition was detained using the optical emission spectrophotometry method on the quantometer MA – ARL and by oxygen incineration of cutting chips on the Leco analyzers CS – 230 and TC – 500. Table 1 presents the weight content limits of each determined chemical element, as well as the mean value and the standard deviation.

The simple statistical analyses showed that the limits of carbon content from 0.10 to 0.22, and manganese from 0.42 to 0.85 wt. % comply to the European standard Chemical analysis of ferrous materials - Determination of manganese in steels and irons - Electrometric titration method (EN 10071:2014). This European standard describes an electrometric titration method for the determination of manganese in steel and iron. The method is applicable to unalloyed, low alloyed or alloyed steels, and to iron materials with manganese content greater than or equal to 0.5 wt. %. The principle is the following: the test portion is dissolved with an appropriate acid mixture and the excess acid is largely neutralized with sodium hydrogen carbonate. Interfering cations are precipitated with zinc oxide. Titration of Mn (II) takes place with a potassium permanganate solution, in a sodium pyrophosphoric medium at a pH-value of about 6.5. The end point of this redox reaction, i.e. the oxidation of Mn (II) to Mn (III), is determined by an electrometric measurement [4].

Table 1. Chemical composition of analyzed steel melts

[wt. %]	C	Mn	Si	P	S	Al	Ni	Cr	N
Min.	0.10	0.42	0.05	0.007	0.01	0.02	0.01	0.00	0.004
Max.	0.22	0.85	0.37	0.100	0.05	0.07	0.07	0.30	0.009
Average	0.147	0.622	0.138	0.0203	0.017	0.043	0.033	0.026	0.0058
St. dev.	0.027	0.152	0.080	0.0225	0.009	0.012	0.014	0.061	0.0013

Mechanical properties were determined on an Instron universal testing machine in the laboratory of the same Croatian mill factory were the steel strips were produced. Some of the testing results were cross-validated in laboratory of the Faculty of Metallurgy in Sisak, Croatia, using the Zwick 50 kN universal testing machine. All mechanical testing was done according to EN 10002-1. Table 2 presents the limits of each determined mechanical property, as well as the mean value and the standard deviation.

Table 2. Mechanical properties of analyzed steel strips

	R_{eH} [MPa]	R_m [MPa]	A [%]
Min.	243	328	21.9
Max.	408	502	39.4
Average	355.0	459.4	33.78
St. dev.	28.4	30.1	4.52

RESULTS AND DISCUSSION

It was determined that for every 0.1 wt. % of carbon there was an increase of 15 MPa in tensile strength and 10 MPa in yield strength of the hot-rolled steel strips. Conversely, for every 0.1 wt. % carbon there was an average reduction of 2 % (absolute value) on the elongation. The influence of the manganese on the steel tensile properties was not so straightforward, but it can be also concluded that the manganese does increase the tensile and yield strength, as well as reduces the elongation. The sum of carbon and manganese was also analyzed.

A logarithmic regression model was fitted to the data in order to try to find a connection between the analyzed properties, Figure 3 to 11.

$$R_m = 114.42\ln(\%C) + 680.55$$
$$R^2 = 0.4184$$
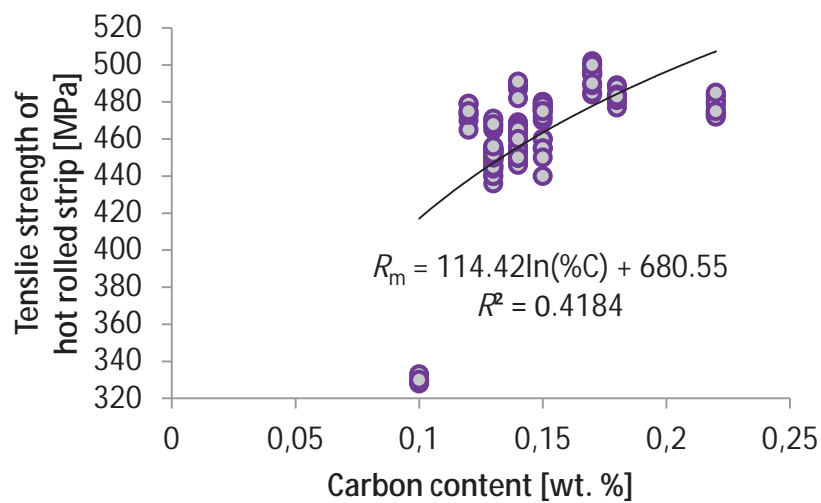
Figure 3. Steel carbon content vs. hot-rolled strip tensile strength

$$R_m = 49.008\ln(\%Mn) + 484.15$$
$$R^2 = 0.1625$$
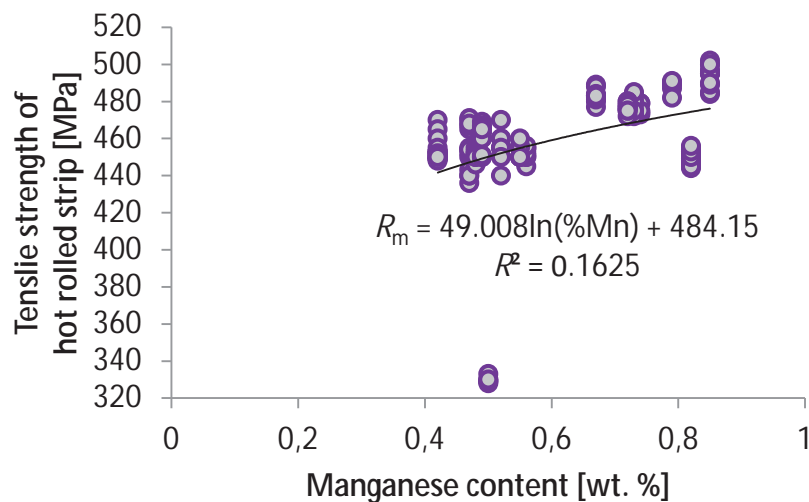
Figure 4. Manganese carbon content vs. hot-rolled strip tensile strength
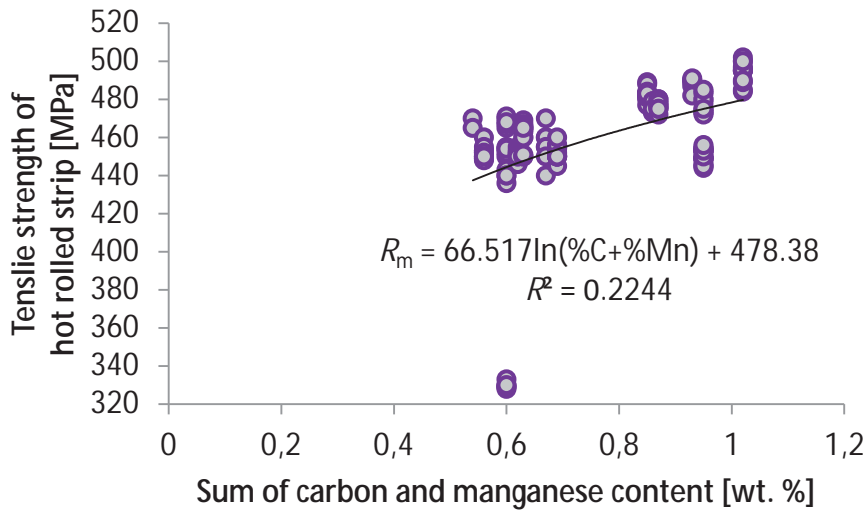
Figure 5. Sum of steel carbon and manganese content vs. hot-rolled strip tensile strength

The equation shown in Figure 5:

$$R_m = 66.517\ln(\%C + \%Mn) + 478.38$$
$$R^2 = 0.2244$$
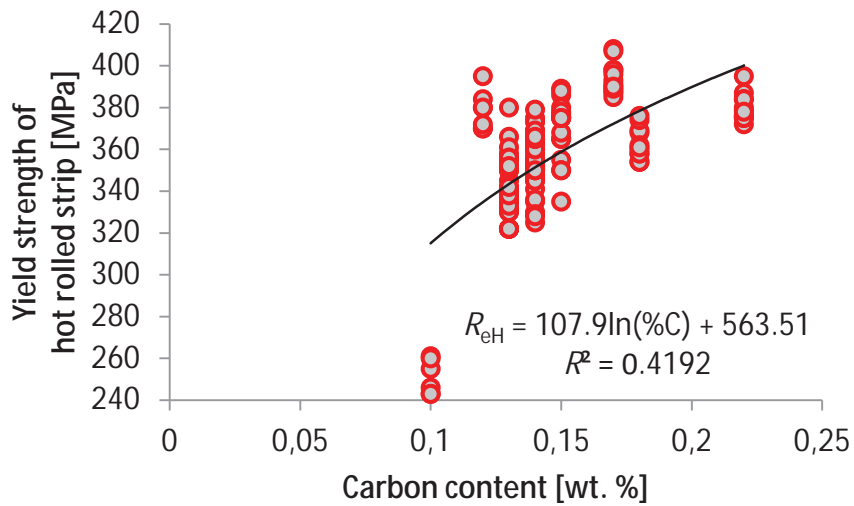
Figure 6. Steel carbon content vs. hot-rolled strip yield strength

The equation shown in Figure 6:

$$R_{eH} = 107.9\ln(\%C) + 563.51$$
$$R^2 = 0.4192$$
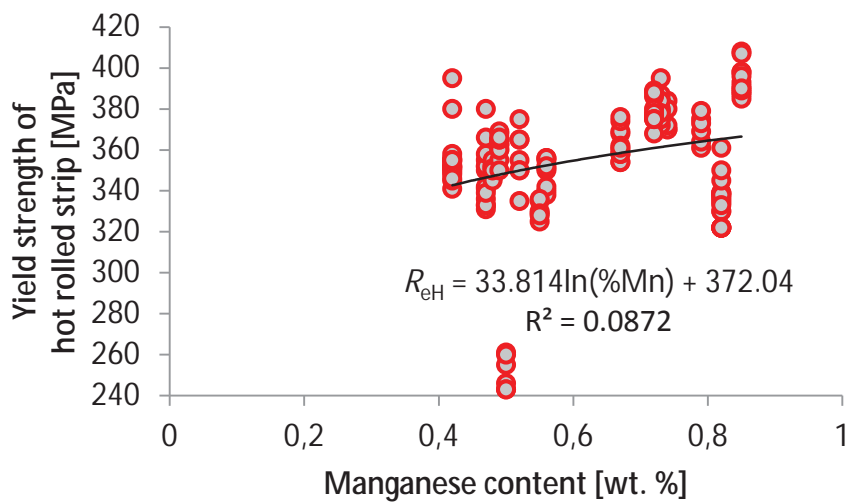
Figure 7. Steel manganese content vs. hot-rolled strip yield strength

The equation shown in Figure 7:

$$R_{eH} = 33.814\ln(\%Mn) + 372.04$$
$$R^2 = 0.0872$$
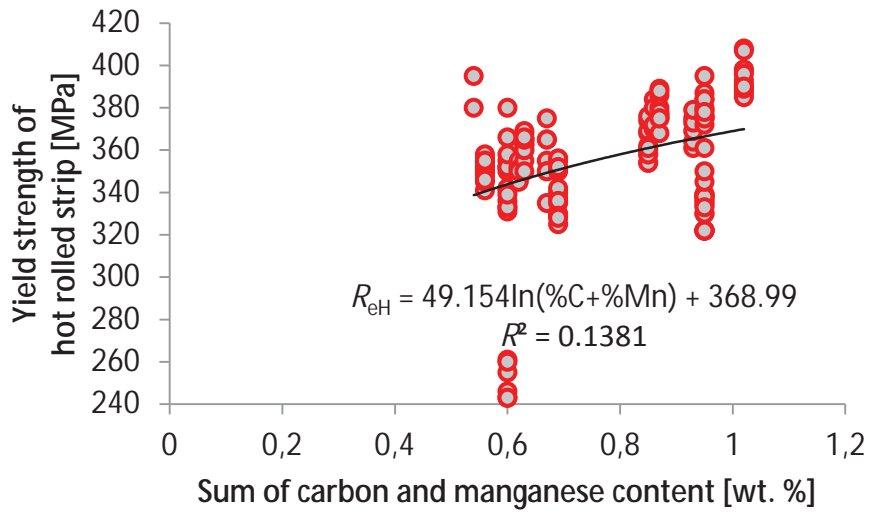
Figure 8. Sum of steel carbon and manganese content vs. hot-rolled strip yield strength
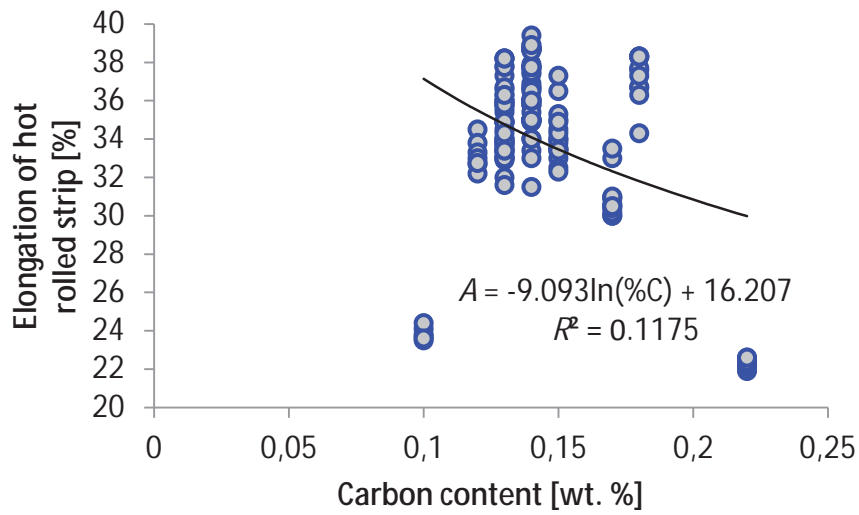
Figure 9. Steel carbon content vs. hot-rolled strip elongation
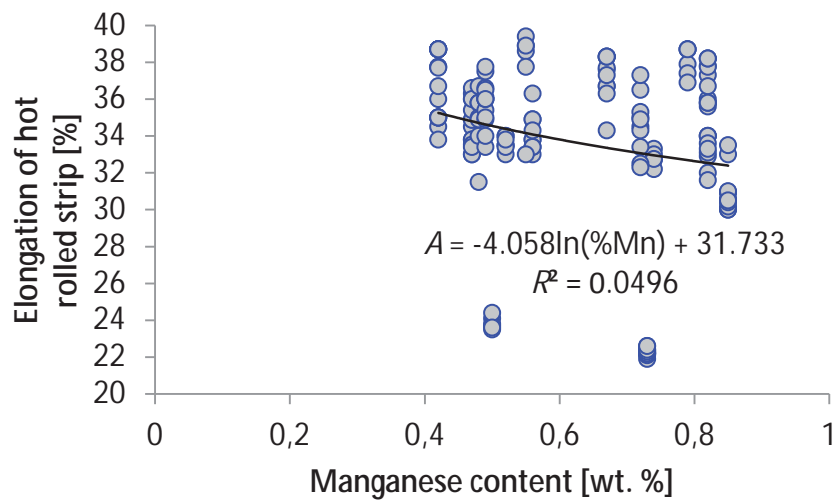
Figure 10. Steel manganese content vs. hot-rolled strip elongation
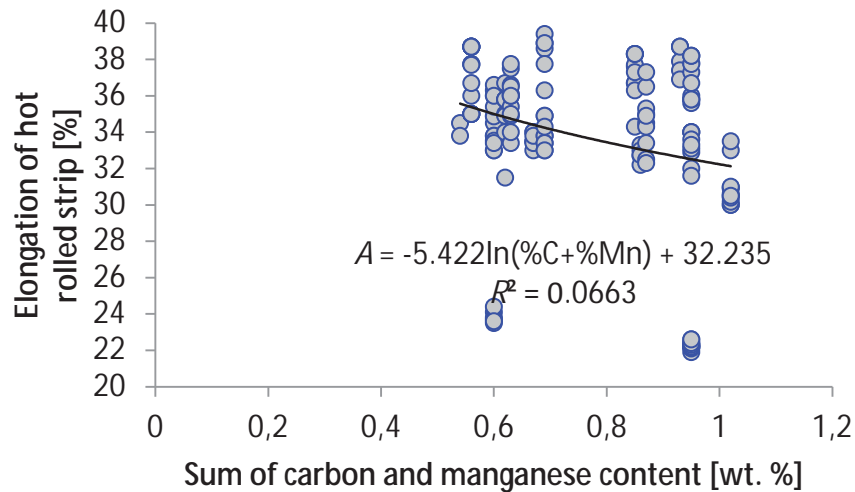
Figure 11. Sum of steel carbon and manganese content vs. hot-rolled strip elongation

The regression equation is included on the respective chart for each analyzed problem, and the calculated correlation coefficients as a statistical measure are also presented. The R-squared shows how close are the data to the regression line fitted by the selected model. The values of the R-squared are satisfactory for the carbon content influence, but much lower for the possible determination of a regression a logarithmic model for fitting tensile properties to manganese content.

Conversely, the correlation of the sum of manganese and carbon to mechanical properties was between the stated two single elements analysis. It is evident that the link to mechanical properties is not as simple as one chemical element influence. There are obviously other dependent and independent variables that influence the tensile and yield strength, and elongation of the hot-rolled steel strips.

CONCLUSIONS

The paper presented the results of a regression analysis of the influence of the most important variables, i.e. carbon, manganese and the sum of these two elements, on the mechanical properties of hot-rolled steel strips.

A logarithmic regression model was fitted to the data in order to try to find a connection between the analyzed properties and the most relevant chemical elements. The values of the R-squared are satisfactory for the carbon content influence, but much lower the manganese. Also, the correlation of the sum of manganese and carbon to mechanical properties was between the stated two single elements analysis.

It was concluded that the link to mechanical properties is not as simple as one chemical element influence. There are obviously other dependent and independent variables that influence the tensile and yield strength, and elongation of the hot-rolled steel strips.

In such a complex prediction problem, other, more complex prediction models would be more appropriate. One possible mathematical model that could correlate the chemical composition of the steel melt to the mechanical properties of the hot-rolled strip could be artificial neural networks. This method has advanced prediction properties and is adequate

for solving very complex prediction problems. The application of artificial neural networks in materials property prediction was already studied and confirmed in literature [5-11]. Therefore, the next step in a better prediction of mechanical properties of hot-rolled steel strips based on the chemical composition of the steel melt is planned to be undertaken.

REFERENCES

[1] E. P. DeGarmo, J. T. Black, R. A. Kohser, DeGarmo's Materials and Processes in Manufacturing, 11th ed., Wiley, Hoboken, NJ, 2011.

[2] W. Jacobs, Quantification of Microstructure in Plate Steels using EM sensor Technology, Accessible on Internet: http://www2.warwick.ac.uk/fac/sci/wmg/research/steel_processing/projects/phdprojects/, April 12th 2017.

[3] S. Rešković, Teorija oblikovanja deformiranjem - interna skripta, Metalurški fakultet, Sveučilište u Zagrebu, Sisak, 2015.

[⬜⬜] DIN EN 10071 2013-01 - Beuth.de, Accessible on Internet: https://www.beuth.de/en/standard/din-en-10071/165734519, April, 13th 2017.

[5] V. Alar, I. Žmak, B. Runje, A. Horvatić, Development of Models for Prediction of Corrosion and Pitting Potential on AISI 304 Stainless Steel in Different Environmental Conditions. International Journal of Electrochemical Science, 11(2016), pp. 7674-7689.

[6] T. Filetin, I. Žmak, D. Novak, Nitriding parameters analyzed by neural network and genetic algorithm, Journal de physique IV, 120(2004), pp. 355-362.

[7] I. Žmak, T. Filetin, Predicting Thermal Conductivity of Steels Using Artificial Neural Networks, Transactions of FAMENA, 34(2010)3, pp. 11-20.

[8] I. Žmak, T. Filetin, S. Hren, Modeliranje vlačne čvrstoće nodularnog lijeva pomoću umjetnih neuronskih mreža, Ljevarstvo, 51(2009)3, pp. 59-64.

[9] P. Saravanakumar, V. Jothimani, L. Sureshbabu, S. Ayyappan, D. Noorullah, P. G. Venkatakrishnan, Prediction of Mechanical Properties of Low Carbon Steel in Hot Rolling Process Using Artificial Neural Network Model, Procedia Engineering, 38(2012), pp. 3418-3425.

[10] D. Šimek, A. Oswald, R. Schmidtchen, M. Motylenko, G. Lehmann, D. Rafaja, Prediction of Mechanical Properties of Carbon Steels After Hot and Cold Forming by Means of Fast Microstructure Analysis, Steel Research Int., 85(2014), pp. 1369-1378.

[11] E. Kanca, F. Çavdar, M. M. Erşen, Prediction of Mechanical Properties of Cold Rolled Steel Using Genetic Expression Programming, Acta Physica Polonica A, 130(2016), pp. 365-369.

COMMERCIAL PAGES
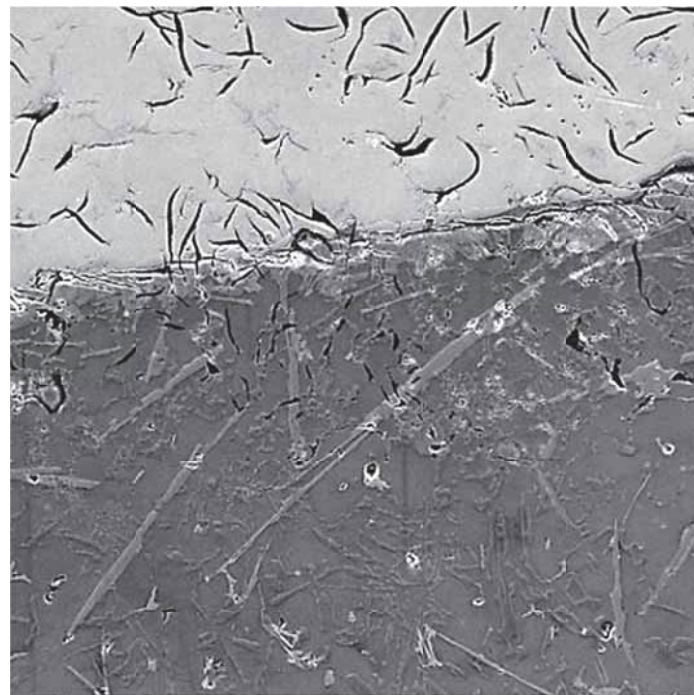
Det: SE
SEM MAG: 300 x   SEM HV: 20.00 kV   200 µm   VEGA\\ TESCAN
Date(m/d/y): 08/19/14   Name: ALFIN_3D.jpg   Performance in nanospace

https://link.springer.com/article/10.1007/BF03356037

By the order of appearance:

SPONSORSHIP CATEGORY	COMPANY
CO-ORGANIZER	ELKEM AS (NO)
GOLDEN SPONSOR	COMET d.o.o., Novi Marof (HR)
	NETZSCH GmbH, Graz (AT) & ASOLUTIC d.o.o., Zagreb (HR)
	MIKROLUX d.o.o., Zaprešić (HR)
SILVER SPONSOR	ANALYSIS d.o.o., Beograd (RS)
	HAGI GmbH, Pyhra (AT)
	LABTIM ADRIA d.o.o., Sesvete (HR)
BRONZE SPONSOR	BENTOPRODUCT d.o.o., Šipovo (BiH)
	BITUS d.o.o., Zagreb (HR)
	EDC d.o.o., Zagreb (HR)
	EKW – KREMEN d.o.o., Šentjerej (SI)
	IDEF d.o.o., Zagreb (HR)
	INDUCTOTHERM EUROPE Ltd, Worcestershire (GB)
	ISTRABENZ PLINI d.o.o., Bakar (HR)
	KONTROLTEST INTERNATIONAL d.o.o., Zagreb (HR)
	MECAS ESI s.r.o., Plzen (CZ) & TC LIVARSTVO d.o.o., Ljubljana (SI)
	TOPOMATIKA d.o.o., Zagreb (HR)
	WERNER METAL – Export Import d.o.o., Zlatar Bistrica (HR)
MEDIA COVER	IRT 3000
	Foundry Lexicon
	Foundry Planet
SUPPORTING ASSOCIATION AND COMPANIES	Croatian Foundry Association, Zagreb (HR)
	Slovenian Foundry Association, Ljubljana (SI)
	Ferročrtalič d.o.o., Dolenjske Toplice (SI)

μikrolux
advantageous technologies consulting

general representative

TESCAN
PERFORMANCE IN NANOSPACE

16th INTERNATIONAL FOUNDRYMEN CONFERENCE

Opatija, May 15th-17th, 2017

It is our pleasure to invite you to come and visit us at the 16th International Foundrymen Conference in Opatija, Croatia

Check out for the latest news at our booth
TESCAN'S Triglav is one of them...

Triglav™
The new cutting-edge
UHR column technology

Key features
Triglav™ - newly designed UHR electron column

- TriLens™ objective system: unique combination of three-lens objective and crossover-free beam path
- Advanced detection system with multiple SE and BSE detectors
- TriSE™ and TriBE™

- Triglav™ - Ultimate ultra-high resolution at low beam energy: 1 nm at 1 keV and 0.7 nm at 15 keV
- EquiPower™ thermal power dissipation system for excellent electron column stability
- Electron beam currents up to 400 nA and rapid beam energy changes
- Optimised column geometry for accommodating large wafers up to 8"
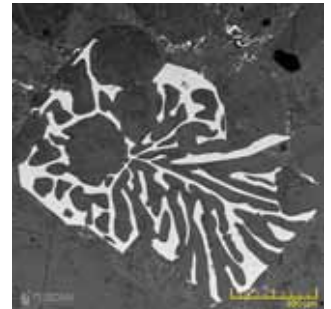
AlSi10 - Metallographic sample - etched

Ag crystals from electrolysis
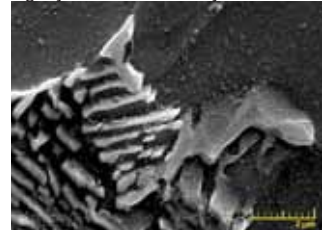
Pearlite structure in steel
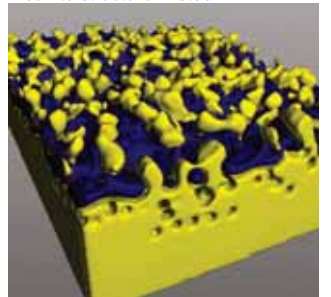
3D BSE reconstruction showing corrosion growing through Cr plating on steel

µikrolux

advantageous technologies consulting

representative

We will give you a better insight into the technological news
We are looking forward to Your visit!

OXFORD INSTRUMENTS

WDS - Wavelength Dispersive Spectroscopy - complements EDS by offering excellent peak separation, accurate trace element analysis, and optimised element detection for low and high energy X-rays to provide...
"Microprobe Accuracy on an SEM"

WDS provides the finest resolution of X-ray peaks

BRUKER

Spectroscopic phase analysis of a ternary alloy

Top: Element map of a ternary alloy with regions for phase map creation. Bottom: Phase map of the alloy

Pt-LA Al-KA Ru-LA

Quorum Technologies
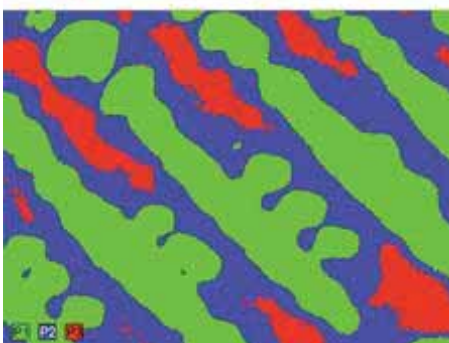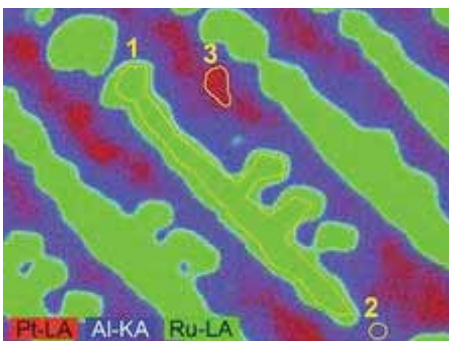
Q150T Turbo-Pumped Sputter Coater/Carbon Coater

The Q150T is available in three formats: sputtering, carbon evaporation or both. Depending upon the selected configuration, the Q150T can be a top-of-the-range sputter coater for high resolution scanning electron microscopy (SEM), a carbon coater suitable for SEM and transmission electron microscopy (TEM), or both - in a single easy-to-use system. Other options include metal evaporation and aperture

Lab tim laboratorijska oprema

Tinius Olsen
The First Name In Materials Testing

www.testingmetal.com

Applied Test Systems
http://www.atspa.com

BENTO PRODUCT

TRUE ALCHEMY

BENTOPRO-A

BENTOPROCARBO
BENTOPROCARBO-20 (BPC-20)
BENTOPROCARBO-25 (BPC-25)
BENTOPROCARBO-30 (BPC-30)
BENTOPROCARBO-35 (BPC-35)
BENTOPROCARBO-A (BPC-A)

BENTOPRO-A je alkalno aktivirani bentonit vrhunskog kvaliteta koji se koristi kao vezivo za pripremu pješčanih kalupa za livenje sivog i nodularnog liva, čelika i nekih obojenih metala.

BENTOPROCARBO je kompozitno vezivo proizvedeno iz mješavine alkalno aktiviranog bentonita i različitog sadržaja prirodnih, mineralnih nosilaca sjajnog ugljenika, u skladu sa zahtjevima kupca.

BENTOPRODUCT DOO je regionalni lider u proizvodnji različitih proizvoda na bazi visokokvalitetnog bentonita. Trenutno, godišnji nivo prodaje iznosi 25-30.000 tona gotovih proizvoda za različite namjene:

- BENTOPRO-A i BENTOPROCARBO, za primjenu u livarstvu
- BENTOPRODRILL, za primjenu u bušaćim radovima
- BENTOPROSEAL, za primjenu u građevinarstvu
- BP GROUND, ispune za poboljšanje elektrovodljivosti kod uzemljenja
- BP FARMA, za primjenu u poljoprivredi (aditivi za stočnu hranu i tretman zemljišta)
- BP CLARIS, za primjenu u prehrambenoj industriji (sredstva za bistrenje vina i voćnih sokova)

BENTOPRODUCT DOO svoje proizvode prodaje u više od 10 zemalja, a preko 70% na teritoriji EU. 50% livačkog programa prodaje se livnicama u sektoru automobilske industrije.

Poslujemo u skladu sa Integrisanim menadžment sistemom koji uključuje ISO 9001, ISO 14001 i OHSAS 18001, a za proizvode za prehrambenu industriju posjedujemo sertifikate HALAL i KOSHER.

Iplex FX
INDUSTRIJSKI VIDEOSKOP

Epoch 600
INDUSTRIJSKI ULTRAZVUČNI UREĐAJ

Now LabVIEW compatible

Induction　　Cuppola　　Rotary　　Channel Furnace

POZIVNICA

Firma Istrabenz plini d.o.o. (Hrvatska) i Ingas d.o.o. (Slovenija)
poziva Vas na naš izložbeni prostor
u sklopu 16. Međunarodne konferencije ljevača , koja će se održati u Opatiji
od 15. do 17. Svibnja 2017. u Grand hotelu Adriatic – Opatija.

Predstaviti ćemo:

a.　Mogućnost suradnje na području tehničkih plinova i UNP-a;
b.　Opremu za upotrebu tehničkih plinova i UNP-a;
c.　Mase za obzidavanje peći za lijevanje firme Insertec;
d.　Skladištenje, pneumatski transport i miješanje praškastih proizvoda i granulata
　　Firme NolTec Europe;
e.　Čišćenje dimnih plinova (SO2, SO3, Hg i NOx).

Čekamo Vas na našem izložbenom prostoru u Opatiji

Istrabenz Plini d.o.o. Bakar　　　　　　　　　Ingas d.o.o. Koper

ISTRABENZ PLINI　　　　　INGAS d.o.o.

SO2　SO3　NO2　Hg　HCl　CO2

trokuttest group

Croatia - Bosnia and Herzegovina - Bulgaria - Serbia
Slovenia - Macedonia - Montenegro - Albania
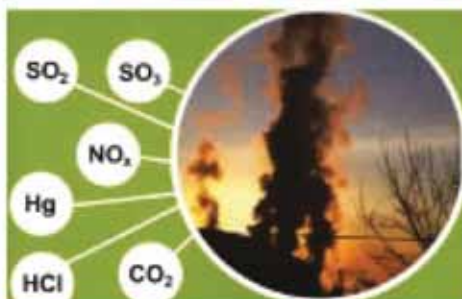
Optimal solutions for:

Non-Destructive Testing
Mechanical Testing
Laboratory Equipment
Predictive Maintenance
Heat Treatment

Qness

INSTRON

GNR ANALYTICAL INSTRUMENTS GROUP

proceq

metkon
Technology behind Systems

YXLON

SciAps

HELLING

- LIEVAONICA BUJAN d.o.o.
- E- ELMES d.o.o,Croatia
- STROJOLJEV ANTOLČIĆ,Croatia
- SVIM, Croatia

|	
Name of company	**WERNER METAL-EXPORT IMPORT d.o.o.**
Address of company	Stjepana Radića 3, HR-49247 Zlatar Bistrica, Republic of Croatia
Contacts	Phone: 00 385 (0)49 462 555 Fax: 00 385 (0)49 461 971 Mail: werner-metal@kr.t-com.hr
Web page	http://www.winko.com/p/werner-metal-export-import-d-o-o-0051311936
Materials of castings:	aluminum alloys, tin bronzes, aluminum bronzes
Capacity of production	150 tons per year
Production program	Foundry:rings , rotors, machine parts, motor parts,transformer parts and other different types of sand castings and gravity die castings according to customer's molds and desires Sales department : Distributor and representative for Croatia and Bosna and Hercegovina of: -MORGAN MOLTEN METAL SYSTEMS GmbH , Germany (crucibles and foundry equipment) -THERMAL CERAMICS (insulation materials) -MOLTEN METAL PRODUCTS, England (furnaces) Distributor of: Vesuvius GmbH,Germany (Foseco); Lanik,Czech Rep.,Lac Czech Rep.
Equipment in foundry	three oil furnaces , gravity die casting machine
Quality	ISO 9001 certificate in progress
References	- KONČAR MJERNI TRANSFORMATORI DD,Croatia - KONČAR- MES DD, Croatia - TELEGRA d.o.o., Croatia - DALEKOVOD – PROIZVODNJA d.o.o., Croatia - WML, Germany - SCHLOSSEREI KRUTISCH, Austria - SAINT JEAN INDUSTRIES d.o.o., Croatia - JEDINSTVO d.o.o., Croatia - STROJAR d.o.o., Croatia - HS PRODUKT d.o.o,Croatia - RS METALI d.o.o., Croatia - METAL PRODUCT d.o.o., Croatia - ALU Llevaonica umjetnina d.o.o., Croatia - LIEVAONICA UMJETNINA UJEVIĆ, Croatia - DUNI-Llevaonica obojenih metala, Croatia - DITRX D.O.O. , Bosna i Hercegovina

SUPPORTING ASSOCIATION AND COMPANIES

Croatian Foundry Association, Zagreb (HR)

Slovenian Foundry Association, Ljubljana (SI)
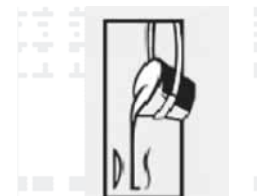
Ferro**Č**rtali**č** d.o.o., Dolenjske Toplice (SI)

MEDIA COVERAGE

IRT 3000

Foundry Lexicon

Foundry Planet